Exploring the Immune Response to the ChAdOx1 MERS Vaccine Candidate



A thesis submitted for the degree of

Doctor of Philosophy in Clinical Medicine

Sarah Batawi

Nuffield Department of Medicine

St Cross College

Hilary Term 2025

Professor Dame Sarah Gilbert

Professor Teresa Lambe OBE

Doctor Rachel Kenneil

Doctor Mustapha Bittaye

Word Counts

~ 50,000

Abstract

Fourteen years after its identification, Middle East respiratory syndrome coronavirus (MERS-CoV) continues to circulate with high case fatality and no licensed vaccines. Key challenges for advancing MERS vaccine development include understanding how different vaccination regimens shape humoral immunity, and elucidating how prior exposure to other coronaviruses influences these immune responses.

This thesis characterises the humoral immune response to the chimpanzee adenovirus Oxford 1 (ChAdOx1)–based MERS vaccine candidate, alongside supporting cellular responses, using clinical trial samples collected before and after the emergence of severe acute respiratory syndrome coronavirus 2 (SARS-CoV-2) to examine how exposure to other coronaviruses influences responses to ChAdOx1 MERS, alongside cross-sectional analyses of the relationship between ChAdOx1 MERS responses and immunity to other coronaviruses. In parallel, pre-clinical studies evaluate humoral and cellular immune responses across different vaccination strategies incorporating ChAdOx1 MERS and Modified Vaccinia Ankara–based MERS (MVA-MERS-S) vaccine candidates to inform optimal MERS vaccine regimens.

In the first half of the thesis, I evaluate data from pre- and post-pandemic trials. Different doses were evaluated in pre-pandemic trials in the UK and Saudi Arabia; higher doses induced stronger peak antibody titres, whereas medium doses sustained responses with a stepwise increase in avidity. Baseline immunity to seasonal coronaviruses influenced the magnitude and antigenic targeting of the IgG response. A post-pandemic trial in a predominantly older cohort revealed further evidence of imprinting, with hybrid immunity enhancing spike-specific responses and baseline SARS-CoV-2 immunity augmenting MERS vaccine immunogenicity. However, prior immunisation with ChAdOx1 nCoV-19 was associated with reduced transgene-specific responses to ChAdOx1 MERS, consistent with anti-vector immunity.

The second half of the thesis uses a design of experiments (DoE) approach to evaluate heterologous MERS vaccination strategies in preclinical models, using different combinations of MVA-MERS-S and ChAdOx1 MERS vaccine candidates. Modelling outputs indicated that an MVA-MERS-S prime/ChAdOx1 MERS boost enhanced immune responses compared to the opposite vaccination order. Booster dose was the strongest determinant of immunogenicity; prime dose and interval length shaped epitope specificity. DoE-guided optimisation identified dose–interval combinations suitable for rapid reactive vaccination, as well as longer-interval regimens for proactive immunisation.

Together, these studies advance understanding of MERS vaccine immunogenicity across preclinical and clinical settings, and provide insights that may inform continued clinical development of MERS-CoV vaccine candidates.

Acknowledgment

In the name of Allah, the Most Gracious and the Most Merciful. All praise and thanks are due to Him. To Him, al-Walī — the Guardian and Protector — who has watched over me throughout this journey. May He accept this work from me and continue to bless me with His guidance and mercy.

The Prophet, peace be upon him, said: “He who does not thank people has not truly thanked God” [Abu Dawood]. With this in mind, I am deeply grateful to everyone who helped me along the way.

My heartfelt thanks go to my supervisors, Sarah Gilbert, Teresa Lambe and Rachel Kenneil, whose mentorship, generosity, and belief in me have guided every step of this journey. Sarah, thank you for taking a chance on me, for giving your time so generously, and for providing opportunities that shaped my growth as a scientist. Working under your leadership during the pressures of the pandemic was inspiring in countless ways; your dedication, clarity of vision, and ability to think ahead have left a lasting impact on me. Teresa, your positivity and encouragement, and the way you approached study planning — always clear, thoughtful, and strategic — taught me how to think scientifically and plan effectively. Your guidance helped me navigate both scientific and personal challenges. Working under both of you during such an unprecedented time strengthened my resilience and deepened my commitment to science. Rachel, thank you for sharing your expertise and for your constant support throughout this project. Your kindness, creativity, and perfectly timed help made each day lighter. Thank you for being a friend, for reading my endless drafts, for helping me refine my ideas, and for gently pushing me forward. Your questions always made me think in new directions. I am deeply grateful for everything you have done.

To Mustafa, and Barbara, thank you for the warmth, support, and guidance you each brought to my journey. Mustafa, your discipline, precision, and careful approach to experiments shaped the way I think and work in the lab. Barbara, working with you was incredibly rewarding; your knowledge, positivity, and constant encouragement enriched my experience. I am deeply grateful for everything I learned from each of you.

Thank you to the members of the Gilbert Group for your constant support. Emilie, thank you for always having my back and keeping everything running smoothly. Marta and Roo, thank you for sharing your expertise in animal work and for your generous help. Nick and Sue, thank you for managing the lab and ensuring it functioned seamlessly. Sean, thank you for introducing me to public engagement and guiding me through it. Wendy, thank you for being Wendy — your presence, support, and kindness are truly irreplaceable. David, thank you for sharing your knowledge of DoE and for your helpful advice throughout.

To everyone in the Gilbert Group, OVG — especially Susanna, Sandra, Sagida, Audrey, Niesha, Allan, and Emma — and to those at the Jenner Institute, including Aadil, thank you for fostering such a supportive, collaborative, and kind environment. Your guidance, help in the lab, and daily encouragement made this journey much easier and far more enjoyable.

To my colleagues—Cameron, Jack, Alex, and Matej—thank you for your continued support and friendship. Cameron, thank you for the late nights in the lab, for always being generous with your knowledge, and for a friendship that felt more like having a brother by my side throughout this journey. Alex, thank you for guiding me through countless assays and for your patience and willingness to explain every detail so clearly. Jack, thank you for the humour, energy, and entertainment you brought to long experiments—you made even the hardest days lighter. Matej, thank you for your emotional support during difficult moments and tight deadlines; your presence truly made a difference. Working with you all was a joy, and I feel incredibly fortunate to have shared this journey with you.

To my family: thank you to my parents Mariam and Abdulhalim, my sister Ghadah, and my brothers for your endless love, prayers, and support, and to Sultan for always being there for me, even from afar. To my second family in Oxford— Stephany, Mona, Hira, Bica, Beatrice, Belquees, Mewa, Sophia, Taibah, and Omar — thank you for giving me a taste of home and filling my time here with laughter, unforgettable meals, and comforting companionship. And to Sheikh Tariq, Ibrahim, and Alhasan, thank you for keeping me grounded and on track.

My journey into this field began long before this thesis. I was working as medical intern during the 2014 MERS epidemic in Jeddah. Having the privilege to witness the first reported camel-to-human case was both unforgettable and deeply unsettling. At that time, there were moments of real uncertainty — no vaccine, no antiviral treatments. Experiencing the outbreak from the clinical side shaped my understanding of the urgency and vulnerability that accompany emerging diseases.

Years later, finding myself on the other side — contributing to vaccine development — felt profoundly meaningful. The contrast between these two experiences reinforced my belief in translational research and reminded me why this work matters.

To my country, Saudi Arabia, thank you for supporting and funding me through these years.

Contents

1 Introduction 24
1.1 Vaccines 24
1.2 Cellular immune response 24
1.3 Humoral immunity 26
1.3.1 Antibody structure and subclasses 26
1.3.2 Antibody effector function 28
1.3.3 Murine Immune Response 31
1.3.4 Correlates of protection and vaccine licenses 33
1.3.1 Adenoviral Vectors 35
1.3.2 ChAdOx1 platform 36
1.3.3 Modified vaccinia Ankara (MVA) Vectors 37
1.4 Overview of coronavirus and emerging threats 38
1.4.1 Virology of coronaviruses 39
1.4.2 Seasonal human coronaviruses 39
1.4.3 Zoonotic coronaviruses with epidemic and pandemic potential 39
1.4.4 Spike protein as a coronavirus vaccine target 41
1.5 Immune imprinting and cross-coronavirus immunity 43
1.5.1 Humoral immunity 45
1.5.2 Cellular immunity 46
1.6 SARS-CoV-2 and Variants of Concern (VOCs) 46
1.7 Middle East Respiratory Syndrome Coronavirus (MERS-CoV) 47
1.7.1 Epidemiology 47
1.7.2 Clinical picture 51
1.7.3 Virology, clades and genetic stability 52
1.7.4 Immune pathogenesis 56
1.7.5 MERS protective immunity 59
1.7.6 MERS-CoV in the Context of Human Coronaviruses 59
1.8 MERS-CoV Vaccine 61
1.8.1 ChAdOx1 MERS vaccine candidate 62
1.8.2 MVA-MERS 64
1.9 Aim and objectives of the Present Study 65
2 Study Design and Experimental Methods 67
2.1 Reagents and solutions 67
2.2 Clinical trials and human samples 74
2.2.1 MERS001 (First-in-Human Trial, United Kingdom) 76
2.2.2 MERS002 (Kingdom of Saudi Arabia) 76
2.2.3 MERS003 (Older adults, United Kingdome) 77
2.2.4 MERS-CoV Convalescent Cohort (Pre-pandemic) 78
2.2.5 Convalescent MERS-CoV Cohort with COVID-19 vaccination (Hybrid MERS/SARS-CoV-2 immunity) 78
2.2.6 Hybrid SARS-CoV-2/SARS-CoV-2 and SARS-CoV-2 vaccine immunity 79
2.2.7 Pre-pandemic negative controls 80

2.3 Immunization, Sample Collection and Processing 80
2.3.1 Serum and plasma preparation 80
2.3.2 PBMC isolation and storage 81
2.4 Animal model 81
2.4.1 Pre-clinical Experimental overview 81
2.4.2 Experimental Plan for MERS-IDT001 and MERS-IDT002 81
2.4.3 Immunization, Sample Collection and Processing 83
2.5 Vaccines 84
2.5.1 ChAdOx1-MERS 84
2.5.2 Clinical batch production 84
2.5.3 Preclinical Batch Production 84
2.5.4 MVA-MERS-S 85
2.5.5 ChAdOx1-SEAP Virus 85
2.5.6 Negative control vaccines for pre-clinical studies 86
2.6 Experimental Methods 86
2.6.1 Cell Culture and maintenance 86
2.6.2 Immunological assays 87
2.6.2.1.1.1.5 Avidity indirect ELISA 93
2.6.2.2.2.2 B-cell ELISPOT 103
2.6.3 Application to the MERS-DoE Study 104
2.7 Statistical Analysis 104
3 Exploratory Analysis of Humoral and Cellular Responses to the ChAdOx1 MERS-CoV Vaccine Candidate 106
3.1 Introduction 107
3.2 Results 108
3.2.1 Overview of study design and immunogenicity analyses 108
3.2.2 Immunogenicity of ChAdOx1 MERS after a single dose 109
3.2.3 Induction and durability of humoral antibody responses 126
3.2.4 Immunogenicity of prime-boost vaccination 132
3.2.5 Pre-existing coronavirus immunity and cross-reactive response 139
3.2.6 Comparison of breadth responses and durability between populations 146
3.2.7 T cell responses 155
3.3 Discussion 162
4 Immune imprinting and Its Impact on Coronavirus vaccination 167
4.1 Introduction 168
4.2 Results 169
4.2.1 Hybrid Immunity and Cross-Reactivity Following SARS-CoV-2 Vaccination 169
4.2.2 Post-Pandemic Immunogenicity of ChAdOx1 MERS Vaccination in Older Adults (MERS003 Trial) 206
4.3 Discussion 223
5 Heterologous Prime-Boost Vaccination with ChAdOx1 and MVA-Based MERS-CoV Vaccines in Mice 232

5.1 Introduction 232
5.2 Results 233
5.2.1 Study design and immunization regimens 233
5.2.2 Binding and functional antibody responses 234
5.2.2.1 Binding and neutralising antibodies against full MERS-CoV spike 234
5.2.3 Cellular responses 249
5.2.3.1 ASC in the spleen and Bone Marrow. 249
5.2.4 Determinants of Immune Response 258
5.2.4.4 Antibody pre-boosting modulates post-boost responses. 267
5.3 Discussion 270
6 Design of Experiments (DoE) for Optimising MERS-CoV heterologous Prime-Boost Vaccination in Mouse Model 273
6.1 Introduction 273
6.2 Methods 276
6.2.1 Selection process 277
6.2.2 Treatment generation 278
6.2.3 Experimental data and processing 280
6.2.4 Data analysis and model evaluation 284
6.2.5 Model validation 284
6.3 Results 284
6.1.2 Descriptive summary 284
6.3.2 Statistical models 296
6.3.3 Regimen optimisation 319
6.4 Discussion 326
7 Discussion 330
7.1 Future Work 336
8 Appendix 340
8.1 Publications and presentations as DPhil student 340
8.1.1 Publications / Commentaries 340
8.1.2 Oral presentation 340
8.1.3 Academic service 340
8.1.4 Supplementary 341
9 References 368

List of figures

Figure 1-1. Antibody Structure, Isotypes And Subclasses. 27
Figure 1-2. Fc receptor–mediated immune responses to viral infection. 31
Figure 1-3. Classical adenoviral entry pathway. 36
Figure 1-4. Phylogenetic tree of representative coronaviruses based on complete genome nucleotide sequences 38
Figure 1-5. Schematic structure of the process of mers-cov attachment, fusion and entry to the host cell expressing the dipeptidyl peptidase-4 (DPP4) receptor. 42
Figure 1-6. Beneficial and detrimental cross-reactive immune responses during heterologous secondary infection. 44
Figure 1-7. Zoonotic mode of transmission of MERS-CoV. 48
Figure 1-8. MERS epidemic curve. 49
Figure 1-9. Structural organisation of MERS-CoV. 53
Figure 1-10. MERS-CoV clades and phylogenetic relationships. 54
Figure 1-11. Selected amino-acid substitutions in the MERS-CoV spike protein 56
Figure 1-12. MERS-CoV replication. 57
Figure 1-13. Peptide-level similarity analysis of the MERS-CoV spike protein across human coronaviruses. 60
Figure 2-1. Overview of ChAdOx1 MERS clinical trials and serology assays 75
Figure 3-1. Visual abstract of the study methods and results. 106
Figure 3-2. MERS-CoV spike-specific IgM responses induced by ChAdOx1 MERS vaccination. 110
Figure 3-3. MERS-CoV spike–specific IgA responses after ChAdOx1 MERS Vaccination. 112
Figure 3-4. MERS-CoV spike-specific igg responses following ChAdOx1 MERS vaccination. 115
Figure 3-5. MERS spike-specific igg subclass responses induced by ChAdOx1 MERS vaccination. 116
Figure 3-6. Correlation of total IgG with IgG subclasses and group-specific subclass responses following ChAdOx1 MERS vaccination. 118
Figure 3-7. MERS-CoV spike-subunit specific IgG antibody responses following ChAdOx1 MERS vaccination. 119
Figure 3-8. Anti-MERS-CoV spike IgG avidity index following ChAdOx1 MERS vaccination. 121
Figure 3-9. Fcγr-binding antibody responses following ChAdOx1 MERS vaccination. 122
Figure 3-10. Fcγr-binding antibody responses following ChAdOx1 MERS vaccination, pooled by regimen. 123
Figure 3-11. Longitudinal Fcγr-binding antibody responses following ChAdOx1 MERS vaccination, pooled by regimen. 124
Figure 3-12. Correlation matrix of Fcγr-binding and IgG responses at peak (Day 28) following ChAdOx1 MERS vaccination. 126
Figure 3-13. Induction and maintenance of humoral antibody responses. 128
Figure 3-14. Decay kinetics of antibody isotypes and Fcγ receptor–binding activities over time. 130
Figure 3-15. Comparison of short and long antibody half-lives across isotypes and Fcγ receptor–binding responses. 132
Figure 3-16. Antibody dynamics following short- and long-interval boosting compared with convalescent Responses. 133
Figure 3-17. Fcγr-binding antibody responses following booster vaccination at short and long intervals compared with convalescent responses. 134
Figure 3-18. Antibody subclass and Fcγ receptor–binding responses following short- and long-interval boosting compared with single-dose vaccination and convalescent sera. 136
Figure 3-19. Antibody subclass and Fcγr-binding and profiles following short- and long-interval boosting compared with convalescent sera. 137
Figure 3-20. Antigen-specific IFN-γ ELISPOT responses following prime and prime–boost vaccination. 138
Figure 3-21 Cross-reactive antibody and fcγ receptor–binding responses to seasonal human coronaviruses following ChAdOx1 MERS vaccination . 140
Figure 3-22. Cross-reactive humoral (IgG) And Fcγr-binding responses to SARS-CoV-2 induced by ChAdOx1 MERS vaccination. 141
Figure 3-23. Spearman correlation matrices of MERS-CoV spike–specific antibody responses and baseline seasonal coronavirus immunity. 142
Figure 3-24. Spearman correlation matrices of MERS-CoV spike–specific antibody responses and seasonal *betacoronavirus* back-boosting. 143

Figure 3-25. Humoral immune responses in low and high responders. 145
Figure 3-26. Stepwise regression analysis identifying baseline predictors of vaccine-induced humoral responses. 146
Figure 3-27. Comparison of antibody half-lives between MERS001 and MERS002 studies. 148
Figure 3-28. Induction and durability of humoral antibody responses in MERS001 and MERS002 participants. 149
figure 3-29. durability of humoral antibody responses in MERS001 and MERS002 participants. 150
Figure 3-30. Baseline and longitudinal seasonal coronavirus antibody responses in uk (MERS001) and ksa (MERS002) cohorts. 152
Figure 3-31. Stepwise regression analysis identifying predictors of vaccine-induced S2-specific antibody fold changes. 153
Figure 3-32. Stepwise regression analysis identifying baseline predictors of vaccine-induced iga responses. 154
figure 3-33. Flow cytometric analysis of vaccine-induced activation of $CD8^+$ and $CD4^+$ t cells following ChAdOx1 MERS vaccination. 156
Figure 3-34. assessment of spike-specific $CD4^+$ and $CD8^+$ t cell responses following ChAdOx1 vaccination. 157
Figure 3-35. Intracellular cytokine profile of spike-specific $CD4^+$ and $CD8^+$ t cells following ChAdOx1 MERS vaccination. 158
Figure 3-36. Mapping of $CD8^+$ and $CD4^+$ t cell responses across mers spike peptide minipools in MERS001 participants. 159
Figure 3-37. T cell responses to MERS-CoV and cross-reactivity with other coronaviruses. 161
Figure 4-1 Visual abstract of the study methods and results 167
Figure 4-2. Study design overview. 170
Figure 4-3. Baseline characteristics of the hybrid MERS-CoV immunity cohort and comparison groups. 172
Figure 4-4. Distribution of sample collection dates by immune status group 174
Figure 4-5. Fcγ receptor binding responses to the nucleocapsid protein. 176
Figure 4-6. Binding IgG and neutralisation responses to the SARS-CoV-2 spike protein and its subunits. 177
Figure 4-7. Fcγr binding antibodies titres against SARS-CoV-2 spike, S1 and S2 across fcγr subclasses. 179
Figure 4-8. Fcγ receptor binding responses to the omicron variant protein. 181
Figure 4-9. Spearman correlation between Fcγ receptor (Fcγr) binding to the omicron spike and days after omicron emergence in the hybrid mers-cov/sars-cov-2 group. 182
Figure 4-10. Summary of anti–SARS-CoV-2 humoral immune responses across immune groups. 183
Figure 4-11. Lasso feature selection for antibody responses. 184
Figure 4-12. Multivariate discrimination of hybrid immunity groups using PLS-DA. 185
Figure 4-13 Correlation matrix of humoral immune responses. 187
Figure 4-14. SARS-CoV-2 antibody responses in individuals with hybrid mers immunity. 188
Figure 4-15. SARS-CoV-2 antibody responses in individuals with hybrid SARS-CoV-2/SARS-CoV-2 immunity and vaccine-only immunity. 190
Figure 4-16. Breadth of Fcγr-binding responses to seasonal coronaviruses. 193
Figure 4-17.IgG binding and neutralisation responses to the mers-cov spike protein and its subunits. 195
Figure 4-18. Fcγr-Binding antibody titres against MERS spike, S1, and S2 across Fcγr subclasses. 197
Figure 4-19. Lasso feature selection for antibody responses. 198
Figure 4-20 Correlation matrix of humoral immune responses in hybrid immunity group. 199
Figure 4-21. SARS-CoV-2 antibody responses in individuals with hybrid mers immunity. 200
Figure 4-22. Comparison of anti–MERS-CoV and anti–SARS-CoV-2 spike-specific antibody responses within the hybrid mers immunity group. 201
Figure 4-23. Cross-reactive anti-MERS fc responses in hybrid SARS-CoV-2–immune individuals. 203
Figure 4-24. Correlation of Fcγr-binding antibody responses to MERS-CoV and SARS-CoV-2 spike and subunit antigens following SARS-CoV-2 hybrid or vaccine-induced immunity. 204
Figure 4-25. Participant distribution and stratification in the MERS003 clinical trial. 206
Figure 4-26. Baseline MERS-CoV and SARS-CoV-2 antibody responses in pre- and post-pandemic participants. 208
Figure 4-27. Baseline correlation between MERS-CoV and SARS-CoV-2 antibody responses in post-pandemic participants. 209

Figure 4-28. Kinetics of anti-MERS spike IgG and pseudoneutralisation antibody (PNA) responses following ChAdOx1 MERS vaccination in ChAdOx1-experienced and ChAdOx1-naïve participants. 211
Figure 4-29. Anti–MERS -CoV spike igg and pseudoneutralisation antibody (PNA) responses following chadox1 mers vaccination compared with negative controls in chadox1-experienced and chadox1-naïve. 211
Figure 4-30. Comparison of anti–MERS-CoV spike igg and pseudoneutralisation antibody (PNA) responses between ChAdOx1-naïve and ChAdOx1-experienced participants following chadox1 mers vaccination. 213
Figure 4-31. Antibody decay kinetics and half-life following ChAdOx1MERS vaccination. 214
Figure 4-32. Spearman correlation between binding IgG and neutralising antibody (PNA) responses to MERS-CoV 214
Figure 4-33 ChAdOx1 anti-vector neutralising antibodies following vaccination. 215
Figure 4-34. Spearman correlation between anti-vector immunity and mers-specific antibody responses. 217
Figure 4-35 Baseline and post-vaccination SARS-CoV-2 antibody responses following ChAdOx1MERS vaccination. 218
Figure 4-36. Anti-MERS spike antibody responses following primary and booster vaccination. 222
Figure 5-1. Study design of mouse vaccination experiments. 234
Figure 5-2. Binding IgG and neutralising responses to MERS-CoV spike protein. 236
Figure 5-3. Binding IgG to MERS-CoV spike protein subunits. 239
Figure 5-4. Binding IgA and IgM responses to MERS-CoV spike protein. 241
Figure 5-5. MERS-CoV spike-specific IgG subclasses. 243
Figure 5-6. IgG Avidity following homologous and heterologous vaccination. 245
Figure 5-7. Fc receptor (Fcr) binding for MERS-CoV . 247
Figure 5-8. Overview of vaccine-induced Fcγ receptor binding profiles and functional correlations. 248
Figure 5-9. Antibody-secreting cell (ASC) responses in spleen and bone marrow. 251
Figure 5-10. Correlations between serum antibody titres and asc responses in spleen and bone marrow. 252
Figure 5-11. IFNγ ELISPOT responses to MERS-CoV spike. 254
Figure 5-12. Flow cytometric analysis of $CD8^+$ and $CD4^+$ t-cell cytokine responses. 256
Figure 5-13. Fcγ Receptor (Fcγr) binding responses following homologous MVA/MVA vaccination at low or high dose. 259
Figure 5-14. Humoral responses following homologous and heterologous prime–boost vaccination. 261
Figure 5-15. Fcγ Receptor (Fcγr) binding responses following homologous and heterologous prime–boost vaccination. 263
Figure 5-16. Antibody-secreting cell (ASC) and T cell responses following homologous and heterologous prime–boost vaccination. 264
Figure 5-17. Paired analysis of humoral responses following heterologous Ad/MVA and MVA/Ad boosting. 266
Figure 5-18. Humoral response profiling following heterologous Ad/MVAand MVA/Ad boosting. 267
Figure 5-19. Baseline antibody responses prior to heterologous boosting. 268
Figure 5-20. Pearson correlation analyses between pre- and post-boost antibody responses. 269
Figure 5-21. Principal component analysis (PCA) of baseline serology with outcomes projected as supplementary variables. 270
Figure 6-1. Visual abstract of the study methods and results 273
Figure 6-2. Determinants of secondary b cell response 275
Figure 6-3. DoE workflow applied in this study. 277
Figure 6-4 Experimental design and timeline. 281
Figure 6-5. Humoral immune responses induced by heterologous vaccination. 285
Figure 6-6. Splenic cell viability measured by flow cytometry differed significantly across groups 286
Figure 6-7. Correlations between spike-specific IgG ASC frequencies and serum antibody responses. 287
Figure 6-8. Antibody-secreting cell (ASC) responses following heterologous vaccination. 288
Figure 6-9. Correlation of serum antibody titres with asc frequencies in spleen and bone marrow. 289
Figure 6-10. Comparison of cell counting methods for T cell ELISPOT. 290
Figure 6-11. IFN-γ responses measured by elispot and intracellular cytokine staining. 291
Figure 6-12. Spike-specific humoral and T-cell memory after heterologous vaccination. 293
Figure 6-13. Correlation between pre-boosting igg titres and post-boost igg responses (pearson correlation). 295

Figure 6-14. Correlation of pre-boost IgG titres with post-boost humoral and cellular immune readouts. 296
Figure 6-15. Primary humoral outcomes for the MVA-prime,ChAdOx1-boost regimen. 297
Figure 6-16. Model Fitting results for the humoral composite outcome in the MVA/Ad regimen. 299
Figure 6-17. Model fitting results for IgG ASC responses in spleen and bone marrow for the MVA/Ad regimen. 301
Figure 6-18. Primary humoral outcomes for the Ad-prime, MVA-boost regimen. 302
Figure 6-19. Model fitting results for the humoral composite outcome in the Ad/MVA regimen. 304
Figure 6-20. Model fitting results for IgG ASC responses in spleen and bone marrow for the Ad/MVA regimen. 305
Figure 6-21. Primary cellular outcomes for the MVA-prime,ChAdOx1-boost regimen. 306
Figure 6-22. Model fitting results for the primary cellular composite outcome in the MVA/Ad regimen. 308
Figure 6-23. Prediction profiler for the primary cellular composite (spleen) in the MVA/Ad regimen at 4 weeks. 309
Figure 6-24. Secondary cellular outcomes for the MVA/Ad regimen. 309
Figure 6-25. Model fitting results for immunodominant, S1, and S2 epitopes in the MVA/Ad regimen. 310
Figure 6-26. Primary cellular outcomes for the Ad/MVA regimen. 312
Figure 6-27. Model fitting results for the primary cellular composite outcome in the Ad/MVA regimen. 313
Figure 6-28. Secondary cellular outcomes for the Ad/MVA regimen. 314
Figure 6-29. Model fitting results for immunodominant, S1, and S2 epitopes in the Ad/MVA regimen. 315
Figure 6-30. Memory outcomes for MVA/Ad and Ad/MVA regimens. 316
Figure 6-31. Model fitting results for the memory composite outcome in the MVA/Ad regimen. 318
Figure 6-32. Model fitting results for the memory composite outcome in the Ad/MVA regimen. 319
Figure 6-33. Model fitting results for composite immune responses in the MVA/Ad regimen. 320
Figure 6-34. Model fitting results for composite immune responses in the Ad/MVA regimen. 321
Figure 6-35. Optimized heterologous prime–boost vaccination regimens. 323

List of Tables

Table 1-1. Summary of major human immunoglobulin isotypes and subclasses. 28
Table 1-2. Summary of human Fcγ receptor characteristics. 30
Table 1-3. Summary of major mice immunoglobulin isotypes and subclasses. 33
Table 1-4. Summary of mouse Fcγ receptor characteristics. 33
Table 1-5. Genus, subgenus, known non-human hosts, and cellular receptors of representative human and zoonotic coronaviruses. 42
Table 1-6. Sequence similarity between the MERS-CoV spike protein and other human coronaviruses. 61
Table 1-7. MERS-CoV vaccine candidates across major vaccine platforms. 62
Table 2-1. Commercially available reagents and materials used in this study 67
Table 2-2. Buffers and media prepared in this study 70
Table 2-3. Antibody panel used for the AIM multiparametric flow cytometry 72
Table 2-4. Antibodies used for ICS staining 72
Table 2-5. Antibodies used for AIM sorting 72
Table 2-6. Antibodies used for flow cytometry (T-cell cytokine panel) 73
Table 2-7. Summary of clinical and observational study cohorts included in this study. 74
Table 2-8. Vaccination regimens and sample collection timeline. 82
Table 2-9. Origin, culture medium, and application of cell lines used in this study. 87
Table 2-10. Immunological assays and analytical parameters across human and pre-clinical studies. 89
Table 2-12. Plasmids used for pseudovirus production and receptor expression. 96
Table 3-1. Comparison of vaccine-induced antibody responses between UK (MERS001) and KSA (MERS002) cohorts... 147
Table 4-1 Baseline demographics and clinical characteristics of study participants. 173
Table 4-2. Median anti-nucleocapsid FcγR binding responses. 175
Table 4-3. Median IgG binding to SARS-CoV-2 spike (S), S1, and S2 proteins, and pseudovirus neutralisation assay (PNA) titres. 177
Table 4-4. Median FcγRI responses to MERS-CoV spike, S1, and S2 proteins. 179
Table 4-5. Median Omicron FcγR binding responses. 181
Table 4-6. Median IgG binding to MERS spike (S), S1, and S2 proteins, and pseudovirus neutralisation assay (PNA) titres. 194
Table 4-7. Median FcγRI responses to MERS-CoV spike, S1, and S2 proteins. 198
Table 4-8. Median FcγR responses to MERS-CoV spike, S1, and S2 proteins 202
Table 4-9. Characteristics of trial volunteers. 207
Table 4-10. Median (IQR) antibody responses between groups at each time point. 212
Table 4-11. Spearman correlation between anti-ChAdOx1 neutralising antibody titers and MERS-specific IgG or PNA responses. 217
Table 4-12. Spearman correlation between anti–SARS-CoV-2 and MERS-specific IgG or PNA responses. 220
Table 5-1. Median IgG binding and neutralising antibody titres. 234
Table 5-2. Median IgG binding responses to S1 and S2 subunit proteins. 237
Table 5-3. Median IgM and IgA binding responses to MERS-CoV spike protein. 240
Table 5-4. Median IgG subclass responses to MERS-CoV spike protein. 242
Table 5-5. Median IgG avidity index to MERS-CoV spike protein. 244
Table 5-6. Median FcγRI responses to MERS-CoV spike, S1, and S2 proteins. 246
Table 5-7. Median ASC IgG responses to MERS-CoV spike protein before and after expansion in spleen and bone marrow (BM). 249
Table 5-8. Median IFN-γ producing spots by ELISpot in response to the immunodominant epitope in spleen. 253
Table 5-9. Median ICS responses to the immunodominant epitope in spleen. 255
Table 5-10. Median FcγRI responses to MERS-CoV spike, S1, and S2 proteins in low and high dose MVA. 259
Table 6-1. D-optimal design showing treatment combinations of MVA and ChAdOx1 with corresponding doses and vaccination intervals. MVA doses are expressed in plaque-forming units (PFU/mL), ChAdOx1 doses in international units (IU/mL), and intervals in weeks. The table includes 14 treatment regimens, each referencing specific dosing and scheduling conditions. Central points are highlighted in bold. 278
Table 6-2. Full experimental design. 280
Table 6-3. Overview of immunological assays performed in this study. 282
Table 6-4. Summary of immunological outcomes used in DoE modelling. 283
Table 6-5. Model fitting results for primary humoral outcomes in the MVA/Ad regimen. 298
Table 6-6. Model fitting results for secondary humoral outcomes in the MVA/Ad regimen. 300
Table 6-7. Model fitting results for primary humoral outcomes in the Ad/MVA regimen. 303
Table 6-8. Model fitting results for secondary humoral outcomes in the Ad/MVA regimen. 305
Table 6-9. Model fitting results for primary cellular effector outcomes in the MVA/Ad regimen. 307
Table 6-10. Model fitting results for secondary cellular effector outcomes in the in the MVA/Ad regimen. 310
Table 6-11. Model fitting results for primary cellular effector outcomes in the Ad/MVA regimen.. 312
Table 6-12. Model fitting results for secondary cellular effector outcomes in the Ad/MVA regimen. 314

Table 6-13. Model fitting results for memory outcomes in the MVA/Ad regimen. 317
Table 6-14. Model fitting results for memory outcomes in the Ad/MVA regimen. 318
Table 6-15. Summary of the composite immunological outcome in the combined predictive model 319
Table 6-16. Validation of model predictions against independent datasets of individual model. 325

Supplementary Material

Table S1. WHO reference materials used in this study. WHO reference samples were used as standardized positive and negative controls for evaluation of the PNA and Fcγ receptor binding assays. 341
Table S2. Samples used for assay optimisation 342
Figure S1. Dynamic range across assay conditions comparing Oxford and NIBSC methods 343
Table S3. Summary comparison of Oxford and NIBSC assay workflows. 343
Figure S2. Comparison of heat-inactivated serum (HIS) and heat-inactivated plasma (HIP) performance in the pseudoneutralisation assay (PNA) 344
Figure S3. Internal control performance and variability across assay plates. 345
Table S4. Qulification parameters, assessment approach, and acceptance criteria 345
Table S5. Binding and neutralising antibodies measurements for cross-reactive seasonal coronavirus 346
Table S6. MERS-CoV isolates used for testing MERS PNA assay sensitivity 347
Figure S4. Neutralisation of MERS pseudovirus by a spike-specific monoclonal antibody. 347
Table S7. Curve fit assessment comparing starting dilution points 347
Table S8. Summary of assay precision across diffrent levels. 348
Table S9. Accuracy assessment by recovery experiments using spiked samples. 348
Figure S5. Effect of repeated sample freeze–thaw cycles on assay readouts. 349
Figure S6. Standard curves and quantification limits for Fcγ receptor assays. 350
Figure S7. Fcγ receptor binding to MERS antigens measured by Luminex. 350
Figure S8. Fcγ receptor binding to MERS antigens measured by Luminex. 351
Figure S9. Fcγ receptor binding to endemic human coronavirus spike proteins measured by Luminex. 352
Table S10. Intra-assay precision of Fcγ receptor binding assays. 352
Table S11. Clinical and vaccination data of individuals with prior MERS infection and COVID-19 vaccination (hybrid MERS immunity) based on the presence of positive MERS PCR in sputum. 359
Table S12. Clinical and vaccination data of individuals with prior SARS-CoV-2 infection and COVID-19 vaccination (hybrid SARS-CoV2 infection) based on the presence of anti-N antibodies at the time of vaccination. 360
Table S13. Clinical and vaccination data of individuals with negative SARS-CoV-2 infection and COVID-19 vaccination (vaccine immunity) based on the absence of anti-N antibodies 361
Figure S10. Humoral and cellular immune responses following single-dose MVA-MERS vaccination 362
Figure S11. Gating strategy to identify MERS-specific T cells in mouse splenocytes. 363
Figure S12. Gating strategy to identify MERS immunodominant peptide–specific effector and central memory T cells in mouse splenocytes 364
Table S14. Summary of primary immunological outcomes for MVA-prime/ChAdOx1-boost regimens. 365
Table S15. Summary of humoral and cellular outcomes for the Ad/MVA regimen. 366
Table S16. Prediction based on composite model outcomes 367

List of abbreviations

6-HB	6-helix bundle
ACE2	angiotensin-converting enzyme 2
ACK	Ammonium–Chloride–Potassium
ADCC	antibody-dependent cellular cytotoxicity
ADCD	antibody-dependent complement deposition
ADCP	antibody-dependent cellular phagocytosis
ADE	antibody-dependent enhancement
ADNP	antibody-dependent neutrophil phagocytosis
AF	Alexa Fluor
AI	avidity index
AID	activation-induced cytidine deaminase
AIM	activation-induced markers
ALP	alkaline phosphatase
AWERB	Animal Welfare and Ethical Review Board
APC	antigen-presenting cell
ARDS	acute respiratory distress syndrome
ASC	antibody-secreting cell
AU	absorbance-equivalent arbitrary units
BAC	bacterial artificial chromosome
BAL	bronchoalveolar lavage
BCR	B cell receptor
BM	bone marrow
BSA	bovine serum albumin
BSL	biosafety level
BUV	brilliant ultraviolet
BV	brilliant violet
CAR	coxsackievirus–adenovirus receptor
CD	cluster of differentiation
CDC	Centers for Disease Control
CDR	complementarity-determining regions
CEF	chicken embryo fibroblast cells
CEPI	Coalition for Epidemic Preparedness Innovations
cGMP	current Good Manufacturing Practice
CMV	cytomegalovirus

ChAd	Chimpanzee adenovirus
ChAdOx1	Chimpanzee adenovirus Oxford 1 recombinant vector
CHIM	Controlled human infection models
Conv	Convalescent
CoV	CoV coronavirus
COVID-19	coronavirus disease 2019
CP	cytoplasmic tail
CsCl	caesium chloride
CSR	class-switch recombination
ChAd	chimpanzee adenovirus
CTD	C-terminal domain
CTL	cytotoxic T lymphocyte
CVA	Chorioallantois vaccinia virus Ankara
CVST	cerebral venous sinus thrombosis
CVT	cerebral venous thrombosis
CXCR	CXC-chemokine receptor
DAPI	4',6-diamidino-2-phenylindole
DC	dendritic cell
DF-1	Douglas–Foster 1 (chicken embryo fibroblast cell line)
DMEM	Dulbecco's modified eagle medium
DMSO	dimethyl sulfoxide
DoE	Design of Experiments
DPBS	Dulbecco's phosphate buffered saline
DPP4	dipeptidyl peptidase 4
DVT	deep vein thrombosis
E	envelope
ECL	electrochemiluminescence
ELISA	enzyme-linked immunosorbent assay
ELISpot	enzyme-linked immunospot assay
EU	Elisa unit
EUA	emergency use authorisation
Fab	fragment antigen binding
FACS	fluorescence-activated cell sorting
FBS	foetal bovine serum
Fc	fragment crystallisable

FcR	Fc receptor
FDA	Food and Drug Administration
FITC	FITC fluorescein isothiocyanate
FOXP3	forkhead box protein 3
FP	fusion peptide
GC	germinal centre
GM-CSF	granulocyte-macrophage colony-stimulating factor
HAd	human adenovirus
HCoVs	human seasonal coronaviruses
HE	haemagglutinin-esterase
HIP	heat-inactivated plasma
HIS	heat-inactivated serum
HLA	human leukocyte antigen
HR	heptad repeat
IC	internal control
IC50	half-maximal inhibitory concentration
ICH	intracerebral haemorrhage
ICS	intracellular cytokine staining
IFN	interferon
IFN-γ ELISpot	interferon-γ enzyme-linked immunospot assays
Ig	immunoglobulin
IHC	immunohistochemistry
IL	interleukin
IM	intramuscular
IN	intranasal
IQR	interquartile range
IRS	International Reference standard
ITAMs	immunoreceptor tyrosine-based activation motifs
ITIMs	immunoreceptor tyrosine-based inhibitory motifs
IU	infectious units
IVCs	individually ventilated cages
KNIH	Korea National Institute of Health
LASSO	least absolute shrinkage and selection operator
LB	Luria–Bertani
LCMV	lymphocytic choriomeningitis virus

LLD	lower limit of detection
LLPC	long-lived plasma cell
LOD	limit of detection
M	membrane
mAb	monoclonal antibody
MHRA	Medicines and Healthcare products Regulatory Agency
MERS	Middle East Respiratory Syndrome
MERS-CoV	Middle East Respiratory Syndrome coronavirus
MERSr-CoVs	MERS-related coronaviruses
MFI	Median fluorescence intensity
MHC	major histocompatibility complex
MSD	Meso Scale Discovery
MV	measles virus
MVA	modified vaccinia virus Ankara
N	nucleocapsid
nAb	neutralising antibodies
NETosis	neutrophil extracellular traps
NHP	non-human primate
NIAID	National Institute of Allergy and Infectious Disease
NIBSC	National Institute for Biological Standards and Control
NIH	National Institutes of Health
NIHR	National Institute for Health and Care Research
NK	natural killer
NP	nucleoprotein
NTD	N-terminal domain
NGS	next-generation sequencing
OD	optical density
ORF	open reading frame
OVC	Oxford Vaccine Centre
Oxford BRC	Oxford Biomedical Research Centre
OxTREC	Oxford Tropical Research Ethics Committee
PAMP	pathogen-associated molecular patterns
PBMC	peripheral blood mononuclear cell
PB	Prime boost
PBS	phosphate buffered saline

PCA	principal component analysis
PerCP	peridinin-chlorophyll-protein
PE	phycoerythrin
PF4	platelet factor 4
PFA	paraformaldehyde
PFU	plaque forming units
PIgR	polymeric immunoglobulin receptor
PLS-DA	partial least squares discriminant analysis
P:I ratio	particle-to-infectious unit
PITCH	Protective Immunity through T Cells in Healthcare workers
PMA	phorbol myristate acetate
PNA	pseudovirus neutralisation assay
pNPP	p-nitrophenyl phosphate
PRR	pattern-recognition receptors
PV	pseudovirus
QP	Qualified Person
R_0	basic reproduction number
RABV	rabies virus
RBC	red blood cell
RBD	receptor binding domain
RBM	receptor binding motif
REC	Research Ethics Committee
RLU	relative light unit
RMSE	root mean squared error
RSV	respiratory syncytial virus
RT	Room temperature
S	spike protein
SA	streptavidin
SAPE	streptavidin–phycoerythrin
SARS-CoV-2	Severe Acute Respiratory Syndrome Coronavirus 2
SD	standard deviation
SEAP	secreted alkaline phosphatase
SEM	standard error of the mean
SFU	spot forming units
SIREN	SARS-CoV-2 Immunity and Reinfection Evaluation study

SNP	single-nucleotide polymorphism
SPF	specific pathogen-free
TCID50	median tissue culture infectious dose
TCR	T cell receptor
TCM	central memory T cell
TE	effector T cell
TEM	effector memory T cell
Tfh	T follicular helper cell
Th	helper T cell
TLR	Toll-like receptors
TM	transmembrane region
TMPRSS2	transmembrane serine protease 2
TNF	tumour necrosis factor
tPA	tissue plasminogen activator
Tregs	regulatory T cells
TRM	tissue-resident memory T cells
VVCF	Viral Vector Core Facility
VITT	vaccine-induced immune thrombotic thrombocytopenia
VIP	Variable importance plot
VLP	virus-like particle
VOC	variants of concern
VP	viral particle
VSV	vesicular stomatitis virus
WHO	World Health Organization

Statement of Authorship

I optimised and standardised all Luminex-based serological assays and performed all serological work on the samples unless otherwise specified. MERS-CoV enzyme-linked immunosorbent assay (ELISA) optimisation was conducted jointly with Dr. Mustapha Bittaye, and optimisation of the MERS-CoV pseudovirus neutralisation assay (PNA) was performed by me, with contributions from master's student Ferdinand Haas and technical input from Dr. Rachel Kenneil. Given the large number of samples in the MERS003 clinical trial, sample running was performed collaboratively with Emilie Vannaxay, Dr. Rachel Kenneil. The SARS-CoV-2 ELISA was performed by me together with other members of the group using an established protocol developed by the Lambe group, and the SARS-CoV-2 PNA assay was carried out jointly with Alex Sampson using his optimised protocol. I contributed minor input to the anti-vector assay, which built on earlier work by Dr. Mustapha Bittaye and Caitlin Blundell, with additional assay development later performed by Emilie Vannaxay.

T-cell assays and data visualisation on clinical MERS001 samples were performed by Dr. Mariana Pereira Pinho, a postdoctoral researcher in the Radcliffe Department of Medicine, University of Oxford, under the supervision of Dr. Giorgio Napolitani. Mouse handling, vaccinations, and associated pre-clinical work before take-down were carried out by the team led by Dr. Barbara Dema Jimenez, including Marta Ulaszewska and Roo Bhasin, and I independently performed all downstream analyses, including serological assays. The DoE plan was developed jointly by Barbara Dema Jimenez and me, with guidance from Dr. David Pulido-Gomez. Flow cytometry data acquisition was performed by Barbara Dema Jimenez, and I carried out all subsequent data analysis and visualisation for this project. This thesis includes content previously published, including clinical trial data and commentary from other studies. Parts of this research were disseminated through scientific presentations, and representative material is included in the Appendix. The MERS003 trial was led by Chief Investigator Prof. Maheshi Ramasamy (Oxford Vaccine Group, University of Oxford), with Prof. Sarah Gilbert (Pandemic Sciences Institute, University of Oxford) as lead scientific investigator, and Dr. Andrea Collins (Liverpool Vaccine Group, Liverpool School of Tropical Medicine, Liverpool, UK) as Site Principal Investigator. Clinical procedures were conducted by healthcare professionals at the Liverpool School of Tropical Medicine (Liverpool, UK) and the Liverpool University Hospitals NIHR Liverpool Clinical Research Facility at Royal Liverpool University Hospital, with sample processing performed by the Liverpool Vaccine Group laboratory team.

I gratefully acknowledge the support of the Protective Immunity through T Cells in Healthcare workers (PITCH) Consortium, the National Institute for Health and Care Research (NIHR) Oxford Biomedical Research Centre (Oxford BRC), and the Oxford Vaccine Centre (OVC) Biobank for the provision of samples, infrastructure, and resources used in this research. I am grateful to Dr Giada Mattiuzzo and

Dr Emma Bentley at the National Institute for Biological Standards and Control (NIBSC) and the World Health Organization (WHO) for providing the MERS convalescent serum panel and the NIBSC MERS panel, as well as for their input into the PNA. I also thank Dr Bandar Alosaimi for providing the hybrid MERS immunity samples.

1 Introduction

1.1 Vaccines

Vaccines have been one of the most powerful tools in the control of infectious diseases since Edward Jenner developed the smallpox vaccine in 1796 [1, 2]. Modern technologies can now rapidly develop emerging pathogen vaccines, as seen in the rapid global response to the coronavirus disease 2019 (COVID-19) pandemic. In 2023, the Nobel Prize in Physiology or Medicine recognised Katalin Karikó and Drew Weissman for discoveries that enabled the development of mRNA vaccines, which were deployed at unprecedented speed during the pandemic [3]. The various COVID-19 vaccinations prevented between 14 and 20 million deaths worldwide in their first year of rollout [4]. Their success exemplified how rapid development of vaccines against novel pandemic pathogens are enabled by pre-pandemic research to optimise vaccine platform technologies and understand immunity to related viruses.

Vaccines work by presenting the immune system with pathogen-derived antigens or epitopes in a safe form, allowing immunity to develop without causing disease [5]. Vaccine or adjuvant components activate the innate immune system, which generates inflammatory signals, leading to maturation of antigen presenting cells such as dendritic cells, and to activation of B cells and T cells, which are responsible for coordinating the humoral and cellular components of the adaptive immune response.

T-cell activation results in the formation of effector T cells that regulate immune functions, and memory T cells that persist long-term. B-cell activation drives the humoral response, leading to production of antigen-specific antibodies and establishment of long-lived memory B cells. These coordinated immune processes generate both immediate and durable protection: effector mechanisms act rapidly to control infection shortly after exposure, while memory B and T cells provide long-lasting immunity that enables effective responses during future encounters with the pathogen [5-7].

1.2 Cellular immune response

Antigens processed by dendritic cells are transported to secondary lymphoid organs, where they are presented by these cells on major histocompatibility complex (MHC) molecules [8]. MHC class I molecules, which are expressed on most nucleated cells, present peptides derived from intracellular antigens and are recognised by CD8 T cells, whereas MHC class II molecules, which are expressed primarily on professional antigen-presenting cells, present peptides derived from extracellular antigens and are recognised by CD4 T cells [8, 9].

Following antigen encounter and appropriate co-stimulatory signals, naïve T cells undergo activation, clonal expansion, and differentiation into specialised effector subsets. Effector populations contribute to immune defence through direct killing of infected cells by $CD8^+$ T cells, and immunomodulation by

$CD4^+$ T cells, which produce a diverse range of cytokines (e.g. interleukin and interferon families) to support and influence the function of other immune cells.

$CD8^+$ T cells differentiate into cytotoxic T lymphocytes (CTLs) capable of eliminating intracellular pathogens through several well-defined effector mechanisms: secretion of pro-inflammatory cytokines TNF-α and IFN-γ; release of cytotoxic granules containing perforin and granzymes, leading to apoptosis of target cells [10], and Fas–FasL interactions, in which engagement of Fas on target cells triggers caspase activation and programmed cell death [11-13]. Together, these complementary mechanisms allow $CD8^+$ T cells to efficiently control and clear intracellular infections.

$CD4^+$ T cells diversify into multiple subsets, including Th1, Th2, Th17, regulatory T cells (Tregs), and T follicular helper (Tfh) cells, according to the cytokine milieu and transcriptional programmes induced during priming [9, 14]. Th1 cells promote immunity to intracellular pathogens by secreting IFN-γ, TNF-α, and IL-2, thereby enhancing macrophage activation and supporting cytotoxic T-cell responses. Th2 cells produce IL-4, IL-5, and IL-13, which facilitate B-cell responses and immunity to extracellular organisms such as helminths [15]. Th17 cells secrete IL-17, IL-22, and IL-26, contributing to mucosal barrier protection and neutrophil recruitment [16-18]. Tregs maintain peripheral tolerance through the production of immunomodulatory cytokines such as IL-10 and TGF-β, which suppress effector T-cell activation and limit excessive inflammation, thereby preserving tissue homeostasis and preventing autoimmunity [19]. Tfh cells secrete IL-21 and migrate to germinal centers, where they are indispensable for B-cell affinity maturation, class-switch recombination, and the development of long-lived plasma cells and memory B cells [20-22]. Following activation, T cells also differentiate into memory subsets with distinct homing properties [23]. Circulating memory T cells include central memory T cells (TCM) and effector memory T cells (TEM), while tissue-resident memory T cells (TRM) remain localized within peripheral tissues [24].

TCM reside primarily in lymphoid organs and possess high proliferative capacity. They show reduced dependence on co-stimulatory signals, which allows them to interact efficiently with dendritic cells and B cells. Upon antigen re-encounter, TCM rapidly proliferate and produce effector cytokines such as IFN-γ, supporting a strong secondary immune response.

In contrast, TEM express adhesion molecules and chemokine receptors that enable their migration through peripheral tissues [24]. This positioning allows them to respond quickly upon antigen re-exposure. TEM produce high levels of perforin and granzymes, equipping them for immediate cytotoxic activity.

TRM are a distinct subset that permanently inhabit peripheral tissues such as skin, mucosa, and organs. They do not recirculate but provide rapid local protection by initiating immediate effector functions upon antigen recognition [25, 26].

1.3 Humoral immunity

Humoral immunity is mediated by B cells and the antibodies they produce. B cells acquire intact antigen in the follicle through their B-cell receptor (BCR), typically by binding antigen displayed on subcapsular sinus macrophages or follicular dendritic cells. The BCR–antigen complex is then internalised and processed. B-cell responses can be T-independent or T-dependent [5]. T-independent responses are triggered directly by certain antigens without T-cell involvement and typically generate rapid but relatively low-affinity antibody production. T-dependent responses require cognate help from $CD4^+$ T cells and usually give rise to germinal-centre formation, class-switch recombination, and the production of high-affinity antibodies [27].

Effector B cells, collectively termed antibody-secreting cells (ASCs), comprise plasmablasts—rapidly proliferating cells generated in secondary lymphoid tissues—and terminally differentiated plasma cells, which may be short- or long-lived depending on their anatomical niche. Following activation in secondary lymphoid tissues, B cells differentiate via two major pathways. In the extrafollicular response, activated B cells rapidly give rise to short-lived plasma cells that produce the early wave of antibodies, predominantly low-affinity IgM, with some early IgG [28-32]. Alternatively, activated B cells enter germinal centres (GCs) within B-cell follicles, where, with cognate T follicular helper cell support, they undergo class-switch recombination and somatic hypermutation, enabling affinity maturation and selection of high-affinity clones [32,33]. GC B cells ultimately differentiate into long-lived plasma cells that migrate to the bone marrow (BM), where stromal survival signals support sustained secretion of high-affinity, class-switched antibodies for years, and into memory B cells that mediate rapid recall responses upon antigen re-exposure [5, 33, 34].

1.3.1 Antibody structure and subclasses

Antibodies are Y-shaped molecules composed of two main functional domains linked by a flexible hinge region. The antigen-binding fragments (Fab domain) mediates antigen-specific recognition and binding, and the crystallisable fragment (Fc domain) orchestrates downstream immune responses (Figure 1-1).

Antigen specificity is determined by variable regions in the Fab domain. These undergo somatic hypermutation and affinity maturation in the germinal centre, allowing the immune system to generate antibodies with progressively higher affinity for a given antigen [35, 36]. Class-switch recombination (CSR) occurs in the Fc region of the antibody heavy chain. During CSR, the B cell replaces one constant-region gene segment with another, thereby changing the antibody isotype without altering antigen specificity. As a result, antibodies acquire different Fc-mediated effector functions, enabling engagement of distinct immune receptors and pathways. Antibodies also undergo post-translational glycosylation. This occurs predominantly in the Fc region, where it regulates receptor binding and

effector functions; variable Fab glycosylation can modulate antigen binding in a context-dependent manner [37, 38].

A summary of the key structural and functional properties of IgM, IgG, and IgA is provided in Table 1-1. IgG and IgA are further subdivided into IgG1, IgG2, IgG3, IgG4 and IgA1, IgA2 respectively, with each subclass having unique structural and functional characteristics [39], illustrated in Figure 1-1. Together, these differences give rise to the diverse effector roles of each isotype. IgD and IgE contribute minimally to Fc-mediated antiviral effector functions and are therefore not discussed in detail here.

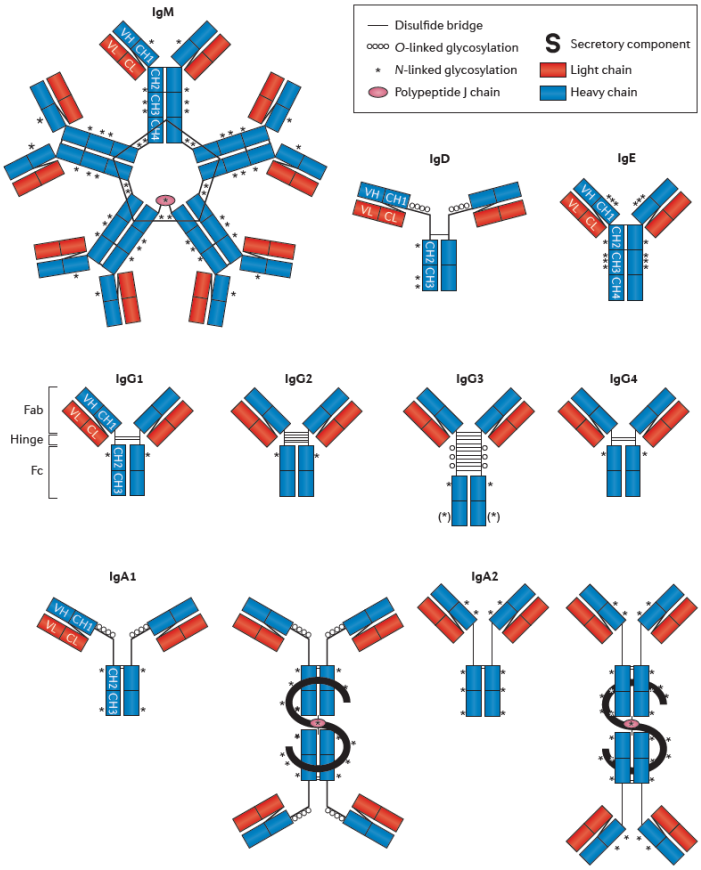


Figure 1-1. Antibody structure, isotypes and subclasses.

Antibodies consist of paired heavy and light chains linked by disulfide bonds and organized into Fab and Fc domains. Isotypes (IgM, IgD, IgG, IgA, IgE) and subclasses differ in structure, multimerization and Fc features. IgM and IgA form multimers via J chains, and dimeric IgA includes a secretory component that enhances stability. Structural variation—including hinge flexibility, disulfide bonding and glycosylation—modulates receptor interactions and effector functions. Adapted from [39].

Isotype	Structure	Key Functions	Receptors	Serum Abundance	Intrinsic Half-life
IgM	Secreted as a pentamer; high valency increases antigen-binding capacity [40].	Potent neutralisation early in infection; strong activation of the classical complement pathway via C1q binding [41]	No classical Fc receptor; complement activation is the primary effector route.	~5–10% of serum Ig.	~5 days
IgG (IgG1–IgG4)	Four subclasses differing in hinge length and flexibility. IgG1 and IgG3 have longer, more flexible hinges [42].	High-affinity neutralisation; IgG1 and IgG3 dominate antiviral responses [42]; mediate complement activation [43]; engage FcγRs for ADCP, ADCC, and inflammatory signalling [44].	Activating: FcγRI, FcγRIIA, FcγRIIC*, FcγRIIIA. Inhibitory: FcγRIIB.	~70–75% of serum Ig.	~21 days (FcRn-dependent).
IgA (IgA1, IgA2)	IgA1 mainly monomeric in serum IgA1 and IgA2 form J-chain–linked dimers at mucosal sites [45, 46].	Primary mediator of mucosal neutralisation; prevents pathogen adherence and invasion; contributes to immune exclusion.	FcαRI on neutrophils, eosinophils, monocytes, Kupffer cells [47, 48].	~15% of serum Ig. >90% of Ab at mucosal surfaces.	~6 days

Table 1-1. Summary of major human immunoglobulin isotypes and subclasses.

The table compares the structural organisation, effector functions (including neutralisation, complement activation, and Fc receptor engagement), receptor-binding profiles, serum abundance, and intrinsic half-lives of IgM, IgG1–IgG4, and IgA1–IgA2. These features collectively illustrate how isotype and subclass diversification contributes to functional specialisation within the humoral immune response.

1.3.2 Antibody effector function

Antibodies bound to viral particles or infected cells protect through two complementary mechanisms: Fab-mediated neutralisation and Fc-mediated engagement of innate immunity. Neutralisation occurs when Fab regions bind viral surface proteins, bacterial toxins, or other essential microbial structures, thereby blocking receptor attachment, membrane fusion, or toxin activity. Direct neutralisation measured *in vitro* is a primary correlate of protection for many vaccines. While such measurements are independent of Fc signaling, neutralisation *in vivo* may be augmented through Fc-dependent mechanisms.

When neutralising activity is low, or when antibodies bind non-neutralising or sub-neutralising epitopes, Fc-mediated effector functions provide a critical second layer of defence. These include antibody-dependent cellular phagocytosis (ADCP), antibody-dependent cellular cytotoxicity (ADCC), and antibody-dependent complement deposition (ADCD) [39, 49], which together enhance pathogen clearance through opsonisation—defined as the coating of pathogens with antibodies and/or

complement to promote their recognition and uptake by immune cells [50]—and Fc receptor engagement [39, 49]. Complement deposition further amplifies these processes and supports additional Fc-dependent mechanisms, including NETosis, enhanced antigen presentation, and retention of immune complexes on follicular dendritic cells [51-54]. NETosis involves the release of chromatin-based extracellular structures that trap and immobilise pathogens [55].

The magnitude and quality of Fc responses depend on antibody subclass, affinity, glycosylation, epitope specificity, and the distribution of Fc receptors on innate immune cells. Activating Fcγ receptors (e.g. FcγRI, FcγRIIA, FcγRIIIA) initiate phagocytosis, cytotoxicity, and inflammatory signalling, whereas FcγRIIB—the only inhibitory Fcγ receptor—attenuates activation and prevents excessive inflammation. Immune cell activation is regulated by a balance between activating and inhibitory signals, mediated in part by immunoreceptor tyrosine-based activation motifs (ITAMs) and immunoreceptor tyrosine-based inhibitory motifs (ITIMs). ITAM-associated receptors promote cellular activation and inflammatory responses, whereas ITIM-containing receptors limit activation by transmitting inhibitory signals [38]. Disruption of this balance, either through enhanced activating Fc receptor signalling or sustained overstimulation by immune complexes and their deposition within tissues [56], can shift Fc-mediated responses from protective immunity to pathological inflammation [57]. This process, known as antibody-dependent enhancement (ADE) [58], often occurs when viruses exploit non-neutralising antibodies to infect Fc receptor–bearing cells such as macrophages or monocytes [59], and has been associated with a Th2-biased immune profile, which may permit intracellular viral survival through reduced activation of antiviral myeloid responses [60, 61].

ADCP is mediated by IgG through Fcγ receptors and by IgA through FcαRI (CD89) on macrophages, monocytes, and neutrophils, reflecting the distinct Fc receptor families engaged by each isotype. ADCC is driven primarily by NK-cell engagement of FcγRIIIA, resulting in degranulation and targeted killing of antibody-coated cells [62, 63]. Fc-mediated ‘classical pathway’ complement activation, most efficiently triggered by IgM and select IgG subclasses (notably IgG1 and IgG3), promotes opsonization, inflammatory recruitment, and membrane-attack-complex–mediated lysis.

Together, Fab- and Fc-mediated mechanisms form an integrated system in which antibody structure, subclass, glycosylation, and receptor engagement shape the quality and durability of protective immunity. Figure 1-2 illustrates the major Fc-mediated effector pathways and their cellular interactions during viral infection, providing a visual overview of how activating and inhibitory Fcγ receptors coordinate or restrain immune activation. Following this, Table 1-2 summarises the key human Fcγ receptors, and how receptor distribution and signalling architecture leads to different effector outcomes.

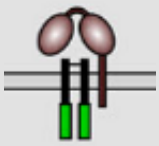
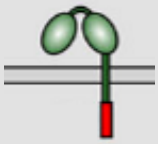
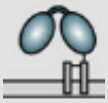
	FcγRIIA (CD32A)	FcγRIIIA (CD16A)	FcγRIIB (CD32B)	FcγRIIIB (CD16B)
Structure				
Function	Antibody-dependent cellular phagocytosis; Immune-complex clearance; antigen presentation; cytokine release	Antibody-dependent cellular cytotoxicity; NK-cell activation; perforin/granzyme-mediated killing	Inhibitory control of immune activation; suppression of B-cell signaling; regulation of inflammation	Antibody-induced NETosis
IgG subclasses	IgG1, IgG2, IgG3, IgG4	IgG1, IgG2, IgG3, IgG4	IgG1, IgG2, IgG3, IgG4	IgG1, IgG3
Major expressing cells	Monocytes, neutrophils, dendritic cells, basophils, mast cells, eosinophils, platelets	B cells, Monocytes, neutrophils, dendritic cells, basophils, mast cells, eosinophils	NK, neutrophils, dendritic cells, basophils, mast cells, eosinophils	Monocytes, neutrophils)
Signalling Motif	ITAM	ITAM (via FcεRIγ chain)	ITIM	GPI-anchored (no signaling tail)

Table 1-2. Summary of human Fcγ receptor characteristics.

Overview of human Fcγ receptors. Activating (ITAM) receptors include FcγRIIA and FcγRIIIA; the inhibitory (ITIM) receptor is FcγRIIB; FcγRIIIB is GPI-anchored and neutrophil-restricted. IgG1 and IgG3 preferentially engage activating receptors. Colour coding indicates signalling domain: activating (green), inhibitory (red), GPI-anchored (grey). Adapted from [64]

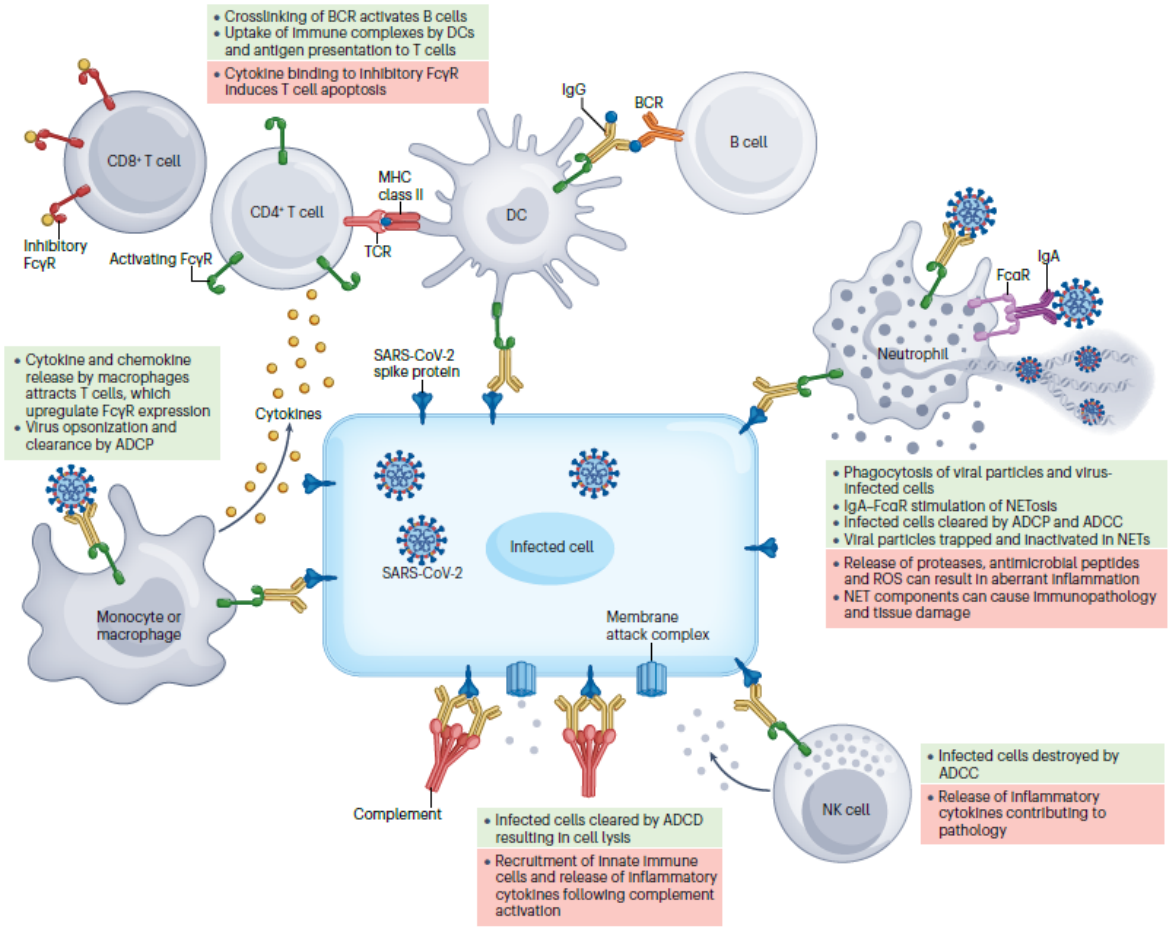


Figure 1-2. Fc receptor–mediated immune responses to viral infection.

Antibodies bound to viral particles or infected cells engage Fc receptors on immune cells, triggering antiviral or inflammatory pathways. Macrophages and dendritic cells opsonize virus, present antigen, and release cytokines. Neutrophils recognize IgA or IgG through FcαR/FcγR, leading to phagocytosis or NET formation. NK cells and other effector cells clear infected cells through ADCC. Complement activation further lyses infected cells and recruits inflammatory cells. These mechanisms contribute to both viral control and potential immunopathology. Figure was reproduced from [65] (The schematic displays SARS-CoV-2 for illustration, but the mechanisms shown are general to antibody-mediated antiviral immunity).

1.3.3 Murine Immune Response

Because of practical and ethical limitations in human studies, murine models are commonly used to explore immunobiology and vaccine mechanisms, guiding the selection of immune parameters that can be examined in humans. However, important species-specific differences must be considered when interpreting murine data. At the cellular level, humans and mice differ in the composition and function of innate and adaptive immune compartments. Notably, adult human peripheral blood is neutrophil-dominant, whereas murine blood is characterised by a relative predominance of lymphocytes, a distinction that can influence early immune activation and downstream effector responses [66].

In the humoral compartment, mice express IgG subclasses (IgG1, IgG2a/c, IgG2b, and IgG3) that do not directly correspond to human IgG1–IgG4, and they possess a single IgA isotype compared with two in humans (IgA1 and IgA2). These distinctions in antibody structure and effector potential are summarised in Table 1-3. In addition, Fc receptor expression patterns and IgG binding properties differ markedly between species (Table *1-4*). In humans, all activating Fcγ receptors generally bind IgG1, whereas in mice only FcγRIII efficiently binds murine IgG1. The inhibitory receptor FcγRIIB also displays species-specific binding characteristics, and several Fcγ receptors are uniquely expressed, including FcγRIV in mice and FcγRIIA, FcγRIIC, and FcγRIIIB in humans [67]. Transgenic mouse models expressing human Fcγ receptors, and in some cases human IgG, have been developed to improve the translational relevance of Fc-mediated immune studies [68].

Together, differences in cellular immune composition, antibody isotype distribution, and Fc receptor biology highlight important limitations in directly extrapolating murine findings to human immune responses and should be considered when interpreting data from animal models.

Isotype	Structure	Key Functions	Receptors	Serum Abundance	Intrinsic Half-life
IgM	• Secreted as a pentamer • High valency increases antigen-binding capacity	• Potent neutralisation early in infection • Strong activation of the classical complement pathway via C1q [69]	No classical Fc receptor; complement activation is the primary effector route	~5–10% of serum IgG	~5 days
IgG1	• Monomeric • Structurally similar to other IgG subclasses	• Efficient neutralisation (steric hindrance) • Commonly associated with Th2-type responses • Weak complement activation [70]	Low affinity for activating FcγRs	Variable	~6–8 days
IgG2a / IgG2c *	Monomeric	• Strong FcγR-mediated effector functions; efficient ADCC, ADCP, and complement activation [69] • Associated with Th1-type responses	High affinity for activating FcγRs	Variable	~6–8 days
IgG2b	Monomeric	• Moderate complement activation[69] and FcγR engagement • Contributes to inflammatory effector functions	Moderate affinity for FcγRs	Variable	~6–8 days
IgG3	• Monomeric • Prone to self-association	• Strong complement activation [69] • Commonly induced by T-independent carbohydrate antigens • Limited FcγR-mediated activity	Does not efficiently bind FcγRs	Variable	~6–8 days

IgA	• Single IgA isotype • predominantly dimeric at mucosal sites via J-chain • Transported across epithelium as secretory IgA (sIgA)	• Primary mediator of mucosal neutralisation • Prevents pathogen adherence and invasion • Contributes to immune exclusion	• No classical Fcα receptor • mucosal transport via polymeric Ig receptor (pIgR)	• Low in serum • Predominant antibody at mucosal surfaces	• ~1–2 days (serum) • Longer persistence at mucosa

Table 1-3. Summary of major mice immunoglobulin isotypes and subclasses.

*IgG2c expression is strain-dependent [71]

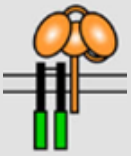
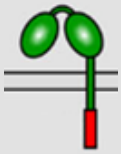
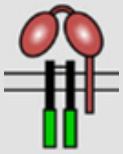
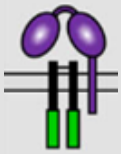
	FcγRI (CD64)	FcγRII (CD32)	FcγRIII (CD16)	FcγRIV
Structure				
Function	ADCP	Inhibitory control of immune activation	ADCC, ADCP	Strong activating receptor; binds IgG2a/IgG2b
Antibody subclasses	IgG2a, IgG2b, IgG3	IgG2a, IgG2b	IgG1, IgG2a, IgG2b	IgG2a, IgG2b
Major expressing cells	Monocytes, dendritic cells	B cells, dendritic cells	NK cells, monocytes, neutrophils, dendritic cells, basophils, mast cells, eosinophils	Monocytes, Neutrophil
Signalling Motif	ITAM	ITIM	ITAM (via FcRγ chain)	ITAM (via FcRγ chain)

Table 1-4. Summary of mouse Fcγ receptor characteristics.

Activating FcγRs signal through ITAM motifs provided by the associated FcRγ chain, whereas FcγRIIb contains an inhibitory ITIM domain. FcγRIII and FcγRIV preferentially bind IgG2a and IgG2b, shaping effector responses in murine systems. Adapted from [64].

1.3.4 Correlates of protection and vaccine licenses

Correlates of protection are measurable immune markers that are statistically associated with protection from infection or disease. These may be mechanistic, where the immune response directly mediates protection, or non-mechanistic, where readily measurable immune responses are statistically associated with protection but not necessarily causally linked. In practice, such biomarkers—most commonly

pathogen-specific antibody responses—are used as practical indicators of the immunological processes underlying vaccine-induced immunity [72] to evaluate the level of immunogenicity. Correlates of protection may additionally be used to assess the durability of immune responses and inform the need for booster immunisation (e.g. pertussis) [73].

Common antibody-based correlates are total antigen-specific antibody titres (e.g. hepatitis B) [74], neutralising antibody levels for viral or toxin-mediated diseases (e.g. influenza, tetanus) [75, 76], and opsonophagocytic antibody activity for bacterial pathogens (e.g. *Streptococcus pneumoniae)* [77]. While cellular immune responses, including $CD4^+$ T-cell responses, often contribute to protection (e.g. herpes zoster), quantitative protective thresholds are more difficult to define [73].

The use of correlates of protection has become an important tool in vaccine regulatory evaluation [72]. Traditional licensure pathways rely on large-scale clinical efficacy trials, which require sufficient disease incidence and are not always feasible [78]. In such situations, vaccine licensure may be supported by alternative regulatory pathways, including immunobridging [79], emergency or conditional authorisation [78], rolling review processes [80], and immunogenicity-based non-inferiority assessments [81].

Immunobridging studies can support vaccine licensure either by extrapolating protective immune thresholds defined in animal models to humans or by applying correlates of protection established in prior human efficacy studies to subsequent clinical trials [79]. The former approach was used for the Ebola vaccine regimen Ad26.ZEBOV and MVA-BN-Filo (Zabdeno/Mvabea), where Ebola glycoprotein–specific IgG and neutralising antibody responses correlated with protection in nonhuman primates and informed protective antibody thresholds in humans [82-85]. In contrast, for vaccines such as influenza, respiratory syncytial virus (RSV), and SARS-CoV-2, immunobridging has more commonly relied on correlates derived from earlier human efficacy trials to support later immunogenicity-based studies [86-88].

Viral vector vaccines

Viral vector vaccines are laboratory-engineered viruses designed to deliver pathogen-specific antigens to host cells. These platforms can be broadly classified as either replication-defective or replication-competent, depending on whether the vector retains the ability to replicate in vaccinated hosts. In replication-defective systems, viral genes required for replication are deleted and replaced with foreign antigen sequences, rendering the vector incapable of productive replication while enabling antigen expression. Removal of additional non-essential genes can further increase transgene capacity, allowing the insertion of multiple or relatively large antigens.

A key advantage of viral vectors is their intrinsic ability to activate innate immune sensing pathways, including endosomal Toll-like receptors and cytosolic nucleic acid sensors such as cGAS–STING [89, 90]. Recognition of virus-derived nucleic acids and structural components induces type I interferons, pro-inflammatory cytokines, and dendritic cell maturation, providing potent adjuvant-like stimulation without the need for exogenous adjuvants [89-92].

Adenoviruses and modified vaccinia Ankara (MVA) are among the most widely used viral vector platforms for human vaccines and are typically employed in replication-defective forms.

1.3.1 Adenoviral Vectors

Adenoviruses are non-enveloped, double-stranded DNA viruses that have been widely used as vaccine vectors due to their genetic stability, capacity for transgene insertion, and strong immunogenicity. For vaccine applications, deletion of the E1 gene renders adenoviruses replication-defective, while removal of the E3 region increases transgene capacity and enhances safety [93]. Early vaccine vectors mainly used human adenovirus type 5 (HAd5), and its entry pathway is shown in Figure 1-3 [94]. This pathway is considered broadly representative of adenoviruses, although differences in receptor usage and cell tropism exist between serotypes. However, pre-existing immunity to HAd5 in human populations led to the development of alternative vectors based on rare human adenovirus serotypes and nonhuman adenoviruses.

Multiple adenoviral-vectored vaccines were deployed during the COVID-19 pandemic, including ChAdOx1 nCoV-19/AZD1222/Covishield (AstraZeneca, University of Oxford, and Serum Institute of India) based on a chimpanzee adenovirus vector (ChAd) [95-97]; Ad26.COV2.S (Johnson & Johnson/Janssen) [98, 99], which uses human adenovirus type 26; the heterologous Sputnik V regimen using Ad26 and Ad5 vectors (Gamaleya Institute) [100, 101]; and the Ad5-nCoV vaccine (CanSino Biologics) [90, 102, 103].

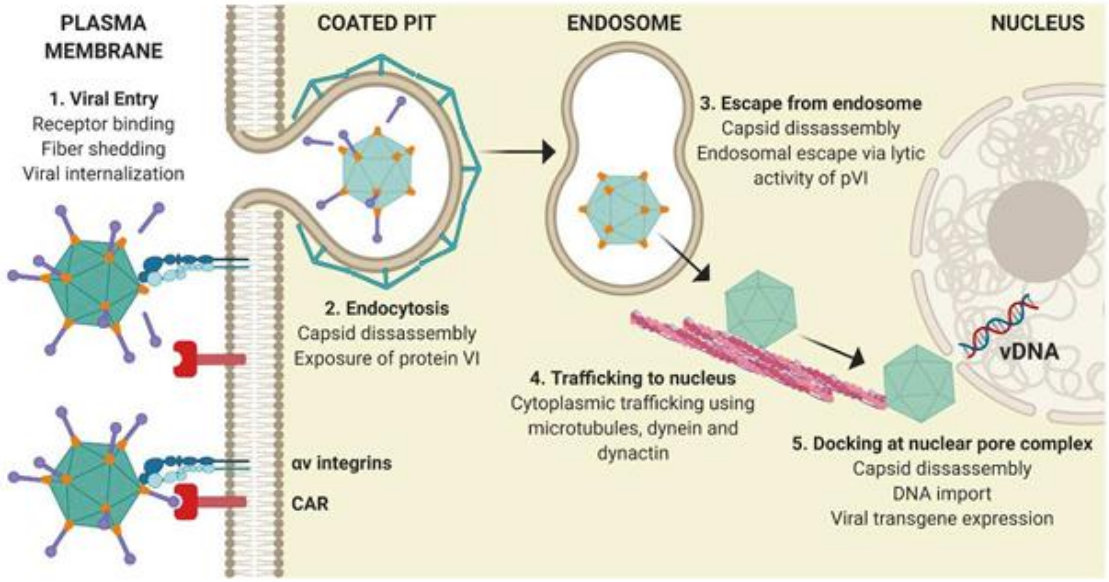


Figure 1-3. Classical adenoviral entry pathway.

(1) Adenovirus type 5 (Ad5) binds to host cells through interactions between its fiber knob and the coxsackievirus–adenovirus receptor (CAR). Subsequent recognition of cellular integrins via the RGD motif in the penton base initiates capsid destabilization and fiber release. **(2)** Integrin engagement promotes uptake of the virion by endocytosis. **(3)** Within the endosome, exposure of the internal protein VI enables membrane disruption and viral escape into the cytosol. **(4)** The partially uncoated viral core is transported along microtubules toward the nucleus and associates with the nuclear pore complex. **(5)** Viral DNA is then imported into the nucleus, where expression of the encoded transgene begins. Figure reproduced from Coughlan et al [94].

1.3.2 ChAdOx1 platform

ChAdOx1 is a non-replicating chimpanzee adenoviral vector derived from adenovirus serotype Y25. Originally developed at the University of Oxford, the platform offers several advantages, including low seroprevalence in humans, scalable and low-cost manufacturing, and ease of storage, facilitating deployment in resource-limited settings [104].

Prior to the licensure of ChAdOx1 nCoV-19, extensive clinical evaluation of the ChAdOx1 platform for pathogens such as malaria, influenza, and Ebola demonstrated an acceptable safety profile and robust immunogenicity [105-107]. Across several studies, ChAdOx1 vaccines consistently induced strong antigen-specific antibody and T-cell responses in healthy adults, older individuals, and immunocompromised populations [108, 109].

The global impact of the platform became evident during the COVID-19 pandemic. ChAdOx1 nCoV-19 was widely deployed and is estimated to have prevented more than six million deaths during its first

year of use [4, 110]. Clinical trials demonstrated an overall efficacy of approximately 70% against symptomatic SARS-CoV-2 infection, with substantial reductions in hospitalization and COVID-19–related mortality [97, 111].

A rare but clinically important adverse event associated with adenoviral vector vaccines is named vaccine-induced immune thrombotic thrombocytopenia (VITT) [112, 113]. It most commonly presents with severe thrombotic complications, including cerebral venous thrombosis (CVT), deep vein thrombosis (DVT), and thrombosis at atypical sites such as the splenic vein [114]. VITT has been reported following vaccination with multiple adenoviral vector platforms, including ChAdOx1- and Ad26-based vaccines, with estimated ultra-rare incidence rates of approximately 1 per 100,000 to 500,000 vaccinations [115]. Mortality of up to 24% have been reported, particularly in cases complicated by cerebral venous sinus thrombosis (CVST) and intracerebral haemorrhage (ICH) [114] Similar thrombotic events have also been described following natural adenoviral infection, suggesting a potential adenovirus family associated risk [116, 117].

Mechanistically, VITT is thought to result from an immune-mediated process involving the generation of pathogenic antibodies against platelet factor 4 (PF4). These antibodies trigger Fc-mediated platelet activation, leading to thrombocytopenia and thrombosis [113, 118-120]. Despite its association with significant morbidity and mortality, risk–benefit analyses demonstrate that the benefits of adenoviral vector vaccination far outweigh this risk, which remains exceedingly rare [121].

1.3.3 Modified vaccinia Ankara (MVA) Vectors

MVA is a highly attenuated strain of vaccinia virus belonging to the *Poxviridae* family. This family also includes the variola virus responsible for smallpox, declared eliminated in 1980 after global vaccination efforts [122]; and mpox virus, which caused the recent multi-country mpox outbreak in 2022 [71–73].

MVA contains a large linear double-stranded DNA genome of approximately 170 kb and retains the characteristic brick-shaped morphology of orthopoxviruses [123]. It was generated through more than 500 serial passages of the chorioallantois vaccinia virus Ankara (CVA) strain in chicken embryo fibroblasts, a process that resulted in the deletion of roughly 30 kb of genomic material, including several host-range and immune-modulatory genes essential for replication in mammalian cells [124-126]. Consequently, MVA is replication-deficient in most mammalian hosts, a feature that underlies its strong safety profile and reduced reactogenicity, and has supported its extensive application as a viral-vectored vaccine platform.

MVA-based smallpox/mpox vaccines manufactured by Bavarian Nordic (MVA-BN) have been approved in Europe, the UK, USA, and Canada [127, 128]. More broadly, MVA has been extensively

evaluated as a vaccine vector across numerous preclinical and clinical studies, with targets including influenza virus, HIV, malaria, Ebola virus, respiratory syncytial virus, and coronaviruses [73, 80–83]. It consistently induces strong $CD4^+$ and $CD8^+$ T-cell responses as well as durable antibody production. During the COVID-19 pandemic, several MVA-based vaccine candidates expressing SARS-CoV-2 antigens were developed and evaluated in clinical studies. These candidates demonstrated high immunogenicity and favourable safety profiles, although none were deployed at mass scale [129, 130].

1.4 Overview of coronavirus and emerging threats

Over the past two decades, members of the coronavirus family have caused several major disease outbreaks, highlighting their capacity to produce severe emerging diseases in humans in addition to relatively long-known endemic infections. Coronaviruses belong to the order *Nidovirales*, family *Coronaviridae*, and subfamily *Orthocoronavirinae*, and infect a wide range of mammals and birds. The subfamily is divided into four genera: *Alphacoronavirus*, *Betacoronavirus*, *Gammacoronavirus*, *and Deltacoronavirus*. Evolutionary relationships among representative coronaviruses across these genera are illustrated in Figure 1-4.

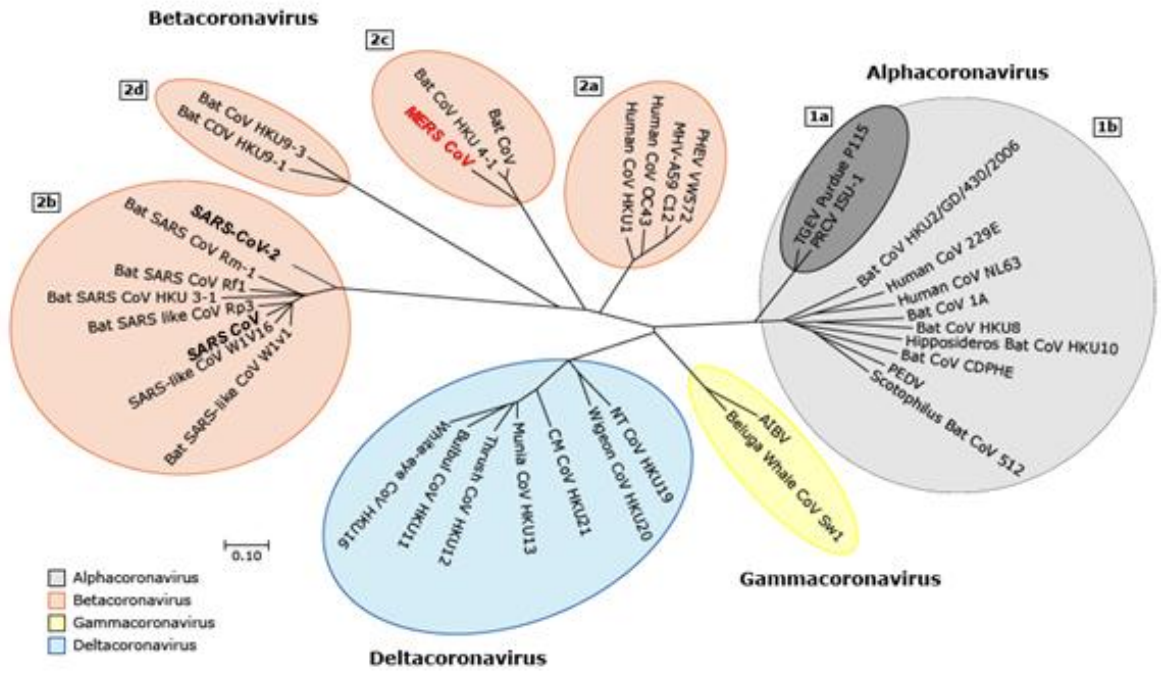


Figure 1-4. Phylogenetic tree of representative coronaviruses based on complete genome nucleotide sequences

Viruses are grouped into four genera: Alphacoronavirus (sky blue), Betacoronavirus (pink), Gammacoronavirus (green), and Deltacoronavirus (light blue), with subgroups 1a–1b and 2a–2d indicated. The tree was reconstructed from RNA-dependent RNA polymerase (RdRp) gene sequences using the maximum likelihood method (MEGA 7.2). Representative viruses include SARS-CoV, SARS-related CoV, MERS-CoV (red), porcine epidemic diarrhoea virus (PEDV), and Wuhan-Hu-1. Reproduced from [114].

1.4.1 Virology of coronaviruses

The family *Coronaviridae* comprises enveloped viruses with the largest known positive-sense, single-stranded RNA genomes among RNA viruses (approximately 22–36 kb). Virions are pleomorphic but typically quasi-spherical, with diameters of ~80–160 nm. All coronaviruses encode four structural proteins: spike (S), membrane (M), nucleocapsid (N), and envelope (E). The M protein is central to virion assembly [131], the highly conserved N protein binds the viral RNA genome and mediates genome assembly and packaging [132], and the E protein is required for efficient virus assembly and release [133]. The endemic betacoronaviruses HCoV-OC43 and HCoV-HKU1 additionally encode a haemagglutinin-esterase (HE) protein, which functions as a receptor-destroying enzyme by cleaving sialic acid-containing receptors [134].

1.4.2 Seasonal human coronaviruses

Several human coronaviruses circulate globally in an endemic and often seasonal manner and are a common cause of upper respiratory tract infections. These are collectively termed human seasonal coronavirus (HCoVs), and include HCoV-229E and HCoV-NL63 (alphacoronaviruses) and HCoV-OC43 and HCoV-HKU1 (betacoronaviruses). Infection typically occurs early in life [135], with age-related distribution patterns. There is increased incidence during winter months in temperate regions [136], although seasonality is not consistently observed [137]. Reinfections are common throughout adulthood, likely due to waning immunity and viral antigenic variation [138]. These viruses transmit efficiently via respiratory routes, particularly in households, hospitals, and long-term care facilities, contributing to their widespread circulation and high cumulative exposure in human populations [135, 139, 140].

Although disease is generally mild, seasonal human coronaviruses account for approximately 5–10% of acute respiratory infections in adults [141] and can cause severe disease in elderly individuals and residents of long-term care facilities, where outbreaks have been associated with mortality rates of up to 8% [142, 143]. Their widespread circulation and repeated exposure have important implications for population immune responses to newly emerging coronaviruses.

1.4.3 Zoonotic coronaviruses with epidemic and pandemic potential

Several zoonotic betacoronaviruses have demonstrated the ability to cross species barriers and cause severe disease in humans. Severe acute respiratory syndrome coronavirus (SARS-CoV) and Middle East respiratory syndrome coronavirus (MERS-CoV) were responsible for major outbreaks in 2002–2004 and from 2012 onwards, respectively [144, 145]. Although the SARS-CoV outbreak was successfully contained through intensive public health interventions [146], MERS-CoV continues to cause sporadic cases and localized outbreaks, primarily in the Middle East [147]. SARS-CoV was

associated with a case fatality rate of approximately 9–10%, while MERS-CoV exhibited a substantially higher mortality rate of around 26–35% [148]. However, these estimates are largely derived from hospitalised and laboratory-confirmed cases and may therefore overestimate true infection fatality rates, as milder or asymptomatic infections are likely to be under-represented. The overall spread of both viruses remained limited.

The emergence of severe acute respiratory syndrome coronavirus 2 (SARS-CoV-2) in late 2019 represented a critical shift in the epidemiology of human coronaviruses [149]. The resulting outbreak of coronavirus disease 2019 (COVID-19) was declared a global pandemic by the World Health Organization (WHO) in March 2020 [150]. Unlike SARS-CoV and MERS-CoV, SARS-CoV-2 demonstrated sustained and highly efficient human-to-human transmission, leading to rapid global dissemination. Ongoing viral evolution, characterized by the accumulation of mutations that enhanced viral fitness, further facilitated transmission and adaptation to human hosts [151]. This unprecedented spread highlighted fundamental differences in viral fitness, host susceptibility, and transmission dynamics among zoonotic coronaviruses.

Zoonotic coronaviruses are maintained in animal reservoirs, with bats recognized as the primary natural hosts for a wide diversity of coronaviruses, including those closely related to SARS-CoV, MERS-CoV, and SARS-CoV-2. Spillover into humans, often involving intermediate hosts, provides opportunities for viral adaptation to human infection and onward transmission [152]. Once introduced into human populations, the epidemic or pandemic potential of a coronavirus is strongly influenced by its transmissibility, commonly reflected by the basic reproduction number (R_0). Reported R_0 values for SARS-CoV-2 generally range from 2 to 2.5 or higher, compared with approximately 1.7–1.9 for SARS-CoV and below 1 for MERS-CoV [142, 153]. The higher transmissibility of SARS-CoV-2 was a key determinant of its rapid and sustained global spread.

Differences in epidemic and pandemic potential among zoonotic coronaviruses are strongly influenced by receptor usage, tissue tropism, and viral shedding dynamics. Both SARS-CoV and SARS-CoV-2 utilize the angiotensin-converting enzyme 2 (ACE2) receptor for cellular entry; however, SARS-CoV-2 exhibits a higher binding affinity for ACE2, enabling more efficient infection of human cells [154]. ACE2 is abundantly expressed in the upper respiratory tract, facilitating effective person-to-person transmission. In contrast, MERS-CoV uses dipeptidyl peptidase 4 (DPP4) as its cellular receptor. DPP4 is predominantly expressed in the lower respiratory tract and other tissues; this limits transmissibility while contributing to severe clinical disease [155].

Additional factors influencing transmission include differences in incubation periods and viral shedding patterns. SARS-CoV-2 is characterized by a relatively long incubation period and substantial viral shedding during the presymptomatic period and in asymptomatic individuals [156], which significantly

enhances transmission potential. By contrast, viral shedding in SARS-CoV and MERS-CoV largely coincided with symptomatic illness [157, 158], allowing more effective case detection and isolation.

Research conducted in response to SARS-CoV and MERS-CoV outbreaks established critical knowledge regarding coronavirus antigens, immune responses, and vaccine platforms. This foundational understanding was rapidly leveraged during the development of vaccines against SARS-CoV-2; an example of the importance of a broad understanding of coronavirus virology, host interactions, and transmission dynamics to pandemic preparedness.

1.4.4 Spike protein as a coronavirus vaccine target

A defining structural feature of coronaviruses is the spike (S) glycoprotein. This assembles as homotrimers forming large, club-shaped projections on the virion surface, and gives rise to the characteristic crown-like appearance from which coronaviruses derive their name [159]. The spike protein is essential for viral entry and represents the primary target of neutralising antibodies, monoclonals and vaccines [160-162]. The S protein has two subunits, S1 trimer and S2 stalk, which are subject to distinct evolutionary pressures. S1 contains the receptor-binding domain (RBD) [163], which mediates binding to host cells and is highly variable across coronavirus species, reflecting strong selection driven by host receptor specificity and immune evasion. The receptors used by representative human and zoonotic coronaviruses are summarized in Table 1-5. In contrast, S2 mediates viral and host membrane fusion and is markedly more conserved due to its indispensable role in viral entry [159, 164, 165]. Coronavirus entry generally involves receptor engagement followed by proteolytic activation of the spike protein by host proteases, such as furin or Transmembrane Protease, Serine 2 (TMPRSS2), triggering large conformational rearrangements in S2 that drive membrane fusion. A representative schematic of spike-mediated receptor binding, proteolytic activation, and membrane fusion is shown in Figure 1-5.

Virus genus/species	Subgenius	Other host than human	Main receptor
Genus Alphacoronavirus			
Human coronavirus 229E	*Duvinacovirus*	Bats [166], Alpacas [167]	Aminopeptidase N [168]
Human coronavirus NL63	*Setracovirus*	Bats [169]	Angiotensin- converting enzyme 2 [170] and Heparan sulfate [167]

Genus Betacoronavirus			
Human coronavirus OC43	*Embecovirus*	Rodent [171], Cattle [172]	9-O-Ac-sialic acid [173]
Human coronavirus HKU1	*Embecovirus*		9-O-Ac-sialic acid [174]
Severe acute respiratory syndrome -related coronavirus	*Sarbecovirus*	Bats, palms civet, diverse mammals [175]	Angiotensin- converting enzyme 2 [176-178]
Middle East respiratory syndrome-related coronavirus	*Merbecovirus*	Bats, Camel	Dipeptidyl-peptidase 4, Sialic acid [179]

Table 1-5. Genus, subgenus, known non-human hosts, and cellular receptors of representative human and zoonotic coronaviruses.

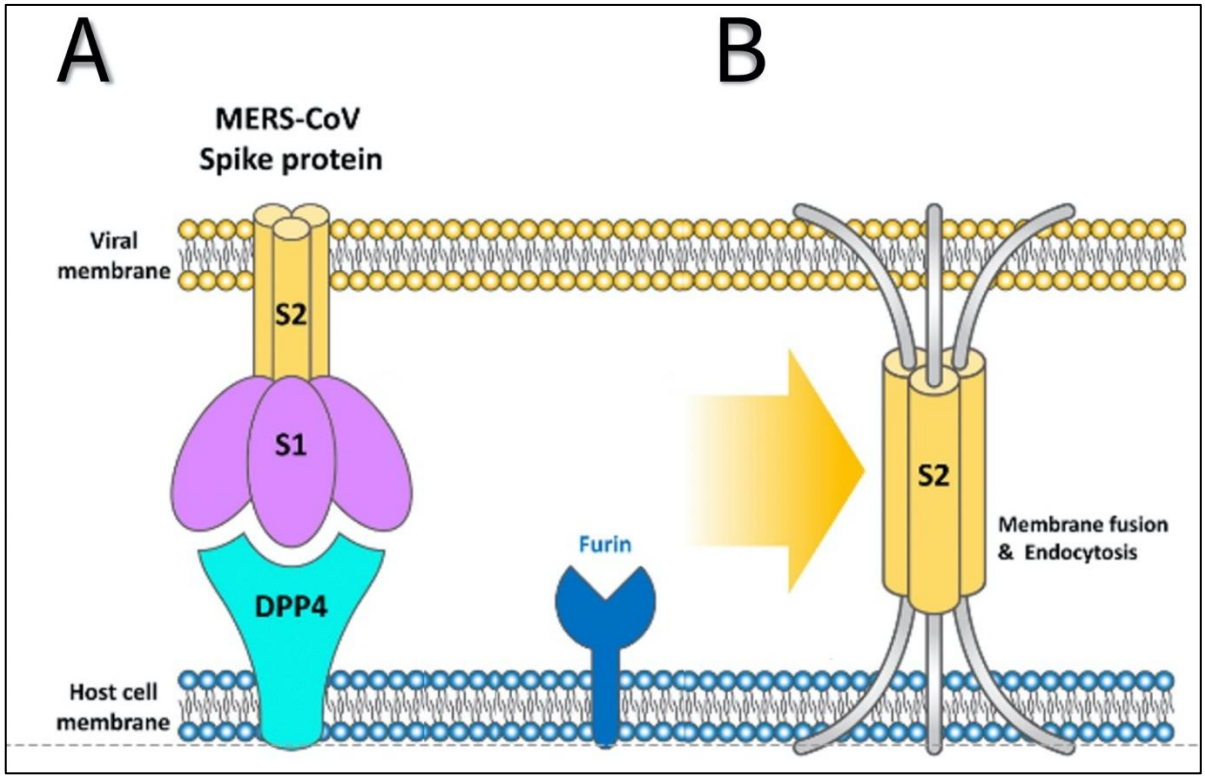


Figure 1-5. Schematic structure of the process of MERS-CoV attachment, fusion and entry to the host cell expressing the dipeptidyl peptidase-4 (DPP4) receptor.

(A) To enter the cell, MERS-CoV utilizes the trimeric spike glycoprotein, which consists of a trimeric S1 located at the surface and a transmembrane S2 subunit. First, the trimeric S1 binds to the host DPP4 receptor via the receptor binding domain (RBD) which activates the cleavage of S1 and S2 by the host furin proteolytic enzymes. **(B)** Fusion occurs by additional proteolysis of the S2 subunit which form a 6-helix bundle (6-HB) fusion core (adapted from Yang et al) [180].

1.5 Immune imprinting and cross-coronavirus immunity

Immune imprinting describes how a person's first exposure to a virus biases immune responses to antigenically distinct variants encountered later. Originally described by Thomas Francis Jr. as "original antigenic sin", early influenza studies showed that immune recall preferentially targets the first strain encountered, even after subsequent exposure to antigenically different viruses [181]. This bias can suppress *de novo* responses to new strains, which may lead to suboptimal protection.

Subsequent work demonstrated that imprinting is not inherently detrimental, but instead reflects a hierarchy of recall termed "antigenic seniority", in which antibody responses remain quantitatively strongest to the earliest encountered strain [182], Age-structured analyses of H3N2 influenza provide population-level evidence for this effect, with neutralisation profiles closely mirroring inferred childhood exposure histories [183]. In parallel, the phenomenon of back boosting describes how exposure to a new but related strain can amplify antibody responses to both the new antigen and previously encountered strains, highlighting how imprinting shapes both breadth and magnitude of recall responses [184, 185].

Beneficial imprinting arises when high-avidity cross-reactive memory T and B cells rapidly expand and recognize conserved, protective epitopes, leading to efficient viral clearance. In contrast, detrimental imprinting can occur through at least two distinct mechanisms. First, when recalled memory responses exhibit low avidity for the new variant due to increased antigenic divergence, binding and effector function may be insufficient for protection. Second, imprinting may be mismatched, whereby high-avidity memory responses are directed toward non-neutralising or otherwise non-protective epitopes, thereby dominating the response while suppressing de novo activation of naïve T and B cells. Both scenarios can skew immunity toward outdated antigenic features and limit the generation of variant-specific responses, with potential consequences for inflammation, immune pathology, or suboptimal vaccine efficacy [186]. These mechanisms are illustrated in Figure 1-6.

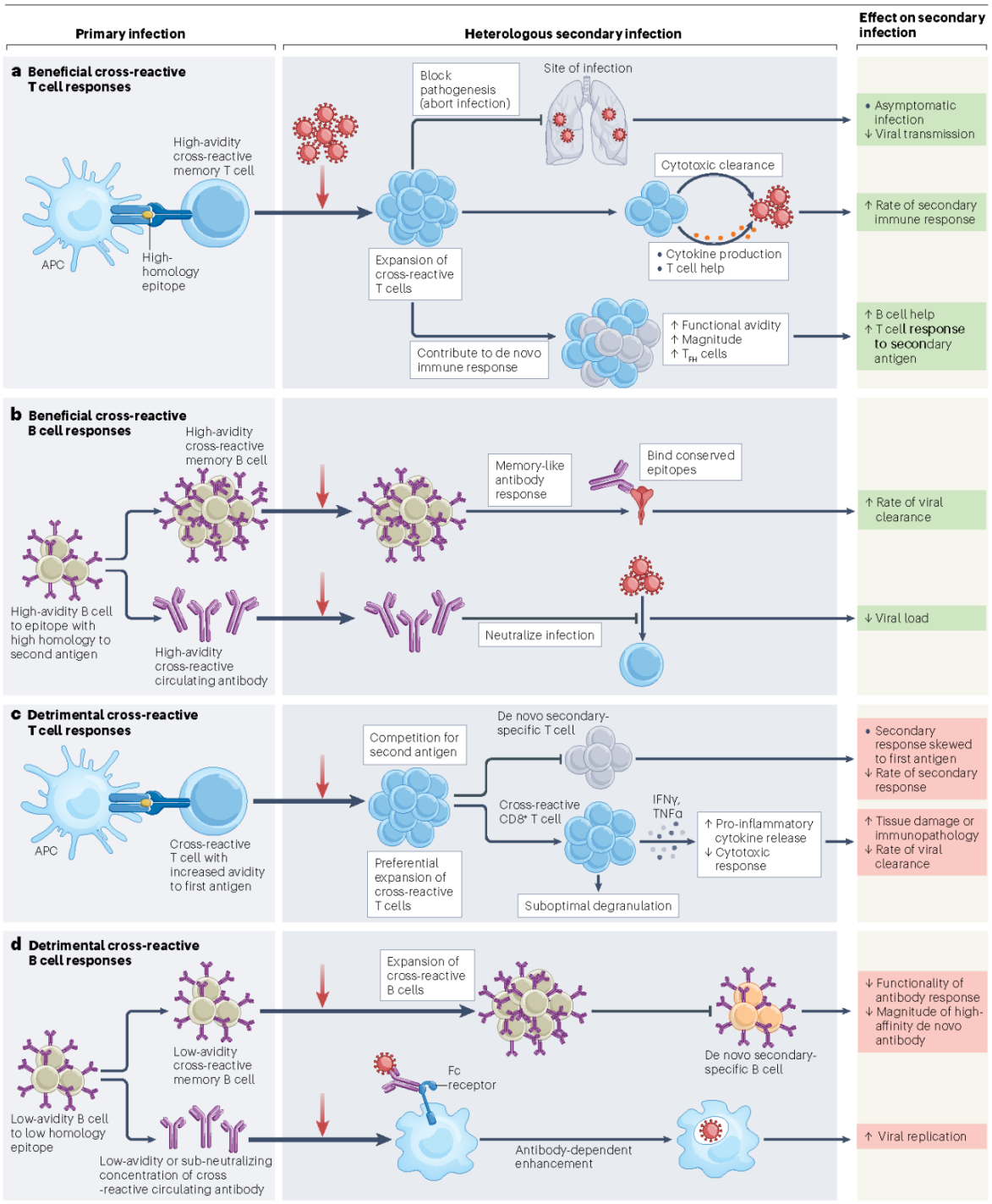


Figure 1-6. Beneficial and detrimental cross-reactive immune responses during heterologous secondary infection.

This schematic illustrates how immune imprinting can generate either protective or harmful outcomes during secondary infection with an antigenically distinct virus. During primary infection, cross-reactive memory T and B cells may form in response to epitopes shared between the original and the heterologous virus. Beneficial imprinting arises when high-avidity cross-reactive T cells enhance cytotoxic clearance and T-helper support, or when cross-reactive memory B cells produce high-affinity antibodies that neutralise the heterologous virus. Detrimental imprinting occurs when low-avidity cross-reactive T cells dominate and limit effective de novo T-cell activation, leading to inflammatory cytokine release and reduced viral clearance, or when low-affinity cross-reactive B cells suppress production of high-affinity antibodies and may contribute to antibody-dependent enhancement. Figure reproduced from [186].

1.5.1 Humoral immunity

Early in the COVID-19 pandemic, children were hypothesised to be partially protected from severe disease due to pre-existing immunity generated by prior exposure to seasonal human coronaviruses. This hypothesis was supported by the frequent detection of cross-reactive immune responses, particularly antibodies targeting regions of the spike S2 subunit conserved among endemic coronaviruses and SARS-CoV-2 [187]. Mechanistic insight into cross-reactive immunity has subsequently been provided by the identification of broadly reactive monoclonal antibodies targeting the conserved stem helix within the S2 fusion subunit. These antibodies recognize spike proteins from multiple betacoronaviruses, including SARS-CoV, SARS-CoV-2, MERS-CoV, and HCoV-OC43, and are generated following both vaccination and natural infection with SARS-CoV-2. Notably, they confer protection against lethal MERS-CoV challenge in mice in both prophylactic and therapeutic settings [188], demonstrating functional cross-reactivity mediated by conserved S2 epitopes.

Pre-pandemic cross-reactive antibodies directed against conserved S2 epitopes are commonly detectable but generally exhibit limited neutralising activity against SARS-CoV-2. During natural infection, expansion of cross-reactive B-cell clones lacking effective neutralisation capacity has been associated with severe COVID-19, suggesting that antibody imprinting may, in some contexts, bias responses toward non-neutralising specificities [189, 190].

Vaccination studies provide a more controlled framework for assessing these effects, but have not provided a consistent conclusion. Some studies report reduced induction of de novo SARS-CoV-2–neutralising antibodies in individuals with higher baseline seasonal coronavirus immunity [190], whereas others observe no association between pre-existing seasonal coronavirus antibodies and vaccine-induced humoral responses [189]. Conversely, in specific settings, baseline antibodies to endemic coronaviruses have been associated with enhanced SARS-CoV-2 antibody responses. In recipients of the inactivated BBIBP-CorV vaccine, baseline antibodies against HCoV-OC43 spike and S1 correlated with higher SARS-CoV-2 RBD-neutralising titres at later time points [191], and multivariable analyses linked higher baseline anti-spike IgG against HCoV-229E and HCoV-NL63 to increased SARS-CoV-2 anti-spike IgG responses [192].

SARS-CoV-2 vaccination has also been shown to boost antibody responses to endemic coronaviruses, particularly HCoV-HKU1 and HCoV-OC43, consistent with bidirectional serological cross-reactivity [190, 192]. Age further modulates these responses, with younger adults exhibiting higher antibody titres and greater back-boosting following ChAdOx1 nCoV-19 vaccination [180]. These findings indicate that pre-existing coronavirus immunity can modulate immune responses to subsequent exposures, although its effects are not uniform

1.5.2 Cellular immunity

Pre-existing $CD4^+$ T-cell responses arising from seasonal coronavirus exposure predominantly target conserved epitopes within the spike S2 subunit. Following primary SARS-CoV-2 vaccination, rapid recruitment of these cross-reactive $CD4^+$ T cells has been observed, with characteristics of a recall response [193].

Higher baseline frequencies of cross-reactive $CD4^+$ T cells have been associated with enhanced early vaccine immunogenicity, including increased T follicular helper responses, elevated early IgG production, and greater T-cell receptor avidity [193]. Consistent associations have been reported in people with HIV vaccinated with ChAdOx1 nCoV-19 [194] and in low-dose mRNA-1273 vaccination studies, where baseline cross-reactive $CD4^+$ T cells correlated with increased polyfunctional $CD4^+$ T-cell responses and higher early antibody titres [195].

While cross-reactive $CD4^+$ T cells may contribute to early immune priming, there is limited information regarding their role in long-term antibody maintenance and durable protection.

Collectively, these findings indicate that pre-existing seasonal coronavirus immunity exerts context-dependent effects on SARS-CoV-2 vaccination. Cross-reactive antibodies primarily target conserved, weakly neutralising epitopes and variably influence humoral responses, whereas cross-reactive $CD4^+$ T cells more consistently support early vaccine-induced immune priming.

1.6 SARS-CoV-2 and Variants of Concern (VOCs)

Since late 2020, SARS-CoV-2 has accumulated mutations arising from continuous RNA virus replication and prolonged infections in immunocompromised hosts, resulting in the gradual accumulation of replication errors despite the presence of a proofreading mechanism [151]. These mutations have subsequently been shaped by evolutionary pressures, leading to the emergence of variants with altered transmissibility and immune escape capacity. Key spike protein mutations, such as D614G and the N501Y substitution, enhanced viral binding affinity to the ACE2 receptor, contributing to increased transmissibility and viral fitness [196, 197]. As a result, the WHO designated several lineages as variants of concern (VOCs) based on their demonstrated impact on public health.

The first major VOC, Alpha (B.1.1.7), emerged in the United Kingdom in late 2020 and exhibited a 50–70% increase in transmissibility compared with ancestral strains [197]. This was followed by the emergence of Beta (B.1.351), which showed substantial resistance to neutralisation by antibodies elicited through prior infection or vaccination and reduced efficacy of several therapeutic monoclonal antibodies [197, 198]. Fc-mediated effector functions of antibodies, including engagement of Fcγ receptors on innate immune cells, have emerged as important contributors to protection, particularly

against antigenically divergent variants for which neutralisation is reduced. Gamma (P.1) was associated with increased transmissibility and an elevated risk of reinfection [199]. Delta (B.1.617.2) became globally dominant in mid-2021 due to markedly enhanced transmissibility and high viral loads, leading to widespread breakthrough infections, including among vaccinated individuals [200].

The most antigenically divergent variant to date, Omicron (B.1.1.529), emerged in late 2021 with over 50 spike protein mutations [201]. These changes shifted viral entry toward endosomal pathways, which has been associated with diminished innate immune activation, contributing to partial evasion of innate immune responses [202, 203] and rapid global spread [187, 188]. Omicron subsequently diversified into multiple sub-lineages, including BA.1, BA.2, BA.4/5, and later XBB and JN.1, each exhibiting varying degrees of transmissibility and immune evasion [204-206].

Subvariants of Omicron continue to evolve under strong immune pressure, resulting in lineages with progressively higher escape from neutralising antibodies [202]. However, T-cell responses remain relatively conserved across variants, contributing to protection against severe disease even when infection or reinfection occurs [200]. Across VOCs, declining neutralising antibody activity has underscored the importance of additional immune mechanisms. Fc-mediated effector functions of antibodies, including engagement of Fcγ receptors on innate immune cells, have emerged as important contributors to protection, particularly against antigenically divergent variants for which neutralisation is reduced [207].

1.7 Middle East Respiratory Syndrome Coronavirus (MERS-CoV)

1.7.1 Epidemiology

MERS-CoV is a zoonotic virus first identified in Saudi Arabia in 2012, in a 60-year-old patient with acute respiratory failure [208]. A MERS-related coronavirus sequence was subsequently detected in a faecal pellet from a *Taphozous perforatus* bat captured near the residence of the index case [209], supporting bats as a likely ancestral reservoir; retrospective serological analyses indicate that MERS-CoV had been circulating in dromedary camels since at least the 1980s [210]. As of 23 November 2025, more than 2,640 laboratory-confirmed cases have been reported globally with 958 deaths, resulting in an approximate case fatality rate of 36 % across 27 countries. Established risk factors for mortality include advanced age, smoking, and the presence of comorbidities [211]. Most reported cases have been concentrated in the Arabian Peninsula, particularly Saudi Arabia [212]. European countries with cases include Austria, Germany, Greece, Italy, the Netherlands, Turkey, and the UK; most cases were imported and did not lead to further spread of the virus.

MERS-CoV is believed to have originated in bats, which are considered the natural reservoir [213]. Dromedary camels act as the primary intermediate host, and the virus circulates endemically within camel populations across the Arabian Peninsula, Africa, and parts of Asia. Transmission intensity

within camels varies regionally, with estimated R_0 values of 7–14 in West Asia, 3–5 in Africa, and 2–3 in South Asia [214]. Zoonotic transmission to humans occurs through direct contact with infected camels, their secretions, or contaminated environments [215, 216]. Genomic similarity between viruses from infected humans and linked camels has provided molecular evidence of camel-to-human transmission [217]. However, the precise factors that lead to spillover from camels to humans remain poorly understood in Figure 1-7.

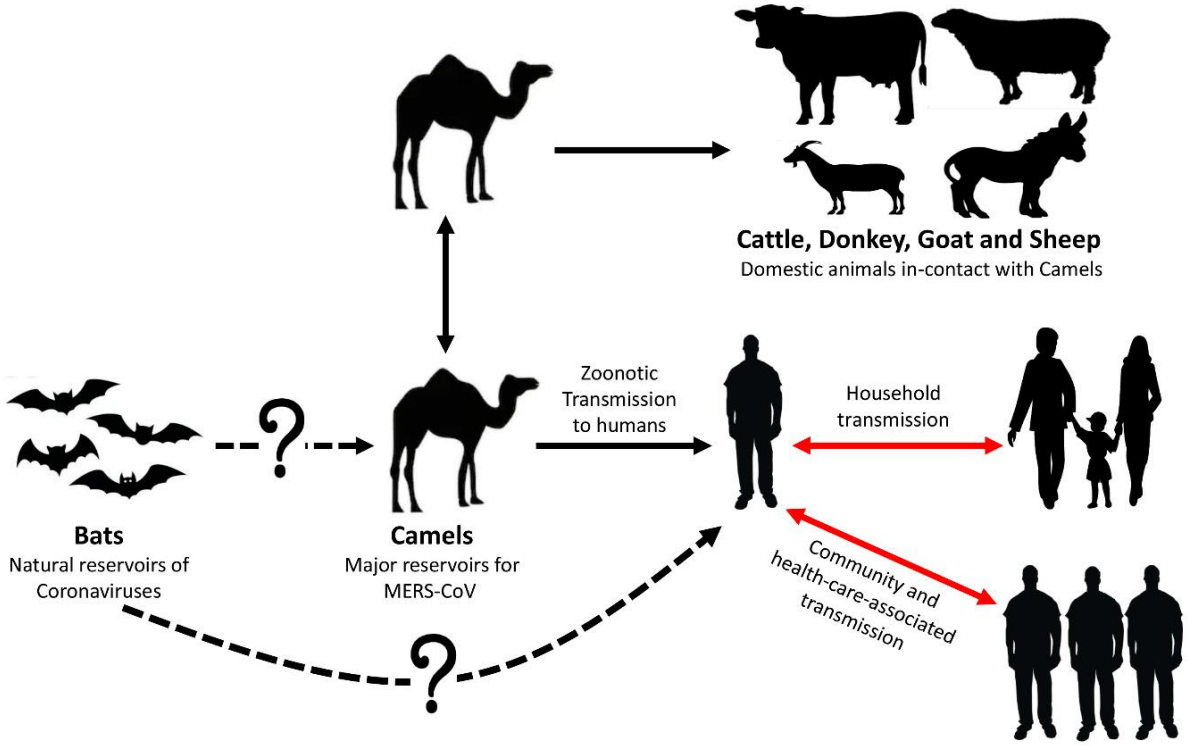


Figure 1-7. Zoonotic mode of transmission of MERS-CoV.

Three transmission routes have been confirmed: camel-to-camel, camel-to-human, and human-to-human. MERS-CoV is prevalent in dromedary camels and has also been detected in domestic animals in contact with camels [43]. As indicated by the dotted lines, direct bat-to-camel and bat-to-human transmission of MERS-CoV has not been confirmed. Reproduced from [218]

Human-to-human transmission is also well documented. The largest regional outbreak was in Riyadh and Jeddah in 2014. Household clusters were reported, but secondary attack rates are low, indicating limited community spread. Transmission is largely concentrated in healthcare settings [219]. In the 2014 outbreak, of the 255 confirmed cases, nearly all secondary infections (87.5 percent) resulted from exposure within healthcare facilities. Notably, 31 percent of all cases were healthcare workers [219], with transmission largely associated with close-contact encounters and aerosol-generating procedures [220].

The 2015 outbreak in the Republic of Korea originated from a single imported case, and resulted in 186 confirmed cases and 38 deaths [221, 222]. The index patient had camel exposure in the Middle East, but the rapid spread within Korea was driven primarily by host-related superspreading and healthcare-associated transmission, including overcrowded emergency rooms [223]. The viral isolate showed near-identity to Riyadh strains [222-224], indicating that viral evolution played little role in the scale of the outbreak. Retrospective analysis of this outbreak identified individuals with a history of autologous stem cell transplantation as being significantly associated with MERS infection [225]. Studies in KSA have also highlighted host genetic factors, with two HLA class II alleles, HLA-DRB111:01 and HLA-DQB102:02, being associated with disease [226].

Following the emergence of COVID-19, reported MERS cases declined substantially (Figure 1-8), likely reflecting decreased testing and surveillance. However, sporadic cases continue to occur, including two elderly individuals from France who had travelled to Oman and had a history of camel contact, reported in December 2025 [147]. These cases indicate that MERS-CoV continues to circulate and that imported infections remain possible despite lower global case numbers.

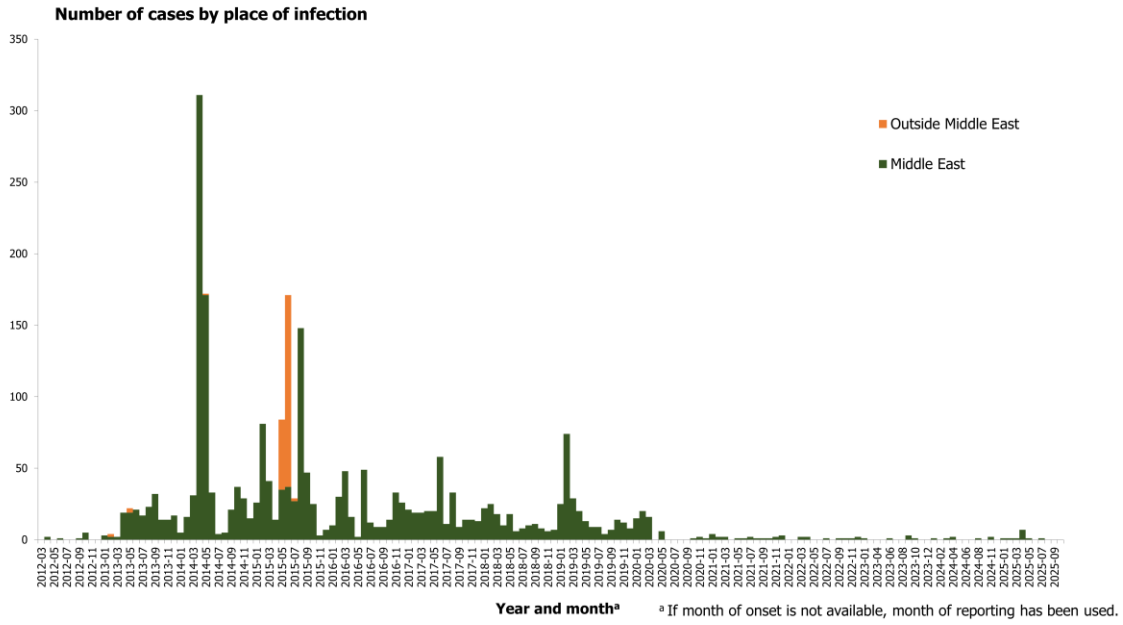


Figure 1-8. MERS Epidemic curve.
Epidemic curve showing laboratory-confirmed MERS-CoV cases (n = 2,640) and associated deaths (n = 958) reported in the Middle East (green) and outside the region (orange) between April 2012 and 3 November 2025. Figure reproduced from the European Centre for Disease Prevention and Control [212].

1.7.1.1 Epidemic potential and risk of resurgence

MERS-CoV remains a significant zoonotic pathogen due to its high case-fatality rate and continued circulation in dromedary camels across the Middle East, Africa, and parts of Asia. Although human-to-human transmission has historically been limited compared to SARS-CoV-2, repeated spillover events and occasional outbreaks in healthcare settings demonstrate a persistent risk of resurgence and emphasize the need for ongoing surveillance.

In the Middle East region, mass gatherings such as the Qatar FIFA World Cup and camel pageant championships increase the risk of MERS-CoV transmission and potential global spread [227]. These risks may be further influenced by seasonal factors. Because the Islamic lunar calendar cycles through all seasons, Hajj remains in each season for several consecutive years—approximately eight—before shifting to the next [228]. When Hajj eventually falls during the colder months, lower winter temperatures in Saudi Arabia may create more favourable conditions for MERS-CoV survival. Experimental studies show that MERS-CoV is particularly stable at around 20 °C and 40% relative humidity, remaining viable on surfaces for up to 48 hours, which raises concern for increased fomite transmission during cooler periods [229].

A key factor underlying the differing transmission patterns of MERS-CoV and SARS-CoV-2 is their receptor usage. SARS-CoV-2 utilizes the ACE2 receptor, which is highly expressed in the upper respiratory tract, enabling efficient human-to-human spread. In contrast, MERS-CoV binds the DPP4 receptor, predominantly expressed in the lower respiratory tract, resulting in limited respiratory shedding and reduced transmissibility despite severe clinical outcomes. This receptor distribution contributes to the lack of sustained community transmission observed with MERS-CoV.

Recent surveillance efforts across Asia, Europe, and Africa have identified multiple MERS-related coronaviruses (MERSr-CoVs) in bats, some of which use ACE2 instead of DPP4 for cellular entry [230]. While many interact primarily with bat ACE2, several viruses, including HKU5-2 and NeoCoV/PDF-2180, show limited compatibility with human ACE2, with enhanced entry in the presence of human proteases. Others, such as HKU5-19, can utilize ACE2 from a broad range of mammalian species, including livestock, rodents, and humans, indicating potential for cross-species transmission. Notably, a single amino-acid substitution (Y560K) in NeoCoV has been shown to confer efficient human ACE2 usage. This demonstrates how small genetic changes may alter host specificity and transmission characteristics. Similar mutation-driven shifts were observed during the emergence of SARS-CoV-2 variants, suggesting that related coronaviruses could acquire adaptations facilitating more efficient human infection.

Additionally, the identification of ACE2-using MERS-like coronaviruses has raised questions about the possibility of recombination between merbecoviruses and ACE2-dependent coronaviruses such as

SARS-CoV-2 [231]. Recombination has already been documented within each lineage independently—for example, several SARS-CoV-2 variants, including Omicron, are believed to have emerged through recombination among circulating strains, and the 2015 MERS outbreak virus was itself the product of recombination between multiple MERS-CoV lineages [232, 233]. Several theoretical scenarios have been proposed in which cross-lineage recombination could occur, including co-infection of MERS-CoV and SARS-CoV-2 in cells that co-express both DPP4 and ACE2 (such as subsets of alveolar and intestinal epithelial cells), or in cells expressing DPP4 alongside alternative SARS-CoV-2 entry factors such as CD147, NRP1, ASGR1, KREMEN1 or AXL [231]. Although speculative, these possibilities underscore the evolutionary plasticity of coronaviruses and raise concerns that recombination could facilitate the emergence of novel variants with meaningful epidemiological implications.

1.7.2 Clinical picture

The clinical presentation of MERS is highly variable, ranging from asymptomatic infection to severe pneumonia and life-threatening multi-organ failure requiring intensive care unit (ICU) admission. Severe cases often require mechanical ventilation, renal replacement therapy, and vasopressor support for refractory shock [5–8]. This wide clinical spectrum is reflected in the histopathological findings observed in fatal cases. In an immunocompetent 45-year-old man, post-mortem examination demonstrated more localised pneumonia [234]. In contrast, a 31-year-old immunocompromised man with lymphoma showed markedly more extensive tissue involvement, including necrotising pneumonia, diffuse alveolar damage, acute kidney injury, portal and lobular hepatitis, and myositis with muscle atrophic changes. Viral particles were detected in these affected tissues but not in liver tissue [235]. These findings indicate that the extent of tissue involvement in fatal MERS cases varies and tends to be more widespread in immunocompromised hosts.

Survivors of MERS generally show reduced quality of life, and those who required ICU care tend to experience greater limitations than non-ICU survivors. However, their overall quality-of-life scores are comparable to those of patients hospitalized for other respiratory illnesses [236].

Therapeutic options for MERS are limited, and no specific antiviral treatment has been firmly recommended. Supportive therapy remains the cornerstone of management. Combination therapy with lopinavir/ritonavir and subcutaneous (SC) IFN-β1b has shown clinical efficacy, demonstrating a reduction in all-cause 90-day mortality in a double-blind study of 95 laboratory-confirmed MERS patients (28% vs. 44%) compared with placebo treatment administered for 14 days [237]. Other treatment options include ribavirin and IFN-α, which have shown antiviral activity in in non-human primates (NHP) studies [238]. A retrospective evaluation in a small cohort found that treatment with ribavirin in combination with IFN-α2a was associated with improved 14-day survival compared with patients receiving supportive care alone [239]. However, a larger retrospective multicentre study

conducted in Saudi Arabia among critically ill patients reported that crude 90-day mortality did not differ between those receiving antiviral therapy and those who did not (after adjusting for confounders) [240]. Notably, antiviral therapy appears to be most effective when administered early in the disease course [237, 239]. The use of glucocorticoids in MERS management has not been shown to affect clinical outcomes or reduce hospitalisation and has been associated with delayed viral clearance [241].

Other potential therapies under investigation include remdesivir [242], convalescent plasma [243], and hyperimmune plasma derived from transchromosomic cattle immunised with a MERS coronavirus vaccine, for which safety and tolerability been evaluated in phase 1 [244]. Moreover, monoclonal antibodies have been developed for MERS-CoV, primarily targeting the RBD of the spike glycoprotein. Among these, the most advanced candidates are the fully human antibodies REGN3048 and REGN3051 [243], which bind distinct RBD epitopes and act synergistically to reduce the risk of viral escape; both have been evaluated for safety and tolerability in a phase 1 clinical trial in healthy adults. Other potent neutralising antibodies include LCA60, isolated from a MERS survivor and targeting a conserved RBD region with strong protective activity in animal models [245], and m336, a highly potent RBD-directed antibody demonstrating exceptional neutralising activity in preclinical studies [246]. Together, these monoclonal antibodies represent the leading therapeutic and prophylactic strategies under investigation for MERS-CoV.

1.7.3 Virology, clades and genetic stability

MERS-CoV has a ~30.1 kb genome encoding the structural spike (S), envelope (E), membrane (M), and nucleocapsid (N) proteins, along with several non-structural and accessory open reading frame (ORF) proteins such as ORF1a, ORF1ab, ORF3, ORF4a, ORF4b, and ORF5. The spike glycoprotein structure is shown below in Figure 1-9.

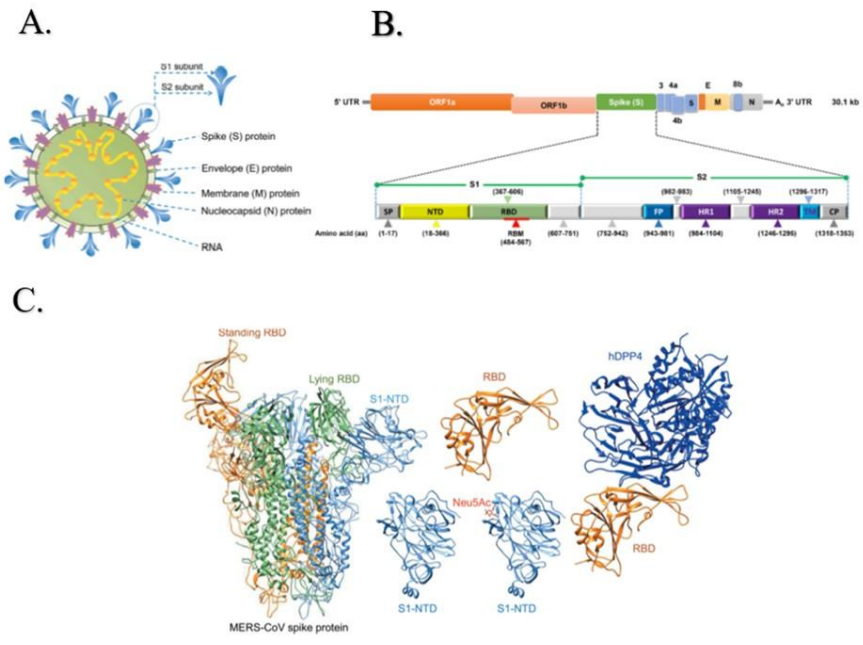


Figure 1-9. Structural organisation of MERS-CoV.

(A) Schematic representation of the MERS-CoV virion showing the spike (S), envelope (E), membrane (M), and nucleocapsid (N) proteins. **(B)** Genome organisation of MERS-CoV, including major open reading frames and the spike (S) gene with annotated functional domains. **(C)** Structural model of the MERS-CoV spike glycoprotein highlighting the S1 and S2 subunits and receptor-binding domain. Image A and C were reproduced from [247] and B was reproduced from [218].

Viral entry begins with S1–DPP4 binding, followed by furin-mediated cleavage at the S1/S2 junction and additional activation within S2, exposing the fusion peptide and promoting formation of the six-helix bundle (6-HB) fusion core [180, 248]. This mechanism enables membrane fusion and release of the viral genome into the host cytoplasm, shaping the infection dynamics, host specificity, and evolutionary trajectory of MERS-CoV.

Genomic surveillance has identified three major MERS-CoV clades (A, B, and C), each further subdivided into multiple lineages Figure 1-10. Clade A circulated only during the early phase of the epidemic (2012–2015), and has not been detected in either humans or camels since that period [144]. Clade B, which includes seven recognized lineages [232, 249, 250], emerged early in the epidemic and remains the predominant clade circulating in dromedary camels [251]. The most recently detected lineage in Saudi Arabian camels is clade B.5, particularly the B.5 2023.1–2023.5 sublineages [252], which continue to dominate infections in both camels and humans across the Middle East. Clade C circulates widely in African camel populations but has not been virologically confirmed in human infections [253, 254]. *In vitro* studies indicate that clade C viruses replicate less efficiently in human cell lines [255]. This could explain cross-reactive T-cell responses suggesting that some individuals in Africa, including slaughterhouse workers, may have experienced unrecognized or subclinical exposure to these viruses [256].

A.

Clade	Lineage	Origin	Most common in	First Detection
Clade A	A1	Arabian Peninsula	Human	2012
Clade B	B	Arabian Peninsula	Humans and Camels	2013
	B1		Humans	
	B2		Camels	
	B3			
	B4			
	B5		Humans and Camels	2014-2015
	B5-2023		Camels	2023
	B5-2023.1			
	B5-2023.2			
	B5-2023.3			
	B5-2023.4			
	B5-2023.5			
Clade C	C1	West/North Africa	Dromedary Camels	2013-2014
	C2	East Africa		2014
	C3	Egypt-specific lineage		2015

B.

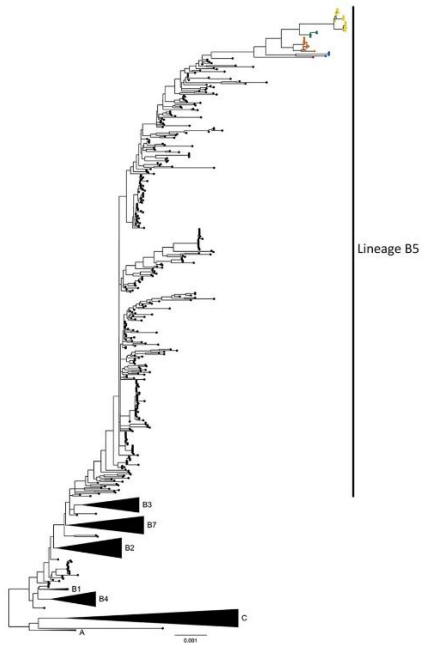


Figure 1-10. MERS-CoV clades and phylogenetic relationships.
(A) Summary table of major MERS-CoV clades and lineages, including geographical origin, primary host species, and year of first detection. Reproduced from [257], courtesy of Prof. Ezam I. Azhar **(B)** Maximum-likelihood phylogenetic tree showing the evolutionary relationships among MERS-CoV lineages, with lineage B5 highlighted as the most recently evolving cluster. Figure B is reproduced from [252]

MERS-CoV circulates endemically in dromedary camels, where as an RNA virus it will generate genetic diversity. Over time, this diversity creates opportunities for the virus to cross species barriers. Spillover into humans occurs when conditions allow the virus to exploit shared host factors—most notably the DPP4 receptor, which is expressed in both camel and human airway tissues. Bioinformatic analyses suggest that repeated camel–human transmission cycles impose selection pressures on the viral genome, gradually shaping variants that are better suited for human infection [258].

1.7.3.1.1 MERS-CoV Evolution

Multiple mutations have been identified across both non-structural proteins and the spike receptor-binding domain (RBD). Several RBD mutations appear particularly relevant to host switching. These include K511R and G521N in the receptor-binding motif, with K511R directly contacting the human DPP4 receptor, as well as Q419S, G436N, D472S, and R479L within the RBD core subdomain. At the C-terminal part of spike, the L775S substitution has also been described [258]. Such mutations illustrate how incremental changes may enhance receptor interaction, immune evasion, or cellular entry, thereby facilitating more efficient spillover. Figure 1-11 illustrates selected amino-acid substitutions in the MERS-CoV spike protein identified in human and camel isolates, highlighting notable changes within the N-terminal domain, receptor-binding domain, and other functional regions implicated in viral adaptation and host switching.

By 2014, clade A viruses had largely disappeared, and clade B became the dominant lineage detected in human infections. During this period, important adaptations also emerged outside the spike gene. One notable example is the nsp6 L232F mutation, which became enriched in human clade B strains, including viruses associated with hospital outbreaks in 2014–2015. Experimental studies show that L232F enhances viral replication in ex vivo human nasal and bronchial tissues and in the lungs of infected mice [259]. These findings suggest that once MERS-CoV enters the human population, it can acquire additional mutations that increase replication efficiency in the human airway, potentially contributing to the persistence or severity of localized outbreaks.

Further variation was observed during specific outbreak events. In the 2014 Jeddah outbreak, four characteristic single-nucleotide polymorphisms relative to the EMC/2012 reference genome were identified in the viruses sampled at the time in cluding L411F substitution in the RBD. Because viable virus could not be isolated for functional analysis, these sequence differences were considered unlikely to explain the sharp increase in cases; instead, the outbreak was attributed largely to healthcare-associated amplification [260]. By contrast, during the 2015 South Korea outbreak, two RBD substitutions—D510G and I529T—were detected in most human infections [261]. Experimental studies demonstrated that these substitutions reduce sensitivity to antibody-mediated neutralization without significantly altering receptor binding or entry efficiency. Therefore, these mutations may not enhance intrinsic transmissibility but could facilitate increased viral spread within infected individuals and reduce susceptibility to neutralizing antibodies [262].

Between 2015 and 2019, MERS-CoV remained relatively stable, likely due to the low number of reported cases and the absence of major outbreaks. Viral isolates from this period still accumulated several amino-acid substitutions, including changes in ORF1ab, the N protein, the spike protein, and ORF4b. During this time, lineage 5 emerged as a successful clade with clear functional advantages. Experimental comparisons showed that lineage 5 viruses replicate more efficiently than earlier strains, induce lower levels of interferon and cytokines, and are less sensitive to interferon pretreatment in Calu-3 cells, exhibiting approximately a ten-fold replication advantage [263]. These findings indicate that lineage 5 increases viral fitness through more efficient replication and an enhanced ability to interfere with interferon responses.

By 2020, reduced testing and fewer human cases limited the availability of recent MERS-CoV sequences, but surveillance in camels shows that lineage B—particularly lineage 5—continues to circulate. In 2023–2024, MERS-CoV was detected in about 39 percent of sampled camels, and a B5-2023 clade was identified. Across its sublineages, 25 amino-acid substitutions and two deletions were found in the spike protein, including changes in the RBD and N-terminal domain. Notably, the RBD substitutions L495P and V527L occur on the exposed ridge of the receptor-binding motif, a major target of human neutralizing antibodies, while A763S in the cathepsin-L cleavage site may affect spike

activation in cells lacking TMPRSS2 [252]. These mutations may influence receptor binding or immune evasion and warrant further investigation.

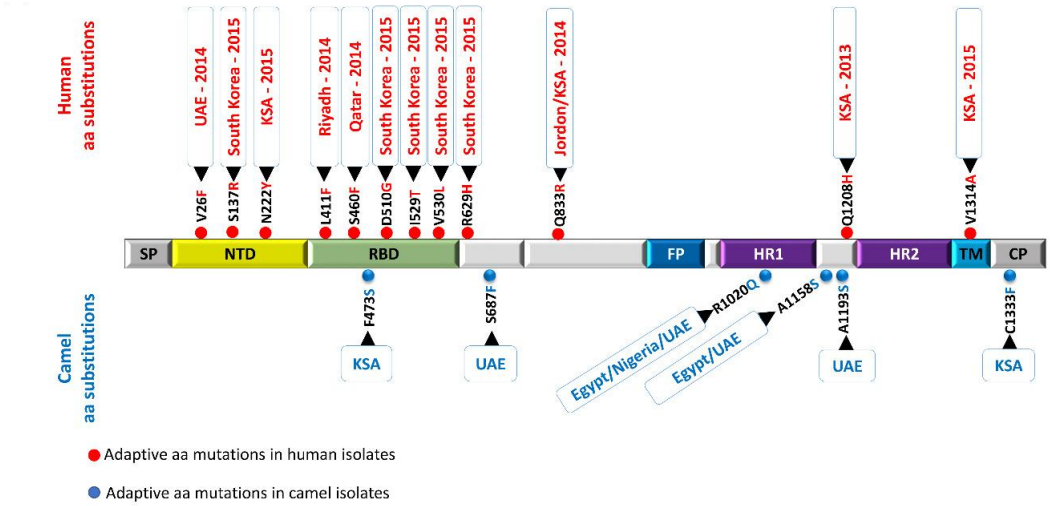


Figure 1-11. Selected amino-acid substitutions in the MERS-CoV spike protein

Schematic structure CoV S protein and its functional domains, including the N-terminal domain (NTD), receptor-binding domain (RBD), receptor-binding motif (RBM), fusion peptide (FP), heptad repeat region 1 and 2 (HR1 and HR2), transmembrane region (TM), and cytoplasmic tail (CP). Human-associated substitutions are shown in red and camel-associated substitutions are shown in blue. Figure is reproduced from [218].

1.7.4 Immune pathogenesis

DPP4, the cellular receptor for MERS-CoV, is broadly expressed across multiple tissues, including the kidney, intestinal tract, liver, and vascular endothelium, as well as the lower respiratory tract. This widespread distribution provides a biological basis for the multisystem involvement and organ dysfunction reported in severe MERS cases. Within the lungs, MERS-CoV preferentially infects DPP4-expressing bronchial non-ciliated epithelial cells, alveolar type I and II pneumocytes, endothelial cells, and alveolar macrophages, accounting for its tendency to cause severe lower-respiratory tract disease and pneumonia [264]. In vitro studies further demonstrate that MERS-CoV can replicate in kidney, intestinal, and hepatic cell lines, supporting its capacity for extrapulmonary infection [265]. Consistent with these findings, postmortem examinations from fatal cases have revealed viral particles and tissue injury in both the lung and kidney [235].

The key steps of MERS-CoV genome organisation and replication are summarised in Figure 1-12. After binding to DPP4 and entering the host cell, MERS-CoV releases its genome into the cytoplasm and rapidly produces viral proteins that antagonize the type I/III interferon system and allow infection to be established. Several accessory proteins—most notably ORF4a and ORF4b—suppress IFN induction and signalling, as shown in multiple mechanistic studies. ORF4a blocks IFN-β promoter activation and IRF-3/7, NF-κB, and ISRE pathways [266], while ORF4b interferes with nuclear import proteins to

inhibit NF-κB–dependent responses [267]. Additional proteins, including M, ORF5, and ORF8b, further dampen IFN expression according to recent reports [266, 268]. Deletion of these antagonists (ORF3, ORF4a, ORF4b, ORF5) leads to enhanced IFN responses and reduced viral replication in cell culture and mouse models [269, 270]. Importantly, studies in mice show that early IFN treatment can limit viral replication and disease severity, underscoring the central role of IFN antagonism in MERS-CoV pathogenesis. The importance of intact interferon (IFN) responses is further underscored by analyses of bronchoalveolar lavage and serum from two patients with different clinical outcomes: the fatal case exhibited markedly reduced IFN-α, IL-12, and IFN-γ, whereas the surviving patient showed no such suppression [271, 272].

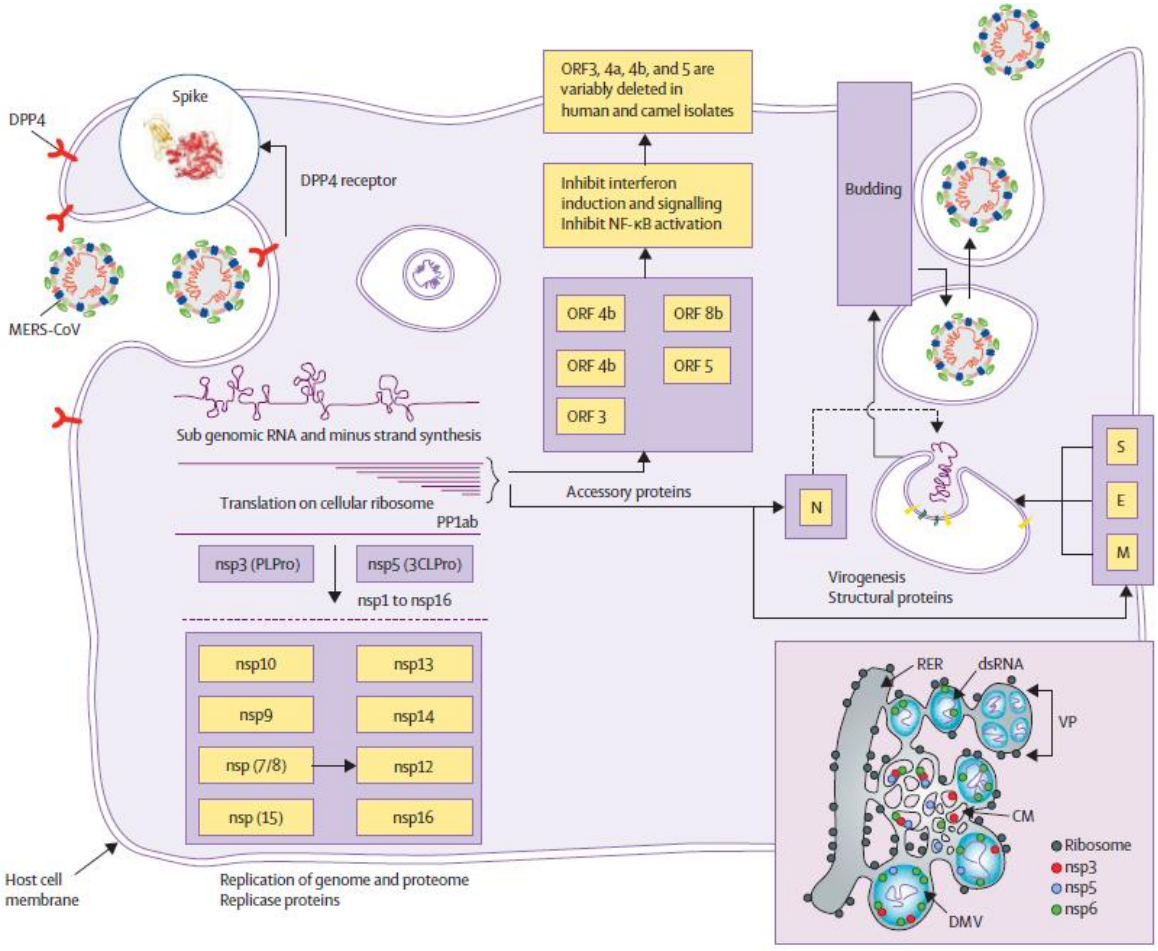


Figure 1-12. MERS-CoV replication.

The MERS-CoV genome encodes two large replicase polyproteins that are cleaved into 16 non-structural proteins forming the replicase–transcription complex. Structural (S, E, M, N) and accessory proteins (ORFs 3, 4a, 4b, 5, 8b) are located in the 3′ region of the genome. Viral entry occurs through spike binding to the DPP4 receptor and protease-mediated activation, followed by fusion and release of the genome into the cytoplasm. RNA synthesis takes place on virus-induced membrane structures, including double-membrane vesicles. Subgenomic RNAs encode structural and accessory proteins, and assembled virions bud into the ER–Golgi compartment before release from the cell. Reproduced from [273].

MERS-CoV can also infect innate immune cells; infection of macrophages leads to increased production of cytokines and chemokines [274], which is thought to enhance neutrophil infiltration and amplify inflammation. Infection of DC enables viral dissemination throughout the host [275] and contributes to dysregulated immune responses, including aberrant cytokine production and impaired antigen-presentation pathways.

Innate cellular responses in MERS include activation of DCs, alveolar macrophages and recruited monocytes/neutrophils that release cytokines and chemokines (for example TNFα, IL-6, IL-8 and others) and thereby recruit additional inflammatory cells into the lung. However, because the virus can dampen early interferon signalling, the initial antiviral state may be delayed or reduced, permitting high viral loads in the lower airway and promoting downstream inflammation and lung injury [274, 276, 277]. Animal and *ex-vivo* human lung studies support productive MERS-CoV replication in alveolar cells together with inflammatory responses that contribute to alveolar damage [278].

Murine studies demonstrate caspase-1 activation in the spleen accompanied by high circulating IL-1β, indicating robust inflammasome activation that may contribute to increased complement signalling during infection [279]. The role of complement in the enhancement of MERS-induced disease has been explored in a mouse challenge model: treatment with anti-C5aR mAb before challenge (to block the C5-C5aR axis) was associated with controlled local and systemic inflammatory response, decreased viral replication in lungs, and reduced spleen and lung damage [280]. In humans, elevated complement was higher in non-survivors [281].

Collectively, these findings demonstrate that MERS-CoV accessory proteins, together with infection of innate immune cells, subvert host defences and create a replication-permissive environment that drives disease progression [268].

MERS-CoV interacts with the adaptive immune system in several important ways. Experimental studies have shown that the virus can infect human T cells *in vitro*, including T cell from peripheral blood, spleen, and tonsils [282]. In marmoset models, T-cell infection leads to pronounced apoptosis, a process believed to enhance pathogenesis by depleting critical immune cell populations and impairing antiviral responses [282]. Despite this immunopathology, MERS-CoV infection triggers detectable virus-specific adaptive immunity. Both T-cell and B-cell responses arise following infection, with $CD4^+$ and $CD8^+$ T cells targeting several structural antigens, including the spike protein, membrane protein, and nucleocapsid protein. A higher frequency of activated $CD8^+$ T cells has been observed in patients with moderate to severe disease in the acute stage [283], suggesting a relationship between disease severity, viral antigen burden, and the magnitude of the cytotoxic T-cell response, or alternatively, $CD8^+$ T cells contributing to immunopathogenesis.

Seroconversion in MERS-CoV infection generally occurs within the first 2 weeks after symptom onset [284]. Critically ill patients who seroconvert early show significantly better survival than those who do not [285], suggesting that a rapid humoral response contributes to improved clinical outcomes. The magnitude and durability of neutralising antibodies correlate with disease severity, with higher and more persistent titres observed in patients who experienced more severe illness. In contrast, individuals with mild disease often fail to develop detectable neutralising antibodies [286], indicating that low-level infection may not provide sufficient antigenic stimulation to induce a measurable or durable humoral response.

Notably, neutralising antibody titres do not correlate with viral load in the lower respiratory tract, implying that immune mechanisms other than humoral immunity—particularly innate antiviral pathways and T-cell responses—likely work together to control viral replication in these patients. This heterogeneity highlights that while early seroconversion is beneficial in severe disease, effective viral control in mild cases may depend more on non-humoral branches of the immune response.

1.7.5 MERS protective immunity

In the case of MERS-CoV, an optimal vaccination strategy is particularly important, because protection is not mediated by a single immune arm. Neutralising antibodies reduce pathology and viral load in animal models after challenge or passive transfer [287, 288]. T-cell studies show that $CD8^+$ cells help control disease but are insufficient for clearance [289], and in human survivors both $CD4^+$ and $CD8^+$ responses are consistently detected, while antibody titres correlate only weakly with viral load during the acute stage [284]. These findings suggest that durable protection requires coordinated activity of both antibodies and T cells.

1.7.6 MERS-CoV in the Context of Human Coronaviruses

Although MERS-CoV is genetically distinct from other human coronaviruses, comparative analysis of the spike glycoprotein reveals patterns of sequence conservation, with important implications for immunity and vaccine design. Quantitative comparison of MERS-CoV spike sequences with representative human coronaviruses demonstrates consistently higher sequence similarity within the S2 vs. the S1 subunit (Table 1-6.), reflecting strong evolutionary constraints on elements essential for viral entry.

To further localize conserved determinants, peptide-level similarity analysis using overlapping 15-mer peptides across the MERS-CoV spike protein was performed and compared with spike sequences from endemic and highly pathogenic human coronaviruses (Figure 1-). This identified discrete regions of local sequence conservation shared between MERS-CoV and other betacoronaviruses, including OC43, HKU1, SARS-CoV-1, and SARS-CoV-2. These conserved peptide regions are not readily apparent

from full-length amino acid alignments but may be immunologically relevant, particularly for T-cell–mediated immune responses.

The presence of conserved spike regions across antigenically distinct coronaviruses is particularly relevant in the context of immune imprinting, especially in the post–SARS-CoV-2 era. Extensive population-level exposure to SARS-CoV-2 through infection and vaccination has demonstrated that pre-existing immunity can preferentially recall responses targeting conserved epitopes upon subsequent heterologous exposure. Such recall may contribute to cross-reactive immunity but may also constrain the induction of novel responses against more variable regions. In the case of MERS-CoV, conserved peptide regions shared with other human coronaviruses provide a framework for considering how prior coronavirus exposure, including SARS-CoV-2, could influence both natural and vaccine-induced immune responses.

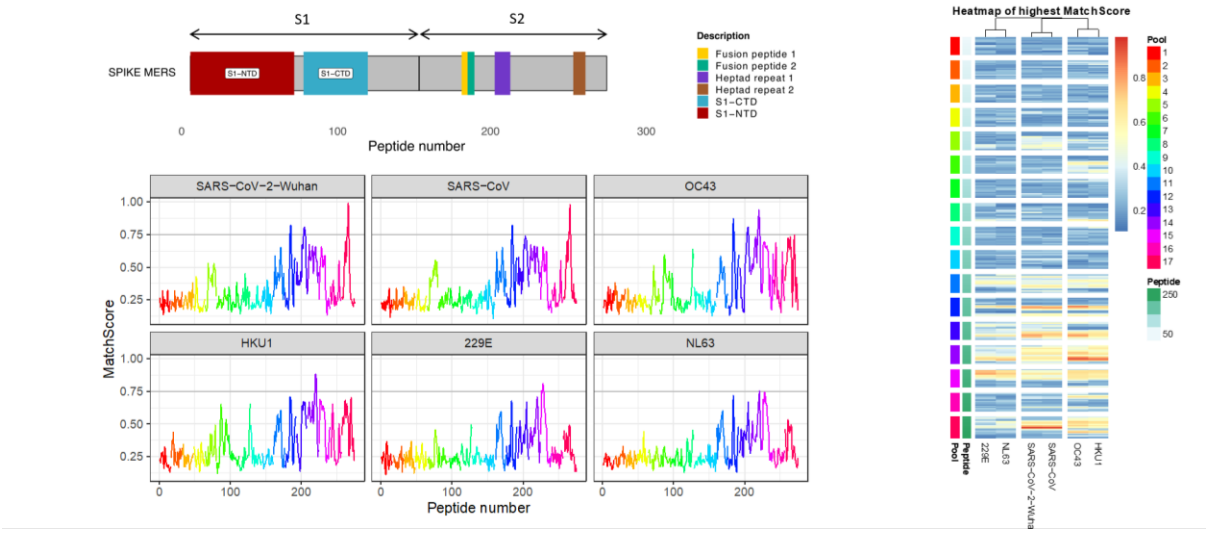


Figure 1-13. Peptide-level similarity analysis of the MERS-CoV spike protein across human coronaviruses.

The MERS-CoV spike protein was divided into overlapping 15-mer peptides spanning the S1 and S2 regions in Supplementary table 8.1.4.1.5 and compared with spike sequences from SARS-CoV-2, SARS-CoV-1, OC43, HKU1, 229E, and NL63. Line plots show peptide match scores along the spike sequence, and the heatmap summarizes the highest match scores across peptide pools. Localized regions of sequence similarity, particularly within S2, are evident despite limited overall amino acid similarity. highest MatchScore for each MERS Spike peptide was computed, and displayed in heatmap and line charts. A MatchScore of 0.75 or higher was considered as a high similarity score.

Virus (Accession number)	S1 (%)	S2 (%)	Overall (%)
HCoV-HKU1 spike (Q0ZME7)	21	42	30
HCoV-OC43 spike (P36334)	19	43	29
SARS-CoV2 (NC_45512.2)	20	42	29
HCoV-229E (Y10052.1)	12	30	20
HCoV-NL63 spike (JX504050.1)	13	33	13

Table 1-6. Sequence similarity between the MERS-CoV spike protein and other human coronaviruses. Percent amino acid identity between the MERS-CoV spike protein (accession number: QBM11748) and spike proteins from human coronaviruses (HKU1, OC43, SARS-CoV-2, 229E, and NL63) is shown for the S1 and S2 subunits and for the full-length spike protein. Higher sequence similarity is observed within the S2 subunit compared with S1 across all viruses analysed, consistent with greater conservation of regions involved in membrane fusion.

1.8 MERS-CoV Vaccine

Despite ongoing research, no licensed vaccine is currently available for the prevention of MERS-CoV. A summary of the different categories of MERS-CoV vaccine platforms is shown in Table 1-7. The most extensively studied approaches include viral-vectored vaccines such as HAd [290], ChAd [291, 292], MVA [293-295], vesicular stomatitis virus (VSV) [296], and other recombinant adenoviral vectors, several of which have progressed into clinical evaluation. Genetic vaccine approaches, including DNA [297] and mRNA platforms [298], have also been developed to induce expression of the MERS spike antigen and have benefited considerably from advances made during the COVID-19 pandemic. Protein-based vaccines, namely protein subunit [299] and protein nanoparticle formulations [300], represent another major category, designed to present the spike antigen in its immunogenic prefusion conformation; recent candidates incorporate the stabilized MERS S-2P [301] to enhance immune responses. Additional strategies include virus-like particle (VLP) vaccines, which mimic viral structure without containing genetic material, and whole-virus vaccines such as live-attenuated [302] and inactivated approaches [303], though these remain largely experimental due to safety and production challenges. The vast majority of candidate vaccines target the MERS-CoV spike protein or its key functional domains, including the S1 and S2 subunits and the RBD, reflecting their central role in viral entry and immune recognition.

To guide global vaccine development priorities, the WHO has outlined target product profiles for three key use cases [304]: vaccines for dromedary camels to reduce zoonotic transmission from animals to humans; long-term human vaccines intended for high-risk groups such as healthcare workers; and reactive-use human vaccines capable of generating rapid immunity during outbreak situations. These priorities reflect the need for tailoring vaccination strategies to the MERS-CoV epidemiology.

The Coalition for Epidemic Preparedness Innovations (CEPI) has invested in five MERS-CoV vaccine candidates; this advanced preparedness for MERS-CoV but also provided critical scientific groundwork that facilitated the rapid development of COVID-19 vaccines. Three of the five MERS-CoV candidates remain in active development. ChAdOx1-MERS and MVA-MERS-S represent the leading candidates to reach human testing, and are covered in later subsections. A plasmid DNA vaccine expressing full-length MERS-CoV spike protein (GLS-5300) completed phase I/IIa clinical testing and demonstrated acceptable safety and immunogenicity in healthy adults [297, 305]. However, further development was discontinued following a strategic decision by CEPI, which, according to public statements from the

developer, reflected that the candidate did not meet CEPI's criteria for progression, although these criteria were not publicly disclosed [306].

Candidate	Platform or technology	MERS antigen (s)	Developers	Stage
rAd/Spike	Recombinant adenovirus	Full-length S	Ewha Womans University (Chang Lab)	Preclinical
Ad5.MERS-S	Recombinant adenovirus	Full-length S	Graduate School of Pharmaceutical Sciences, Ewha Woman's University, Seoul, Republic of Korea	Preclinical
ChAdOx1 MERS	Recombinant adenovirus	Full-length S	University of Oxford & Barinthus Biotherapeutics	Phase I
MVA-MERS-S	MVA vector	Full-length S	IDT Biologika GmbH	Phase I
VSVΔG-MERS	Recombinant attenuated VSV vector	Full-length S	Harbin Veterinary Research Institute, Chinese Academy of Agricultural Sciences, China	Preclinical
MV_{vac2}-MERS-S(H)	MV MERS-S (Measles vector)	Full-length S	Themis Bioscience GmbH	Preclinical
GLS-5300 MERS	Plasmid DNA	Full-length S	GeneOne Life Science and Inovio Pharmaceuticals	Phase I
MERS-CoV RBD-mRNA	mRNA	RBD	Kimball Research Institute, New York Blood Center, New York, USA.	Preclinical
Multiple under testing	Protein nanoparticle	Multiple under testing	Uvax Bio	Preclinical
MERS SClamp	Protein Subunit	Full-length S	The University of Queensland	Preclinical
MERS-CoV VLP	VLP	Full-length S	Department of Molecular and Cell Biology, Centro Nacional de Biotecnología (CNB-CSIC), Madrid, Spain	Preclinical
rSRV9-$MERS_{S1}$	Inactivated rabies virus-vectored MERS-CoV vaccin	S1	Changchun Veterinary Research Institute, Chinese Academy of Agricultural Sciences, Changchun, China	Preclinical
MERS-CoV-E*Δ2	Attenuated Virus	Virus	Universidad Autonoma de Madrid, Spain	Preclinical
Whole inactivated virus (WIV)	Inactivated Virus	Virus	University of Texas Medical Branch (UTMB); Jazan University	Preclinical

Table 1-7. MERS-CoV vaccine candidates across major vaccine platforms.

1.8.1 ChAdOx1 MERS vaccine candidate

The ChAdOx1 MERS vaccine is based on the full-length MERS-CoV spike (S) gene (GenBank: KJ65008.1). The sequence was codon-optimized for human expression, and a 32-amino-acid human tissue plasminogen activator (tPA) signal sequence was added at the N-terminus to further enhance expression; the addition of tPA improves *in-vivo* immunogenicity [307], although the underlying mechanisms remain unclear. The tPA–spike sequence was synthesized by GeneArt (Thermo Fisher Scientific), cloned into a transgene expression plasmid containing a modified human cytomegalovirus (CMV) immediate early promoter with tetracycline operator sites and a bovine growth hormone

polyadenylation signal. This expression cassette was then inserted into the E1 region of the replication-deficient ChAdOx1 vector, following methods described previously [104].

Immunogenicity studies in BALB/c mice demonstrated that a single vaccine dose elicited robust immune responses, including strong neutralising antibody and $CD8^+$ T-cell activity. The antibody titres induced by one dose were comparable to those achieved with a two-dose MVA-based regimen, and these responses were further augmented by heterologous boosting with MVA [307].

Challenge models for preclinical evaluation of MERS-CoV vaccine efficacy are constrained by the limited distribution of the DPP4 receptor, which restricts productive viral infection to certain animal species [308]. Consequently, most efficacy studies rely on transgenic mice expressing human DPP4 [309] and on non-human primates such as rhesus macaques and marmosets. Rhesus macaques typically develop mild to moderate disease, whereas marmosets display more severe pathology that better mirrors human MERS [310-313]. However, despite their closer resemblance to human disease, marmosets are used less frequently because their small size makes clinical monitoring, repeated sampling, and certain procedures technically challenging [308].

Challenge studies showed that a single dose of ChAdOx1 MERS completely protected susceptible hDPP4 mice from lethal infection with six genetically diverse MERS-CoV strains across clades A, B, and C [314, 315]. In rhesus macaques, vaccination significantly reduced viral replication and resulted in reduced radiological and histopathological disease scores. Although one dose was sufficient for protection, animals given a prime–boost regimen had even lower viral loads, indicating superior efficacy. Although NHPs were only challenged with one strain, sera from vaccinated animals showed in vitro neutralising activity against all of the panel of six viruses tested in hDPP4 mice [315]. In dromedary camels, the vaccine elicited robust immune responses, with neutralising antibodies detectable in nasal swabs. Indeed, vaccination markedly reduced nasal discharge and viral shedding in a stringent natural transmission model [160]. Although it did not achieve sterile immunity, this suggests the vaccine's potential to limit camel-to-camel transmission and, consequently, reduce the likelihood of onward transmission to humans.

The safety and immunogenicity of ChAdOx1 MERS have been evaluated across three phase 1 clinical trials. The first two studies—MERS001 (UK, 2018) and MERS002 (Saudi Arabia, 2019)—were open-label, non-randomised, dose-escalation trials conducted before the COVID-19 pandemic and enrolled healthy adults aged 18–55 years [291, 292]. Participants received a single intramuscular (IM) dose of 2.5×10^9, 5×10^9, or 5×10^{10} viral particles (vp). The vaccine demonstrated an acceptable safety profile, with no serious adverse events reported. A single dose elicited strong MERS-specific cellular and humoral immune responses. Total spike-specific IgG responses, measured by binding ELISA, were comparable between the two trials [292]. In MERS001, neutralisation assays using live virus and

pseudotyped viruses representing three strains—MERS-CoV EMC/2012, KOR/KNIH/002, and England-1—showed the highest seropositivity rates at the 5×10^{10} dose [291]. These findings contributed to the trajectory of vaccine development and to the regulatory confidence that ultimately supported the rapid authorization of the ChAdOx1 SARS-CoV-2 vaccine.

The post-pandemic MERS003 trial, a double-blind, placebo-controlled phase Ic study conducted in the UK, extended earlier findings to older adults aged 50–70 years—an age group representing one of the most vulnerable populations for severe MERS disease. In this most recent study, participants received two doses of 5×10^{10} vp administered 84 days apart, with saline placebo serving as a control. Assessments are ongoing. The primary objective is to evaluate safety, tolerability, and reactogenicity in this high-risk group, with immunogenicity as a secondary endpoint. To examine the influence of prior adenoviral-vector exposure, participants were stratified according to whether they had previously received a ChAdOx1-based vaccine. Overall MERS001, MERS002, and MERS003 evaluate vaccine response in MERS-CoV endemic regions and high-risk populations.

1.8.2 MVA-MERS

The MVA vector has been extensively explored as a platform for vaccine development against Middle East respiratory syndrome coronavirus (MERS-CoV). The recombinant, replication-deficient MVA-MERS construct encodes the full-length MERS-CoV spike (S) protein (derived from GenBank accession JX869059, S sequence produced synthetically). In preclinical studies, MVA-based vaccination generated neutralising antibodies in BALB/c mice [316], and induced both neutralising antibodies and $CD8^+$ T-cell responses in DPP4-transgenic mouse models following IM or SC delivery [317]. In dromedary camels, a two-dose intranasal and IM regimen elicited strong systemic and mucosal immune responses, reduced viral shedding, and conferred protection correlated with neutralising antibody levels [318].

Clinical development of MVA-MERS-S began with a first-in-human phase 1 trial conducted between 2017 and 2019. In this study, 23 adults received two doses of either 1×10^7 or 1×10^8 plaque forming units (PFU) administered 28 days apart. The vaccine was well tolerated and induced both humoral and cellular immune responses against the MERS-CoV S1 antigen. Seroconversion occurred in most participants, although antibody titres declined within six months [294]. To assess longer-term immunity, ten participants were offered a delayed booster dose approximately one year after the primary series, with seven individuals subsequently monitored for an additional two years [293]. Both antibody and T cell responses were sustained for at least 24 months following this delayed third dose [319].

A phase 1b, multicentre, double-blind, randomised, placebo-controlled trial was conducted in Hamburg and Rotterdam (NCT04119440) [295]. Healthy adults aged 18–55 years received three IM doses of $1x10^7$ or $1x10^8$ PFU of MVA-MERS-S, with either 28- or 56-day intervals between the first two doses,

and the third dose was administered 224 days after the first. MVA-MERS-S demonstrated an acceptable safety profile with no vaccine-related serious adverse events. Vaccination induced measurable antibody and T-cell responses, and the $1x10^8$ PFU dose produced stronger humoral immunity when the second dose was given 56 rather than 28 days after the first.

Two generations of MVA-vectored MERS vaccines have been developed by IDT Biologika GmbH (Dessau, Germany), a biopharmaceutical manufacturer specialising in viral-vector vaccine production. The second-generation vaccine was designed to enhance antigen expression compared with the original vaccine produced on primary chicken embryo fibroblast (CEF) cells. This updated manufacturing platform employed the DF-1 cell line (immortalised continuous CEF cells); this enabled more efficient viral production, with a 2.4- to 3.4-fold increase in viral yield. Both approaches demonstrated comparable immunogenicity in BALB/c mice, eliciting similar neutralising antibody titres, T-cell responses, and viral clearance following MERS-CoV challenge. Preclinical safety, including repeat-dose toxicology evaluation in rabbits, confirmed an acceptable tolerability profile [295]. The first-generation MVA-MERS-S vaccine was evaluated in phase I/phase Ib clinical trials, whereas the second-generation DF-1–based vaccine progressed to phase IIa clinical evaluation [294, 295, 297].

MVA-MERS was constructed using the vaccinia virus early/late promoter mH5 (also referred to as PmH5 in some publications) to drive spike protein expression [316]. Early preclinical work in our lab also evaluated an alternative MVA construct employing the vaccinia F11 promoter. Although overall immunogenicity was broadly comparable between promoter systems, a homologous F11/F11 prime–boost regimen elicited significantly higher IFN-γ responses than the corresponding mH5-based schedule [307].

1.9 Aim and objectives of the Present Study

Aim

To optimize MERS vaccine responses to strengthen preparedness for future MERS outbreaks through both proactive and reactive vaccination strategies

Objectives

- To evaluate the magnitude, Fc-mediated functionality, and cross-reactivity of the antibody response to MERS-CoV vaccination, and to determine how these features are shaped by population differences and prior coronavirus exposure.
- To understand how immune imprinting and post-pandemic exposure to SARS-CoV-2 influence the quality and breadth of vaccine-induced MERS-CoV immunity.
- To assess homologous Omicron's subvariaChAdOx1 MERS vaccination strategies for improved immunogenicity in vulnerable populations.

- To optimize the ChAdOx1–MVA heterologous viral-vectored platform for enhanced immune potency and breadth.

2 Study Design and Experimental Methods

This chapter describes the experimental procedures used to evaluate immune responses in clinical and pre-clinical settings. Clinical analyses included serum and plasma samples from individuals vaccinated with the ChAdOx1 MERS candidate vaccine, convalescent MERS patients sampled before and after the COVID-19 pandemic, and unexposed control participants, with or without SARS-CoV-2 exposure. Pre-clinical studies assessed immune responses in mice immunised with ChAdOx1 MERS and MVA-MERS-S vaccines to optimise heterologous vaccination strategies.

Humoral immune responses were characterised using enzyme-linked immunosorbent assay (ELISA) to quantify MERS-CoV spike-specific IgG, isotypes, and subclasses, alongside pseudovirus neutralisation (PNA) assays to assess neutralising activity. SARS-CoV-2–specific antibody responses were assessed at the individual level to investigate immune imprinting and cross-reactive recall responses. Fc-mediated effector potential and antibody cross-reactivity with SARS-CoV-2 and endemic human coronaviruses were evaluated using Luminex-based Fcγ receptor binding assays, with antibody avidity assessed by avidity ELISA. Cellular immune responses were analysed using interferon-γ enzyme-linked immunospot assays (IFN-γ ELISpot) and intracellular cytokine staining (ICS) by flow cytometry, using peripheral blood mononuclear cell (PBMCs) for clinical studies and spleen and BM for pre-clinical studies. Spike-specific B-cell memory responses were additionally assessed in mice.

2.1 Reagents and solutions

All commercially available reagents and materials used in this study are listed in Table 2-1. Buffers and media prepared in-house are detailed in Table 2-2. Flow cytometry antibodies and staining panels used for phenotyping and ICS are summarised in Table 2-3, Table 2-4, Table 2-5 for human assays, and Table 2-6 for mouse assays.

Table 2-1. Commercially available reagents and materials used in this study

Reagent	Supplier	Catalogue number
0.45 µM cellulose acetate filter	Millipore	HABG04700
2.5mL syringes		
0.5 mL Amicon ultrafiltration device	Merck Millipore	UFC501096
10 L PBS powder	Thermo Fisher Scientific (Invitrogen)	21600-069
10 mM MEM Non Essential Amino Acids	Thermo Fisher Scientific (Invitrogen)	11140-050
15 mL falcons	Corning Incorporated	430052
175 cm^2 tissue culture flask	Corning Incorporated	431080
25cm^2 tissue culture flask	Corning Incorporated	430639
4% paraformaldehyde in PBS	Biotium	22023
4-Nitrophenyl Phosphate Tablets (20 mg)	Merck Life Sciences	N2765
5 mL polypropylene FACS tubes	Becton Dickinson	352063

50 mL falcons	Corning Incorporated	430290
6 well culture plates	Corning Incorporated	3516
70 μM Falcon™ Cell Strainers	Fisher Scientific	352350
75cm^2 tissue culture flask	Corning Incorporated	430641
96-well Microplates	Greiner Bio-One	655096
96-well solid black assay plate, non-treated	Corning/SLS	3915
96-well tissue culture plate	Nunc	167008
AlumaSeal® film, non-sterile	Merck Life Sciences	Z722634-100EA
Aluminum foil	Scientific Laboratory Supplies Limited	ALU1005
Amicon® Ultra Centrifugal Filter, 50 kDa MWCO	Merck Life Sciences	UFC505096
Anti-IgG Biotinylated antibody	Mabtech	3825-2H
Aspirator and aspirating pipettes		
Bio-Plex Amine Coupling Kit	Bio-Rad Laboratories	171406001
Bio-plex Pro Magnetic COOH Beads	Luminex Corporation	MC10013-01, MC10018-01, MC10019-01, MC10021-01, MC10029-01, MC10034-01, MC10035-01, MC10037-01, MC10043-01, MC10046-01, MC10052-01, MC10055-01
Blocker Casein in PBS	Thermo Fisher Scientific (Thermo Scientific)	37528
Bovine serum albumin (BSA)	Thermo Fisher Scientific (Thermo Scientific)	A9418
BrightGlo	Promega	E2620
BSA Powder	Merck Life Sciences	A7906-100G
Counting Chamber Slides	Thermo Fisher Scientific (Invitrogen)	C10228
Dimethyl sulphoxide (DMSO)	Merck Life Sciences	D2650
Dulbecco's Modified Eagle Media (DMEM)	Thermo Fisher Scientific (Gibco)	21969035
Dulbecco's Modified Eagle Media (DMEM) (Phenol red free)	Thermo Fisher Scientific (Gibco)	31053-028
Dulbecco's phosphate buffered saline (DPBS)	Merck Life Sciences	D8537
Dulbecco's phosphate buffered saline (DPBS)	Thermo Fisher Scientific (Gibco)	14190250
eBioscienceTM Cell Stimulation Cocktail (PMA/ionomycin)	Thermo Fisher Scientific (Invitrogen)	00-4970-03
EasySeal® plate sealer, transparent	Greiner Bio-One	676001
ELISPOT AEC Substrate Set	BD Bioscience	551951
Elispot Colour Development Kit	Bio-Rad Laboratories	170-6432
Fisherbrand™ Polypropylene Microcentrifuge Tubes, 1.5 mL	Thermo Fisher Scientific (Thermo Scientific)	FB74031
Fetal Bovine Serum (FBS)	Merck Life Sciences	F2442
FuGENE-HD	Promega	E2311
Geneticin 50 mg/mL solution	Thermo Fisher Scientific (Invitrogen)	10131-027
gentleMACS Dissociator	Miltenyi Biotec	130-093-235
gentleMACS™ C Tubes	Miltenyi Biotec	130-096-334
Goat anti mouse IgG	Mabtech	3825-2H
Goat anti-human IgA-AP	SouthernBiotech	2050-04

Goat anti-human IgG (γ-chain)-AP	Sigma-Aldrich	A3187
Goat anti-human IgM-AP	SouthernBiotech	D2219-X540
Goat Anti-Mouse IgA-AP	Southern Biotech	1040-04
Goat Anti-Mouse IgG1-AP	Southern Biotech	1071-04
Goat Anti-Mouse IgG2a-AP	Southern Biotech	1081-04
Goat Anti-Mouse IgG2b-AP	Southern Biotech	1091-04
Goat Anti-Mouse IgG3 heavy chain	Abcam	ab98705
Goat Anti-Mouse IgG-AP	Sigma-Aldrich	A3562
Goat Anti-Mouse IgM-AP	Abcam	ab98672
GolgiPlug (Brefeldin A)	BD	555029
HRP-detection antibody	Mabtech	3825-2H
Human Fc receptor CD16A/Fcgr3a	Native antigen	REC32069
Human Fc receptor CD16B/Fcgr3b	Native antigen	REC32071
Human Fc receptor CD32A/Fcgr2a	Native antigen	REC32070
Human Fc receptor CD32B/Fcgr2b	Native antigen	REC32068
IFN-gamma ELISpot ALP Kit	Mabtech	3321-2A
Magnetic 96-Well Separator	Thermo Fisher Scientific (Invitrogen)	A14179
Magpix® drive fluid	Thermo Fisher Scientific (Invitrogen)	4050030
MAIP ELISpot Plates	Merck Life Sciences	MAIPS4510
MERS-CoV Spike S1+S2 Protein	Sinobiological	40069-V08B-B
MERS-CoV Spike/S1 Protein	SinoBiological	40069-V08B1
MERS-CoV Spike/S2 Protein	SinoBiological	40070-V08B
MERS-CoV–specific peptide (VYDTIKYYSIIPHSI)	Mimotopes	Custom made
MERS-CoV–specific full spike peptides	ProImmune Ltd., thinkpeptides	Custom made
MidiPrep Kit	Qiagen	12143
Mouse anti-human IgG1 Fc-AP	SouthernBiotech	9054-04
Mouse anti-human IgG3 Hinge-AP	SouthernBiotech	9210-04
Mouse CD32 / FCGR2B Protein	SinoBiological	50030-M27H-B
NUNC Immuno Plates	Thermo Fisher Scientific (Thermo Scientific)	442404
Opti-MEM™	Thermo Fisher Scientific (Gibco)	31985062
Penicillin-streptomycin	Thermo Fisher Scientific (Gibco) Merck Life Sciences	25030164 P0781
Phospha-Light™ SEAP Reporter Gene Assay System	Thermo Fisher Scientific (Invitrogen)	T1017
Phosphate Buffered Saline (without Ca^{2+} and Mg^{2+})	Merck Life Sciences Thermo Fisher Scientific (Gibco)	D8537 14190
Pierce™ Diethanolamine Substrate Buffer (5X)	Thermo Fisher Scientific (Thermo Scientific)	34064
Reagent Reservoirs (Costar 4870)	Merck Life Science	CLS4870
Recombinant Mouse CD16/FCGR3/Fc gamma RIII Protein (ECD, His & AVI Tag), Biotinylated, HPLC-verified	SinoBiological	50326-M27H-B
Recombinant Mouse CD16-2/FCGR4/Fc gamma RIV Protein	SinoBiological	50036-M27H-B
Recombinant Mouse CD64/FCGR1 Protein	SinoBiological	50086-M27H-B
SARS-CoV2 Spike		
SARS-CoV-2 Spike S1 Subunit protein	R&D Systems	10569-CV
SARS-CoV-2 Spike S2 Subunit protein	R&D Systems	10549-CV
Sodium thiocyanate solution	Sigma-Aldrich	80518
Stericup Quick Release-GV Sterile Vacuum Filtration System	Merck Life Sciences	S2GVU11RE
Streptavidin, R-Phycoerythrin Conjugate (SAPE)	Thermo Fisher Scientific (Invitrogen)	S866

TrypLE™ Express	Thermo Fisher Scientific (Gibco)	12604013
Tween-20	Merck Life Sciences	P9416
Versene	Merck Life Sciences	15040-066
Vivaspin 500	Sartorius	202000107
V-PLEX® Coronavirus Panel 3 (IgG) Kit.	Meso Scale Discovery	K15399U-2
Water (sterile-filtered, Bioreagent)	Merck Life Sciences	W3500
White 96-well flat-bottom plates	Thermo Fisher Scientific (Thermo Scientific)	10182831

Table 2-2. Buffers and media prepared in this study

Buffer name	Components (with concentration or dilution)	Supplier	Catalogue number	
Developer	4-Nitrophenyl Phosphate Tablets (20 mg)	Merck Life Sciences	N2765	Prepare fresh by diluting 5× DEA buffer to 1× in sterile-filtered Bioreagent Water. Add one 20 mg pNPP tablet per 20 mL, wrap in foil, and mix thoroughly. Use 10 mL per plate (minimum 20 mL total) to develop and read ELISA plates with AP-conjugated antibodies.
	5x Diethanolamine Buffer	Thermo Fisher Scientific	34064	
ACK lysis buffer	NH_4Cl (0.15 M)	Merck	A4514	Adjust pH 7.2–7.4 with 1 N HCl; autoclave
	$KHCO_3$ (10 mM)	Merck	P9144	
	Na_2EDTA (0.1 mM)	Merck	EDS	
Carbonate–Bicarbonate Coating Buffer	Coating buffer capsules	Merck	C3041	Dissolve in Milli-Q H_2O and autoclave — used for coating peptides for ELISPOT plates
Complete DMEM	Dulbecco's Modified Eagle Media (DMEM)	Thermo Fisher Scientific	D6546	Used for routine maintenance and growth of HEK-293/T17 cells for the SARS-CoV-2 PNA assay and preclinical cellular mouse studies
	Fetal Calf Serum (FCS) 10 % (v/v)	Thermo Fisher Scientific	F2442	
	L-Glutamine 200mM (1%)	Thermo Fisher Scientific (Gibco)	25030	
	Penicillin-streptomycin (1%)	Thermo Fisher Scientific (Gibco) Merck Life Sciences	25030164 P0781	
Complete DMEM (Phenol Red–Free, 0% FBS)	Dulbecco's Modified Eagle Media (DMEM) (Phenol red free)	Thermo Fisher Scientific (Gibco)	31053-028	Anti-vectro assay
	Penicillin-streptomycin (1%)	Thermo Fisher Scientific (Gibco) Merck Life Sciences	25030164 P0781	
	L-Glutamine 200mM (1%)	Thermo Fisher Scientific (Gibco)	25030	
Complete DMEM (Phenol Red–Free, 10% FBS)	Dulbecco's Modified Eagle Media (DMEM) (Phenol red free)	Thermo Fisher Scientific (Gibco)	31053-028	Anti-vectro assay
	Fetal Calf Serum (FCS) 10 % (v/v)	Thermo Fisher Scientific	F2442	
	L-Glutamine 200 mM (1%)	Thermo Fisher Scientific (Gibco)	25030	

	Penicillin-streptomycin (1%)	Thermo Fisher Scientific (Gibco) Merck Life Sciences	25030164 P0781	
Expansion medium	β-Mercaptoethanol (1 : 1000)	Gibco	31350-010	B-Cell ELISPOT
	Fetal Calf Serum (FCS) 10 % (v/v)	Thermo Fisher Scientific	F2442	
	L-Glutamine (4 mM)	Thermo Fisher Scientific	G7513	
	Penicillin-streptomycin (1%)	Thermo Fisher Scientific (Gibco) Merck Life Sciences	25030164 P0781	
	Pokeweed mitogen (1 : 100,000)	Merck	L8777-SMG	
	Protein A from Staphylococcus aureus (1 : 10,000)	Merck	P7155-10ML	
	R848 (Resiquimod) (1 : 1000)	Merck	SML0196-10ML	
	RPMI-1640 Medium	Merck	R8758	
GripTite Culture medium	Dulbecco's Modified Eagles Media (DMEM)	Thermo Fisher Scientific	D6546	Used for routine maintenance and growth of GripTite cells
	Fetal Calf Serum (FCS) 10 % (v/v)	Thermo Fisher Scientific	F2442	
	Geneticin 50 mg/mL	Thermo Fisher Scientific (Gibco)	10131-027	
	L-Glutamine 200mM	Thermo Fisher Scientific (Gibco)	25030	
	Non Essential Amino Acids (100X)	Thermo Fisher Scientific (Gibco)	11140-050	
	Penicillin-streptomycin (1%)	Thermo Fisher Scientific (Gibco) Merck Life Sciences	25030164 P0781	
LAB buffer	0.25 µm Stericup Quick Release-GV units	Merck	S2GVU02RE	Prepare 1X PBS from 10X stock (diluted 1:10 with dH_2O), add Tween-20 to 0.05% and BSA to 0.1%. Mix thoroughly, filter through a 0.25 µm Stericup unit, label with preparation date, and store at 4˚C.
	Bovine Serum Albumin (BSA) 0.1 %	Merck Life Sciences	A7906-100G	
	PBS powder	Merck	P3813	
	Tween-20 (0.05%)	Merck Life Sciences	P7949-500ML	
Phosphate-Buffered Saline (PBS) – Sterile	PBS powder	Thermo Fisher Scientific (Invitrogen)	21600-069	Dissolve in Milli-Q H_2O and autoclave. Used for pre-clinical work.
Phosphate-Buffered Saline (PBS) – Non-sterile	PBS powder	Thermo Fisher Scientific (Invitrogen)	21600-069	Dissolve in Milli-Q H_2O. Used for plate washing (non-sterile).
PBS-Tween 20 (PBS-T),	PBS powder	Thermo Fisher Scientific (Invitrogen)	21600-069	Prepared by dissolving PBS powder in deionised water, adding Tween-20 tom mixing thoroughly, and used for ELISA and MSD plate washing.
	Tween-20 (0.05%)	Merck Life Sciences	P7949-500ML	
R10 media	Fetal Calf Serum (FCS) 10 % (v/v)	Thermo Fisher Scientific	F2442	Used for routine maintenance and growth

	L-Glutamine (4 mM)	Thermo Fisher Scientific	G7513	of HUH-7 cells for the MERS-PNA assay
	Penicillin-streptomycin (1%)	Thermo Fisher Scientific (Gibco) Merck Life Sciences	25030164 P0781	
	Fetal Calf Serum (FCS) 10 % (v/v)	Thermo Fisher Scientific	F2442	
	RPMI-1640 Medium	Merck	R8758	

Table 2-3. Antibody panel used for the AIM multiparametric flow cytometry

Marker	Fluorophore	Clone	Supplier	Catalogue No.
CD8	BUV395	RPAT8	BD	563795
CD4	BUV496	SK3	BD	612936
PDL1	BUV615-P	MIH1	BD	624297
CD28	BUV737	L293	BD	748475
CD3	BUV805	UCHT1	BD	612895
CXCR3	BV421	G025H7	Biolegend	353716
CD14	BV510	M5E2	Biolegend	301842
CD19	BV510	HIB19	Biolegend	302242
CCR4	BV605	L291H4	Biolegend	359418
41BB (CD137)	BV650	4B41	BD	564092
CD45RA	BV711	HI100	Biolegend	304137
HLA-DR	BV785	L243	Biolegend	307642
CD40L	AF488	24-31	Biolegend	310815
KLRG1	Percpefluor710	13F12F2	eBioscience	46-9488-41
CD38	BB790-P	HIT2	BD	624296
TIM3	PE	7D3	BD	563422
CD25	PE-CF594	M-A231	BD	562403
CCR6	PECY7	G034E3	Biolegend	353418
CD69	AF647	FN50	Biolegend	310918
CCR7	APCCY7	G043H7	Biolegend	353212
CD27	AF700	0323	Biolegend	302813

Table 2-4. Antibodies used for ICS staining

Marker	Fluorophore	Clone	Supplier	Catalogue No.
CD8	PercpCy5.5	SK1	Biolegend	344710
CD4	AF700	RPAT4	ThermoFisher	56-0049-42
CD3	BV650	17A2	Biolegend	100229
IL-10	PECy7	JE53-9D7	Biolegend	501420
TNF-α	BUV395	MAb11	BD	563996
IL-13	PE	JES10-5A2	Biolegend	501903
IL-4	BV605	MP4-25D2	Biolegend	500828
IFN-y	APC-eFluor 780	4S.B3	Invitrogen	47-7319-42
IL-2	APC	MQ1-17H12	eBioscience	17-7029-41
IL-17	BV711	BL168	Biolegend	512328

Table 2-5. Antibodies used for AIM sorting

Marker	Fluorophore	Clone	Supplier	Catalogue No.
CD25	BB515	2A3	BD	564468
CD8	PercpCy5.5	SK1	Biolegend	344710

41BB	PE	4B41	Biolegend	309804
CD4	BV650	SK3	BD Bioscience	563876
CD40L	BV605	24-31	Biolegend	310826
CD25	BB515	2A3	BD	564468
CD8	PercpCy5.5	SK1	Biolegend	344710
41BB	PE	4B41	Biolegend	309804
CD4	BV650	SK3	BD Bioscience	563876
CD40L	BV605	24-31	Biolegend	310826

Table 2-6. Antibodies used for flow cytometry (T-cell cytokine panel)

Marker	Fluorophore	Clone	Supplier	Catalogue No.	Dilution
IFN-γ	BV421	XMG1.2	BioLegend	505829	1:100
CD27	BV510	LG.3A10	BioLegend	124229	1:200
CD8	BV570	53-6.7	BioLegend	100740	1:200
IL-10	BV605	JES5-16E3	BioLegend	505031	1:200
CD127	BV650	A7R34	BioLegend	135043	1:200
IL-4	BV711	11B11	BD Biosciences	564005	1:200
CD44	BV785	IM7	BioLegend	103044	1:100
CD19	BUV737	1D3	BD Biosciences	612781	1:200
CD4	BUV496	GK1.5	BD Biosciences	612952	1:200
TNF-α	AF488	MP6-XT22	BioLegend	506313	1:100
IL-2	PE	JES6-5H4	Invitrogen	12-7021-81	1:100
CD69	PE-Cy5	H1.2F3	BioLegend	104510	1:100
CD62L	PE-CF594	MEL-14	BD Biosciences	562404	1:100
CD103	PE-Cy7	2E7	BioLegend	121416	1:100
CD107a	AF647	1D4B	BioLegend	121610	1:200
CD3	AF700	17A2	BioLegend	100216	1:100
Live/Dead	Zombie NIR	—	BioLegend	423106	1:500

2.2 Clinical trials and human samples

An overview of all study cohorts, including their sources, sample sizes, and exposure histories, is provided in Table 2-7.

Cohort	Source study	Location	n	Initial exposure	Most recent exposure	Type of immunity
MERS001	Phase Ia Clinical trial [292]	UK-Oxford	27	MERS-CoV	–	Vaccine-induced
MERS002	Phase Ib Clinical trial [291]	KSA -Riyadh	24	MERS-CoV	–	Vaccine-induced
MERS003 (Hybrid SARS-CoV-2/MERS-CoV)	Phase Ic Clinical trial [320]	UK -Liverpool	89	SARS-CoV-2 or	MERS-CoV	Hybrid immunity
MERS-CoV Convalescent (Pre-pandemic)	WHO–NIBSC [321, 322]	South Korea	9	MERS-CoV	–	Natural immunity
Hybrid MERS/SARS-CoV-2)	KFMC observational study [323]	KSA	13	MERS-CoV	SARS-CoV-2	Hybrid immunity
Hybrid SARS-CoV-2/SARS-CoV-2	PITCH [324]	UK-Oxford	12	SARS-CoV-2	SARS-CoV-2	Hybrid immunity
SARS-CoV-2 vaccine-only	PITCH[324]	UK-Oxford	12	None	SARS-CoV-2	Vaccine-induced
Pre-pandemic controls	MERS001/002 pre-screening [291, 292]	UK/KSA	35	None	None	Unexposed

Table 2-7. Summary of clinical and observational study cohorts included in this study.

Overview of all cohorts, indicating the study origin, location, sample size (n), initial and most recent exposures, and the resulting immunity type. Icons denote exposure type: the syringe symbol represents vaccination, and the biohazard symbol represents infection.

Clinical trial designs and sample collection timelines are summarised in Figure 2-1. The immunogenicity of the ChAdOx1 MERS vaccine was evaluated using samples from three phase I clinical studies: MERS001 (United Kingdom), MERS002 (Saudi Arabia), and MERS003 (United Kingdom, older adults). Serum, plasma, and PBMCs were collected at predefined time points following vaccination, as illustrated in Figure 2-1. Further details of each study cohort and the corresponding immunological assays are described in the sections below.

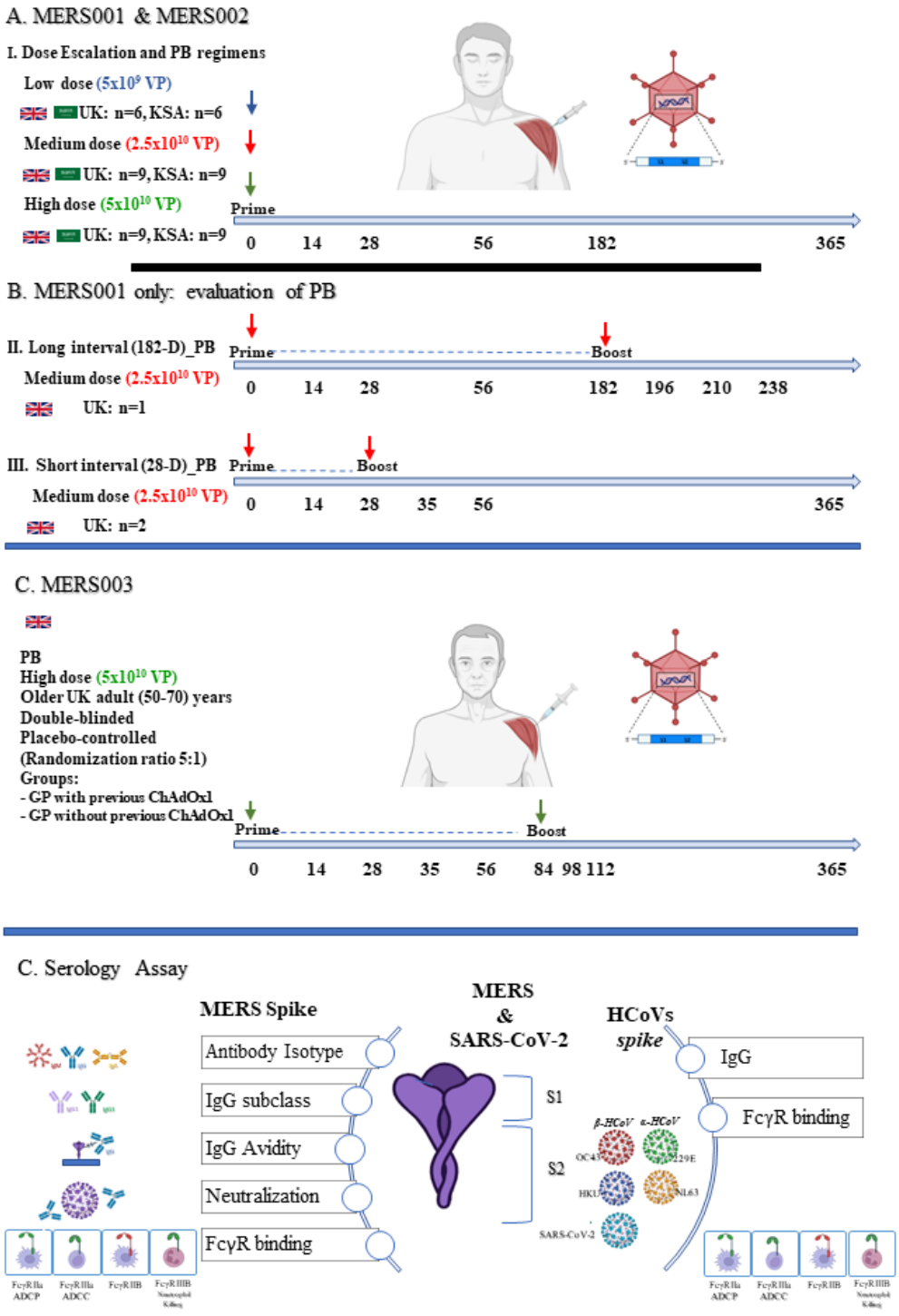


Figure 2-1. Overview of ChAdOx1 MERS clinical trials and serology assays

(A) Schematic representation of phase I MERS001 (UK) and MERS002 (KSA) clinical trials showing dose-escalation and prime–boost (P–B) regimens. **(B)** MERS001 included an additional P–B cohort not present in MERS002. Participants received IM doses of ChAdOx1 MERS at the indicated intervals. **(C)** Phase Ic MERS003 (Liverpool, UK) trial in older adults (50–70 years), conducted as a double-blinded, placebo-controlled study (randomization ratio 5:1), evaluating high-dose P–B regimens in groups with and without prior ChAdOx1 exposure. **(D)** Summary of immunological assays used in this study.

2.2.1 MERS001 (First-in-Human Trial, United Kingdom)

The MERS001 clinical trial was an open-label, non-randomised, dose-escalation phase Ia study [292]. The primary objective was to evaluate the safety and tolerability of ChAdOx1 MERS, based on the incidence of solicited, unsolicited, and serious adverse events following vaccination. The secondary objective was to characterise vaccine-induced humoral immune and cellular responses, measured by ELISA targeting the full-length spike (S) glycoprotein and IFN-γ ELISpot. Virus neutralisation assays were included as exploratory endpoints. The trial was conducted at the University of Oxford, United Kingdom, between March 2018 and September 2021. Healthy adult volunteers aged 18–55 years received a single intramuscular injection of ChAdOx1 MERS at one of three dose levels: low (5×10^9 vp, $n = 6$), medium (2.5×10^{10} vp, $n = 9$), or high (5×10^{10} vp, $n = 9$) (Figure 2-1A). Two additional participants received homologous prime–boost vaccinations at short (28-day, $n = 2$) and long (182-day, $n = 1$) intervals using the medium dose) (Figure 2-1B). Recruitment for these groups was limited due to the onset of the COVID-19 pandemic.

Blood samples were collected at defined timepoints post-vaccination (days 0, 14, 28, 56, 182, and 365) for serum, plasma, and PBMC isolation. Additional samples were collected for participants receiving a booster dose (days 14, 28, and 56 post-boost), as shown in Figure 2-1. Exploratory immunological analyses, including anti-MERS serology and cross-reactivity assays using MERS001 samples, are described in Chapter 3. Detailed assay methodologies are provided in 2.6.2.

Ethical approval for the study was granted by the UK Medicines and Healthcare products Regulatory Agency (MHRA) and the Research Ethics Committee (REC), and the trial was registered at ClinicalTrials.gov under identifier NCT03399578.

2.2.2 MERS002 (Kingdom of Saudi Arabia)

The MERS002 clinical trial was an open-label, non-randomised, phase Ib study [291]. The overall study design and sample collection schedule were identical to those of the prime-only groups of MERS001 (no prime-boost groups were included in MERS002) as show in Figure 2-1A. The MERS002 trial was conducted at King Abdulaziz Medical City, Ministry of National Guard Health Affairs, Riyadh, Saudi Arabia. Participant recruitment took place between December 2019 and June 2020, shortly before the onset of the COVID-19 pandemic. Healthy Middle Eastern adults aged 18–50 years were screened for eligibility and enrolled following written informed consent.

Serum, plasma, and PBMCs were collected at predefined time points post-vaccination, following the same schedule as in MERS001. IFN-γ ELISpot assays were performed at King Abdullah International Medical Research Centre (KAIMRC) using fresh PBMCs, and the completed IFN-γ ELISpot plates

were subsequently shipped to the University of Oxford for data quality control and analysis. Serum and plasma samples, collected in Riyadh, were shipped to Oxford for humoral immunogenicity analysis as described for the MERS001 trial (see Section 1.5.1.1).

The study was approved by the Institutional Review Board and Ethical Committee at King Abdullah International Medical Research Centre (KAIMRC; approval number CT18/004/R) and by the Saudi Food and Drug Authority (SFDA; reference SCTR 18121302). The trial was registered at ClinicalTrials.gov under identifier NCT04170829.

2.2.3 MERS003 (Older adults, United Kingdome)

The MERS003 clinical trial was a double-blind, placebo-controlled, phase Ic study conducted in Liverpool, United Kingdom, after the onset of the COVID-19 pandemic [320]. Healthy adults aged 50–70 years received two doses of ChAdOx1 MERS (5×10^{10} vp) administered 84 days apart. The placebo consisted of sterile saline (salt water) with no active ingredient and served as a separate negative control group. Participants were stratified by prior exposure to ChAdOx1-based vectors (Figure 2-1C).

The primary objective was to evaluate the safety, tolerability, and reactogenicity of ChAdOx1 MERS in this age group, and the secondary objective was to assess vaccine-induced humoral and cellular immune responses. Participants were stratified into two exposure groups: individuals with prior vaccination using ChAdOx1-based vectors and those without previous exposure.

Serum, plasma, and PBMCs were collected in Liverpool, stored at –80˚C or in liquid nitrogen (PBMCs), and subsequently shipped to the University of Oxford for immunological analysis. Analyses included anti-MERS spike-specific IgG ELISA, MERS PNA, SARS-CoV-2 spike-specific ELISA and PNA, IFN-γ ELISpot assays, and anti-vector neutralisation assays.

Ethical approval for the study was obtained from the UK Medicines and Healthcare products Regulatory Agency (MHRA) and the Research Ethics Committee (REC; reference 23/SC/0047). The trial was registered in the ISRCTN registry under identifier ISRCTN17936606.

Convalescent and Control Samples

To evaluate the impact of previous MERS-CoV infection on immune responses to COVID-19 vaccination, several convalescent and control cohorts were included as summarised in Table 1. Pre-pandemic MERS-CoV convalescent samples served as reference comparators for naturally acquired immunity; post-pandemic MERS survivors who subsequently received COVID-19 vaccination represented hybrid MERS/SARS-CoV-2 immunity; additional SARS-CoV-2–infected and vaccinated individuals were included as comparator groups to contextualise hybrid and vaccine-only responses.

2.2.4 MERS-CoV Convalescent Cohort (Pre-pandemic)

This cohort comprised convalescent-phase serum samples collected from individuals infected with MERS-CoV in South Korea prior to the COVID-19 pandemic. A total of nine samples from recovered participants were obtained through collaborations with the National Institute for Biological Standards and Control (NIBSC) [321, 322].

The first set of samples (n = 5) was obtained through aWHO study in 2019 that aimed to compare serological methods for MERS-CoV antibody detection [321]. These samples were originally donated by the Korea National Institute of Health (KNIH) and were derived from PCR-confirmed MERS-CoV–infected individuals.

The second set (n = 4) was contributed to a multi-centre international collaborative study coordinated by NIBSC and supported by the CEPI [321]. The Jenner Institute, University of Oxford, participated as one of 11 international laboratories involved in validating the MERS-CoV International Reference Standard (IRS), developed to harmonise antibody measurements across laboratories and assay platforms. This study established the first international standard for MERS-CoV antibodies (NIBSC code: 19/178) in 2020.

The second set of samples were originally donated by Dr Manki Song of the International Vaccine Institute (IVI), Korea, and were collected over a four-month period, more than one year after hospital discharge, representing long-term convalescent immune responses. Donors were selected for high anti-MERS-CoV antibody titres, and sample collection was coordinated by Dr Manki Song (IVI) and Prof. Yeon-Sook Kim (Chungnam National University Hospital, South Korea). Samples were provided in both freeze-dried and liquid formulations [321].

To ensure biosafety, all serum and plasma samples were inactivated using a validated solvent–detergent method before transfer, eliminating any potential residual infectious virus [325]. Samples were stored at –20˚C or below until analysis. Sample collection was approved by the NIBSC Human Material Advisory Committee (project number: 16/005MP). All donors provided informed consent, and samples were anonymised before use.

2.2.5 Convalescent MERS-CoV Cohort with COVID-19 vaccination (Hybrid MERS/SARS-CoV-2 immunity)

This cohort comprised plasma samples from individuals previously infected with MERS-CoV who were either subsequently vaccinated against COVID-19 or remained unvaccinated. All samples were collected after the onset of the COVID-19 pandemic, representing hybrid MERS/SARS-CoV-2 immune histories. Samples were obtained at King Fahad Medical City (Riyadh, Saudi Arabia) between 2020

and 2023 as part of an observational study investigating MERS-CoV–specific humoral and cellular immune responses following COVID-19 vaccination, including cross-neutralisation of SARS-CoV-2 and MERS-CoV variants [323].

The source dataset consisted of 70 MERS-CoV convalescent individuals sampled 5–10 years post-infection, with and without a history of COVID-19 vaccination, as previously described in detail [323]. That study addressed research questions related to cross-reactive and vaccine-induced immunity in the post–COVID-19 pandemic context, with a particular focus on subunit-specific antibody responses and functional profiling using detailed serological assessments. For the present analysis, a subset of 13 plasma samples was utilised. Due to additional consent requirements for international transfer, only a subset of the original samples was available for inclusion. These samples were kindly provided by Dr Bander Alosaimi and were selected to address the specific aims of this study.

All sample collections were conducted under protocols approved by the King Fahad Medical City Institutional Review Board (IRB log number: 20-703). Use of these samples for the current study was additionally reviewed and approved by the Oxford Tropical Research Ethics Committee (OxTREC reference: 550-22). Samples were registered as a collection under the University of Oxford Human Tissue Act (HTA) licence, and all transfers were conducted in accordance with applicable regulatory and ethical requirements, including a formal Material Transfer Agreement (MTA) between the providing and receiving institutions.

2.2.6 Hybrid SARS-CoV-2/SARS-CoV-2 and SARS-CoV-2 vaccine immunity

Samples were obtained from the Protective Immunity from T cells to COVID-19 in Health Workers (PITCH) study [324], a prospective, multicentre sub-study of the SARS-CoV-2 Immunity and Reinfection Evaluation (SIREN) study [326]. The PITCH study investigates cellular and humoral immune responses to SARS-CoV-2 infection and vaccination among healthcare workers in the United Kingdom. All participants provided written informed consent. The PITCH study was approved by the Berkshire Research Ethics Committee and the UK Health Research Authority (IRAS ID: 284460; REC reference: 20/SC/0230) and is registered with ISRCTN (Trial ID: ISRCTN11041050).

Healthcare workers aged 18 years or older were eligible for inclusion, with no exclusion criteria applied. Baseline risk factors were recorded at enrolment, symptom status was updated every two weeks, and vaccination data were obtained through linkage with the National Immunisations Management System and participant questionnaires. Prior SARS-CoV-2 infection status among participants was assessed at baseline using available records at the start of the analysis period (7 December 2020) using historic PCR results and detection of anti-SARS-CoV-2 nucleocapsid antibodies, with all external test results (including symptomatic testing) captured.

For the present analysis, samples collected at the Oxford site of the PITCH study (Oxford University Hospitals NHS Foundation Trust) were used. All participants in this subset (n = 24) were recruited at the Oxford site and are covered by Oxford-specific ethical approvals. Sample collection, storage, and secondary use were conducted under the GI Biobank Study protocol, approved by the Yorkshire & The Humber–Sheffield Research Ethics Committee (REC reference: 16/YH/0247). Two age- and sex-matched comparison groups were selected to correspond to the MERS-CoV/SARS-CoV-2 hybrid immunity cohort: individuals with prior SARS-CoV-2 infection who had received two doses of SARS-CoV-2 vaccine (hybrid SARS-CoV-2/SARS-CoV-2 immunity; n = 12), and individuals who had received two doses of SARS-CoV-2 vaccine without prior infection (SARS-CoV-2 vaccine-only immunity; n = 12). Infection status was defined by detection of anti–SARS-CoV-2 nucleocapsid IgG at recruitment or by documented infection occurring after the second dose; a history of COVID-19 illness during the trial was also recorded.

2.2.7 Pre-pandemic negative controls

Pre-pandemic negative control samples were obtained from healthy adult volunteers enrolled at baseline in the MERS001 and MERS002 clinical trials prior to vaccination [291, 292]. These samples were used to establish assay background and serological cut-off thresholds.

2.3 Immunization, Sample Collection and Processing

Participants in clinical trials received IM immunization administered into the deltoid muscle of the non-dominant arm. Vaccine volumes and doses were determined according to the individual clinical trial protocols (MERS001–MERS003). All vaccinations were performed by qualified clinical staff under appropriate aseptic conditions, and participants were monitored on-site for at least 30 minutes post-immunization for immediate adverse events.

Sample handling procedures varied according to the specific clinical trial protocols (MERS001–MERS003) and relevant ethical approvals. In all studies, peripheral blood was collected at predefined time points for the preparation of serum, plasma, and PBMCs. Blood was drawn into EDTA or serum separator tubes and processed within 4–6 hours of collection.

2.3.1 Serum and plasma preparation

Serum samples were obtained by allowing blood to clot at room temperature for 30–60 min, followed by centrifugation at 10,000×g for 10 min. Plasma was prepared from whole blood collected in EDTA tubes and centrifuged at 10,000×g for 10 min without prior clotting. The resulting serum or plasma was transferred to sterile cryovials and stored at –80˚C until analysis.

2.3.2 PBMC isolation and storage

PBMCs were separated by Ficoll-Paque density-gradient centrifugation, washed twice in phosphate-buffered saline (PBS), and cryopreserved in fetal bovine serum containing 10 % dimethyl sulfoxide (DMSO) for long-term storage in liquid nitrogen. PBMC processing differed among the clinical trials: in MERS001 and MERS002, PBMCs were isolated from fresh blood and used immediately for functional assays such as IFN-γ ELISpot and intracellular cytokine staining, whereas in MERS003, PBMCs were isolated then cryopreserved, and shipped on dry ice for subsequent analysis. Before use, frozen PBMCs were thawed rapidly at 37˚C, washed twice in complete medium, and rested for at least 2 hours prior to stimulation.

2.4 Animal model

Female BALB/c mice were used in accordance with the *UK Animals (Scientific Procedures) Act 1986* under project licence number PP2352929, granted by the UK Home Office, and with approval from the local Animal Welfare and Ethical Review Board (AWERB) at the University of Oxford.

Inbred, age-matched female mice were purchased from commercial suppliers (Inotiv Ltd., UK) in separate batches for each of the main experiments. Upon arrival, animals were allowed to acclimatize for at least one week before the start of procedures and were randomly assigned to experimental groups. Animals were group-housed in individually ventilated cages (IVCs) under specific pathogen-free (SPF) conditions, maintained at a constant temperature of 20–24˚C and relative humidity of 45–65%, on a 13:11 h light–dark cycle.

2.4.1 Pre-clinical Experimental overview

Three experiments were conducted. Two independent replicate studies, MERS-IDT001 and MERS-IDT002, were performed using identical protocols to confirm the reproducibility of the findings. Each of these studies used a single batch of animals. The third experiment, MERS-DoE, employed a design-of-experiments (DoE) framework to investigate multiple experimental factors simultaneously. This study used one batch of animals but was conducted in two experimental blocks due to logistical considerations.

General animal and immunization procedures common to all three experiments are described in this chapter, while details of the experimental design, group allocation, and additional methods specific to DoE are presented in Chapter 6.

2.4.2 Experimental Plan for MERS-IDT001 and MERS-IDT002

Eight groups were included: vector controls for each vaccine platform (‘Ad GFP’ and ‘MVA GFP’); prime only for each vaccine (‘Ad’ and ‘MVA’); homologous prime boost for each vaccine (‘Ad/Ad’ and ‘MVA/MVA’), and heterologous prime boost in both configurations (‘Ad/MVA’ and ‘MVA/Ad’) (Table 2-8). Within each experiment, six mice were allocated per group (n = 6). Results from the two

replicate experiments were combined when no significant statistical differences were observed between corresponding groups, while maintaining the relative hierarchy of group responses. This approach increased statistical power to detect differences between vaccine regimens.

Two exploratory groups were included in only one of the replicate experiments. In MERS-IDT001, a high-dose homologous prime–boost group (MVAH/MVAH) was incorporated to evaluate the effect of dose escalation. In MERS-IDT002, a prime-only group (MVA) was included to assess the kinetics of the primary immune response. Sampling for the MVA groups was performed at D14 post-prime, corresponding to the expected peak immune response. In the exploratory prime-only group, an additional sampling time point at D28 post-prime was included to assess response persistence. For comparative analyses, D14 data were used across all groups to ensure consistency and adequate sample size.

#	Label	Group description	Prime	Boost	Total n
1	MVA GFP	Vector control MVA GFP	MVA GFP	MVA GFP	12
2	Ad GFP	Vector control ChAdOx1 GFP	ChAdOx1 GFP	ChAdOx1 GFP	12
3	MVA	Prime only MVA MERS 14-days response	MVA MERS	n/a	12
4	MVA	Prime only MVA MERS 28-days response	MVA MERS	n/a	6 (MERS-IDT002)
5	Ad	Prime only ChAdOx1 MERS 4-week response	ChAdOx1 MERS	n/a	12
6	Ad/Ad	Homologous prime/boost ChAdOx1 MERS	ChAdOx1 MERS	ChAdOx1 MERS	12
7	MVA/MVA	Homologous prime/boost MVA MERS	MVA MERS	MVA MERS	12
8	Ad/MVA	Heterologous prime/boost ChAdOx1 prime, MVA boost	ChAdOx1 MERS	MVA MERS	12
9	MVA/Ad	Heterologous prime/boost MVA MERS prime, ChAdOx1 MERS boost	MVA MERS	ChAdOx1 MERS	12
10	MVAH/MVAH	Homologous prime/boost MVA MERS high dose	MVA MERS high dose	MVA MERS high dose	6 (MERS-IDT001)

Table 2-8. Vaccination regimens and sample collection timeline.

Mice were primed with either ChAdOx1 (Ad) or Modified Vaccinia Ankara (MVA) expressing MERS-CoV spike (MERS) or GFP (control). Boosts, when given, were administered 28 days after prime either as homologous or heterologous. Mice were bled prior to booster administration. Blood, spleen and BM were collected 14 or 28 days after boost (endpoint). BM was collected for MERSIDT002 only. The table details each group's label, description, prime and boost vaccines, and sample size (n). ChAdOx1 MERS at $1x10^8$ IU/mL, MVA MERS (IDT GMP batch) at $1x10^6$ PFU; or for the high-dose MVA MERS group, 100 µL total (50 µL

per leg) at 7.08×10^6 PFU/mL. Abbreviations: Ad = ChAdOx1; MVA = Modified Vaccinia Ankara; MERS = MERS-CoV spike; GFP = green fluorescent protein control; n/a = no boost administered. For MVA-only groups, samples were analysed at either 14 days or 28 days post-prime, depending on the assay. Both MVA groups are labelled as "MVA" to match the figure legends. These represent prime-only MVA MERS groups analysed at either 14 days or 28 days post-prime, with the specific time point indicated in each figure legend.

2.4.3 Immunization, Sample Collection and Processing

Animals were immunised IM into the hind leg (tibialis muscle) under short-term anaesthesia with vaporized IsoFlo®. The standard injection volume was 50 µL per animal; where a higher total volume was required to achieve the target immunising dose, the injection was split equally between both hind legs (50 µL/leg). All animals were humanely euthanised at the end of each experiment by an approved Schedule 1 method.

Mice were bled via the tail vein prior to booster administration (4 weeks post-prime) for the collection of serum to assess humoral immunity. At study termination, whole blood was collected by cardiac puncture into serum separator tubes. Samples were allowed to clot at room temperature for 30–60 min and centrifuged at 10,000×g for 10 min. The resulting serum was transferred to sterile cryovials and stored at –20 °C until analysis.

Post-mortem examination, spleens and femurs/tibias (for BM isolation) were harvested aseptically and immediately placed into ice-cold phosphate-buffered saline (PBS). All tissues were processed within 4 hours of collection.

Single-cell suspensions from spleens were prepared using C-tubes (Miltenyi Biotec) and the gentle MACS Dissociator (Miltenyi Biotec), following the manufacturer's instructions for spleen tissue. BM cells were obtained by mechanically flushing femurs and tibias with cold sterile PBS using a 25-gauge needle and syringe. The resulting cell suspensions were combined and passed through a 70 µm cell strainer (Fisher Scientific) into a 50 mL conical tube. An additional 10 mL of PBS was used to rinse the C-tube and strainer, and the rinse was added to the cell suspension. Samples were centrifuged at 1350 rpm for 5 min at room temperature.

After removal of the supernatant, red blood cells were lysed using ammonium–chloride–potassium (ACK) lysis buffer. Briefly, 5 mL of ACK buffer was added to the cell pellet, gently mixed, and incubated at room temperature for no longer than 5 min. Lysis was stopped by adding 25 mL of PBS, followed by gentle mixing by inversion and centrifugation at 1350 rpm for 5 min. The resulting cell pellet was resuspended in 5 mL of complete medium, and any residual cell debris ("ghosts") was removed.

Cell concentration and viability were determined using both a CASY cell counter and a Countess II Automated Cell Counter (Thermo Fisher Scientific). For CASY analysis, 5 µL of each sample was diluted in 10 mL of CASYton solution, and viable cell numbers were recorded. For cell counting using the Countess analyzer, cell suspensions were mixed with trypan blue solution at a 1:9 ratio and loaded

onto Countess cell counting slides (Thermo Fisher Scientific). Viable and total cell numbers were automatically quantified using the instrument's standard settings. Following counting, cells were resuspended in complete culture medium and used immediately for downstream applications without normalization to a fixed concentration. Spot-forming units per million cells were calculated retrospectively based on the recorded cell counts. Serum (collected both before and after boosting), spleen, and BM samples collected four weeks after the final vaccination were used to assess humoral and cell-mediated immune responses. The only exception was the MVA prime-only group, which was terminated 14 days post-prime to capture the peak immune response.

2.5 Vaccines

2.5.1 ChAdOx1-MERS

The ChAdOx1 MERS vaccine construct encoded the MERS-CoV spike glycoprotein from strain Camel/Qatar/2/2014 (GenBank accession no. KJ650098.1) was codon optimized for humans and synthesized by GeneArt (Thermo Fisher Scientific). To enhance expression, the transgene included a 32-amino-acid human tissue plasminogen activator (tPA) signal sequence at the N-terminus, which has been shown to improve immunogenicity [307], The vector was generated by Gateway recombination between the ChAdOx1 destination bacterial artificial chromosome (BAC) vector and entry plasmids containing the MERS-CoV spike coding sequence. Plasmid assembly followed standard molecular cloning protocols as previously described [104].

2.5.2 Clinical batch production

The ChAdOx1 MERS vaccine used in the MERS001, MERS002 and MERS003 clinical studies was manufactured according to current Good Manufacturing Practice (cGMP) standards by the Clinical Biomanufacturing Facility, University of Oxford (Oxford, UK). The viral vector vaccine was purified and sterile-filtered to generate a clinical lot with a final concentration of 1.74×10^{11} vp/mL. At the CBF the vaccine was certified and labelled for the trial by a qualified person before transfer to the clinical sites. The vaccine is supplied as a liquid in glass vials and was stored at nominal -80°C in a secure freezer at the clinical sites.

2.5.3 Preclinical Batch Production

Preclinical ChAdOx1-MERS vaccine material was produced at the Pandemic Sciences Institute's Viral Vector Core Facility (VVCF) by Dr Claire Powers. Vaccine batch #4378 was generated by re-bulking pre-master stock adenovirus material (batch #3521).

T-REx™ 293 cells were infected with an archived pre-master stock of adenovirus, and the rescued virus was serially passaged to obtain sufficient material for purification. Viral particles were purified by

caesium chloride (CsCl) gradient ultracentrifugation as previously described [104], followed by buffer exchange and aliquoting.

Quality control (QC) assays were performed on the purified material. Sterility was verified by microbial culture, and viral particle concentration was determined spectrophotometrically. Infectious units (IU) were quantified by titration in T-REx™ 293 cells followed by immunostaining. Viral infectivity was assessed by calculating the particle-to-infectious unit (P:I) ratio, which was within the expected range for ChAdOx1-based vectors (≈ 70:1).

The presence and integrity of the transgene insert were confirmed by polymerase chain reaction (PCR). Insert-dependent (ID) PCR verified antigen expression, while flank–flank PCR confirmed the integrity of the antigenic DNA sequence and excluded contamination with wild-type adenovirus. The complete transgene sequence was further validated by next-generation sequencing (NGS).

2.5.4 MVA-MERS-S

The vaccine encoded the full-length MERS-CoV spike glycoprotein (strain EMC/2012, GenBank accession number JX869059). The MVA-MERS-S vaccine was manufactured by IDT Biologika GmbH (Dessau, Germany), a biopharmaceutical manufacturer specialising in viral vector vaccines [294, 295]. For the present study, the second-generation MVA-MERS-S vaccine produced in DF-1 cells was used. The rationale of development and differences from earliest generation are outlined in Chapter 1.

Vaccine material (lot number: CTM0221) was shipped from Germany and supplied as a GMP-grade product prepared for clinical trial use. The same GMP batch was also employed in the phase Ib clinical study [295], where the production and manufacturing process has been described in detail.

2.5.5 ChAdOx1-SEAP Virus

The ChAdOx1-SEAP virus, a replication-deficient chimpanzee adenovirus expressing the secreted alkaline phosphatase (SEAP) reporter gene, was used in anti-vector neutralisation assay as previously described [104]. This vector is based on the ChAdOx1 backbone, similar to ChAdOx1-MERS, but carries the SEAP gene in place of the antigen insert. Viral stocks (VVCF #1041 and #3708) were produced at the Pandemic Sciences Institute's Viral Vector Core Facility (VVCF) under the supervision of Dr. Claire Powers. The virus was propagated in HEK-293 or HEK-293T cells and purified using standard adenoviral purification methods. Viral titres were determined as infectious units per millilitre (IU/mL), and aliquots were diluted 1:100 to prepare working stocks and stored at −80˚C until use in neutralisation assays.

2.5.6 Negative control vaccines for pre-clinical studies

Negative controls consisted of ChAdOx1 or MVA vectors encoding green fluorescent protein (GFP) instead of the MERS-CoV spike protein. These controls accounted for non-specific immune responses induced by the viral vector itself and enabled differentiation between vector-specific and antigen-specific responses.

Control vaccines were produced at the Pandemic Sciences Institute's Viral Vector Core Facility (VVCF) under the supervision of Dr. Claire Powers. Vaccine material (batch #4377) was generated by re-bulking pre-master stock adenovirus material (batch #4046A). The MVA #3290 vector was propagated in DF-1 cells, produced as a large batch, and subsequently divided into aliquots designated A–D. The present report pertains specifically to parts B and C (batch #4232 B&C).

2.6 Experimental Methods

2.6.1 Cell Culture and maintenance

All cell lines were maintained at 37˚C in a humidified atmosphere containing 5% CO_2. The origin and specific experimental applications of each cell line are summarized in Table 2-9 and composition of the cell culture media used for each cell line is provided in Table 2-2.

HEK293T/17 cells (Cytion) were subcultured every 2–3 days at a ratio of 1:5 using 0.25% trypsin–EDTA (Thermo Fisher Scientific). Huh-7 cells (CLS Cell Lines Service GmbH, Eppelheim, Germany) were subcultured according to the manufacturer's recommended procedure, which included detachment with 0.25% trypsin–EDTA, gentle centrifugation, and removal of residual trypsin prior to resuspension in fresh medium. GripTite™ 293 MSR cells (Thermo Fisher Scientific) were pre-treated with versene (EDTA) solution (Merck Life Science) prior to trypsinization to facilitate detachment.

HEK293T/17 cells were used for pseudovirus (PV) production for MERS-CoV and SARS-CoV-2 assays, and in the SARS-CoV-2 PNA. Huh-7 cells were used for MERS-CoV PNA, and GripTite™ 293 MSR cells were used for ChAdOx1-SEAP anti-vector neutralisation assays.

Cell line	Description	Source / supplier	Catalogue	Culture medium	Application in this study
HEK293T/17	Human embryonic kidney cell line	Cytion	305117	Complete DMEM	Pseudovirus production and SARS-CoV-2 PNA
Huh-7	Human hepatocellular carcinoma cell line	CLS Cell Lines Service GmbH (Eppelheim, Germany)	300156	R10 medium	MERS-CoV PNA
GripTite™ 293 MSR	HEK293-derived adherent cell line with enhanced adherence properties	Thermo Fisher Scientific (Invitrogen)	R79507	GripTite™ medium	ChAdOx1-SEAP anti-vector neutralisation assay

Table 2-9. Origin, culture medium, and application of cell lines used in this study.

2.6.2 Immunological assays

Immunological assays were performed to evaluate antigen-specific humoral and cellular immune responses following vaccination. Comparable assay platforms were used for both human and murine samples, with species-specific modifications in secondary antibody reagents and sample processing. The assays included ELISA, enzyme-linked immunospot (ELISpot) assay, intracellular cytokine staining (ICS) by flow cytometry, and multiplex immunoassays, including Fc receptor (FcR) profiling by Luminex and electrochemiluminescence (ECL) assays using the Meso Scale Discovery (MSD) platform. A summary of the key assay parameters and species-specific differences is presented in Table 2-10.

Assay Type	Species	Sample Type	Antigen / Target	Measured Component(s)	Readout	Notes
ELISA	Human	Serum / Plasma	MERS-CoV Spike (S)	Total IgG	Optical density (OD_{450}) converted to ELISA Units (EU) via a 4-parameter logistic (4PL) standard curve	MERS001–MERS003, MERS Convalescents and hybrid immunity groups
ELISA	Human	Serum / Plasma	MERS-CoV Spike (S)	IgG subclass (IgG1, IgG3) and IgM, IgA	OD_{450} converted to EU via standard curve	MERS001–MERS002, MERS Convalescents and hybrid immunity groups
ELISA	Mouse	Serum	MERS-CoV Spike (S)	Total IgG	OD_{450} converted to EU via standard curve	MERS-IDT001-003

ELISA	Mouse	Serum	MERS-CoV Spike (S)	subclasses (IgG1, IgG2a, IgG2b, IgG3)	OD_{450} normalised to EU	MERS-IDT001-002
ELISA	Human /mouse	Serum / Plasma	MERS-CoV S1, S2	IgG	OD_{450} converted to EU via standard curve	Clinical: MERS001–MERS003, MERS Convalescents and hybrid immunity groups Pre-clinical: MERS001 and MERSIDTG002
ELISA	Human	Plasma	SARS-CoV-2 (Wuhan-Hu-1)	Total IgG	OD_{450} converted to EU via standard curve	MERS003, MERS Convalescents and hybrid immunity groups
ELISA	Human	Plasma	SARS-CoV-2 S1, S2 (Wuhan-Hu-1)	Total IgG	OD_{450} converted to EU via standard curve	MERS Convalescents and hybrid immunity groups
ELISA (Avidity)	Human / Mouse	Serum / Plasma	MERS-CoV Spike (S)	IgG avidity index	Avidity index NaSCN concentration resulting in 50% reduction of binding from samples normalized to OD = 1.0	Clinical: MERS001-002 pre-clinical: IDT001-002
MSD Multiplex ECL	Human	Serum / Plasma	MERS-CoV Spike and HCoV and SARS-CoV-2	IgG	Electrochemiluminescence (ECL) signal converted to AU/mL via standard curve	MERS001-002
FcR Profiling (Luminex)	Human	Serum / Plasma	MERS-CoV Spike (S) protein, S1 and S2, HCoV	FcγRIIa FcγRIIIa FcγRIIB FcγRIIIB	Median Fluorescence Intensity (MFI) converted to Arbitrary Units (AU) via standard curve	MERS001–MERS002, MERS Convalescents and hybrid immunity groups
FcR Profiling (Luminex)	Mouse	Serum / Plasma	MERS-CoV Spike (S)	FcγRIa, FcγRIIb, FcγRIII FcγRIV	MFI converted to AU via standard curve	MERS-IDT001-002
Pseudovirus Neutralisation (PNA)	Human	Heat-inactivated Plasma	MERS-CoV pseudoviruses: MERS001 – EMC/2012 and KOR/KNIH/002/England-1 [292] MERS002 – EMC/2012 [291] MERS003 –Qatar/2/2014	Neutralising antibodies	% inhibition of luciferase signal; IC_{50} calculated	MERS001–MERS003; measures neutralising capacity
Pseudovirus Neutralisation (PNA)	Human	Heat-inactivated Plasma	SARS-CoV-2 pseudovirus (Wuhan-Hu-1)	Neutralising antibodies	% inhibition of luciferase signal; IC_{50} calculated	MERS003, MERS convalescents and hybrid immunity
Pseudovirus Neutralisation (PNA)	Mouse	Heat-inactivated Plasma	MERS-CoV pseudovirus (Camel/Qatar/2/2014)	Neutralising antibodies	% inhibition of luciferase signal; IC_{50} calculated	MERS-IDT001-003
Anti-vector neutralisation assay	Human	Heat-inactivated Plasma	ChAdOx1 SEAP	Neutralising antibodies	RLU converted to AU via standard curve	MERS003

ELISpot	Human	PBMC	Full Spike peptide pools	IFN-γ–secreting cells	Spot-forming units (SFU) per 10^6 PBMC	MERS001-003
ELISpot	Mouse	Splenocytes	Spike peptide pool (S1 immunodominant peptide)	IFN-γ–secreting cells	SFU per 10^6 splenocytes	MERS-IDT001-003
ELISpot	Mouse	Splenocytes and bone marrow	MERS-CoV Spike (S)	MERS-specific B cells IgG (ASC)	SFU per 10^6 cells	MERS-IDT002-003
Flow Cytometry (ICS)	Human	PBMC	Spike peptide pools	$CD3^+$ $CD4^+$ / $CD8^+$ T cells producing IFN-γ, TNF-α, IL-2	% $cytokine^+$ cells	MERS001–MERS003; BD LSRFortessa;
Flow Cytometry (ICS)	Mouse	Splenocytes /BM	MERS-IDT002 (S1 immunodominant); MERS-IDT003 (S1, S2, + S1 immunodominant peptides)	$CD3^+$ $CD4^+$ / $CD8^+$ T cells producing IFN-γ, TNF-α	% $cytokine^+$ cells	MERS-IDT002-3 Sony ID7000 flow cytometer

Table 2-10. Immunological assays and analytical parameters across human and pre-clinical studies.

The table summarises the experimental assays used to characterise vaccine-induced humoral and cellular immune responses in human (clinical and convalescent) and mouse (pre-clinical) studies. Each assay is listed with the corresponding sample source, antigen or target, readout type, and associated study or cohort. Abbreviations: ASC, antibody-secreting cell; SFU, spot-forming unit; MFI, mean fluorescence intensity; PBMCs, peripheral blood mononuclear cells. Pseudovirus neutralisation assays for MERS001 and MERS002 were not performed as part of this project; data were obtained from previously published work see References [291, 292].

2.6.2.1 Serological assays

2.6.2.1.1 ELISA to MERS-CoV spike protein

ELISA assays were optimised for the detection of MERS-CoV S protein-specific total IgG and IgG subclasses, as well as IgM and IgA, in human serum or plasma, with additional adaptations for avidity analyses. Equivalent ELISA platforms were applied to pre-clinical mouse samples with protocol modifications as described below.

All assays were performed using high-binding 96-well MaxiSorp plates (NUNC, Thermo Fisher Scientific) coated with recombinant MERS-CoV S-clamp protein, based on the MERS-CoV KFU-HKU-13 strain spike glycoprotein (amino acids 1–1297; GenBank accession AHX00711.1) and stabilised in the prefusion trimeric conformation (provided by Dr Keith Chappell, Australian Infectious Disease Research Centre, University of Queensland, Australia) [327]. Plates were incubated for more than 18 hours at 4˚C, washed six times with 0.05% PBS–Tween 20 (PBS-T), and blocked with casein blocking buffer (Thermo Fisher Scientific) for one hour at room temperature (RT).

2.6.2.1.1.1.1 Human ELISA Assays

The assay for total IgG was established and performed in-house following previously published protocols [291, 292]. Plates were coated with MERS-CoV S clamp protein at a concentration of 1 µg/mL for total IgG detection and 6 µg/mL for antibody isotypes (IgA and IgM) and subclasses (IgG1 and IgG3), diluted in phosphate-buffered saline (PBS) at 50 µL per well. Coated plates were incubated at 4˚C overnight or for up to one week before use. Following coating, plates were washed and blocked as above. Serum samples were diluted in casein blocking buffer (Thermo Fisher Scientific) to fall within the dynamic range of detection, and plated in triplicate.

Standard curves were generated from pooled human reference serum exhibiting high antibody titres. The same reference pool was used to prepare standard curves for each antibody isotype (IgG, IgM, and IgA) and subclass (IgG1 and IgG3). The top standard was assigned a distinct arbitrary ELISA unit value for each antigen–antibody isotype and subclass. Serial dilutions were performed as follows: 10-point serial dilutions, with two-fold dilutions starting at 1:100 for IgG, two-fold from 1:20 for IgM, IgA, and IgG3, and 1.5-fold from 1:20 for IgG1, all diluted in casein. Antibody concentrations of the test samples were expressed as ELISA Unit (EU), derived from optical density (OD) values interpolated against a four-parameter logistic (4-PL) standard curve generated using Gen5 software (version 3.10; BioTek Instruments, Winooski, VT, USA).

In addition to the standard curve, a single dilution of the pooled reference serum corresponding to standard point 4 was included on each plate as a positive control at 1:800 (IgG) or 1:160 (IgM, IgA, IgG3) to ensure measurements remained within the optimal working range for each target. Following a two-hour incubation at 20˚C, plates were washed and incubated for one hour at room temperature with alkaline phosphatase (AP)-conjugated goat anti-human secondary antibodies (Sigma-Aldrich for IgG, 1:1000 dilution; SouthernBiotech for IgM, 1:500; IgA, 1:1000; IgG1, 1:675; and IgG3, 1:500), all diluted in casein.

After a final wash, plates were developed with 4-nitrophenyl phosphate substrate prepared in diethanolamine buffer (Fisher Scientific, UK). Optical density was measured at 405 nm using an ELx808 microplate reader (BioTek Instruments), and data were analysed using Gen5 software. The limit of detection (LOD) was defined as the mean OD plus three standard deviations (SD) of blank wells.

2.6.2.1.1.1.2 Mouse (Pre-clinical) ELISA Assays

Pre-clinical assays followed the same general procedure as described for human samples, with minor modifications. Plates were coated with MERS-CoV S clamp protein at concentrations of 2 µg/mL for IgG and 5 µg/mL for IgM and IgA detection, and incubated under identical blocking and washing conditions.

Standard curves were applied only for the quantification of total antibody isotypes, whereas subclass assays were analysed without the use of standard curves. A three-fold serial dilution starting at 1:100 was used to detect MERS-CoV–specific IgG antibodies, while a two-fold serial dilution starting at 1:100 was applied for IgM and IgA assays. A positive control derived from the standard reference serum was included on each plate, corresponding to standard point 5 for IgG and standard point 4 for IgM and IgA, at dilutions of 1:8100 (IgG) and 1:800 (IgM and IgA), representing the optimal working range for each isotype.

Alkaline phosphatase (AP)-conjugated goat anti-mouse secondary antibodies were used at optimised dilutions specific to each isotype: 1:5000 for IgG, 1:500 for IgM, and 1:1000 for IgA (all diluted in casein). Antibodies were sourced from Sigma-Aldrich, Abcam, and SouthernBiotech. Plates were developed as described for the human assays.

In contrast to the human assay, serum samples for IgG subclass measurements were diluted in casein to achieve an OD of approximately 1.0 based on total IgG readings, ensuring normalisation across samples. Samples were plated in duplicate and incubated for two hours at 37˚C. Development was stopped when a representative sample for each target reached an optical density (OD) of approximately 1.0, which served as the internal control for endpoint determination across plates. Subclass-specific detection antibodies conjugated to alkaline phosphatase (AP) were used at the following dilutions: IgG1, IgG2a, IgG2b, and IgG2c at 1:4000 (SouthernBiotech), and IgG3 at 1:1000 (Abcam). Following a one-hour incubation at 37 °C, plates were washed, developed, and read as described above. Results were expressed as OD values.

2.6.2.1.1.1.3 Antibody responses to MERS spike S1 and S2 proteins

IgG binding to MERS-CoV spike and subunit proteins (S1 and S2) was measured by ELISA, following the procedure described for total anti–MERS-CoV spike IgG detection in human samples (Section 2.6.2.1.1.1.1) and mouse samples (Section 2.6.2.1.1.1.12.6.2.1.1.1.2) with minor modifications. Ninety-six–well MaxiSorp plates (NUNC, Thermo Fisher Scientific) were coated with recombinant MERS-CoV spike (S) protein (provided by Dr Keith Chappell, Australian Infectious Disease Research Centre, University of Queensland, Australia) and recombinant S1 and S2 subunit proteins (Sino Biological) at a concentration of 1 µg/mL for all antigens in human assays and 2 µg/mL for all antigens in mouse assays, diluted in phosphate-buffered saline (PBS), and incubated overnight at 4˚C. Quantification of antigen-specific IgG responses was performed using a MERS-CoV spike–based standard curve, which was subsequently used to interpolate antibody concentrations for S1- and S2-binding assays.

A four-parameter logistic (4-PL) standard curve was generated for the MERS-CoV spike protein using species-matched pooled serum standards, with separate pooled standards generated for human and mouse IgG assays. For each species, the same pooled standard was used consistently across all

corresponding IgG assays. The MERS-CoV spike standard curve was used to interpolate antibody concentrations for spike (S), S1, and S2 binding assays, as previously described for MERS-CoV ELISA analyses. Each assay plate incorporated three internal antigen-specific controls derived from the standard curve to monitor responses against the spike (S), S1, and S2 proteins.

Bound antibodies were detected using alkaline phosphatase–conjugated goat anti-human IgG (Sigma-Aldrich) at a 1:1000 dilution. Plates were developed using 4-nitrophenyl phosphate substrate prepared in diethanolamine buffer (Fisher Scientific, Loughborough, UK) and read at 405 nm using an ELx808 microplate reader (BioTek Instruments). Antibody concentrations were expressed as EU, interpolated from the MERS-CoV–specific 4-PL standard curve using Gen5 software (version 3.10; BioTek Instruments).

Human serum IgG binding to SARS-CoV-2 spike and subunit proteins (S1 and S2) was measured by enzyme-linked immunosorbent assay (ELISA), as described previously [95] and in Section 1.4.2.1.1 for total anti-MERS spike IgG detection, with minor modifications.

2.6.2.1.1.1.4 Antibody responses to SARS- CoV-2 spike, S1 and S2 proteins

Human serum IgG binding to SARS-CoV-2 spike was measured by ELISA, as described previously [95] and in Section 1.4.2.1.1 for total anti-SARS-CoV-2 spike IgG detection with minor modification. IgG binding for S1 and S2 subunits was measured using the same ELISA approach with minor modifications. Ninety-six–well MaxiSorp plates (NUNC, Thermo Fisher Scientific) were coated with recombinant SARS-CoV-2 spike (native Antigen), S1, and S2 proteins (R&D Systems) at a concentration of 2 µg/mL in phosphate-buffered saline (PBS) and incubated overnight at 4˚C. Plates were washed six times with 0.05% PBS–Tween20 (PBS-T). Serum samples were plated in triplicate and diluted in casein blocking buffer (Thermo Fisher Scientific) to ensure readings fell within the linear detection range.

A four-parameter logistic (4-PL) standard curve was generated for the SARS-CoV-2 spike (S) protein only using pooled human reference serum with high anti–SARS-CoV-2 antibody titres. This spike-based standard curve served as the reference for quantification of IgG binding to spike (S) and was also used to interpolate antibody concentrations for the S1 and S2 binding assays, as previously described for MERS-CoV ELISA analyses. A series of ten two-fold serial dilutions was prepared in duplicate, starting at 1:300. A single dilution corresponding to standard point 4 (1:2400) was included on each plate as a positive control. Each assay plate also incorporated three internal antigen-specific controls derived from the standard curve to monitor responses against the spike (S), S1, and S2 proteins. Bound antibodies were detected using AP–conjugated goat anti-human IgG (Sigma-Aldrich) at a 1:1000 dilution. Plates were developed with 4-nitrophenyl phosphate substrate prepared in diethanolamine buffer (Fisher Scientific, Loughborough, UK) and read at 405 nm using an ELx808 microplate reader

(BioTek Instruments). Antibody concentrations were expressed as EU, interpolated from the SARS-CoV-2-specific 4-PL standard curve using Gen5 software (version 3.10; BioTek Instruments).

2.6.2.1.1.1.5 Avidity indirect ELISA

2.6.2.1.1.1.5.1 Human avidity

Antibody avidity of MERS-CoV–specific IgG was evaluated using sodium thiocyanate (NaSCN; Sigma-Aldrich) as a chaotropic reagent to dissociate bound antibodies. The assay followed the IgG ELISA setup described previously (Section 1.4.2.1.1) with modification. Serum or plasma samples were diluted in casein blocking buffer (Thermo Fisher Scientific) to achieve an optical density (OD) of approximately 1.0 (between 0.75 and 1.2 accepted) based on the total IgG assay readout; samples were plated in duplicate. Plates were incubated for 2 hours at 20 °C before washing as previously described.

For each sample, one set of duplicates was treated with PBS (control) and the other with increasing concentrations of NaSCN (0.5, 1.0, 1.5, 2.0, 2.5, and 3.0 M diluted in PBS), applied for 15 minutes at 20 °C. Following treatment, plates were washed before incubation for 1 hour at 20˚C with alkaline phosphatase AP–conjugated goat anti-human IgG (Sigma-Aldrich) at a 1:1000 dilution. Plates were developed and read as previously described for MERS-CoV ELISA. The IgG standard curve described for the total spike assay was included on each plate as an additional internal control to monitor assay performance but was not used for quantification.

The avidity index (AI) was defined as the molar NaSCN concentration that reduced the OD by 50% relative to the PBS-treated control. NaSCN concentration versus OD values were plotted, and Avidity Index (AI) values were interpolated from the regression curve using GraphPad Prism (version 10.6.1; GraphPad Software, San Diego, CA, USA).

2.6.2.1.1.1.5.2 Pre-clinical avidity assay

For pre-clinical mouse samples, the same procedure was applied with minor modifications. Plates were coated with MERS-CoV S clamp protein at 2 µg/mL, and a narrower NaSCN range (1.0, 1.4, 1.8, 2.2, 2.6, and 3.0 M) was used to accommodate species-specific differences in antibody binding strength. Detection was performed using AP–conjugated goat anti-mouse IgG (Sigma-Aldrich) at a 1:5000 dilution. Mouse assays did not include a standard curve; instead, a single high-titre reference serum was included on all plates as an internal control to ensure assay reproducibility. Plates were developed and read as described above.

2.6.2.1.1.1.6 Fcγ Receptor (FcγR) Binding Assay (Luminex-based)

2.6.2.1.1.1.6.1 Multiplex FcγR Binding Assay (Human Samples)

Antigen-specific Fcγ receptor (FcγR) binding activity was assessed for FcγRIIa, FcγRIIb, FcγRIIIa, and FcγRIIIb using an in-house multiplexed Luminex assay developed and standardised for this study. The

assay was designed to characterise antibody effector functions targeting MERS-CoV, SARS-CoV-2 and their subunits, as well as human seasonal coronaviruses (HCoVs).

2.6.2.1.1.1.6.1.1 Antigen coupling

Prior to coupling, antigen storage buffers for the MERS-CoV spike (S-clamp), S1, and S2 proteins were exchanged with phosphate-buffered saline (PBS) using a 0.5 mL Amicon ultrafiltration device (Merck Millipore) to remove residual stabilisers, following the manufacturer's instructions. The MERS-CoV S-clamp protein (provided by Dr Keith Chappell, Australian Infectious Diseases Research Centre, University of Queensland, Australia) and the S1 and S2 subunits (Sino Biological) were covalently coupled to Bio-Plex Magnetic COOH beads (Bio-Rad) via a two-step carbodiimide reaction using the Bio-Plex Amine Coupling Kit (Bio-Rad), according to the manufacturer's protocol. Similarly, the SARS-CoV-2 spike (S), S1, and S2 subunits, along with spike proteins from seasonal human coronaviruses (HCoV-OC43, HCoV-HKU1, HCoV-229E, and HCoV-NL63) (Native Antigen Company), were coupled using the same method to generate a comprehensive coronavirus antigen panel. Coupled beads (Bio-Rad Laboratories; currently supplied by Luminex Corporatio) were stored in the dark at –20 °C until use.

2.6.2.1.1.1.6.1.2 Assay procedure

Ninety-six–well plates (Greiner Bio-One) were loaded with the coupled bead mixture at a final concentration of 1×10^6 beads per antigen target in a total volume of 50 µL per well Luminex assay buffer (LAB buffer; prepared in-house, with composition detailed in Table 2-2). LAB buffer was filter-sterilised using 0.25 µm Stericup Quick Release-GV units (Merck Life Sciences) to ensure consistency and prevent bead aggregation. Plates were incubated on a plate shaker (700 rpm, room temperature) for 30 min, followed by two washes with 100 µL per well of the same buffer, performed using a magnetic plate separator (Thermo Fisher Scientific).

A pooled serum standard, derived from participants who had received a two-dose MERS vaccination regimen and exhibited high antibody titres, was included on each plate to enable calibration and inter-assay comparability. For all Fc receptor profiling assays, standards were prepared by serial 2-fold dilutions starting at 1:100. Serum samples were diluted within the linear range of the standard curve and analyzed in duplicate. Following a one-hour incubation of samples on a plate shaker (700 rpm) at 37˚C, plates were washed two times in in LAB buffer.

Secondary detection of FcγR activity was performed using biotinylated recombinant Fcγ receptor proteins (FcγRIIa, FcγRIIb, FcγRIIIa, and FcγRIIIb; Native Antigen Company). The FcγR proteins were pre-incubated with streptavidin–phycoerythrin (SAPE; Thermo Fisher Scientific). The FcγR–SAPE conjugate mixture was gently rolled for 10 minutes at room temperature to allow complex formation. The resulting FcγR–SAPE complexes were then added to the assay plates at a final FcγR concentration of 2 µg/mL (SAPE dilution 1:2000) in LAB buffer at 50 µl/well and incubated for 1 hour

on a plate shaker (700 rpm) at room temperature. After incubation, plates were washed three times, and 100 µl/well Magpix fluid added (Thermo Fisher Scientific). Relative antigen-specific activity was subsequently determined using a Bio-Plex MAGPIX Multiplex Reader (Bio-Rad).

The antigen target for standard curve quantification was selected based on assay reproducibility: the full MERS-CoV spike protein was used for FcγRIIa, FcγRIIIa, and FcγRIIb, while the S1 subunit was used for FcγRIIIb. A positive control derived from the pooled serum standard was included on each plate at its optimal working dilution (1:1600 for FcγRIIa and 1:800 for FcγRIIb, FcγRIIIa, and FcγRIIIb). For quality control, interpolated values of the positive control for each antigen target were reviewed to verify assay performance. The limit of detection (LOD) was defined as the lowest concentration of the standard yielding a signal exceeding the mean blank plus two standard deviations, as determined from the standard curve.

2.6.2.1.1.1.6.1.3 Data analysis

Median fluorescence intensity (MFI) values were exported from xPONENT software and analysed using fitted standard curves in GraphPad Prism v10.6.1 (GraphPad Software, USA), analogous to ELISA-based quantification. This approach enabled semi-quantitative comparison of FcγR-binding responses across plates and experiments, with higher MFI values indicating stronger antigen-specific FcγR engagement. Assay reproducibility was confirmed by consistent performance of the positive control and pooled standard sera across independent runs.

2.6.2.1.1.1.6.2 FcγR Binding Assay (Mouse Samples)

The same multiplex Luminex platform was applied to preclinical mouse serum samples following the same workflow, with adjustments for species-specific Fcγ receptors (FcγRIa, FcγRIIb, FcγRIII and FcγRIV; Sino Biological), standard curve concentration ranges, sample dilution factors, and FcγR concentrations to account for differences in antibody titres between species. All other assay conditions, including bead coupling, incubation, and readout, were identical to those used for the human assays.

A two-fold serial dilution starting at 1:100 was used for selected samples analysed for FcγRIa, FcγRIIb, and FcγRIV, while a three-fold serial dilution starting at 1:100 was used for FcγRIII to optimize the dynamic range for each target. Only MERS-CoV antigens were assessed in this assay. Antigen curves used for quantification were selected based on assay reproducibility: the S2 subunit was used for FcγRIa, FcγRIIb, and FcγRIV, and the full spike (S) protein was used for FcγRIII. A positive control (Standard 5), derived from the standard serum, was included on each plate at the optimal working dilution for each receptor assay (1:1600 for FcγRIa, FcγRIIb, and -IV, and 1:8100 for FcγRIII).

The FcγR–SAPE complexes were then added to the plates at a final FcγR concentration of 1 µg/mL in LAB buffer (50 µL per well), followed by incubation and readout as described above.

2.6.2.1.2 Neutralisation assays

Neutralisation assays were performed to assess antibody-mediated inhibition of viral entry. The plasmids used for pseudovirus production and receptor expression are summarized in Table 2-11.

Plasmid	Description / gene	Source / supplier	Application
p8.91	HIV-1 packaging plasmid encoding Gag and Pol	[326]	Pseudovirus production
pCSFLW	Luciferase reporter plasmid carrying firefly luciferase	[328]	Pseudovirus production
pENTR4-LPTOS MERS-S (without tPA)	Full-length MERS-CoV spike glycoprotein	University of Oxford	MERS-CoV pseudovirus production
pcDNA3.1-SARS-CoV-2-S	Full-length SARS-CoV-2 spike glycoprotein (Wuhan-Hu-1)	University of Oxford	SARS-CoV-2 pseudovirus production
pcDNA3.1-hACE2	pCAGGS-ACE2	S. Pöhlmann & M. Hoffmann, Leibniz Institute for Primate Research	Co-transfection for SARS-CoV-2 PNA
human TMPRSS2 protease	pCAGGS-TMPRSS2		

Table 2-11. Plasmids used for pseudovirus production and receptor expression.

2.6.2.1.2.1 MERS-CoV

2.6.2.1.2.1.1 Pseudovirus production

MERS-CoV pseudovirus expressing the full-length spike (S) glycoprotein was produced in HEK-293T cells using a three-plasmid transfection system. For each transfection (corresponding to one well of a 6-well plate), cells were transfected with 250 ng of p8.91 (HIV-1 packaging plasmid encoding Gag and Pol), 375 ng of pCSFLW (transfer plasmid carrying a firefly luciferase reporter gene flanked by HIV-1 LTRs and the packaging signal), and 150 ng of pENTR4-LPTOS MERS S (without tPA), which encodes the full-length spike glycoprotein from the MERS-CoV isolate Camel/Qatar_2_2014 (GenBank accession no. KJ650098.1).

If plasmid amplification was required, Escherichia coli strain DH5α was transformed with the respective plasmids and cultured on Luria–Bertani (LB) agar or in LB broth supplemented with 100 µg/mL carbenicillin or ampicillin. Plasmid DNA was subsequently purified using standard procedures, following the manufacturer's instructions for the Qiagen MidiPrep Kit (Qiagen).

HEK-293T/17 cells (Cytion) were seeded in 6-well plates (Corning Incorporated) at a density of 2.0 × 10^5 cells/mL in complete DMEM and allowed to grow until they reached roughly 60–80% confluency. Transfection mixes were prepared in 100 µL of Opti-MEM (Thermo Fisher Scientific) by combining the plasmid DNA with FuGENE-HD (Promega) at a ratio of 0.3 µL FuGENE-HD per 100 ng of total

DNA. The mix was incubated for about 20 minutes at room temperature before being added dropwise to each well.

While the complexes were forming, the culture medium in the wells was replaced with 2 mL of fresh, pre-warmed DMEM. Following transfection, cells were incubated at 37˚C in a humidified 5% CO_2 incubator for 48 hours. The supernatants containing pseudovirus particles were then collected, passed through a 0.45 µm filter (Millipore) to remove cell debris, and pooled. The filtered virus was aliquoted into 1.5 mL tubes and stored at −80˚C until use.

2.6.2.1.2.1.2 Pseudovirus titration

To determine the viral titre, pseudovirus preparations were thawed from −80 °C and immediately serially diluted twofold using 100 µL of neat virus in R10 medium directly in a white Nunc 96-well plate (Thermo Scientific). Huh-7 cells (CLS Cell Lines Service GmbH, Eppelheim, Germany) were then added under conditions identical to those used in the neutralisation assay (4.0×10^4 cells/50 µL, corresponding to 8.0×10^5 cells/mL), and an additional 50 µL of medium was added to each well to bring the total volume to 150 µL. The plates were then incubated at 37 °C with 5% CO_2 for 48 hours.

After incubation, the culture medium was removed by inverting and gently tapping the plate, and a 1:1 mixture of Bright-Glo reagent (Promega) and PBS was prepared (3 mL per plate, sufficient to cover all wells) and 30 µL/well added to the plate. The plate was then left at room temperature for five minutes to allow the luminescent signal to develop. Luciferase activity was measured as relative light units (RLU) using a CLARIOstar plate reader. RLU values were adjusted according to the dilution used in each well to estimate the viral concentration in the original stock. The adjusted RLU values were plotted against the logarithm of the final dilution, and the viral titre was determined from the portion of the curve showing a clear linear relationship between dilution and signal.

2.6.2.1.2.1.3 Pseudovirus neutralisation assay

Plasma (human) or serum (mouse) samples were incubated at 56˚C for 30 minutes prior to use to heat-inactivate it. Samples were then serially diluted twofold in R10 medium to a final volume of 50 µL per well. MERS-CoV pseudovirus was diluted in R10 to a concentration of 2.0×10^6 RLU/mL, and 50 µL of the diluted virus was added to each well. The serially diluted serum or plasma samples and pseudovirus were mixed at a 1:1 ratio and incubated at 37˚C with 5% CO_2 for two hours to allow neutralisation.

Following this incubation, Huh-7 cells (CLS Cell Lines Service GmbH, Eppelheim, Germany) were added at a density of 8.0×10^5 cells/50 µL (equivalent to 2.0×10^6 cells/mL) to each well. The plates were then incubated for 48 hours at 37˚C with 5% CO_2. After incubation, media was removed, BrightGlo/PBS added, and RLU signal read as described above.

The results of the pseudovirus neutralisation assay were expressed as IC_{50} values, representing the inhibitory concentration at which 50% of viral entry was blocked. IC_{50} values were calculated using GraphPad Prism software, as described previously [329]. Each assay plate included positive controls, as well as virus-only and cell-only controls to ensure assay validity.

2.6.2.1.2.2 SARS-CoV-2 Pseudovirus Neutralisation Assay

The neutralising activity of serum samples against SARS-CoV-2 was measured using a lentivirus-based pseudovirus neutralisation assay, adapted from the procedure described for MERS-CoV (Section 2.6.2.1.2.1). The SARS-CoV-2 pseudovirus expressed the full-length spike (S) glycoprotein from the Wuhan-Hu-1 isolate (GenBank accession no. MN908947.3) and contained a firefly luciferase reporter gene.

HEK293T/17 (Cytion) cells were subcultured in T275 flasks (Corning Incorporated) and transfected 24 hours prior to infection with plasmids encoding human ACE2 and TMPRSS2 at a 1:1 ratio, using FuGENE® HD (Promega) in Opti-MEM (Thermo Fisher Scientific) at a ratio of 0.3 µL transfection reagent per 100 ng of total plasmid DNA. Transfected cells were maintained at 37 °C with 5% CO_2 until use in pseudovirus titration and neutralisation assays.

Heat-inactivated serum samples were serially diluted threefold in R10 medium, starting at 1:50 or 1:150 depending on sample titre. Diluted samples were mixed at a 1:1 ratio with SARS-CoV-2 pseudovirus and incubated for 2 hours at 37˚C with 5% CO_2. Following incubation, the ACE2-/TMPRSS2 transfected HEK293T/17 cells were added and incubated at 37 °C with 5% CO_2 for 48 hours.

After incubation, the culture medium was carefully removed using an aspirator to avoid disturbing the cell monolayer. Bright-Glo reagent (Promega), diluted 1:1 in PBS, was added at 30 µL per well, and plates were incubated for 5 minutes at room temperature in the dark. Luminescence was measured using a CLARIOstar Plus luminometer (BMG Labtech).

The 50% inhibitory concentration (IC_{50}) was determined using nonlinear regression analysis in GraphPad Prism (version 10.6.1). Neutralisation titres were expressed as the reciprocal serum dilution at which 50% inhibition of pseudovirus entry was achieved.

2.6.2.1.2.3 ChAdOx1-SEAP Anti-Vector Neutralisation Assay

Anti-ChAdOx1 vector neutralising antibody titers were measured using a cell-based assay with secreted alkaline phosphatase (SEAP) readout. The protocol was as described previously for serum and plasma measurement [104] with modification to include a standard curve for quantification. Briefly, GripTite MSR 293 cells (Thermo Fisher Scientific) were seeded in 96-well flat bottom plate (Nunc) for 24±2 hours, to reach 80-90% confluency at the point of transfection.

Samples were heat-inactivated for 90 minutes at 56°C in heat block or water bath, then diluted at 1/100 in Complete DMEM (Phenol Red–Free, 0% FBS). Samples were randomized and tested blind in triplicates. Pool of serum from volunteers with high anti-ChAdOx1 vector neutralising antibody titres was used to prepare a standard curve consisting of a two-fold ten-point serial dilution from 1/20, which was assigned arbitrary units (AU). Each plate also included a positive internal control prepared from the standard pool and a virus-only negative control.

Recombinant ChAdOx1–SEAP virus at a multiplicity of infection (MOI) of 500, diluted in Complete DMEM (Phenol Red–Free, 0% FBS), was mixed with samples at a 1:1 ratio and incubated for 1 hour at 37˚C. Triplicate aliquots of each sample were then applied to GripTite MSR 293 cells and incubated for 1 hour at 37 °C to permit infection. The mixture was subsequently removed using an aspirator and replaced with Complete DMEM (Phenol Red–Free, 10% FBS), and cells were incubated for an additional 24 ± 2 hours. Culture supernatants were then collected, and SEAP activity was quantified using the Phospha-Light™ SEAP Reporter Gene Assay System (Thermo Fisher Scientific), following the manufacturer's instructions. Luminescence was measured using a ClarioStar Plus plate reader (BMG Labtech).

Using BMG ClarioStar MARS software, the relative light unit (RLU) output of the standard curve was fitted to a four-parameter logistic curve against arbitrary standard units (AU) (AU and RLU log-transformed), and the curve was used to convert RLU of individual test samples into AU. Responses were reported based on the average of triplicates.

2.6.2.1.3 MESO Scale Discovery (MSD) Multiplexed Immunoassay

The MESO Scale Discovery (MSD) platform is an electrochemiluminescence-based assay that enables highly sensitive detection and quantification of multiple analytes simultaneously. The assay was performed according to the manufacturer's instructions using the V-PLEX® Coronavirus Panel 3 (IgG) Kit (Meso Scale Discovery).

Briefly, MSD plates pre-coated with spike proteins from a panel of human coronaviruses (HCoVs) were used. The panel included nine antigens: HCoV-229E Spike, HCoV-HKU1 Spike, HCoV-OC43 Spike, HCoV-NL63 Spike, SARS-CoV-1 Spike, SARS-CoV-2 Nucleocapsid (N), MERS-CoV Spike, SARS-CoV-2 S1 Receptor Binding Domain (RBD), and SARS-CoV-2 Spike. Plates were first blocked to prevent non-specific binding, then washed and incubated with test samples, reference standards, and controls. Following incubation, plates were washed three times with washing buffer, and a SULFO-TAG™ anti-human IgG detection antibody was added. After a final set of three washes, MSD GOLD Read Buffer B was added, and the plates were immediately read using a MESO SECTOR S 600 plate reader. Electrochemiluminescent signals were recorded and analyzed using MSD DISCOVERY

WORKBENCH® software, with results expressed in arbitrary units (AU/mL) or normalized to reference standards as appropriate.

2.6.2.1.4 Normalization of Data

As the supply of the NIBSC international standard (IS; 19/178) is limited [321], it is not feasible to include it on every assay plate. Therefore, an internal control (IC) was established and used as a plate control for data normalization in the pseudovirus neutralisation assay (PNA), which is inherently more variable between runs. The relationship between the IS and IC was determined by running both standards in parallel, allowing the IC to serve as a secondary reference standard. Once characterized, the IC is included on each PNA plate to normalize assay data and ensure consistency across experiments. The mean IS readout was determined from five plates analysed across three independent assays, providing a reliable calibration reference.

In contrast, the ELISA IgG assay demonstrates higher inter-assay consistency. Therefore, ELISA results are converted directly from EU to international units per millilitre (IU/mL) based on ratio of EU to IU from repeated tests of International Standard (concentration set by NIBSC/WHO at 1000 IU/mL).

2.6.2.2 Cellular assays

2.6.2.2.1 Human assays

2.6.2.2.1.1 Peptides sequence and matrix pools

To stimulate T cells, 275 synthetic peptides (15mers overlapping by ten amino acids) spanning the entire vaccine insert were used, including the tissue plasminogen activator leader sequence to test the signal peptide response as a positive control. To determine the region of the protein that was responsible for the activation, these peptides were divided into 17 pools containing 16 or 19 consecutive peptides. The sequence of the peptides and the pools they belong are described in Supplementary Table 1.

2.6.2.2.1.2 Culture medium

Medium for T cell cultures (R10HS) was prepared using RPMI-1640 supplemented with 10% human AB serum (Merck), 2 mM L-glutamine, 1% non-essential amino acids, 1% sodium pyruvate, 1% pen/strep, 5×10^{-5} β-mercaptoethanol (all from Gibco).

2.6.2.2.1.3 Multiparametric flow cytometry analysis of PBMC and subsequent clustering analysis

PBMC were thawed, incubated for 1 hour with 2.5U/mL Benzonase® Nuclease (Millipore) and rested overnight in R10HS medium supplemented with 25 ng/mL IL-7 and 0.5 uL CD40 antibody (Miltenyi Biotec). Cells were recovered, stained with Acqua Live/Dead (ThermoFisher) and antibodies listed in Supplementary Table 2. Samples were then acquired in X50 FACSymphony instrument (BD Bioscience). Normalization (using the Cytonorm plugin) and gating of live CD4 and CD8 T cells was done using FlowJo. Clustering of CD4 and CD8 T cells was done using FlowSOM and ConsensusClusterPlus in RStudio.

2.6.2.2.1.4 Ex vivo frequency of Spike-specific T cells using activated induced markers (AIM)

Thawed PBMCs were loaded with either MERS peptide pool or, as a control, a mix of CEF (3616-1, Mabtech) and CEFTA (3617-1, Mabtech) peptide pools, at a final concentration of 2 μg/mL of each peptide, for 1 hour in the incubator. Subsequently, the volume of medium was adjusted, and cells were cultured overnight in R10HS supplemented with 25 ng/mL IL-7 and 0.5 uL CD40 antibody (Miltenyi Biotec). In the next day, cells were stained with Acqua Live/Dead (ThermoFisher) and antibodies (Supplementary Table 2) and acquired in X50 FACSymphony instrument (BD Bioscience). The percentage of CD25+41BB+ CD8 T cells and CD25+CD40L CD4 T cells were determined using FlowJo.

2.6.2.2.1.5 Expansion of Spike-specific T cells

Thawed PBMCs were loaded for 1 hour with 2 μg/mL MERS peptide pool or a mix of CEF and CEFTA peptide pool as a positive control. Cells were cultured for 3 days in R10HS supplemented with 25 ng/mL IL-7. Half the medium was replaced with R10HS supplemented with 1000 IU/mL Proleukin (IL-2), on day 3, and then every 2 to 3 days. On day 13, IL-2 was removed by washing the cells with R10HS, and ICS was performed the following day.

2.6.2.2.1.6 Intracellular staining of cytokines (ICS)

PBMC was expanded for two weeks with CD3/CD28 Dynabeads (ThermoFisher) to be used as target cells. Target cells were loaded with 2 μg/mL MERS peptide pool for 1 hour. T cells expanded for two weeks from blood of the same patient taken at day 0, 14 and 28 were barcoded with CFSE and CTV dyes as previously described [330]. The cells from the three time points and the loaded target cells were pooled and cultured for 4 hours in the presence of brefeldin A (Biolegend) and monensin (eBioscience). After incubation, cells were stained with Acqua Live/Dead, fixed with Fixation buffer (Biolegend), and stained in the presence of Permeabilization Buffer (ThermoFisher) with the antibodies listed in Table 2-4. Samples were acquired in LSRFortessa X-20 (BD Bioscience), and analysed using FlowJo v10 (BD Bioscience). The Boolean analysis was done by creating combination gates in FlowJo and the program SPICE was used to allow for a better visualization of the results.

2.6.2.2.1.7 Sorting of Spike-specific T cell lines and clones

After expanding the T cells for 2 weeks with spike peptide pool, cells were cultured overnight with the same pool in the presence of CD40 antibody. After incubation, cells were stained with Acqua Live/Dead and antibodies listed in Table 2-5. CD25+41BB+ and CD25+CD40L+ double positive T cells were

sorted either as bulk lines or clones. T cells were then expanded, as previously described [330], by stimulation with phytohaemagglutinin (PHA), irradiated allogeneic PBMC and IL-2.

2.6.2.2.1.8 LCL generation and coculture with T cells

Autologous EBV-LCLs were generated as previously reported [330], by culturing PBMC in the presence of supernatant from B95-8 marmoset cells and cyclosporin A. LCL were, then, incubated overnight with 10 µg/mL recombinant Spike proteins (kindly provided by Gavin Scraeton), washed, and co-cultured with Spike-specific CD4 T cell lines in the presence of brefeldin A and monensin for 4 hours. Cells were then stained with the ICS panel (Table 2-6), acquired in LSRFortessa X-20, and analysed using FlowJo.

2.6.2.2.2 Mouse assays

2.6.2.2.2.1 IFNγ ELISPOT, Intracellular Cytokine Staining and Flow Cytometry and ICS staining

Splenic T-cell ELISpot assays were performed following stimulation with the immunodominant epitope in the S1 region, as described previously [307]. Hydrophobic PVDF membrane ELISpot plates (Millipore) were coated with 50 µL per well of 5 µg/mL anti-mouse IFNγ capture antibody (clone AN18; Mouse IFNγ ELISpot ALP Kit, Mabtech) in carbonate–bicarbonate buffer and incubated overnight at 4˚C. On the following day, plates were blocked with 100 µL per well of complete DMEM for at least one hour at room temperature. Spleen cell suspensions were prepared on the same day, as described in section 2.4.3. After removing the blocking medium, splenocytes were plated in duplicate at twofold serial dilutions over five dilutions and stimulated with 2 µg/mL of the MERS-CoV–specific peptide (VYDTIKYYSIIPHSI; Mimotopes) prepared in complete DMEM. Plates were then incubated for 18–20 hours at 37˚C in a humidified CO_2 incubator. After incubation, plates were washed six times with PBS, and 50 µL per well of biotinylated anti-mouse IFNγ detection antibody (Mabtech) was added and incubated for 2 hours at room temperature. Plates were then washed six times with PBS and treated with 50 µL per well of streptavidin–alkaline phosphatase (Mabtech) for 1 hour. Spots were developed using the ELISpot Colour Development Kit (Bio-Rad) according to the manufacturer's instructions, and incubating at room temperature until spots were clearly visible. Plates were then gently washed with tap water, air-dried overnight on paper towels, and the spots were counted using an AID ELISpot reader and software.

For analysis of intracellular cytokine production, single-cell suspensions of splenocytes were stimulated at 37˚C for 6 hours with 2 µg/mL of the immunodominant peptide and overlapping peptide pools spanning the MERS-CoV spike protein, divided into S1 (ELISpot pools 1–8) and S2 (ELISpot pools 9–12) regions (ProImmune Ltd., thinkpeptides®; see Supplementary Table X). Phorbol 12-myristate 13-acetate (PMA) (Thermo Fisher) was used as a positive control, while unstimulated cells cultured in medium only served as negative controls. GolgiPlug (BD Biosciences) was added during stimulation to

inhibit cytokine secretion and permit intracellular accumulation, and anti-CD107a–Alexa 647 antibody (BioLegend) was included at the start of incubation to identify degranulating cells.

Following stimulation, cells were washed and stained with fluorochrome-conjugated antibodies specific for surface markers (listed in Table 7-9). Cells were then fixed with 4% paraformaldehyde (Biotium), permeabilized, and stained intracellularly for IFN-γ, TNF-α, and IL-4.

2.6.2.2.2.2 B-cell ELISPOT

Hydrophobic PVDF membrane ELISpot plates (Millipore) were coated with MERS S-clamp protein (kindly provided by Dr. Keith Chappell, Australian Infectious Disease Research Centre, Queensland, Australia) at 5 µg/mL in PBS (50 µL per well) and incubated overnight at 4˚C. As a positive control, wells were coated with anti-mouse IgG (Mabtech) at 15 µg/mL in PBS (50 µL per well), according to the manufacturer's instructions, and incubated under the same conditions. The following day, plates were blocked with 100 µL per well of R10 medium for at least one hour at 37˚C.

Single-cell suspensions from spleen and BM were prepared as described previously (Section 1.2.3). Cells were plated in duplicate at twofold serial dilutions in R10 medium, maintaining a final volume of 200 µL per well. Cell concentrations were adjusted for each dilution to ensure consistent total volumes across wells. The concentration of viable cells was determined prior to plating using a Countess (Invitrogen) or Casy (Roche) automated cell counter. Plates were incubated for 18–20 h at 37˚C in a humidified 5% CO_2 incubator.

After incubation, plates were washed five times with PBS. Biotinylated anti-IgG antibody (Mabtech), prepared according to the manufacturer's instructions, was added (50 µL per well) and incubated for 2 hours at room temperature. Plates were washed five times with PBS and then incubated for 1 hour at room temperature with HRP-streptavidin (Mabtech) prepared according to the manufacturer's instructions. Spots were developed using an AEC (3-amino-9-ethylcarbazole) substrate kit (BD Biosciences) according to the manufacturer's instructions and incubated at room temperature until spots were fully developed. Plates were gently washed with tap water and air-dried before counting. Spots corresponding to antibody-secreting cells were enumerated using an AID ELISpot reader and software (AID).

To detect antibody-secreting memory B cells, splenocytes and BM cells were stimulated for six days in expansion medium at 37˚C in a humidified 5% CO_2 incubator prior to the ELISpot assay. The expansion medium was refreshed every other day to maintain optimal cell viability and activation.

2.6.3 Application to the MERS-DoE Study

A subset of these assays (specifically, IgG and PNA) were used in the MERS-DoE experiment, which also included other immunological techniques such as flow cytometry and ELISpot. The methods unique to the DoE study are presented in Chapter 6.

2.7 Statistical Analysis

All statistical analyses were performed using GraphPad Prism version 10.6.1 (892) (GraphPad Software), JMP Student Edition version 19 (SAS Institute Inc.), and Microsoft Excel. Data were first assessed for normality using the Shapiro–Wilk test, and appropriate parametric or non-parametric tests were applied accordingly. Statistical significance was defined as $p < 0.05$.

Comparisons between two groups were performed using unpaired t-tests or Mann–Whitney U tests, while multiple group comparisons were analysed using ordinary one-way ANOVA followed by Tukey's multiple comparisons test, or the Kruskal–Wallis test with post hoc multiple comparisons, depending on data distribution. Differences in IgG titres were determined using one-way ANOVA with Tukey's correction, whereas neutralisation titres were compared using the Kruskal–Wallis test. Correlations between continuous variables were assessed using Pearson's or Spearman's correlation coefficients, as appropriate.

Antibody decay was assessed using two complementary approaches, as described previously [331, 332]. First, decay rates were estimated using an exponential decay model assuming first-order kinetics. For each participant, post-peak antibody titres were fitted to an exponential decay curve, where antibody levels decrease over time from the peak response according to a constant decay rate. Antibody half-life was calculated from the estimated decay constant [332]. Second, decay rates were independently estimated using linear regression of $\log_2$-transformed post-peak antibody titres. Log_2-transformed titres were modelled as a linear function of time, consistent with first-order decay on a logarithmic scale. The decay rate was derived from the slope of the fitted regression line, and antibody half-life was calculated from this slope [331].

For multivariate analysis, principal component analysis (PCA) was used to explore clustering and variance among experimental groups, while partial least squares (PLS) regression was applied to identify relationships between immunological parameters and outcomes such as antibody titres or neutralisation activity. Least absolute shrinkage and selection operator (LASSO) regression was also performed in JMP Student Edition for variable selection and identification of key predictors of immune responses. Model performance was evaluated using R^2, Q^2, and root mean square error (RMSE) values, and variable importance in projection (VIP) scores were used to identify influential variables within each model.

Data were $\log_{10}$-transformed where appropriate to improve normality. Percentage data, particularly from cellular assays, were arcsine square-root transformed to stabilize variance prior to analysis. Data used in multivariate models were z-score normalized to standardize variable scales. Graphical outputs, including scatter plots, correlation matrices, PCA and PLS score plots, and night plots, were generated using GraphPad Prsm, JMP, and Microsoft Excel.

3 Exploratory Analysis of Humoral and Cellular Responses to the ChAdOx1 MERS-CoV Vaccine Candidate

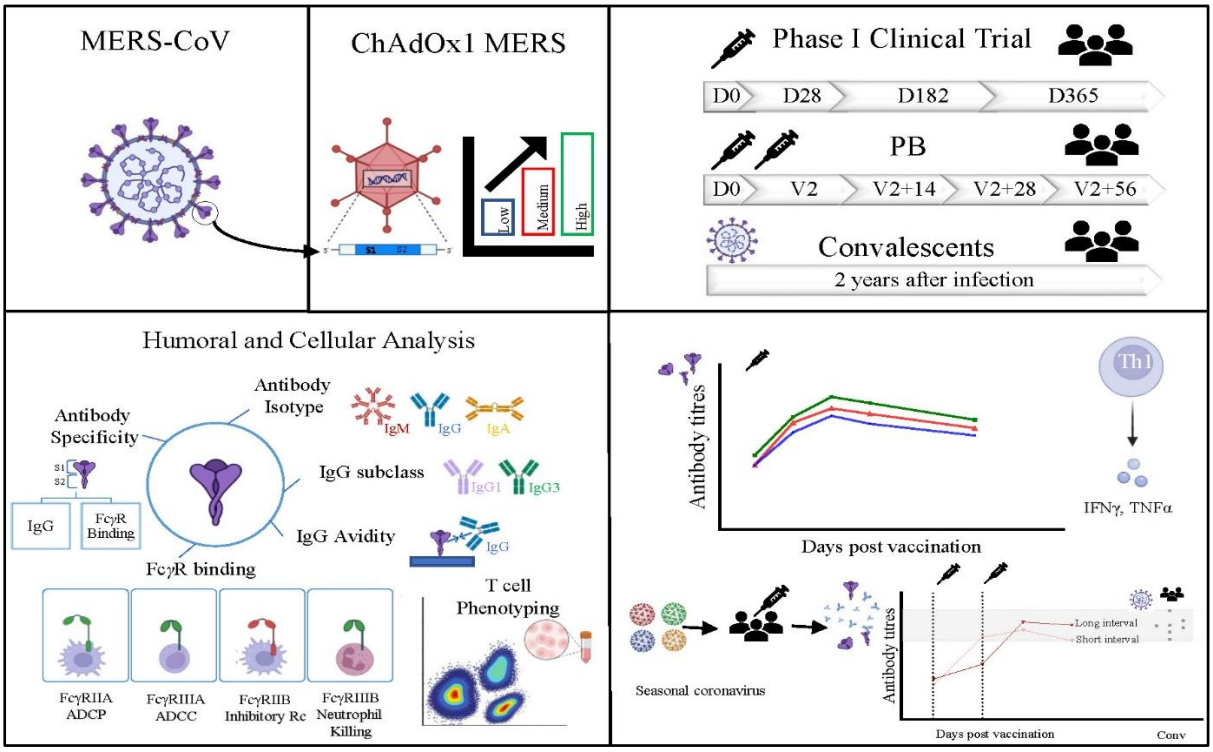


Figure 3-1. Visual abstract of the study methods and results.

Highlight

- A single dose of ChAdOx1 MERS induces durable, multifunctional immune responses detectable up to one-year post-vaccination.
- The medium dose of ChAdOx1 MERS elicited a durable and progressively increasing antibody avidity, indicating ongoing maturation of the humoral immune response.
- Higher single doses broaden spike recognition, while boosting further increases responses to levels seen in convalescent individuals.
- A longer prime–boost interval produces more sustained immune responses than a short interval.
- Vaccination induces strong Th1-biased $CD4^+$ and $CD8^+$ T cell responses, with $CD8^+$ T cells predominantly S1-specific.
- Cross-reactive antibody and T cell responses against other betacoronaviruses are detected post-vaccination and shaped by pre-existing immunity to seasonal coronaviruses.

3.1 Introduction

MERS-CoV continues to pose a global health threat, with sporadic cases associated with high mortality still reported in Saudi Arabia [333]. MERS-CoV is listed on the World Health Organisation (WHO) blueprint of priority pathogens for research and development [334]. To date, there is no licensed vaccine to prevent MERS infection. The vaccine candidate ChAdOx1 MERS has been evaluated in phase I dose-escalation clinical studies in both the United Kingdom (UK) and the Kingdom of Saudi Arabia (KSA) [291, 292].

Findings from the ChAdOx1 MERS UK trial contributed directly to dose selection strategies for the AstraZeneca/Oxford COVID-19 vaccine (Vaxzevria), which later received WHO emergency use authorization in February 2021 [335]. Importantly, the initiation of MERS vaccine trials before the COVID-19 pandemic and before licensure of ChAdOx1 nCOV-19 provided a unique opportunity to investigate detailed humoral immune responses without the confounding effects of widespread SARS-CoV-2 exposure and immune imprinting. Interestingly, early efficacy data for ChAdOx1 nCOV-19 suggested unexpectedly higher protection following a lower dose priming (comparable to the medium dose tested in our study). Subsequent post-hoc analyses indicated that this effect was largely driven by the dosing interval [97], underscoring the importance of understanding how doses and intervals shape the humoral response to adenovirus vectored coronavirus vaccination.

In the case of MERS vaccination, optimising dose and schedule is of particular importance because infection is associated with a much higher mortality rate than COVID-19 [336]. Initial clinical trials of ChAdOx1 MERS demonstrated that neutralising antibody responses were strongest at the highest dose tested (5×10^{10} vp) with similar overall IgG induction across both the MERS001 and MERS002 trials. However, the breadth and functionality of humoral immunity beyond neutralisation remain poorly defined.

The aim of this chapter is therefore to conduct a comprehensive characterisation of the humoral immune response to ChAdOx1 MERS, employing detailed further analyses, including antibody isotypes, IgG subclasses, Fc receptor binding, avidity, and recognition of distinct spike subunits (S1 and S2). By comparing responses across three dose levels, booster regimens with different intervals, and two geographically distinct populations, this analysis provides new insights into how dose and schedule shape the quality of humoral immunity induced by ChAdOx1 MERS. In addition, we assess data from T-cell assays performed in a subset of MERS-001 participants, including multiparametric flow cytometry to evaluate the phenotype and cross-reactivity of vaccine-induced T cells, and IFNγ ELISpot assay, thereby complementing the humoral findings.

3.2 Results

3.2.1 Overview of study design and immunogenicity analyses

The immunogenicity of ChAdOx1 MERS was evaluated in participants from the phase I MERS001 (UK) and MERS002 (KSA) clinical trials, as described in the methods section (see Figure 2-1 for the overall study design). Volunteers received a single intramascular injection (IM) of ChAdOx1 MERS at one of three doses: low (5×10^{9} vp, n=12), medium (2.5×10^{10} vp, n=18), or high (5×10^{10} vp, n=18). For each dose group, participants were evenly split between the two study sites. In addition, two subgroups from MERS001 received a medium-dose prime–boost regimen, with either a long (182-day, n=1) or short (28-day, n=2) interval between doses.

In accordance with pre-established quality control criteria, one sample from the medium-dose cohort in MERS002 was excluded from the final serological analysis. The exclusion was necessitated by a significant physical opacity in the sample matrix that interfered with optical detection and precluded acquisition of reliable ELISA measurements.

Two participants were not included in the complete immunogenicity analysis: one from the high-dose group in MERS001 withdrew consent, and all of that participant's samples were subsequently destroyed, while one from the medium-dose group in MERS002 had missing post-vaccination samples.

Immunological responses were assessed by measuring antibody isotypes, IgG subclass distribution, avidity, Fc receptor binding, and spike subunit (S1/S2) recognition, and were compared with convalescent samples (n=9), including the WHO International Reference Standard (NIBSC 19/178). Antibody cross-reactivity against spike proteins from seasonal human coronaviruses was evaluated in group 3 participants from both MERS001 (n=8) and MERS002 (n=9).

T-cell responses were evaluated through IFN-γ ELISpot assays performed in MERS001 participants, which allowed assessment of T-cell responses after boosting and direct comparison with previously published prime-only data. Multiparametric flow cytometry was conducted in a subset of MERS001 participants to characterise the magnitude, phenotype, and functional profile of vaccine-induced $CD4^{+}$ and $CD8^{+}$ T cells (n=9). Cross-reactive T-cell responses were assessed within this same subset. The number of participants included in each assay differed because not all immunological analyses were performed across the full cohort.

This chapter focuses on the analysis of these immunogenicity data and their comparison between dose groups, study sites, and vaccination regimens.

3.2.2 Immunogenicity of ChAdOx1 MERS after a single dose

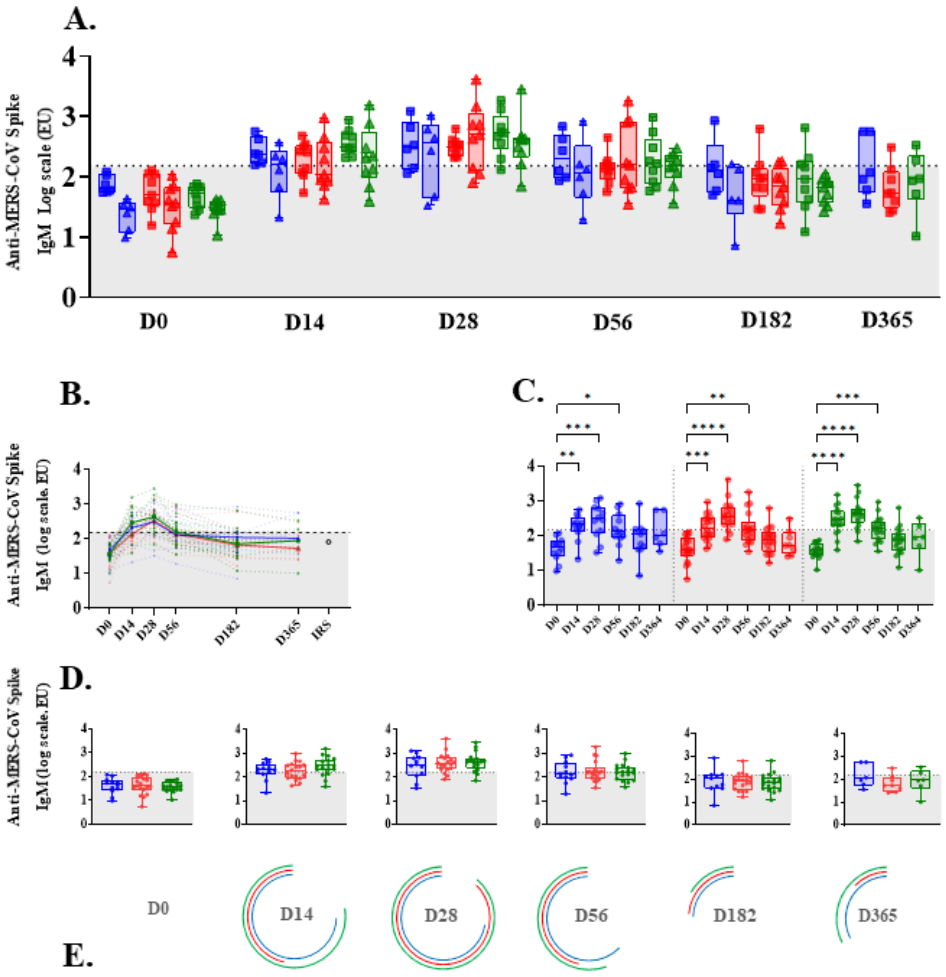
3.2.2.1 Isotype induction

3.2.2.1.1 IgM responses

IgM responses showed similar trends between cohorts, with low-dose differences falling below the assay limit of detection and considered background (Figure 3-2A). Data for subsequent analyses were therefore combined across the two trials.

MERS-specific IgM responses were dose dependent, detectable by D14 in medium- and high-dose groups, peaking at D28 with significant increases from baseline across all doses before declining by D56 (Figure 3-2B). At the peak time point, all three dose groups showed significant increases from baseline (low dose: $p = 0.0004$; medium dose: $p < 0.0001$; high dose: $p < 0.0001$). Median IgM titres at D28 were 316 EU (interquartile range [IQR] 121–652) in the low-dose group, 359 EU (IQR 214–653) in the medium-dose group, and 437 EU (IQR 244–583) in the high-dose group (Figure 1C). By D56, IgM levels remained detectable in all doses compared to their baseline ($P<0.05$).

No significant differences in IgM magnitude were observed between dose groups at any timepoint (Figure 3-2D). In contrast, seroconversion rates were highest in the high-dose group, with 78% of participants positive at D14, 89% at D28, and 56% at D56 (Figure 3-2E). Together, these results indicate robust priming of B cells in the high-dose groups, with responses persisting until D56.



Gp	D0	D14	D28	D56	D182	D365
1	0	9/12 (75%)	**8/12 (67%)**	5/12 (43%)	3/11 (12%)	2/6 (33%)
2	0	8/17 (47%)	**15/17 (88%)**	8/17 (47%)	4/17 (24%)	1/8 (13%)
3	0	14/18 (78%)	**16/18 (89%)**	10/18 (56%)	3/18 (17%)	2/6 (33%)

Figure 3-2. MERS-CoV spike-specific IgM responses induced by ChAdOx1 MERS vaccination.

(A) Comparison of IgM titres between MERS001 (UK, squares) and MERS002 (KSA, triangles) cohorts across dose groups. **(B)** Time course of IgM responses by dose group, including comparison with the WHO International Reference Standard (NIBSC 19/178). **(C)** Pooled analysis of IgM responses across doses, comparing each group's baseline with post-vaccination timepoints. **(D)** Magnitude of IgM titres across groups at each timepoint. **(E)** Seropositivity analysis showing the proportion of responders by dose group (upper plots) and responder counts (table, lower panel). IgM responses were quantified by ELISA and expressed as ELISA units (EU). EU are plotted on a log10 scale. The dashed line indicates the seropositivity threshold (153 EU), calculated as the mean plus 3 standard deviations of baseline pre-vaccination samples. Boxes represent the interquartile range (IQR) with the medians indicated by horizontal lines; whiskers extend to 1.5× IQR, and data points represent individual participants. Dose groups are colour-coded as follows: blue = low dose (5×10^9 vp; n = 12), red = medium dose (2.5×10^{10} vp; n = 17), and green = high dose (5×10^{10} vp; n = 18). Statistical analyses included the Mann–Whitney test for head-to-head comparisons between MERS001 and MERS002 (A) and the Kruskal–Wallis test with Dunn's post hoc comparisons for dose and timepoint effects (C,D). Asterisks (*) denote statistical significance for within-group and between-cohort comparisons, as defined by P-values: * (P<0.05), ** (P<0.01), *** (P<0.001), **** (P<0.0001).

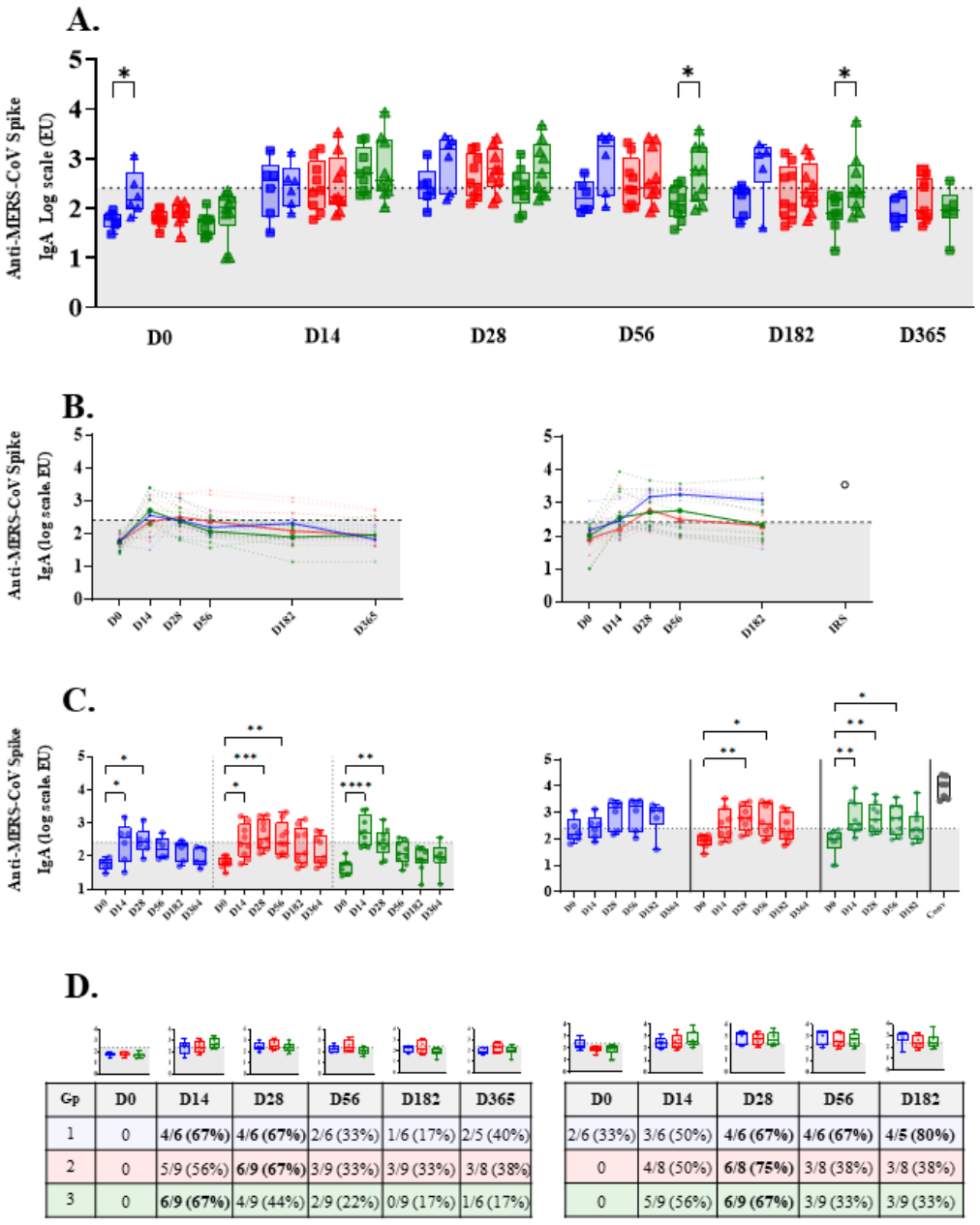
3.2.2.1.2 IgA responses

IgA titres differed between cohorts, with higher baseline and post-vaccination responses in MERS002, including baseline seropositivity in some low-dose participants (Figure 3-3A). To account for baseline differences between cohorts, IgA responses were analysed separately for MERS001 and MERS002 (Figure 3-3B–C).

In MERS001, IgA titres in the medium-dose group rose more gradually than in the high-dose group, peaking at D28 compared with D14 for high-dose vaccination. Notably, in MERS001, the medium-dose group exhibited sustained IgA induction, with seropositivity rates from D28 onwards comparable to or exceeding those of the low- and high-dose groups.

In MERS002, elevated baseline IgA titres—particularly in low-dose participants—were further boosted following vaccination, consistent with back-boosting of pre-existing cross-reactive immunity (Figure 3-3C, right panel). This suggests back-boosting of pre-existing cross-reactive responses. Seropositivity rates in MERS002 were consistently high across all dose groups (Figure 3-3D), and overall detection rates at six months were higher than in MERS001, although no clear dose-dependent trends were observed.

The highest vaccine-induced IgA titres were observed at D56 in the low-dose group of MERS002 (median 1830 EU, IQR 177–2798), which remained approximately 2.7-fold lower than titres in convalescent samples (median 11,644 EU, IQR 3274–24,924). By D182, median IgA responses across all dose groups had declined below the limit of detection, except for the low-dose group in MERS002, where the median titre remained above the limit of detection. These findings suggest cohort-specific modulation of IgA induction, likely influenced by baseline immunity, and support the potential role of booster vaccination in enhancing IgA responses.



Gp	D0	D14	D28	D56	D182	D365
1	0	**4/6 (67%)**	**4/6 (67%)**	2/6 (33%)	1/6 (17%)	2/5 (40%)
2	0	5/9 (56%)	**6/9 (67%)**	3/9 (33%)	3/9 (33%)	3/8 (38%)
3	0	**6/9 (67%)**	4/9 (44%)	2/9 (22%)	0/9 (17%)	1/6 (17%)

D0	D14	D28	D56	D182
2/6 (33%)	3/6 (50%)	**4/6 (67%)**	**4/6 (67%)**	**4/5 (80%)**
0	4/8 (50%)	**6/8 (75%)**	3/8 (38%)	3/8 (38%)
0	5/9 (56%)	**6/9 (67%)**	3/9 (33%)	3/9 (33%)

Figure 3-3. MERS-CoV spike–specific IgA responses after ChAdOx1 MERS vaccination.

(A) Comparison of IgA titres between the MERS001 cohort (UK; open circles) and MERS002 cohort (KSA; triangles) across dose groups. **(B)** Time course of IgA responses by dose group, shown separately for each cohort (left, MERS001; right, MERS002). NIBSC international reference serum (IRS) is shown for comparison. **(C)** Pooled IgA responses across doses (left, MERS001; right, MERS002), including human convalescent sera (HCS). **(D)** Seropositivity by dose group (upper panels: left = MERS001, right = MERS002) and responder counts (lower tables). Individual participant data points are shown. Dose colours: low (5×10^9 vp, blue; n = 12), medium (2.5×10^{10} vp, red; n = 17), high (5×10^{10} vp, green; n = 18). IgA responses were quantified by ELISA and expressed as ELISA units (EU). EU are plotted on a log10 scale. The dashed line indicates the seropositivity threshold (257 EU), calculated as the mean plus 3 standard deviations of baseline pre-vaccination samples. Statistical comparisons: Mann–Whitney test for pairwise cohort comparisons in (A); Kruskal–Wallis with Dunn's post hoc correction for within–group comparisons to baseline (D0) in (C,D). Asterisks (*) denote statistical significance for within-group and between-cohort comparisons, as defined by P-values: * (P<0.05), ** (P<0.01), *** (P<0.001), **** (P<0.0001).

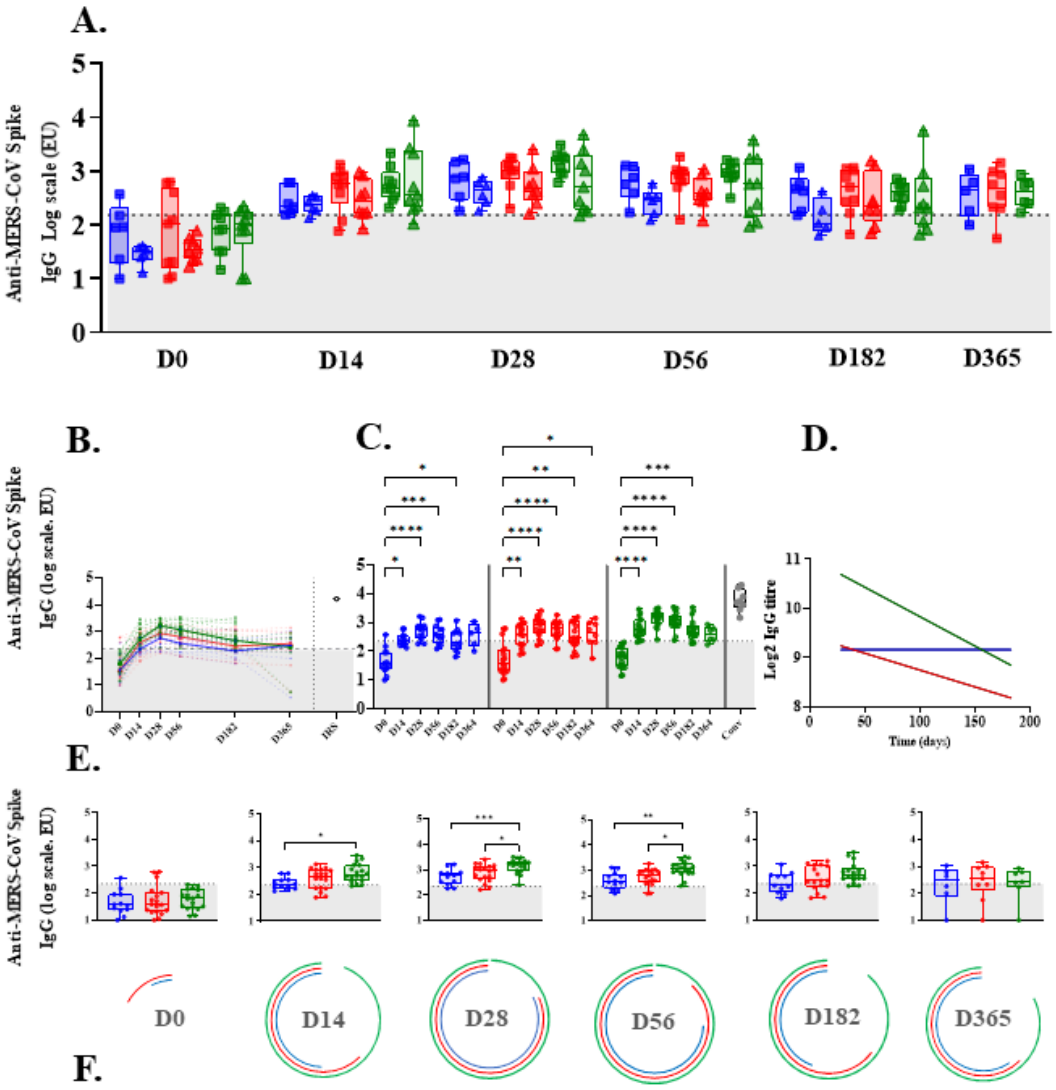
3.2.2.1.3 IgG responses

3.2.2.1.3.1 Spike total IgG

IgG titres were comparable between cohorts across dose groups (Figure 3-4A). Individual cohort-level data have been reported previously [291, 292], the analyses presented here are based on the pooled dataset from both trials to increase statistical power.

Anti-MERS-CoV IgG responses were dose dependent, with medium- and high-dose groups showing significant increases from baseline at all assessed timepoints and higher peak titres in the high-dose group at D28 (Figure 3-4B-C). At D28, the high-dose group reached a median of 1655 EUs (IQR, 929–2195) compared with 892 EUs (IQR, 512–1154) in the medium-dose group ($p = 0.01$). Seroconversion rates mirrored this pattern, reaching 100% on both D28 and D56 in the high-dose group (Figure 3-4C). Nevertheless, titres induced by the high-dose group at D28 remained approximately tenfold lower than the NIBSC International Reference Standard (16,707 EUs; Figure 3-4B) and were also below those observed in convalescent individuals, highlighting the need for a booster dose to achieve convalescent titres.

Following the peak response, IgG titres declined in all groups, with slower decay and greater durability observed in the medium-dose group compared with the high-dose group (Figure 3-4D). The estimated IgG half-life, calculated using $\log_2$-transformed titres between D28 and D182, was 129 days (IQR; 98–196) in the medium-dose group compared with 106 days (IQR; 66–123) in the high-dose group (Figure 3-4D). Importantly, antibody titres in both groups remained above baseline for most of the follow-up period; however, at D365 titres in the high-dose group were statistically similar to baseline, whereas the medium-dose group maintained titres above baseline. Together, these findings indicate that while dose escalation enhances peak antibody magnitude, moderate dosing may better support durable humoral immunity.



Gp	D0	D14	D28	D56	D182	D365
1	1/12 (8%)	6/12 (50%)	**10/12 (83%)**	9/12 (75%)	5/11 (45%)	3/5 (60%)
2	3/17 (17%)	14/17 (71%)	14/17 (82%)	**15/17 (88%)**	11/17 (65%)	5/8 (63%)
3	0/18 (0%)	18/18 (94%)	**18/18 (100%)**	**18/18 (100%)**	16/18 (89%)	5/6 (83%)

Figure 3-4. MERS-CoV spike-specific IgG responses following ChAdOx1 MERS vaccination.

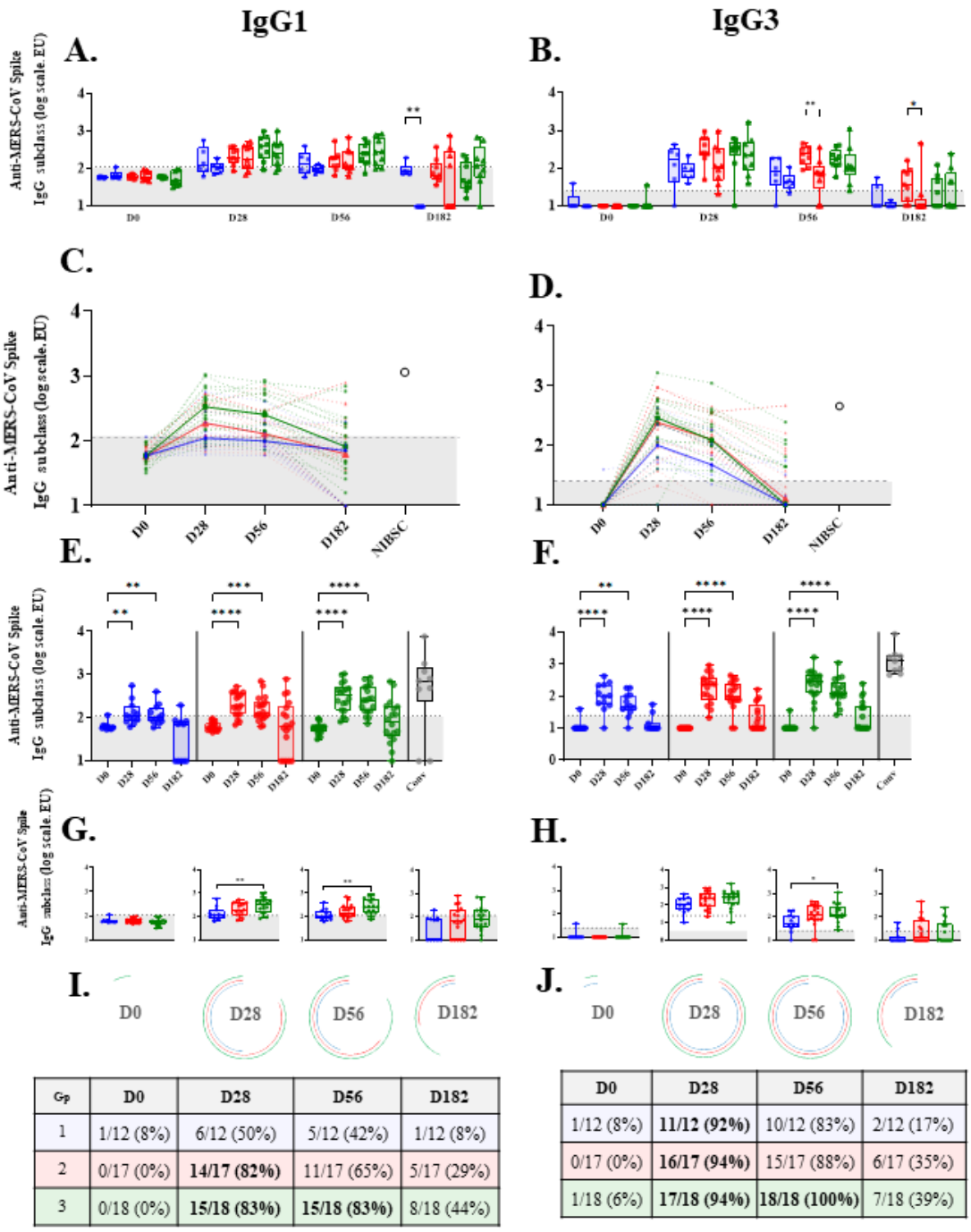
(A) Comparison of spike-specific IgG titres between the UK cohort (MERS001, open circles) and the KSA cohort (MERS002, triangles) across dose groups. **(B)** Longitudinal IgG responses by dose group. **(C)** Pooled analysis of IgG titres across all doses. **(D)** Decay rate of anti–MERS-CoV spike IgG responses over time. Log2-transformed IgG titres are plotted against time (days), with lines representing the rate of decline in antibody levels for each group. **(E)** IgG titres stratified by dose group at each timepoint. **(F)** Seropositivity analysis: proportion of responders by dose group (upper panels) and responder counts (lower table). Data are shown as boxplots with individual participant points; dose group colours and cohort symbols are as defined in Figure 1. Data are plotted on a log10 scale. The dashed line indicates the seropositivity threshold (225 EU). The cut-off was defined as described previously [292] and corresponds to the mean plus 3 standard deviations of pre-pandemic MERS negative controls (n = 40). Statistical analyses: (A) Mann–Whitney test for cohort comparisons; (C, D) Kruskal–Wallis test with Dunn's post hoc correction for multiple comparisons within each group. Asterisks (*) denote statistical significance for within-group and between-cohort comparisons, as defined by P-values: * (P<0.05), ** (P<0.01), *** (P<0.001), **** (P<0.0001).

3.2.2.1.3.2 IgG subclass composition

Vaccination predominantly induced IgG1 and IgG3 subclasses. Which were dose dependent. Whereas IgG2 and IgG4 were undetectable by ELISA. Although, overall IgG titres were similar between trials, subclass responses showed cohort-specific differences, particularly at D182, with greater IgG1 persistence in MERS001 than MERS002 in the low-dose group (Figure 3-5). Similarly, IgG3 responses showed greater persistence in MERS001 than MERS002 at D56 and D182. Notably, high-dose vaccination yielded consistent subclass responses between populations at D182, indicating more robust IgG class switching at higher antigen doses (Figure 3-5A-B). Despite these differences, pooled data are presented to highlight dose-dependent effects.

The median levels for IgG1 and IgG3 remained higher than baseline in D28 and D56 (Figure 3-5C-F). Median lgG1 levels at D28 peak time point were 189 and 318 EUs for the medium and high-dose group, respectively. D28 seroconversion rates were similar in both the medium and high dose groups (82 and 83% of participants, respectively). However, at D56, only 67% of the medium-dose group remained seropositive compared to 83% in the high-dose group (Figure 3-5I). At D28, median levels of IgG1 induced by the high-dose group (median 318 EUs, IQR 144– 465) were 3.6-fold lower than NIBSC IRS (1143 EUs).

IgG3 responses showed a pronounced early peak at Days 28–56 across all dose groups, particularly in high-dose recipients (Figure 3-5). Median levels of IgG3 at D28 induced by the high dose group (median 288 EUs, IQR 122– 462) were close to the NIBSC IRS (452 EUs) by 1.6 fold.



Gp	D0	D28	D56	D182
1	1/12 (8%)	6/12 (50%)	5/12 (42%)	1/12 (8%)
2	0/17 (0%)	**14/17 (82%)**	11/17 (65%)	5/17 (29%)
3	0/18 (0%)	**15/18 (83%)**	**15/18 (83%)**	8/18 (44%)

D0	D28	D56	D182
1/12 (8%)	**11/12 (92%)**	10/12 (83%)	2/12 (17%)
0/17 (0%)	**16/17 (94%)**	15/17 (88%)	6/17 (35%)
1/18 (6%)	**17/18 (94%)**	**18/18 (100%)**	7/18 (39%)

Figure 3-5. MERS Spike-specific IgG subclass responses induced by ChAdOx1 MERS vaccination.

(A–B) Comparison of IgG1 **(A)** and IgG3 **(B)** titres between MERS001 (UK, squares) and MERS002 (KSA, triangles) cohorts across dose groups at the indicated timepoints. **(C–D)** Time course of IgG1 **(C)** and IgG3 **(D)** responses by dose group, including comparison with the WHO International Reference Standard (NIBSC 19/178). **(E–F)** Pooled analysis of IgG1 **(E)** and IgG3 **(F)** responses across doses, showing changes from baseline to post-vaccination timepoints. **(G–H)** Fold increase of IgG1 **(G)** and IgG3 **(H)** antibody titres relative to baseline, stratified by dose group. **(I–J)** Seropositivity analysis for IgG1 **(I)** and IgG3 **(J),** showing proportions of responders over time (upper circular plots) and responder counts by group (tables, lower panels).

IgG subclass responses were quantified by ELISA and expressed as ELISA units (EU). EU are plotted on a log10 scale. The dashed lines indicate the seropositivity thresholds (113 EU for IgG1 and 25 EU for IgG3). Corresponding to the mean plus 3 standard deviations of pre-pandemic MERS negative controls. Boxes represent the interquartile range (IQR) with median lines; whiskers extend to 1.5× IQR, and individual points represent participants. Dose groups are colour-coded as follows: blue = low dose (5×10^9 vp; n = 12), red = medium dose (2.5×10^{10} vp; n = 17), and green = high dose (5×10^{10} vp; n = 18). Statistical analyses included the Mann–Whitney test for comparisons between cohorts (A–B) and the Kruskal–Wallis test with Dunn's post hoc comparisons for dose and timepoint effects (C–H). Asterisks (*) denote statistical significance for within-group and between-cohort comparisons, as defined by P-values: * (P<0.05), ** (P<0.01), *** (P<0.001), **** (P<0.0001).

To facilitate comparison of IgG subclass responses on a common scale, EU readouts were normalised to IU/mL using the NIBSC standard. Although this normalisation does not imply absolute equivalence between subclasses, it supports relative within-cohort comparisons. Both subclasses correlated strongly with total IgG (IgG1: R = 0.80, p < 0.0001; IgG3: R = 0.70, p < 0.0001), with IgG1 showing the stronger association (Figure 3-6A). Despite this, paired analyses confirmed significantly higher IgG3 than IgG1 at peak timepoints (D28–D56) (Wilcoxon signed-rank test; p-values shown in Figure 3-6B-I). Across dose groups, IgG3 titres were consistently higher than IgG1 during early responses before declining to similar levels by D182. These findings suggest that IgG1 mirrors total IgG more closely, whereas IgG3 shows a sharper early peak following priming.

Convalescent sera also showed IgG3-dominated responses, with higher median titres than IgG1 (Figure 3-6E). Overall titres were greater in convalescents, but the subclass pattern mirrored vaccination. Together, these data indicate that ChAdOx1 MERS elicits an IgG3-skewed response that resembles natural infection.

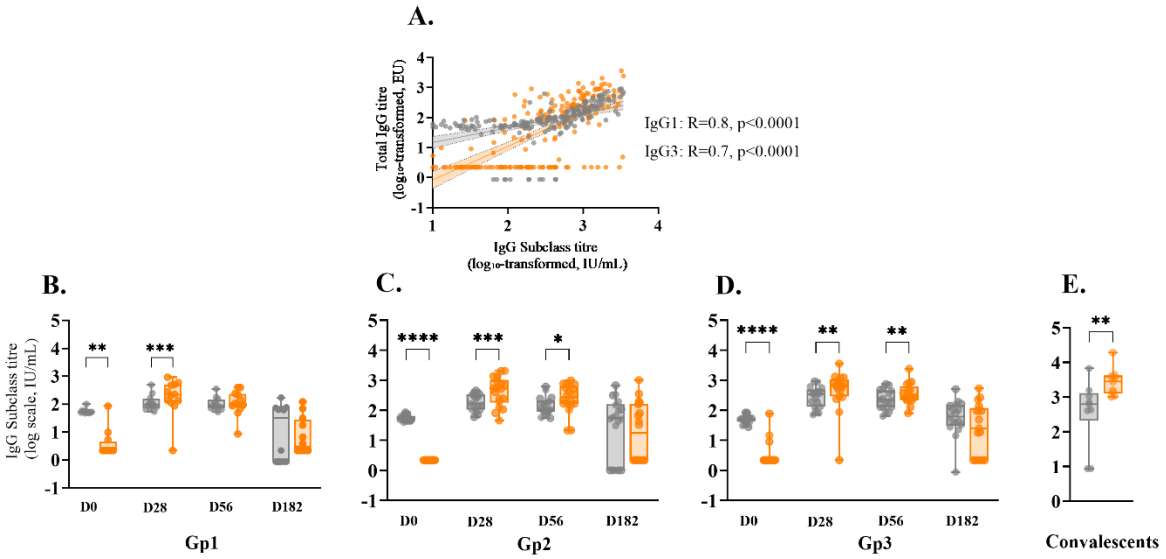


Figure 3-6. Correlation of total IgG with IgG subclasses and group-specific subclass responses following ChAdOx1 MERS vaccination.

(A) Correlation of total IgG titres (log_{10} EU) with IgG1 (grey) and IgG3 (orange) subclass titres (log_{10} IU/mL) across all participants and timepoints. Lines represent linear regression with 95% confidence intervals; ρ and p values were calculated using Spearman's rank correlation. **(B–D)** IgG1 (grey) and IgG3 (orange) titres expressed in IU/mL across timepoints in participants receiving low-dose (Gp1, B), medium-dose (Gp2, C), or high-dose (Gp3, D) vaccination. **(E)** convalescent individuals. Data are shown as boxplots (interquartile range, median, whiskers = 1.5× IQR); individual points represent participants. Statistical significance between IgG1 and IgG3 titres at each timepoint was assessed using paired non-parametric testing (Wilcoxon signed-rank test).

3.2.2.1.3.3 Antigen-Specific IgG Responses to Spike S1 and S2 subunits

Epitope recognition of MERS-CoV–specific IgG following ChAdOx1 MERS vaccination was characterized by a standardized indirect ELISA to quantify responses to the S1 and S2 subunit antigens at baseline (D0) and at the post-vaccination peak (D28). Results were consistent across cohorts (Figure 3-7A), and data were therefore combined for analysis. Antibody titres increased significantly at D28 compared with baseline across all dose groups [low dose: S1 (p = 0.0284), S2 (p = 0.0291); medium dose: S1 and S2 ($p < 0.0001$); high dose: S1 and S2 ($p < 0.0001$)] (Figure 3-7A-B). At D28, median titres were 507 [IQR: 141–600] for S1 and 367 [IQR: 151–475] for S2 in the low-dose group, 533 [IQR: 327–909] and 545 [IQR: 194–881] in the medium-dose group, and 1,225 [IQR: 712–1,617] and 618 [IQR: 418–1,098] in the high-dose group. S1 responses were significantly higher in the high-dose group compared with low and medium doses ($p = 0.0005$ and $p = 0.0081$, respectively), whereas differences for S2 were not significant. S1 responses also mirrored those to the full spike, showing a strong correlation with total S ($r = 0.80$, $p < 0.0001$) Figure 3-7D, while no significant association was observed for S2. Collectively, these results demonstrate that ChAdOx1-induced antibody responses are dose-dependent and primarily target the S1 subunit, as illustrated in the heat map presented in Figure 3-7E.

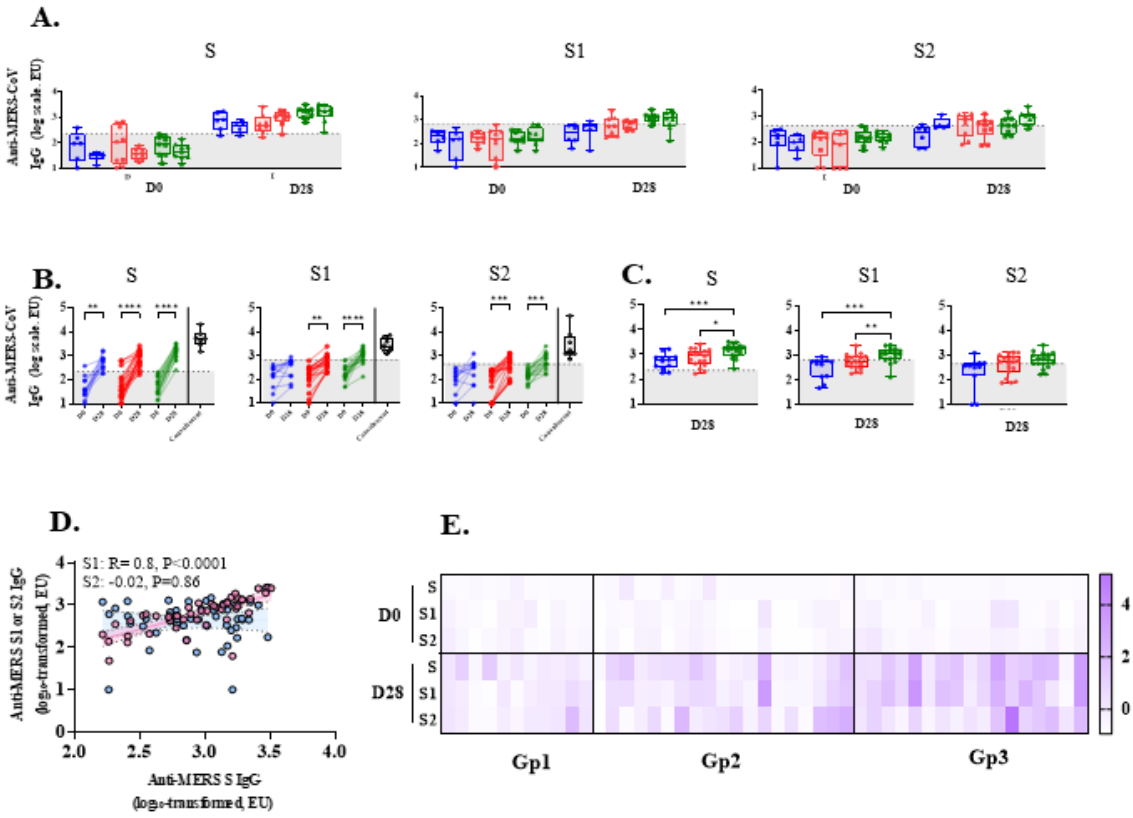


Figure 3-7. MERS-CoV spike-subunit specific IgG antibody responses following ChAdOx1 MERS vaccination.

(A) Comparison of S, S1, and S2-specific IgG titres (left to right) between the UK cohort (MERS001, squares) and the KSA cohort (MERS002, triangles) across dose groups. **(B)** Pooled analysis of IgG responses by dose group between baseline (Day 0) and peak (Day 28). **(C)** Pooled IgG titres across all doses comparing groups at Day 28. **(D)** Correlation of S responses with S1 (pink) and S2 (blue) at Day 28. Regression lines and Spearman correlation coefficients are shown. (E) Heatmap of IgG3 titres to S, S1, and S2 at Day 0 and Day 28 across the three dose groups (Gp1–Gp3). Colour intensity represents antibody magnitude (log EU). Data are shown as boxplots with individual participant points unless otherwise indicated; dose group colours and cohort symbols are as defined in Figure 3. The horizontal dashed line shows the threshold for seropositivity (225, 670 and 445 EUs) for S, S1 and S2 respectively. Statistical analyses: (A) Mann–Whitney test for cohort comparisons; (B) Wilcoxon signed-rank test for paired samples; (C) Kruskal–Wallis test with Dunn's post hoc correction for multiple comparisons.

3.2.2.2 IgG binding strength (avidity)

We assessed MERS spike-specific IgG avidity following single vaccination in MERS001 and MERS002. A sodium thiocyanate displacement, standardised indirect ELISA was used to evaluate avidity indices (AI) at D28, D56, and D182 post-vaccination, combining data from both populations as no differences in IgG titres were observed between them at each time point (Figure 3-8A).

IgG avidity increased over time in all dose groups. Between D28 and D182, fold changes were 0.65-, 0.95-, and 0.64-fold in the low-, medium-, and high-dose groups, respectively (Figure 3-8B). Statistically significant increases were observed in the low- and medium-dose groups, but not in the high-dose group. In particular, the medium-dose group showed a progressive rise in AI, with significant differences between D28 and D56 ($p = 0.004$; ; Figure 3-8C) and between D56 and D182 ($p < 0.0001$; Figure 3-8C).

No statistically significant differences in IgG avidity index (AI) were detected between dose groups at any individual time point (Figure 3-8D). However, longitudinal paired analyses demonstrated significant increases in AI over time in the low- and medium-dose groups, indicating progressive affinity maturation following vaccination (Figure 3-8C). In contrast, the high-dose group did not show a consistent increase in avidity over time and exhibited greater inter-individual variability, including one participant with an atypical decline in AI.

At D182, the median AI in the medium-dose group (1.3 M, IQR 1.2–1.4) remained lower than that of the NIBSC international reference serum (2.28 M), providing contextual benchmarking rather than evidence of inter-dose differences. Together, these data suggest that while avidity maturation occurs following vaccination, the medium dose may support a more consistent progression towards higher-quality antibody responses, favouring gradual affinity maturation over time.

.

+

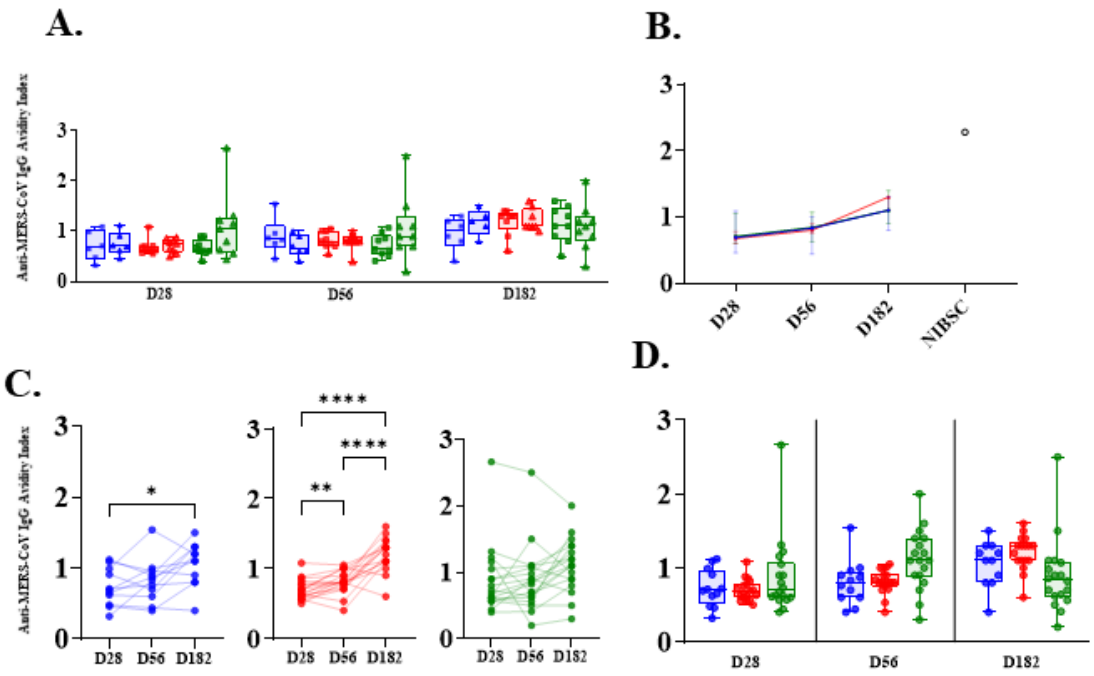


Figure 3-8. Anti-MERS-CoV Spike IgG avidity index following ChAdOx1 MERS vaccination.
(A) Avidity index of Spike-specific IgG across dose groups at D28, D56, and D182. **(B)** Mean avidity indices over time by dose group, with NIBSC reference serum included for comparison. **(C)** Paired analysis of Spike-specific IgG avidity within each dose group. **(D)** Comparison of avidity indices between dose groups at each timepoint. Avidity was assessed by ELISA using a chaotropic agent and expressed as the avidity index. Boxes represent the interquartile range (IQR) with median lines; whiskers extend to 1.5× IQR. Data points represent individual responses. Dose groups are colour-coded: blue = low dose (5×10^9 vp), red = medium dose (2.5×10^{10} vp), green = high dose (5×10^{10} vp).
Statistical analyses: (C) Friedman test with Dunn's post hoc comparisons for paired analyses across timepoints. (D) Kruskal–Wallis test with Dunn's post hoc comparisons between dose groups.

3.2.2.3 FcγR-binding activity

FcγR-binding antibody responses against S, S1, and S2 antigens were measured at baseline (Day 0), Day 28, and Day 182, with additional measurements at Day 365 available for MERS001 only. Only medium- and high-dose groups were analysed, as the low-dose vaccination elicited lower total anti-spike IgG responses. Convalescent samples will be presented in the prime-boost (PB) (section 3.2.4.1), so are not presented here to avoid redundancy.

3.2.2.3.1 Cohort-specific response

Cohort-specific differences in FcγR-binding responses were modest and inconsistent across receptors and timepoints; data were therefore pooled for subsequent analyses to increase statistical power (Figure 3-9).

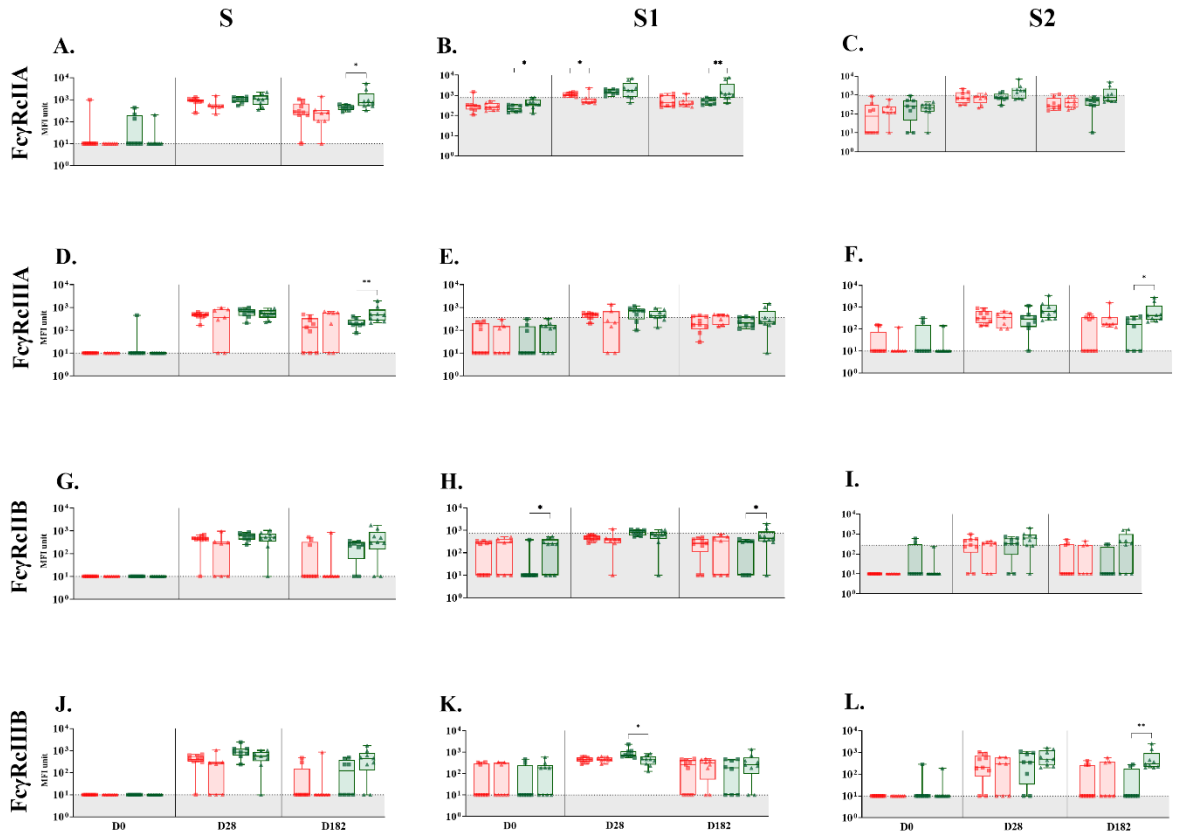


Figure 3-9. FcγR-binding antibody responses following ChAdOx1 MERS vaccination.

(A–C) FcγRI-binding antibody responses against MERS-CoV antigens S, S1, and S2 in participants from the UK cohort (MERS001, square) and the KSA cohort (MERS002, triaangle). **(D–F)** FcγRIIA-binding antibody responses against S, S1, and S2. **(G–I)** FcγRIIB-binding antibody responses against S, S1, and S2. **(J–L)** FcγRIIIB-binding antibody responses against S, S1, and S2. Responses were measured at baseline (Day 0), Day 28, and Day 182. Day 365 data are not shown here because they were only available for MERS001. Data are displayed as boxplots with individual participant points; MERS001 is shown in red, MERS002 in green. Red = 2.5×10^{10} vp (n = 17); Green = 5×10^{10} vp (n = 17). The horizontal dashed line represents the assay cutoff, corresponding to the mean ± SD of pre-pandemic serum samples from MERS001 and MERS002 collected prior to vaccination (n = 32). Statistical comparisons between regimens at each timepoint were performed using the Mann–Whitney U test or an unpaired t-test, depending on data normality.

3.2.2.3.2 Durability over time

FcγR-binding antibody responses were significantly induced at Day 28 across all targets, with several responses—particularly FcγRIIa and FcγRIIIa binding to S1 and S2—persisting to Day 182 (Figure 3-10).

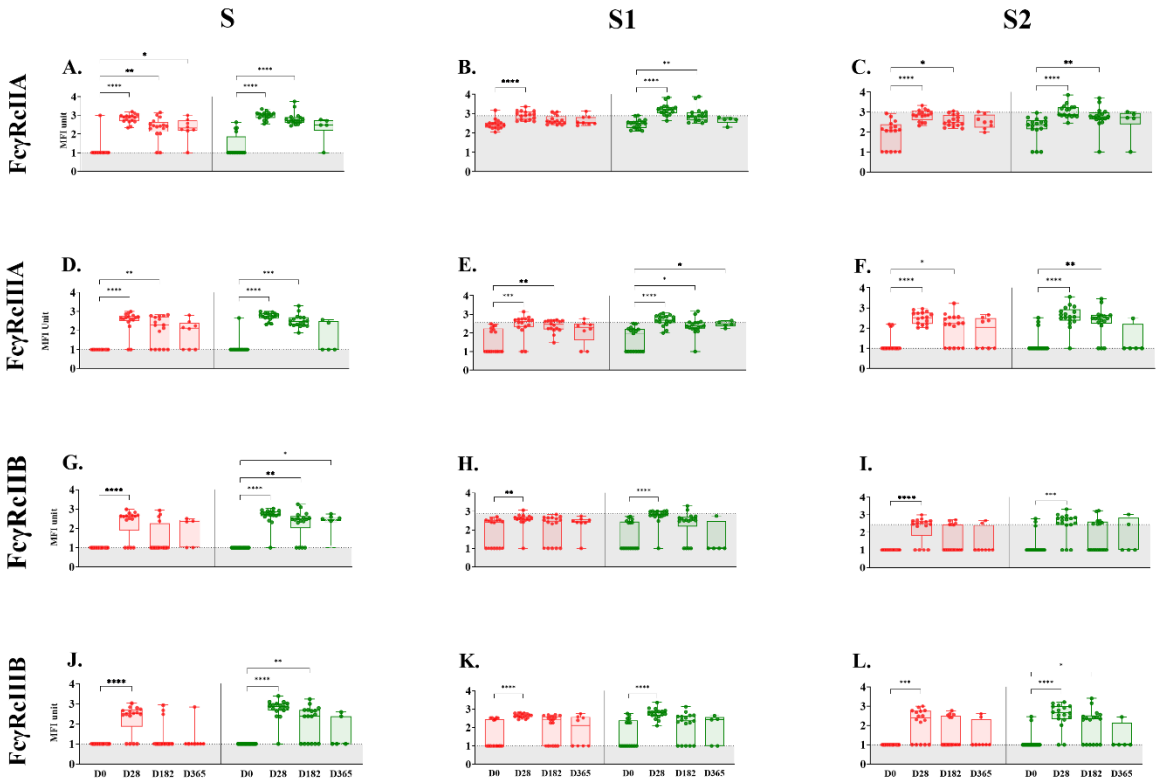
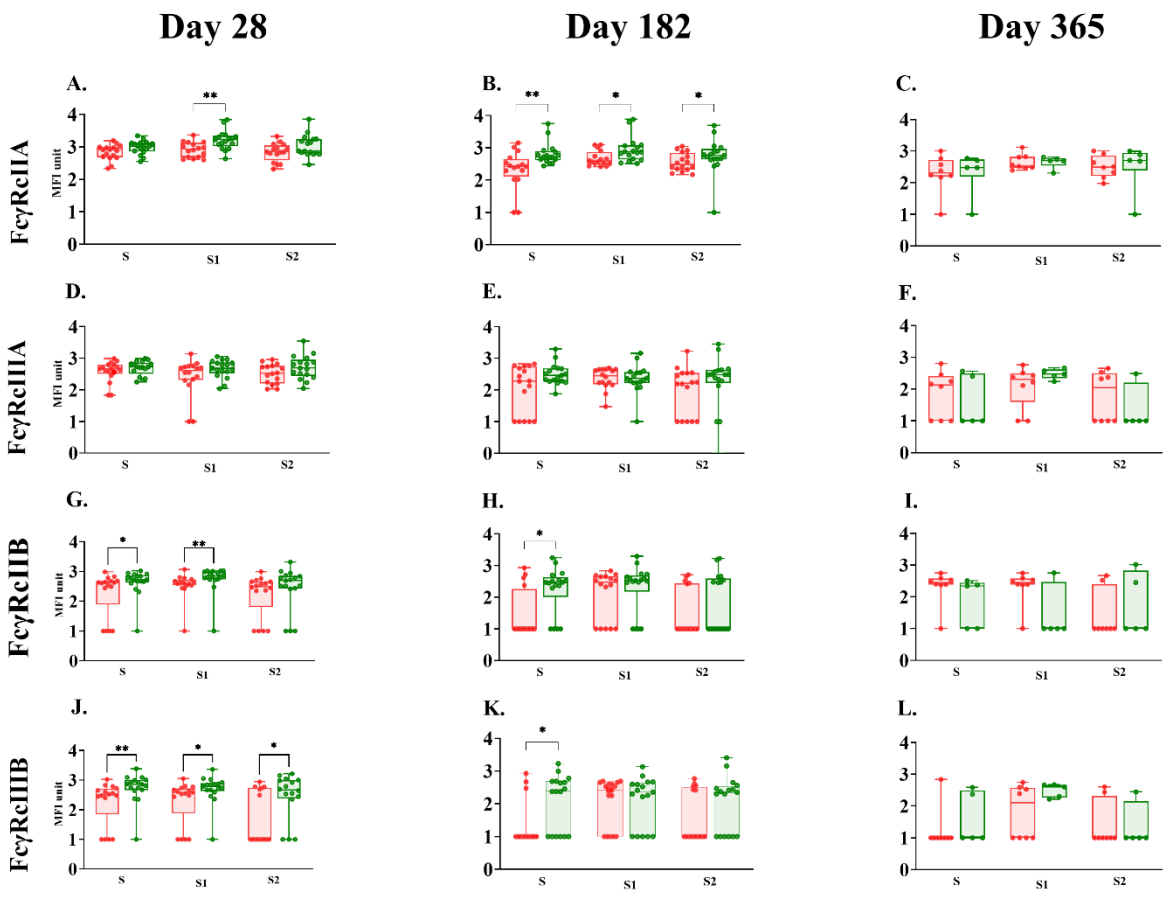


Figure 3-10. FcγR-binding antibody responses following ChAdOx1 MERS vaccination, pooled by regimen.

(A–C) FcγRI-binding antibody responses against MERS-CoV antigens S, S1, and S2 in participants receiving either medium dose (red) or high dose (green) vaccination. **(D–F)** FcγRIIA-binding antibody responses against S, S1, and S2. **(G–I)** FcγRIIB-binding antibody responses against S, S1, and S2. **(J–L)** FcγRIIIB-binding antibody responses against S, S1, and S2. Responses were measured at baseline (Day 0), Day 28, and Day 182 in pooled data from MERS001 and MERS002, with additional measurements at Day 365 for MERS001 only. Data are displayed as boxplots with individual participant points; medium dose is shown in red (n=17) and high dose in green (n=17). The horizontal dashed line indicates the assay cutoff. Statistical analyses were performed using the Kruskal–Wallis test with Dunn's post hoc correction for multiple comparisons against baseline. Each dose group was analyzed independently, and comparisons were made relative to the corresponding group's own baseline values. Asterisks (*) denote statistical significance for within-group and between-cohort comparisons, as defined by P-values: * (P<0.05), ** (P<0.01), *** (P<0.001), **** (P<0.0001).

3.2.2.3.3 Comparison between medium and high dose

High-dose vaccination elicited significantly higher FcγRIIa, FcγRIIb, and FcγRIIIB binding responses to spike and S1 at Day 28, with several of these differences persisting to Day 182, indicating enhanced magnitude and durability compared with the medium-dose regimen (Figure 3-11).



Antibody type	Target	Timepoint	Gp2	Gp3	Pvalue
FcγRIIA	S1	28	854 [486–1332]	1679 [1035–2206]	0.003
FcγRIIB	S	28	416.5 [77–481]	528 [429–743]	0.03
FcγRIIB	S1	28	398[342–527]	691 [541–997]	0.003
FcγRIIIB	S	28	320 [71–513]	724 [458–1013]	0.006
FcγRIIIB	S1	28	373 [76–527]	619 [428–795]	0.02
FcγRIIIB	S2	28	10 [10–553]	470 [240–1004]	0.02
FcγRIIA	S	182	264 [128–454]	525 [416–786]	0.002
FcγRIIA	S1	182	386 [320–742]	751 [435–1198]	0.02
FcγRIIA	S2	182	305 [215–692]	585 [439–913]	0.03
FcγRIIB	S	182	10 [10–182]	296 [103–429]	0.01
FcγRIIIB	S	182	10 [10–425]	239 [10–490]	0.02

Figure 3-11. Longitudinal FcγR-binding antibody responses following ChAdOx1 MERS vaccination, pooled by regimen.

Responses are shown at Day 28 (left column), Day 182 (middle column), and Day 365 (right column; available for MERS001 only). **(A–C)** FcγRIIa-binding antibody responses against MERS-CoV antigens S, S1, and S2 in participants receiving either medium dose (red) or high dose (green) vaccination. **(D–F)** FcγRIIIA-binding antibody responses against S, S1, and S2. **(G–I)** FcγRIIB-binding antibody responses against S, S1, and S2. **(J–L)** FcγRIIIB-binding antibody responses against S, S1, and S2. Data are displayed as boxplots with individual participant points; the medium dose is shown in red (n = 17) and the high dose in green (n = 17). As each target has its own cutoff, cutoff lines were removed for clarity. Statistical comparisons between dose groups at each time point for each target were performed using the Mann–Whitney U test. Asterisks (*) denote statistical significance for within-group and between-cohort comparisons, as defined by P-values: * (P<0.05), ** (P<0.01), *** (P<0.001), **** (P<0.0001).

3.2.2.3.4 Correlation of FcγR-binding and IgG responses

To explore functional relationships between antibody binding and Fc effector potential, correlation analyses were performed at the peak response on D28 (Figure 3-12). Strong positive correlations were observed among FcγR-binding responses targeting the same antigen (S, S1, or S2), indicating potential coordinated activation of multiple Fcγ receptors. FcγRIIA, FcγRIIIA, FcγRIIB, and FcγRIIIB binding responses were highly correlated with total IgG levels across all antigenic targets, suggesting that FcγR engagement was largely driven by antigen-specific IgG concentrations. Notably, FcγR binding correlated more strongly with IgG1 than with IgG3 at peak timepoints, consistent with the strong association between IgG1 and total IgG despite the predominance of IgG3 at this timepoint (Figure 3-6). This indicates that inter-individual variation in FcγR engagement more closely tracks IgG1 levels.

Stronger correlations were observed between responses to the spike (S) and its S1 subunit, whereas correlations with S2 were generally weaker. In particular, FcγRIIIB binding to S2 showed the weakest correlations with other FcγR- and IgG-mediated responses, indicating distinct or less coordinated recognition of epitopes within the S2 region.

Overall, these findings demonstrate that, at peak immunogenicity, FcγR-binding activity is closely linked to IgG levels, highlighting a coordinated induction of antibody magnitude and Fc-mediated effector potential following ChAdOx1 MERS vaccination.

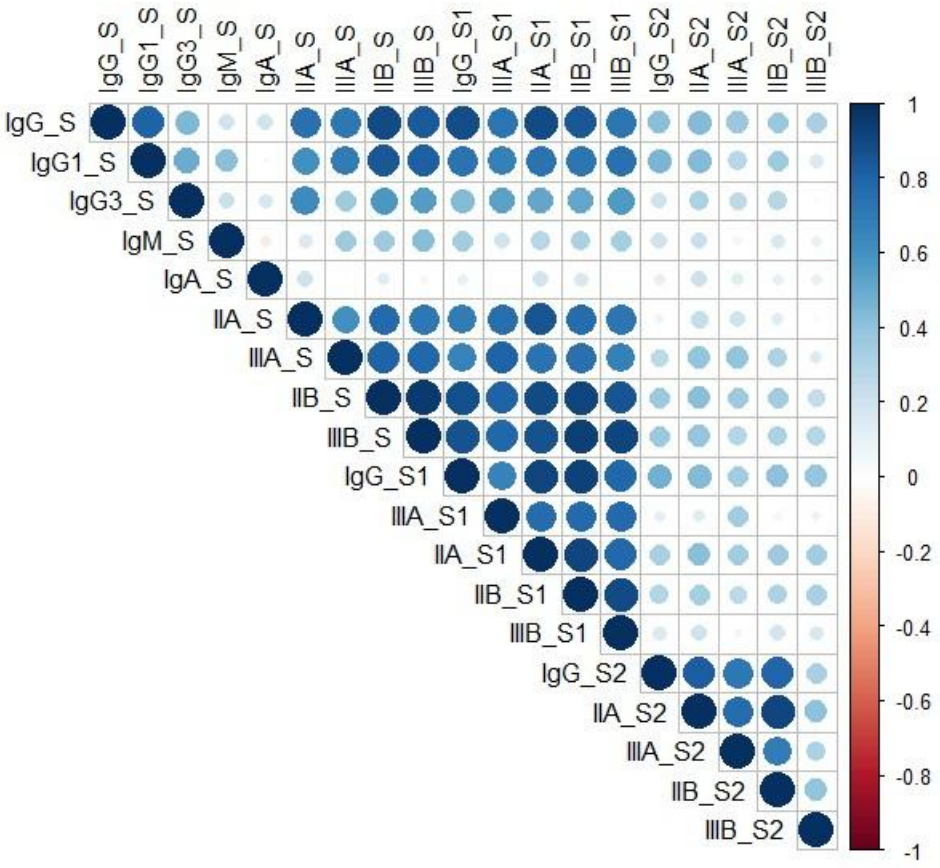


Figure 3-12. Correlation matrix of FcγR-binding and IgG responses at peak (Day 28) following ChAdOx1 MERS vaccination.
Pairwise Spearman correlation coefficients are shown for FcγR-binding activities (FcγRIIA, FcγRIIIA, FcγRIIB, and FcγRIIIB) and total IgG responses to MERS-CoV spike (S), S1, and S2 antigens. The colour scale represents the strength and direction of correlation (blue = positive, red = negative), with circle size proportional to the absolute correlation coefficient (r). Strong positive correlations were observed among FcγR-binding responses and with IgG binding to the same antigen. Correlations were highest between responses to spike (S) and S1, while weaker associations were noted for S2, particularly for FcγRIIIb binding to S2, which showed the least correlation with other parameters.

3.2.3 Induction and durability of humoral antibody responses

Following the comparative evaluation of individual antigen-specific responses, overall patterns of induction and durability were assessed (Figure 3-13). Although antibody neutralisation was not included in the comparative analysis due to methodological differences between plasma and serum assays where MERS001 we had available plasma samples and MERS002 we were only provided with serum plasma (see supplementary 8.1.4.1.2.2), specifically the use of plasma samples in MERS001 and serum samples in MERS002, which were not directly comparable in the neutralisation assay.

At peak (D28), vaccination elicited broad Ig and FcγR-binding antibody responses against spike antigens (Figure 3-13A). Heatmaps of z-score–normalized data revealed robust induction of IgG, IgA, and FcγR engagement, with a more expansive and higher-magnitude profile observed in the high-dose

group compared with the medium-dose group. Radar plots supported this finding, illustrating broader FcγR engagement and stronger subclass responses at D28 in high-dose recipients (Figure 3-13B).

Subsequent analyses focused on antibody retention, expressed as the median percentage of the D28 peak maintained at later timepoints. Between D182 and D365, the high-dose group exhibited a smaller decline from the D28 peak in FcγRIIA and FcγRIIIA binding to S2, together with more sustained FcγRIIB and FcγRIIIB engagement to the Spike antigen, whereas responses in the medium-dose group declined more markedly. However, S1-specific responses showed a smaller decrease in the medium-dose group (Figure 3-13C).

Population-level persistence, assessed by the proportion of participants remaining seropositive, showed that at D182, a higher proportion of high-dose recipients retained FcγRIIA responses to S (100% vs. 88%) and S1 (42% vs. 25%), and FcγRIIIA responses to S (100% vs. 69%), whereas FcγRIIIA responses to S1 were slightly higher in the medium-dose group (24% vs. 44%). By D365, seropositivity rates remained higher in the high-dose group across most receptors, with FcγRIIA (80% vs. 88%), FcγRIIIA (40% vs. 6%), FcγRIIB (60% vs. 25%), and FcγRIIIB (40% vs. 13%) responses all persisting at greater frequencies compared with the medium-dose group (Figure 3-13, Panel D).

Together, these analyses demonstrate that high-dose vaccination elicited broader and more functionally diverse FcγR engagement at peak and conferred enhanced long-term persistence of binding and Fc-functional antibody responses compared with the medium-dose group.

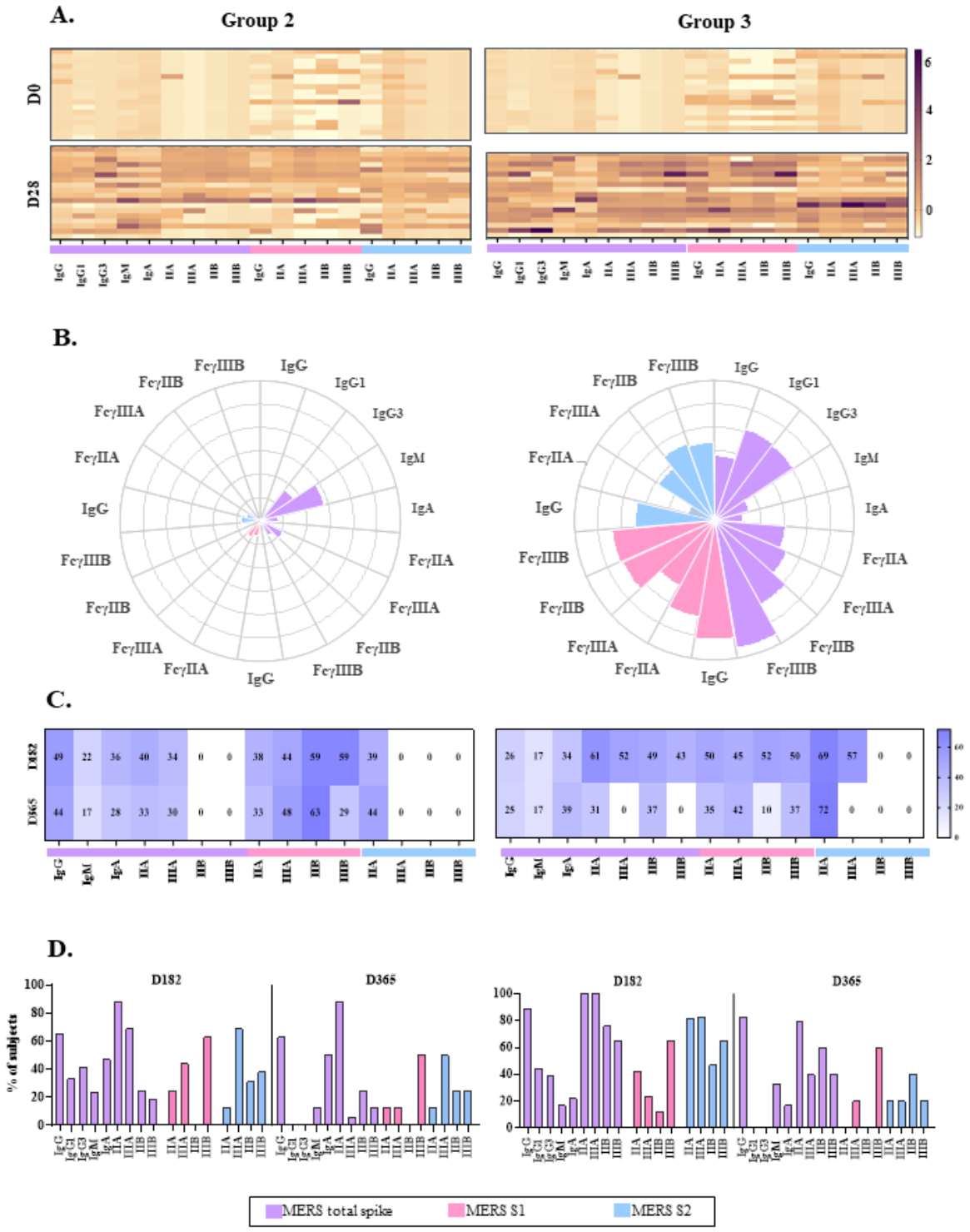


Figure 3-13. Induction and maintenance of humoral antibody responses.
(A) Heatmaps of z-score–normalized data showing Ig isotype and FcγR-binding antibody responses against spike antigens in Group 2 (left) and Group 3 (right) participants before vaccination (Day 0) and at peak (Day 28). **(B)** Radar plots summarizing the breadth of responses at Day 28 for Group 2 (left) and Group 3 (right). **(C)** Heatmaps showing the median percentage of the Day 28 response retained at Days 182 and 365 for each antigen–FcγR combination. Values inside cells indicate group medians. **(D)** Bar plots showing the proportion of participants who remained seropositive at Day 182 (top) and Day 365 (bottom) for Group 2 (left) and Group 3 (right).

Longitudinal analysis revealed distinct decay kinetics among antibody isotypes and Fcγ receptor–binding activities over time (Figure 3-14). The durability of the antibody response was evaluated in MERS001 using exponential decay modelling, as this cohort included three available time points (Days 28, 182, and 365). IgG responses (Figure 3-14A) exhibited a biphasic decline, with a rapid reduction within the first 50–100 days followed by a slower decay phase, indicating relatively sustained antibody persistence. IgA responses (Figure 3-14B) showed a steeper and more uniform decline, consistent with the shorter half-life with durable response in the medium dose group. FcγRIIA-binding antibodies (Figure 3-14C–E) demonstrated gradual decreases in activity, maintaining detectable levels for up to 400 days as extrapolated from the slope, suggesting extended Fc-mediated effector functionality. In contrast, FcγRIIIA- and FcγRIIIB-binding antibodies (Figure 3-14 F–H) decayed more rapidly, particularly beyond 100 days post-peak, reflecting a faster loss of these Fc receptor interactions.

Although the medium-dose group exhibited lower overall IgG magnitudes compared to the high-dose group after the booster (up to D56), these responses were more sustained over time, remaining detectable and relatively stable for at least the first 200 days post vaccination. This trend was especially evident for FcγRIIB-associated functions, suggesting that moderate antigen exposure may favour longer-lived antibody maintenance despite lower initial titres.

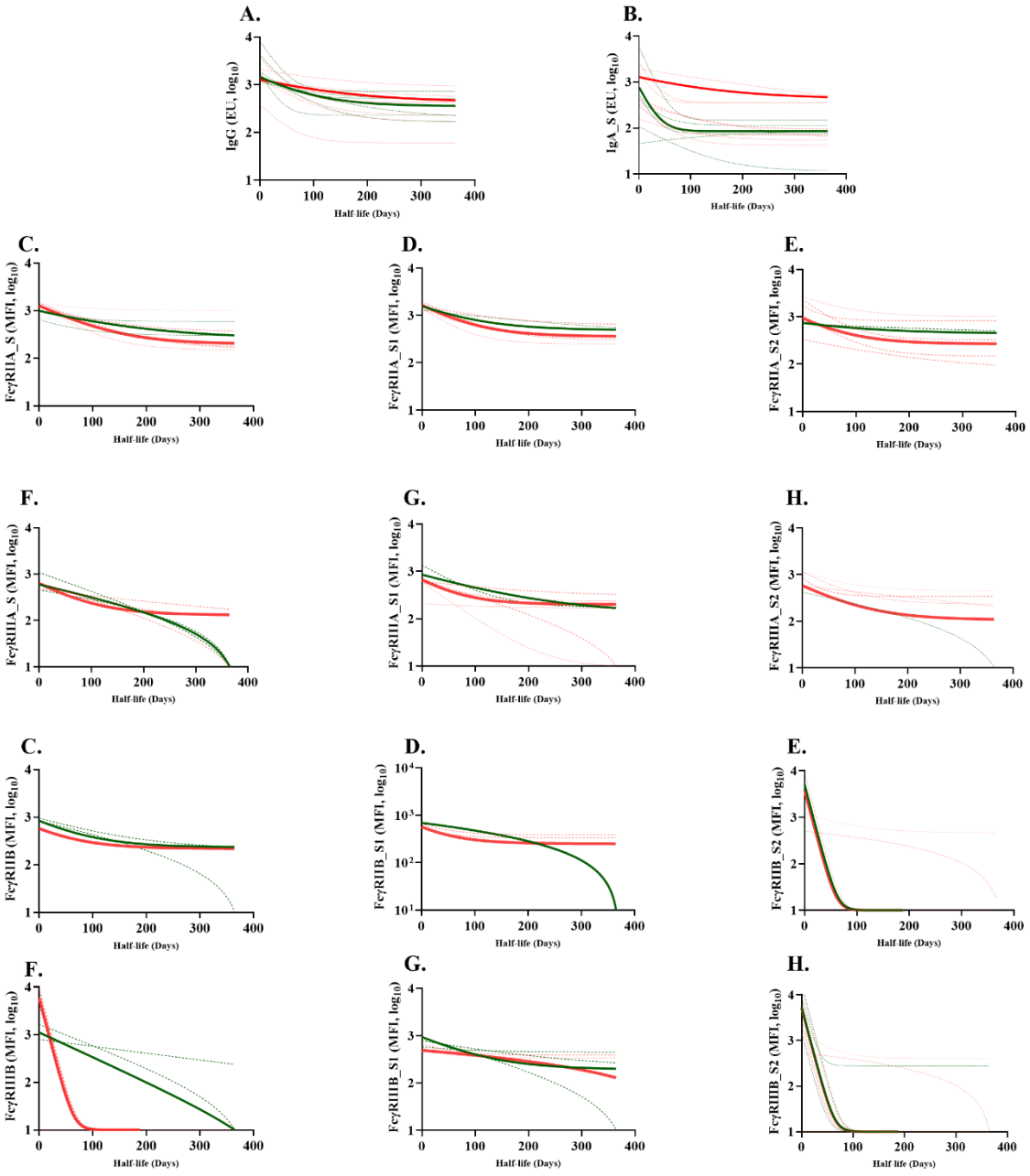


Figure 3-14. Decay kinetics of antibody isotypes and Fcγ receptor–binding activities over time.
Longitudinal decay of antibody responses is shown for **(A)** IgG, **(B)** IgA, **(C–E)** FcγRIIA-, and **(F–H)** FcγRIIIA/IIIB-binding antibodies. Red lines represent the medium-dose group and green lines the high-dose (Group 3) cohort. Thick lines indicate group medians, and thin lines show individual responses. Data were modelled using an exponential decay fit including MERS001 study data from days 28, 56, 182, and 365 (day 65 when available). IgG and FcγRIIA responses decayed more slowly than IgA and FcγRIIIA/B responses, indicating greater persistence of certain antibody functions.

For participants with only a single post-peak measurement (D182), half-life estimates were calculated following previously described methods [331]. The short-term analysis (Days 28–182) indicated a relatively rapid decline in both MERS001 and MERS002, whereas long-term analysis (up to Day 365) was limited to MERS001 (Figure 3-15). The cohort size and sampling timepoints constrain the precision

of these models. Despite these constraints, the models reveal clear kinetic trends and provide a foundational estimate of antibody persistence that can be refined in future studies with larger cohorts and more frequent sampling.

Further analysis using alternative half-life calculations with log_2-transformed data confirmed these findings (Figure 3-15). The median IgG half-life in the medium-dose group was 129 days (IQR 98–196), compared with 106 days (IQR 66–123) in the high-dose group (Figure 3-15A, p = 0.03). This difference was not apparent in the long-term analysis, where median half-lives were 172 days (IQR147–330) for the medium-dose group and 195 days (IQR167–316) for the high-dose group. In contrast, the half-life of FcγRIIA-binding antibodies was higher in the high-dose group than in the medium-dose group, with median values of 158 days (IQR97–274) and 80 days (IQR47–139), respectively (Figure 3-15C, p = 0.0056). These findings suggest that medium-dose vaccination may enhance the persistence of binding antibodies, whereas the high-dose regimen favours more durable Fc-mediated functional responses.

When comparing half-lives of binding IgG and FcγR-associated responses, no significant differences were observed between IgG and the activating FcγRIIA or FcγRIIIA features in either the short- or long-term analyses. In contrast, inhibitory FcγRIIB and FcγRIIIB binding displayed shorter apparent half-lives than IgG during the short-term phase, with differences in FcγRIIB binding persisting into the long-term analysis. Notably, these effects were evident only in the medium-dose group, where FcγRIIB-associated functions showed prolonged persistence despite lower overall IgG magnitudes compared with the high-dose group.

The median short-term half-life of FcγRIIB-binding antibodies in the medium-dose group was 29 days (IQR, 27–68), while FcγRIIIB-binding antibodies in the same group had a median half-life of 30 days (IQR, 27–32) (Figure 3-15C). Both were significantly shorter than the corresponding IgG half-life of 129 days (IQR, 98–196; p = 0.004 and p = 0.0056, respectively; Figure 3-15I). No significant differences were observed within the high-dose group. These findings confirm a trend toward more sustained responses in the medium-dose group, suggesting that moderate antigen exposure may promote longer-lasting antibody functions despite lower overall magnitudes. Nevertheless, both groups demonstrated long-lasting antibody responses extending beyond one year. However, despite the induction of these durable responses, peak antibody levels following a single dose vaccination remained lower than those observed in convalescent individuals, underscoring the potential need for a booster dose to further enhance and prolong protective immunity.

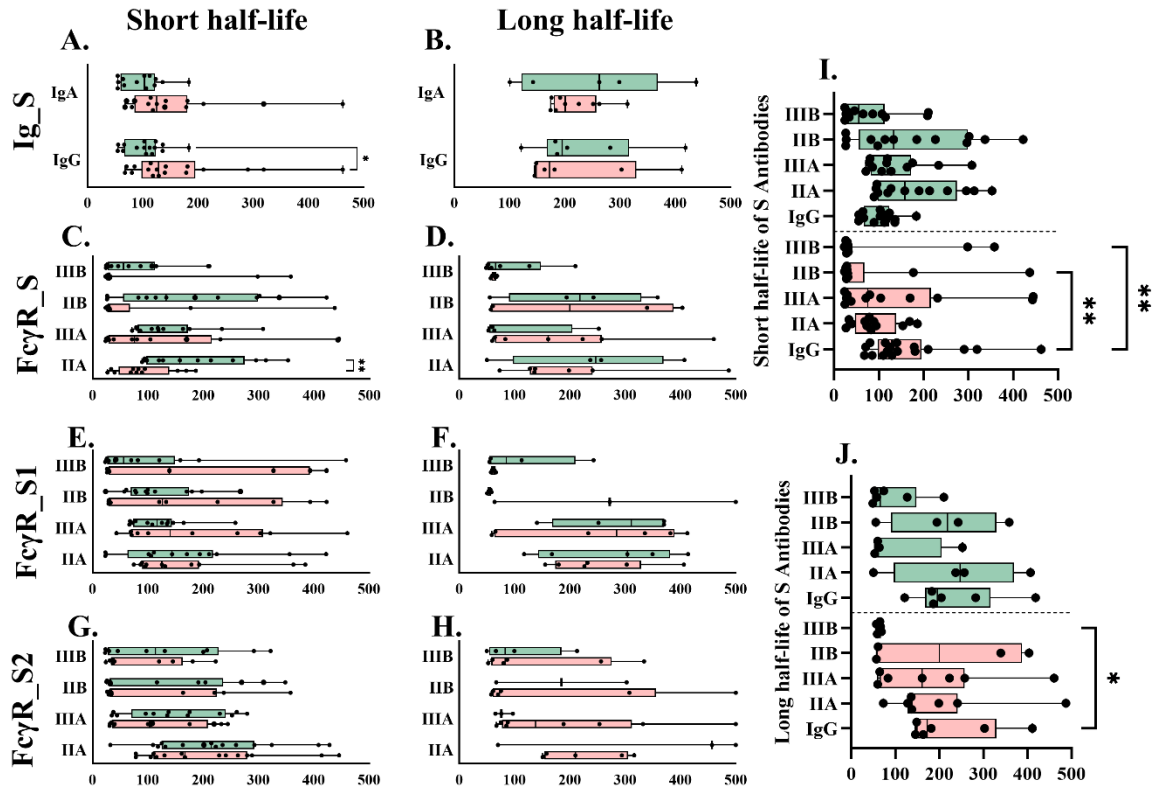


Figure 3-15. Comparison of short and long antibody half-lives across isotypes and Fcγ receptor–binding responses.
Box plots depict the distribution of antibody half-lives for **(A–B)** IgG and IgA**, (C–D)** FcγRIIA-, FcγRIIIA-, and FcγRIIIB-binding antibodies against the S antigen, **(E–F)** FcγR-binding to S1, and **(G–H)** FcγR-binding to S2. Panels A, C, E, and G represent short half-lives, while panels B, D, F, and H show long half-lives. Red boxes correspond to the medium-dose group and green boxes to the high-dose (Group 3) cohort. Each dot represents an individual participant; box plots indicate medians and interquartile ranges. Short half-life calculations included data from the MERS001 and MERS002 studies up to day 182, whereas long half-life estimates were derived from MERS001 data up to day 365. Statistical significance was assessed using the Mann–Whitney U test for panel A-H and the Kruskal–Wallis test for panels I and J within each group. Asterisks indicate significant differences (*$p < 0.05$, **$p < 0.01$).

3.2.4 Immunogenicity of prime-boost vaccination

Humoral and cellular immune responses were assessed in a small subset of MERS001 participants who received a medium-dose prime–boost vaccination at either short or long intervals and were compared with responses from prime-only recipients and convalescent individuals. Analyses were restricted to MERS001 participants to ensure consistency within a single study population.

3.2.4.1 Humoral immune responses following prime and prime–boost vaccination

Boosting induced a rapid increase in antibody responses, with titres peaking at Day 14 post-boost, particularly following longer prime–boost interval (Figure 3-16). Nevertheless, total IgG reached a median of 6,985 EUs in the long-interval participant (representing a 46.5-fold increase from pre-boost levels) and a median of 3,409 EUs in the short-interval group (1.9-fold increase), with both remaining below the NIBSC International Reference Standard (IRS; 16,707 EUs) (Figure 3-16A). Long-interval

boosting preferentially enhanced IgG1 responses and avidity, whereas IgG3 responses were less dependent on dosing interval (Figure 3-16B-C). IgA titres were stabilised by boosting but remained below the IRS (3,557 EUs), whereas IgM remained undetectable (Figure 3-16E–F). IgG responses to S1 increased in both groups, with a 3.8-fold rise in the long-interval participant compared with a 1.4-fold median increase in the short-interval group, while S2 responses rose only modestly (~1-fold) and were similar between intervals (Figure 3-16G–H). Antibody avidity was higher in the long-interval participant (AI 1.8 M) than in the short-interval group (1.23 M) at D28 post-boost (Figure 3-16D). Notably, avidity had already increased between the 28-day and 6-month pre-boost timepoints, indicating progressive maturation of antibody binding strength before booster administration. Overall, these findings indicate that long-interval boosting further enhanced IgG—particularly IgG1—and avidity, whereas IgG3 responses were less dependent on dosing interval.

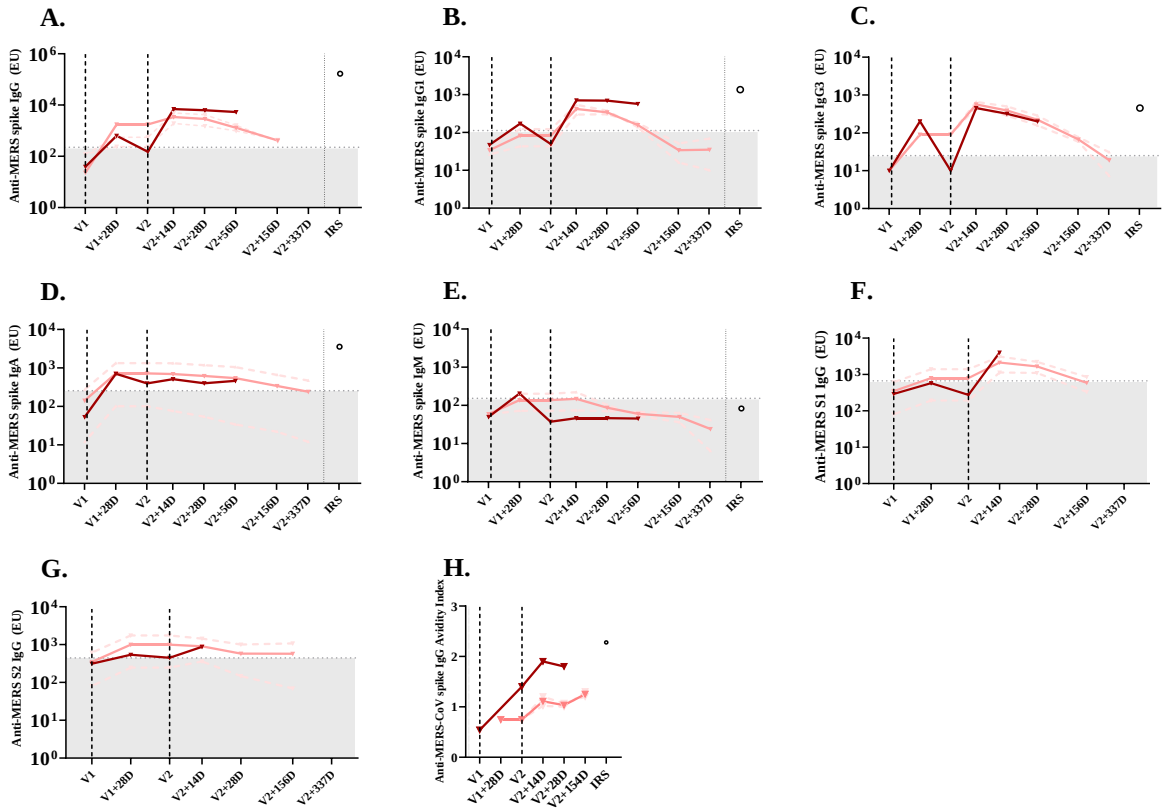


Figure 3-16. Antibody dynamics following short- and long-interval boosting compared with convalescent responses.

(A) Total IgG titres following boosting at short and long intervals, with convalescent sera from naturally infected individuals included as a reference group. Convalescent samples provide a benchmark for infection-induced antibody levels and are shown here for context, while detailed comparisons with peak vaccine-induced responses are presented in subsequent panels. **(B–C)** IgG1 and IgG3 subclass responses showing distinct kinetics between dosing intervals. **(D)** Antibody avidity measured at Day 28 post-boost. **(G–H)** S1- and S2-specific IgG responses following boosting. The International Reference Standard (IRS) is included as a benchmark to contextualize antibody titres. Data are expressed as ELISA units (EUs). Lines indicate medians; dashed line represents the assay detection limit.

Boosting enhanced FcγR-binding antibody responses, particularly to spike and S1, with stronger and more sustained responses following longer dosing intervals (Figure 3-17). The largest increases were observed against full-length spike and S1 (Figure 3-17B, E, H, K), with kinetics that were similar across groups but consistently higher in the long-interval participant than in the short-interval group at D56 post-boost. In contrast, S2 responses rose only modestly at the peak and were less affected by interval (Figure 3-17C, F, I, L).

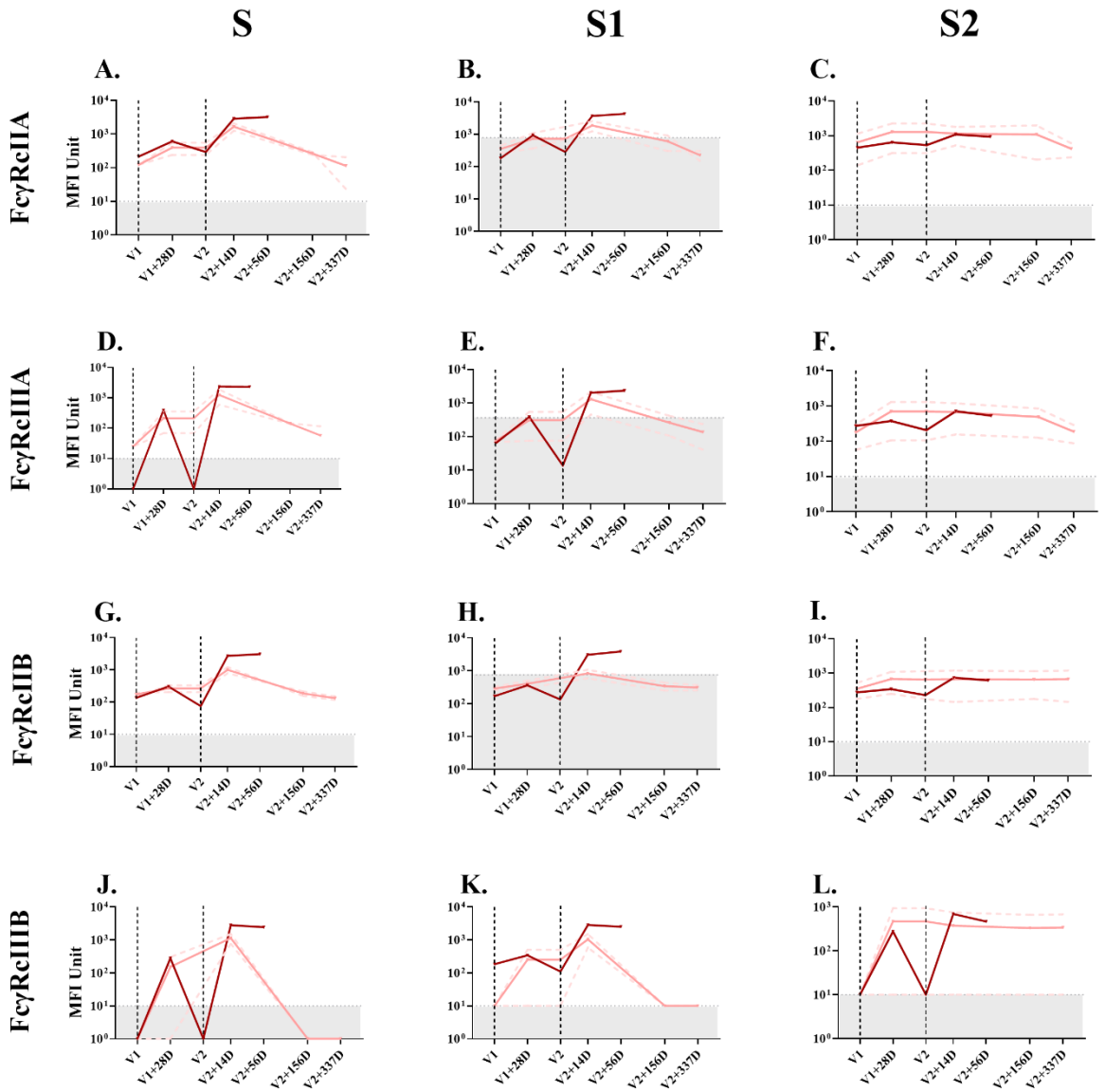


Figure 3-17. FcγR-binding antibody responses following booster vaccination at short and long intervals compared with convalescent responses.

Binding to full-length spike (S), S1, and S2 was assessed for FcγRIIA **(A–C),** FcγRIIIA **(D–F)**, FcγRIIB **(G–I),** and FcγRIIIB **(J–L).** Participants received a booster dose at either a short interval (Day 28, n = 2, pale red) or a long interval (Day 182, n = 1, dark red). Shaded areas indicate the baseline range, and dotted lines represent the detection threshold.

Compared with convalescent sera, convalescent samples exhibited consistently higher antibody levels than those observed following medium-dose prime vaccination (Figure 3-18), with the exception of IgG1 (Figure 3-18B), which was comparable across groups. In several readouts, convalescent responses also exceeded those induced by high-dose prime vaccination, with significant differences detected for the IgG3 subclass (Figure 3-18F), the IgA isotype (Figure 3-18J), and FcγRIIIA binding to spike, S1 (Figure 3-18G), and S2 (Figure 3-18H) ($p < 0.05$; Figure 3-18). Prime–boost responses generally fell between high-dose prime and convalescent levels. The participant who received a longer prime–boost interval displayed antibody titres comparable to convalescent sera across multiple measures (Figure 3-18).

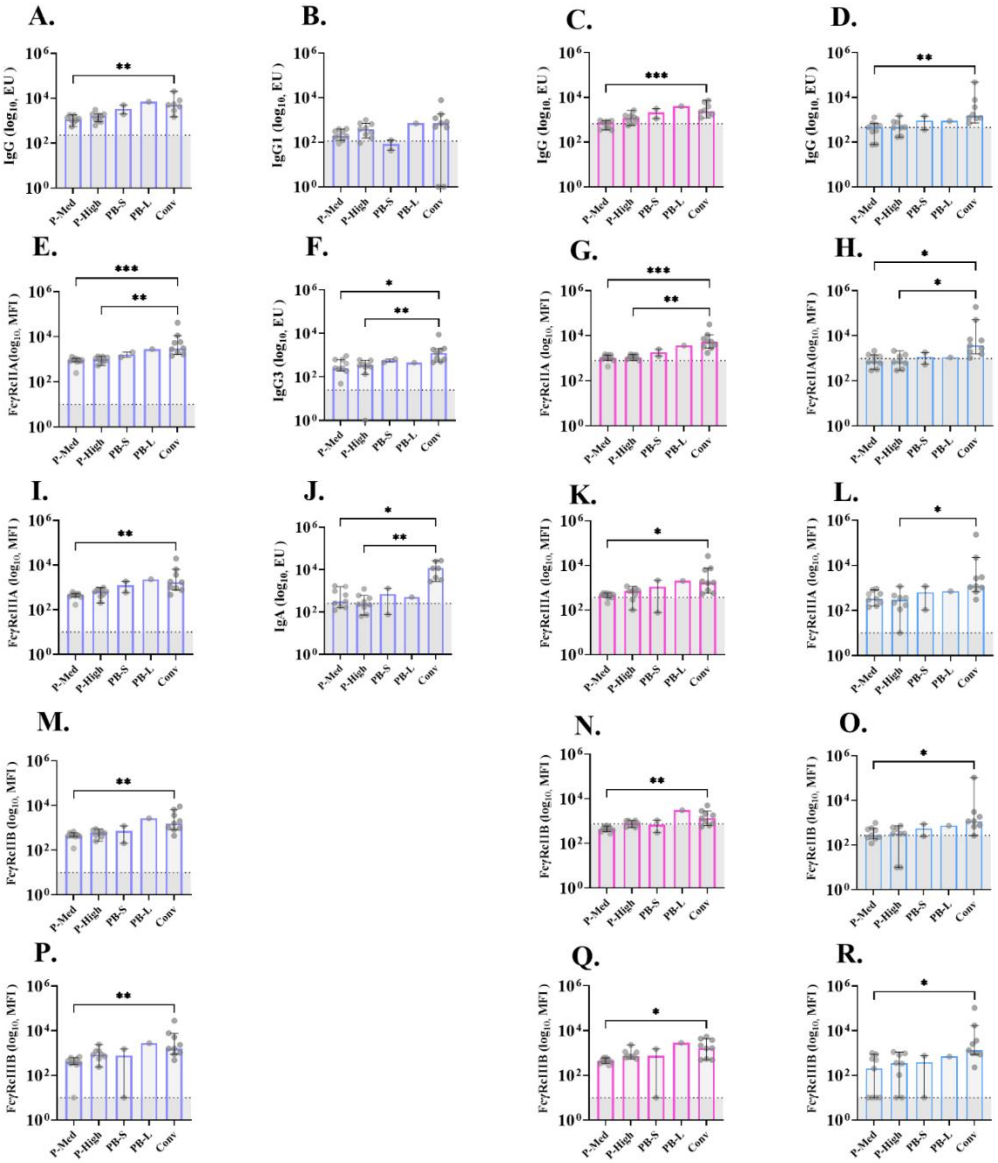


Figure 3-18. Antibody subclass and Fcγ receptor–binding responses following short- and long-interval boosting compared with single-dose vaccination and convalescent sera.

Antibody and FcγR-binding responses were measured at peak immunogenicity (Day 28 for prime-only groups and Day 14 post-boost for prime–boost regimens) and compared with convalescent samples. Bar graphs show ELISA units (EUs, $\log_{10}$) for total IgG, IgG1, IgG3, and IgA responses, as well as FcγRIIA-, FcγRIIIA-, and FcγRIIB-binding antibody responses to MERS-CoV spike (S), S1, and S2 antigens. Colours indicate antigen specificity: purple for spike (S), pink for S1, and blue for S2. Vaccine groups include medium-dose (P-Med) and high-dose (P-High) single-dose recipients, short-interval prime–boost (PB-S), long-interval prime–boost (PB-L), and convalescent (Conv) samples. Bars represent group medians with individual data points overlaid; error bars indicate interquartile ranges. The horizontal dashed line denotes the assay cutoff (seropositivity threshold) for each readout. Statistical analyses were performed using the Kruskal–Wallis test with Dunn's post hoc correction for multiple comparisons (*$p < 0.05$; **$p < 0.01$; ***$p < 0.001$)

Antibody-binding and FcγR- profiles were compared across prime-only, combined prime–boost, and convalescent groups (Figure 3-19). Heatmap analysis showing overall increases in both subclass diversity and FcγR-binding magnitude following boosting (Figure 3-19A). Among boosted participants, those with longer intervals tended to display higher and more sustained responses, particularly for IgG and FcγR engagement with spike and S1. Convalescent sera remained the most enriched and evenly distributed across all subclasses and FcγR-binding features, highlighting the broader functional profile of infection-induced immunity.

Radar plots supported these findings, revealing prime-only responses were modest and dominated by spike-specific features (Figure 3-19B). Combined prime–boost profiles demonstrated enhanced responses, particularly to spike and S1, while convalescent sera exhibited the broadest and most balanced activity across S, S1, and S2 subunits. The durability of antibody half-life was not assessed in boosted individuals due to the absence of later timepoints, which limited direct comparison of long-term responses between regimens.

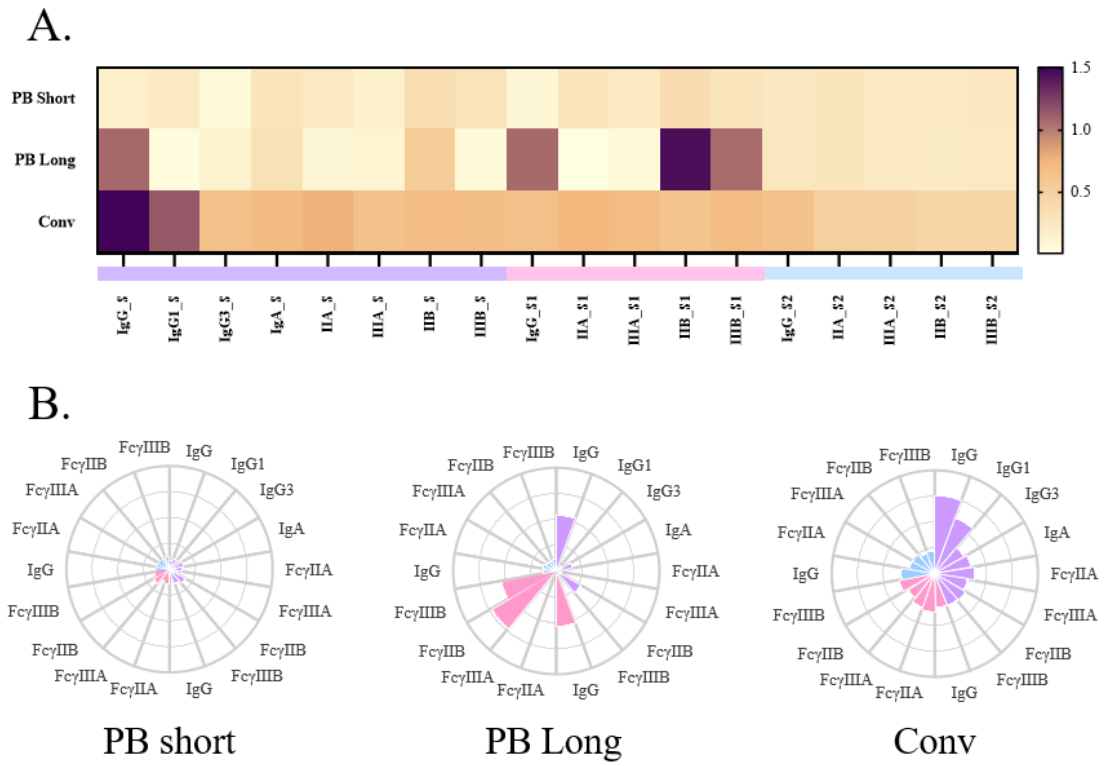


Figure 3-19. Antibody subclass and FcγR-binding and profiles following short- and long-interval boosting compared with convalescent sera.

(A) Heatmap showing normalized antibody and FcγR-binding features for spike (S), S1, and S2 antigens in prime–boost short-interval (PB Short) and long-interval (PB Long) groups, and convalescent samples (Conv). Each column represents a specific antibody subclass or FcγR interaction; values are normalized to the global maximum across all samples. **(B)** Radar plots illustrating composite immune profiles for PB Short, PB Long, and Convalescent groups. Axes represent antibody subclasses and FcγR-binding features; data are normalized to the global maximum. Colours indicate antigen specificity: purple for spike (S), pink for S1, and blue for S2.

3.2.4.2 Cellular immune responses following prime and prime–boost vaccination

IFN-γ ELISpot assays were used to evaluate vaccine-induced T-cell responses against spike, S1, and S2 peptide pools (Figure 3-20). Increases in T-cell activity after boosting were limited, with responses peaking at D14 post-boost in both short- and long-interval groups, but not exceeding the levels observed after the initial prime (Figure 3-20A-C). In the long-interval participant, pre-boost responses had declined close to baseline by six months and remained low for spike and S1, both falling below the detection threshold. Only S2-specific T-cell responses showed a measurable increase following the booster. In the short-interval group, boosting induced a modest rise in T-cell activity, reaching levels comparable to or slightly exceeding those observed after the primary vaccination for spike and S1, but not for S2. The highest overall IFN-γ responses were observed in the high-dose prime-only group at D28 (Figure 3-20D), consistent with trend of stronger T-cell priming at higher antigen exposure previously reported in MERS001 and MERS002 [291]. Although further validation in a larger cohort

is needed to confirm this effect, the observed trend strongly suggests that antigen dose is a critical factor in shaping the magnitude of the T-cell response.

These findings indicate that booster vaccination had limited capacity to further enhance the magnitude of T-cell responses, with minimal post-boost activation of spike- and S1-specific (Figure 3-20D-E) cells and only modest induction of S2 reactivity (Figure 3-20F). Boosting can still refine qualitative aspects of T-cell immunity, including cytokine polyfunctionality, cytotoxic effector potential, memory subset distribution, and epitope breadth or avidity. Such qualitative modulation may hold immunological relevance even in the absence of substantial quantitative expansion, underscoring the rationale for deeper functional T-cell analyses in future studies.

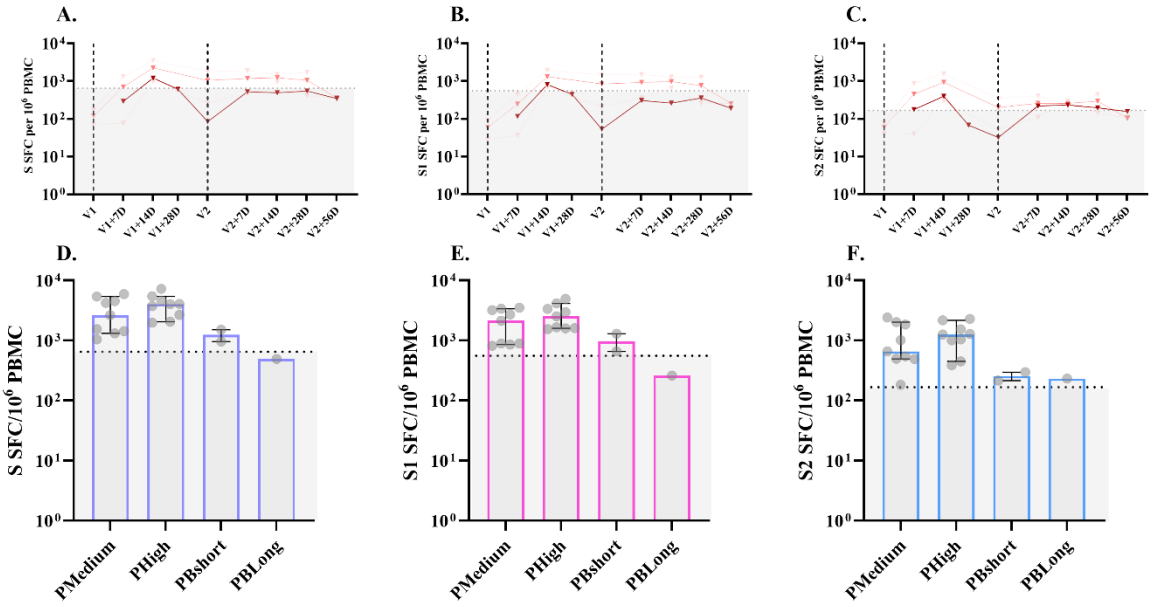


Figure 3-20. Antigen-specific IFN-γ ELISpot responses following prime and prime–boost vaccination.

(A–C) Longitudinal kinetics of IFN-γ spot-forming cells (SFCs) per 10^6 PBMCs in response to pooled peptide pools from spike **(A)**, S1 **(B),** and S2 **(C).** Each line represents an individual participant; vertical dashed lines indicate the timing of vaccine doses. Shaded areas represent background range based on unstimulated controls. **(D–F)** Comparison of peak responses to spike **(D)**, S1 **(E)**, and S2 **(F)** across prime-only medium-dose (PMedium), prime-only high-dose (PHigh), and prime–boost short-interval (PBShort) and long-interval (PBLong) groups. Bars indicate group medians with individual datapoints overlaid; error bars represent interquartile ranges. Responses are shown as background-subtracted SFCs per 10^6 PBMCs. Dotted lines denote the assay detection threshold, defined as the mean plus three standard deviations of Day 0 responses. Statistical analyses were performed using the Kruskal–Wallis test with Dunn's multiple-comparison correction (*P < 0.05; **P < 0.01; ***P < 0.001). Data generated by clinical trial team.

Overall, booster vaccination restored and broadened humoral responses beyond those induced by a single dose, with the long-interval regimen eliciting higher peak antibody titres, greater avidity, and more sustained responses. In contrast, the impact of boosting on cellular immunity was limited, with only modest increases in IFN-γ–producing T cells and minimal activation of spike- and S1-specific responses. Boosted participants approached the magnitude of infection-induced antibody responses

observed in convalescents, but retained a narrower spectrum of FcγR engagement and weaker cellular activity. Although IFN-γ–producing T-cell responses showed only modest boosting, other forms of T-cell help, such as T follicular helper and memory $CD4^+$ T cells, support class-switch recombination and affinity maturation, processes that influence antibody subclass distribution and FcγR engagement. Together, these findings indicate that while booster vaccination enhanced antibody magnitude and quality, it did not fully recapitulate the breadth of Fc-mediated effector potential observed following natural infection.

3.2.5 Pre-existing coronavirus immunity and cross-reactive response

Given widespread exposure to seasonal human coronaviruses, baseline immunity may influence vaccine-induced responses through cross-reactivity or immune imprinting [186]. To investigate this, we measured antibody responses to the four seasonal HCoVs—229E and NL63 (alphacoronaviruses), and OC43 and HKU1 (betacoronaviruses)—and SARS-CoV-2. This was tested in MERS001/2 high dose group only (n=17) as this dose elicited the highest immunogenicity and offered the most informative samples available, given logistical and reagent constraints. Importantly, the majority of samples were collected prior to the widespread circulation of SARS-CoV-2, with the final specimen in MERS002 obtained in June 2020, shortly after the COVID-19 pandemic was declared in May 2020. Any observed SARS-CoV-2 reactivity is therefore most likely to reflect cross-reactive antibodies rather than prior infection. We first assessed longitudinal changes in these responses following vaccination to identify evidence of back-boosting of seasonal coronavirus (CoV) immunity. We then examined correlations between baseline reactivity, and post-vaccination seasonal CoV and MERS-CoV antibody responses, both at the peak of the response and at a later time point (D182), as well as overall fold changes following vaccination.

3.2.5.1 Longitudinal responses

Antibody responses to seasonal coronaviruses increased significantly from baseline following ChAdOx1 MERS vaccination. Back-boosting was observed for the Betacoronaviruses OC43 and HKU1, with significant increases in IgG and FcγR-binding responses at Day 28 and sustained FcγRIIA/IIIA activity to Day 182, whereas responses to Alphacoronaviruses (229E, NL63) remained unchanged (Figure 3-21).

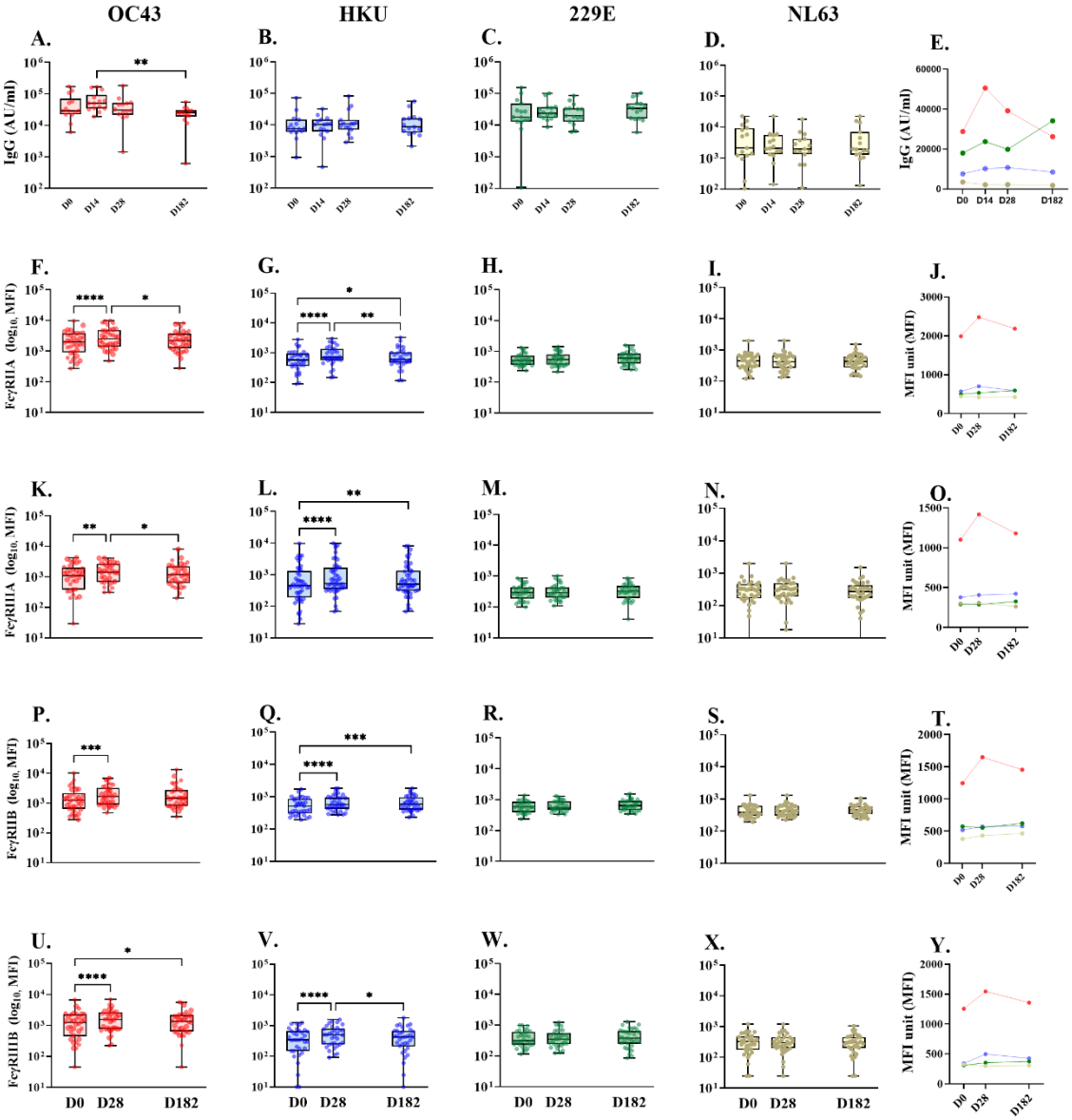


Figure 3-21 Cross-reactive antibody and Fcγ receptor–binding responses to seasonal human coronaviruses following ChAdOx1 MERS vaccination.

Shown are antibody (IgG) and FcγR-binding responses to Betacoronaviruses OC43 and HKU1 **(A–B, F–G, K–L, P–Q, U–V)** and Alphacoronaviruses 229E and NL63 **(C–D, H–I, M–N, R–S, W–X)** measured at baseline (D0), Day 28 (D28), and Day 182 (D182) after vaccination. IgG binding responses were quantified using a Meso Scale Discovery (MSD) assay, while FcγR-binding activities were measured using a Luminex-based multiplex assay for FcγRIIA, FcγRIIIA, FcγRIIB, and FcγRIIIB interactions. Corresponding median fluorescence intensity (MFI) trends over time are shown in **E, J, O, T**, and **Y**. Boxplots represent group medians with interquartile ranges; individual datapoints are shown. Statistical analyses were performed using the Wilcoxon matched-pairs signed-rank test; only paired samples from the same participants were included, and missing data were excluded from the analysis. Data are presented as arbitrary units (AU/mL, $\log_{10}$ scale) or median fluorescence intensity (MFI, $\log_{10}$ scale). Colour indicates viral antigen specificity: red = OC43, blue = HKU1, green = 229E, and yellow = NL63. Significance values are indicated as *p < 0.05; **p < 0.01; ***p < 0.001; ****p < 0.0001*. Analysis included individuals from the MERS high-dose group: MERS001 (n = 8) and MERS002 (n = 9). No assay cut-off was applied because seronegative reference samples were not available and the commercial MSD assay does not provide validated cut-off values

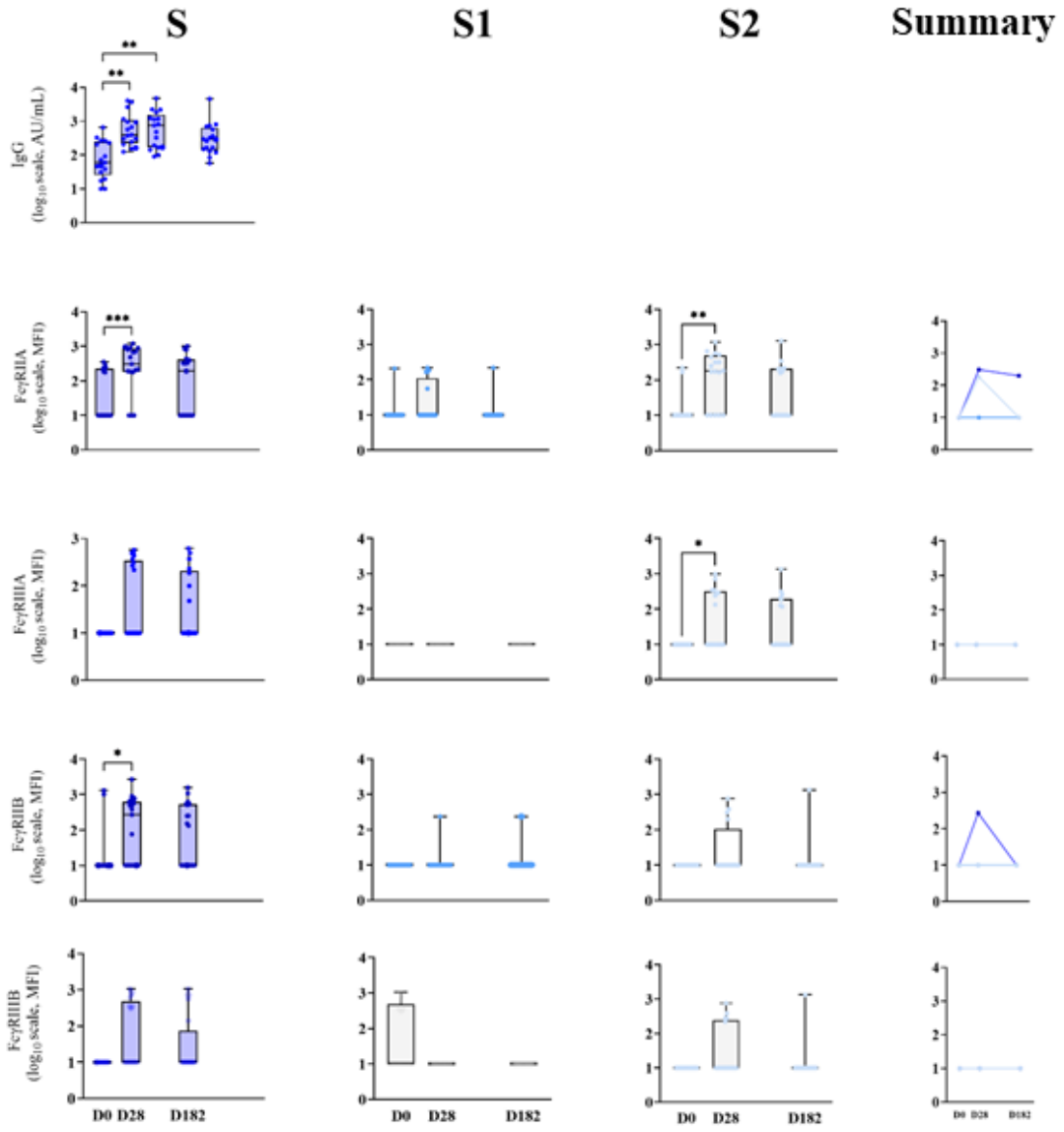


Figure 3-22. Cross-reactive humoral (IgG) and FcγR-binding responses to SARS-CoV-2 induced by ChAdOx1 MERS vaccination.

Columns are ordered by antigen specificity (S, S1, and S2), followed by a summary of median response trajectories over time. Boxplots represent group medians with interquartile ranges, with individual data points overlaid. Summary panels depict median values only and are intended to illustrate overall response trends rather than statistical comparisons. Statistical analyses were performed using the Wilcoxon matched-pairs signed-rank test; only paired samples from the same participants were included, and missing data were excluded from the analysis. Data are presented as arbitrary units (AU/mL, $\log_{10}$ scale) or median fluorescence intensity (MFI, $\log_{10}$ scale). Colours indicate viral antigen specificity: dark blue (S), medium blue (S1), and light blue (S2). Significance values are indicated as * $p < 0.05$; ** $p < 0.01$; *** $p < 0.001$

ChAdOx1 MERS vaccination generates transient cross-reactive IgG responses to SARS-CoV-2, consistent with antibody targeting of conserved spike domains, particularly within S2, and associated FcγRIIA and FcγRIIB engagement. These responses peak at D28 but wane by D182 (Figure 3-22).

3.2.5.2 Baseline and back-boosting associations with vaccine responses

Next, we investigated whether baseline antibody responses to seasonal coronaviruses influenced the magnitude and durability of vaccine-induced immunity. To assess this, baseline IgG and FcγR-binding responses were correlated with a composite vaccine score, calculated as the average z-score across all antibody and FcγR readouts for MERS-CoV spike (S, S1, and S2) at peak (D28) and sustained (D182) time points. Baseline OC43 FcγRIIA and FcγRIIIA responses correlated positively with composite S2 responses both at the peak (D28; r = 0.60, p = 0.016; Figure 3-23A) and at D182 (r = 0.60, p = 0.016; Figure 3-23E). In contrast, baseline IgG responses to 229E correlated positively with composite S1 responses at D182, whereas baseline FcγRIIIB responses correlated negatively with composite S2 responses (Figure 3-23G), indicating that distinct components of pre-existing coronavirus immunity may exert both facilitating and inhibitory effects on vaccine-induced responses.

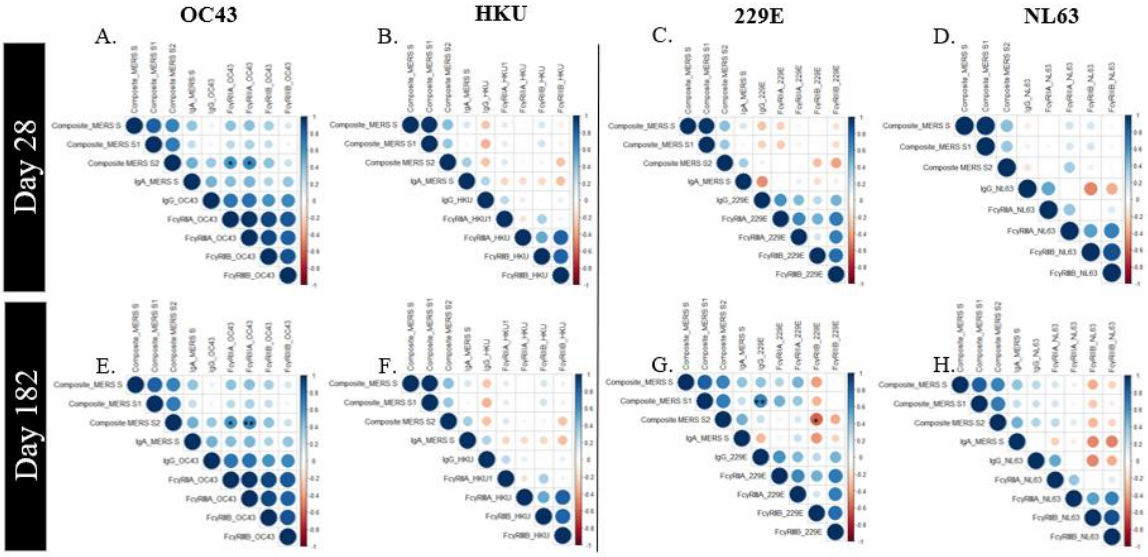


Figure 3-23. Spearman correlation matrices of MERS-CoV spike–specific antibody responses and baseline seasonal coronavirus immunity.

Spearman correlation matrices showing associations between MERS-CoV spike–specific antibody responses measured at Day 28 **(A–D)** and Day 182 **(E–H)** post-vaccination and baseline antibody responses to seasonal *Betacoronavirus* (OC43, HKU1) and *Alphacoronavirus* (229E, NL63) antigens. Composite MERS-CoV responses were calculated as the average z-score of binding IgG and FcγR responses to each subunit (S, S1,and S2). Each circle represents a Spearman correlation coefficient (ρ), with circle size indicating the strength and colour indicating the direction of correlation (blue = positive, red = negative). Panels A–B show correlations for *Betacoronavirus* OC43 and HKU1, and panels C–D for *Alphacoronavirus* 229E and NL63 at Day 28. Panels E–H display the same analyses at Day 182.

Because back-boosting was most evident for OC43 and HKU1, we next asked whether the magnitude of back-boosting correlated with vaccine-induced titres at D28 and D182 (Figure 3-24). At D28, the extent of back-boosting (fold change between D0 and D28) in OC43 FcγRIIIA and FcγRIIB responses correlated positively with MERS-CoV S and S1 responses (Figure 3-24A), suggesting that individuals with stronger OC43 functional boosting mounted higher vaccine responses. At D182, HKU1 back-boosting responses correlated with MERS-CoV S and S1 titres, indicating that cross-reactive HKU1 immunity contributed to the maintenance of vaccine-induced responses over time (Figure 3-24D).

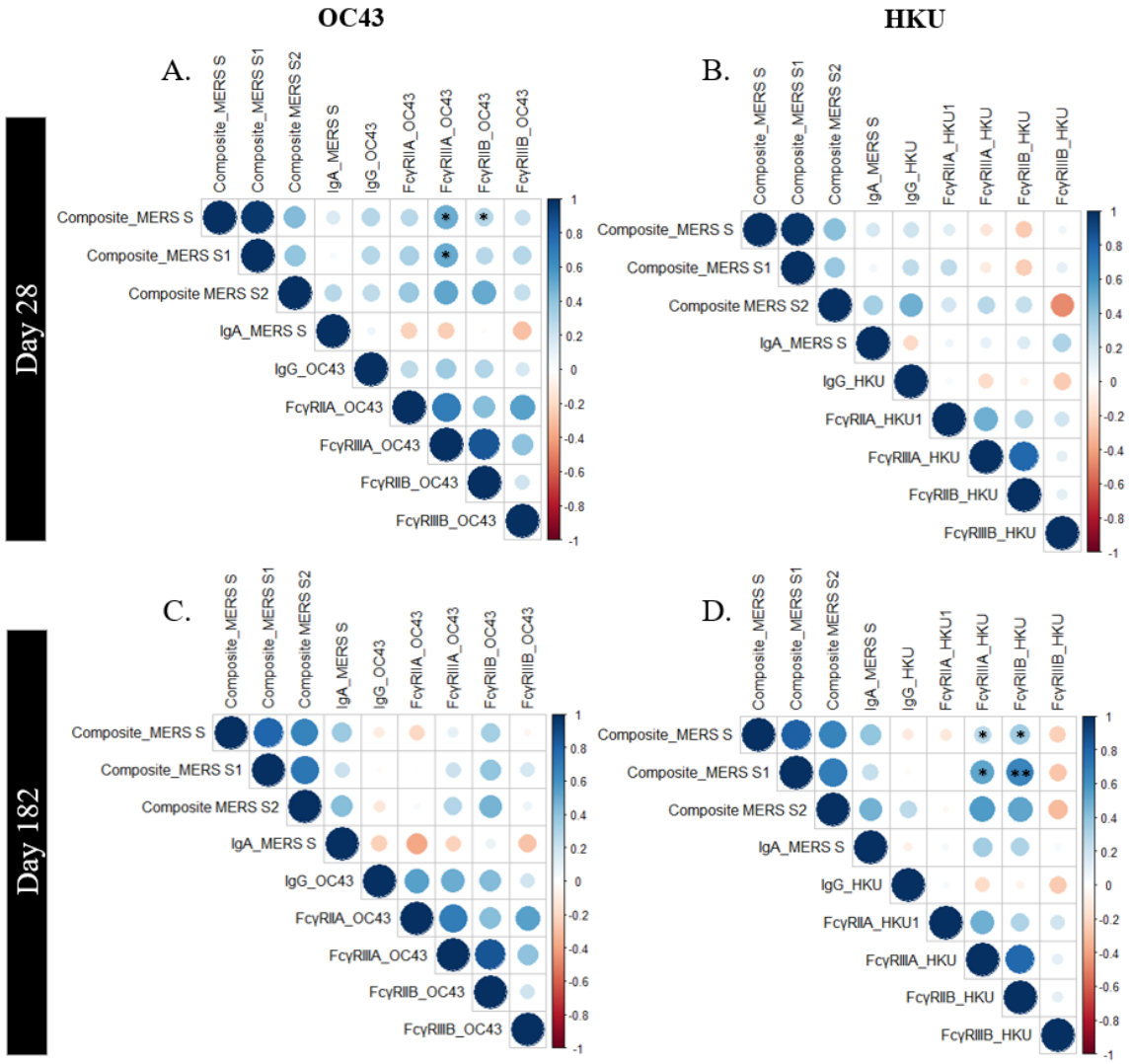


Figure 3-24. Spearman correlation matrices of MERS-CoV spike–specific antibody responses and seasonal *Betacoronavirus* back-boosting.
Spearman correlation matrices showing associations between MERS-CoV spike–specific antibody responses measured at Day 28 **(A–B)** and Day 182 **(C–D)** post-vaccination and the fold changes (baseline to Day 28) in antibody responses to seasonal *Betacoronavirus* OC43 and HKU1, representing back-boosting effects. Composite MERS-CoV responses were calculated as the average z-score of binding IgG and FcγR responses to each subunit (S, S1, and S2). Each circle represents a Spearman correlation coefficient (ρ), with circle size indicating the strength and colour indicating the direction of correlation (blue = positive, red = negative).

These data show a positive association between the magnitude of MERS-CoV vaccine responses and the extent of back-boosting to OC43 and HKU1. While this may reflect a contribution of pre-existing cross-reactive immunity to vaccine outcomes, the reverse is also possible, whereby individuals mounting stronger vaccine responses exhibit greater boosting of cross-reactive seasonal coronavirus antibodies. Given the small sample size, the directionality of these relationships cannot be determined.

3.2.5.3 Influence of baseline seasonal coronavirus immunity on vaccine responses

To investigate whether baseline seasonal coronavirus immunity influenced vaccine-induced responses, participants were stratified into high and low responder groups using principal component analysis (PCA) of D28 readouts. Spike- and S1-associated responses clustered together, whereas IgA and S2 responses formed a separate group (Figure 3-25A). High and low responders were clearly separated, with both MERS001 and MERS002 participants distributed across these clusters, indicating no cohort-specific bias. IgG titres were significantly higher in high responders compared with low responders, but baseline antibody responses to seasonal coronaviruses did not differ between groups (Figure 3-25B–C). This analysis was limited to vaccine responses at D28, as the distribution of high and low responders between MERS001 and MERS002 became unequal at D182, potentially confounding cohort comparisons.

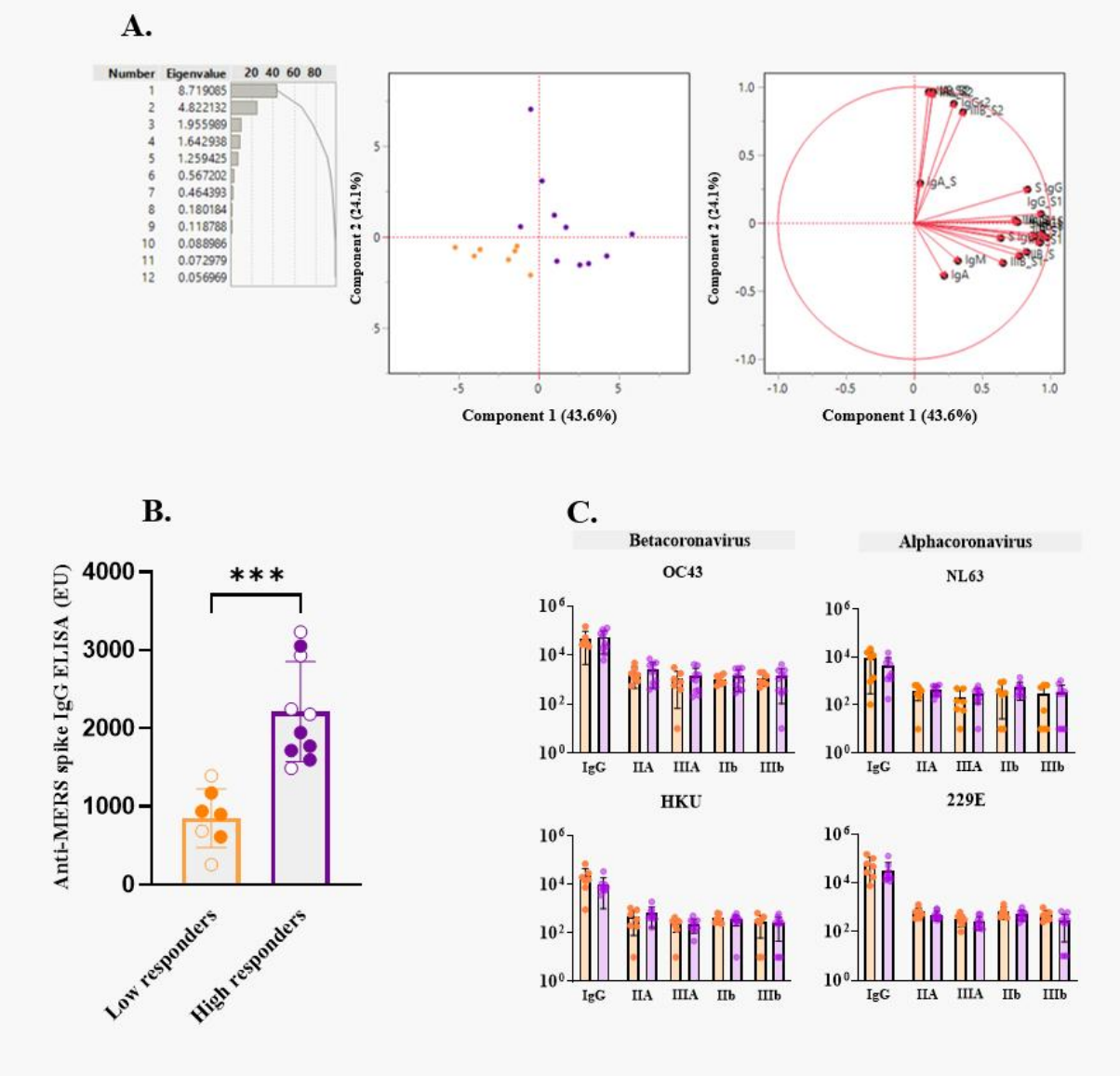


Figure 3-25. Humoral immune responses in low and high responders.

(A) Principal component analysis (PCA) of humoral responses. The left panel shows the percentage of variance explained by each principal component. The middle plot illustrates sample clustering based on antibody features, with filled purple circles representing high responders and orange circles representing low responders. The right biplot displays the loading vectors indicating the contribution of individual antibody variables to the principal components, highlighting clustering of S, S1, and FcγR features together, and IgA and S2 responses grouping together. (**B)** Comparison of anti-MERS spike IgG levels between low and high responders identified by PCA. Filled circles correspond to MERS001 and open circles to MERS002. **(C)** Baseline antibody responses (IgG and subclasses IIA, IIIA, IIb, and IIIb) to common human coronaviruses—Betacoronaviruses (OC43, HKU) and Alphacoronaviruses (NL63, 229E)—in low and high responders. Statistical significance was determined using the Mann–Whitney test (***$p < 0.001$).

We next applied stepwise regression models to identify baseline predictors of vaccine responses. For IgG at D28, baseline OC43 FcγRIIB emerged as a significant independent predictor of vaccine-induced titres ($p = 0.011$; adjusted $R^2 = 0.50$), whereas baseline IgG responses to OC43 or 229E were not significant. A simplified model including only OC43 FcγRIIB confirmed this association ($p = 0.010$;

adjusted $R^2 = 0.32$). The trial variable (MERS001 vs. MERS002) was included as a covariate and was not significant, indicating no trial-specific effect on IgG outcomes. As shown in Figure 3-26, baseline OC43 FcγRIIIB levels were higher in high responders than in low responders, although the difference was not statistically significant.

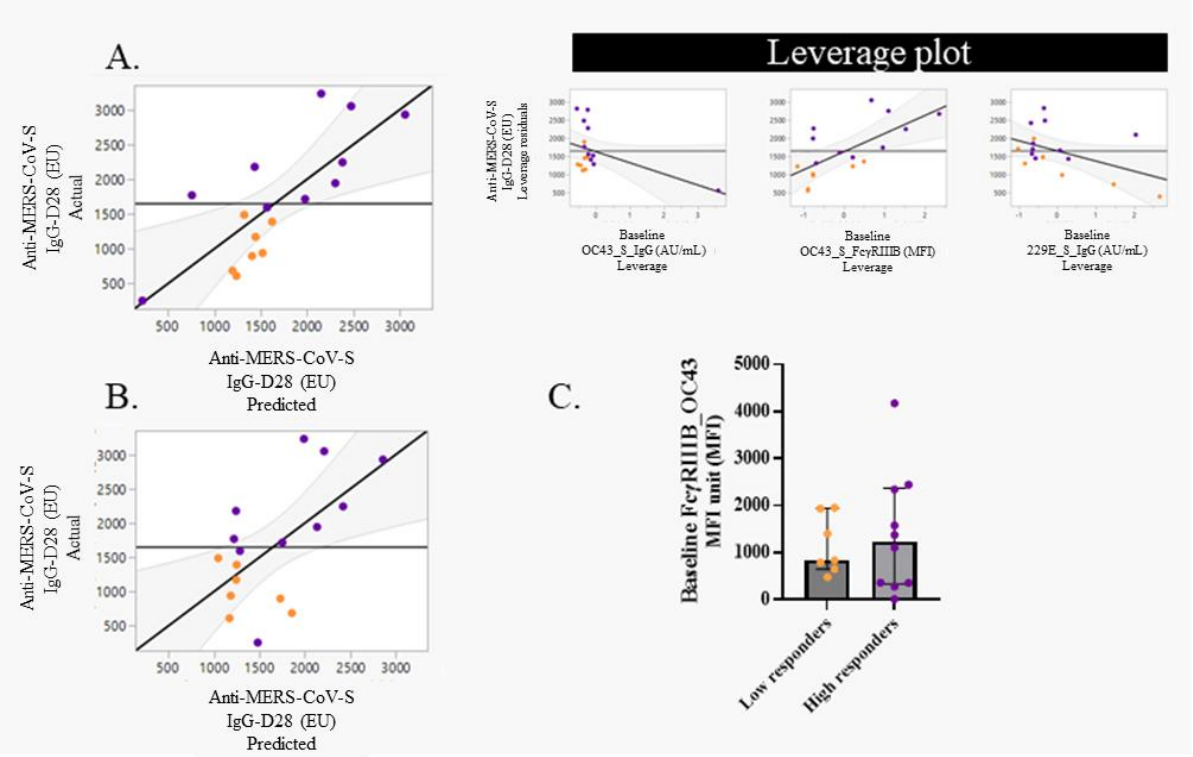


Figure 3-26. Stepwise regression analysis identifying baseline predictors of vaccine-induced humoral responses.

(A) Actual vs predicted plot showing the fit of the full regression model for MERS-CoV spike-specific IgG titres at Day 28. **(B)** Leverage plots illustrating associations between baseline OC43 IgG, OC43 FcγRIIB, and 229E IgG features and vaccine-induced IgG responses. Baseline OC43 FcγRIIB was identified as a significant independent predictor ($p = 0.011$; adjusted $R^2 = 0.50$), whereas OC43 and 229E IgG were not significant. **(C)** Simplified regression model including only OC43 FcγRIIIB, confirming its association with vaccine-induced IgG titres ($p = 0.010$; adjusted $R^2 = 0.36$). (D) Baseline OC43 FcγRIIIB levels in low and high response.

Models using fold changes were not significant, with only a weak association observed for composite S2, at D28 ($p = 0.03$; adjusted $R^2 = 0.30$). These findings suggest that absolute baseline functional responses, rather than fold changes, were stronger predictors of vaccine-induced IgG titres.

3.2.6 Comparison of breadth responses and durability between populations

Across all readouts examined in this study, significant differences were observed between the UK (MERS001) and KSA (MERS002) cohorts. Differences in antibody magnitude were most pronounced in the high-dose groups at D182 (Table 3-1). When viewed collectively, a distinct pattern emerged: responses in MERS001 were predominantly directed toward the spike (S) protein and its S1 subunit,

whereas MERS002 showed stronger reactivity toward the S2 subunit, accompanied by higher IgA titres and enhanced FcγR-binding activity at the peak time point.

The longevity of these antibody responses also differed between cohorts. The median IgG1 half-life was significantly higher in MERS001 compared with MERS002 [114 days (IQR, 79–180) vs. 53 days (IQR, 49–84); Figure 3-27A, $p = 0.04$]. However, given the modest p-value and small sample sizes, this finding should be interpreted with caution. In contrast, FcγRIIB-binding responses to the S2 subunit were longer-lived in MERS002, with a median half-life of 204 days (IQR, 32–309) compared with 31 days (IQR, 26–71) in MERS001 (Figure 3-27D, $p = 0.0082$). These cohort-specific differences in both antibody magnitude are further illustrated by the heatmap and nightplot analyses below (Figure 3-27A-B).

Antibody type	Target	Gp	Timepoint	MERS001	MERS002	p-value
IgA	S	Gp3	D56	119 [66-276]	583 [143-1717]	0.03
	S	Gp3	D182	80 [58-167]	213 [100-732]	0.02
IIA	S	Gp3	D182	438 [341-562]	746 [519-1931]	0.02
	S1	Gp2	D28	1102 [918- 1398]	486 [413-710]	0.01
	S1	Gp3	D0	215 [154-322]	360 [299-621]	0.02
	S1	Gp3	D182	528 [349-697]	1166 [756-3830]	0.0037
IIIA	S	Gp3	D182	190 [169-290]	472 [268-801]	0.0037
	S2	Gp3	D182	166 [10-311]	418 [273-1192]	0.02
IIB	S1	Gp3	D0	10 [10-10]	244 [10-394]	0.05
	S1	Gp3	D182	305 [10-335]	444 [328-881]	0.02
IIIB	S1	Gp3	D28	723 [628-1115]	465 [259-629]	0.01
IIIB	S2	Gp3	D182	10 [10-180]	297 [212-936]	0.0027

Table 3-1. Comparison of vaccine-induced antibody responses between UK (MERS001) and KSA (MERS002) cohorts.
Median [IQR] values are shown for each antibody type, antigen target (S, S1, or S2), and timepoint (Day 0, Day 28, Day 56, Day 182). Only readouts with significant differences between cohorts are included. P-values were derived from Mann–Whitney U tests. Overall, responses were higher in MERS002 compared with MERS001, with the exception of FcγRIIIB binding to S1, which was higher in MERS001. Sample sizes: MERS001 (n = 8), MERS002 (n = 9).

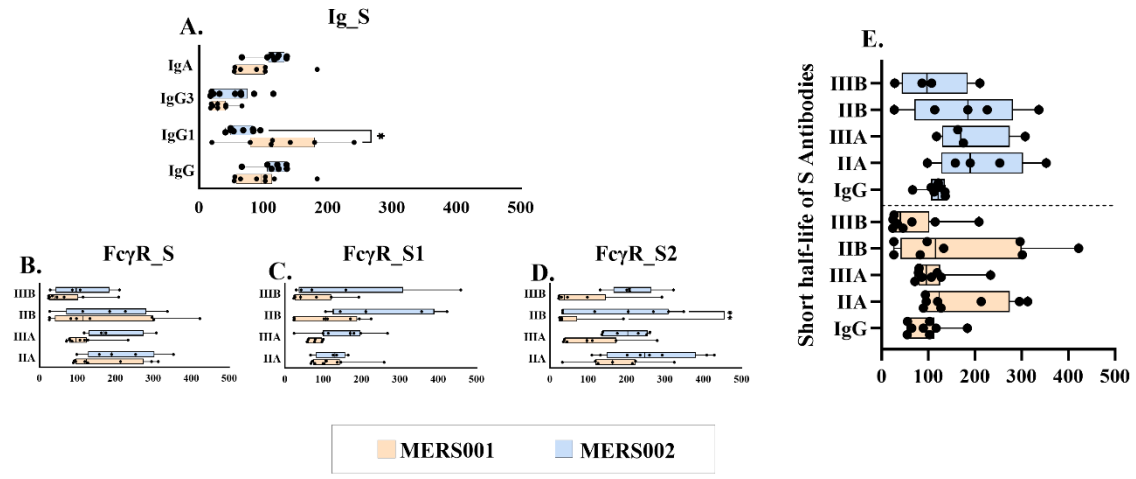


Figure 3-27. Comparison of antibody half-lives between MERS001 and MERS002 studies.

Box plots depict the distribution of short half-lives for **(A)** total and subclass-specific IgG and IgA binding antibodies, **(B)** FcγR-binding to the S antigen, **(C)** FcγR-binding to S1, and **(D)** FcγR-binding to S2. Panel **(E)** summarizes short half-lives of IgG and FcγR-binding antibodies across both studies. Blue boxes represent the MERS001 study and orange boxes represent the MERS002 study. Each dot corresponds to an individual participant, with box plots showing medians and interquartile ranges. Statistical comparisons between groups were performed using the Mann–Whitney U test, and within-group comparisons in panel (E) were assessed using the Kruskal–Wallis test. Asterisks denote significant differences within each group separately (*$p < 0.05$). All data lacking reliable readouts were excluded from the analysis to ensure accuracy and consistency in the comparison.

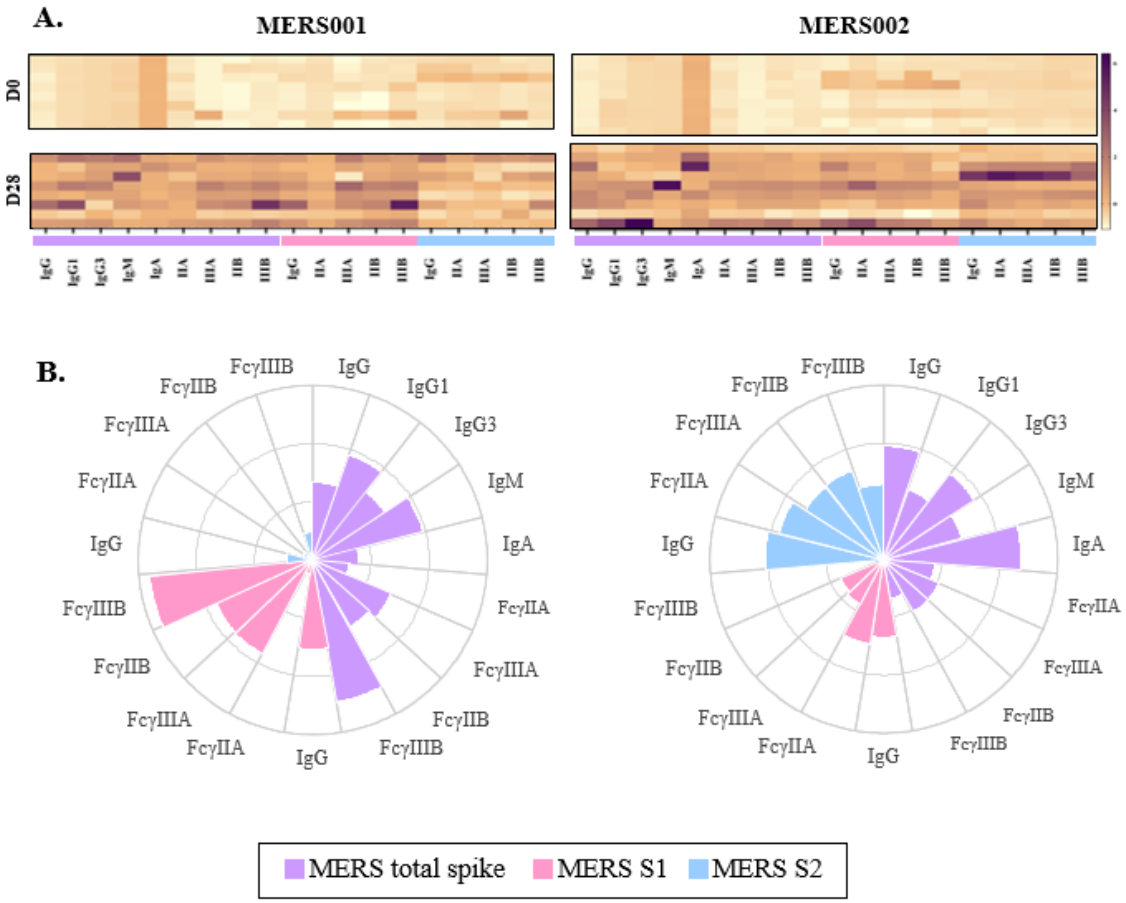


Figure 3-28. Induction and durability of humoral antibody responses in MERS001 and MERS002 participants. **(A)** Heatmaps of z-score–normalized data showing Ig isotype and FcγR-binding antibody responses against MERS-CoV spike antigens in participants from the MERS001 (left) and MERS002 (right) trials before vaccination (Day 0), at the peak response (Day 28). **(B)** Radar plots illustrating the breadth and relative magnitude of antibody responses at Day 182 for MERS total spike (purple), S1 (pink), and S2 (blue) antigens in MERS001 (left) and MERS002 (right) participants.

At D182, antigen-specific antibody responses remained detectable in both MERS001 and MERS002 participants but were generally higher in MERS002. As shown in the heatmaps (Figure 3-29A), a greater proportion of the D28 peak response was retained at D182 across multiple FcγR-binding features in MERS002 compared with MERS001. Consistently, a higher percentage of MERS002 participants remained seropositive at D182 for total spike, S1, and S2 antigens (Figure 3-29B). Estimated antibody half-lives were also longer in MERS002, particularly for FcγRIIA- and FcγRIIIA-binding antibodies (Figure 3-29C). However, these half-life estimates were derived from only two time points (D28 and D182) and should therefore be interpreted cautiously, as they may not accurately capture non-linear decay kinetics. Collectively, these analyses indicate higher antibody levels and slower estimated decay rates at D182 in the MERS002 cohort relative to MERS001, based on between-cohort comparisons at matched post-vaccination time points.

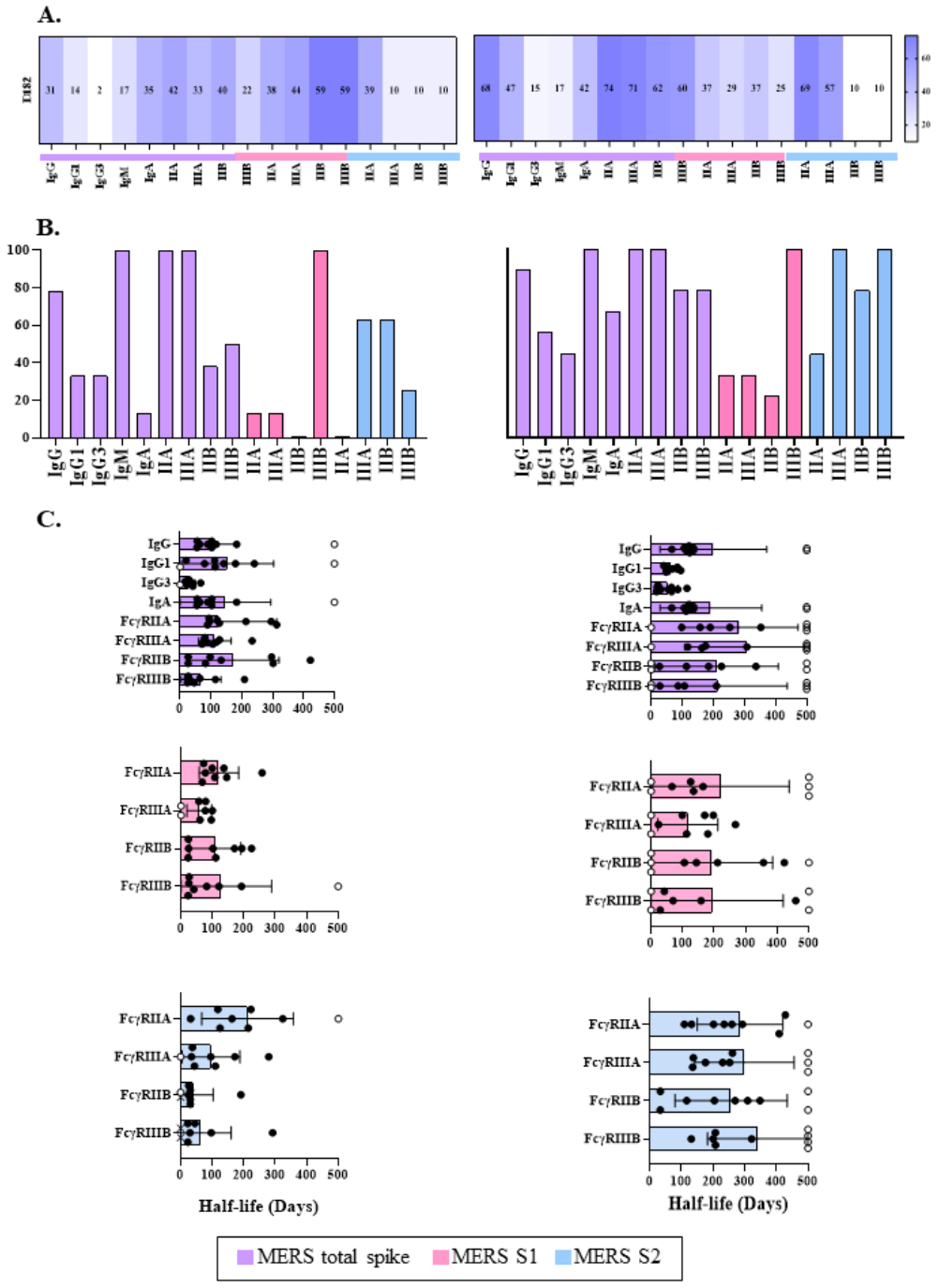


Figure 3-29. Durability of humoral antibody responses in MERS001 and MERS002 participants.
(A) Heatmaps summarizing the median percentage of the Day 28 response retained at Day 182 for each antigen–FcγR combination in the MERS001 (left) and MERS002 (right) trials, illustrating changes between the peak response (Day 28) and the follow-up (Day 182). **(B)** Bar plots showing the proportion of participants who remained seropositive at Day 182 for each antigen–FcγR feature. Seropositivity was defined as a signal exceeding the mean plus 3 standard deviations (SD) of pre-immune samples. **(C)** Estimated half-lives of antigen-specific and FcγR-binding antibody responses. Empty circles indicate responses for which the half-life could not be calculated because antibody levels were stable (right side) or increasing after the peak (left side). "X" denotes non-responders. Half-lives were calculated using log-transformed decay data with a single post-peak time point (Day 182). Analyses were performed for MERS001 (left, n = 8 high-dose participants) and MERS002 (right, n = 9 high-dose participants).

To investigate whether these population-specific patterns reflected variation in seasonal coronavirus exposure, we compared baseline immunity and post-vaccination kinetics. Baseline IgG and FcγRIIIA responses to OC43 were significantly higher in MERS002 ($p < 0.05$), whereas α-coronavirus (229E) FcγRIIB and FcγRIIIA responses, as well as NL63 FcγRIIB responses, were elevated in MERS001 (Figure 3-30A). Following vaccination, kinetics also differed between cohorts: OC43 FcγRIIA and FcγRIIIA-binding antibodies were higher in MERS002 (Figure 3-30B), while HKU1 FcγRIIB and 229E FcγRIIB and FcγRIIIB responses were consistently higher in MERS001 at all time points assessed. Notably, differences in OC43 and 229E responses observed at baseline persisted over time; however, in pooled analyses, only OC43 demonstrated a significant back-boosting effect, whereas 229E responses remained relatively stable Figure 3-30), suggesting that vaccine-induced recall was largely restricted to pre-existing OC43-specific immunity.

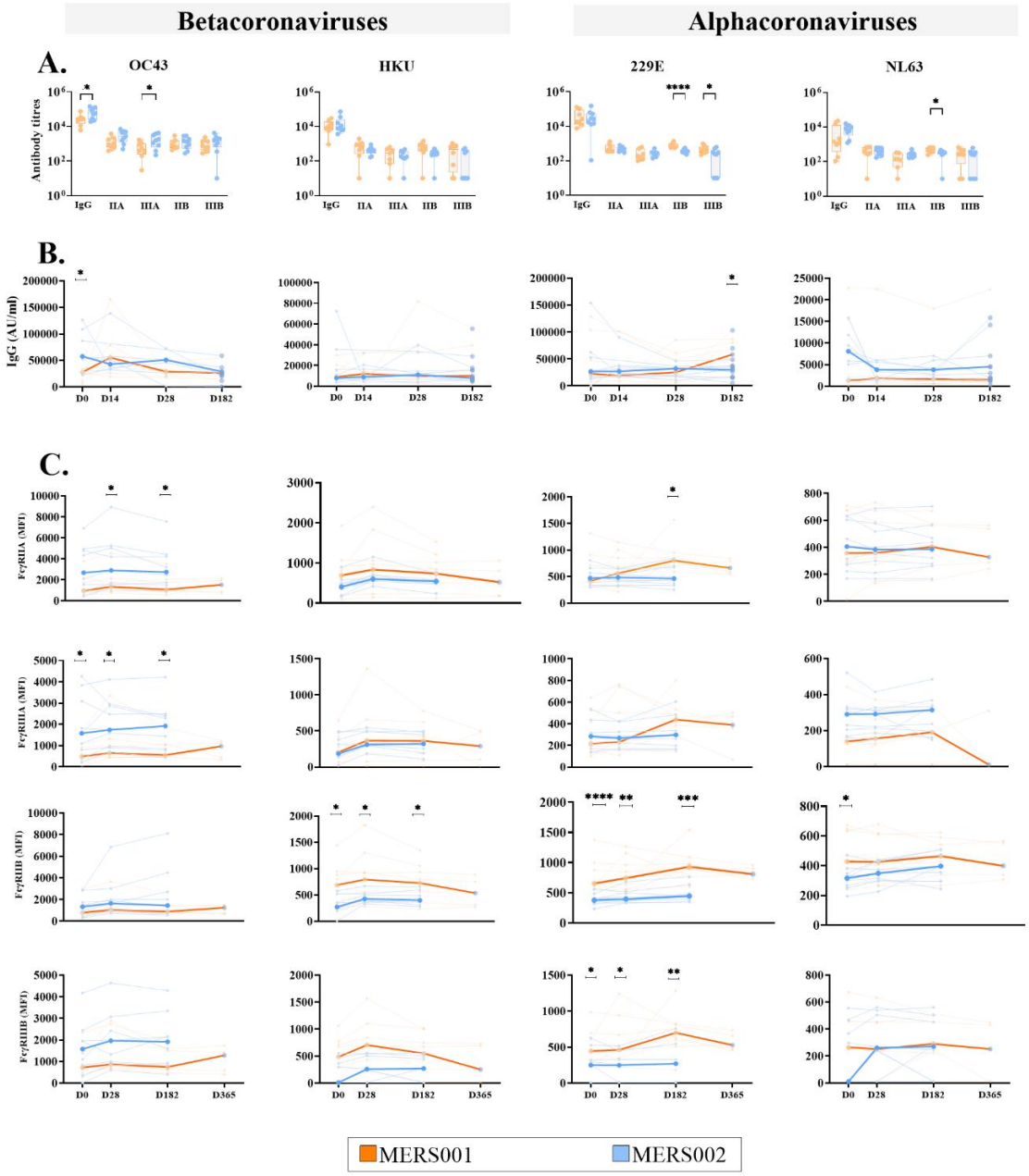
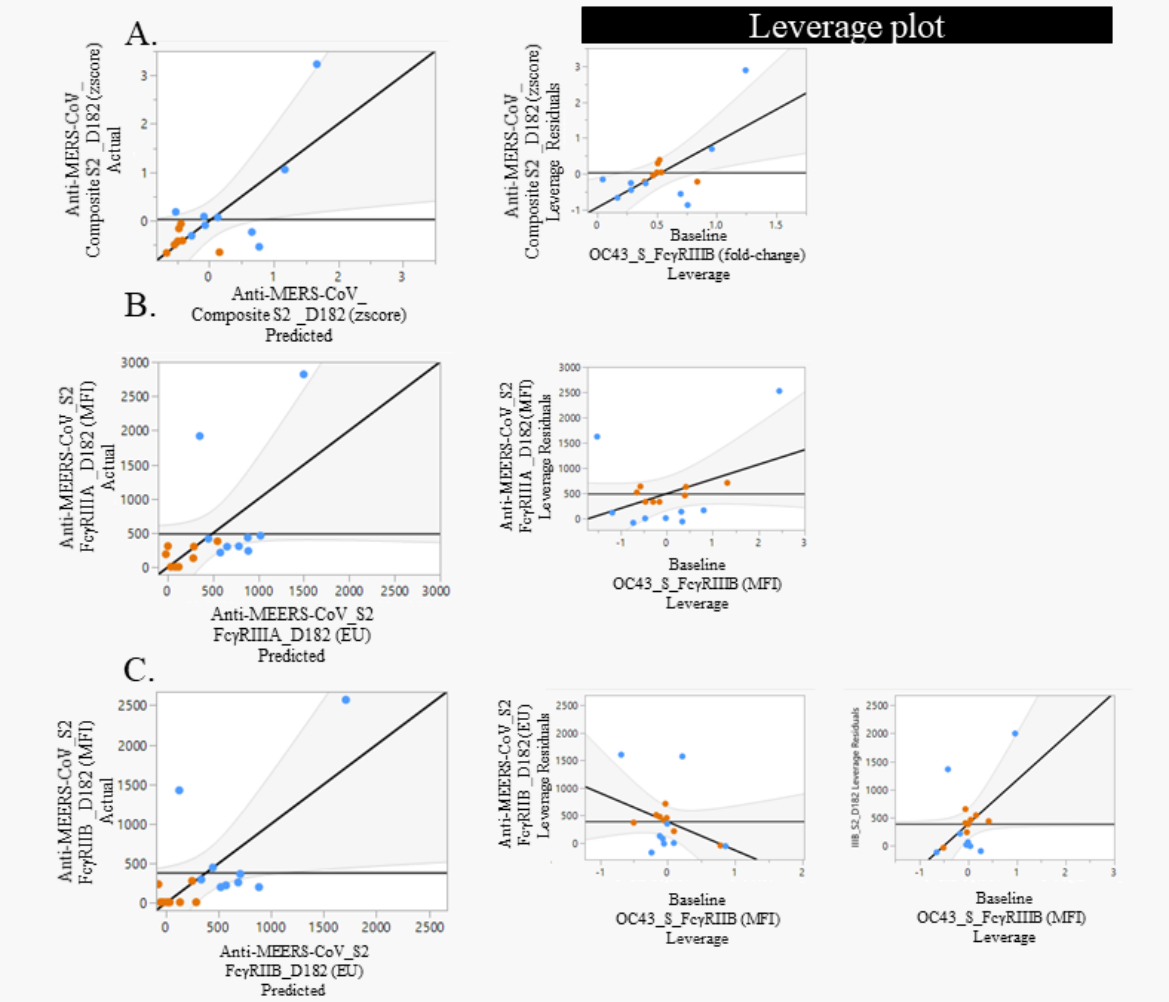


Figure 3-30. Baseline and longitudinal seasonal coronavirus antibody responses in UK (MERS001) and KSA (MERS002) cohorts.

(A) Baseline IgG and FcγR-binding antibody responses to OC43, HKU1, 229E, and NL63. Boxplots represent medians and interquartile ranges; individual data points represent participants. **(B)** Longitudinal kinetics of IgG and FcγR-binding antibodies to OC43, HKU1, 229E, and NL63 measured at Day 0, Day 14, Day 28, Day 56, and Day 182. Solid lines indicate median responses per cohort; thin lines represent individual trajectories. **(C)** FcγR-binding responses were additionally measured at Day 0, Day 28, Day 182, and Day 365. Statistical comparisons between cohorts were performed using the Mann–Whitney U test or unpaired *t*-test, depending on data normality; significant differences are indicated by $p < 0.05$ (*). Colour coding: MERS001 (orange) and MERS002 (blue).



Regression modelling confirmed that baseline OC43 responses were strongly associated with vaccine-induced S2-specific outcomes, which differed between cohorts (Figure 3-31). In particular, the fold change in FcγRIIB_OC43 between baseline and D28 was a positive predictor of the S2-specific composite fold change between D182 and D28 (Figure 3-31A). Baseline FcγRIIIB_OC43 levels were positively associated with MERS S2-specific FcγRIIIA fold changes at D182 (Figure 3-31B). Additionally, baseline FcγRIIB_OC43 levels were positively, and baseline FcγRIIIB_OC43 levels were negatively, associated with S2-specific FcγRIIIB fold changes at Day 182 (Figure 3-31C).

Figure 3-31. Stepwise regression analysis identifying predictors of vaccine-induced S2-specific antibody fold changes.

(A) Composite S2-specific FcγR fold changes. **(B)** FcγRIIIA-specific S2 fold changes. **(C)** FcγRIIIB-specific S2 fold changes. Regression models included baseline seasonal coronavirus FcγR features and fold changes between Day 182 and Day 28 as predictors. Significant associations are shown as coloured regression lines (red = positive; blue = negative) with shaded 95 % confidence intervals. Statistical significance was determined using stepwise linear regression ($p < 0.05$). Orange circles represent MERS001 (UK) participants, and blue circles represent MERS002 (KSA) participants.

IgA responses exhibited distinct kinetics. Stepwise regression analyses using IgA titres at D28 and D182 as outcomes revealed significant associations with baseline seasonal coronavirus features at both timepoints. At D28, the model was significant ($p = 0.0019$; adjusted $R^2 = 0.70$), with positive predictors including OC43 FcγRIIIB and HKU1 IgG, and negative associations with OC43 FcγRIIB and 229E IgG (Figure 3-32A–B). At D182, the model remained significant ($p = 0.0012$; adjusted $R^2 = 0.62$), with OC43 FcγRIIB emerging as a positive predictor and OC43 IgG as a negative predictor (Figure 3-32C–D). The regression models included trial (MERS001 vs. MERS002) as a covariate, which was not significant at either timepoint, indicating no trial-specific effect on IgA outcomes. Together, these findings highlight the importance of baseline OC43 immunity in shaping IgA responses, with FcγRIIIB associated with early IgA induction at D28 and FcγRIIB contributing to IgA maintenance at D182.

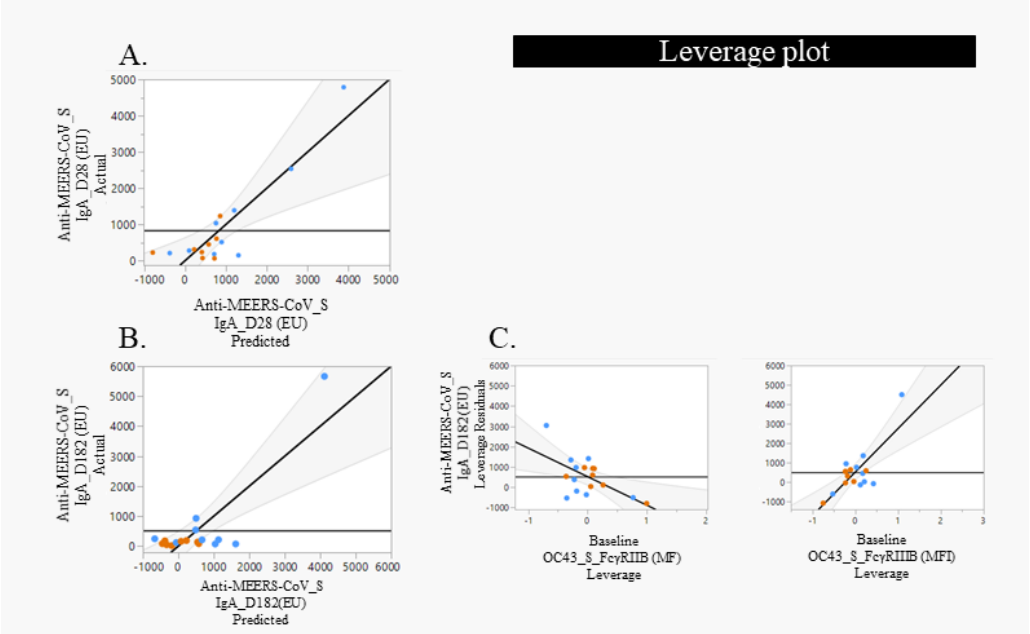


Figure 3-32. Stepwise regression analysis identifying baseline predictors of vaccine-induced IgA responses.

(A) Actual versus predicted plot showing the fit of the regression model for Day 28 IgA titres ($p = 0.0019$; adjusted $R^2 = 0.70$). **(B)** Actual versus predicted plot for the Day 182 model ($p = 0.0012$; adjusted $R^2 = 0.62$). **(C)** Leverage plots for Day 182 showing a positive association with OC43 FcγRIIB and a negative association with OC43 IgG. Together, these analyses highlight the role of baseline OC43 immunity in shaping IgA responses, with FcγRIIIB linked to early induction (Day 28) and FcγRIIB to long-term maintenance (Day 182). Filled purple circles represent high responders (MERS001), and open orange circles represent low responders (MERS002).

Taken together, these findings suggest that differences in baseline seasonal coronavirus immunity—particularly functional responses to OC43—contributed to the distinct vaccine response profiles observed between MERS001 and MERS002.

3.2.7 T cell responses

The results described so far indicate multifaceted and broad humoral immunity in response to vaccination with the ChAdOx1 MERS vaccine. Vaccination with the ChAdOx1 MERS vaccine has been shown to induce robust and sustained T cell responses as measured by IFN-γ ELISPOT [291, 292]. To better characterize the phenotypic and functional diversity of vaccine-induced T cell responses, multiparameter flow cytometry was used to identify changes in the phenotype of $CD4^+$ and $CD8^+$ T cells following vaccination.

PBMCs from the MERS001 cohort were selected based solely on cell counts (see Methods), not by treatment group. Six participants contributed samples (n = 6): at D0 there was one participant from group 1, two from group 2, and three from group 3; the same distribution was available at D14; by D28 samples remained for only three participants (one from group 1 and two from group 2). Therefore, these data are presented to illustrate the overall cellular response rather than to support comparisons between dose groups.

Multidimensional analysis using the FlowSom algorithm revealed a transient accumulation at D14 of a distinct cluster of $CD8^+$ T cells (cluster 7) (Figure 3-33A), characterized by co-expression of $CD38^+$ and HLA-DR—activation markers typically associated with effector $CD4^+$ and $CD8^+$ T cell responses. In contrast, no significant changes were observed in the frequency of the eight clusters identified by FlowSom within the $CD4^+$ T cell population (Figure 3-33B).

To validate the multidimensional analysis, manual gating was performed to identify cells expressing $CD38^+$ and HLA-DR among both $CD4^+$ and $CD8^+$ T cells. This analysis confirmed an increased frequency of $CD38^+$HLA-DR^+ $CD8^+$ T cells at D14 following vaccination (Figure 3-33C), with no corresponding change in the frequency of $CD38^+$HLA-DR^+ $CD4^+$ T cells (Figure 3-33D).

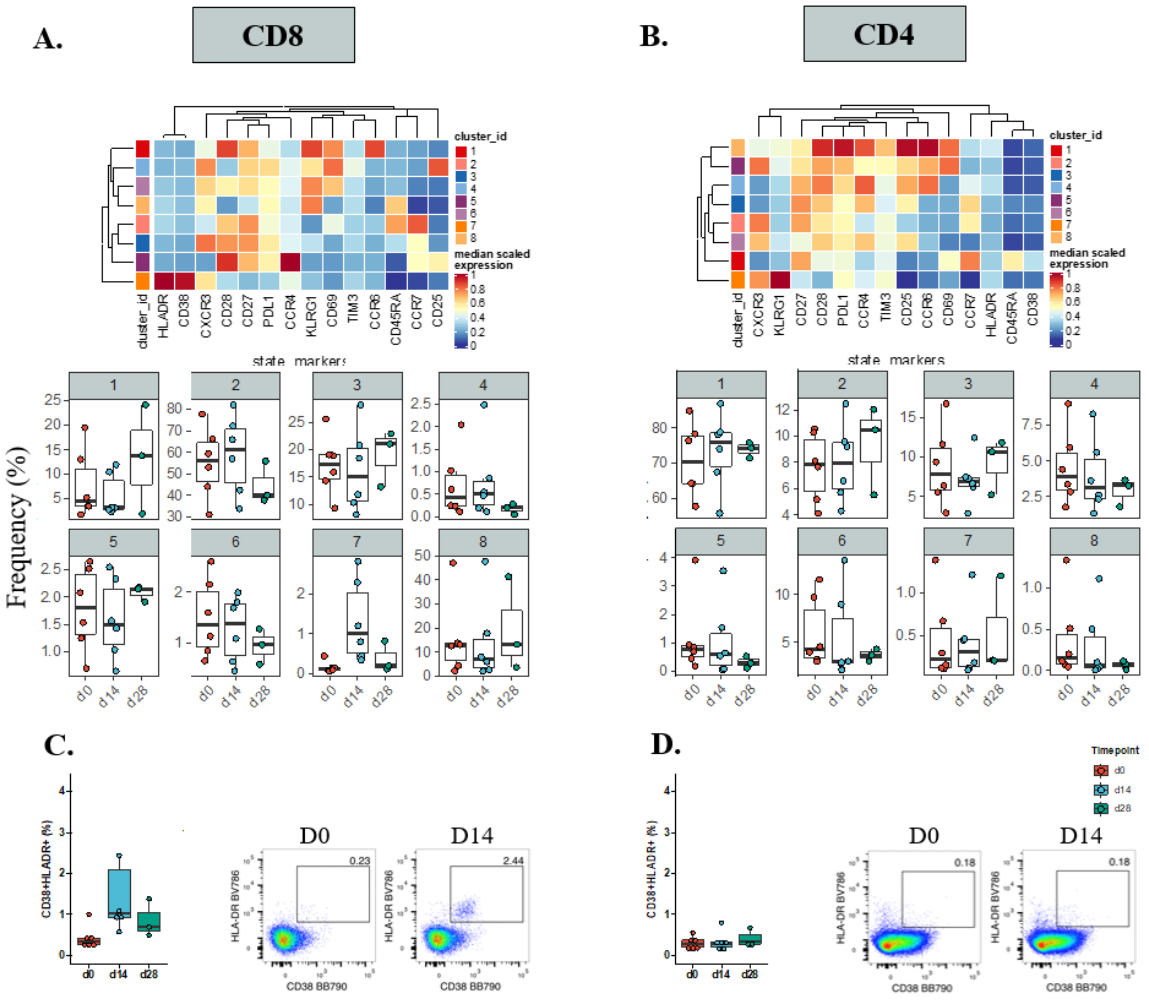


Figure 3-33. Flow cytometric analysis of vaccine-induced activation of CD8⁺ and CD4⁺ T cells following ChAdOx1 MERS vaccination.
(A) Multidimensional FlowSom analysis of CD8⁺ T cells identified eight distinct clusters based on the expression of activation and differentiation markers. A transient increase in the frequency of cluster 7, characterized by co-expression of CD38 and HLA-DR, was observed at Day 14 post-vaccination. **(B)** FlowSom clustering of CD4⁺ T cells revealed eight phenotypically distinct clusters, with no significant changes in frequency detected across timepoints. **(C)** Manual gating analysis confirmed a higher frequency of CD38⁺HLA-DR⁺ CD8⁺ T cells at Day 14 compared with baseline and Day 28. Representative flow cytometry plots illustrate CD38 and HLA-DR co-expression at Day 0 and Day 14. **(D)** The frequency of CD38⁺HLA-DR⁺ CD4⁺ T cells remained unchanged over time. Representative plots show comparable CD38 and HLA-DR expression at Day 0 and Day 14. Data represent PBMCs from participants in the MERS001 study (Day 0: n = 6; Day 14: n = 6; Day 28: n = 3).

3.2.7.1 Spike-specific CD4⁺ and CD8⁺ T cells activation-induced markers (AIM)

Next, the potential association between the magnitude of effector CD8⁺ and CD4⁺ T cell responses and the accumulation of Spike-specific T cells following vaccination was examined. The frequency of Spike-specific CD4⁺ and CD8⁺ T cells was assessed by measuring the upregulation of activation-

induced markers (AIM) after overnight stimulation with an overlapping peptide pool spanning the entire MERS-CoV Spike protein. This analysis was conducted using both freshly thawed PBMCs and cells subjected to a two-week *in vitro* expansion with MERS peptide pools to evaluate the proliferative capacity of vaccine-induced T cells.

In freshly thawed PBMCs, increased frequencies of $CD25^{+}4\text{-}1BB^{+}$ $CD8^{+}$ T cells (Figure 3-34A) and $CD25^{+}CD40L^{+}$ $CD4^{+}$ T cells (Figure 3-34B) were observed at D14 compared with baseline in most participants (five of six for $CD8^{+}$ and four of six for $CD4^{+}$). Following two weeks of *ex vivo* expansion, AIM analysis demonstrated further increases in the frequency of MERS-specific $CD25^{+}4\text{-}1BB^{+}$ $CD8^{+}$ T cells (Figure 3-34C) and $CD25^{+}CD40L^{+}$ $CD4^{+}$ T cells (Figure 3-34D). This response was detected in all six participants for $CD8^{+}$ and in five of six for $CD4^{+}$ T cells, indicating that vaccination with ChAdOx1 MERS induces both $CD8^{+}$ and $CD4^{+}$ T cell responses with strong proliferative potential.

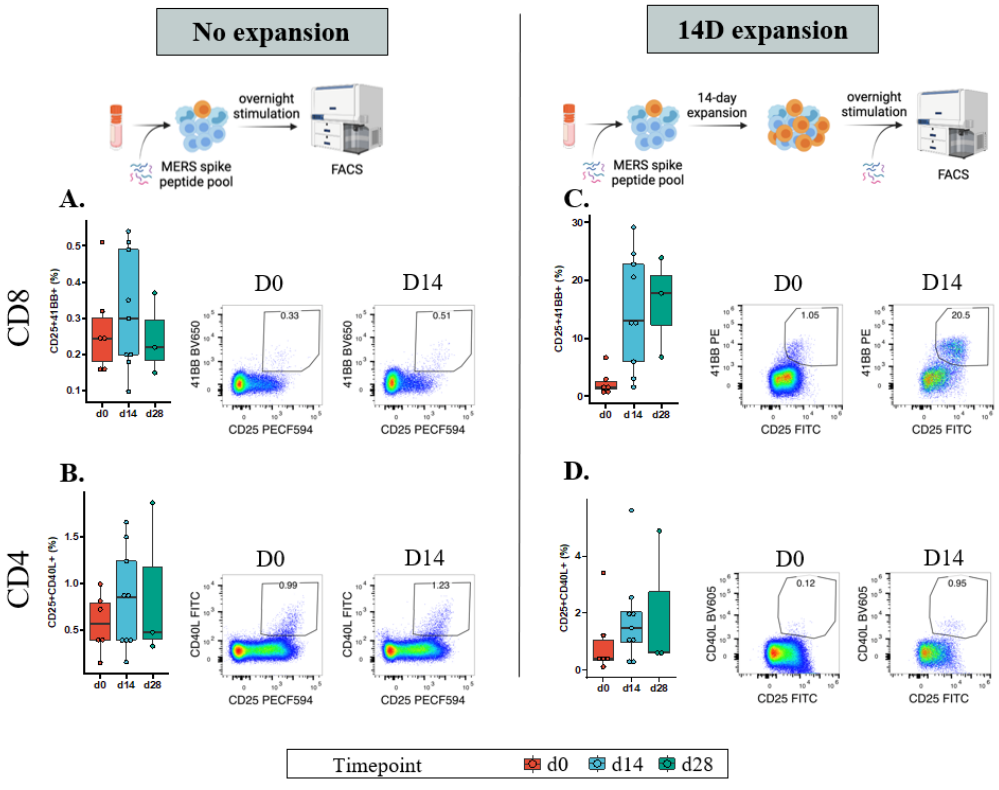


Figure 3-34. Assessment of Spike-specific $CD4^{+}$ and $CD8^{+}$ T cell responses following ChAdOx1 MERS vaccination.

PBMCs from vaccinated participants were stimulated with an overlapping MERS Spike peptide pool either directly (no expansion) or after a 14-day in vitro expansion. **(A–B)** Frequency of $CD25^{+}41BB^{+}$ $CD8^{+}$ T cells **(A)** and $CD25^{+}CD40L^{+}$ $CD4^{+}$ T cells **(B)** measured by AIM assay in freshly thawed PBMCs. **(C–D)** Following 14-day expansion, increased frequencies of Spike-specific $CD25^{+}41BB^{+}$ $CD8^{+}$ T cells **(C)** and $CD25^{+}CD40L^{+}$ $CD4^{+}$ T cells **(D)** were observed. Representative flow cytometry plots illustrate AIM expression at baseline (Day 0) and Day 14 post-vaccination. Data represent participants from the MERS001 study (Day 0: n = 6; Day 14: n = 6; Day 28: n = 3).

3.2.7.2 ICS

To further characterize vaccine-primed Spike-specific T cells proliferating after *in vitro* rechallenge, intracellular cytokine staining was performed on expanded PBMCs following restimulation with the same peptide pool. Spike-specific $CD4^+$ and $CD8^+$ T cells were both enriched for IFN-γ–producing populations, with detectable TNF-α expression, consistent with a Th1-type cytokine profile.

Spike-reactive $CD4^+$ and $CD8^+$ T cells from vaccinated participants exhibited a shift toward this type 1 cytokine pattern between D0 and D14, whereas responses to the control CEF peptide pool remained largely unchanged (Figure 3-35A–B). These findings indicate that vaccination with ChAdOx1 MERS elicits antigen-specific, Th1-polarized T cell responses characterized by IFN-γ and TNF-α production.

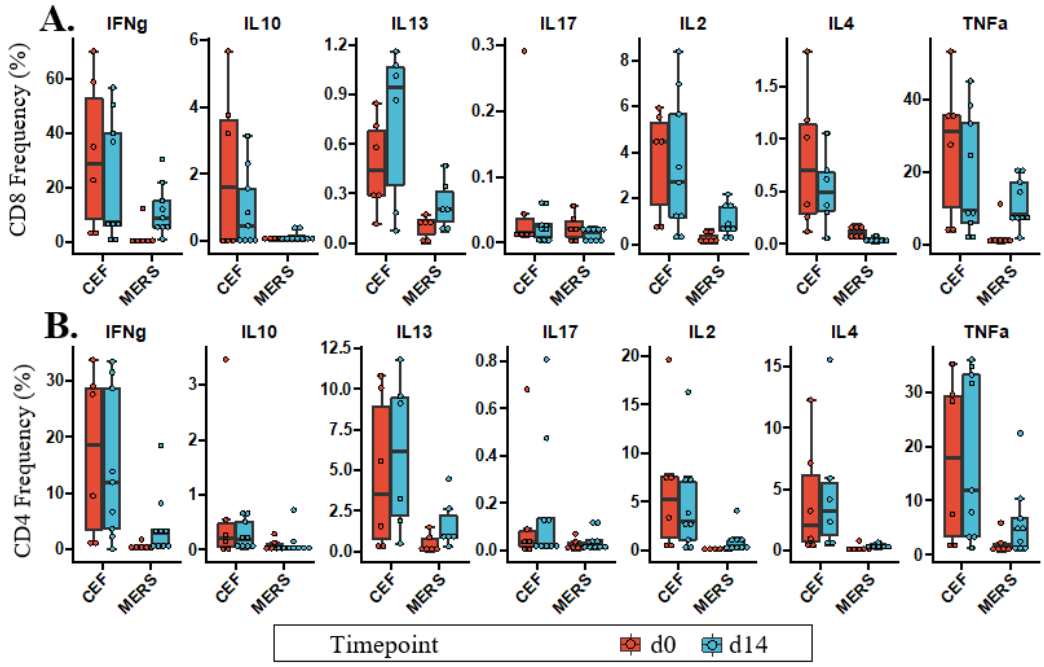


Figure 3-35. Intracellular cytokine profile of spike-specific $CD4^+$ and $CD8^+$ T cells following ChAdOx1 MERS vaccination.
(A) Frequencies of cytokine-producing $CD8^+$ T cells detected after restimulation of expanded PBMCs with CEF control peptides or MERS Spike peptide pools at baseline (Day 0) and post-vaccination (Day 14). **(B)** Corresponding frequencies of cytokine-producing $CD4^+$ T cells under the same conditions. Cytokines measured included IFN-γ, IL-10, IL-13, IL-17, IL-2, IL-4, and TNF-α. Increased frequencies of IFN-γ^+ and TNF-α^+ cells were observed in response to MERS Spike stimulation at Day 14, consistent with a Th1-biased immune response. Boxplots represent data from individual participants (Day 0: n = 6; Day 14: n = 6).

To gain a more detailed understanding of the regions of the Spike protein targeted by vaccine-induced T cells, an in-depth analysis of responses to individual peptide minipools was performed. PBMCs collected at Days 0, 14, and 28 from participants in the MERS001 study were stimulated with 17 overlapping minipools spanning the entire MERS-CoV Spike protein, minipools A01–A11 covering the S1 subunit and A12–A17 corresponding to the S2 subunit, to assess region-specific T cell reactivity. Spike-specific $CD8^+$ T cell responses were predominantly directed toward peptides located within the

S1 region, particularly in minipools A04, A05, and A13, indicating a focused recognition pattern (Figure 3-36A). The cytokine profile of these responses, represented by IFN-γ, IL-2, and TNF-α production, further confirmed strong Th1-type activity (Figure 3-36B). In contrast, Spike-specific $CD4^+$ T cells recognized a wider range of peptide regions, with responses distributed across multiple minipools, including A03–A07 and A11–A13, suggesting broader epitope coverage (35 Z, C). Corresponding cytokine analysis revealed IFN-γ–dominated responses with variable contributions of IL-2 and TNF-α (35 Z, D). This restricted $CD8^+$ and widespread $CD4^+$ reactivity pattern observed in MERS001 participants confirmed the antibody data, indicating that vaccination with ChAdOx1 MERS induces both humoral and cellular immune responses primarily directed toward the S1 domain of the spike protein.

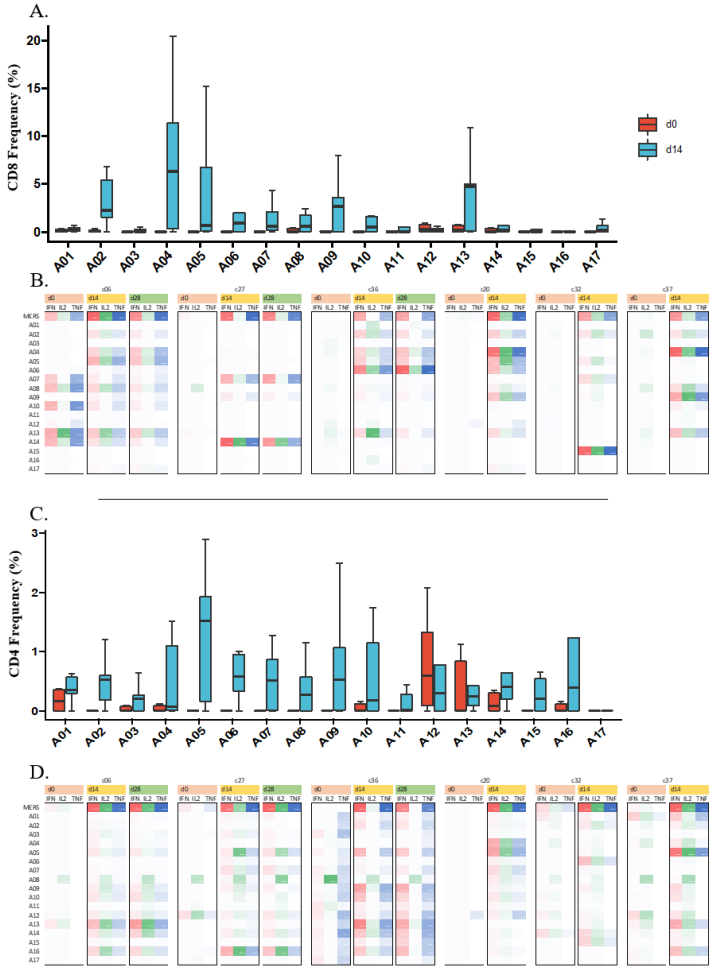


Figure 3-36. Mapping of $CD8^+$ and $CD4^+$ T cell responses across MERS Spike peptide minipools in MERS001 participants.
PBMCs collected at Days 0, 14, and 28 were stimulated with 17 overlapping peptide minipools (A01–A17) spanning the MERS-CoV Spike protein. **(A)** $CD8^+$ T cell frequencies and **(B)** corresponding cytokine heatmaps (IFN-γ, IL-2, TNF-α) show focused responses mainly against peptides within the S1 region. **(C)** $CD4^+$ T cell frequencies and **(D)** heatmaps reveal broader epitope recognition with IFN-γ–dominant Th1-type profiles.

3.2.7.3 Cross reactive responses

Cross-reactive $CD4^+$ T cell responses against Spike proteins from different coronaviruses have been described in the context of COVID-19 vaccination and infection [193]. However, the samples analysed in this study were collected in 2018 and 2019, prior to the emergence of SARS-CoV-2. To investigate the cross-reactive potential of ChAdOx1 MERS vaccine-induced $CD4^+$ T cells, fluorescence-activated cell sorting (FACS) was performed to isolate AIM^+ $CD4^+$ T cells from both D0 and D14 PBMCs following two weeks of in vitro expansion with MERS spike peptide pools. The sorted AIM^+ cells were further expanded in the presence of PHA and IL-2 to generate MERS Spike–specific $CD4^+$ T cell lines (Figure 3-37).

The specificity of these $CD4^+$ T cell lines was evaluated by co-culturing them with autologous EBV-transformed B cell lines pulsed with recombinant MERS Spike protein. $CD4^+$ T cell lines derived from all D14 samples contained a high frequency (25–90%) of cells capable of recognizing the recombinant protein, whereas only one of four lines generated from D0 samples showed a small population of reactive cells. These findings suggest that the AIM^+ cells detected at baseline most likely represented non-specific or artefactual responses to the peptide pools rather than genuine cross-reactive T cells targeting the MERS Spike protein.

To further examine potential cross-reactivity, the Spike-specific $CD4^+$ T cell lines generated from D14 samples were stimulated with autologous EBV-transformed cell lines pulsed with recombinant Spike proteins from SARS-CoV, SARS-CoV-2, and the pre-pandemic human coronaviruses HKU1, NL63, OC43, and 229E. Only one of the five $CD4^+$ T cell lines exhibited cross-reactivity, recognizing the Spike proteins from HKU1 and OC43. Computational peptide similarity analysis identified a peptide within pool 14 that shared high sequence similarity with HKU1 and OC43 Spike peptides, potentially explaining the observed cross-reactive response.

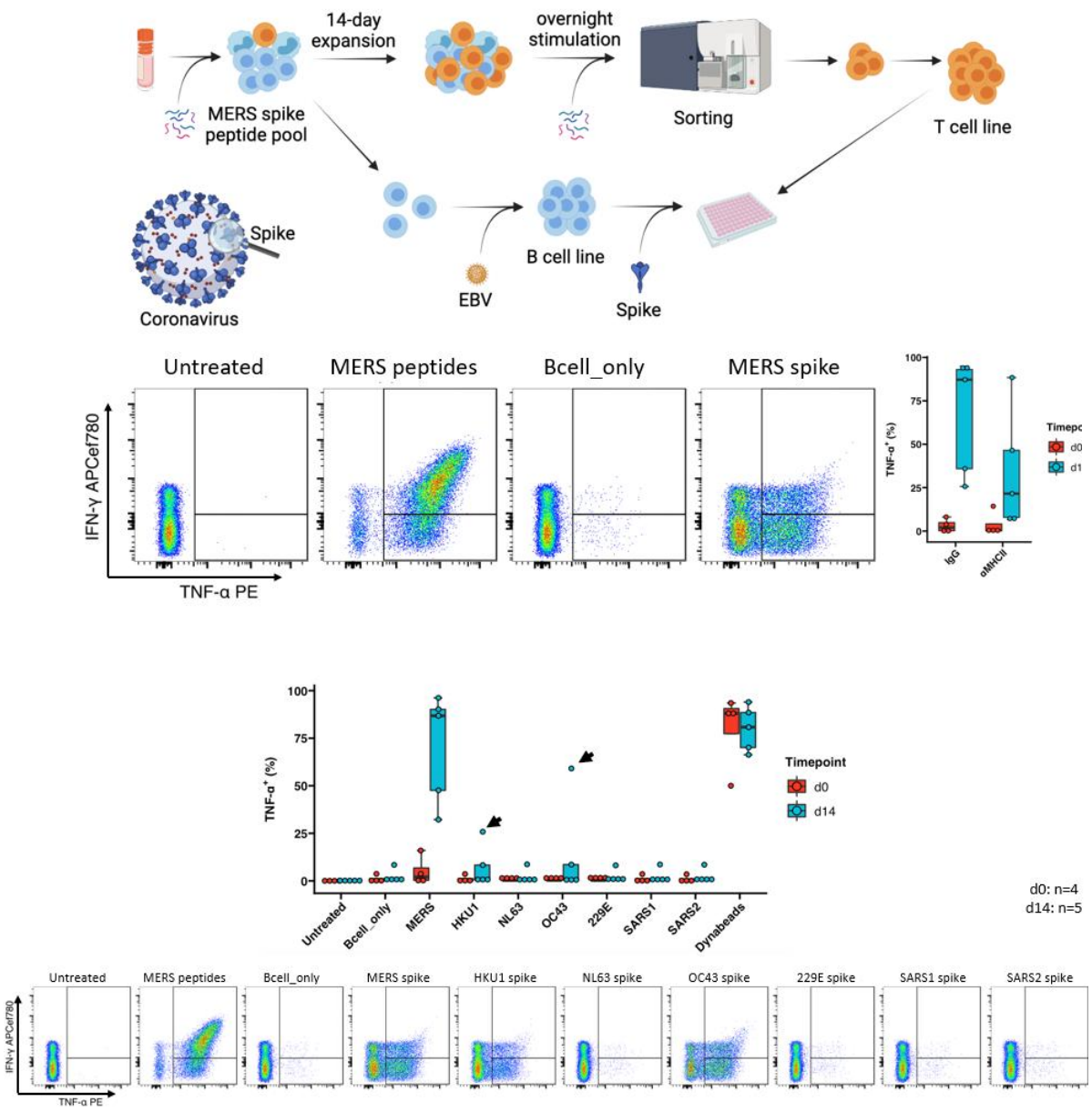


Figure 3-37. T cell responses to MERS-CoV and cross-reactivity with other coronaviruses.

PBMCs were expanded for 14 days with a MERS spike peptide pool, then restimulated overnight with MERS or other coronavirus spike antigens. IFN-γ^+ TNF-α^+ T cells were quantified by flow cytometry. Representative plots and box plots show cytokine responses at baseline (day 0) and after expansion (day 14). One donor exhibited cross-reactive responses to two seasonal coronaviruses (HKU1 and NL63). Arrows indicate paired samples from the same participants.

In summary, vaccination with ChAdOx1 MERS induced robust and durable T cell responses, characterized by Th1-polarized $CD4^+$ T cells and $CD8^+$ T cells predominantly targeting epitopes within the S1 region of the spike protein.

3.3 Discussion

A successful vaccine against MERS-CoV is expected to elicit a broad, polyfunctional and polyclonal antibody response targeting the spike protein, accompanied by a robust and sustained T cell response that supports viral clearance and long-term immune protection across diverse populations. Previous studies have demonstrated that neutralising antibodies play a key role in limiting viral replication and reducing pathology, whereas $CD8^+$ and $CD4^+$ T cell responses are essential for achieving viral control and establishing lasting immunity [284, 287-289]. The findings presented in this chapter expand on these observations by providing a detailed characterisation of the quality, magnitude, and kinetics of vaccine-induced immune responses in individuals from both the UK and Saudi Arabia, as well as phenotypic analysis of cellular immune responses in the UK cohort.

A clear dose-dependent immune response to ChAdOx1 MERS vaccination was observed, consistent with patterns reported for other adenoviral [337] and mRNA-based vaccine platforms [338]. The antibody features characterized in this study were guided by systems serology findings from COVID-19, which identified multiple immune markers associated with favourable outcomes, including spike-specific IgM antibodies and FcγRIIIB engagement as key correlates of protection [339, 340]. Although FcγR-mediated effector functions are primarily driven by IgG antibodies, these mechanisms often persist longer than neutralising responses [332] and have been shown to contribute to cross-variant protection in SARS-CoV-2 [207]. Due to challenges in conducting efficacy studies, it remains difficult to establish definitive correlates of protection for MERS-CoV. However, given the conserved structural architecture of coronaviruses, it is plausible that similar Fc-mediated pathways underpin protective immunity against MERS-CoV.

The dose-dependent effect of ChAdOx1 MERS vaccination was most pronounced for total spike and S1-specific responses. This was consistent with previously published findings from the UK MERS vaccine trial, where only a high prime dose induced live-virus neutralisation in the majority of participants [292]. The S1 subunit contains the receptor-binding domain (RBD), and RBD-specific monoclonal antibodies derived from convalescent MERS patients have demonstrated potent neutralising activity against MERS-CoV *in vitro* and conferred protection in mouse challenge studies [341]. Beyond the S1 domain, one dose of ChAdOx1 also induced antibodies targeting the S2 subunit, including IgG and FcγR-binding antibodies, whereas other MERS vaccine candidates, such as MVA-based vaccines, elicited measurable S2-specific IgG only after two doses [342]. Analyses of convalescent samples further revealed an enrichment of S2-directed responses, underscoring the contribution of this region to naturally acquired immunity. Consistent with these findings, monoclonal antibodies recognising epitopes within the S2 subunit have also been reported to confer protection in

mouse models, reinforcing the potential role of S2-targeted responses in viral neutralisation and protection [188].

Parallel T-cell analyses demonstrated responses predominantly directed toward the S1 region. A single dose elicited robust $CD8^+$ T-cell responses with a Th1-biased cytokine profile—a hallmark of effective viral clearance and reduced risk of antibody-dependent enhancement (ADE), as previously reported in MERS-challenged *in vivo* rabbit models lacking neutralising antibody development [343]. Similar targeting of S1 epitopes has been reported for MVA-based MERS vaccines in humans, suggesting that this region represents a conserved target for cytotoxic T-cell priming across vaccine platforms [344].

Collectively, these data establish that the ChAdOx1 vector can induce broad and polyfunctional humoral and cellular immunity, underscoring its utility as a rapid and effective vaccine platform for reactive immunization against emerging pathogens like MERS-CoV.

The immune IgG subclass profile induced by vaccination with ChAdOx1 MERS was primarily of IgG1 and IgG3 antibodies, consistent with previous findings describing the subclass profiles induced after priming with ChAdOx1 nCoV-19 [345] and other viral-vectored vaccine candidates [346]. In these earlier studies, low levels of antigen-specific IgG2 and IgG4 were also detected. By contrast, IgG2 was not detected in our cohort, possibly due to the small sample size. IgG4 responses have been observed following mRNA vaccination only after three doses [347]; therefore, as this study involved only a single priming vaccination, the absence of IgG4 was expected. IgG1 and IgG3 are the principal antibody subclasses induced in response to viral infections [42]. They mediate key effector functions, including complement activation[43] owing to their unique structure [348] and high affinity for Fcγ receptors [44]. In alignment with this, we observed an enrichment of Fc-associated antibody features in convalescent MERS patients, suggesting a role for these mechanisms in natural viral control. These Fc-mediated responses were more pronounced in participants receiving high-dose ChAdOx1 MERS and demonstrated notable durability even after a single immunization, with several readouts persisting up to day 182 and a subset maintained through day 365. Collectively, these observations provided a strong rationale for the deep characterization of humoral responses performed in this study to define the magnitude and functional quality of ChAdOx1 MERS-induced immunity.

Intriguingly, the medium-dose group in this study demonstrated higher antibody avidity indices and slower decay rate following a single dose of ChAdOx1 MERS, suggesting that lower antigen exposure may promote more efficient affinity maturation. The progressive increase in avidity observed over time is consistent with findings from ChAdOx1 nCoV-19 [345], where continued maturation of the humoral response was also reported. Importantly, the divergence in antibody avidity between the medium- and high-dose groups in our study became apparent only at six months post-vaccination, indicating that affinity maturation continues well beyond the early post-vaccination period. This pattern mirrors

observations from ChAdOx1 nCoV-19 studies, in which longer prime–boost intervals using a medium-dose regimen were associated with improved antibody quality and higher efficacy [97]. Similar phenomena have also been described in animal models, where lower antigen doses produced antibodies of greater avidity [349]. Although the underlying mechanism remains incompletely understood, Garg et al. [350] demonstrated through stochastic modelling of germinal-centre dynamics that limited antigen availability enhances B-cell competition, promoting stringent selection and the survival of high-affinity clones. Collectively, these findings underscore the critical influence of dose and timing in shaping the quality and durability of the antibody response. Accordingly, studies incorporating extended prime–boost intervals are warranted to evaluate the potential advantages of medium-dose priming, which may optimise the induction of high-affinity, long-lived antibody responses and strengthen durable immunological memory.

The results presented here provide strong evidence supporting the inclusion of a booster dose, aligning with the dosing regimen recommended for the licensed ChAdOx1 nCoV-19 (COVID-19) vaccine primary series [351]. In MERS001, administration of a second dose of ChAdOx1 MERS markedly increased antibody titres, elevating responses from single-dose levels to values comparable to those observed in convalescent MERS patients. These findings demonstrate that the booster dose effectively amplifies the primary immune response, with its overall impact closely influenced by the interval between doses. Across multiple studies, extended prime–boost intervals have consistently been shown to enhance immunogenicity, resulting in higher and more durable antibody responses [97, 295, 352-355]. This includes a clinical trial of ChAdOx1 nCoV-19, where efficacy increased by 26.2% when the interval was extended to 12 weeks, compared with shorter intervals of less than six weeks [356, 357]. In contrast, the increase in T-cell immunity was limited after a booster dose given at a longer interval [353, 358]. Collectively, these findings indicate that optimizing the dosing interval enhances not only the magnitude but also the quality and longevity of vaccine-induced antibody responses, particularly humoral responses, supporting strategies that promote durable and broad protection against MERS-CoV and related pathogens. Furthermore, optimizing dosing intervals may also facilitate a better understanding of the mechanisms of protection will be especially important when optimizing dosing intervals, to inform which immune arms should be preferentially induced for durable and protective immunity. Nevertheless, the practical feasibility of implementing such extended boosting schedules remains an important consideration in the development of proactive vaccination strategies.

In addition to IgG-mediated functions, IgA represents an important component of the humoral response. As the predominant secretory antibody at mucosal surfaces, IgA plays a key role in neutralising pathogens during infection [45]. The role of serum IgA in vaccine mediated protection is less defined. Infection with MERS-CoV induces robust serum IgA class switching in patients who recovered from pneumonia [286]. In our convalescent analysis, we also observed marked enrichment of serum IgA

responses, further supporting its potential role in protective or recovery-associated immunity against MERS-CoV. We observed induction of MERS-specific serum IgA following ChAdOx1 MERS vaccination, detectable even after a single dose and maintained after booster vaccination, indicating that ChAdOx1 MERS is capable of eliciting and sustaining this antibody isotype. Interestingly, the Saudi cohort demonstrated higher IgA antibody responses and increased S2-specific anti-MERS reactivity, potentially reflecting elevated baseline reactivity to OC43. This pre-existing immunity to OC43 could have provided a stronger foundation for cross-reactive boosting upon vaccination. Together, these findings suggest that background immune landscapes, including prior exposure to endemic coronaviruses and differential mucosal antibody activity, may shape both the magnitude and quality of vaccine-induced responses across populations.

In our study, participants with higher baseline OC43 FcγRIIB reactivity tended to exhibit stronger spike-specific IgG responses, supporting the concept of immune "backboosting," [359] whereby prior exposure to related coronaviruses enhances certain aspects of vaccine-induced immunity. FcγRIIB is an inhibitory receptor [38]; however, in mouse models, antibodies targeting FcγRIIB (CD32B) have been shown to enhance immune responses in vivo by promoting cross-linking and signalling through activating Fcγ receptors [360]. Consistent with this, fold changes in FcγRIIB- and FcγRIIIB-binding responses to OC43 between baseline and Day 28 were associated with fold changes in anti-MERS S2-specific responses at Day 182. In line with these findings, pre-existing immunity to other Betacoronaviruses has also been linked to more favourable outcomes following COVID-19 infection in previous studies [339], and vaccination with the mRNA COVID-19 vaccine BNT162b2 has been shown to expand T cells recognizing conserved regions within the S2 subunit shared among human coronaviruses, correlating with enhanced antibody responses [193]. Together, these findings suggest that pre-existing immunity to common human coronaviruses may influence the magnitude and quality of vaccine-induced immune responses. Nevertheless, such associations are not universally beneficial; some studies have reported that elevated baseline antibody levels can correlate with reduced vaccine responsiveness, implying possible immune interference or competition between cross-reactive epitopes. These contrasting effects highlight the complexity of immune imprinting, in which pre-existing immunity may either facilitate or hinder new responses depending on antigenic overlap and an individual's immune history. These interpretations, informed by both the present study and the published literature, should be considered in light of certain study limitations, including incomplete characterisation of antibody glycosylation, IgG subclass distributions, and responses to specific regions of seasonal coronavirus spike proteins, as well as the relatively small sample size. Despite these constraints, our data demonstrate a clear backboosting effect, with increased baseline reactivity to Betacoronaviruses OC43 and HKU, whereas MVA-MERS vaccination has previously been associated with enhanced OC43 reactivity only [342].

Subtle yet consistent differences were observed between the two populations studied, with participants in the MERS002 cohort generally exhibiting higher antibody responses following vaccination and more durable responses at Day 182. This difference may, at least in part, be attributable to higher baseline reactivity to OC43, which could have provided a stronger foundation for cross-reactive boosting, as discussed earlier. Differences in the timing of participant recruitment may also have contributed to baseline anti-OC43 reactivity. Human seasonal coronaviruses such as OC43 circulate endemically and exhibit clear seasonal peaks during colder months in the Northern Hemisphere [361], coinciding with December recruitment for MERS002, whereas recruitment for MERS001 began in March, after the winter peak. Although regional surveillance data are limited [362], these observations suggest that seasonal exposure timing may have contributed to enhanced baseline OC43 immunity in the MERS002 cohort.

These distinctions extended to Fc-mediated features, with persistent differences observed in FcγRIIA and FcγRIIIA engagement profiles. Other factors—such as variations in prior infection history, environmental exposures, or genetic background—may also have contributed; for example, SARS-CoV-2 antibody responses were reported to be higher in South Asian than in White healthcare workers in the UK [363]. Although not all comparisons reached statistical significance, the overall trend suggests that population-level immune landscapes can meaningfully influence vaccine immunogenicity. These findings underscore the importance of considering background immunity when interpreting and comparing vaccine responses across geographically or demographically distinct populations.

Strengths of the study include the standardization of all ELISA based assays, which improves reliability and reproducibility of data [364]. Assessment of the immunological responses from replicate trials in two diverse population increases the generalizability of findings. Limitations of the study include the relatively small sample size, particularly in the booster group, as recruitment was halted prematurely due to the COVID-19 pandemic; consequently, the study was not powered to detect differences between groups or to support extensive longitudinal analyses.

Taken together, these findings underscore the intricate relationship between humoral and cellular immunity, pre-existing seasonal coronavirus exposure, and population-specific factors. The data suggest that vaccine-induced immunity is not solely determined by the vaccine platform but is shaped by the immunological context of each individual. Optimising vaccination for diverse populations will therefore require a mechanistic understanding of how individual immune baselines, established by a lifetime of genetic, environmental, and immunological experiences, dictate vaccine effectiveness.

4 Immune imprinting and Its Impact on Coronavirus vaccination

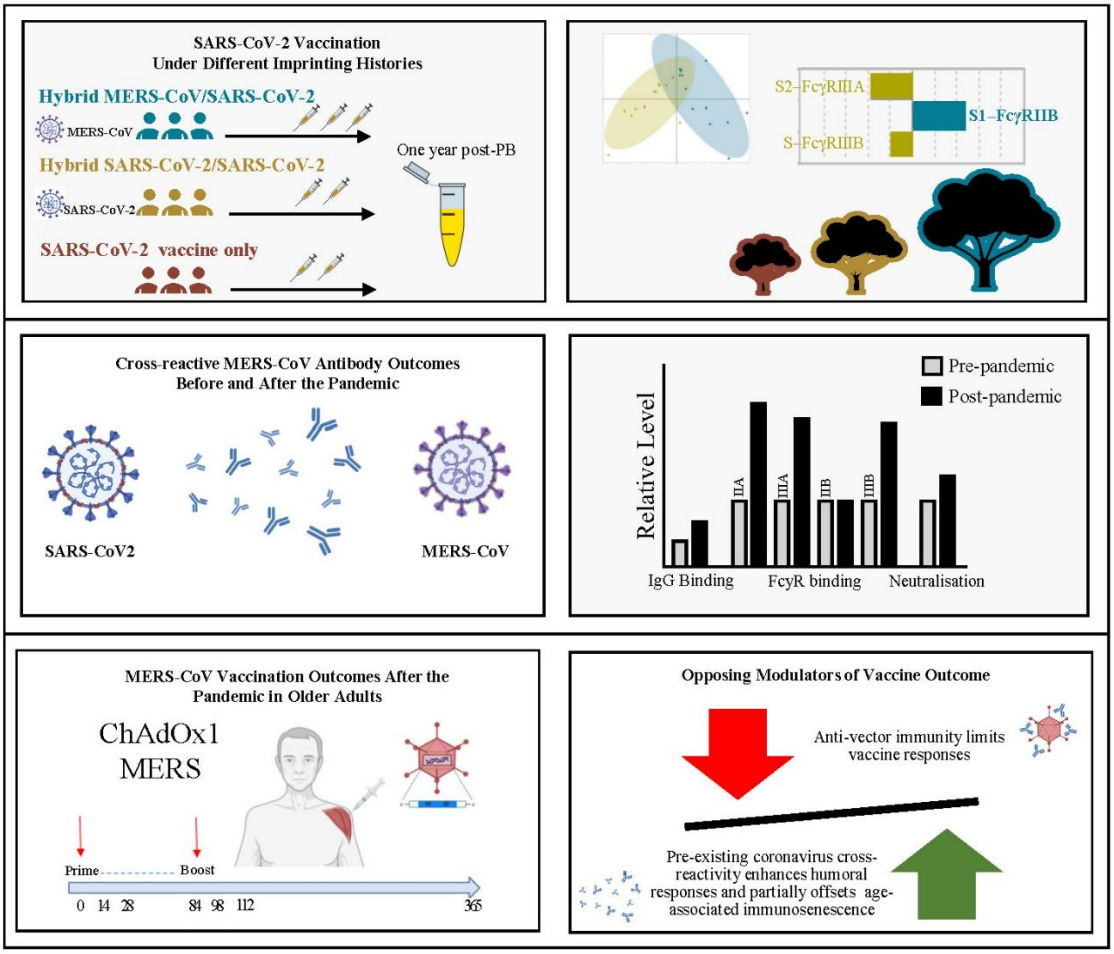


Figure 4-1 Visual abstract of the study methods and results

Highlight

- Hybrid immunity from prior coronavirus infection broadens antibody and enhances vaccine-induced immunity compared to vaccine only immunity.
- COVID-19 vaccination after MERS-CoV infection drives predominantly S1-focused responses, whereas after SARS-CoV-2 infection, it drives conserved S2 responses.
- SARS-CoV-2 exposure is associated with low-level MERS cross-reactive antibodies, which are substantially lower than post-MERS vaccination or MERS-convalescent responses.
- ChAdOx1 MERS induces robust humoral immunogenicity in older adults, enhanced by pre-existing cross-reactivity, and helps to mitigate immunosenescence
- Anti-vector immunity can interfere with immune responses to ChAdOx1 MERS.

Note: Some observed effects in hybrid MERS immunity may be influenced by later sampling and recent SARS-CoV-2 infection, which could bias immune readouts.

4.1 Introduction

The landscape of MERS-CoV vaccination has evolved considerably since the virus was first identified in 2012 [144]. Nearly the entire global population has been exposed to SARS-CoV-2 by infection, vaccination, or both. Interestingly, reported cases of MERS-CoV infection have declined since emergence of SARS-CoV-2 [365]. This decline may be attributed to multiple factors, including lockdown-related travel restrictions, diversion of surveillance efforts toward SARS-CoV-2, and the implementation of public-health and social measures aimed at limiting viral transmission [366]. Nevertheless, cases did not reappear following the lifting of travel restrictions; therefore, cross-reactive immune responses induced by SARS-CoV-2 have also been proposed as a potential contributing factor to the reduced number of MERS-CoV cases. Several studies have reported antibodies recognising MERS-CoV antigens following SARS-CoV-2 infection [367, 368]. Yet, cross-reactivity does not necessarily translate into cross-protection, and the extent to which such immune responses confer meaningful protection against MERS-CoV remains uncertain.

Evidence also suggests that cross-coronavirus exposure can shape subsequent immune responses in suboptimal ways. This phenomenon, known as immune imprinting, is best exemplified for coronaviruses by SARS-CoV-2: initial vaccination with the ancestral Wuhan strain has been associated with suboptimal immune responses upon subsequent exposure to the Omicron variant, resulting in breakthrough infections [369, 370]. These observations informed the World Health Organization's recommendation to update booster formulations and antigen composition [371], and highlight the importance of considering immune imprinting in future coronavirus vaccine strategies.

In Chapter 3, I demonstrated that ChAdOx1 MERS vaccination induces cross-reactive antibodies recognizing the betacoronaviruses SARS-CoV-2, OC43, and HKU1. Antigen-specific FcγR-binding, measured by Luminex as a surrogate of functional activity, revealed responses were transient for SARS-CoV-2 and OC43 but persisted for HKU1. These findings highlight the potential for functional cross-reactivity between MERS-CoV and SARS-CoV-2 and raise questions about the mechanisms and implications of such responses—particularly how widespread SARS-CoV-2 exposure may affect subsequent MERS-CoV vaccination [371].

Recent outbreaks of MERS-CoV have demonstrated that older adults still remain at highest risk of severe disease and mortality [366]. This continued vulnerability underscores the importance of evaluating MERS-CoV vaccination in older populations. In this chapter, I present data from the MERS003 clinical trial, which evaluated ChAdOx1-MERS-CoV immunogenicity in older adults post-COVID-19 pandemic. Conducted after the widespread use of ChAdOx1-based COVID-19 vaccines, the trial also assessed the impact of prior ChAdOx1 vaccination and explored the implications of using the ChAdOx1 platform in this context.

To fully interpret vaccine-induced immunity in this trial, it is first necessary to examine the immunological relationship between MERS-CoV and SARS-CoV-2. I begin by characterizing SARS-CoV-2–specific responses in a unique group of individuals with prior MERS-CoV infection who subsequently received COVID-19 vaccination. These are compared to SARS-CoV-2–vaccinated individuals, with and without a history of SARS-CoV-2 infection. I then assess MERS-CoV spike–specific responses in these groups to explore evidence of cross-reactivity and potential back-boosting. Using comprehensive serological profiling, I examine how exposure history shapes vaccine-induced immunity, focusing on spike-specific responses and epitope targeting. By comparing anti-MERS-CoV and anti-SARS-CoV-2 responses across distinct exposure profiles, I identify patterns of cross-reactivity and back-boosting unique to each group. Collectively, these analyses clarify how prior coronavirus infection influences humoral immunity in a post-pandemic population and provide critical context for designing next-generation coronavirus vaccines.

4.2 Results

Immune responses were compared across individuals with distinct coronavirus exposure histories. Seven immunity groups were analysed, defined by different combinations of prior infection and vaccination with MERS-CoV and/or SARS-CoV-2 (see Methods and Table 2-7 for group definitions and exposure histories). These group definitions are used consistently throughout the chapter to facilitate direct comparisons. Individual-level participant characteristics are provided in Appendix 8.1.4.2.

4.2.1 Hybrid Immunity and Cross-Reactivity Following SARS-CoV-2 Vaccination

4.2.1.1 Overview of study design and immunogenicity analyses

To investigate the impact of prior MERS-CoV infection on responses to COVID-19 vaccination, we identified a cohort of MERS-CoV convalescent individuals from Saudi Arabia with samples collected between December 2021 and February 2022, who had subsequently received COVID-19 vaccination or had recently been exposed to SARS-CoV-2 (hybrid MERS-CoV/SARS-CoV-2 immunity; n = 13). Immune status was defined based on self-reported vaccination history and detection of anti–SARS-CoV-2 nucleocapsid IgG.

Two age- and sex-matched comparison groups were selected from the UK: individuals with prior SARS-CoV-2 infection who had received two doses of SARS-CoV-2 vaccine (hybrid SARS-CoV-2/SARS-CoV-2 immunity; n = 12), and individuals who had received two doses of SARS-CoV-2 vaccine without prior SARS-CoV-2 infection (SARS-CoV-2 vaccine-only immunity; n = 12). Initially, each group was compared with pre-pandemic negative control samples from MERS001 (UK) and MERS002 (KSA); overall 17 samples from each (combined n = 34), which served as reference controls.

Infection status was defined by anti–SARS-CoV-2 nucleocapsid IgG positivity at recruitment or by documented SARS-CoV-2 infection or COVID-19 illness during the trial, with corresponding anti-nucleocapsid antibody responses, prior to sample analysis (Figure 4-2). Detailed participant characteristics, recruitment procedures, and matching strategies are described in Chapter 2, with additional details provided in relevant sections where appropriate. These comparisons used the corresponding negative controls to account for potential differences due to seasonal coronavirus differences between populations as discussed in chapter 3. Subsequently, the study groups were compared with each other.

The analyses presented in this section assess both SARS-CoV-2–specific and MERS-CoV–specific humoral immunity, focusing on antibody binding and Fcγ receptor–mediated activity as surrogates of functional responses. Neutralisation assay were included where available to further explore how prior exposures shape antibody profiles across coronavirus species.

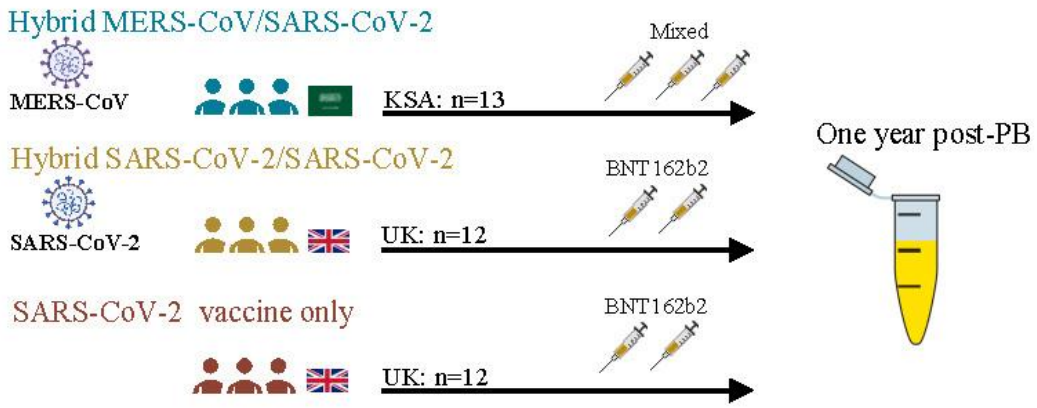


Figure 4-2. Study design overview.

Schematic representation of the three study groups included in the analysis. The hybrid MERS-CoV/SARS-CoV-2 group comprised participants from Saudi Arabia (KSA; n = 13) with prior MERS-CoV infection who subsequently received COVID-19 vaccination with mixed vaccine platforms. The hybrid SARS-CoV-2/SARS-CoV-2 group included UK participants (n = 12) with prior SARS-CoV-2 infection followed by two doses of BNT162b2 vaccine. The SARS-CoV-2 vaccine-only group consisted of UK participants (n = 12) who received two doses of BNT162b2 without prior SARS-CoV-2 infection. All samples were collected approximately one year post–prime-boost vaccination (post-PB).

4.2.1.2 Baseline Characteristics

Participants with hybrid MERS-CoV/SARS-CoV-2 immunity were predominantly male (77%) with a median age of 40 years [IQR 35–52; range 15–72]. Three participants were over 50 years of age. MERS-CoV infection had occurred a median of six years earlier (range 3–8 years), and three individuals had experienced severe disease requiring intensive care unit (ICU) admission. Among these participants, 77% (n = 10) had received two doses of COVID-19 vaccine with varying combinations, three (15%) had received three doses, and one participant (n=1) had not received any COVID-19 vaccination. This participant was retained in the analysis due to the small cohort size (n = 13) and because their prior MERS-CoV infection and likely SARS-CoV-2 exposure, owing to the late sampling point after the pandemic, made them relevant to the study objectives. Details of sample collection and timing are presented in the next section.

The matched comparison groups were of similar age, with a median [IQR] of 40 [35–47] years (p = 0.88) for the hybrid SARS-CoV-2 group and 43 [35–49] years (p = 0.99) for the SARS-CoV-2 vaccine-only group, as determined by ordinary one-way ANOVA with Tukey's multiple comparisons test. Sex distribution was also comparable across groups. Baseline demographics and clinical features are summarised in Table 4-1 and illustrated in Figure 4-3, with complete participant details provided in Appendix 8.1.4.2.

The interval between prime and boost vaccination was slightly longer, and the time from the second dose to sample collection was shorter, in the hybrid SARS-CoV-2/SARS-CoV-2 immunity group compared with the SARS-CoV-2 vaccine-only group. Although these timing differences could theoretically bias toward higher immune responses in the hybrid group, as discussed in Chapter 3, no statistically significant differences were observed in either the prime–boost interval or the time between the second dose and sampling; the median [IQR] prime–boost interval was 63 [23–77] days versus 25 [21–45] days (p = 0.06), and the median [IQR] time from the second dose to sample collection was 196 [193–266] versus 264 [242–270] days (p = 0.80) for the hybrid SARS-CoV-2/SARS-CoV-2 and SARS-CoV-2 vaccine-only groups, respectively. The potential influence of these timing differences on immune responses will be examined further later in the chapter.

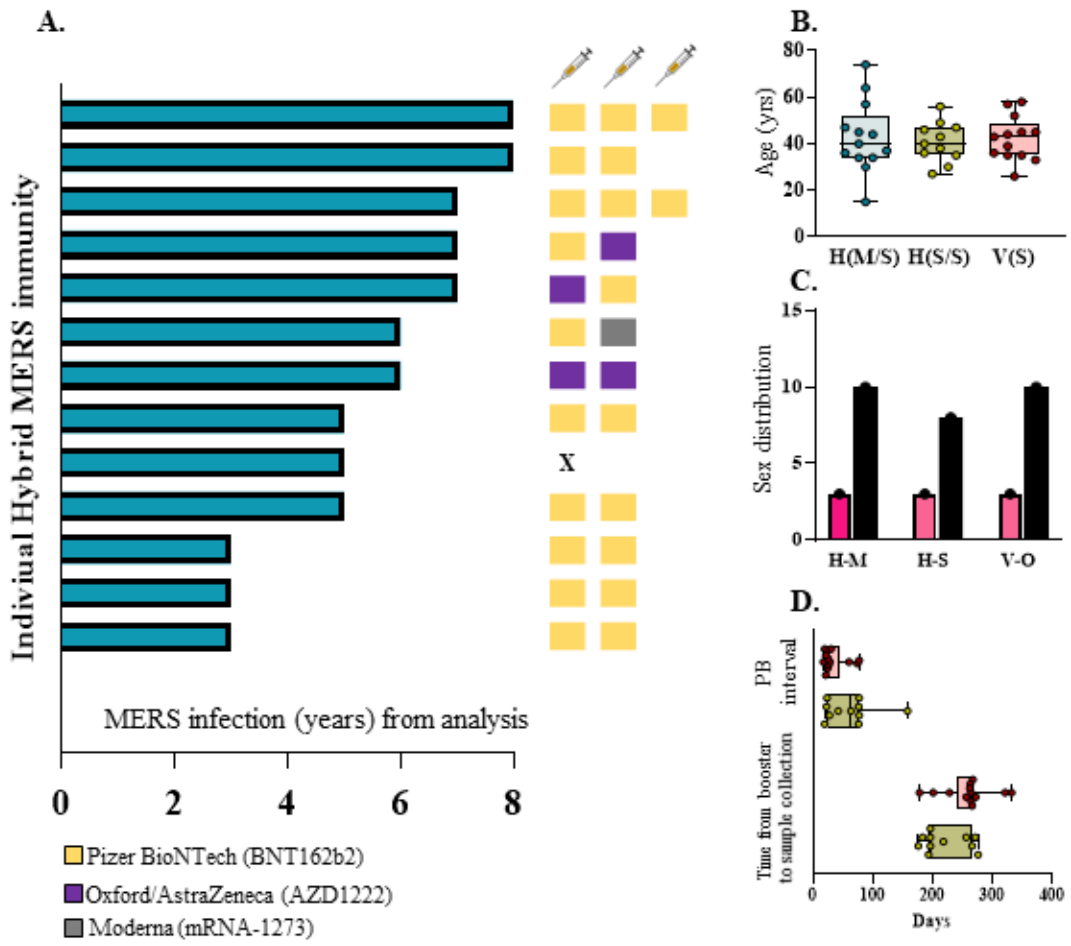


Figure 4-3. Baseline characteristics of the hybrid MERS-CoV immunity cohort and comparison groups.

Samples were collected approximately one year after completion of COVID-19 vaccination, estimated from the national vaccine rollout timeline in Saudi Arabia. **(A)** COVID-19 vaccine type and timing of sample collection among participants with hybrid MERS-CoV immunity: yellow = Pfizer–BioNTech BNT162b2, purple = Oxford–AstraZeneca AZD1222, grey = Moderna mRNA-1273, and X = unvaccinated. **(B)** Age distribution across the three study groups; dots represent individual participants and boxes indicate the median and interquartile range (IQR). **(C)** Sex distribution across the three groups, shown as bars (black = male, pink = female). **(D)** Time intervals between prime and boost (PB) doses and between the second vaccination and sample collection; boxes indicate the median and IQR. Statistical significance was assessed using one-way ANOVA (B) and multiple t-tests with false discovery rate (FDR) correction (D). Study groups: MERS-CoV convalescents with subsequent SARS-CoV-2 vaccination ("MERS-CoV/SARS-CoV-2 hybrid immunity," n = 13, turquoise, H(M/S)), SARS-CoV-2 convalescents with subsequent vaccination ("SARS-CoV-2/SARS-CoV-2 hybrid immunity," n = 12, gold, H(S/S)), and vaccine-only recipients ("SARS-CoV-2 vaccine-only immunity," n = 12, red, V(S)).

Characteristic	Hybrid MERS immunity (n=13)	Hybrid SARS-CoV-2 immunity (n=11)	SARS-CoV-2 vaccine Immunity (n=13)
Age, years mean ± SD median [IQR]	43 ± 15 40 [34-52]	41 ± 9 40 [35-47]	43 ± 10 43 [35-49]
Sex, n (%) male	10/13 (77%)	8/11 (72%)	10/13 (77%)
Time since MERS-CoV infection, median (range), years	6 (3-8)	NA	NA
ICU admission (if applicable) n (%)	3 (23%)	NA	NA
Prime-boost interval, median [IQR] days	NA	63 [23-77]	25 [21-45]
Days between boost and sampling, median [IQR] days	NA	196 [193-266]	264 [242-270]

Table 4-1 Baseline demographics and clinical characteristics of study participants. Full participant details are available in Appendix X.

4.2.1.3 Sample collection

Samples from participants with hybrid MERS-CoV/SARS-CoV-2 immunity were collected significantly later than those from participants with hybrid SARS-CoV-2/SARS-CoV-2 or SARS-CoV-2 vaccine-only immunity. In the hybrid MERS-CoV/SARS-CoV-2 group, 92% (12/13) of samples were collected between December 2021 and February 2022, a period marked by the rapid emergence and global dominance of the Omicron variant [372]. In contrast, most samples from the hybrid SARS-CoV-2/SARS-CoV-2 (10 of 12, 83%) and vaccine-only (9 of 12, 75%) groups were collected earlier, between July 2021 and October 2021, during the Delta wave [373]. The timing of sample collection and corresponding variant distribution are illustrated in Figure 4-4. This difference introduces a substantial confounding factor between immune status and sample collection date, which should be taken into account when interpreting the results presented in this chapter.

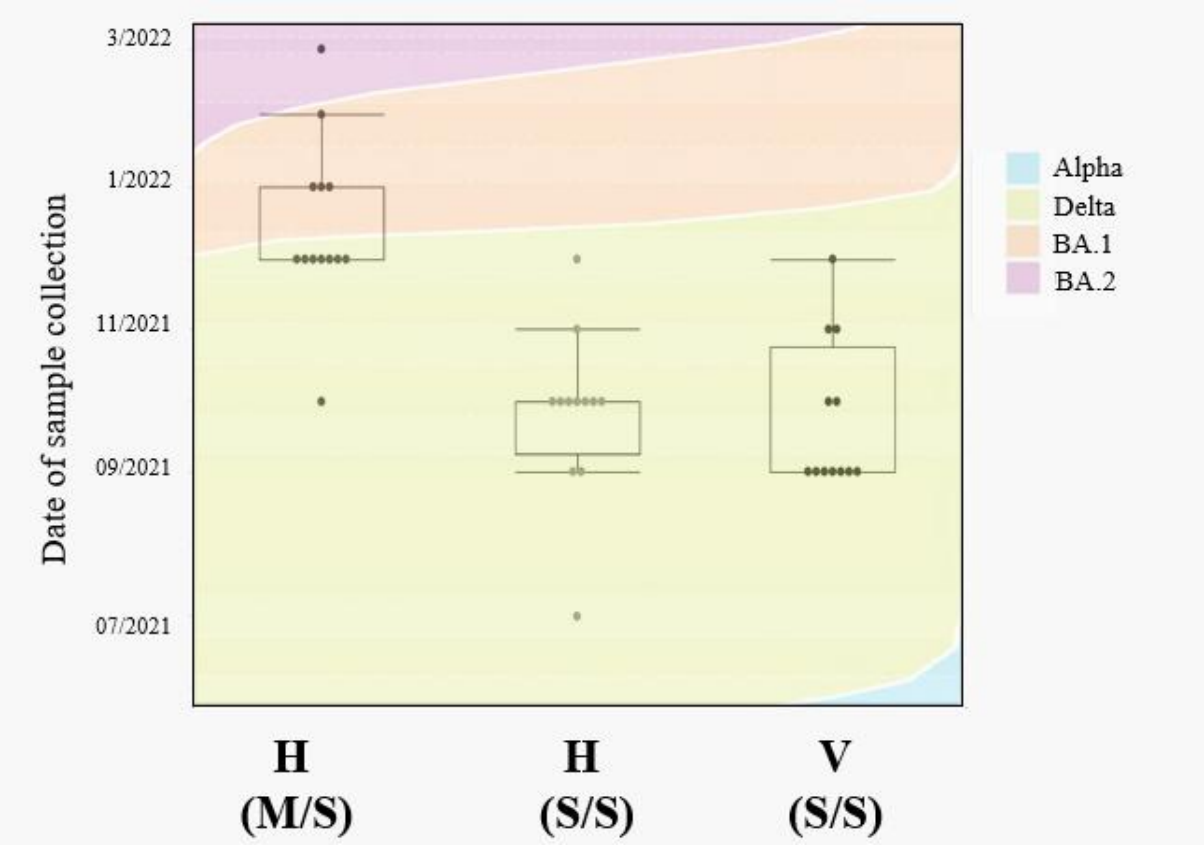


Figure 4-4. Distribution of sample collection dates by immune status group.

Stacked area plot showing the proportion of typed SARS-CoV-2 cases in the UK from July 2021 to May 2022, stratified by variant (Alpha, Delta, BA.1, and BA.2), figure was adapted and modified from [373]. SARS-CoV-2 variant epidemiology in the Middle East, including Saudi Arabia, was reported to be similar during this period [374, 375]. Coloured boxes indicate the timeframes during which samples were collected for each immune status group, with individual sample dates shown as points within each box.

4.2.1.4 FcγR binding analysis of anti-nucleocapsid responses

Anti-nucleocapsid IgG responses following COVID-19 infection can persist for up to one year [376]; however, Fcγ-receptor (FcγR) binding to nucleocapsid is less well characterized. To explore the FcγR-binding profile of anti-nucleocapsid responses across different coronavirus exposure histories—particularly between hybrid immunity groups—FcγR binding to the SARS-CoV-2 Wuhan strain nucleocapsid was measured and compared among the three study groups. IgG binding was not assessed due to unavailability of the MSD assay at the time of analysis. Results of group comparisons are presented in Figure 4-5, and corresponding median values with IQR for each vaccination group are summarized in Table 4-2.

Group	FcγRIIA (MFI, median [IQR])	FcγRIIIA (MFI, median [IQR])	FcγRIIIA (MFI, median [IQR])	FcγRIIIA (MFI, median [IQR])
H (M/S)	765 [440–2988]	246 [169–1223]	31 490 [5999–41 385]	282 [241–1046]
H (S/S)	501 [339–773]	262 [179–315]	228 [183–317]	297 [219–366]
V(S/S)	217 [199–247]	10 [10–108]	10 [10–169]	10 [10–156]
NC	61 [10-163]	10 [10–10]	10 [10–10]	10 [10–10]

Table 4-2. Median anti-nucleocapsid FcγR binding responses.

Data are presented as median values with IQR (CI). Fcγ receptor (FcγR) binding is expressed as median fluorescence intensity (MFI) in plasma samples from individuals with different immune histories: hybrid MERS-CoV immunity (H(M/S); n = 13, turquoise), hybrid SARS-CoV-2 immunity (H(S/S); n = 12, gold), and vaccine-induced SARS-CoV-2 immunity (V(S); n = 12, red). Pre-pandemic control data (n = 34, grey) were combined from the MERS001 and MERS002 cohorts.

No significant differences were observed between the vaccine-only group and pre-pandemic negative controls across all FcγR targets ($p > 0.9999$). Although FcγRIIA MFI values were slightly higher in the vaccine-only group (median [IQR]: 264 [199–247]) compared with negative controls (62 [10–163]; Table 4-2), this trend did not reach statistical significance ($p = 0.25$). Notably, two participants in the vaccine-only group showed detectable FcγR binding across all targets (Figure 4-5A), suggesting possible low-level SARS-CoV-2 exposure after enrolment and highlighting the difficulty of recruiting individuals with completely unexposed, or "sterile," immunity. In contrast, individuals with hybrid immunity displayed significantly higher anti-nucleocapsid FcγR responses than pre-pandemic controls across all FcγR subclasses ($p < 0.0001$). Individual negative-control data are shown in the heat map (Figure 4-5A), and corresponding group medians with IQRs are indicated in Figure 4-5B.

Both hybrid immunity groups showed significantly higher median FcγR MFI levels compared with the vaccine-only group ($p < 0.05$), although the level of significance varied across FcγR subclasses (Figure 4-5; Table 4-2). Hybrid MERS-CoV/SARS-CoV-2 immunity exhibited the highest responses across all FcγR targets. A significant difference was observed for FcγRIIB, with median [IQR] MFI responses of 31,490 [5999–41,385] compared with 228 [183–317] in the hybrid SARS-CoV-2/SARS-CoV-2 group ($p = 0.007$) and 10 [10–169] in the vaccine-only group ($p < 0.0001$). These data highlight a distinct FcγRIIB profile in hybrid MERS-CoV/SARS-CoV-2 immunity, suggesting an inhibitory preference relative to other groups.

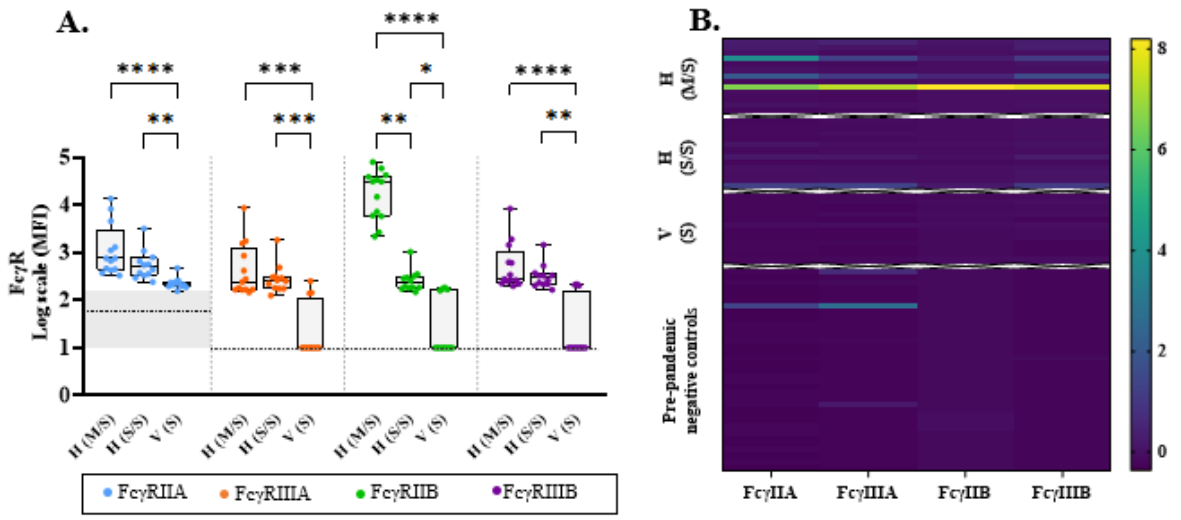


Figure 4-5. Fcγ receptor binding responses to the nucleocapsid protein.

(A) Box-and-whisker plots show median fluorescence intensity (MFI) of Fcγ receptor (FcγR) binding in plasma samples from individuals with different immune histories: hybrid MERS-CoV immunity [H (M/S); n = 13, including one unvaccinated participant shown in black], hybrid SARS-CoV-2 immunity [H (S/S); n = 12], and vaccine-induced SARS-CoV-2 immunity [V (S); n = 12]. Data from pre-pandemic controls (n = 34) are not shown; their group median is indicated by a dotted horizontal line, with the interquartile range (IQR) shaded in grey. FcγR binding was assessed across subclasses (FcγRIIA, FcγRIIIA, FcγRIIB, and FcγRIIIB; left to right). Colours indicate FcγR subclass: blue = FcγRIIA, orange = FcγRIIIA, green = FcγRIIB, and purple = FcγRIIIB. Statistical comparisons were performed using Kruskal–Wallis tests with Dunn's post-hoc correction for multiple comparisons within each target. Asterisks (*) denote statistical significance for within-group and between-cohort comparisons, as defined by P-values: * (P<0.05), ** (P<0.01), *** (P<0.001), **** (P<0.0001). **(B)** Heatmap showing normalized z-scores for FcγR binding responses across study groups. Each row represents an individual participant, and each column a distinct FcγR target. Groups are separated for clarity. Colour scale indicates relative response magnitude (purple = low, yellow = high).

4.2.1.5 IgG and FcγR Profiling of SARS-CoV-2 Spike-Specific Responses

To evaluate the magnitude and functional properties of SARS-CoV-2–specific antibody responses across the three immune-status groups, IgG binding to the full-length spike protein and its subunits (S1 and S2) of the Wuhan strain was quantified, along with neutralisation activity measured using a lentivirus-based pseudovirus neutralisation assay. FcγR binding to spike/S1/S2 was then assessed as a surrogate marker of Fc-mediated antibody function, providing complementary insight into qualitative differences in humoral responses among the groups. Results for IgG binding and pseudovirus neutralisation assays (PNA) are presented in Table 4-3 and Figure 4-6, while FcγR binding results for each antigen are shown in Table 4-4 and Figure 4-7.

Group	IgG_S (EU, median [IQR])	IgG_S1 (EU, median [IQR])	IgG_S2 (EU, median [IQR])	Neutralizing Ab titre (IU/mL, IQR
H (M/S)	12543 [4617–43315]	11932 [4022–37347]	866 [367–4366]	1940 [173–3185]
H (S/S)	5909 [3127–9506]	4633 [2563–8440]	424 [330–764]	141 [103–185]
V(S)	545 [411–1184]	521 [380–869]	48 [28–118]	45 [35–53]
NC	10 [10-96]	10 [10–10]	10 [10–68]	10 [10–10]

Table 4-3. Median IgG binding to SARS-CoV-2 spike (S), S1, and S2 proteins, and pseudovirus neutralisation assay (PNA) titres.

Data are presented as median values with interquartile range (IQR). Binding antibody levels (ELISA units, EU) and neutralisation titres (PNA IC_{50}) were measured in plasma samples from individuals with different immune histories: hybrid MERS-CoV immunity [H (M/S); n=13, including one unvaccinated participant; turquoise], hybrid SARS-CoV-2 immunity [H (S/S); n=12; gold], vaccine-induced SARS-CoV-2 immunity [V (S); n=12; red], and pre-pandemic controls [n=8; grey].

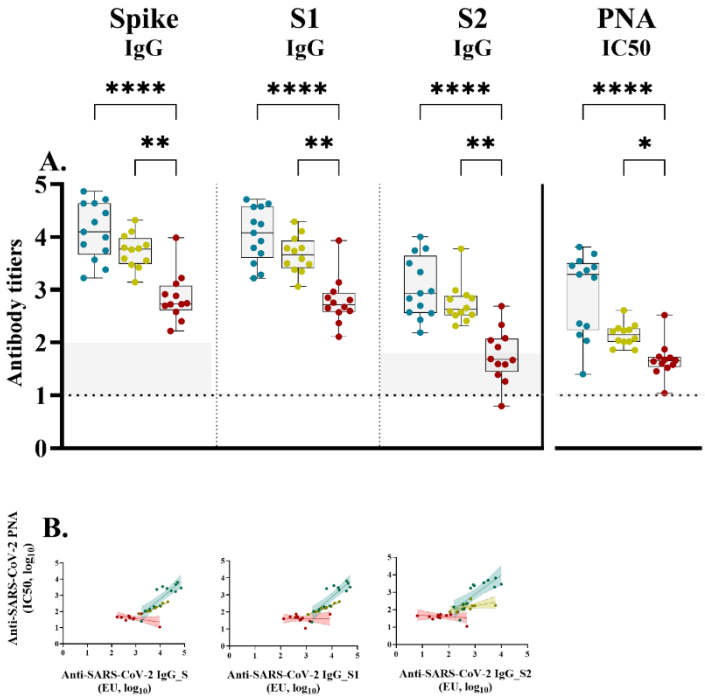


Figure 4-6. Binding IgG and neutralisation responses to the SARS-CoV-2 spike protein and its subunits.
(A) Box-and-whisker plots showing median values for plasma IgG binding (left) and pseudovirus neutralisation (right). The left plots display ELISA units (EU) of plasma IgG binding to the full-length spike (S) protein and its subunits (S1, S2) among three groups: hybrid MERS-CoV/SARS-CoV-2 immunity (H [M/S]; n = 13), hybrid SARS-CoV-2/SARS-CoV-2 immunity (H [S/S]; n = 12), and SARS-CoV-2 vaccine-only immunity (V [S]; n = 12). Data from pre-pandemic controls (n = 8) are not displayed; however, the group median is indicated by a dotted horizontal line, with the interquartile range (IQR) shaded in grey. The right plots show median half-maximal inhibitory concentration (IC_{50}) values for neutralisation of the SARS-CoV-2 Wuhan strain, measured using a lentivirus-based pseudovirus neutralisation assay (PNA) with heat-inactivated plasma. Statistical significance was assessed using the Kruskal–Wallis test with Dunn's post hoc correction within each group.
(B) Pearson correlations between binding antibody responses (S, S1, S2) and neutralising antibody titres. Colours indicate immune groups: turquoise = H (M/S), gold = H (S/S), and red = V (S). Asterisks (*) denote statistical significance for within-group and between-cohort comparisons, as defined by P-values: * (P<0.05), ** (P<0.01), *** (P<0.001), **** (P<0.0001).

At the time of sampling, both hybrid immunity groups exhibited significantly higher anti-spike, S1, and S2 IgG and neutralising antibody titres compared with negative controls (NCs). In contrast, the vaccine-only group did not differ significantly from pre-pandemic NCs in anti-spike, S1, or S2 IgG titres ($p = 0.5$ for spike and S1; $p > 0.9$ for S2), indicating that by the time of sampling (260 ± 35 days post-vaccination, mean ± SD), vaccine-induced antibody levels had waned to baseline.

Binding and neutralising antibody (nAb) titres were significantly higher in both the hybrid MERS-CoV and hybrid SARS-CoV-2 groups compared with the vaccine-only group, with varying levels of significance (Figure 4-6A). A trend toward higher antibody responses was observed in the hybrid MERS-CoV group compared with the hybrid SARS-CoV-2 group, although these differences were not statistically significant (spike: $p = 0.59$; S1: $p = 0.60$; S2: $p > 0.99$; PNA: $p = 0.21$).

Pearson correlation analysis showed that, within the hybrid MERS-CoV group, IgG responses to spike ($r = 0.80$, $p = 0.006$), S1 ($r = 0.83$, $p = 0.0007$), and S2 ($r = 0.87$, $p = 0.003$) were strongly correlated with neutralisation activity. Similarly, in the hybrid SARS-CoV-2 group, spike ($r = 0.99$, $p < 0.001$) and S1 ($r = 0.98$, $p < 0.001$) titres showed strong correlations with neutralisation, while the association with S2 and with neutralisation was weaker ($r = 0.60$, $p = 0.029$). No significant correlations were observed in the vaccine-only group (all $p > 0.05$), likely reflecting uniformly low titres comparable to those in negative controls (Figure 4-6B).

These findings suggest possible cross-neutralisation mediated by antibodies targeting the conserved S2 subunit in individuals with hybrid MERS-CoV/SARS-CoV-2 immunity, consistent with the higher sequence conservation of S2 across coronaviruses. However, the strong correlations observed between binding and neutralising antibody titres may also reflect the overall magnitude of the antibody response, as individuals with higher total IgG levels tended to exhibit correspondingly greater neutralisation activity. To further investigate the functional aspects of the humoral response, FcγR-binding activity was quantified as a surrogate measure of Fc-mediated antibody function.

Group		FcγRIIIA (MFI, median [IQR])	FcγRIIIA (MFI, median [IQR])	FcγRIIIA (MFI, median [IQR])
H (M/S)	FcγRIIA	93430 [21481–130717]	20119 [4581–36663]	1743 [444.8–4843]
H (S/S)		35178 [27656–56901]	7950 [3790–18233]	1049 [841.8–1718]
V(S/S)		4473 [2669–14427]	1168 [647.7–2654]	180.0 [168.0–241.2]
NC		10.00 [10.00–120.00]	10.00 [10.00–10.00]	10.00 [10.00–10.00]
H (M/S)	FcγRIIIA	26591 [6197–64581]	12809 [2913–39775]	895.4 [191.4–2850]
H (S/S)		19864 [11965–26751]	8073 [5128–14807]	639.0 [453.4–812.8]
V(S/S)		1164 [907.7–5769]	445.9 [259.1–941.7]	10.00 [10.00–10.00]
NC		10.00 [10.00–10.00]	10.00 [10.00–10.00]	10.00 [10.00–10.00]
H (M/S)	FcγRIIB	54393 [13003–82317]	11029 [2309–25234]	794.0 [261.6–2373]
H (S/S)		22170 [17596–35727]	2908 [1525–6883]	348.2 [265.0–464.5]
V(S/S)		1724 [1158–6339]	325.2 [210.0–664.0]	10.00 [10.00–10.00]
NC		10.00 [10.00–10.00]	10.00 [10.00–10.00]	10.00 [10.00–10.00]

H (M/S)	FcγRIIIB	17412 [4345–43085]	8141 [1625–23731]	804.0 [201.3–2174]
H (S/S)		19964 [12207–27614]	4100 [1811–11196]	442.4 [326.5–616.9]
V(S/S)		1430 [1134–1940]	451.9 [245.1–872.9]	10.00 [10.00–10.00]
NC		10.00 [10.00–10.00]	10.00 [10.00–10.00]	10.00 [10.00–10.00]

Table 4-4. Median FcγRI responses to MERS-CoV spike, S1, and S2 proteins.

Data are presented as median values with IQR (CI). Binding antibody levels (EU) and neutralisation titres (PNA IC_{50}) were measured in plasma samples from individuals with distinct immune histories: hybrid MERS-CoV/SARS-CoV-2 immunity (H[M/S]; n = 13, including one unvaccinated participant; turquoise), hybrid SARS-CoV-2/SARS-CoV-2 immunity (H[S/S]; n = 12; gold), and vaccine-induced SARS-CoV-2 immunity (V[S]; n = 12; red). Pre-pandemic negative controls (NC; n = 34; grey) are included for reference.

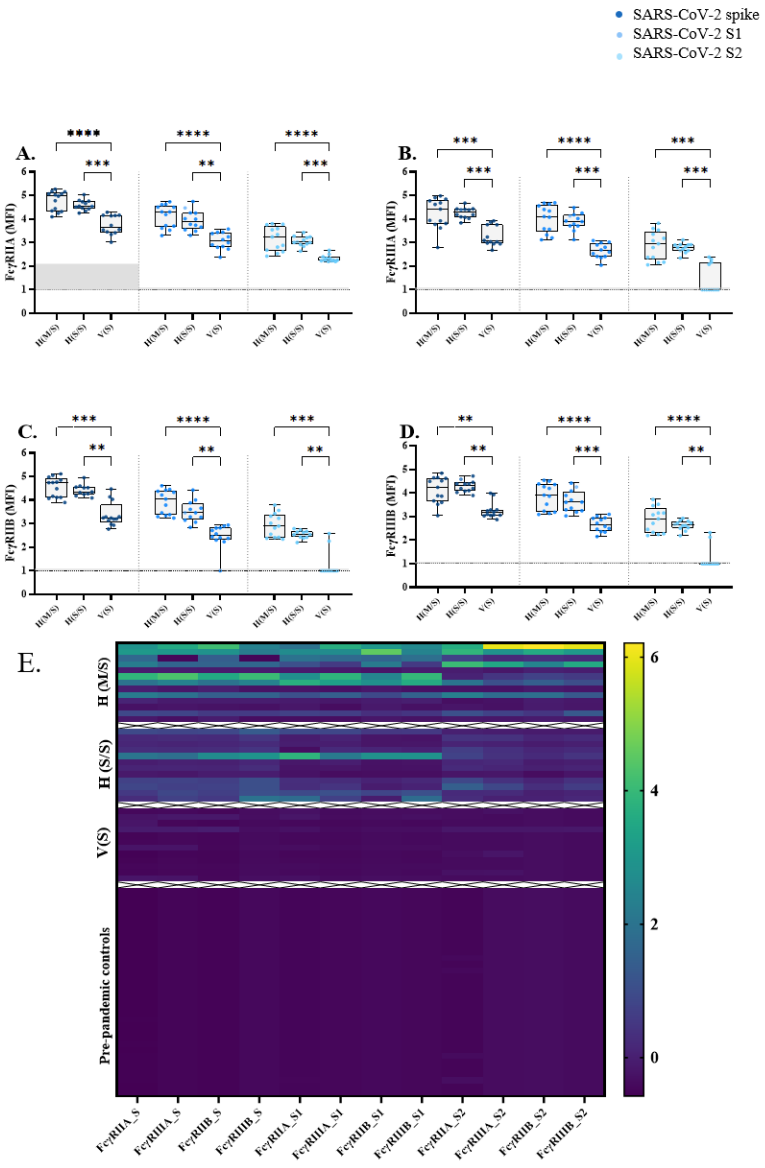


Figure 4-7. FcγR binding antibodies titres against SARS-CoV2 spike, S1 and S2 across FcγR subclasses.

(A) Individual titres of FcγRIIa, FcγRIIb, FcγRIIIa, FcγRIIIB in serum samples from cohort with different immune histories: Hybrid MERS immunity (n=13), Hybrid SARS-CoV-2 (n=12) immunity, Vaccine-induced immunity (n=12). Pre-pandemic controls data (n=34) are not shown; the median of this group is shown in indicated by dotted horizontal line, with (IQR) shaded in grey; panels left to right). Colours indicate distinct

target (dark Blue = spike, medium blue=S1, light blue=S2). Statistical comparisons were performed using Kruskal–Wallis tests with Dunn's post hoc correction for multiple comparisons. * $p < 0.05$, ** $p < 0.01$, *** $p < 0.001$, **** $p < 0.0001$. **(B)** Heatmap showing normalized z-score for each FcγR target with each comparison group. Each row represents the response of an individual participant; groups are separated, and each column represents the response of distinct FcγR target. Colour scale indicates relative magnitude of the measured response (purple = low, yellow = high).

Across all groups, Fcγ receptor (FcγR) engagement was generally higher than in pre-pandemic controls, except for FcγRIIB and FcγRIIIB binding to S2 in the SARS-CoV-2 vaccine-only group, which was comparable to NCs. As summarized in Table 4-4, these results suggest that FcγR-mediated effector activity may persist longer than neutralisation capacity in the vaccine-only group, particularly for spike and S1, whereas S2 responses appeared less durable. Apparent differences may also reflect assay sensitivity between ELISA- and luminescence-based detection methods.

Consistent with total IgG and neutralisation data, FcγR-binding activity was highest in the hybrid MERS-CoV/SARS-CoV-2 group, followed by the hybrid SARS-CoV-2 and vaccine-only groups. These patterns were consistent across all FcγR types, with hybrid immunity groups showing universally higher responses than vaccine-only immunity ($p < 0.01$). Median FcγR responses were consistently highest in the hybrid MERS-CoV/SARS-CoV-2 group, showing approximately 2–4-fold higher activity relative to hybrid SARS-CoV-2 immunity and up to ~30-fold higher than vaccine-only immunity across most receptors Table 4-4. Although no significant differences were detected between the two hybrid groups overall, FcγRIIB showed the largest fold differences, particularly for S1 and S2, suggesting that prior MERS-CoV exposure may uniquely enhance inhibitory FcγRIIB engagement, consistent with higher nucleocapsid FcγRIIB responses observed earlier.

4.2.1.6 Breadth of response to omicron variants

To assess whether multiple coronavirus exposures enhance the breadth of antibody responses, Fcγ receptor-binding activity to the Omicron spike was quantified. Data are summarised in Table 5 and Figure 4-8. As expected, individuals exposed to SARS-CoV-2 through vaccination (with or without infection) had significantly higher FcγR titres to Omicron compared to pre-pandemic controls ($P<0.05$). Prior infection conferred additional benefit beyond vaccination alone, with individuals in the hybrid MERS-CoV and hybrid SARS-CoV-2 groups exhibiting significantly higher FcγR binding than those in the vaccine-only group, as reflected in Table 5.

Group	FcγRIIIA (MFI, median [IQR])	FcγRIIIA (MFI, median [IQR])	FcγRIIIA (MFI, median [IQR])	FcγRIIIA (MFI, median [IQR])
H (M/S)	38634 [12798–76487]	12077 [4257–29673]	31490 [5999–41385]	13403 [3981–27249]
H (S/S)	18570 [12963–29316]	9597 [5900–16946]	15097 [4815–24572]	12306 [2196–23373]
V(S/S)	1883 [1374–7396]	860.6 [700.1–1223]	1007 [820.1–1203]	1106 [963.4–1358]
NC	200.7 [10.00–438.0]	10.00 [10.00–27.04]	10.00 [10.00–22.91]	10 [10–79]

Table 4-5. Median Omicron FcγR binding responses.

Data are presented as median values with IQR. Fcγ receptor (FcγR) binding is expressed as median fluorescence intensity (MFI) in plasma samples from individuals with different immune histories: hybrid MERS-CoV immunity (H(M/S); n = 13, including one unvaccinated participant, turquoise), hybrid SARS-CoV-2 immunity (H(S/S); n = 12, gold), and vaccine-induced SARS-CoV-2 immunity (V(S); n = 12, red). Pre-pandemic control data (n = 34, grey) were combined from the MERS001 and MERS002 cohorts.

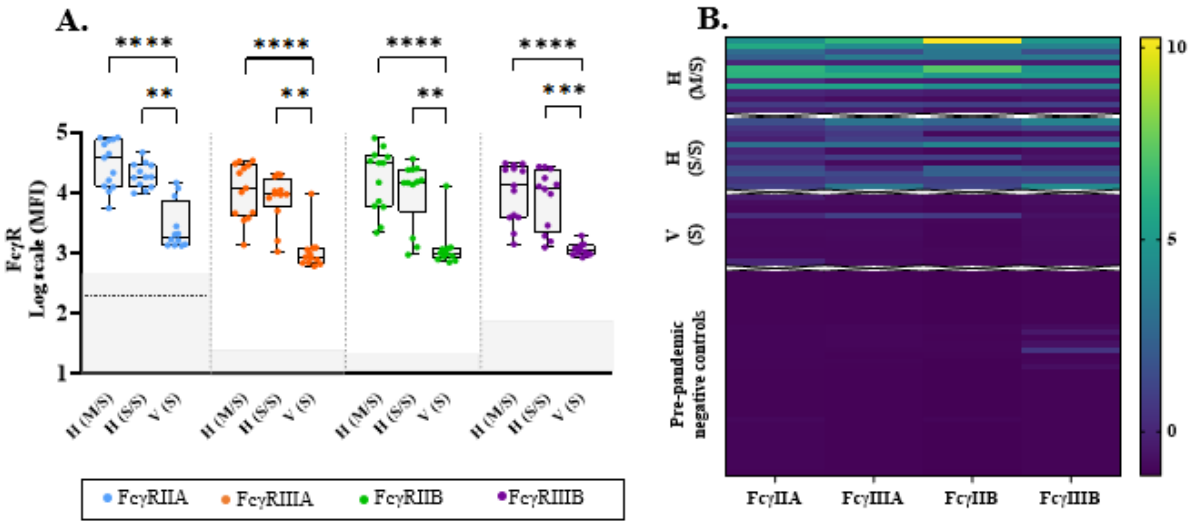
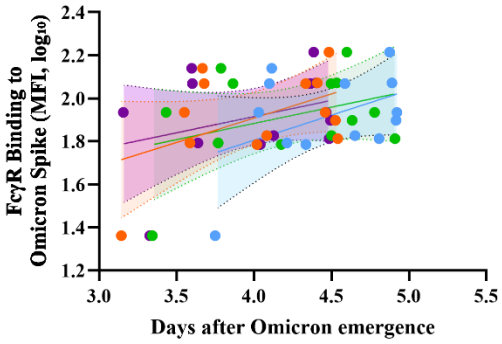


Figure 4-8. Fcγ receptor binding responses to the Omicron variant protein.
(A) Box and whisker plots represent median fluorescence intensity (MFI) of Fcγ receptor (FcγR) binding in serum samples from individuals with different immune histories: Hybrid MERS immunity (n=13), Hybrid SARS-CoV-2 (n=12) immunity, Vaccine-induced immunity (n=12). Pre-pandemic controls data (n=34) are not shown; the median of this group is shown in indicated by dotted horizontal line, with (IQR) shaded in grey. FcγR binding was assessed across FcγR subclasses (e.g. FcγRIIA, FcγRIIIA, FcγRIIB, FcγRIIIB; panels right to left). Colours indicate distinct immunity target (blue = FcγIIA, orange =FcγIIIA, green=FcγRcIIB, purple=FcγRcIIIB). Statistical comparisons were performed using Kruskal–Wallis tests with Dunn's post hoc correction for multiple comparisons.* $p < 0.05$, ** $p < 0.01$, *** $p < 0.001$, **** $p < 0.0001$. **(B)** Heatmap showing normalized z-score for each FcγR target with each comparison group. Each row represents the response of an individual participant; groups are separated, and each column represent the response of distinct FcγR target. Colour scale indicates relative magnitude of the measured response (purple = low, yellow = high).

As discussed earlier, 10 of 12 (83%) samples in the hybrid SARS-CoV-2 group were collected in October 2021, before the emergence of the Omicron variant. Sampling time did not differ between the hybrid SARS-CoV-2 and vaccine-only groups, with nearly all samples collected during the Delta wave, thereby minimising the risk of temporal bias as a confounding factor. This suggests that the enhanced FcγR binding observed in the hybrid SARS-CoV-2 group is more likely to reflect cross-reactive immunity to ancestral or early variants rather than recent Omicron infection. In contrast, 12 of 13 (92%) samples in the hybrid MERS-CoV group were collected after the emergence of Omicron. Although Omicron-specific responses did not correlate with the timing of sample collection relative to Omicron emergence (Figure 4-9), their association with nucleocapsid-specific immunity is examined in the next section to clarify the potential contribution of recent Omicron infection



Omicron S specific	Spearman R
FcγRIIA	0.3
FcγRIIIA	0.3
FcγRIIB	0.2
FcγRIIIB	0.7

Figure 4-9. Spearman correlation between Fcγ receptor (FcγR) binding to the Omicron spike and days after Omicron emergence in the hybrid MERS-CoV/SARS-CoV-2 group.

FcγR binding is shown as mean fluorescence intensity (MFI, log scale). Colours indicate distinct FcγR targets: blue = FcγRIIA, orange = FcγRIIIA, green = FcγRIIb, and purple = FcγRIIIB. No significant correlation was observed between FcγR binding magnitude and time since Omicron emergence. The table on the right shows the corresponding R values.(n=13).

4.2.1.7 Summary, coordination and correlation analysis of antibody features

To gain a comprehensive overview of the magnitude and functional breadth of antibody responses to SARS-CoV-2 antigens, we integrated the system serology comparisons across all immune-status groups. As shown in the night-plot summary and heatmap (Figure 4-10), hybrid immunity was associated with the highest overall responses across all measured antibody features, including IgG titres, Fcγ receptor binding, and pseudovirus neutralisation. In contrast, vaccine-only individuals exhibited markedly reduced responses across most antigen targets and Fc-mediated surrogate effector functions, with several features approaching baseline (Figure 4-10B). Notably, responses in the vaccine-only group were lower than those captured in the night-plot visualisation, further emphasising the observed hierarchy of immunity.

Clear Omicron-specific activity was evident in the hybrid groups, particularly in the hybrid MERS-CoV/SARS-CoV-2 group, with one individual displaying exceptionally strong nucleocapsid reactivity (Figure 4-10B). While SARS-CoV-2 nucleocapsid antibodies typically wane within 6–9 months after infection, the durability of MERS-CoV nucleocapsid responses remains poorly defined. The persistence of robust nucleocapsid reactivity in the hybrid MERS-CoV group may therefore reflect recent SARS-CoV-2 infection with the Omicron variant, particularly given the timing of sample collection relative to MERS exposure. The late time points in this group are also consistent with recent infection.

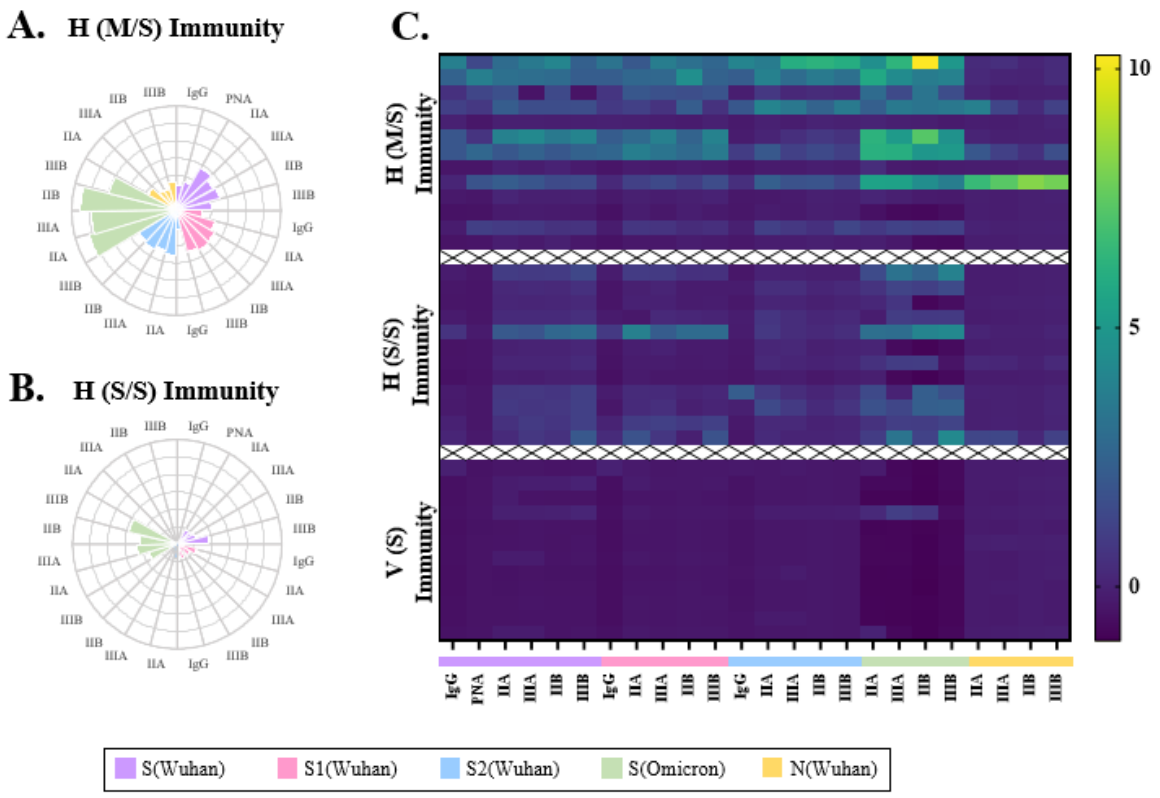


Figure 4-10. Summary of anti–SARS-CoV-2 humoral immune responses across immune groups.

(A, B) Night plots illustrating the aggregate distribution and mean z-scores of antibody responses across hybrid immune groups, representing the overall magnitude and breadth of humoral immunity. All targets and features were normalized independently as z-scores to reflect within-feature variation. **(C)** Heatmap showing normalized z-scores for all measured antibody features, including IgG binding, Fcγ receptor (FcγR) engagement, and pseudovirus neutralization titres. Each row represents an individual participant, and each column corresponds to a distinct antigen-specific response. From left to right, features include IgG binding to SARS-CoV-2 spike (purple), S1 (pink), and S2 (blue) antigens (Wuhan strain); FcγR binding to Omicron spike (green); and FcγR responses to SARS-CoV-2 nucleocapsid (yellow, Wuhan strain). Groups are separated by horizontal dividers. The colour scale indicates the relative magnitude of the measured response (purple = low, yellow = high).

To gain a more profound understanding of the specific and unique features of the humoral immune response induced by hybrid immunity, we performed a multivariate analysis using least absolute shrinkage and selection operator (LASSO) feature selection followed by partial least squares discriminant analysis (PLS-DA). Prior to analysis, all measurements were normalized using z-score transformation. A total of 20 antibody features were included, comprising all measured SARS-CoV-2 antigen responses except those specific to Omicron, which were excluded from this analysis.

LASSO regularization reduced the dataset to a small subset of non-zero predictors, while most features were shrunk to zero. The coefficient path illustrated the progressive elimination of weak predictors (Figure 4-11A), and the corresponding AICc curve identified the optimal penalty that retained only the strongest discriminating antibody features (Figure 4-11B). At this optimal point, LASSO selected a

limited set of FcγR-binding responses, including S2-FcγRIIIA, S1-FcγRIIIB, S2-FcγRIIIB, and Spike-FcγRIIIB, which were subsequently carried forward into the PLS-DA.

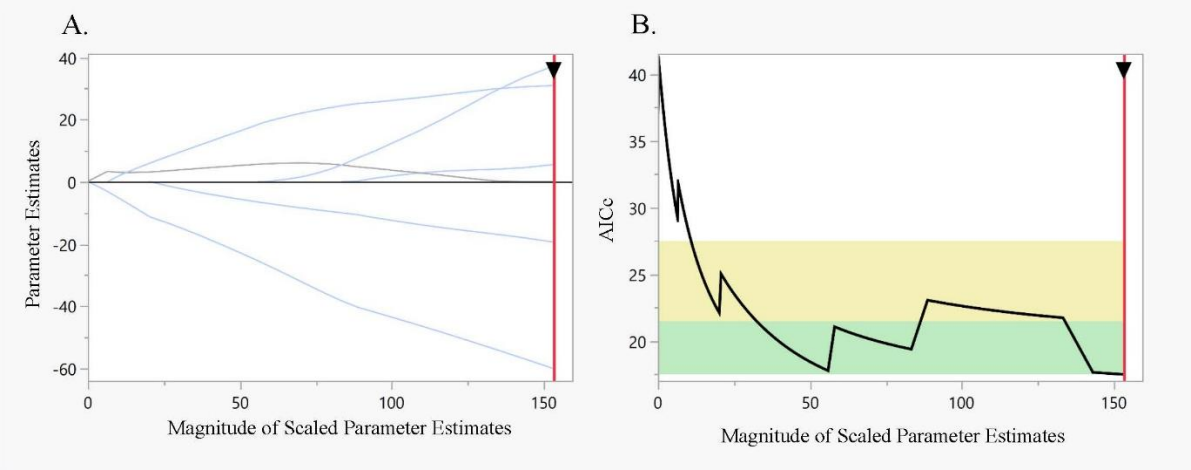


Figure 4-11. LASSO feature selection for antibody responses.
(A) Coefficient path showing the shrinkage of predictor coefficients as the LASSO penalty increases. Most features approach zero, while only a small subset retains non-zero values at the optimal penalty.
(B) AICc curve used to determine the optimal model complexity. The minimum AICc value (vertical red line) identifies the penalty that yields the most parsimonious set of discriminating antibody features.

PLS-DA revealed that only 2 of the 20 antibody features analyzed were sufficient to discriminate hybrid MERS/SARS-CoV-2 immunity from hybrid SARS-CoV-2/SARS-CoV-2 immunity. As shown in the variable importance plot (Figure 4-12A), S2-specific antibodies with FcγRIIIA binding and S1-specific antibodies with FcγRIIB binding were the only features exceeding the VIP > 1 threshold. Based on the model coding (1 = hybrid MERS/SARS-CoV-2; 0 = hybrid SARS-CoV-2/SARS-CoV-2), the PLS-DA coefficients (Figure 4-12B) indicated that S1–FcγRIIB responses were enriched in the hybrid MERS/SARS-CoV-2 group, whereas S2–FcγRIIIA responses were enriched in the hybrid SARS-CoV-2/SARS-CoV-2 group. Consistent with these feature-level differences, the PLS-DA scores plot (Figure 4-12C), demonstrated clear separation between the two hybrid-immunity groups.

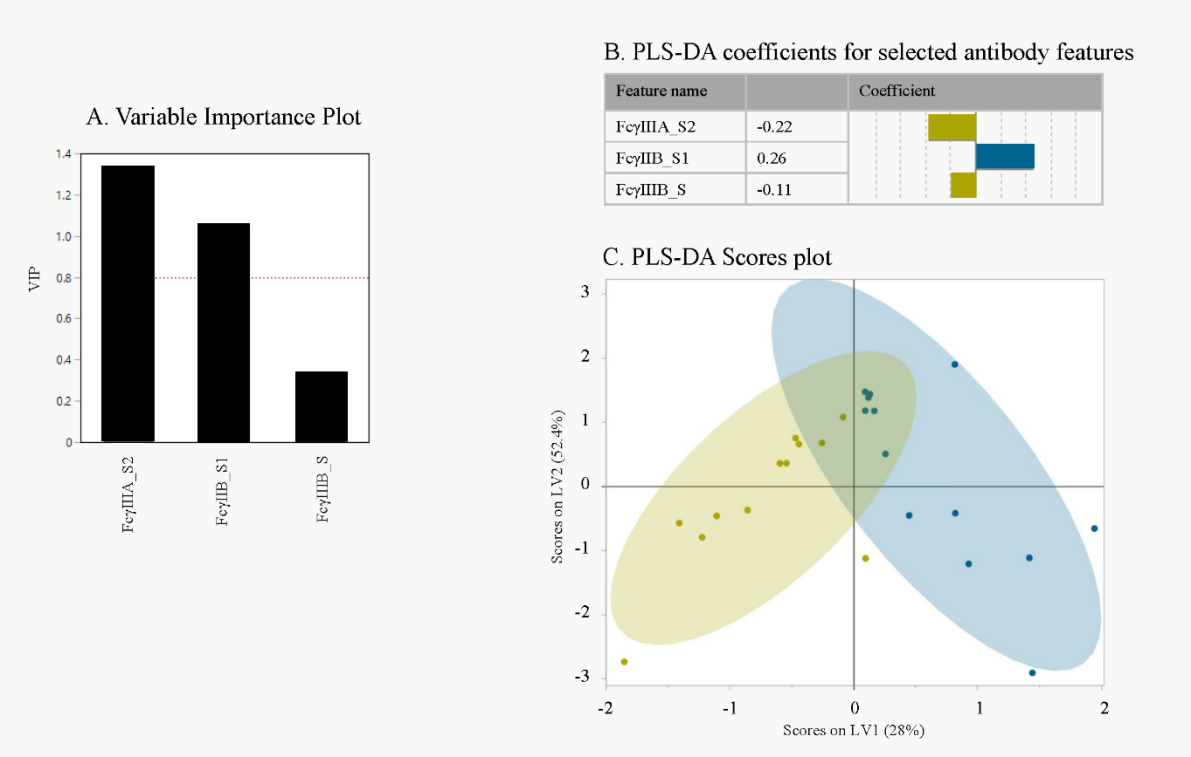


Figure 4-12. Multivariate discrimination of hybrid immunity groups using PLS-DA. **(A)** Variable importance plot (VIP) for the three LASSO-selected antibody features. FcγRIIIA_S2 and FcγRIIB_S1 exceeded the VIP > 1 threshold, indicating their dominant contribution to group separation. **(B)** PLS-DA coefficients for the selected features. Based on the model coding (1 = hybrid MERS/SARS-CoV-2; 0 = hybrid SARS-CoV-2/SARS-CoV-2), FcγRIIB_S1 responses were enriched in the hybrid MERS/SARS-CoV-2 group, whereas FcγRIIIA_S2 responses were enriched in the hybrid SARS-CoV-2/SARS-CoV-2 group. **(C)** PLS-DA scores plot showing clear separation between hybrid MERS/SARS-CoV-2 (n = 13, turquoise) and hybrid SARS-CoV-2/SARS-CoV-2 (n = 12, gold). Ellipses represent 90% confidence intervals.

To explore this further, we examined correlations within each hybrid group separately, focusing on the relationship between nucleocapsid responses and SARS-CoV-2 Wuhan- and Omicron-specific antibodies (Figure 4-13). Correlation analysis using Pearson's correlation coefficient revealed strong positive associations between nucleocapsid responses and all SARS-CoV-2– and Omicron-specific antibody features in the hybrid MERS-CoV/SARS-CoV-2 group (Figure 4-13A). IgG titres, FcγR-binding responses, and neutralisation activity were significantly correlated, indicating a highly correletaed humoral immune profile in this group and supporting the possibility of recent SARS-CoV-2 infection.

In contrast, more modest correlations were observed in the hybrid SARS-CoV-2 group. Here, associations were limited primarily to correlations between nucleocapsid FcγRIIB and S1-specific FcγRIIA responses to the Wuhan strain (R = 0.6, p = 0.5), with no broader coordinated pattern identified. Furthermore, Wuhan-specific antibody responses did not correlate with Omicron-specific

responses, indicating that activity induced by infection with the ancestral strain provides limited cross-reactive functional immunity against Omicron.

As this work is a cross-sectional observational study based on single time-point sampling and limited exposure history, recent SARS-CoV-2 infection cannot be definitively confirmed. Nevertheless, several findings point toward this possibility, particularly in the hybrid MERS-CoV/SARS-CoV-2 group. The strong correlations observed between nucleocapsid-specific responses and both binding and neutralising antibodies support the likelihood of recent natural infection, as nucleocapsid is not included in current COVID-19 vaccines. High antibody levels in some individuals may therefore reflect recent exposure rather than vaccination alone, although a contribution from broader cross-reactive immunity in this hybrid group cannot be excluded.

Interpretation is further complicated by several practical constraints. The small sample size and the absence of precise vaccination dates in this group prevented assessment of how timing or dosing interval may have influenced antibody profiles. Consequently, it remains unclear whether the observed patterns reflect vaccine-induced boosting or recent exposure during the Omicron wave. In addition, the dynamics of MERS-specific nucleocapsid responses are not well characterised, making it difficult to determine whether the strong nucleocapsid reactivity in this group represents long-lived responses or recent SARS-CoV-2 infection. These uncertainties also highlight the methodological challenges of selecting suitable control groups during periods of active viral circulation. Moreover, because Omicron-specific neutralisation assays—particularly competition-based formats—were not performed, the functional specificity of the observed responses could not be fully determined.

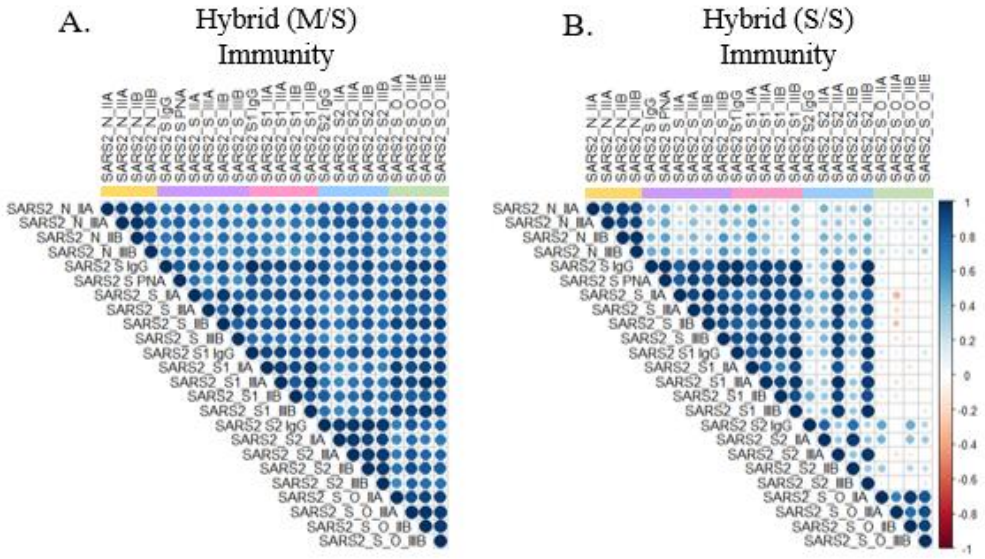


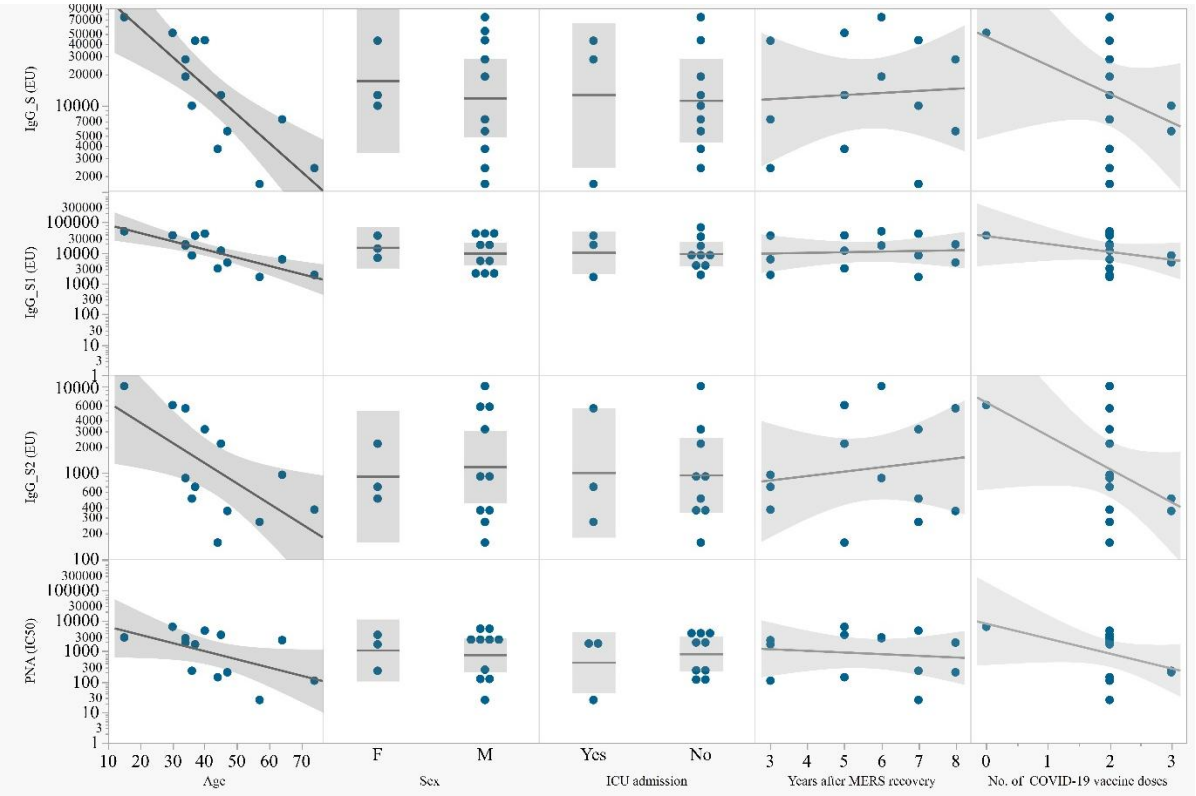
Figure 4-13 Correlation matrix of humoral immune responses. Pairwise Spearman correlation coefficients between all measured antibody features are shown.

Antibody features include IgG binding titres and Fcγ receptor (FcγR) engagement across SARS-CoV-2 spike, S1, S2, Omicron spike, and nucleocapsid antigens, as well as pseudovirus neutralisation titres (PNA). Each circle represents the strength and direction of a correlation, with colour indicating the coefficient value (–1 to +1) and circle size reflecting the magnitude of the correlation. Blue denotes positive correlations, whereas red denotes negative correlations. Age displayed negative correlations with several antibody features. All correlations were computed using Spearman's rank method. The left panel shows the hybrid MERS-CoV/SARS-CoV-2 group (n = 13), and the right panel shows the hybrid SARS-CoV-2 group (n = 12). Antibody features are colour-coded as follows: FcγR responses to SARS-CoV-2 nucleocapsid (yellow, Wuhan strain); IgG binding to SARS-CoV-2 spike (purple), S1 (pink), and S2 (blue) antigens (Wuhan strain); and FcγR binding to the Omicron spike (green).

4.2.1.8 Host and Exposure Factors Shaping Anti–SARS-CoV-2 Antibody Responses

4.2.1.8.1 Hybrid MERS-CoV/SARS-CoV-2 immunity

Next, we investigated if MERS-related factors are associated with SARS-CoV-2 immune responses. Specifically, we examined the relationship between SARS-CoV-2 binding IgG antibody levels against the S, S1, and S2 subunits, as well as neutralising antibody responses, comparing these measures between male and female individuals and between those who required ICU admission during acute MERS infection and those who did not. We also assessed correlations between antibody levels and patient age, time since recovery, the number of COVID-19 vaccine doses received. Results are illustrated in Figure 4-14.



	Age	Years after MERS	No. of doses
S	-0.8 ***	0.03	-0.19
S1	-0.8 **	0.07	-0.19
S2	-0.64 **	0.02	-0.32
PNA	-0.57 *	0.05	-0.3

Figure 4-14. SARS-CoV-2 antibody responses in individuals with hybrid MERS immunity.
Scatterplots and boxplots depict associations between serum antibody levels and demographic or clinical variables among individuals recovered from MERS and later exposed to SARS-CoV-2 or vaccinated against COVID-19. Measured responses include IgG against the spike protein (IgG_S), S1 subunit (IgG_S1), and S2 subunit (IgG_S2), as well as pseudovirus neutralising activity (PNA, IC50). Each dot represents one participant. Grey shaded areas indicate 95% confidence intervals for regression lines, and gray boxes represent interquartile ranges for categorical variables. Antibody titres are displayed on a logarithmic scale (EU or IC50). n = 13. The accompanying table summarizes Pearson correlation coefficients for each group. Statistical significance is indicated as * $p < 0.05$, ** $p < 0.01$, *** $p < 0.001$, **** $p < 0.0001$.

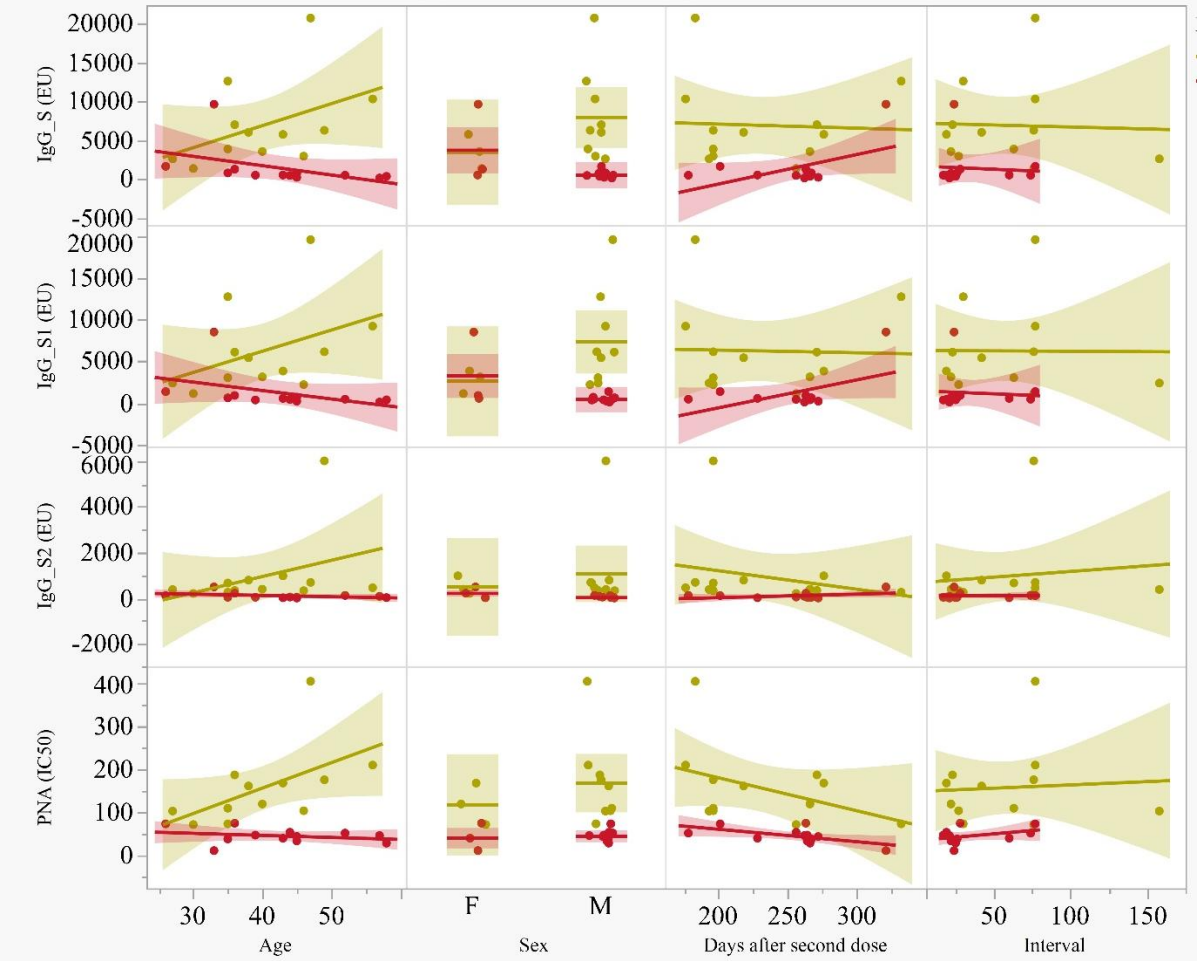
Age showed a negative correlation with both binding (S IgG: R = –0.80, p = 0.0009; S1 IgG: R = –0.80, p = 0.0018; S2 IgG: R = –0.60, p = 0.02) and neutralising antibody responses (R = –0.57, p = 0.04), indicating reduced immunity in older individuals. No significant differences were observed between sexes, although the small number of female participants (3 out of 13) may have limited our ability to detect sex-related effects. ICU admission status had no significant impact on either binding or

neutralising antibody levels following recovery. Similarly, the number of years since MERS recovery was not associated with differences in antibody magnitude or function.

Interestingly, the number of COVID-19 vaccine doses received showed weak negative correlations with antibody responses (R = –0.2 to –0.3), although none were statistically significant. Only 2 out of 13 participants (15%) had received three vaccine doses. These observations raise the question of whether repeated vaccination might influence SARS-CoV-2–specific antibody responses, or alternatively, whether individuals requiring repeated vaccination represent a subgroup with generally poorer health or diminished immune responsiveness. To clarify these relationships, paired longitudinal studies assessing immune responses before vaccination and following each vaccine dose are needed.

4.2.1.8.2 Hybrid SARS-CoV-2/SARS-CoV-2 and vaccine-only immunity groups

Vaccination dates and sample collection timepoints after booster vaccination were available for both matched groups. The hybrid immunity group (SARS-CoV-2 infection plus vaccination) and the vaccine-only group each had documented vaccination histories and intervals. To assess the effects of age, the PB interval, and the sampling time after the second dose, we performed correlation analyses using binding IgG and neutralising antibody levels. Correlations were analysed separately for each group, as shown in Figure 4-15.



	H (S/S)			V (S)		
	Age	Days after second dose	Interval between PB	Age	Days after second dose	Interval between PB
S	0.49	-0.04	0.06	0.86***	0.07	0.48
S1	0.5	-0.06	0.13	-0.73**	-0.007	0.58*
S2	0.54	-0.25	0.03	-0.3	-0.24	0.43
PNA	0.36	-0.15	0.02	0.33	0.49	-0.55

Figure 4-15. SARS-CoV-2 antibody responses in individuals with hybrid SARS-CoV-2/SARS-CoV-2 immunity and vaccine-only immunity.

Scatterplots and boxplots depict associations between serum antibody levels and demographic or clinical variables (n = 12 per group). Measured responses include IgG against the spike protein (IgG_S), S1 subunit (IgG_S1), and S2 subunit (IgG_S2), as well as pseudovirus neutralising activity (PNA, IC_{50}). Each dot represents an individual participant. Grey shaded areas indicate 95% confidence intervals for regression lines, and grey boxes represent interquartile ranges for categorical variables. Antibody titres are shown on a logarithmic scale (EU or IC_{50}). The accompanying table summarises Pearson correlation coefficients for each group. Statistical significance is indicated as *** $p < 0.001$.

In the hybrid SARS-CoV-2/SARS-CoV-2 immunity group, antibody responses were largely independent of age and the other factors assessed, with no significant correlations observed. In contrast, the vaccine-only group demonstrated strong inverse associations between age and antibody responses: age negatively correlated with spike IgG (R = –0.86, p = 0.0006) and S1 IgG (R = –0.73, p = 0.0097), indicating a more pronounced age-related decline in vaccine-induced immunity. A positive correlation was also observed between S1 IgG and the interval since the most recent booster (R = 0.58, p = 0.05), suggesting that S1-specific responses are sensitive to both age and dosing intervals.

Together, these findings imply that hybrid SARS-CoV-2 immunity may mitigate the negative effects of age on antibody responses and highlight the role of prior infection in sustaining humoral immunity following vaccination.

4.2.1.8.3 Factors influencing Anti-SARS-CoV-2 antibody responses across and within immune groups.

Based on these observations, we next performed multivariable linear regression analyses to identify the strongest independent predictors of antibody magnitude and function across key readouts. Variables included in the models were immune status, age, sex, and nucleocapsid-specific FcγR-binding responses as a proxy for prior infection.

Next, we examined whether the immune profile of the spike region differed between individuals with exposure to coronaviruses of distant origin (hybrid MERS-CoV/SARS-CoV-2) and those with repeated exposure to the same virus (hybrid SARS-CoV-2/SARS-CoV-2). To address this, we applied a least absolute shrinkage and selection operator (LASSO) model to reduce the dataset to a minimal set of features that best distinguished the two hybrid groups. These selected features were then visualized using partial least squares discriminant analysis (PLS-DA). A total of 20 features—including binding, FcγR activity, and neutralisation—were evaluated per sample (Fig. 2A; $P < 0.001$, permutation test; leave-one-out cross-validation [LOO-CV] accuracy = 1.0). Features enriched in the hybrid MERS-CoV/SARS-CoV-2 group included S1-specific IgG and FcγRIIB activity, consistent with de novo responses to less conserved regions of the spike. In contrast, the hybrid SARS-CoV-2/SARS-CoV-2 group was enriched for S2-specific responses, particularly FcγRIIIA activity.

4.2.1.9 Cross-reactivity to seasonal coronaviruses

To assess whether exposure to other coronaviruses enhances cross-reactive responses to seasonal coronaviruses, we first compared each immune-history group with its respective negative control (NC) population—consisting of pre-pandemic, pre-vaccination samples (i.e., the hybrid MERS-CoV/SARS-CoV-2 group with MERS002 controls from KSA, and the hybrid SARS-CoV-2 and SARS-CoV-2 vaccine-only groups with MERS001 controls from the UK)—followed by direct comparisons between

immune-history groups (Figure 4-16). These comparisons were performed separately for each cohort due to differences in baseline coronavirus exposure and immune profiles between populations, as discussed in the previous chapter.

Hybrid groups showed overall higher responses to betacoronaviruses. Compared with their respective NCs, both the hybrid MERS-CoV/SARS-CoV-2 and hybrid SARS-CoV-2/SARS-CoV-2 groups exhibited elevated responses to HKU1, although the magnitude and patterns varied across Fc subclasses. Increases were most notable for FcγRIIA in both hybrid groups (Fig. 12A); for FcγRIIIA (Figure 4-16B) and FcγRIIIB (Figure 4-16D) in the hybrid SARS-CoV-2 group; and for the inhibitory FcγRIIB (Figure 4-16C) in the hybrid MERS-CoV/SARS-CoV-2 group. Responses to OC43 were also higher in the hybrid SARS-CoV-2 group ($p = 0.026$ for both FcγRIIA and FcγRIIIA; Figure 4-16A–B).

In contrast, an opposite pattern emerged for inhibitory responses against the alphacoronaviruses. Both the hybrid SARS-CoV-2/SARS-CoV-2 and the SARS-CoV-2 vaccine-only groups demonstrated reduced FcγRIIB activity compared with their respective NC cohorts (Figure 4-16C). FcγRIIB responses to 229E were consistently lower in both groups relative to the UK NC cohort. For NL63, however, diminished FcγRIIB responses were observed only within the hybrid SARS-CoV-2/SARS-CoV-2 group when compared with its corresponding NCs (Figure 4-16D).

Notably, FcγRIIIB responses to NL63 were higher in the hybrid SARS-CoV-2 group compared with both the hybrid MERS-CoV/SARS-CoV-2 group and their corresponding NCs ($p = 0.01$, Figure 4-16D). No other significant differences were observed in direct comparisons across the groups. Although these data are cross-sectional, the findings suggest that cross-reactive antibody responses are directed primarily toward the betacoronavirus HKU1, with enhanced activating responses to OC43 in individuals with hybrid SARS-CoV-2 immunity compared with the negative control group. FcγRIIB responses to HKU1 were also elevated in the hybrid MERS-CoV/SARS-CoV-2 group, mirroring the pattern observed for nucleocapsid-specific responses. This may indicate a predominant role for inhibitory FcγRIIB signalling in modulating antibody activity within hybrid MERS immunity. Collectively, these observations highlight distinct patterns of Fc-mediated coronavirus immunity shaped by prior exposure history.

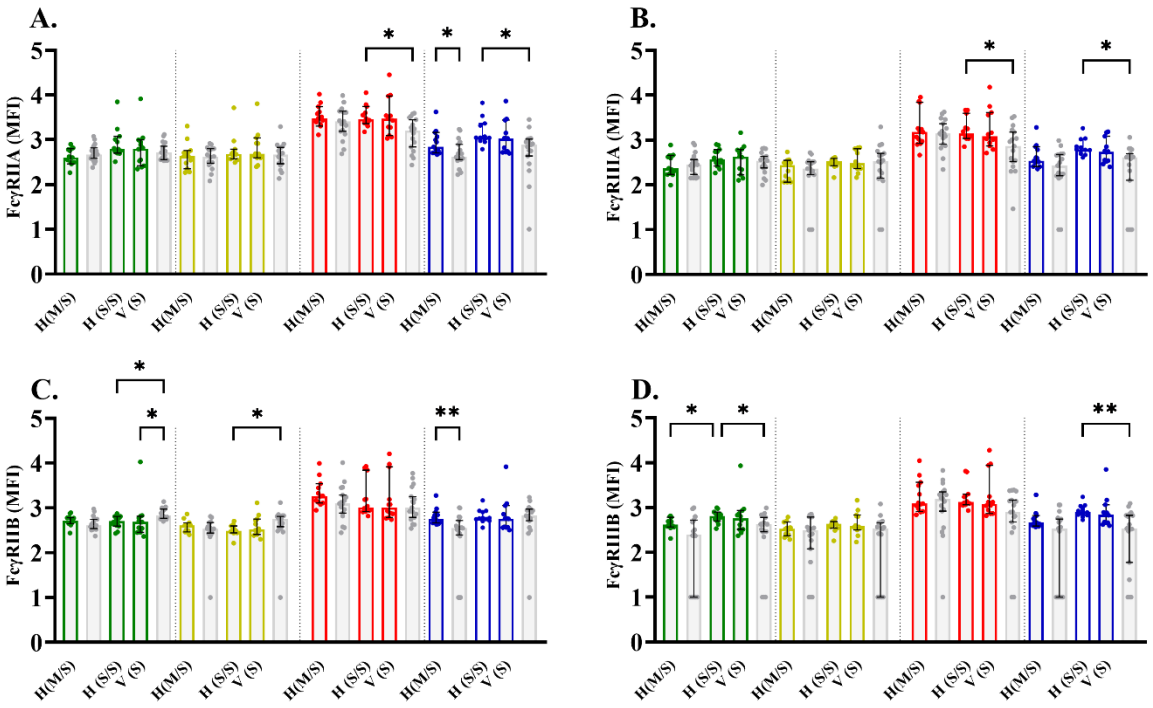


Figure 4-16. Breadth of FcγR-binding responses to seasonal coronaviruses.

(A) FcγRIIA, **(B)** FcγRIIIA, **(C)** FcγRIIB, and **(D)** FcγRIIIB binding responses. Hybrid MERS-CoV/SARS-CoV-2 immunity [H(M/S), n = 13] is compared with negative controls (NCs) from Saudi Arabia (n = 17), whereas the hybrid SARS-CoV-2 [H(S/S), n = 12] and SARS-CoV-2 vaccine-only [V(S), n = 12] groups are compared with pre-pandemic NCs from the UK (n = 17). Individual responses are shown as points, with bars indicating the median and 95% confidence interval. Colours represent the four seasonal coronaviruses: 229E (green), NL63 (yellow), OC43 (red), and HKU1 (blue). Grey bars denote the corresponding NCs for each population. Comparisons between H(M/S) and NCs were performed using the Mann–Whitney test, while comparisons involving the H(S/S), V(S), and NC groups were conducted using the Kruskal–Wallis test with Dunn's multiple-comparison correction. A secondary comparison among the H(M/S), H(S/S), and V(S) groups was also performed using the Kruskal–Wallis test. Asterisks (*) denote statistical significance for within-group and between-cohort comparisons, as defined by P-values: * (P<0.05), ** (P<0.01), *** (P<0.001), **** (P<0.0001).

4.2.1.10 MERS-CoV responses in hybrid MERS immunity

In the previous section, I showed that immune imprinting from prior MERS-CoV infection is likely to enhance the antibody response to SARS-CoV-2 vaccination. In Chapter 2, I also demonstrated that vaccination with ChAdOx1 MERS elicited cross-reactive antibody responses against the seasonal betacoronaviruses OC43 and HKU1. However, unlike seasonal coronaviruses, immunity to MERS-CoV is known to persist for several years following infection [377-380].

We therefore sought to determine whether COVID-19 vaccination could elicit back-boosting of MERS-CoV-specific antibody responses in individuals with a history of MERS-CoV infection. Ideally, paired pre- and post-vaccination samples would be required to directly quantify such effects. However, for

individuals with hybrid MERS-CoV immunity, only a single post-vaccination sample was available. To indirectly evaluate the extent of antigenic back-boosting, as well as the long-term persistence of MERS-CoV-specific antibody responses in this hybrid group, we conducted comparative serological analyses across three cohorts: individuals with hybrid MERS-CoV/SARS-CoV-2 immunity (defined as prior MERS-CoV infection followed by SARS-CoV-2 exposure), individuals with natural MERS-CoV infection alone (a pre-pandemic Korean cohort sampled approximately two years after recovery), and individuals who received a single high-dose ChAdOx1 MERS vaccination pre-pandemic (MERS001 and MERS002) sampled at the day 28 peak described in Chapter 3.

This comparative approach enabled us to assess whether SARS-CoV-2 vaccination can enhance or recall MERS-CoV-specific immune responses in individuals previously infected with MERS-CoV. Results for IgG binding and PNA are presented in Table 4-6 and Figure 4-17, while FcγR binding results for each antigen are shown in Table 4-7 and Figure 4-18.

Group	FcγRIIIA (EU, median [IQR])	IgG_S1 (EU, median [IQR])	IgG_S2 (EU, median [IQR])	Neutralizing Ab titre (IU/mL, median [IQR])
Conv (M)	5022 [2849–7959]	2452 [1671–5617]	1481 [1169–6708]	807.8 [426.9–2195]
H (M/S)	1725 [806.5–4503]	600.9 [199.8–1932]	1031 [456.4–1406]	111.0 [39.5–270.5]
V(M)	1339 [791.1–2269]	1225 [712.4–1617]	605.7 [451.1–1046]	326.1 [203.3–432.2]
NC	41 [24-105]	164 [112-293]	146 [64-213]	10 [10-10]

Table 4-6. Median IgG binding to MERS spike (S), S1, and S2 proteins, and pseudovirus neutralisation assay (PNA) titres.

Data are presented as median values with IQR. Binding antibody levels (ELISA units, EU) and neutralisation titres (PNA IC_{50}) were measured in plasma samples from individuals with different immune histories: pre-pandemic MERS convalescent individuals (Conv (M); n=9), individuals with hybrid MERS-CoV immunity [H (M/S); n=13, including one unvaccinated participant], individuals with vaccine-induced MERS immunity [V (S); n=12], and pre-pandemic controls (n=48 for S, S1, and S2; n=34 for PNA).

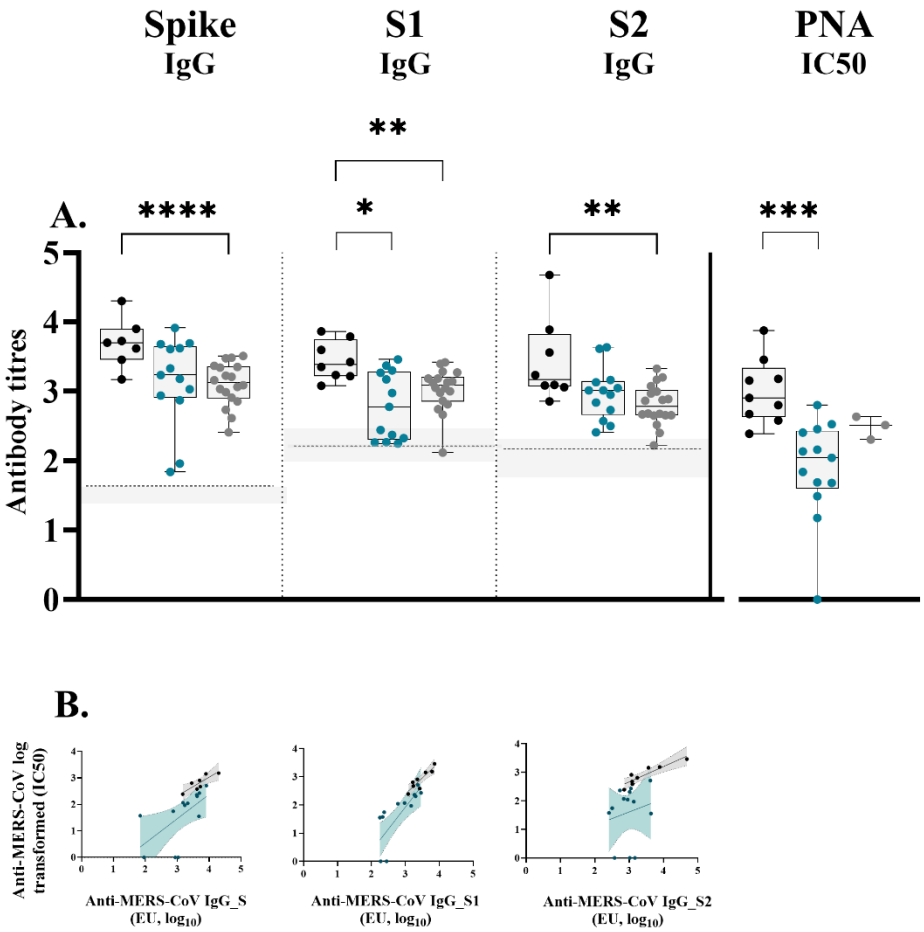


Figure 4-17.IgG binding and neutralisation responses to the MERS-CoV spike protein and its subunits.

(A) Box-and-whisker plots show plasma IgG binding (left) and pseudovirus neutralisation activity (right). The IgG binding plots display ELISA units (EU) measured against the full-length spike (S) protein and its subunits (S1 and S2) in three groups: individuals with MERS-CoV convalescent immunity (H [Conv]; n = 9), individuals with hybrid MERS-CoV/SARS-CoV-2 immunity (H [M/S]; n = 13), and individuals with MERS-CoV vaccine-induced immunity (V [M]; n = 17). Data from pre-pandemic controls (n = 34) are not shown; however, the group median is indicated by a dotted line, with the interquartile range (IQR) shaded in grey. Neutralisation activity (right) is represented by median half-maximal inhibitory concentration (IC_{50}) values against the MERS Qatar strain, measured using a lentivirus-based pseudovirus neutralization assay (PNA) with heat-inactivated plasma. Statistical significance was assessed using the Kruskal–Wallis test with Dunn's post hoc correction for comparisons within each immune group**. (B)** Pearson correlation analyses between binding antibody responses (S, S1, and S2) and neutralising antibody titres. Colours represent immune groups: grey = H (Conv), turquoise = H (M/S). Asterisks (*) denote statistical significance for within-group and between-cohort comparisons, as defined by P-values: * (P<0.05), ** (P<0.01), *** (P<0.001), **** (P<0.0001).

The magnitude of MERS-CoV–specific binding IgG levels, pseudovirus neutralisation assay (PNA) titres, and FcγR-binding activities in the hybrid MERS immunity group was significantly higher than in pre-pandemic negative controls for spike, S1, and S2 antigens, as summarised in Table 4-6 and Table 4-7. These findings suggest that MERS-specific antibody responses persist in individuals with hybrid immunity, or that SARS-CoV-2 vaccination may induce back-boosting of pre-existing MERS immunity.

The MERS convalescent group, sampled within two years of recovery, consistently exhibited the highest antibody responses across all binding IgG and neutralisation assays (Figure 4-17A), whereas individuals in the hybrid immunity group were sampled at a median of six years (range 3–8 years) following MERS-CoV infection. Significant differences were also observed between the hybrid and convalescent groups in S1-binding antibody levels ($p = 0.0065$), with convalescent individuals exhibiting higher neutralising antibody titres ($p = 0.0006$) (Figure 4-17A, Table 4-6). Neutralisation analyses in the vaccine-only group were limited by the small sample size ($n = 3$), due to freeze–thaw–related assay constraints affecting pre-pandemic samples, as detailed in Supplementary Section 8.1.4.1.2.3.7.

While no significant differences were observed between the hybrid and vaccine-only groups (Figure 4-17A), S1-specific IgG responses were approximately 2-fold higher in the vaccine-induced immunity group, whereas S2-specific responses were around 1.7-fold higher in the hybrid group (Table 4-6). This pattern suggests that vaccine-induced immunity preferentially boosts *de novo* S1 responses, whereas hybrid immunity enhances the recall and amplification of more conserved S2-targeted antibodies, consistent with boosting of conserved epitopes following prior MERS exposure.

Correlation analysis revealed strong positive associations between binding IgG and neutralising antibody levels for spike and S1 in MERS convalescent individuals ($R = 0.80$, $p < 0.05$), and for S2 ($R = 0.82$, $p = 0.03$). In contrast, in the hybrid MERS-CoV group, strong correlations were observed for spike ($R = 0.70$, $p = 0.007$) and S1 ($R = 0.90$, $p < 0.0001$), whereas S2-binding antibodies showed no association with neutralising activity ($R = 0.09$, $p = 0.76$). These findings indicate that although cross-reactive, S2-directed antibodies are detectable, they show limited association with neutralisation activity in the hybrid MERS-CoV group. Notably, in the hybrid MER-CoV/SARS-CoV-2, the SARS-CoV-2–specific neutralising responses correlated with anti–SARS-CoV-2 IgG levels, suggesting that dominant neutralising antibody targets differ between the two viruses and/or that individuals with hybrid immunity mount higher overall responses to SARS-CoV-2 Figure 4-6.

Similar to the binding and neutralisation data, FcγR responses were overall higher for spike in MERS convalescent individuals compared with the hybrid MERS group, with particularly strong S1-mediated activation of FcγRIIIA and FcγRIIA ($p < 0.05$, Figure 4-18, Table 7). Interestingly, other FcγR responses—including those mediated by the inhibitory receptors FcγRIIB and FcγRIIIB for S1, as well as all S2-directed FcγR responses—were comparable between the two groups ($p > 0.05$; Figure 4-18C-D). Furthermore, no differences were observed between hybrid and vaccine-induced immunity for any FcγR activity, indicating that Fc-mediated antibody functionality is maintained in the hybrid group despite the substantially longer time since MERS-CoV exposure compared with vaccine-induced immunity.

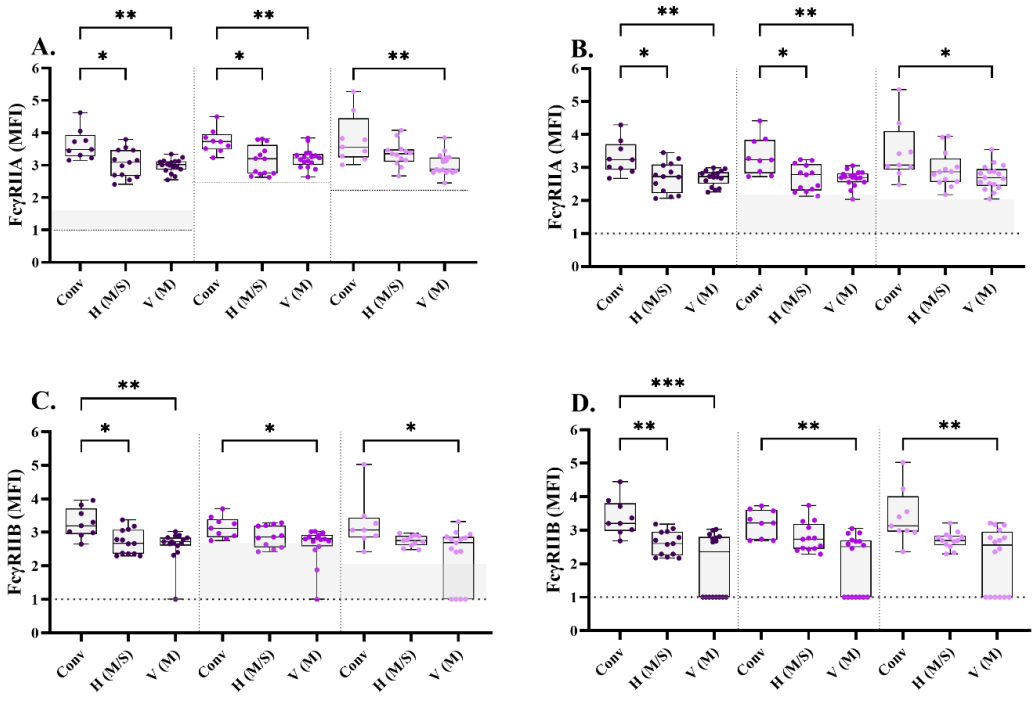


Figure 4-18. FcγR-binding antibody titres against MERS spike, S1, and S2 across FcγR subclasses.

(A-D) Individual titres of FcγRIIA, FcγRIIIA, FcγRIIB, and FcγRIIIB in serum samples from cohorts with different immune histories: pre-pandemic MERS convalescent (Cov, n = 9), hybrid MERS immunity (MERS/SARS-CoV, n = 13), and MERS vaccine-induced immunity (n = 17) Data from pre-pandemic controls (n = 34) are not shown; the median of this group is indicated by a dotted horizontal line, with the interquartile range (IQR) shaded in grey. Colours represent distinct antigen targets: dark purple = spike, medium purple = S1, and light purple = S2. Statistical comparisons were performed using Kruskal–Wallis tests with Dunn's post hoc correction for multiple comparisons. *p < 0.05; **p < 0.01; ***p < 0.001; ****p < 0.0001.

Group		Spike (MFI, median [IQR])	S1 (MFI, median [IQR])	S2 (MFI, median [IQR])
Conv	FcγRIIA	3090 [1863–8570]	5332 [3041–9063]	3646 [1724–28410]
H (M/S)		1217 [461.3–2915]	1575 [548.2–4263]	2243 [1294–3041]
V(M)		1033 [723.0–1320]	1679 [1035–2206]	746.7 [632.2–1734]
NC		10 [10–40]	313 [193 –377]	177 [118–334]
Conv	FcγRIIIA	1730 [855.9–5081]	1706 [662.7–6769]	1189 [855.4–12488]
H (M/S)		535.5 [166.4–1240]	606.8 [201.8–1261]	734.1 [366.4–1902]
V(M)		535.5 [325.4–722.6]	496.7 [357.3–664.9]	492.7 [278.7–894.3]
NC		10 [10–10]	10 [10–143]	10 [10–112]
Conv	FcγRIIB	1583 [899.8–5092]	1324 [712.4–2472]	1173 [370.2–2781]
H (M/S)		466.0 [230.5–1191]	731.5 [356.4–1590]	573.6 [410.7–777.7]
V(M)		527.0 [401.0–694.0]	632.3 [377.6–839.4]	490.4 [490.4–738.4]
NC		10 [10–10]	243 [10–487]	10 [10–118]
Conv	FcγRIIIB	1603 [960.5–6453]	1644 [517.7–4053]	1343 [919.1–10315]
H (M/S)		402.0 [176.0–897.1]	538.7 [276.8–1532]	495.3 [351.3–686.0]
V(M)		226.5 [10.0–633.3]	321.5 [10.0–497.2]	361.5 [10.0–910.6]
NC		10 [10–10]	10 [10–10]	10 [10–10]

Table 4-7. Median FcγRI responses to MERS-CoV spike, S1, and S2 proteins.

Data are presented as median values with IQR. Binding antibody levels (EU) and neutralisation titers (PNA IC_{50}) were measured in plasma samples from individuals with different immune histories: pre-pandemic MERS convalescent individuals (Conv (M); n=9), individuals with hybrid MERS-CoV immunity [H (M/S); n=13, including one unvaccinated participant], individuals with vaccine-induced MERS immunity [V (S); n=12], and pre-pandemic controls (n=48 for S, S1, and S2; n=34 for PNA).

To identify the specific antibody features distinguishing MERS convalescent individuals from those with hybrid MERS/SARS-CoV-2 immunity, we applied least absolute shrinkage and selection operator (LASSO) feature selection. All antibody measurements were normalized using z-score transformation prior to analysis, and a total of 20 MERS-CoV–reactive features were included.

LASSO regularization reduced the dataset to a single non-zero predictor, with all other features shrunk to zero. The coefficient path demonstrated the progressive removal of weak predictors, and the AICc curve identified the optimal penalty yielding the most parsimonious model (Figure 4-19). At this optimal penalty, LASSO selected MERS-CoV Spike-specific FcγRIIIB-binding antibodies as the only feature capable of differentiating MERS convalescent individuals from those with hybrid MERS/SARS-CoV-2 immunity. This feature was therefore examined independently in downstream analyses.

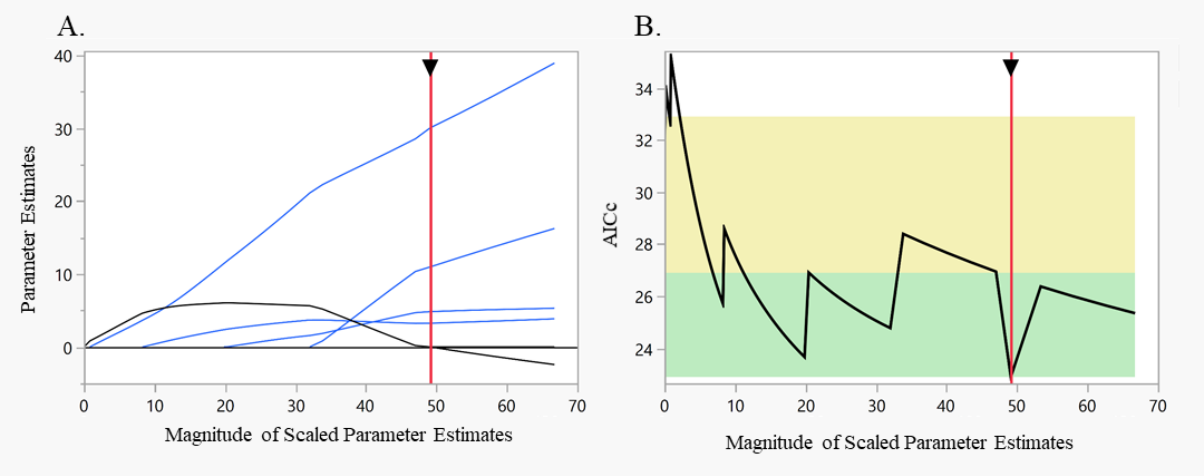


Figure 4-19. LASSO feature selection for antibody responses.

(A) Coefficient paths showing the shrinkage of predictor coefficients as the LASSO penalty increases. As regularisation strength increases, most antibody features are progressively reduced toward zero, with only a small subset retaining non-zero coefficients near the optimal penalty. **(B)** AICc curve used to identify the optimal model complexity. The minimum AICc value (red vertical line) corresponds to the most parsimonious model. At this penalty, only a single antibody feature remains non-zero, indicating that it is the sole feature selected as significant by the LASSO procedure.

Given the evidence for MERS–SARS-CoV-2 cross-reactivity and potential back-boosting in individuals with hybrid MERS immunity, we next examined correlations between SARS-CoV-2– and MERS-CoV–specific antibody responses within the hybrid MERS group. Strong positive associations were observed between MERS-CoV S2–specific responses and multiple SARS-CoV-2 antibody features, with particularly strong correlations involving FcγR-mediated functions (Figure 4-20). Anti-MERS S2 IgG correlated significantly with SARS-CoV-2 S2 and spike IgG responses, as well as with FcγRIIIA and FcγRIIIB engagement of SARS-CoV-2 spike, with even stronger associations observed for FcγR responses targeting SARS-CoV-2 S2. In addition, MERS S2–specific FcγR activity correlated with FcγR engagement of SARS-CoV-2 spike and S1 to varying degrees. Correlations with SARS-CoV-2 nucleocapsid antibodies were also observed, suggesting that some individuals may have experienced natural SARS-CoV-2 infection in addition to vaccination. Collectively, these correlations highlight substantial cross-reactivity centred on the conserved S2 domain.

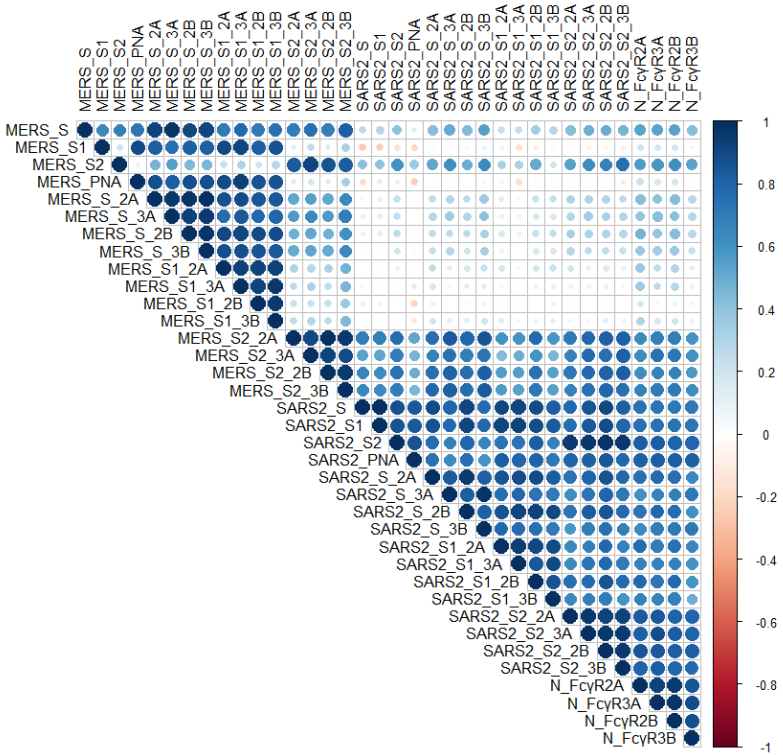
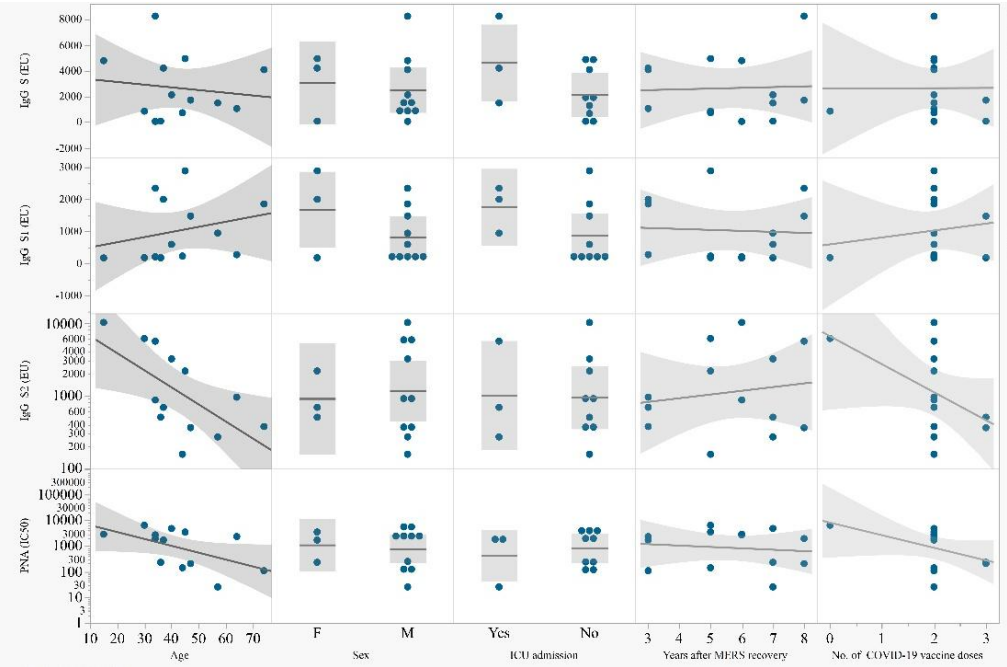


Figure 4-20 Correlation matrix of humoral immune responses in hybrid immunity group.

Pairwise Spearman correlation coefficients between all measured MERS- and SARS-CoV-2–specific antibody features are shown. Each circle represents the strength and direction of a correlation, with colour indicating the coefficient value (–1 to +1) and circle size reflecting the magnitude of the correlation. Blue denotes positive correlations, whereas red denotes negative correlations. Data shown are for the hybrid MERS-CoV/SARS-CoV-2 group (n = 13).

No significant associations were observed between MERS-related immune responses and age, years since recovery, or the number of COVID-19 vaccine doses received. In contrast, a clear separation in MERS-CoV–specific responses was evident between individuals who required ICU admission during MERS-CoV infection and those who did not (Figure 4-21). ICU admission was associated with higher MERS-CoV S1-specific functional antibody responses, particularly FcγRIIA and FcγRIIIB engagement (Figure 4-22B). Median FcγRIIA-binding titres were 6173 [2082–6527] in ICU patients compared with 608 [512–1906] in non-ICU individuals (p = 0.02), while FcγRIIIB-binding titres were 1985 [579–5547] versus 317 [264–741], respectively (p = 0.49). In contrast, ICU status was not associated with differences in SARS-CoV-2–specific antibody responses (Figure 4-21) indicating that the observed separation by disease severity was restricted to MERS-CoV–specific immunity.



	Age	Years after MERS	No. of doses
S	0.01	0.03	-0.32
S1	0.48	-0.04	-0.19
S2	-0.15	0.12	-0.06
PNA	0.28	0.09	-0.35

Figure 4-21. SARS-CoV-2 antibody responses in individuals with hybrid MERS immunity.

Scatterplots and boxplots depict associations between serum antibody levels and demographic or clinical variables among individuals recovered from MERS and later exposed to SARS-CoV-2 or vaccinated against COVID-19. Measured responses include IgG against the spike protein (IgG_S), S1 subunit (IgG_S1), and S2 subunit (IgG_S2), as well as pseudovirus neutralising activity (PNA, IC_{50}). Each dot represents one participant. Grey shaded areas indicate 95% confidence intervals for regression lines, and grey boxes represent interquartile ranges for categorical variables. Antibody titers are displayed on a logarithmic scale (EU or IC_{50}). n = 13. The accompanying table summarizes Pearson correlation coefficients for each group. Statistical significance is indicated as *** $p < 0.001$.

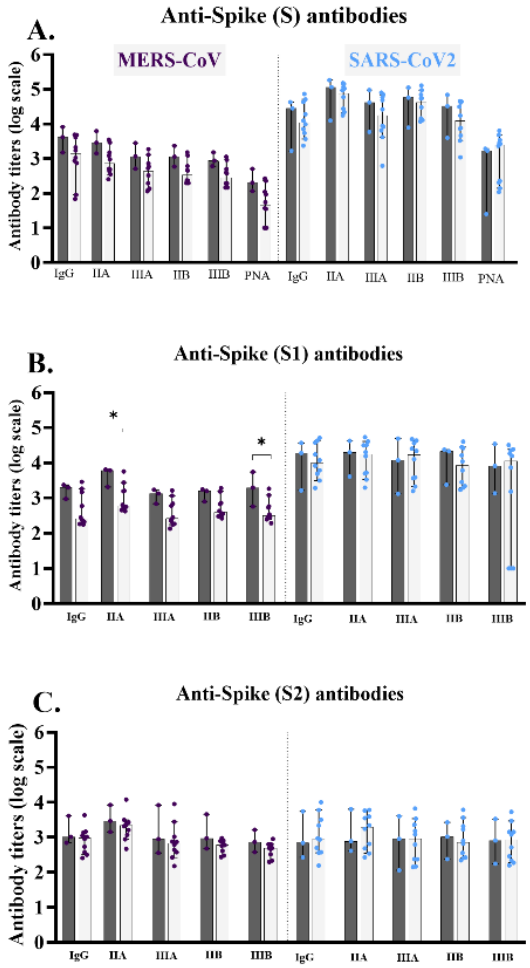


Figure 4-22. Comparison of anti–MERS-CoV and anti–SARS-CoV-2 spike-specific antibody responses within the hybrid MERS immunity group.

Antibody titres (log scale) are shown for individuals with prior ICU admission (dark grey, n = 3) and non-ICU individuals (light grey, n = 10) during MERS-CoV infection. MERS-CoV responses are displayed in blue, and SARS-CoV-2 responses in purple. Antibody binding and FcγR engagement were assessed against **(A)** full-length spike (S), **(B)** S1, and **(C)** S2 subunits. Comparisons between ICU and non-ICU groups within each antigen target were performed using the Mann–Whitney test. Asterisks indicate statistically significant differences (*$p < 0.05$).

4.2.1.10.1 Cross-reactive MERS-CoV Humoral Responses Following Post-pandemic SARS-CoV-2 Vaccination With and Without Prior SARS-CoV-2 Infection.

As previously noted, MERS incidence has declined in recent years, and cross-reactivity between MERS-CoV and SARS-CoV-2 has been proposed as a possible contributing factor. To investigate this, we assessed antibody binding and Fc-mediated effector functions as surrogate measures of potential immunity against the MERS-CoV spike protein and its subunits, using the same cohort described

above—comprising individuals with prior SARS-CoV-2 infection and vaccination (hybrid SARS-CoV-2 immunity, n = 12), SARS-CoV-2 vaccination only (vaccine-only, n = 12), and pre-pandemic negative controls (n = 34) (Figure 4-23). Samples were collected at a median of 77 days (IQR 24–196 days) after the most recent vaccination, providing insight into the durability of cross-reactive humoral responses over time. To determine whether SARS-CoV-2 infection or vaccination elicits cross-reactive responses, we first compared results to those of pre-pandemic negative controls. To determine whether the magnitude of these cross-reactive responses approaches that elicited by direct MERS-CoV antigen exposure, we compared them with responses observed in MERS pre-pandemic convalescent individuals (n = 9) and in recipients of a ChAdOx1 MERS vaccine (prime-only; n = 17; comprising MERS001, n = 8, and MERS002-KSA, n = 9), as described in the previous section. Corresponding data are presented in Table 4-8 and illustrated in Figure 4-23.

Group		Spike (MFI, median [IQR])	S1 (MFI, median [IQR])	S2 (MFI, median [IQR])
Conv	FcγRIIA	3090 [1883–8570]	5332 [3041–9063]	3846 [1724–28410]
V (M)		1033 [723.0–1320]	746.7 [832.2–1734]	1016 [667.7–1742]
H (S/S)		280.7 [202.2–316.5]	435.8 [341.9–481.8]	405.1 [228.5–713.5]
V(S)		144.9 [128.7–162.1]	327.9 [323.1–1356]	392.1 [221.8–1589]
NC		10.0 [10.0–10.0]	313.2 [132.5–376.2]	10.0 [10.0–333.5]
Conv	FcγRIIIA	1730 [855.9–5081]	1706 [862.7–6769]	1189 [856.4–12448]
V (M)		535.5 [325.4–722.6]	497.6 [357.3–864.9]	203.0 [32.71–1048]
H (S/S)		168.8 [10.0–209.3]	188.3 [147.1–248.3]	224.7 [120.4–409.2]
V(S)		10.0 [10.0–10.0]	173.5 [304.4–898.2]	492.7 [278.7–894.3]
NC		10.0 [10.0–10.0]	10.0 [10.0–170.8]	10.0 [10.0–10.0]
Conv	FcγRIIB	1683 [899.8–5092]	924.8 [638.5–2070]	1182 [289.3–4559]
V (M)		527.0 [401.0–694.9]	832.3 [377.6–839.4]	490.4 [10.0–738.4]
H (S/S)		10.0 [10.0–178.6]	321 [217-396]	10.0 [10.0–254.8]
V(S)		10.0 [10.0–10.0]	207.9 [123.0–836.8]	160.9 [10.0–326.1]
NC		10.0 [10.0–10.0]	126.5 [10.0–345.6]	10.0 [10.0–10.0]
Conv	FcγRIIIB	1603 [950.5–6453]	1644 [517.7–4053]	1343 [919.1–10315]
V (M)		227 [10-633]	321.5 [10.0–497.2]	361.5 [10.0–910.6]
H (S/S)		141.7 [103.7–203.7]	553.4 [323.1–1356]	198.7 [163.3–320.8]
V(S)		10.0 [10.0–10.0]	289.5 [207.5–499.5]	176.5 [88.2–638.9]
NC		10.0 [10.0–10.0]	10.0 [10.0–313]	10.0 [10.0–10.0]

Table 4-8. Median FcγR responses to MERS-CoV spike, S1, and S2 proteins

Data are presented as median values with IQR. Fcγ receptor-binding antibody levels (MFI) were measured in plasma samples from individuals with different immune histories: hybrid SARS-CoV-2 immunity [H(S/S); n = 12; gold], vaccine-induced SARS-CoV-2 immunity [V(S); n = 12; red], and pre-pandemic negative controls [NC; n = 34; light grey]. For reference, responses from pre-pandemic MERS convalescent individuals [Conv; n = 9; dark grey] and ChAdOx1 MERS vaccine prime-only recipients [V(M); n = 17; comprising MERS001, n = 8, and MERS002-KSA, n = 9; medium grey] are also shown.

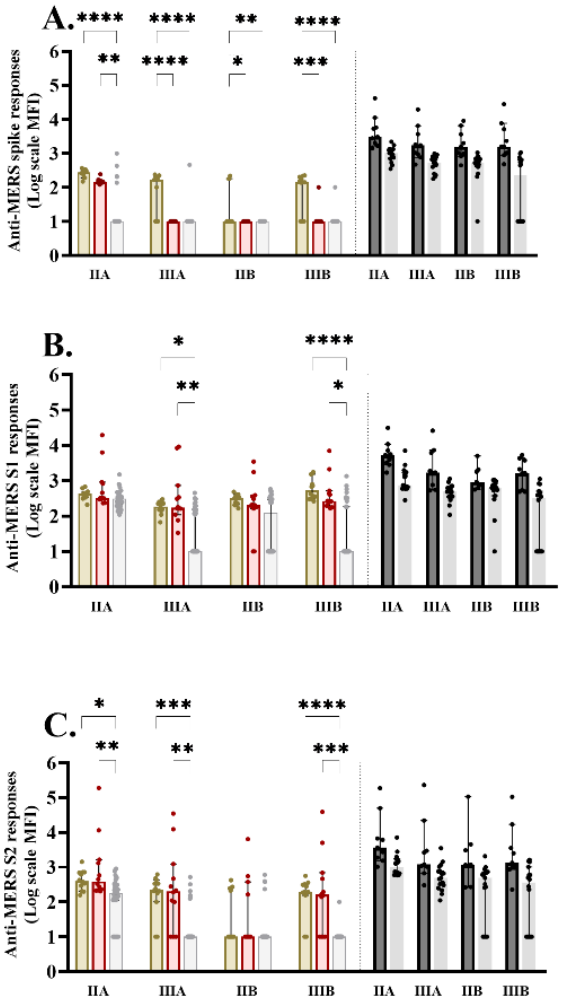


Figure 4-23. Cross-reactive anti-MERS Fc responses in hybrid SARS-CoV-2–immune individuals.

(A) Anti-MERS spike, **(B)** anti-MERS S1, and **(C)** anti-MERS S2 IgG Fc responses were measured across study groups. Hybrid SARS-CoV-2–immune individuals [H(S/S), n = 12] (gold) and SARS-CoV-2 vaccine-only individuals [V(S), n = 12] (red) were compared with pre-pandemic negative controls (NC; n = 34, gray), while MERS convalescent and MERS vaccine recipients (black and medium gray, respectively) shown on the right side of each graph were included as reference groups. Each point represents an individual sample; bars indicate the median and 95% confidence interval. Comparisons among groups were performed using the Kruskal–Wallis test with Dunn's multiple-comparison correction. Asterisks (*) denote statistical significance for within-group and between-cohort comparisons, as defined by P-values: * (P<0.05), ** (P<0.01), *** (P<0.001), **** (P<0.0001).

Both hybrid and vaccine-induced SARS-CoV-2 immunity showed elevated FcγR-binding responses against MERS antigens compared with negative controls, with the strongest activity directed toward the S2 subunit (Figure 4-23C). Hybrid SARS-CoV-2/SARS-CoV-2 immunity elicited higher and more functionally diverse FcγR responses—spanning FcγRIIA, FcγRIIIa, FcγRIIB, and FcγRIIIb ($p < 0.05$)—with the exception of FcγRIIB and FcγRIIA binding to S1, which remained comparable to negative controls. In contrast, the vaccine-only group displayed more restricted cross-reactivity, limited to select subunits and following a similar overall pattern to the hybrid group, although without statistically significant differences ($p > 0.05$; Figure 4-23). MERS spike–specific FcγR responses were

generally higher in the hybrid SARS-CoV-2 group compared with the vaccine-only group ($p < 0.05$; Figure 4-23A). Overall, these data indicate that SARS-CoV-2 infection, particularly in the context of prior viral exposure, can induce cross-reactive Fc-mediated responses to MERS-CoV, likely through recognition of conserved epitopes within the spike protein. However, given the late sampling time points, these differences may also reflect enhanced durability of hybrid-induced antibodies rather than differences in peak response magnitude alone.

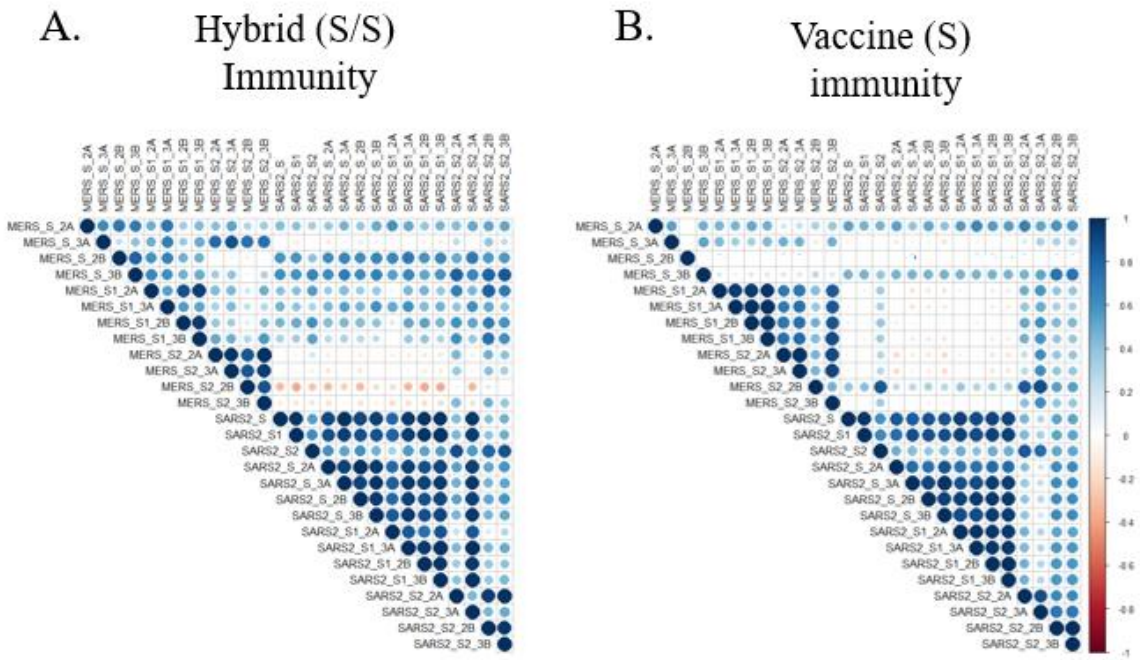


Figure 4-24. Correlation of FcγR-binding antibody responses to MERS-CoV and SARS-CoV-2 spike and subunit antigens following SARS-CoV-2 hybrid or vaccine-induced immunity.

(A) Hybrid SARS-CoV-2 immunity (H(S/S)) and **(B)** vaccine-only SARS-CoV-2 immunity (V(S)) groups. Each panel shows pairwise Spearman correlation matrices of FcγR-binding mean fluorescence intensity (MFI) values measured against MERS-CoV and SARS-CoV-2 spike (S), S1, and S2 antigens. The colour scale represents the strength and direction of correlation (blue = positive; red = negative; white = no correlation). Circle size and colour intensity correspond to the magnitude of correlation. Broader and stronger correlations were observed in hybrid immunity, particularly between MERS-S2 and SARS-CoV-2 S2 responses, indicating enhanced cross-reactive Fc engagement compared with vaccine-only immunity.

To further define the quality and breadth of SARS-CoV-2–induced cross-reactive responses to MERS-CoV, we next examined correlations between FcγR engagement across MERS spike subunits in hybrid and vaccine-only SARS-CoV-2 immunity. Correlation analysis revealed that in the hybrid immunity

group, SARS-CoV-2–induced cross-reactive Fc binding extended across MERS spike, S1, and S2, indicating broad cross-recognition (Figure 4-24A). In contrast, the vaccine-only group displayed a narrower pattern of cross-reactivity, with correlations primarily involving MERS spike FcγRIIA and FcγRIIIB engagement, and most prominently S2-directed Fc binding (Figure 4-24B). Infection-derived immunity was further distinguished by negative correlations with MERS S2–FcγRIIB, whereas vaccination without prior infection showed positive correlations with this feature. Neither group exhibited correlations with spike FcγRIIIA binding, suggesting differences in the regulation of inhibitory Fc receptors and indicating overall limited cross-reactive FcγRIIIA engagement (Figure 4-24A). Collectively, these findings demonstrate that prior infection elicits a more functionally diverse and broadly cross-reactive Fc profile, whereas vaccination alone generates a more focused response centred on conserved S2-mediated Fc interactions.

Nevertheless, when compared with ChAdOx1 MERS vaccine recipients (prime-only, assessed 2 years post-vaccination) and MERS convalescent individuals (assessed approximately two years post-infection), these cross-reactive responses remained markedly lower, as shown in Figure 4-23. This finding underscores the difference in persisting antibody levels following infection or single dose vaccination, supporting further assessment of two-dose vaccination regimens.

Taken together, these results demonstrate that infection with, and vaccination against, SARS-CoV-2 can generate cross-reactive antibodies to the MERS spike capable of binding its subunits and engaging Fcγ receptors, suggesting potential functional activity. Since the precise threshold of antibody titre or Fc-mediated function required for protection against MERS-CoV is unknown, it remains unclear whether these cross-reactive antibody responses (or potential cross-reactive T-cell immunity not measured here) would be sufficient to contribute to the observed reduction in MERS incidence. These findings highlight the importance of targeted MERS vaccination, particularly for vulnerable populations such as older adults, who are at increased risk of severe MERS-CoV disease and in whom antibody magnitude, durability, and vaccine responsiveness are often reduced. To address this, the following section presents data from the MERS003 clinical trial in older adults (50–70 years), a group at increased risk of severe MERS disease.

4.2.2 Post-Pandemic Immunogenicity of ChAdOx1 MERS Vaccination in Older Adults (MERS003 Trial)

4.2.2.1 Overview of study design and immunogenicity analyses

The MERS003 clinical trial evaluated the immunogenicity of the ChAdOx1 MERS vaccine in adults aged 50–70 years in Liverpool, United Kingdom. Detailed methodology, including study design, dosing regimen, and participant stratification, is provided in Chapter 2. Briefly, participants were randomized to receive ChAdOx1 MERS or placebo and stratified by prior exposure to ChAdOx1 nCoV-19 vs. a non-ChAdOx1 COVID-19 vaccine. This section presents post-pandemic immunogenicity findings, focusing on how previous exposure to the closely related SARS-CoV-2 virus may modulate immune responses to MERS vaccination. In addition, we examine whether pre-existing immunity to adenoviral vectors influences vaccine-induced responses

Between September 2023 and January 2024, a total of 84 participants aged 50–70 years were enrolled in the MERS003 clinical trial, a double-blinded, placebo-controlled Phase Ic study conducted in Liverpool, United Kingdom, approximately three years after the onset of the COVID-19 pandemic. Participants were randomized in a 5:1 ratio to receive two IM doses of ChAdOx1 MERS (5×10^{10} viral particles) or placebo, administered 84 days apart. The median age of participants was 62 years (range 50–70), and 51% were female. Participants were stratified according to prior exposure to the ChAdOx1 nCoV-19 vaccine: Group 1 (Gp1) comprised individuals previously vaccinated with ChAdOx1 nCoV-19 (n=45; ChAdOx1 MERS, n=37; placebo, n=8), while Group 2 (Gp2) included ChAdOx1 nCoV-19–naïve individuals (n=39; ChAdOx1 MERS, n=33; placebo, n=6). The distribution of participants by group and treatment is illustrated in Figure 4-25, and baseline demographic characteristics are presented in Table 4-9. Characteristics of trial volunteers.

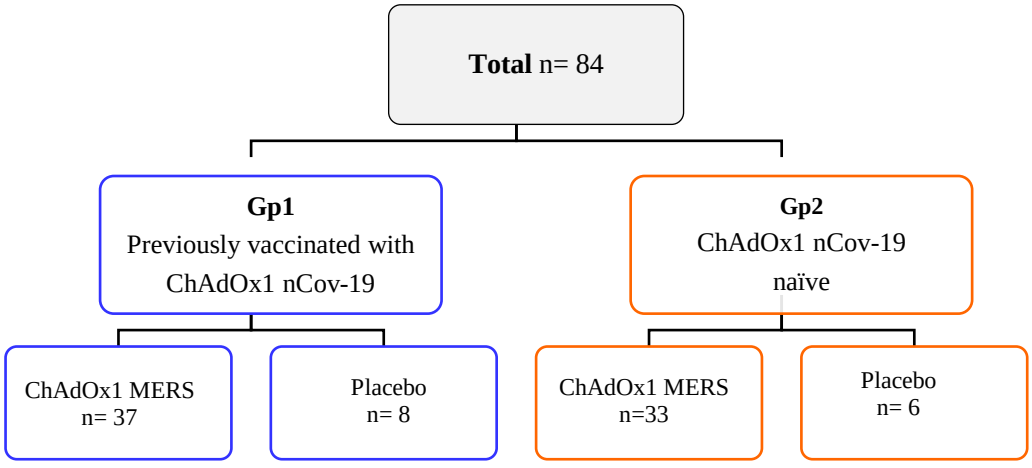


Figure 4-25. Participant distribution and stratification in the MERS003 clinical trial.

		ChAdOx1 exposed group (n=45)	ChAdOx1 naïve (n=39)	All (n=84)
Age, years (range)		63 (51-70)	62 (50-70)	62 (50-70)
Sex	Male	26 (58%)	15 (38%)	41 (49%)
	Female	19 (42%)	24 (62%)	43 (51%)
Ethnicity	White	44 (98%)	36 (92%)	80 (95%)
	Mixed	0	3 (8%)	4 (5%)
	Other	1 (2%)	0	1 (1%)
No. previous ChAdOx1 vaccine doses	0	0	39 (100%)	
	1	0	0	
	2	43 (96%)	0	
	3	2 (4%)	0	

Table 4-9. Characteristics of trial volunteers.
Data are median (range) or n (% of group or trial, depending on column)

4.2.2.2 Baseline SARS-CoV-2 immunity and cross reactivity to MERS-CoV

To investigate whether post-pandemic immunity to SARS-CoV-2 induced cross-reactive anti-MERS responses at baseline, we compared MERS-specific IgG and PNA levels on MERS003 D0 to pre-pandemic MERS001 and MERS002 D0 samples. SARS-CoV-2–specific responses were also measured at baseline and correlated with MERS-specific responses.

Post-pandemic, 16 of 85 (19%) participants were seropositive for MERS-CoV IgG at baseline, compared with 4 of 51 (8%) in the pre-pandemic MERS001 and MERS002 cohorts (Figure 4-26A). Seropositivity was determined as described previously [292] using an in-house ELISA, with the cut-off defined as the mean ± SD of pre-pandemic negative controls (n = 40). Baseline MERS-CoV–specific antibody titres were significantly higher in post-pandemic participants, with median IgG levels of 4.89 [2.34–10.61] IU/mL compared with 2.50 [1.45–6.00] IU/mL in pre-pandemic controls ($p = 0.0269$, Mann–Whitney test). A similar trend was observed for anti-MERS PNA, with median values of 23.8 [1.87–40.41] IU/mL in post-pandemic participants versus undetectable levels in pre-pandemic controls ($n = 17$; $p = 0.0002$) (Figure 4-26B). Baseline anti-MERS S IgG and PNA responses correlated weakly (Figure 4-26C; Spearman $r = 0.22$, $p = 0.04$).

As expected, anti–SARS-CoV-2 responses were detected in MERS003 participants. These were higher than in pre-pandemic controls and IgG and PNA correlated strongly with each other (Figure 4-26D–E; Spearman $r = 0.8$, $p < 0.0001$).

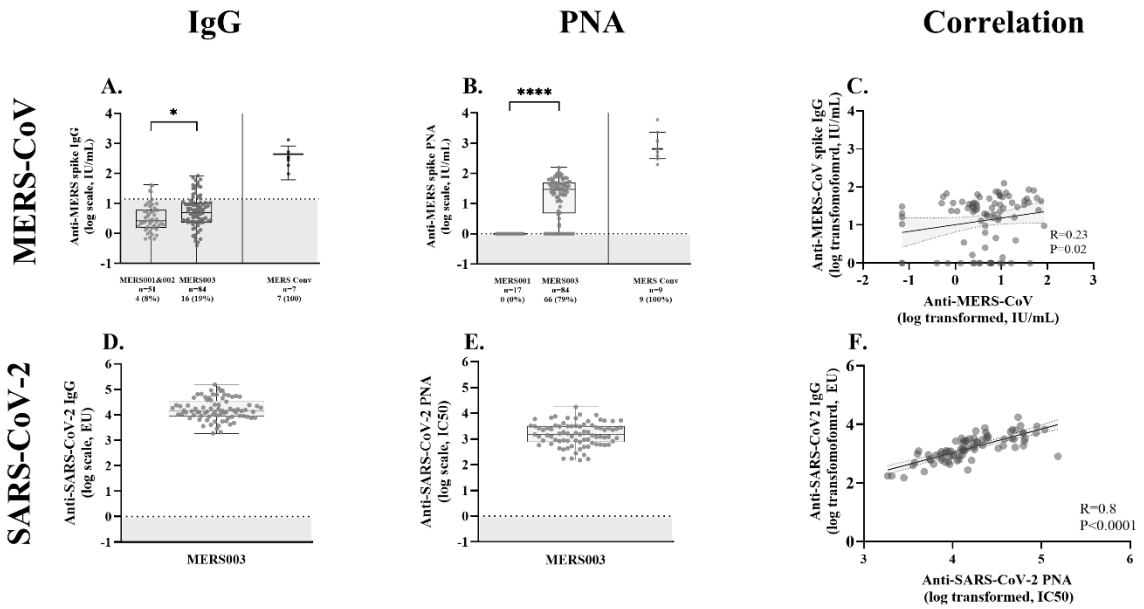


Figure 4-26. Baseline MERS-CoV and SARS-CoV-2 antibody responses in pre- and post-pandemic participants.

(A) Baseline anti–MERS-CoV spike IgG concentrations shown, from left to right, for pre-pandemic participants (MERS001 and MERS002), post-pandemic participants (MERS003), and MERS-CoV convalescent individuals included as a comparator. **(B)** Baseline anti–MERS-CoV pseudoneutralisation assay (PNA) titres displayed in the same group order. **(C)** Correlation between baseline anti–MERS-CoV spike IgG and PNA responses in post-pandemic MERS003 participants (Spearman r = 0.23, p = 0.02). (D–F) Baseline anti–SARS-CoV-2 spike IgG, PNA, and correlation analyses among MERS003 participants, demonstrating a strong association between binding and neutralisation (Spearman r = 0.8, p < 0.0001). Dashed lines indicate seropositivity cut-offs. Statistical comparisons were performed using the Mann–Whitney test; *p < 0.05, ****p < 0.0001.

No significant correlations were observed between MERS-CoV–specific and SARS-CoV-2–specific binding or neutralising antibody responses (Figure 4-27A-B). In MERS003 participants, baseline anti-MERS spike IgG showed only a weak association with SARS-CoV-2 neutralising antibody titres (r = 0.20), which did not reach statistical significance (p = 0.05; Figure 4-27C). No reciprocal association was observed between SARS-CoV-2 binding antibodies and MERS-CoV neutralising activity (Figure 4-27D). Collectively, these findings indicate minimal cross-neutralisation between MERS-CoV and SARS-CoV-2, despite detectable cross-reactive binding responses.

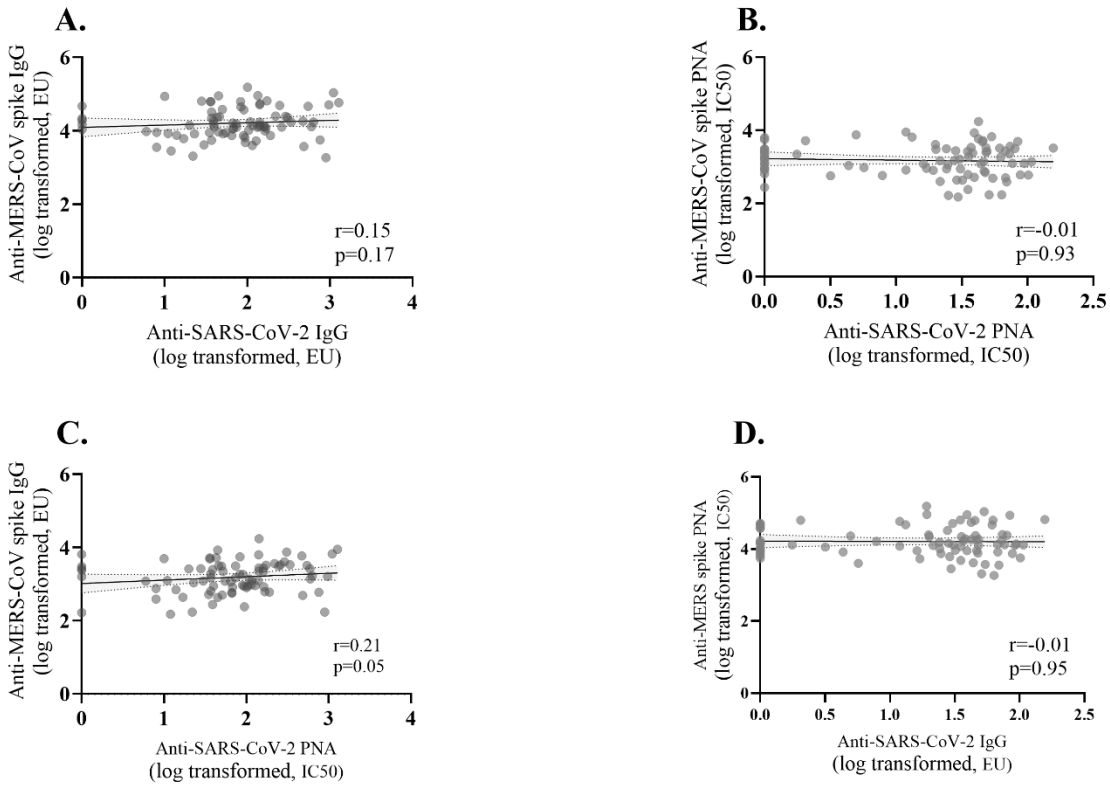


Figure 4-27. Baseline correlation between MERS-CoV and SARS-CoV-2 antibody responses in post-pandemic participants.

(A) Correlation between anti–MERS-CoV spike IgG and anti–SARS-CoV-2 spike IgG responses. **(B)** Correlation between anti–MERS-CoV spike PNA and anti–SARS-CoV-2 PNA responses. **(C)** Correlation between anti–MERS-CoV spike IgG and anti–SARS-CoV-2 PNA responses. **(D)** Correlation between anti–MERS-CoV spike PNA and anti–SARS-CoV-2 IgG responses. Each data point represents an individual participant. Correlations were assessed using Spearman's rank correlation test. No significant associations were observed between MERS-CoV– and SARS-CoV-2–specific antibody responses.

4.2.2.3 Anti-MERS-CoV specific immunogenicity of ChAdOx1 MERS

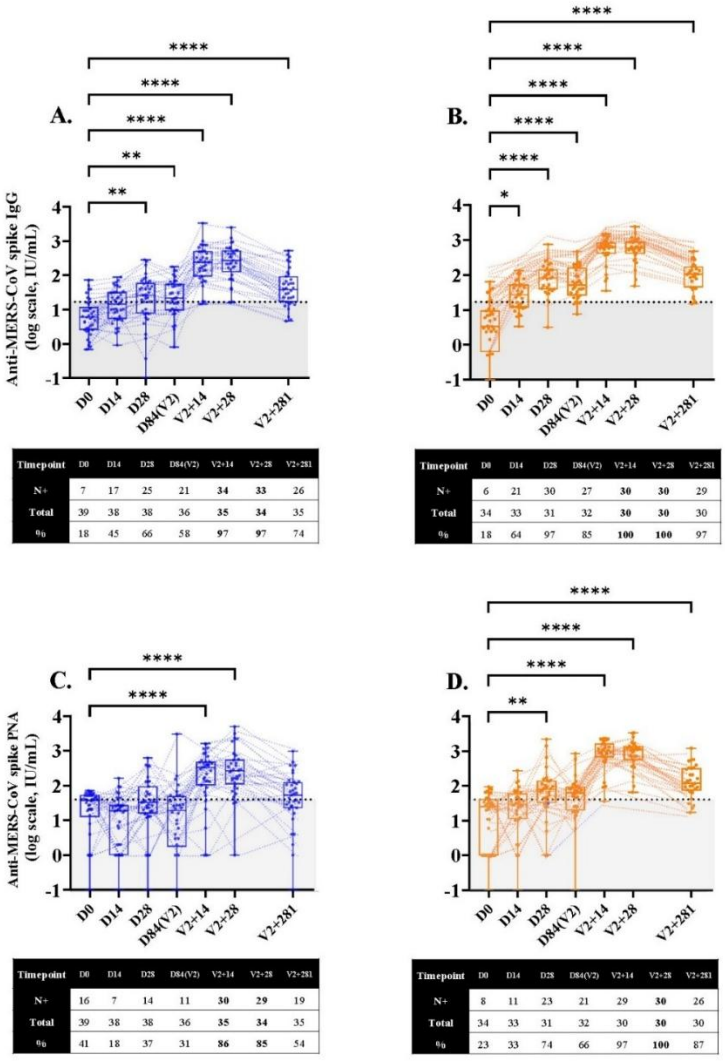
Prime vaccination induced IgG responses that were significantly higher than baseline by day 14 in ChAdOx1-naïve participants (p= 0.04, 64% seropositive; Figure 4-28B); this increase was delayed until day 28 in ChAdOx1-experienced participants (p= 0.0059; 66% seropositive; Figure 4-28A). In both groups, IgG titres peaked at day 28 and remained significantly above baseline at day 84, although the proportion of seropositive individuals declined from 97% to 85% in the ChAdOx1-naïve group and from 66% to 58% in the ChAdOx1-experienced group (Figure 4-28A-B).

Administration of a second dose boosted binding IgG responses in both groups, with peak levels observed at day 28 post-boost (100% seropositive in ChAdOx1-naïve and 97% seropositive in ChAdOx1-experienced participants). The fold change between pre- and post-boost levels was similar in both groups (12.5-fold in ChAdOx1-experienced and 11.5-fold in ChAdOx1-naïve participants).

Anti-MERS spike IgG remained significantly higher than baseline at all post–second-dose time points ($p < 0.0001$) with 74% seropositive in ChAdOx1-experienced participants and 97% in ChAdOx1-naïve participants at 281 days post-boost (i.e. one year post-prime) (Figure 4-28A-B).

Induction of neutralising antibodies was limited in individuals with prior ChAdOx1 exposure (Figure 4-28C). Levels were only significantly above baseline after the second dose at day 14 (86% seropositive; $p < 0.0001$) and day 28 (85% seropositive; $p < 0.0006$). By day 281 post–second dose, the median PNA titre was 53 [23–124] IU/mL, comparable to baseline values of 38 [13–53] IU/mL ($p = 0.31$), indicating limited durability of the neutralising response.

In contrast, ChAdOx1-naïve participants demonstrated a more robust induction of neutralising antibodies (Figure 4-28D). Responses were detectable by day 28 after the first dose (74% seropositive; $p = 0.0045$), and the second dose further boosted neutralising antibody levels (100% seropositive at day 28 post-boost). By day 281, median PNA levels remained significantly above baseline (120 [74–321] vs 25 [1–42] IU/mL; $p < 0.0001$; 87% seropositive).



Timepoint	D0	D14	D28	D84(V2)	V2+14	V2+28	V2+281
N+	7	17	25	21	**34**	**33**	26
Total	39	38	38	36	**35**	**34**	35
%	18	45	66	58	**97**	**97**	74

Timepoint	D0	D14	D28	D84(V2)	V2+14	V2+28	V2+281
N+	6	21	30	27	**30**	**30**	29
Total	34	33	31	32	**30**	**30**	30
%	18	64	97	85	**100**	**100**	97

Timepoint	D0	D14	D28	D84(V2)	V2+14	V2+28	V2+281
N+	16	7	14	11	**30**	**29**	19
Total	39	38	38	36	**35**	**34**	35
%	41	18	37	31	**86**	**85**	54

Timepoint	D0	D14	D28	D84(V2)	V2+14	V2+28	V2+281
N+	8	11	23	21	29	**30**	26
Total	34	33	31	32	30	**30**	30
%	23	33	74	66	97	**100**	87

Figure 4-28. Kinetics of anti-MERS spike IgG and pseudoneutralisation antibody (PNA) responses following ChAdOx1 MERS vaccination in ChAdOx1-experienced and ChAdOx1-naïve participants.

(A–B) Anti-MERS-CoV spike IgG responses in and ChAdOx1-experienced (A; blue) and ChAdOx1-naïve (B; orange) participants. **(C–D)** Corresponding anti-MERS-CoV spike PNA responses in ChAdOx1-experienced (C; blue) and ChAdOx1-naïve (D; orange) participants. Each point represents an individual participant, and box plots indicate the median and interquartile range (IQR). Dotted lines connect paired samples from the same participant over time. Shaded areas represent values below the assay's limit of detection. The number and percentage of seropositive participants (N^+/Total, %) at each time point are listed below each panel. Statistical significance relative to baseline (Day 0) was determined using the Kruskal–Wallis test followed by Dunn's multiple-comparison correction. $p < 0.05$, ** $p < 0.01$, *** $p < 0.001$, **** $p < 0.0001$.

Compared with the placebo, IgG responses at day 28 after the first dose in ChAdOx1-naïve participants transiently exceeded those of the placebo (Figure 4-29B). Otherwise, in both groups, IgG and PNA responses were significantly higher than those of the negative control (placebo) group only after the second dose Figure 4-29A-D, indicating that booster vaccination is required to achieve responses above background.

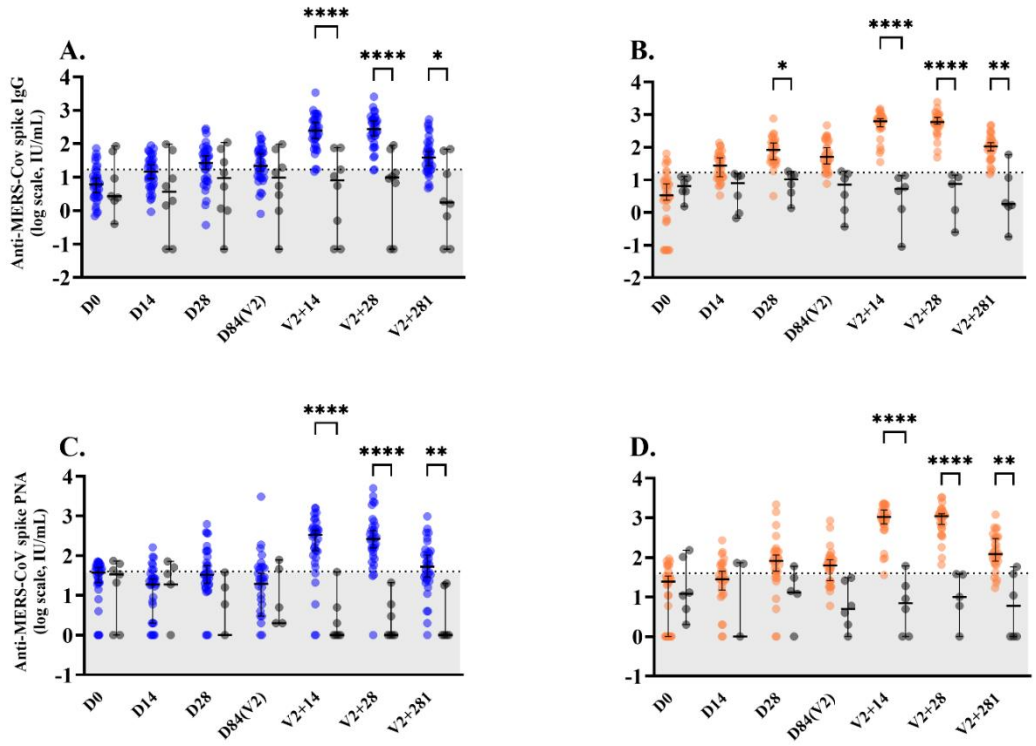


Figure 4-29. Anti–MERS-CoV spike IgG and pseudoneutralisation antibody (PNA) responses following ChAdOx1 MERS vaccination compared with negative controls in ChAdOx1-experienced and ChAdOx1-naïve.

(A–B) Anti–MERS-CoV spike IgG responses in ChAdOx1-experienced participants (B; blue; n = 33) and ChAdOx1-naïve participants (A; orange; n = 37) and **(C–D)** Corresponding anti–MERS-CoV spike PNA responses in ChAdOx1-experienced (D; blue; n = 33) and ChAdOx1-naïve (C; orange; n = 37) participants. Negative control (NC) samples are shown in black (n = 8 for ChAdOx1-naïve comparison; n = 6 for ChAdOx1-experienced comparison). Each point represents an individual participant, with horizontal bars indicating the median and interquartile range (IQR). Shaded regions denote values below the assay limit of detection. Statistical significance at each time point was assessed relative to the negative control (NC) using the Kruskal–Wallis test with Dunn's multiple-comparison correction. *$p < 0.05$, **$p < 0.01$, ***$p < 0.001$, ****$p < 0.000$.

Between-group comparisons demonstrated that antibody levels were consistently higher in ChAdOx1 naïve individuals compared with those with a history of ChAdOx1 vaccination (Figure 4-30A,D) . Differences were evident early after the first dose, appearing by day 14 for binding IgG (Figure 4-30B) and by for neutralising antibodies (Figure 4-30E), and these differences persisted following the second dose through to the final sampling time point (Figure 4-30B,E). The magnitude of these differences is summarised in Table 4-10. Seropositivity rates for both IgG and PNA were higher in ChAdOx1-naïve participants, reaching 100% for both measurements by day 28 after the second dose. At the final time point (day 281), seropositivity rates remained higher in the naïve group compared with the experienced group (97% versus 74% for IgG and 87% versus 54% for PNA) (Figure 4-28C,F). These findings indicate that differences between groups emerged early and were maintained over time, suggesting that both the magnitude and durability of the antibody response were greater in ChAdOx1-naïve participants.

	IgG (IU/mL)			PNA (IU/mL)		
	Gp1	Gp2	P	Gp1	Gp2	P
D0	6 [3–12]	3 [1–10]	0.128977	38 [13–53]	25 [1–42]	0.328283
D14	15 [5–32]	27 [12–53]	0.016808	19 [1–28]	30 [11–61]	0.019467
D28	26 [8–60]	83 [39–143]	0.000148	33 [16–94]	80 [32–140]	0.026281
D84	22 [10–57]	51 [26–161]	0.004170	30 [2–50]	62 [20–93]	0.000875
V2+14	243 [94–513]	627 [409–863]	0.001273	332 [102–489]	997 [668–1657]	0.000004
V2+28	275 [125–536]	589 [413–914]	0.001759	264 [110–554]	1079 [556–1385]	0.000151
V2+281	39 [17–94]	106 [44–175]	0.002852	53 [23–124]	120 [74–321]	0.003146

Table 4-10. Median (IQR) antibody responses between groups at each time point.

Median and interquartile range (IQR) values are shown for each group at all sampling time points. Statistical comparisons between ChAdOx1-experienced (Gp1) and ChAdOx1-naïve (Gp2) participants were performed using the Mann–Whitney U test with false discovery rate (FDR) adjustment for multiple comparisons.

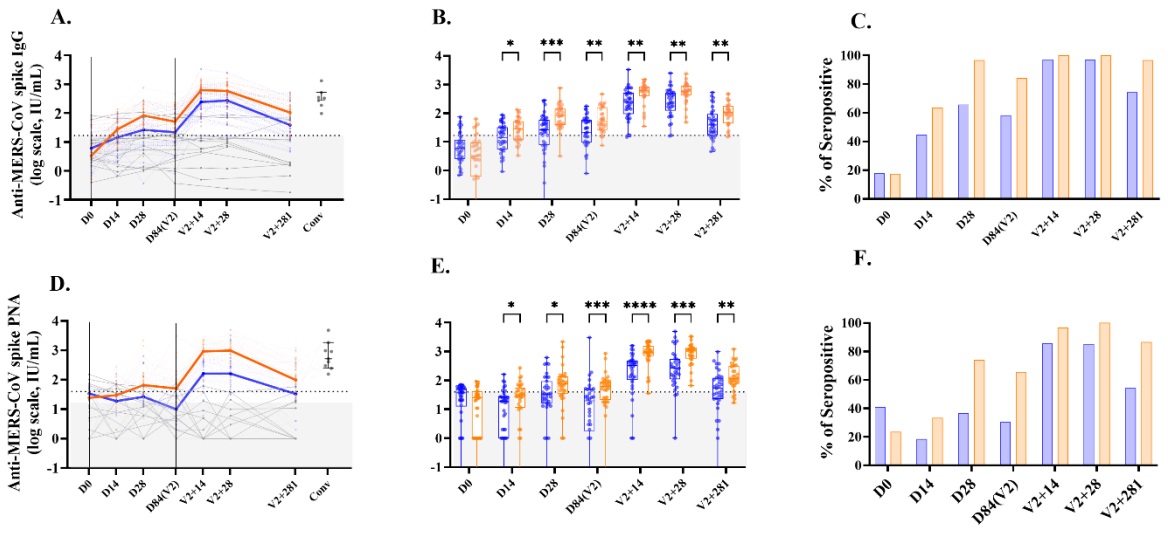


Figure 4-30. Comparison of anti–MERS-CoV spike IgG and pseudoneutralisation antibody (PNA) responses between ChAdOx1-naïve and ChAdOx1-experienced participants following ChAdOx1 MERS vaccination.

(A–C) Anti–MERS-CoV spike IgG responses and seropositivity rates over time. **(D–F)** Corresponding anti–MERS-CoV spike PNA responses and seropositivity rates over time. Responses in ChAdOx1-naïve (orange) and ChAdOx1-experienced (blue) participants are shown across all time points and compared directly at each time point. Statistical comparisons between groups were performed using the Mann–Whitney U test with false discovery rate (FDR) adjustment. *p < 0.05, **p < 0.01, ***p < 0.001, ****p < 0.0001.

To estimate the decay rate of antibodies following the booster dose, an exponential decay model was initially applied. However, as only two early time points (day 14 and day 28) and one late time point (day 281) were available after the booster, the model could not reliably fit a biphasic decay curve and was associated with considerable uncertainty in the data (Figure 4-31A-B). Accordingly, antibody half-life was estimated using an alternative half-life calculation approach based on $\log_2$-transformed data, as described previously [331] and outlined in 3.2.3 of the previous chapter.

The half-life of binding and neutralising antibodies was very similar between groups. The median half-life of anti-MERS spike IgG was 109 days [IQR: 78-170] in ChAdOx1-experienced participants and 110 days [IQR: 76-161] in ChAdOx1-naïve participants (p = 0.7). For detectable PNA titres, the estimated median half-life was 109 days [IQR:83-136] in experienced and 110 days [IQR: 66-178] in naïve participants (p = 0.9).

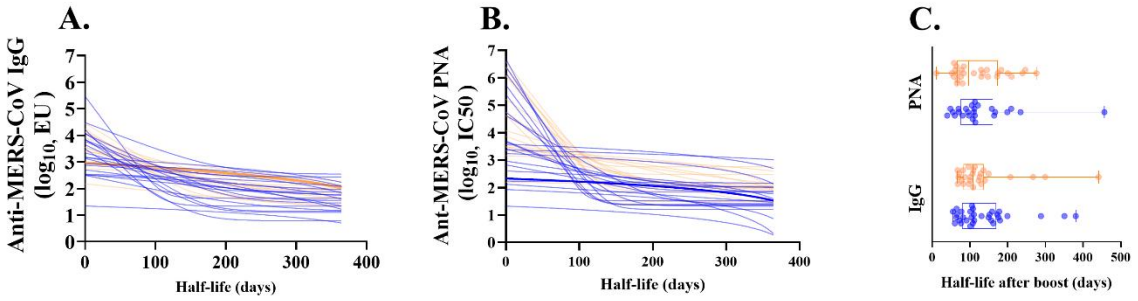


Figure 4-31. Antibody decay kinetics and half-life following ChAdOx1 MERS vaccination.

Panels A and B show the decay of anti-MERS spike IgG **(A)** and pseudoneutralisation antibody (PNA) **(B)** levels over time after the second dose. **(C)** estimated antibody half-life for IgG and PNA in ChAdOx1-experienced (blue) and ChAdOx1-naïve (orange) participants. Statistical comparisons between groups were performed using the Mann–Whitney U test with false discovery rate (FDR) adjustment for multiple comparisons. * $p < 0.05$, ** $p < 0.01$, *** $p < 0.001$.

Binding IgG and neutralising antibody levels correlated strongly overall ($R = 0.8$, $p < 0.0001$; Figure 4-32A).This association was tighter in MERS-naïve participants ($R = 0.90$, $p < 0.0001$; Figure 4-32C) than in ChAdOx1-experienced participants ($R = 0.90$, $p < 0.0001$; Figure 4-32C) than in ChAdOx1-experienced participants ($R = 0.7$, $p < 0.0001$; Figure 4-32B). Although ChAdOx1-experienced participants exhibited lower binding IgG and neutralising antibody levels overall, the weaker correlation indicates greater variability in the relationship between binding and neutralisation rather than a selective reduction in neutralising activity per unit IgG. This is consistent with pre-existing anti-vector immunity primarily reducing the overall magnitude of the humoral response, with secondary effects on neutralising antibody levels.

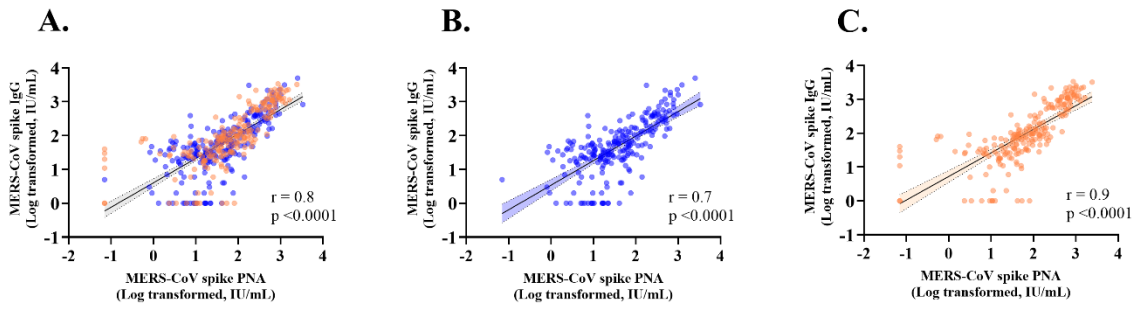


Figure 4-32. Spearman correlation between binding IgG and neutralising antibody (PNA) responses to MERS-CoV.

(A) shows the correlation when all participants were combined, while **(B)** and **(C)** show correlations within the ChAdOx1-experienced (blue) and ChAdOx1-naïve (orange) groups, respectively. Spearman's rank correlation coefficient (r) and corresponding p-values are indicated on each plot.

4.2.2.4 Anti-vector immunity and vaccine induced responses

To assess the extent of anti-vector immunity and its impact on transgene immunogenicity following vaccination, we measured neutralisation of the ChAdOx1 vector at baseline (day 0) and pre-boost (day 84) using a modified ChAdOx1 SEAP assay. The assay was adapted from a previously published protocol with modifications to increase throughput, as described in Chapter 2. These readouts were then correlated with vaccine-induced immune responses at all assessed time points.

As expected, anti-vector immunity was higher in individuals with a prior history of ChAdOx1 vaccination compared to ChAdOx1-naïve individuals. At baseline, the median ChAdOx1 nAb titre in previously vaccinated participants was 116 [70–226], compared with 21 [2–40] in ChAdOx1-naïve participants ($p < 0.000$; Figure 4-33B). Anti-vector immunity increased further after the first dose in both groups, with a 13-fold overall increase ($p < 0.0001$; Figure 4-33A), corresponding to 12-fold and 14-fold increases in previously vaccinated and naïve individuals, respectively, showing comparable fold changes between the two groups ($p = 0.7$). By day 84, anti-vector nAb titres remained higher in individuals with prior ChAdOx1 vaccination compared to naïve individuals ($p = 0.0008$; Figure 4-33B). These findings show that vaccination enhances anti-vector immunity, which remains higher in previously vaccinated individuals, and that baseline anti-vector levels largely determine the magnitude of the response.

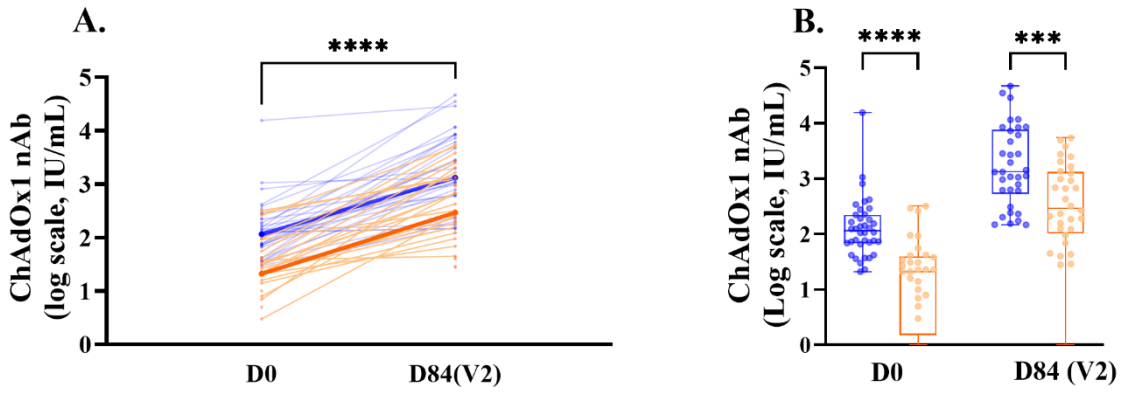


Figure 4-33 ChAdOx1 anti-vector neutralising antibodies following vaccination.

(A) Anti-vector neutralising antibody (nAb) titres measured at baseline (D0) and 84 days before the administration of the second vaccination (D84, V2). Each thin line represents an individual participant; the thick line represents the median value for each group. Statistical significance was determined using a paired Wilcoxon test. **(B)** Anti-vector neutralising antibody (nAb) titers measured at D0 and D84 (V2) in both groups. Data are shown as box-and-whisker plots (median with interquartile range) with individual data points overlaid. Statistical significance was assessed using multiple paired Mann–Whitney tests with false discovery rate (FDR) correction (*$p < 0.05$). Blue indicates participants previously vaccinated with ChAdOx1, and orange indicates ChAdOx1-naive participants.

Baseline anti-vector immunity, analysed across both groups, correlated negatively with anti-MERS IgG and PNA responses (Table 4-11; Figure 4-34A,C,E,G). Significant negative correlations were observed at day 28 after the first dose for anti-MERS IgG ($r = -0.30$, $p = 0.02$; Figure 4-34A) and PNA ($r = -0.32$, $p = 0.0086$; Figure 4-34C). These associations persisted following the second dose, with stronger negative correlations at day 14 post-boost for anti-MERS IgG ($r = -0.46$, $p = 0.0002$; Figure 4-34E) and PNA ($r = -0.32$, $p = 0.0097$; Figure 4-34G).

Pre-boost anti-vector neutralising antibody levels were also negatively associated with anti-MERS IgG induction at day 14 post-boost ($r = -0.32$, $p = 0.009$; Figure 4-34F), whereas no significant association was observed with PNA responses ($r = -0.18$, $p = 0.15$; Figure 4-34H).

When groups were analysed separately, no significant effect of baseline anti-vector immunity was observed in ChAdOx1-experienced participants (Table 4-11). In contrast, among ChAdOx1-naïve participants, higher baseline anti-vector antibody levels were associated with reduced peak anti-MERS binding IgG responses following the second dose at day V2+14 ($R = -0.40$, $p = 0.03$; Table 4-11). This effect was confined to binding anti-MERS antibody responses, with no significant correlations observed for PNA responses (Table 4-11).

When anti-vector antibody levels measured pre-boost (day V2) were considered, higher titres were associated with lower day 28 anti-MERS IgG responses in the combined cohort ($R = -0.32$, $p = 0.009$; Table 4-11; Figure 4-34B). This relationship was evident only in ChAdOx1-naïve participants ($R = -0.40$, $p = 0.04$; Table 4-11) and not in ChAdOx1-experienced participants ($R = -0.01$, $p = 0.95$; Table 4-11), indicating that the effect observed in the combined analysis was largely driven by the ChAdOx1 naïve group. Consistent with this, pre-boost anti-vector neutralising antibody levels in ChAdOx1-naïve participants also correlated negatively with anti-MERS IgG induction at day 14 post-boost ($r = -0.36$, $p = 0.05$).

As anti-vector antibodies were measured only at baseline and pre-boost, these findings should be interpreted as associations rather than evidence of a causal effect of post-prime anti-vector immunity on earlier antibody responses, and may reflect the development of cross-reactive anti-vector immunity following the first dose in the ChAdOx1 naïve participants.

Collectively, these results suggest that ChAdOx1-naïve individuals are more susceptible to the effects of pre-existing or vaccine-induced anti-vector neutralising antibodies. In contrast, the lower responses observed in ChAdOx1-experienced compared with ChAdOx1-naïve participants may indicate the involvement of additional mechanisms of anti-vector immunity that are not fully captured by anti-vector neutralising antibody measurements alone.

These findings suggest that naïve individuals are more affected by pre-existing or vaccine-induced anti-vector neutralising antibodies. Furthermore, the lower responses observed in Group 1 compared to Group 2 may indicate the involvement of alternative mechanisms of anti-vector immunity not captured solely by neutralising antibody measurements.

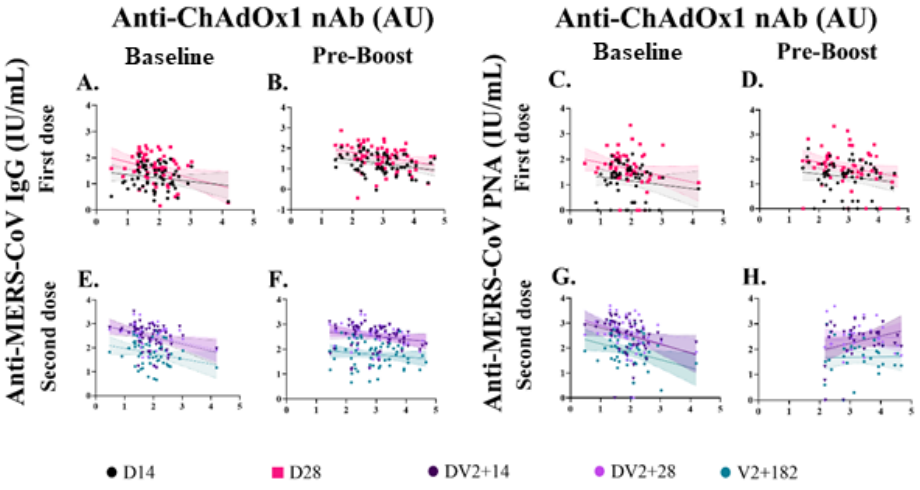


Figure 4-34. Spearman correlation between anti-vector immunity and MERS-specific antibody responses.

Baseline and pre-boost anti-ChAdOx1 neutralising antibody (nAb) titres were correlated with MERS-specific IgG **(A–B, E–F)** and PNA **(C–D, G–H)** responses following the first and second doses. Each dot represents an individual participant, and shaded areas indicate the 95% confidence interval of the regression line. Colours denote sampling time points: black (day 14 post-prime), pink (day 28 post-prime), purple (day 14 post-boost), violet (day 28 post-boost), and turquoise (day 182 post-boost). Negative correlations indicate that higher anti-vector titres were associated with lower vaccine-induced MERS antibody responses.

		MERS_S_IgG_(IU/mL)						MERS_S_PNA_(IU/mL)					
		D14	D28	D84	V2+14	V2+28	V2+281	D14	D28	D84	V2+14	V2+28	V2+281
All	Baseline	-0.16	-0.28*	-0.22	-0.46***	-0.38**	-0.29*	-0.29*	-0.32**	-0.28*	-0.32**	-0.33**	-0.27*
	Pre-boost	-0.32**	-0.32**	-0.27*	-0.32**	-0.33***	-0.2	-0.2	-0.24	-0.14	-0.18	-0.19	-0.22
ChAdOx1 experienced	Baseline	0.01	-0.05	0.02	-0.04	0.1	0.14	-0.2	-0.26	0.08	-0.09	-0.16	0.02
	Pre-boost	-0.18	-0.01	-0.15	-0.08	-0.09	0.03	-0.09	-0.18	0.03	0.09	0.03	-0.02
ChAdOx1 naïve	Baseline	0.17	0.19	0.21	-0.4*	-0.19	-0.01	0.04	-0.14	-0.02	-0.23	-0.21	0.05
	Pre-boost	-0.34	-0.37*	-0.1	-0.36*	-0.3	-0.16	-0.2	-0.17	-0.04	0.01	-0.06	-0.15

Table 4-11. Spearman correlation between anti-ChAdOx1 neutralising antibody titers and MERS-specific IgG or PNA responses.

Shown are correlation coefficients (R) for baseline and pre-boost anti-vector titers across all participants and within each group (Gp1, ChAdOx1-experienced; Gp2, ChAdOx1-naïve). Red and blue shading indicate negative and positive correlations, respectively. *p < 0.05, **p < 0.01, ***p < 0.001.

4.2.2.5 SARS-CoV-2 and effect of immune imprinting.

To assess the effect of pre-existing anti–SARS-CoV-2 antibodies on the response to MERS vaccination, anti–SARS-CoV-2 IgG levels were measured at baseline (day 0) and day 28, while neutralising activity against the SARS-CoV-2 Wuhan strain was evaluated using a lentivirus-based pseudovirus neutralisation assay at day 0, day 28 post-prime, and 28 days post-boost (V2+D28). Compared with baseline, anti–SARS-CoV-2 IgG and neutralising antibody levels did not change after the first dose Figure 4-35A. When compared between groups, SARS-CoV-2 antibody responses were lower in the ChAdOx1-experienced group at baseline, although these differences were not statistically significant (1.4-fold difference in both IgG (p = 0.2) and PNA (p = 0.9); Figure 4-35B). Interestingly, in the ChAdOx1-experienced group, SARS-CoV-2 neutralising antibody levels decreased after the second dose (V2+D28) compared with both baseline and day 28 following the first dose Figure 4-35C. At this day V2+D28, neutralising antibody levels were lower than those observed in the ChAdOx1-naïve group (1049 [688–3003] vs 2602 [1522–3644] IU/mL), representing a 2.5-fold difference (p = 0.04; Figure 4-35D). Overall, these findings indicate that MERS vaccination did not induce cross-reactive or back-boosting effects on SARS-CoV-2 antibodies; instead, a modest decline in SARS-CoV-2 antibody levels was observed, particularly among ChAdOx1-experienced participants.

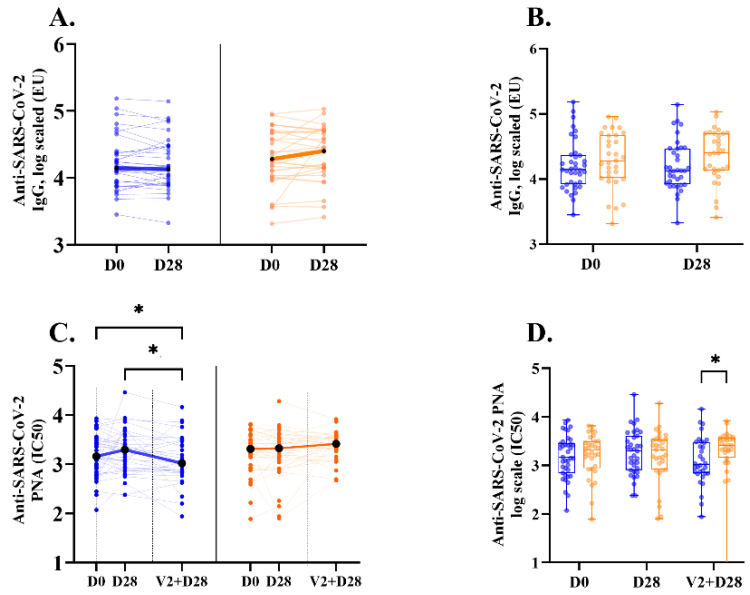


Figure 4-35 Baseline and post-vaccination SARS-CoV-2 antibody responses following ChAdOx1 MERS vaccination.

Panel **A** shows anti–SARS-CoV-2 spike IgG at baseline (D0) and day 28 (D28), and panel **C** shows pseudoneutralisation antibody (PNA) at D0, D28, and 28 days after the second dose (V2+D28) for each group separately. Panels **B** and **D** present between-group comparisons for ChAdOx1-experienced (blue) and ChAdOx1-naïve (orange) participants. Within-group comparisons (A, C) were performed using the Wilcoxon matched-pairs signed-rank test, and between-group comparisons (B, D) using multiple t tests with FDR adjustment. * $p < 0.05$.

No correlation was observed between baseline anti–SARS-CoV-2 antibody levels and MERS vaccine–induced responses when all doses and time points were analysed together (Table 4-12). However, when groups were analysed separately, baseline anti–SARS-CoV-2 IgG levels in ChAdOx1-naïve participants correlated positively with early MERS-specific pseudoneutralisation (PNA) responses at day 14 following the first dose (R = 0.43, p = 0.01; Table 4-12).

In addition, anti–SARS-CoV-2 IgG and anti–SARS-CoV-2 PNA measured at day 28 in ChAdOx1 naïve participants correlated positively with MERS-specific PNA measured at day 14 (R = 0.40, p = 0.02 and R = 0.40, p = 0.05, respectively), suggesting a transient association between early MERS-specific functional responses and contemporaneous SARS-CoV-2 antibody levels. No further correlations were observed at later time points, indicating that this association was short-lived.

Following the second dose, anti–SARS-CoV-2 PNA measured at day V2+D28 correlated positively with MERS-specific IgG measured at the same time point and at day V2+D28+1 (R = 0.27, p = 0.006; Table 4-12). This relationship was evident only when data from both groups were analysed together, suggesting a broadly shared antibody response profile rather than a group-specific effect.

			MERS_S_IgG_(IU/mL)						MERS_S_PNA_(IU/mL)					
	Anti-SARS-CoV-2		D14	D28	D84(V2)	V2+14	V2+28	V2+281	D14	D28	D84(V2)	V2+14	V2+28	V2+281
all	IgG	Baseline	0.01	0.04	-0.01	-0.05	0.06	0.11	0.20	-0.09	-0.03	0.05	-0.02	0.03
		D28	0.10	0.10	0.06	-0.01	0.07	0.17	0.16	-0.04	0.01	0.06	0.01	0.09
	PNA	Baseline	0.12	0.10	0.02	-0.13	-0.02	0.01	0.22	-0.01	-0.03	-0.07	-0.01	-0.10
		D28	0.05	0.18	0.11	-0.02	0.05	0.18	0.12	0.02	0.12	-0.03	-0.02	0.14
		V2+D28	0.29*	0.24	0.23	0.21	0.27*	0.36**	0.27*	0.08	0.19	0.21	0.19	0.24
Gp1	IgG	Baseline	-0.01	-0.07	-0.04	-0.13	-0.21	-0.09	-0.07	-0.16	-0.11	-0.18	-0.24	-0.24
		D28	0.05	-0.03	-0.03	-0.10	-0.17	-0.04	-0.10	-0.14	-0.05	-0.17	-0.18	-0.27
	PNA	Baseline	0.27	0.17	0.09	-0.08	-0.14	0.03	0.12	0.11	-0.10	-0.10	-0.15	-0.26
		D28	0.10	0.19	0.19	0.00	-0.05	0.18	-0.07	0.03	0.18	-0.04	-0.03	0.04
		V2+D28	0.35	0.36	0.27	0.14	0.12	0.30	0.20	0.12	0.23	0.12	0.08	0.03
Gp2	IgG	Baseline	-0.03	0.04	-0.03	0.00	0.18	0.21	0.42*	-0.09	0.03	0.21	0.10	0.14
		D28	0.01	0.03	-0.04	0.00	0.11	0.20	0.40*	-0.08	-0.05	0.06	0.05	0.19
	PNA	Baseline	-0.07	-0.03	-0.11	-0.22	0.00	-0.03	0.31	-0.15	-0.06	-0.11	0.10	-0.05
		D28	-0.02	0.12	0.02	-0.03	0.12	0.18	0.35*	0.04	0.06	-0.05	0.03	0.19
		V2+D28	0.12	0.05	0.08	0.14	0.25	0.25	0.31	-0.06	-0.05	0.18	0.16	0.17

Table 4-12. Spearman correlation between anti–SARS-CoV-2 and MERS-specific IgG or PNA responses. Shown are correlation coefficients (R) at baseline (D0), day 28 (D28), and 28 days after the second dose (V2+D28), calculated across all participants and within each group (Gp1, ChAdOx1-experienced; Gp2, ChAdOx1-naïve). Blue and red shading indicate positive and negative correlations, respectively. *p < 0.05, **p < 0.01, ***p < 0.001.

4.2.2.6 SARS-CoV-2 responses and effect of Immune imprinting on response to MERS-CoV vaccination

To investigate the influence of prior SARS-CoV-2 exposure—through infection or vaccination—on antibody responses to ChAdOx1 MERS vaccination, and to assess the contribution of pre-existing ChAdOx1 anti-vector immunity, antibody responses in MERS003 participants were compared with pre-pandemic cohorts at equivalent peak time points following vaccination (Figure 4-36).

Peak post-prime responses in MERS003 (day 28 post-prime) were compared with those from the pre-pandemic MERS001 trial, in which participants received a single high-dose vaccination identical to that used in MERS003 (day 28 post-prime; n = 9). Peak post-boost responses in MERS003 (day V2+14) were compared with a small exploratory pre-pandemic participant group in the PB study (n = 3) who received two medium doses administered at either short (28 days) or long (182 days) intervals.

In addition, vaccine-induced responses were compared with antibody levels observed in MERS convalescent individuals from both the pre-pandemic (n = 9) and post-pandemic (n = 13) periods, the latter representing the MERS-CoV/SARS-CoV-2 hybrid group examined in this chapter.

MERS003 ChAdOx1-naïve older adults showed post-prime MERS-CoV–specific IgG and PNA responses comparable to those observed in younger pre-pandemic participants (median IgG 83 [39–143] IU/mL vs 105 [61–128] IU/mL, p = 0.9; median PNA 80 [32–140] IU/mL vs 261 [182–389] IU/mL, p = 0.2; Figure 4-36A,C). In contrast, MERS003 ChAdOx1-experienced older adults exhibited significantly lower post-prime IgG and PNA responses than younger pre-pandemic participants (median IgG 26.7 [8–60] AU/mL, p = 0.00071; median PNA 33 [16–94] IU/mL, p = 0.02; Figure 4-36A,C). Together, these findings suggest that age alone has a limited effect on vaccine-induced responses, whereas pre-existing anti-vector immunity resulting from prior ChAdOx1 exposure substantially dampens immunogenicity. This attenuation may need to be considered when designing dosing strategies for individuals with prior adenoviral vector exposure.

At the peak post-boost time point (day V2+14), IgG and PNA antibody levels in vaccinated participants in MERS003 were similar in magnitude to those observed in MERS convalescent individuals. Antibody levels were modestly lower in previously ChAdOx1-vaccinated participants (approximately 1.4-fold lower for both IgG and PNA; IgG p > 0.99, PNA p = 0.2; Figure 4-36B,D), and were also slightly lower

in ChAdOx1-naïve participants compared with convalescent individuals (approximately 1.5-fold lower for both IgG and PNA; $p > 0.99$ for both comparisons; Figure 4-36B,D). These differences were not statistically significant.

The convalescent participants had recovered approximately two years prior to sample collection, indicating that measurable MERS-specific antibody responses can persist long term following natural infection, although the peak antibody levels present shortly after infection are unknown. Importantly, the antibody level required for protection against MERS-CoV infection is currently unknown, and no correlate of protection has been established.

Furthermore, antibody levels in ChAdOx1-naïve vaccinees exceeded those observed in individuals with "hybrid" MERS immunity (previous MERS infection followed by COVID-19 vaccination), with 5.4-fold higher anti-MERS IgG ($p = 0.0007$; Figure 4-36B) and 11-fold higher PNA responses ($p < 0.0001$; Figure 4-36D). Together, these findings demonstrate that ChAdOx1 MERS vaccination can induce antibody responses in older adults that are comparable in magnitude to those observed in individuals with prior MERS infection at a late convalescent time point. In addition, antibody responses in ChAdOx1-naïve vaccinees exceeded those observed in individuals with post-pandemic 'hybrid' MERS immunity, supporting the immunogenicity of this vaccination regimen in older populations.

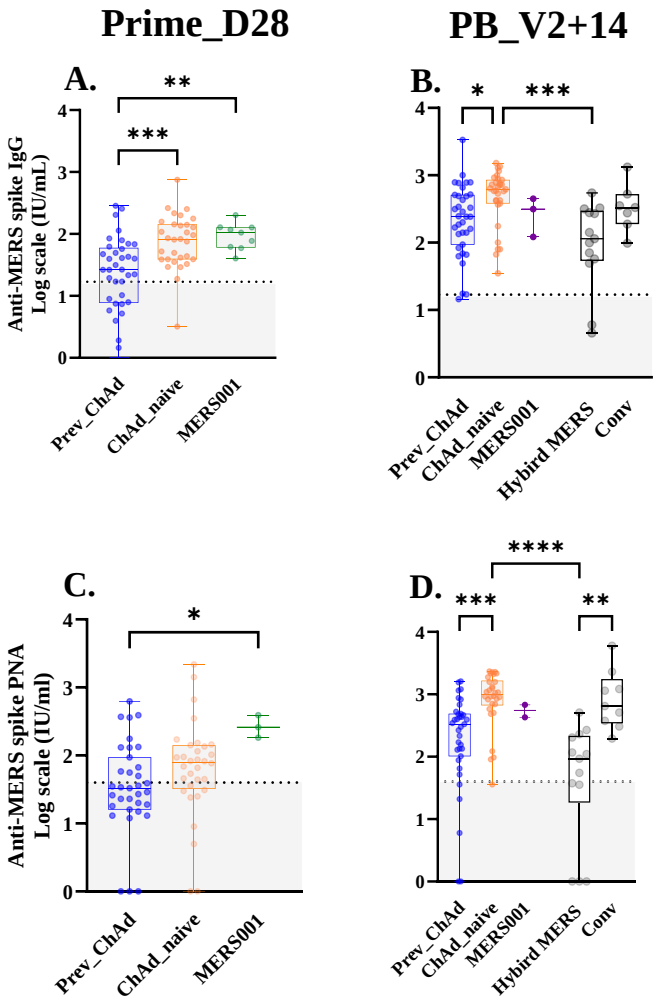


Figure 4-36. Anti-MERS spike antibody responses following primary and booster vaccination.

Anti-MERS spike IgG **(A–B)** and pseudoneutralising antibody (PNA) **(C–D)** responses were measured on day 28 after the first dose (A and C) and at the peak time point following the booster dose (PB_V2+14; B and D). Groups include previously vaccinated ChAdOx1 recipients (MERS003_Prev ChAd; blue), ChAdOx1-naïve participants (ChAd-naïve_MERS003; orange), MERS001 vaccinees (MERS001; green), hybrid MERS participants (homologous PB medium-dose regimen; black), and hybrid convalescent individuals (Conv; MERS-CoV post-pandemic individuals vaccinated with a COVID-19 vaccine; grey). Each dot represents an individual participant. Data are presented as individual responses with boxplots indicating the median, interquartile range, and full range (whiskers). Dashed lines indicate assay lower limits of detection. Statistical analyses were performed using the Kruskal–Wallis test with Dunn's post hoc correction; *p < 0.05, **p < 0.01, ***p < 0.001, ****p < 0.0001.

4.3 Discussion

MERS-CoV remains a significant public health threat, and the development of effective vaccines a global priority. In the aftermath of the COVID-19 pandemic, this chapter extends the pre-pandemic evaluation of ChAdOx1 MERS described in Chapter 3 by examining how prior exposure to either MERS-CoV or SARS-CoV-2 shapes the magnitude, quality, and breadth of subsequent vaccination responses.

Hybrid immunity resulting from prior SARS-CoV-2 infection followed by COVID-19 vaccination has been shown to broaden neutralisation against VOC, and to enhance Fc-mediated effector functions [381] and mucosal immune responses in the respiratory tract [382]. Hybrid SARS-CoV-2 exposure has also been associated with shifted S2-directed responses compared with vaccination alone. This pattern, seen across both mRNA and adenoviral vector platforms, suggests a change in epitope preference [383]. In contrast, the influence of prior exposure to endemic human coronaviruses (HCoVs) on SARS-CoV-2 immune responses appears to be variable - studies report both modest cross-reactive effects and minimal or no impact on vaccine-induced immunity [186]. Far less is known about how prior exposure MERS-CoV might influence immune responses to subsequent SARS-CoV-2 vaccination, largely due to the small number of MERS cases.

Our findings support that prior coronavirus exposure—whether heterologous (MERS-CoV) or homologous (SARS-CoV-2)—directs the epitope specificity of vaccine-induced antibody responses. Immune imprinting following MERS-CoV infection preferentially biased antibody responses towards S1-associated epitopes, whereas prior SARS-CoV-2 exposure favoured responses targeting more conserved S2-associated epitopes, accompanied by enhanced FcγRIIIA engagement directed to S2 and increased FcγRIIB engagement to spike. Notably, enrichment of FcγRIIIA–S2–associated responses has also been reported in independent studies of SARS-CoV-2 vaccination and infection, supporting the reproducibility of this functional signature [383]. In addition, increased FcγRIIB engagement directed to spike has been associated with reduced risk of breakthrough infection following vaccination[339]. Together, these findings indicate that prior coronavirus exposure can direct both the specificity and functional quality of vaccine-induced antibody responses, providing a mechanistic framework for how immune imprinting shapes downstream immune outcomes and potential protective mechanisms.

Following the pandemic and the emergence of SARS-CoV-2, marked changes in the epidemiology of MERS—including reduced case detection—have been observed [384]. Several studies have reported measurable cross-reactivity to MERS-CoV, including detectable binding antibodies [367, 385]; this is largely attributed to the conserved S2 region [386]. Importantly, in-vivo antibody-dependent enhancement (ADE) has not been observed [367].

By comparing baseline MERS-specific antibody responses in pre- and post-pandemic individuals, we found evidence that SARS-CoV-2 exposure can generate low-level cross-reactive and cross-neutralising MERS-specific antibodies with Fc-effector activity. However, these cross-reactive antibody titres were significantly lower than those induced by a single pre-pandemic ChAdOx1 MERS vaccination or by prior MERS infection. This highlights the continued need for targeted MERS vaccination, particularly in vulnerable populations.

Finally, data from the post-pandemic ChAdOx1 MERS clinical trial enabled evaluation of MERS-specific vaccine responses in the context of prior SARS-CoV-2 exposure. Robust immunogenicity was observed following vaccination; however, responses differed according to prior ChAdOx1 exposure, with lower responses observed in ChAdOx1-experienced vs ChAdOx1-naïve participants. Following booster vaccination, antibody responses were enhanced in both groups, reaching levels comparable to those reported in younger vaccinated adults or in MERS convalescents. While pre-existing anti-vector immunity influenced the magnitude of responses after priming, booster vaccination largely mitigated these differences.

Together, these findings provide a snapshot of MERS vaccine performance in the post-pandemic landscape, where prior coronavirus exposure and extensive use of the ChAdOx1 vector are increasingly common. In the following sections, we summarise these key findings and discuss their implications for understanding coronavirus immune imprinting, the optimisation of MERS vaccine strategies, and preparedness for future emerging pathogens

Hybrid Coronavirus Immunity Shapes SARS-CoV-2 FcγR Profiles

Observations from SARS-CoV-1 survivors showed enhanced and more durable responses to SARS-CoV-2 vaccination than SARS-CoV-1–naïve individuals; suggesting that long-lived, cross-reactive memory B cells generated during the 2003 outbreak can be effectively recalled by SARS-CoV-2 vaccination [21]. The strong neutralising activity in the SARS-CoV1/SARS-CoV2 hybrid immunity group extends to SARS-CoV-2 variants of concern and even to cross-clade, pan-sarbecovirus lineages such as bat and pangolin coronaviruses, further highlighting the value of heterologous priming in broadening antiviral immunity [22]. Importantly, prior SARS-CoV-1 infection did not interfere with the induction of *de novo* T-cell responses to SARS-CoV-2, indicating that pre-existing immunity does not limit subsequent T-cell priming to novel epitopes on a related pathogen [387]. Together, these results show how prior exposure to a related sarbecovirus can enhance vaccine-induced immunity.

I assessed whether prior coronavirus exposure influenced vaccine responses to the more distantly related MERS-CoV. I found that previous MERS infection is associated with an enhanced response to COVID-19 vaccination compared with both hybrid SARS-CoV-2 immunity and vaccine-only immunity. These findings align with longitudinal follow-up studies of MERS survivors in Korea, which

reported elevated IgG levels to SARS-CoV-2 as well as cross-reactive antibodies to SARS-CoV-1, compared with individuals with no history of MERS [379].

Conversely, a small cohort study evaluating paired vaccination samples from MERS survivors reported similar anti-SARS-CoV2 responses compared with infection-alone or vaccine-alone groups [388]. Notably, despite survivors showing a significant induction of SARS-CoV-2–specific IgG and pseudoneutralisation activity following vaccination, no SARS-CoV-2–specific IgM was detected - a pattern consistent with a secondary, recall-type immune response rather than a primary response.

Importantly, recall responses do not necessarily result in higher peak circulating antibody titres compared with primary vaccination, as they may be characterised instead by more rapid kinetics, preferential class switching, and qualitative changes in antibody function rather than increased magnitude. Thus, the absence of IgM in the hybrid immunity group likely reflects activation of pre-existing memory B cells rather than de novo responses, even in the absence of substantially higher anti–SARS-CoV-2 IgG titres compared with vaccination alone. Further characterisation of the underlying memory B-cell populations will be important to clarify these mechanisms.

Furthermore, the same study reported limited ADCC increases after SARS-CoV-2 vaccination (in either MERS survivors or vaccine only individuals), compared to high ADCC titres in after SARS-CoV-2 infection. In contrast, our study observed induction of Fc-effector–associated responses following vaccination; this was assessed by Fcγ receptor binding, which serves as a surrogate marker of Fc-mediated functionality. Differences in the assays used to assess Fc-mediated immunity may therefore contribute to the divergent findings, as FcγR binding reflects antibody potential for effector engagement but does not capture downstream cellular activation or effector mechanisms such as ADCC.

In addition, the quality and magnitude of Fc-mediated responses may depend on the nature of prior coronavirus exposure—whether shaped by natural infection, vaccination, or a combination of both—as well as cohort-specific factors including infection severity, timing since exposure, and infection-driven shaping of the humoral repertoire. Together, these considerations highlight the complexity of comparing Fc-mediated immune outcomes across studies using different readouts.

An additional challenge is the difficulty of fully excluding undocumented or asymptomatic SARS-CoV-2 infection in the years following the pandemic, particularly in regions with widespread community transmission. Such undetected exposures could silently boost cross-reactive immunity and confound the interpretation of post-vaccination responses in small cohorts.

Multivariate analysis revealed clear qualitative differences between the two hybrid immunity groups. Hybrid MERS/SARS-CoV-2 immunity was characterised by enhanced S1-specific FcγRIIB activity. FcγRIIB is the only inhibitory Fc receptor, expressed on B cells and myeloid subsets, where it regulates immune activation [6] and mediates the retention of immune complexes on follicular dendritic cells [8].

Prolonged antigen display within germinal centres via FcγRIIB may promote both memory B-cell expansion and the recruitment of naïve B cells, providing a mechanistic basis for the emergence of de novo S1-specific responses. This may also explain the strong association observed between S1-specific FcγRIIB activity and neutralisation in our dataset. Furthermore, FcγRIIB has been shown to potentiate activating FcγR signalling [9,10], offering an additional pathway through which neutralisation capacity may be amplified.

In contrast, hybrid SARS-CoV-2 immunity was enriched for S2-specific FcγRIIIA activity together with Spike-specific FcγRIIIB engagement—signatures previously associated with ADCC and protection against severe COVID-19 [339]. This pattern indicates a functional bias toward Fc-mediated effector responses targeting more conserved regions of the spike protein. The enrichment of S2-FcγRIIIA responses has also been reported in other studies of hybrid immunity [383], lending further support to the robustness of this observation.

Our results are consistent with the original analysis of this cohort, which examined MERS survivors both with and without subsequent COVID-19 vaccination [323]. In that study, neutralisation was assessed post-vaccination in a subset of participants (n=10) using a focus reduction neutralisation test (FRNT50). Broad coronavirus neutralisation capacity was seen, with activity against multiple SARS-CoV-2 variants, including the ancestral strain, Delta, and BA.5, as well as against several MERS-CoV strains. However, no direct comparator groups were included within this analysis, limiting the ability to draw definitive conclusions regarding relative enhancement compared with infection-only or vaccination-only immunity.

Consistent with these observations, the present dataset demonstrates SARS-CoV-2 Wuhan neutralising activity in individuals with hybrid MERS-CoV/SARS-CoV-2 immunity. Although the small sample size and lack of appropriate control groups preclude firm conclusions, these findings are compatible with the hypothesis that prior MERS infection followed by COVID-19 vaccination may synergistically shape coronavirus-neutralizing antibody responses.

Several studies have demonstrated the superior immunogenicity of hybrid SARS-CoV-2 immunity, including induction of cross-reactive responses to viral variants. Our results are consistent with these findings, showing that individuals with prior coronavirus exposure mounted stronger Omicron-specific and neutralising responses than vaccine-only recipients. This enhanced immunity was observed even when some samples were collected at later time points post-vaccination or infection.

Importantly, prior coronavirus exposure also appeared to mitigate factors typically associated with reduced vaccine-induced immunity, including older age and longer intervals between the booster dose and sample collection [96, 97]. In individuals with SARS-CoV-2 vaccine-only immunity, antibody responses showed significant negative associations with both age and post-boost interval. In contrast, in the hybrid SARS-CoV-2/SARS-CoV-2 group, antibody responses were less affected by age and

interval. Together, these observations suggest that prior coronavirus exposure may partially offset age- and post-boost interval–related declines in SARS-CoV-2–specific antibody responses.

Back-Boosting of MERS Immunity

Our findings add to emerging evidence that SARS-CoV-2 exposure or vaccination can shape pre-existing MERS-CoV immunity, but that this back-boosting effect is limited in scope. The original cross-sectional analysis of the MERS–SARS-CoV-2 hybrid immunity cohort from which our comparison samples were drawn, suggested higher MERS-specific antibody levels in individuals who received COVID-19 vaccination within five years of their MERS infection compared with those vaccinated after a longer interval [323]. However, because of the cross-sectional study design, it was not possible to assess individual-level boosting.

Longitudinal follow-up of survivors from the 2015 Korean outbreak compared pre- and post-pandemic samples from the same individuals, and similarly demonstrated only marginal increases in MERS S and S2 IgG titres, stable neutralising antibody responses, and a continued decline in S1 titres [379]. Importantly, linear epitope mapping revealed that COVID-19 vaccination preferentially boosted responses to conserved S2 epitopes—including the fusion peptide, stem helix, and cytoplasmic regions. These S2-directed responses increased after COVID-19 vaccination in individuals without prior MERS infection but remained significantly higher in individuals who had previously been infected with MERS-CoV, highlighting the contribution of pre-existing immunity. In contrast, antibody responses targeting the more variable S1 region showed little change following COVID-19 vaccination in either group and did not differ substantially between individuals with and without prior MERS infection.

Other MERS convalescent studies conducted in Qatar, although limited in sample size, reported increases in MERS-specific responses following COVID-19 vaccination, including elevated IgA targeting S1 [388]. This increase in MERS-specific responses was only significant when analysing paired pre- and post-vaccination samples (n = 4); in unpaired analysis of all samples (n=14) the increase was not significant. This study did not include S2-specific readouts, limiting its ability to provide a comprehensive view of the breadth of boosting across spike domains.

Together, these observations indicate that any augmentation of MERS immunity during the COVID-19 pandemic is modest, population-dependent, and predominantly directed toward conserved regions of spike rather than the more variable S1 domain.

Disease severity during primary MERS infection remained a dominant determinant of antibody magnitude years later, consistent with long-standing evidence for sustained memory B-cell responses after severe coronavirus disease[380]. The longitudinal Korean cohort similarly showed higher spike-specific responses in individuals who experienced more severe primary disease [379]. This severity-associated hierarchy persisted over the years for S1 responses, but shifted after 2019 for S and S2, consistent with SARS-CoV-2 exposure preferentially boosting conserved epitopes rather than broadly restoring the original severity-associated hierarchy.

Our data further show that individuals with severe prior MERS infection displayed higher functional antibody profiles, including elevated FcγRIIA- and FcγRIIIB-binding responses targeting S1 epitopes. These functional features persisted after COVID-19 vaccination, suggesting that the qualitative characteristics of the MERS-specific humoral response—particularly those shaped by severe disease and ICU-level illness—are remarkably stable over time and are not substantially remodelled by heterologous coronavirus exposure. This observation is consistent with findings from the Korean cohort, which similarly reported long-lasting imprinting of antibody functional profiles associated with disease severity. Taken together, these findings suggest that SARS-CoV-2 vaccination induces selective amplification of MERS-CoV antibodies targeting conserved spike regions, while the broader imprint of disease severity on MERS-specific immunity remains largely unchanged.

To further clarify these immunological patterns, future work should incorporate systems serology profiling of MERS convalescents during the acute phase of infection as well as before and after vaccination. Such studies will be important for understanding the evolution of Fc-mediated antibody responses and may ultimately help establish immune correlates relevant for the evaluation and regulatory approval of MERS vaccines.

Cross-reactivity from SARS-CoV-2 exposure toward MERS-CoV antigens

Following the emergence of COVID-19, our findings suggest that SARS-CoV-2 exposure—through infection or vaccination—can generate antibodies with cross-reactive potential against MERS-CoV, which retain the ability to engage Fcγ receptors and mediate effector functions. Such Fc-mediated activity is of particular interest because it often persists longer than neutralising antibody levels [332] and may therefore represent a more durable component of cross-coronavirus immunity.

The enrichment of MERS-CoV–specific responses in individuals with hybrid exposure histories supports the idea that repeated antigenic encounters can broaden the repertoire of cross-reactive antibodies. This pattern suggests an expansion of epitope recognition beyond conserved S2 regions to include more variable regions such as S1. Although SARS-CoV-2 vaccine recipients exhibited higher responses than pre-pandemic negative controls, MERS-spike-directed responses were highest in individuals with hybrid SARS-CoV-2/SARS-CoV-2 exposure. While no significant differences emerged when each spike subunit was analysed individually, comparison with negative controls

revealed that overall FcγR engagement in the hybrid and vaccinated groups was stronger for S2 (three out of four activating FcγRs) than for S1 (two activating FcγRs). This pattern indicates a greater contribution of conserved S2-driven responses, consistent with the structural homology shared between the SARS-CoV-2 and MERS-CoV spike proteins in this region.

Notably, regardless of SARS-CoV-2 infection status, induction of the inhibitory receptor FcγRIIB was limited compared with pre-pandemic controls, suggesting that the regulatory arm of the Fc-effector response may be less prominently engaged. In parallel, cross-reactive T cell immunity—particularly to conserved proteome regions outside spike—has also been identified post-pandemic in hybrid SARS-COV-2/SARS-COV2 immunity [389, 390]. Such T cell memory, derived from prior betacoronavirus encounters, can enhance $CD4^+$ T cell responses and antibody titres [193] potentially amplifying both the magnitude and quality of MERS-CoV vaccine-induced immunity.

Together, these observations raise the possibility that the pandemic has subtly elevated baseline MERS immunity, with both antibody and T cell compartments poised to influence future MERS vaccine responsiveness. While our cross-sectional design captures persistence rather than peak magnitude—since sampling occurred approximately 8 months post-vaccination—the detection of FcγR-engaging antibodies underscores their durability.

Insights from the post-pandemic MERS003 Clinical Trial in elderly adults

Age-dependent declines in vaccine-induced immunity are well documented across multiple platforms [96, 391, 392]; however, in this study, the widespread background of SARS-CoV-2 exposure introduced an additional immunological variable that likely shaped baseline immunity and early vaccine responsiveness.

As anticipated, baseline MERS-specific responses—including binding and neutralising activity—were higher in the post-pandemic cohort than in pre-pandemic population baselines. Consistent with our earlier cross-reactivity findings, baseline anti–SARS-CoV-2 neutralisation titres correlated with baseline anti-MERS-binding IgG, supporting the hypothesis that pre-existing cross-reactive memory contributed to elevated starting immunity.

A similar pattern was observed in the MVA-MERS trials [293, 295], in which participants vaccinated in the post-pandemic period exhibited higher baseline MERS-specific antibody levels and stronger responses after the first dose compared with pre-pandemic recipients, even within matched dose and schedule cohorts. With both ChAdOx1-MERS and MVA-MERS, this advantage was most pronounced following the first dose, with differences between pre- and post-pandemic groups diminishing after the second dose. These findings suggest that prior coronavirus exposure can enhance early vaccine responsiveness, whereas repeated antigen exposure through boosting reduces the relative influence of pre-existing immune imprinting.

Although SARS-CoV-2/MERS-CoV cross-reactivity does not constitute a formal prime–boost regimen, the MERS003 data indicate that prior coronavirus exposure can mimic aspects of priming. Older ChAdOx1-naïve participants achieved post–single dose immunogenicity levels comparable to younger adults vaccinated pre-pandemic. This aligns with our earlier observation that hybrid or cross-reactive immunity can partially offset age-related declines in vaccine responsiveness.

Interestingly, we also observed potential inhibition from anti-vector immunity: vaccine-induced anti-MERS-CoV responses were higher in ChAdOx1-naïve individuals both post-prime and post-boost. We did not observe a correlation between neutralising anti-vector antibodies and anti-MERS-CoV antibodies; previous ChAdOx1 vaccine studies reported a weak but statistically significant negative association between vaccine-induced ChAdOx1-neutralising antibodies and anti-spike IgG responses ($p = 0.037$), and no significant association with anti-spike T-cell responses ($p = 0.22$) [96].

The MERS003 findings suggest that neutralising anti-vector antibodies alone may not fully account for the observed differences in vaccine-induced antibody responses. In a prior study of ChAd68 ME-TRAP vaccination, pre-existing T cell responses to the ChAd63 hexon protein—detected in 8/12 (67%) volunteers —were negatively correlated with post-vaccination anti-ME-TRAP antibody responses ($R = –0.6901$, $p = 0.023$) [393]. Consistent with this, a study evaluating a ChAdOx1-based HBV vaccine reported lower post-vaccination T cell responses in individuals with prior ChAdOx1 exposure; there was a no association with baseline anti-vector neutralisation, and a weak negative correlation of baseline anti-hexon T cells and post-vaccination anti-HBV T cells ($r=-0.3864$, $p=0.0564$) [394]. This raises the possibility that cross-reactive anti-vector immunity to ChAdOx1 is not limited to neutralising antibody responses, and that pre-existing T cell immunity may also influence the magnitude of vaccine-induced responses in certain individuals.

Limitations

Several limitations should be considered. First, there is uncertainty surrounding vaccination dates in the hybrid MERS-CoV/SARS-CoV-2 groups. The matched group analysis at later time points (>190 days post–second dose) likely reflects antibody waning, capturing durability rather than peak post-vaccination responses. Although matching was performed by sex and age, precise alignment of sample collection dates was not possible, and the approximately three-month difference in sample processing—during which the hybrid MERS group was tested at the height of the Omicron wave, whereas the control group was tested earlier in a different country—could bias comparisons toward higher apparent responses in the hybrid group. The small sample size, combined with the use of a geographically distinct control cohort, further introduces the possibility of selection bias and limits the generalisability of the findings.

Second, the absence of systematic recording of SARS-CoV-2 infections in the MERS003 trial limits our ability to fully account for the effect of post-vaccination exposures. Although assessment of

nucleocapsid (N) antibodies was possible and provides an indicator of prior SARS-CoV-2 infection, N-specific responses can persist for extended periods and do not provide information on the timing of infection. This makes it challenging to fully exclude undocumented SARS-CoV-2 exposures that could have occurred between vaccination and sampling.

Third, we were unable to follow up participants from earlier MERS001 and MERS002 vaccine trials after the COVID-19 pandemic to determine whether similar post-pandemic enhancements in cross-reactive immunity occurred in those cohorts. The lack of longitudinal linkage across trials therefore restricts our ability to generalise the imprinting effects observed in MERS003.

Finally, the large number of comparisons performed across multiple immune parameters and exposure groups, which increases the risk of identifying statistically significant findings that may not be biologically meaningful. Some observed differences may therefore reflect false-positive associations due to multiple testing. As formal correction for multiple comparisons was not consistently applied, results were interpreted cautiously, with emphasis placed on biological plausibility and consistency across related immune readouts rather than statistical significance alone. Accordingly, findings were considered in the context of the broader immune response rather than as isolated effects.

Despite these limitations, this study provides a rare opportunity to examine how prior exposure to multiple coronaviruses shapes vaccine-induced immunity in humans. The availability of MERS survivor cohorts, combined with detailed serological and Fc-functional profiling following SARS-CoV-2 vaccination, enabled the assessment of immune imprinting effects in a cross-sectional setting. The consistent patterns observed across independent vaccine platforms and cohorts support the biological relevance of the findings, even where sample sizes were limited. Together, these data establish a framework for understanding how heterologous coronavirus exposures influence the quality and durability of vaccine-induced immunity.

At the same time, the human data presented in this chapter highlight the inherent limitations of observational analyses and the challenges of disentangling the effects of prior exposure, timing, and adenoviral vector immunity. To address these questions under controlled conditions, the following chapter explores heterologous prime–boost vaccination strategies in pre-clinical animal models, enabling systematic optimisation of vaccine order, interval, and platform.

5 Heterologous Prime-Boost Vaccination with ChAdOx1 and MVA-Based MERS-CoV Vaccines in Mice

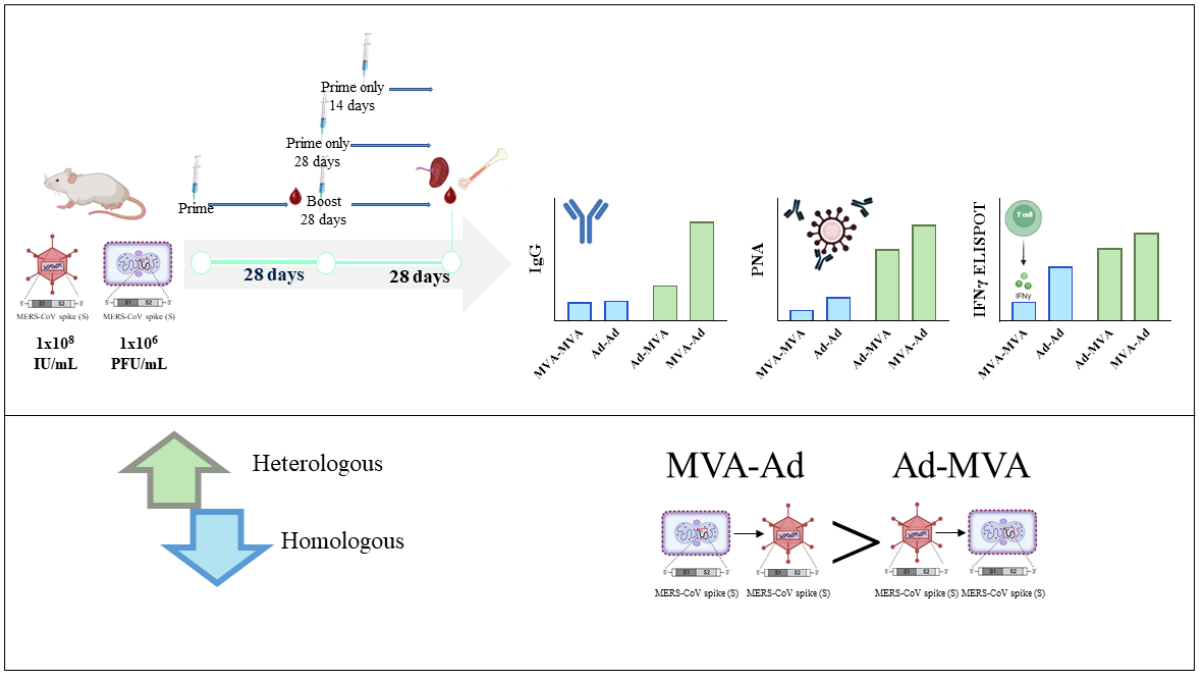


Figure 5.1 Visual abstract of the study methods and results

Highlights

- Heterologous PB induces a higher immune response compared to homologous regimens.
- Immunogenicity was shaped by the order of heterologous vaccination.
- Increasing dose in homologous MVA prime–boost regimens amplified humoral, cellular, and Fc-effector responses.
- Pre-boost antibody titres appear to influence the magnitude of booster responses.

5.1 Introduction

To date, only three MERS vaccine candidates have progressed to human trials [292, 294, 297]: a DNA vaccine (GLS-5300 MERS), chimpanzee adenovirus vector (ChAdOx1 MERS) and modified vaccinia virus Ankara (MVA-MERS-S). The latter two are recombinant replication-deficient viral vector vaccines and together they form the Coalition for Epidemic Preparedness Innovations (CEPI) standalone MERS vaccine portfolio [395]. This chapter focuses on these viral vector platforms, which remain under continued clinical development.

MVA-MERS-S was first tested in a Phase Ia trial in healthy adults in Germany as a two-dose regimen [294], with a late third booster subsequently administered to a subset of participants. Most recently, it was evaluated in a phase Ib three-dose regimen enrolling 140 volunteers [295].

ChAdOx1-MERS has been assessed as a single dose in healthy adults in the UK [292] and in Saudi Arabia, where MERS-CoV is endemic and the risk of exposure is higher [291]. More recently, a two-dose regimen was assessed in older adults (50–70 years) in the UK, an age group particularly susceptible to severe MERS-CoV disease [320]. As discussed in Chapter 4, anti-vector immunity was associated with reduced magnitude and durability of vaccine-induced responses.

This issue is particularly relevant for viral vector platforms, where immune responses directed against the vector may interfere with antigen expression following boosting [396].

Heterologous prime–boost (PB) vaccination is a well-established strategy to enhance immune responses and has shown superior immunogenicity and efficacy over homologous PB regimens in both animal models and humans [106, 397]. By alternating vectors, heterologous PB can help mitigate the impact of vector-specific immunity.

In this chapter, we compare homologous vaccination regimens previously evaluated in clinical trials with a heterologous vaccination regimen using the classical 28-day interval, testing combinations of ChAdOx1 MERS, developed at the University of Oxford, and MVA-MERS, developed by IDT Biologika. A key advantage of this collaborative work with IDT Biologika, a German biopharmaceutical manufacturer of viral vector vaccines, is that both ChAdOx1 MERS and MVA-MERS have already been individually tested in humans, providing an established safety record that facilitates their combination in future clinical trials.

5.2 Results

5.2.1 Study design and immunization regimens

To evaluate the immunogenicity of CEPI's MERS vaccine candidates, two independent mouse experiments (MERS-IDT001 and MERS-IDT002) were conducted. Mice were assigned to prime-only, homologous, or heterologous prime–boost regimens using ChAdOx1-MERS (henceforth referred to as 'Ad') and MVA-MERS-S (referred to as 'MVA'), with a consistent 28-day interval between prime and boost. For single-dose MVA vaccination, immune responses were assessed 2 weeks post-prime, with 4 weeks also assessed in MERS-IDT002. For consistency across comparisons, the 2-week groups (n=12) were designated as the primary dataset, while the 4-week groups (n=6) are presented for comparison (**Error! Reference source not found.**). The overall study design is illustrated in Figure 5-1 and **Error! Reference source not found.** in Methods for full details of vaccination groups, sampling schedules, and group sizes.

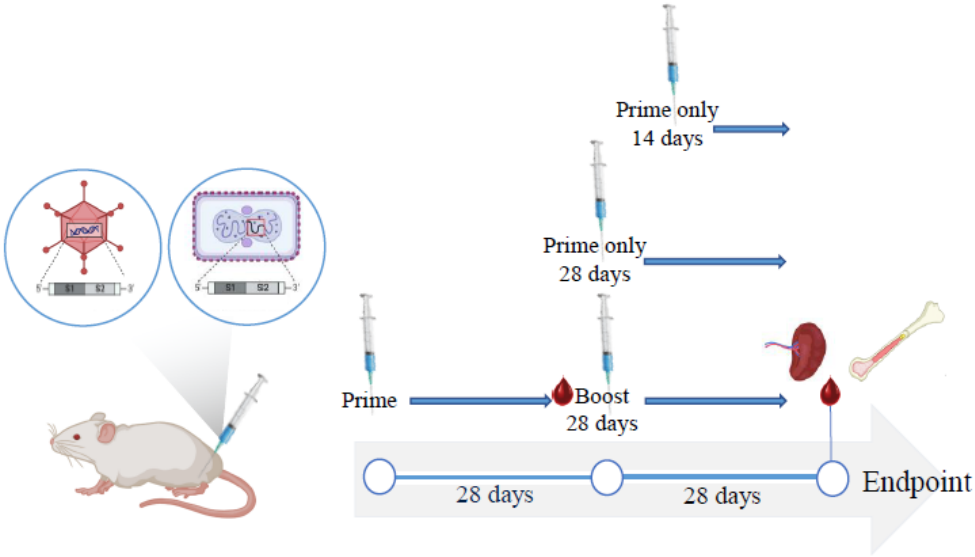


Figure 5-1. Study design of mouse vaccination experiments.

BALB/c mice were primed with either ChAdOx1-MERS or MVA-MERS-S. Prime-only groups were analysed at 14 or 28 days after vaccination, while prime–boost groups were given a booster at day 28 and analysed 28 days later. Sera was collected pre-boost, and at endpoint, blood, spleen, and BM were collected for immunological analyses. See Methods for details of vaccine dose, administration, and group allocation.

5.2.2 Binding and functional antibody responses

5.2.2.1 Binding and neutralising antibodies against full MERS-CoV spike

Levels of MERS spike–specific IgG and MERS-CoV pseudovirus neutralising antibodies were measured in serum (Figure 5-2). Median titres with IQR for each vaccination group are summarized in Table 5-1.

Group	IgG_S (EU, median [IQR])	Neutralizing Ab titre (IU/mL, median [IQR])
MVA	163 [43–259]	50 [7–59]
Ad	2289 [1765–2678]	1311 [815-1859]
MVA/MVA	3793 [2173–6872]	2358 [1601–3398]
Ad/Ad	4176 [3146–5439]	4907 [3588–6162]
Ad/MVA	7222 [3124–12407]	15,836 [9603–21,402]
MVA/Ad	20,186 [16,872–25,154]	19,601[14,219–32,452]

Table 5-1. Median IgG binding and neutralising antibody titres.
Data are shown as median values with IQR. IgG responses are expressed in ELISA units (EU). Neutralising antibody titres were measured using a pseudovirus neutralisation assay (PNA) and are reported in international units per millilitre (IU/mL). Data are pooled from two independent experiments (n = 12 animals per group; Ad/MVA, n = 11 due to one missing sample).

A single vaccination induced only low levels of IgG, particularly with MVA-MERS, which did not differ from the respective GFP control (p>0.999; Figure 5-2A). Ad vaccination elicited a modest but not statistically significant increase compared with Ad-GFP controls (p = 0.08; Figure 5-2A).
Homologous prime–boost vaccination increased IgG titres compared with pre-boost level, rising by ~16.5-fold in the MVA/MVA group (p = 0.01; Figure 5-2C) and ~2-fold in the Ad/Ad group (p = 0.04; Figure 5-2C), with post-boost titres for both significantly higher than negative controls (MVA/MVA: p = 0.0007; Ad/Ad: p = 0.0003; Figure 5-2A). Heterologous boosting further increased antibody responses, with Ad/MVA showing a ~3-fold rise and MVA/Ad a ~99-fold rise over their matched pre-boost titres (p < 0.0001 for both; Figure 5-2C).

Post-boost titres were highest in MVA/Ad and Ad/MVA, with the highest levels observed in MVA/Ad (20,186 [16,872–25,154] EU) and Ad/MVA (7222 [3124–12,407] EU); while homologous Ad/Ad (4176 [3146–5439] EU) and MVA/MVA (3793 [2173–6872] EU) produced lower responses (Figure 5-2A).

The lowest neutralising antibody responses were observed in animals receiving control vaccines or prime-only immunization (Figure 5-2B). Homologous boosting with Ad/Ad or MVA/MVA increased titres compared with their respective negative controls, reaching medians of 4907 [3588–6162] IU/mL and 2358 [1601–3398] IU/mL, respectively. These increases were statistically significant versus controls (Ad/Ad: p = 0.0002; MVA/MVA: p = 0.038) but not when compared with prime-only vaccination (p > 0.05). Heterologous boosting induced the highest neutralising titres, with medians of 19,601 [14,219–32,452] IU/mL in MVA/Ad and 15,836 [9603–21,402] IU/mL in Ad/MVA. These responses were significantly greater than those in prime-only groups (p = 0.0001 for both Ad/MVA and MVA/Ad vs. MVA prime; p = 0.045 for Ad/MVA vs. Ad prime; p = 0.016 for MVA/Ad vs. Ad prime). Although heterologous regimens appeared to elicit stronger IgG and neutralising responses than homologous boosting, no significant differences were detected between them, and titres induced by MVA/Ad and Ad/MVA were comparable (p > 0.99).

IgG and neutralising titres were strongly correlated across all groups. Spearman R= 0.92 [95% CI (0.9-0.95), p=<0.0001; Figure 5-2D. When analysed by regimen, the correlation was stronger for Ad/MVA (R = 0.7, p = 0.01) than for MVA/Ad (R = 0.5, p = 0.07).

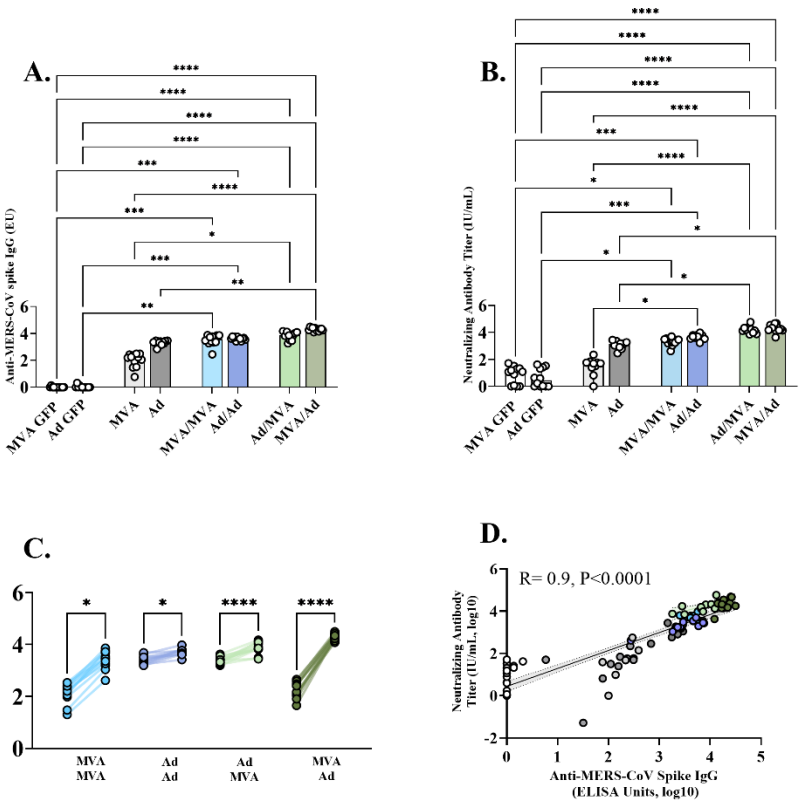


Figure 5-2. Binding IgG and neutralising responses to MERS-CoV spike protein.

(A) IgG binding to full-length MERS-CoV spike protein shown as median ELISA units (EU). Bars represent medians with 95% confidence intervals (CI). **(B)** Neutralising antibody titres (IU/mL) against MERS-CoV pseudovirus. Bars represent medians with 95% CI. **(C)** Paired IgG binding responses for individual animals before and after boosting. Lines connect responses from the same animal. Data were analyzed by repeated-measures one-way ANOVA (matched), with multiple comparisons corrected using Dunn's post-test. **(D)** Correlation between anti-MERS-CoV spike IgG and neutralising antibody titres across all groups. Each point represents an individual animal; the shaded area indicates the 95% CI. Spearman correlation was performed ($R = 0.9$, $p < 0.0001$). Colours indicate groups: MVA GFP (white), Ad GFP (white), MVA (light grey), Ad (dark grey), MVA/MVA (light blue), Ad/Ad (lavender blue), Ad/MVA (light green), MVA/Ad (dark green). Data are combined from both experiments (n = 12). Statistical analysis: Panels A–B: Kruskal–Wallis with Dunn's post-test for between-group comparisons. Panel C: Repeated-measures one-way ANOVA (matched) with Dunn's multiple comparisons post-test for paired pre/post analysis. Panel D: Spearman correlation. Significance is indicated as *p < 0.05, **p < 0.01, ***p < 0.001, ****p < 0.0001.

5.2.2.2 Epitope-specific IgG responses following vaccination

Since we observed a trend toward higher overall spike-specific responses in MVA/Ad compared with Ad/MVA, we next examined whether vector order influenced the distribution of antibody responses across spike subdomains, namely IgG binding to the S1 subunit (containing the RBD) and to the S2 subunit (Figure 5-3). The corresponding median values with IQR for each vaccination group are summarized in Table 5-2.

Group	IgG_S1 (EU, median [IQR])	IgG_S2 (EU, median [IQR])
MVA	16 [12–30]	5 [2–18]
Ad	89 [69–155]	64 [39–91]
MVA/MVA	217 [161–350]	90 [67–181]
Ad/Ad	360 [134–503]	204 [104–268]
Ad/MVA	557 [468–1149]	214 [188–261]
MVA/Ad	1389 [729–1906]	409 [226–503]

Table 5-2. Median IgG binding responses to S1 and S2 subunit proteins.
Data are presented as median values with IQR. IgG responses are expressed in ELISA units (EU). Data are pooled from two independent experiments (n = 12 animals per group), except Ad/MVA (n = 11) due to one missing sample.

For S1-specific IgG (Figure 5-3A), the weakest responses were detected in prime-only groups (MVA: 16 EU [12–30]; Ad: 89 EU [69–155]). Homologous boosting increased titres above controls (MVA/MVA: 217 EU [161–350], $p = 0.0049$; Ad/Ad: 360 EU [134–503], $p = 0.0025$), with Ad/Ad higher than MVA prime ($p = 0.03$), though overall responses remained modest. In contrast, heterologous regimens elicited stronger responses: MVA/Ad induced the highest titres (1389 EU [729–1906]) and Ad/MVA yielded intermediate levels (557 EU [468–1149]). Both exceeded MVA prime-only ($p < 0.05$), but only MVA/Ad was significantly greater than Ad prime ($p < 0.05$). No significant differences were observed between heterologous and homologous boosts overall. Ad/MVA titres varied between experiments (MERS-IDT001: 1075 EU vs. MERS-IDT002: 479 EU; $p = 0.0022$), but pooled analysis revealed no difference between the two heterologous regimens ($p > 0.999$).

The pattern for S2-specific IgG was broadly similar (Figure 5-3D). Prime-only animals again showed the weakest responses, comparable to GFP controls ($p > 0.05$). Homologous boosting with Ad/Ad (268 EU [203–336]) or MVA/MVA (181 EU [90–364]) increased titres above controls ($p < 0.05$), with Ad/Ad higher than MVA prime ($p = 0.01$). However, these responses remained similar to Ad prime-only levels and did not differ between Ad/Ad and MVA/MVA. Heterologous vaccination produced stronger responses: MVA/Ad induced the highest titres (409 EU [226–503]) and Ad/MVA gave intermediate levels (214 EU [188–261]). MVA/Ad was significantly greater than prime-only and controls ($p < 0.05$), but not clearly different from homologous regimens ($p > 0.05$).

When responses were expressed as fold-increase relative to pre-boosting (Figure 5-3B,F), the contrast between regimens became clearer. Homologous boosts produced only small and equivalent increases across subdomains (MVA/MVA: ~1.24-fold for S1, ~2-fold for S2; Ad/Ad: ~1.2-fold for S1, ~2.7-fold for S2). By contrast, heterologous boosting generated both higher magnitude and broader responses.

MVA/Ad produced a ~2.7-fold increase in S1 and a ~36-fold increase in S2, while Ad/MVA resulted in only a minimal rise in S1 ~1-fold but a more substantial ~4.5-fold increase in S2. Notably, the stronger fold-change in S2 with Ad/MVA was accompanied by a very low fold-change in S1, despite absolute titres being higher in that domain.

Across all animals, both S1- and S2-specific IgG strongly correlated with total spike IgG ($p < 0.0001$; Figure 5-3 C, F). However, within the heterologous groups, S1 and S2 responses themselves did not correlate ($R=0.3$, $p =0.4$ for Ad/MVA and $R=0.2$, $p=0.6$ for MVA/Ad S1, ($R=0.-0.24$, $p =0.5$ for Ad/MVA and $R=0.3$, $p=0.3$ for MVA/Ad S2, suggesting that booster vector choice shaped antibody specificity rather than proportionally amplifying both domains. Heatmap analysis further supported this observation (Figure 5-3G): MVA/Ad drove a broad response to both domains, whereas Ad/MVA showed a S2-bias post-boost.

Taken together, these results show that heterologous regimens consistently trended higher IgG and neutralising antibody than homologous vaccination across all readouts, although the differences did not reach statistical significance. Within the heterologous strategies, MVA/Ad generally induced stronger overall responses than Ad/MVA, but this advantage was not as evident when focusing on subunit-specific IgG. Instead, a distinct pattern emerged: MVA/Ad boosted both S1- and S2-specific antibodies, whereas Ad/MVA preferentially enhanced S2. Thus, vector order shaped not only the overall magnitude but also the balance of S1 versus S2 responses.

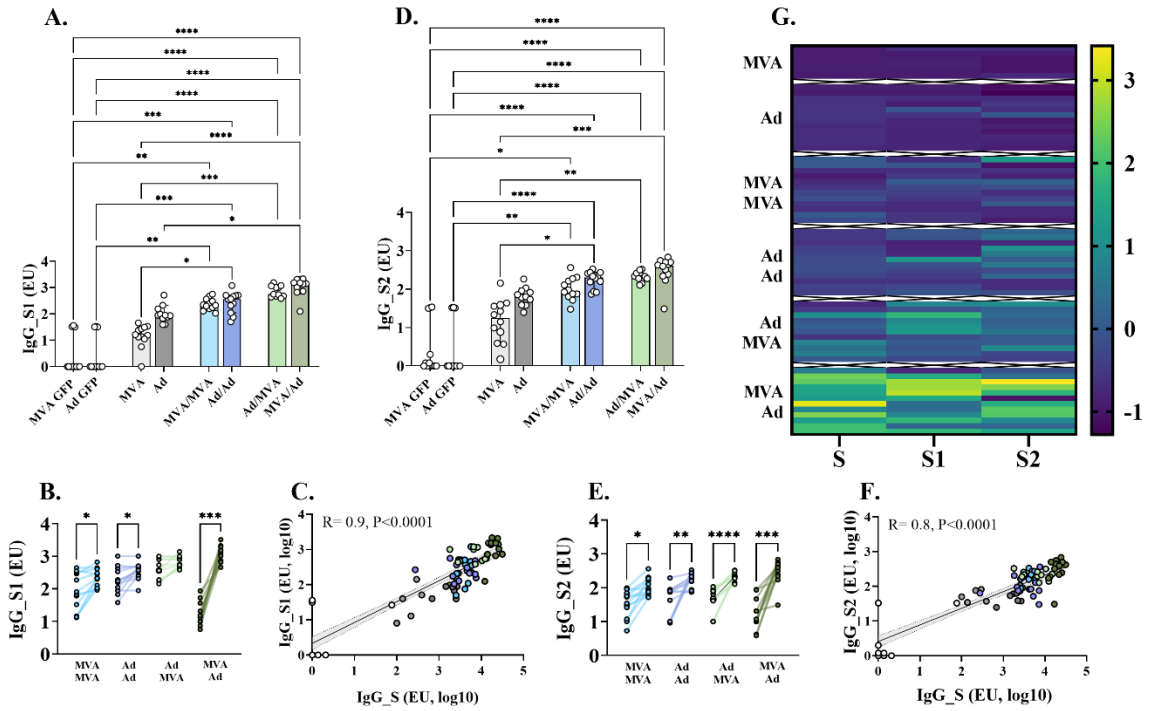


Figure 5-3. Binding IgG to MERS-CoV spike protein subunits.

(A) Median ELISA units (EU) of IgG binding to the MERS-CoV S1 subunit protein. **(B)** Paired IgG binding responses for individual animals before and after boosting (S1). Lines connect responses from the same animal. **(C)** Correlation between S1-specific and full-length spike-specific IgG, analysed by Pearson correlation. The regression line is shown with shaded areas representing the 95% confidence interval (CI). **(D)** Median EU of IgG binding to the MERS-CoV S2 subunit protein. **(E)** Paired IgG binding responses for individual animals before and after boosting (S2). Lines connect responses from the same animal. **(F)** Correlation between S2-specific and full-length spike-specific IgG, analysed by Pearson correlation. The regression line is shown with shaded areas representing the 95% CI. **(G)** Heatmap representation of IgG binding to full-length spike (S), S1, and S2 across groups, Shown as normalized z-scores, with higher levels of binding shown in yellow and low levels of binding shown in blue. Colours denote groups: MVA GFP (white), Ad GFP (white), MVA (light grey), Ad (dark grey), MVA/MVA (light blue), Ad/Ad (lavender blue), Ad/MVA (light green), MVA/Ad (dark green). Data are combined from two independent experiments. Statistical analysis: Panels A and D: Kruskal–Wallis with Dunn's post-test for between-group comparisons. Panel B and E: Repeated-measures one-way ANOVA (matched) with Dunn's multiple comparisons post-test for paired pre/post analysis. Panel C and F: Spearman correlation. Significance is indicated as *p < 0.05, **p < 0.01, ***p < 0.001, ****p < 0.0001.

5.2.2.3 Antibody class switching (IgG subclasses, IgA, IgM, avidity)

To evaluate antibody class switching, IgA and IgM binding titres were measured by ELISA, with results shown in Figure 5-4. Corresponding median values with IQR for each vaccination group are summarized in Table 5-3.

Group	IgM_MERS-IDT001 (EU, median [IQR])	IgM_MERS-IDT002 (EU, median [IQR)	IgA (EU, median [IQR])
MVA	167 [128–250]	191 [132–239]	18 [8–52]
Ad	1134 [454–1590]	1862 [1704–2634]	144 [80–218]
MVA/MVA	167 [128–250]	755 [457–986]	183 [102–359]
Ad/Ad	1322 [712–2853]	1972 [1571–2550]	357 [274–587]
Ad/MVA	686 [154.5–1815]	3413 [2633–3892]	486 [269–1696]
MVA/Ad	1260 [881–2070]	2971 [1957–4204]	945 [380–1696]

Table 5-3. Median IgM and IgA binding responses to MERS-CoV spike protein.
Data are presented as median values with IQR. Antibody responses are expressed in ELISA units (EU). IgM responses are shown separately for MERS-IDT001 and MERS-IDT002 experiments (n = 6 animals per group, except Ad/MVA with n = 5 due to one missing sample) and were not pooled. IgA responses are pooled from two independent experiments (n = 12 animals per group, except Ad/MVA with n = 11).

5.2.2.3.1 IgM responses

IgM responses varied between experiments (MERS-IDT001, Figure 5-4A; MERS-IDT002, Figure 5-4B) and are therefore presented separately. Significant group-specific differences observed in Ad/Ad (1322 [712–2853] vs. 1972 [1571–2550]; p = 0.0022), Ad/MVA (1260 [881–2070] vs. 3413 [2633–3892]; p = 0.0043), and MVA/Ad (3205 [1226–3867] vs. 2971 [1957–4204]; p = 0.0087). Despite this variation, Ad induced robust IgM binding titres, both as a single immunization (Figure 5-4B) and as a homologous boost (Ad/Ad; Figure 5-4A,B). In contrast, IgM induction after MVA alone or following homologous MVA/MVA boosting was limited and comparable to controls (Figure 5-4A,B). Heterologous vaccination further enhanced IgM responses, with both Ad/MVA and MVA/Ad regimens inducing significantly higher titres than controls. Paired fold-change analysis revealed that Ad/MVA produced only a modest increase (median 2.5-fold; p = 0.43; Figure 5-4C). By contrast, using Ad as a booster (MVA/Ad) markedly enhanced IgM induction, yielding consistently high titres across experiments (median 20-fold; p < 0.0001; Figure 5-4C).

5.2.2.3.2 IgA responses

Prime-only vaccination induced minimal IgA titres (Ad prime: 144 [80–218] EU; MVA prime: 18 [8–52] EU), which were not significantly different from negative controls (Ad-GFP: 10 [7–52] EU; MVA-GFP: 10 [7–101] EU; Figure 5-4D–E). Among homologous regimens, Ad/Ad induced detectable IgA responses (357 [274–587] EU), significantly higher than controls and MVA prime (p < 0.05), whereas MVA/MVA generated low titres (183 [102–359] EU) comparable to controls. Heterologous vaccination elicited the strongest IgA titres. MVA/Ad induced the highest responses (945 [380–1696] EU), significantly greater than negative controls (p < 0.0001), Ad prime (p = 0.05), and MVA prime (p = 0.04). Ad/MVA also increased titres (381 [247–637] EU), higher than MVA prime and controls but not different from Ad prime. Paired fold-change analysis confirmed IgA class-switching in heterologous

regimens, significant for both MVA/Ad ($p < 0.0001$) and Ad/MVA ($p = 0.01$; Figure 5-4E), but not for homologous boosts. Overall, heterologous regimens produced stronger IgA responses than homologous boosts, although differences between individual heterologous and homologous groups did not reach statistical significance.

Heatmap of median responses (Figure 5-4F) showed that heterologous regimens outperformed homologous boosts in magnitude and breadth. MVA/Ad gave the strongest IgA, overall Ad as a booster drove higher IgM and IgA than MVA.

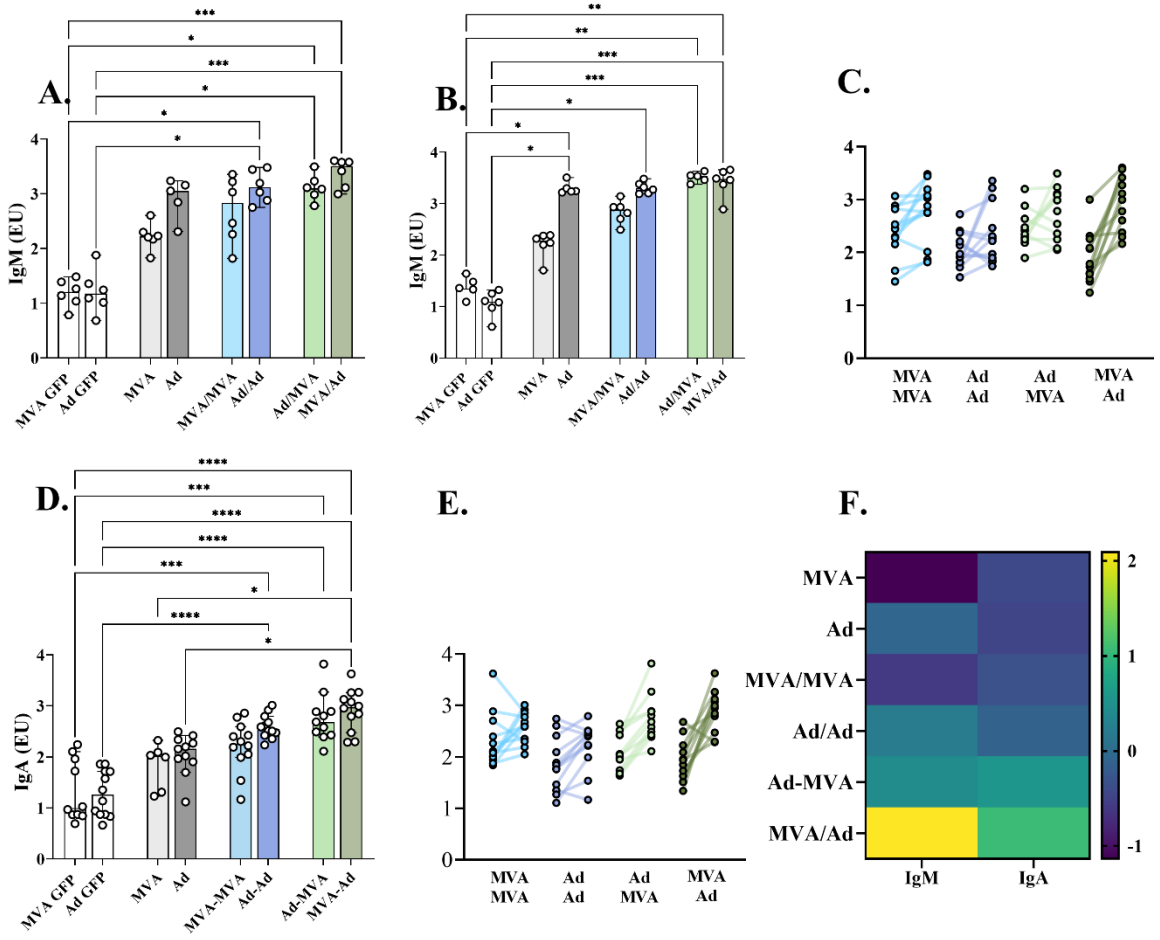


Figure 5-4. Binding IgA and IgM responses to MERS-CoV spike protein.

(A–B) Median ELISA units (EU) of IgM binding to the MERS-CoV spike protein in the MERS-IDT001 and MERS-IDT002 experiments. **(C)** Fold changes (post ÷ pre) in IgM binding responses from both experiments. **(D)** Median ELISA units (EU) of IgA binding responses, pooled from both experiments. **(E)** Fold changes (post ÷ pre) in IgA binding responses from pooled data. **(F)** Heatmap of median fold changes in IgM and IgA responses across homologous and heterologous regimens. Higher levels of fold changes shown in yellow and low levels of fold changes shown in blue. Bars represent medians with 95% confidence intervals (CI). Statistical analysis: Kruskal–Wallis with Dunn's post-test (*$p < 0.05$, **$p < 0.01$, ***$p < 0.001$, ****$p < 0.0001$). Colours denote groups: MVA-GFP (white), Ad-GFP (white), MVA (light grey), Ad (dark grey), MVA/MVA (light blue), Ad/Ad (lavender blue), Ad/MVA (light green), MVA/Ad (dark green).

5.2.2.3.3 IgG subclass responses

Analysis of IgG subclass responses revealed a mixed profile of IgG1, IgG2b, and IgG3 across all vaccination regimens. IgG subclass titres were normalized to total IgG levels, such that comparisons reflect relative subclass distribution rather than absolute antibody magnitude. Assessment was performed in both MERS-IDT001 and MERS-IDT002, giving a combined sample size of n = 12 mice per group. IgG2a titres differed in the MVA/MVA group (0.40 [0.40–0.67] in MERS-IDT001 vs. 0.70 [0.50–0.80] in MERS-IDT002; p = 0.04), IgG2b in the Ad/MVA group (0.30 [0.23–0.34] vs. 0.40 [0.40–0.59]; p = 0.03), and IgG3 in the Ad/Ad group (0.32 [0.30–0.50] vs. 0.20 [0.19–0.30]; p = 0.04). However, these replicate-specific differences did not alter the overall hierarchy across vaccination regimens, and therefore results from both experiments were combined to increase statistical power.

Titres of IgG2b, and IgG3 were comparable among groups, indicating no major differences (Figure 8C and D). The corresponding median values with IQR for each vaccination group are summarized in Table 5-4.

Group	IgG1 (OD, median [IQR])	IgG2a (OD, median [IQR])	IgG2b (OD, median [IQR])	IgG3 (OD, median [IQR])
MVA	0.20 [0.17–0.26]	0.35 [0.25–0.47]	0.26 [0.20–0.36]	0.44 [0.34–0.59]
Ad	0.36 [0.29–0.45]	0.45 [0.42–0.52]	0.32 [0.26–0.38]	0.46 [0.40–0.51]
MVA/MVA	0.37 [0.28–0.50]	0.46 [0.42–0.54]	0.29 [0.21–0.47]	0.51 [0.32–0.73]
Ad/Ad	0.39 [0.18–0.47]	0.51 [0.40–0.73]	0.38 [0.17–0.53]	0.28 [0.21–0.43]
Ad/MVA	0.54 [0.49–0.64]	0.64 [0.62–0.76]	0.35 [0.28–0.42]	0.54 [0.27–0.78]
MVA/Ad	0.54 [0.31–0.78]	0.88 [0.78–1.00]	0.37 [0.25–0.89]	0.50 [0.38–0.52]

Table 5-4. Median IgG subclass responses to MERS-CoV spike protein.

Data are presented as median values with IQR. IgG responses are expressed as optical density (OD). Data are pooled from two independent experiments (n = 12 animals per group), except for Ad (n = 10) and Ad/MVA (n = 11) due to missing samples or unavailable volume.

The most pronounced differences between groups were observed in the induction of IgG1 and IgG2a (Figure 5-5A–B). Heterologous vaccination induced higher levels of IgG1 than MVA alone (p = 0.0027 for MVA/Ad; p = 0.0004 for Ad/MVA; Figure 5-5A). The heterologous MVA/Ad prime–boost regimen also elicited the highest levels of IgG2a, with a median of 0.88 OD [0.78–1.0]. These responses were significantly greater than those induced by single-dose vaccination (MVA: 0.40 [0.30–0.50]; Ad: 0.50 [0.40–0.50]; p < 0.0001) or homologous prime–boost regimens (MVA/MVA: 0.50 [0.40–0.70]; p = 0.01; Ad/Ad: 0.50 [0.40–0.50]; p = 0.0003). Similarly, heterologous Ad/MVA (0.64 [0.62–0.76]) induced higher IgG2a levels compared with MVA prime-only vaccination (p = 0.0002). Responses were also greater than those induced by homologous Ad/Ad vaccination, although this difference did not reach significance (p > 0.99; Figure 5-5B). Direct comparison of the two heterologous regimens showed that MVA/Ad induced higher IgG2a than Ad/MVA (1.4-fold difference), but this did not reach

statistical significance ($p > 0.99$). Nonetheless, there was a consistent trend toward stronger IgG2a induction with MVA/Ad, which may have been underestimated due to the limited sample size.

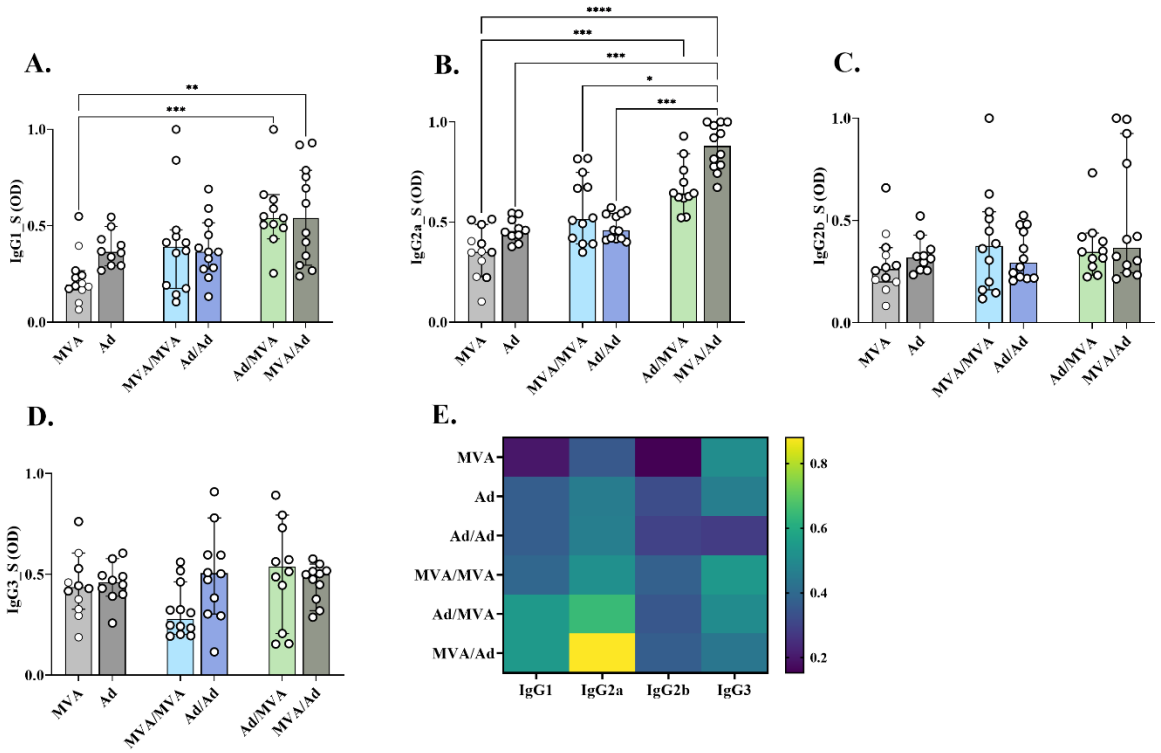


Figure 5-5. MERS-CoV spike-specific IgG subclasses.

(A–E) Individual mouse sera were normalised to 1 IgG EU. Data points represent median responses measured by optical density, with error bars showing median the 95% CI. Data are shown, from left to right, for IgG1**(A),** IgG2a **(B),** IgG2b, **(C)** IgG3 displayed in the second row **(D). (E)** Heatmap summary displaying the median response of each group with representswith higher levels of binding shown in yellow and low levels of binding shown in blue. Statistical analysis: Kruskal–Wallis with Dunn's post-test (*p < 0.05, **p < 0.01, ***p < 0.001, ****p < 0.0001). Colours denote experimental groups: MVA GFP (white), Ad GFP (white), MVA (light grey), Ad (dark grey), MVA–MVA (light blue), Ad–Ad (lavender blue), Ad–MVA (light green), and MVA–Ad (dark green).

5.2.2.3.4 IgG avidity

The avidity of IgG to spike was measured by NaSCN displacement assay, with data combined from MERSIDT001 and MERSIDT002. A small difference between replicates was observed for Ad/Ad in the median avidity index (1.46 [1.25–1.63] in MERSIDT001 vs. 1.41 [1.19–1.73] in MERSIDT002; $p = 0.015$), but this did not alter the overall response hierarchy. Therefore, data from both experiments were combined for analysis. The combined results are shown in Figure 5-6, values are presented as median (IQR) in Table 5-5.

Group	IgG_S avidity index (NaSCN, median [IQR])
MVA	0.9 [0.7–1.4]
Ad	1.1 [0.9–1.2]
MVA/MVA	1.5 [1.2–1.7]
Ad/Ad	1.6 [1.4–1.7]
Ad/MVA	1.4 [1.2–1.5]
MVA/Ad	1.5 [1.4–1.67]

Table 5-5. Median IgG avidity index to MERS-CoV spike protein.
Data are presented as median values with 95% confidence intervals (CI). Antibody avidity is expressed as the sodium thiocyanate (NaSCN) concentration required to dissociate 50% of bound antibody. Responses are pooled from two independent experiments (n = 12 animals per group, except Ad [n = 11] and Ad/MVA [n = 11]).

At the group level, avidity index (AI) was generally higher in boosted regimens than in prime-only vaccination (Figure 5-6A). Significant increases were observed for Ad/Ad, MVA/MVA, and MVA/Ad compared with Ad prime, whereas Ad/MVA did not differ significantly from either Ad or MVA prime ($p > 0.05$). Notably, consistently higher AI was observed when Ad was used as the booster (Ad/Ad and MVA/Ad), suggesting a booster-dependent effect. No significant differences were detected between homologous and heterologous boosted regimens.

Paired analysis showed modest avidity increases after boosting (Figure 5-6B). Homologous regimens showed little to no increase in avidity after boosting (MVA/MVA ~1.8-fold, $p = 0.001$; Ad/Ad ~2-fold, $p = 0.0004$). In contrast, heterologous regimens improved avidity, with Ad/MVA showing a ~1.5-fold increase ($p = 0.01$) and MVA/Ad demonstrating the strongest effect (~2.2-fold, $p = 0.001$). These findings indicate that boosting enhances IgG avidity compared with priming alone, but that this effect is primarily driven by regimens in which Ad is used as the boost, particularly the MVA/Ad combination, which consistently achieved the highest avidity indices.

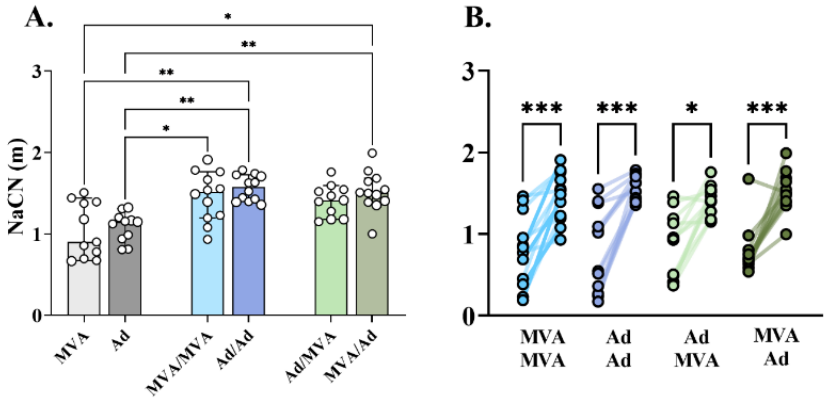


Figure 5-6. IgG avidity following homologous and heterologous vaccination.

(A–B) Avidity of spike-specific IgG was assessed using a NaSCN displacement assay. Data points represent individual mouse sera, with bars indicating the median and error bars showing the 95% CI. **(A)** Group comparisons showing significantly higher avidity in boosted regimens compared with prime-only vaccination, analysed by Kruskal–Wallis test with Dunn's multiple comparisons. **(B)** Paired analysis of pre- and post-boost samples, assessed using the Friedman test with Dunn's multiple comparisons, demonstrated significant increases in avidity following boosting, particularly for heterologous regimens. Colours denote experimental groups: MVA (light grey), Ad (dark grey), MVA–MVA (light blue), Ad–Ad (lavender blue), Ad–MVA (light green), and MVA–Ad (dark green). (*p < 0.05, **p < 0.01, ***p<0.001)

5.2.2.4 FcγR binding profile

FcγR responses were assessed only in the MERS-IDT001 experiment (n = 6 per group). Binding was analysed for FcγRI, FcγRIIB, FcγRIII, and FcγRIV, which are associated respectively with antibody-dependent cellular cytotoxicity (ADCC), regulation of effector function, monocyte/macrophage activation, and neutrophil activity (see Chapter 1). Responses were measured against the full-length spike (S) and its subunits (S1 and S2). Although serum was available from MERS-IDT002 experiment, further FcγR assays required technical optimization that could not be completed within the timeframe of this study. As such, these data should be interpreted with caution, but they provide proof-of-concept evidence of Fc-mediated antibody activity in this vaccine model (Table 5-6).

Group		Spike (MFI, median [IQR])	p-vlaue	S1 (MFI, median [IQR])	p-vlaue	S2 (MFI, median [IQR])	p-vlaue
MVA	FcγRI	18 [8–29]	ns	52 [23–98]	ns	9 [2–21]	ns
Ad		168 [112–290]	ns	720 [528–1291]	0.03	77 [43–121]	ns
MVA/MVA		135 [78–225]	ns	578 [343–1040]	ns	118 [45–252]	ns
Ad/Ad		457 [321–667]	0.03	984 [948–1649]	0.004	174 [75–321]	ns
Ad/MVA		1191 [974–2404]	0.0002	811 [323–1501]	ns	399 [247–691]	0.0038
MVA/Ad		1125 [819–2055]	0.0003	1151 [219–2316]	0.03	1678 [409–2854]	0.0003
MVA	FcγRIIB	2 [1–9]	ns	21 [13–47]	ns	3 [1–10]	ns
Ad		122 [64–148]	ns	484 [348–933]	ns	70 [43–90]	ns

MVA/MVA		105 [50–233]	ns	425 [268–967]	ns	108 [58–181]	ns
Ad/Ad		372 [278–434]	0.002	1342 [1063–1850]	0.01	148 [116–323]	ns
Ad/MVA		259 [221–398]	0.01	1510 [1286–2302]	0.004	648 [308–1366]	0.002
MVA/Ad		1178 [187–2524]	0.001	4182 [1794–5786]	0.0002	1375 [748–2118]	0.0002
MVA	FcγRIII	49 [15–102]	ns	112 [38–214]	ns	11 [1–22]	ns
Ad		1137 [384–6267]	ns	4954 [1142–275647]	0.04	299 [100–1239]	ns
MVA/MVA		637 [338–1110]	ns	1361 [784–3468]	ns	180 [100–526]	ns
Ad/Ad		2088 [948–3017]	0.03	4639 [2095–7354]	ns	362 [256–725]	ns
Ad/MVA		2663 [2058–3734]	0.004	5590 [3747–9311]	0.03	388 [285–641]	0.05
MVA/Ad		5760 [3584–7860]	0.0003	11707 [7471–33649]	0.001	2318 [309–4973]	0.002
MVA	FcγRIV	19 [9–32]	ns	50 [23–89]	ns	12 [3–21]	ns
Ad		145 [100–207]	ns	322 [259–389]	ns	78 [45–124]	ns
MVA/MVA		116 [73–198]	ns	320 [206–512]	ns	100 [77–195]	ns
Ad/Ad		278 [228–339]	0.03	829 [438–2005]	0.007	169 [112–290]	0.03
Ad/MVA		701 [540–1238]	0.0006	1700 [996–2741]	0.0004	283 [264–301]	0.0006
MVA/Ad		1237 [769–2420]	<0.0001	2899 [1332–3957]	0.0001	832 [227–2572]	0.0004

Table 5-6. Median FcγRI responses to MERS-CoV spike, S1, and S2 proteins.

Data are presented as median values with IQR. Antibody responses are expressed as mean fluorescence intensity (MFI). Data are from the MERS-IDT001 experiment (n = 6 animals per group), except for Ad (n = 5) due to missing samples. p-values indicate comparisons with the negative control group.

Ad prime induced detectable binding to activating receptors (Figure 5-7B,H) with FcγRI and FcγRIII against S1 significantly above controls ($p < 0.05$). Both homologous Ad/Ad and heterologous regimens further enhanced FcγR binding to spike, with titres significantly higher than controls ($p < 0.05$) (Figure 5-8).

Across all antigens, the strongest FcyR binding was induced by Ad/Ad, Ad/MVA, and MVA/Ad. Ad/Ad and Ad/MVA frequently gave similar results, while MVA/Ad was consistently the highest regime, although not significantly greater than Ad/Ad and Ad/MVA ($p > 0.05$). Direct comparison of S1 and S2 responses showed that MVA/Ad consistently exceeded Ad/MVA, with only modest differences for S1 (FcγRI = 1.4, FcγRIIB = 1.86, FcγRIII = 2.0, FcγRIV = 1.7), but more pronounced enhancement for S2 (FcγRI = 4.2, FcγRIIB = 2.1, FcγRIII = 5.9, FcγRIV = 2.93). This pattern highlights the broader and functionally more relevant S2 activity elicited by MVA/Ad.

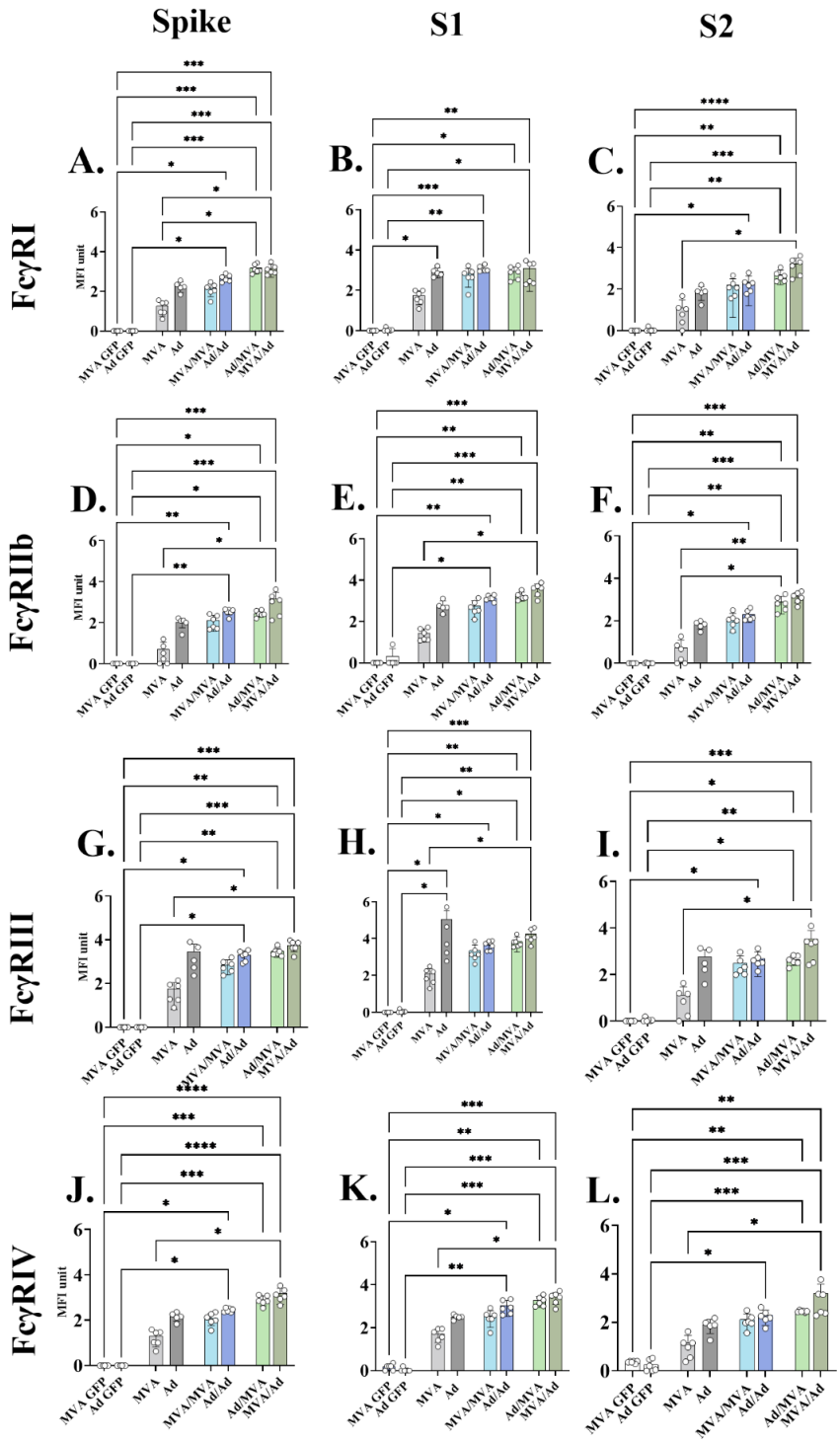


Figure 5-7. Fc receptor (FcR) binding for MERS-CoV.

Median fluorescence intensity (MFI) against MERS-CoV spike protein and its subunits S1 and S2, measured by Luminex as a surrogate for functional activity. Data points represent median responses, with error bars showing median the 95% CI. Statistical analysis was performed using Kruskal–Wallis with Dunn's post-test (*p < 0.05, **p < 0.01, ***p < 0.001, ****p < 0.0001). Panels: **(A–C)** FcγRI binding to Spike, S1, and S2; **(D–F)** FcγRIIb binding to Spike, S1, and S2; **(G–I)** FcγRIII binding to Spike, S1, and S2; (J–L) FcγRIV binding to Spike, S1, and S2.Colours denote experimental groups: MVA GFP (white), Ad GFP (white), MVA (light grey), Ad (dark grey), MVA–MVA (light blue), Ad–Ad (lavender blue), Ad–MVA (light green), and MVA–Ad (dark green). Data are shown for study MERSIDT001.

Consistent with these quantitative analyses, heatmap visualization (Figure 5-8A) revealed that MVA/MVA remained indistinguishable from baseline, Ad and Ad/Ad induced limited activity, while both heterologous regimens elicited broader FcγR engagement, with MVA/Ad displaying the most widespread and intense binding across receptors and spike subdomains. Overall, the hierarchy of FcγR-binding responses was: MVA/Ad > Ad/MVA ≈ Ad/Ad >> MVA/MVA ≈ negative controls, indicating that heterologous regimens clearly outperformed MVA/MVA, which remained at baseline levels, while the most consistent and functionally relevant FcγR engagement was achieved with MVA/Ad. Binding antibodies and FcγRs were found to be highly correlated with each other, highlighting their close relationship in the immune response (Figure 5-9B).

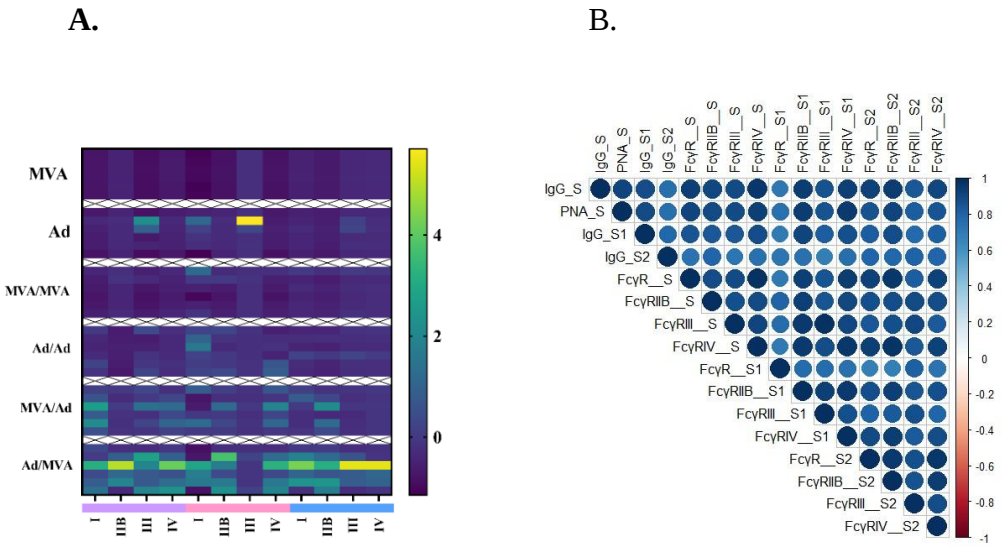


Figure 5-8. Overview of vaccine-induced Fcγ receptor binding profiles and functional correlations. (A) Heatmap of Fcγ receptor (FcγR) binding profiles of vaccine-induced antibodies. Spike-specific antibody FcγR interactions were quantified by Luminex-based multiplex assay using sera from vaccinated mice. Binding to murine FcγRI, FcγRIIB, FcγRIII, and FcγRIV was measured against full-length spike (S, purple), S1 (pink), and S2 (blue) subdomains. Data are presented as normalized z-scores (standard deviations from the mean), with each row representing an individual mouse and each column corresponding to an antigen/receptor combination. The colour scale represents relative binding activity, with purple denoting low and yellow denoting high responses. **(B)** Pairwise Pearson correlation coefficients (R) shown between antibody binding, neutralisation (PNA) and Fcγ receptor engagement (FcγRI, FcγRIIB, FcγRIII, FcγRIV) measured against spike and its subunits (S1, S2). Values in each cell represent correlation coefficients, with colour intensity indicating the strength and direction of correlation (blue = positive, red = negative). The scale bar denotes correlation strength from –1.0 to +1.0.

5.2.3 Cellular responses

Assessments were performed only in the MERS-IDT002 experiment (n = 6 per group), as this analysis was added in an exploratory manner following completion of MERS-IDT001.

5.2.3.1 ASC in the spleen and Bone Marrow.

To assess ASC, we first measured ASC IgG frequencies in spleen and BM. This was followed by a 5-day expansion to detect memory B cell–derived ASC responses. Data are shown in Figure 5-9, and Table 5-7.

Group	Spleen ASC ($ASC/10^6$ cells, median [IQR])	BM ASC ($ASC/10^6$ cells, median [IQR])	Spleen memory ASC ($ASC/10^6$ cells, median [IQR])	Spleen memory ASC ($ASC/10^6$ cells, median [IQR])
MVA	1.276 [1.118–1.583]	2.775 [1.541–4.78]	2.360 [1.255-3.334]	5.947 [2.928–18.56]
Ad	4.539 [4.201–6.461]	2.624 [1.752–3.388]	17.15 [12.99–31.23]	9.1 [1.0–97.22]
MVA/MVA	4.028 [2.272–8.187]	33.54 [25.65–52.1]	26.07 [18.15–61.13]	14.18 [1.542–25.66]
Ad/Ad	16.97 [8.782–23.8]	37.45 [16.59–53.35]	36.97 [23.72–44.71]	189.2 [9.056–226.3]
Ad/MVA	8.84 [7.186–9.89]	73.65 [40.29–110.8]	30.75 [27.56–38.32]	26.72 [21.57–42.81]
MVA/Ad	26.68 [15.62–43.25]	103.6 [59.86–139.2]	39.5 [20.22–64.94]	46.46 [36.89–115.6]

Table 5-7. Median ASC IgG responses to MERS-CoV spike protein before and after expansion in spleen and bone marrow (BM).

Data are presented as median values with IQR. IgG responses are expressed as spot-forming units (SFU) per million cells. Data are from the MERS-IDT002 experiment (n = 6 animals per group), except for Ad/MVA (n = 5) due to missing samples or unavailable data.

Prime-only vaccination with MVA or Ad induced minimal IgG ASC responses in both spleen and BM, comparable to negative controls (Figure 5-9A–B). Homologous boosting regimens resulted in detectable ASC responses with distinct tissue distributions. Ad/Ad vaccination was associated with higher ASC frequencies in the spleen (17 [9–24] SFU/million; p = 0.002; Figure 5-9A) and in the BM (33 [17–53] SFU/million; p = 0.051; (Figure 5-9B). In contrast, MVA/MVA vaccination elicited low ASC frequencies in the spleen (4 [2–17] SFU/million; p = 0.229; Figure 5-9A) but higher frequencies in the BM (37 [26–52] SFU/million; p = 0.03; Figure 5-9B). These patterns suggest regimen-dependent ASC localisation, with more rapid migration and accumulation of ASCs in the BM following MVA/MVA vaccination, whereas Ad/Ad vaccination was characterized by a comparatively stronger splenic response at the point analysed.

Heterologous vaccination regimens also exhibited tissue-specific ASC distributions. Ad/MVA induced low ASC frequencies in the spleen (9 [7–10] SFU/million; Figure 5-9A), which were not significantly different from controls (p = 0.08), but was associated with higher ASC frequencies in the BM (44 [40–111] SFU/million; p = 0.004; Figure 5-9B. In contrast, MVA/Ad elicited robust ASC responses in both the spleen (28 [16–43] SFU/million; p = 0.0001; Figure 5-9A) and the BM (74 [60–109] SFU/million;

$p < 0.0001$; Figure 5-9B). Specifically, MVA priming appears to promote more rapid ASC generation and early accumulation in the BM, whereas Ad priming is associated with a slower build-up of ASCs that remain detectable in the spleen at the analysed time point.

Direct comparison confirmed that MVA/Ad responses were consistently higher than Ad/MVA across tissues, but these differences did not reach significance, likely reflecting the small sample size. Representative B ELISpot wells supported these findings, showing more numerous and intense spots after heterologous boosting—particularly with MVA/Ad—compared with homologous or prime-only regimens. ASC frequencies correlated strongly with both serum IgG and neutralising antibody titres. *Ex vivo* memory B cell responses were quantified by IgG ELISpot following 5-day culture of spleen and BM cells in expansion media (Figure 5-9C–D). In the spleen (Figure 5-9C) all PB regimens induced significant increases in IgG memory B cell ASC compared with negative controls ($p<0.05$), while prime only regimens had no significant response ($p>0.05$ vs. negative controls). Furthermore, there were no significant differences between homologous and heterologous regimens, or between the two heterologous groups (Ad/MVA vs. MVA/Ad).

In contrast, BM cultures showed no significant differences in IgG memory B cell ASC between vaccinated groups. However, these cultures exhibited high background activity (Figure 5-9D), particularly in negative controls, and no significant differences were detected between vaccinated groups.

Together, these results indicate that vaccination induced spike-specific memory B-cell responses in the spleen across multiple regimens. While both homologous and heterologous boosting strategies elicited detectable responses, no consistent differences in response magnitude were observed between PB regimens at the time point analysed.

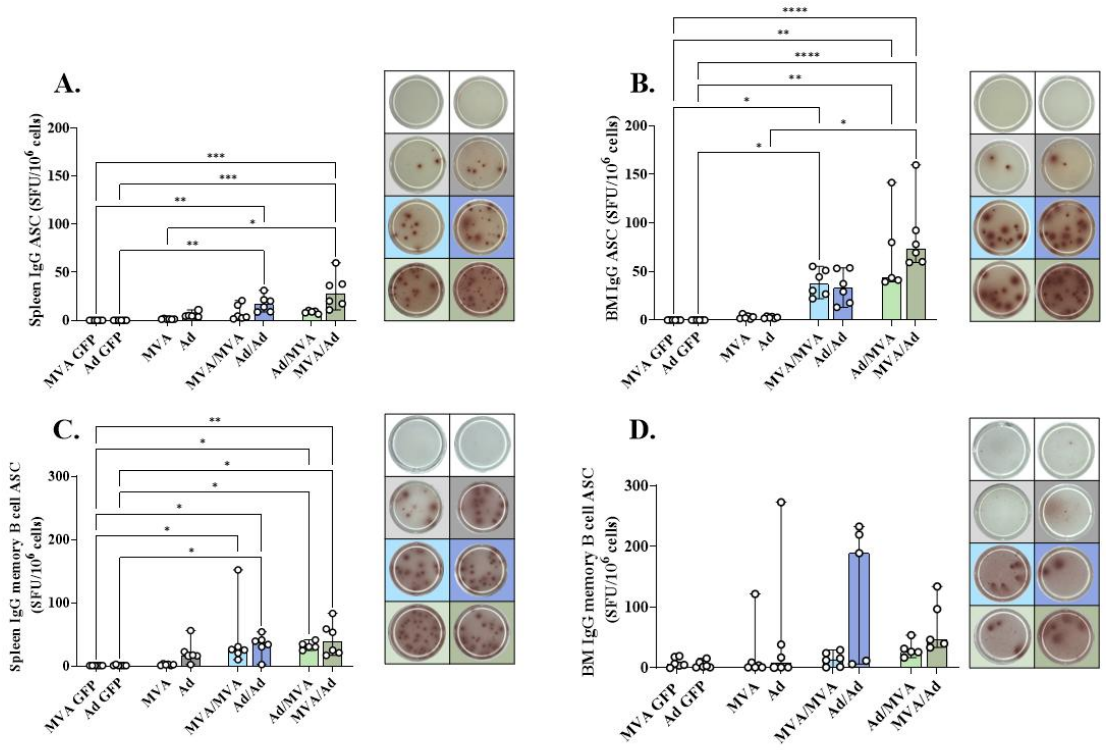


Figure 5-9. Antibody-secreting cell (ASC) responses in spleen and bone marrow.

(A–B) Frequencies of spike-specific IgG ASCs in spleen **(A)** and bone marrow **(B)** measured directly ex vivo by ELISpot with a representative figure of the wells per group. (C–D) Frequencies of spike-specific IgG memory B cell ASCs in spleen **(C)** and bone marrow **(D)** following 5-day expansion culture. Bars indicate median values with 95% confidence intervals (CI). Statistical analysis was performed using Kruskal–Wallis with Dunn's post-test (*p < 0.05, **p < 0.01, ***p < 0.001, ****p < 0.0001). Representative ELISpot wells are shown next to each panel, with background shading corresponding to group colours. Colours denote groups: MVA GFP (white), Ad GFP (white), MVA (light grey), Ad (dark grey), MVA/MVA (light blue), Ad/Ad (lavender blue), Ad/MVA (light green), MVA/Ad (dark green). Data points represent median responses, with error bars showing median the 95% CI.

Serum IgG titres correlated strongly with ex vivo IgG ASC frequencies in both spleen and BM (Spearman R = 0.9, p < 0.0001; Figure 5-10A). PNA titres also correlated closely with ex vivo ASC responses (spleen: R = 0.82, p < 0.0001; BM: R = 0.9, p < 0.0001; Figure 5-10B). Memory IgG ASC responses after 5-day expansion were likewise associated with serum antibody levels. Strong correlations were observed between IgG titres and memory ASC in both spleen (R = 0.82, p < 0.0001) and BM (R = 0.76, p < 0.0001; Figure 5-10C). Associations with PNA were moderate but significant (spleen: R = 0.6, p = 0.0002; BM: R = 0.6, p = 0.0003; Figure 5-10D). These findings support a model in which serum IgG and neutralising antibody levels predominantly reflect ASC/plasma cell activity at the time of sampling. While significant correlations were also observed between IgG titres and memory ASC frequencies, these were weaker than those observed for ex vivo ASC responses. This indicates

that memory B cells, although clearly induced and functionally competent, are not the principal contributors to circulating antibody titres under steady-state conditions.

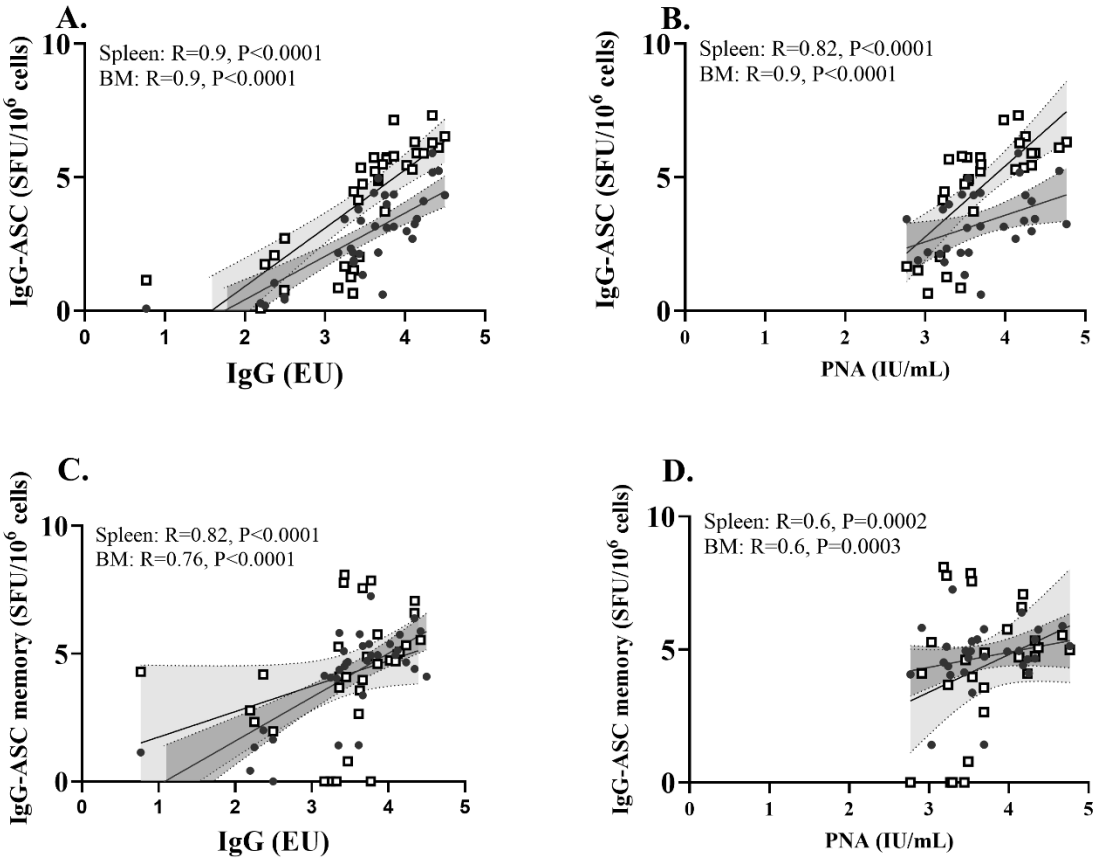


Figure 5-10. Correlations between serum antibody titres and ASC responses in spleen and bone marrow.

(**A–B)** Correlation of serum IgG **(A)** and PNA titres **(B)** with ex vivo IgG ASC frequencies in spleen (black dots) and bone marrow (white squares). **(C–D)** Correlation of serum IgG **(C)** and PNA titres **(D)** with memory IgG ASC frequencies after 5-day expansion. Data points from spleen are depicted as circles and from bone marrow as squares. Shaded areas indicate 95% confidence intervals of the regression fit. Data were log10-transformed prior to analysis. Correlations were assessed using Spearman's rank; coefficients (R) and p-values are shown in each panel.

5.2.3.2 IFNγ ELISPOT and ICS

The magnitude of IFN-γ responses was evaluated by stimulating splenocytes overnight with a single peptide corresponding to the immunodominant epitope VYDTIKYYSIIPHSI of the MERS-CoV spike, as previously described [307]. IFN-γ production was assessed in both MERS-IDT001 and MERS-IDT002. Absolute response levels varied between experiments, with Ad prime ~1.6-fold higher and Ad/MVA ~1.27-fold higher in MERS-IDT002 ($p = 0.0087$). Despite these shifts in magnitude, the hierarchy of responses remained consistent: MVA/Ad induced the strongest IFN-γ production, followed

by Ad/MVA, then the homologous regimens (Ad/Ad and MVA/MVA), with prime-only groups (Ad and MVA) showing the lowest responses (Figure 5-11). Raw data and corresponding medians are summarized in Table 5-8.

Group	IFN-γ producing spots (SFU per 10^6 cells, median [IQR])
MVA	323.7 [161.0–609.0]
Ad	1646.0 [1011.0–1973.0]
MVA/MVA	641.7 [506.6–1055.0]
Ad/Ad	1773.0 [1457.0–2072.0]
Ad/MVA	2375.0 [1983.0–3413.0]
MVA/Ad	2878.0 [2351.0–4098.0]

Table 5-8. Median IFN-γ producing spots by ELISpot in response to the immunodominant epitope in spleen.

Data are presented as median values with IQR. IFN-γ ELISpot responses are expressed as spot-forming units (SFU) per million splenocytes. Responses are pooled from two independent experiments (n = 12 animals per group), except for Ad (n = 11) and Ad/MVA (n = 11).

All vaccination regimens induced higher responses compared with non-vaccinated controls ($p<0.05$), with the exception of MVA prime only ($p=0.97$). Ad regimens were significantly higher than MVA for both prime only and homologous PB (p =0.0067 and p=0.0197, respectively) (Figure 5-11). Homologous boosting did not enhance responses relative to priming for either Ad/Ad or MVA/MVA ($p=0.9955$ and 0.9316, respectively) (Figure 5-11).

The highest responses overall were achieved with heterologous regimens, particularly MVA/Ad, with no significant difference observed between the two heterologous regimens ($p=0.64$). Thus, a single Ad immunisation was sufficient to induce strong IFNγ responses compared with MVA, with the latter not improved by homologous boosting.

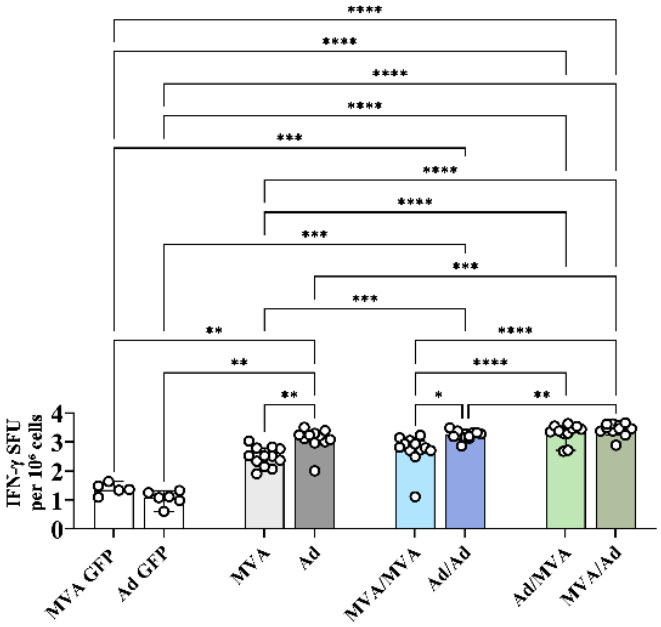


Figure 5-11. IFNγ ELISpot responses to MERS-CoV spike.
Splenocytes were stimulated overnight with the immunodominant spike peptide VYDTIKYYSIIPHSI, and IFNγ-producing cells were quantified using ELISpot reader. Data points represent median responses, with error bars showing median the 95% CI. Statistical analysis was performed using one-way ANOVA with Tukey's post-test *(*$p < 0.05$, *$p < 0.01$, **$p < 0.001$, *$p < 0.0001$). Colours denote experimental groups: MVA GFP (white), Ad GFP (white), MVA (light grey), Ad (dark grey), MVA–MVA (light blue), Ad–Ad (lavender blue), Ad–MVA (light green), and MVA–Ad (dark green).

The phenotype and functional capacity of T-cell responses were assessed by flow cytometry after overnight stimulation of splenocytes with a single peptide corresponding to the immunodominant epitope VYDTIKYYSIIPHSI, using intracellular cytokine staining combined with memory phenotyping profiling (Figure 5-12). Across all experimental groups, splenocyte viability exceeded 65% following processing and stimulation, which falls within acceptable ranges for ICS assays following extended ex vivo stimulation and fixation/permeabilization. Importantly, no significant differences were observed in the overall frequencies of $CD4^+$ or $CD8^+$ T cells among the different vaccination regimens ($p > 0.05$). MERS-CoV–specific responses were predominantly mediated by $CD8^+$ T cells (Figure 5-12A), while $CD4^+$ T-cell responses were low and close to background (Figure 5-12B). The corresponding summary data for $CD8^+$ T cells are presented in Table 9; $CD4^+$ responses were not tabulated due to their low magnitude.

Group	IFN-γ^+ (%, median [IQR])	TNFα^+ (%, median, [IQR])	IFN-γ^+ TNFα^+ (%, median, [IQR])
MVA	0.03 [0.03–0.03]	0.04 [0.03–0.05]	0.02 [0.01–0.02]
Ad	0.02 [0.02–0.04]	0.03 [0.01–0.06]	0.12 [0.08–0.19]
MVA/MVA	0.01 [0.01–0.01]	0.03 [0.03–0.05]	0.04 [0.02–0.05]

Ad/Ad	0.02 [0.01–0.04]	0.16 [0.02–0.38]	0.02 [0.01–0.03]
Ad/MVA	0.02 [0.01–0.04]	0.04 [0.02–0.04]	0.27 [0.15–0.35]
MVA/Ad	0.02 [0.02–0.04]	0.03 [0.02–0.05]	0.21 [0.16–0.24]

Table 5-9. Median ICS responses to the immunodominant epitope in spleen.

Data are presented as median values with IQR. IFN-γ ELISpot responses are expressed as spot-forming units (SFU) per million splenocytes. Responses are pooled from two independent experiments (n = 12 animals per group), except for Ad (n = 11) and Ad/MVA (n = 11) due to missing samples.

$IFN\gamma^+TNF\alpha^+$ $CD8^+$ T-cell frequencies were significantly higher than GFP controls ($p < 0.05$) for all regimens except MVA and MVA/MVA ($p > 0.99$). Responses in the Ad prime group were not significantly different from negative controls ($p = 0.07$) (Figure 5-12A). The highest frequencies of $IFN\gamma^+TNF\alpha^+$ double-positive $CD8^+$ T cells were induced by the heterologous Ad/MVA regimen (median 0.27% [IQR: 0.15–0.35]), followed by MVA/Ad (median 0.2% [IQR: 0.16–0.23]) and Ad/Ad (median 0.2% [IQR: 0.16-0.26]). Representative flow cytometry plots illustrating these cytokine-producing $CD8^+$ T-cell responses across vaccination groups are shown in Figure 5-12C. These findings underscore the limited capacity of MVA to elicit strong T cell immunity as either prime or homologous boost, at least against this immunodominant epitope, while adenovirus-containing regimens—particularly in heterologous combinations—were most effective. Although ELISpot analysis showed comparable IFNγ responses following Ad/MVA and MVA/Ad vaccination, flow cytometric analysis suggested a trend toward higher responses with Ad/MVA, although this did not reach statistical significance. These differences are likely assay-dependent, as ELISpot measures cumulative IFNγ secretion over prolonged stimulation and may capture cytokine production from multiple responding cell types, whereas flow cytometry specifically quantifies IFNγ production by viable T cells following stimulation, potentially revealing differences in activation kinetics.

$CD4^+$ T cell responses specific to the immunodominant epitope were minimal (Figure 5-12B). Reported frequencies represent values after subtraction of media-only background controls. Background-subtracted frequencies of $IFN\gamma^+$ or $TNF\alpha^+$ single-positive cells (≤0.05%) and $IFN\gamma^+TNF\alpha^+$ double-positive cells (≤0.008%) were essentially undetectable. Elevated background activity was observed in negative controls, particularly in the MVA GFP group. Although the MVA/Ad regimen showed the numerically highest frequency of $IFN\gamma^+CD4^+$ cells (median 0.029% [IQR: 0.02–0.04]), these values remained within assay noise and were indistinguishable from negative controls. Collectively, these findings indicate an absence of detectable $CD4^+$ T-cell responses to the immunodominant epitope and support the conclusion that epitope-specific cellular immunity induced by viral-vector vaccination against MERS-CoV is predominantly mediated by $CD8^+$ T cells.

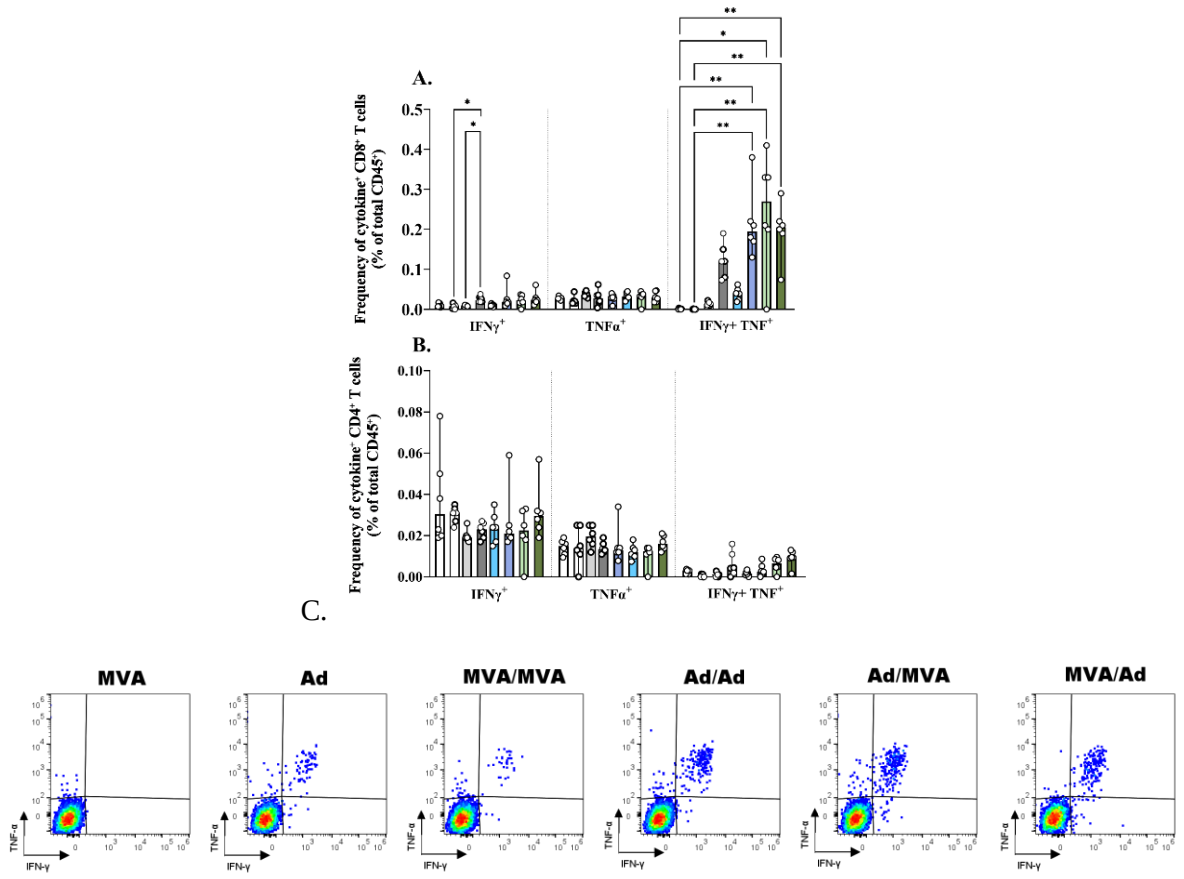


Figure 5-12. Flow cytometric analysis of CD8$^+$ and CD4$^+$ T-cell cytokine responses.

Splenocytes were stimulated overnight with a MERS-CoV spike immunodominant epitope, and intracellular cytokine staining was performed to quantify IFNγ$^+$and TNFα$^+$T cells. **(A)** Frequencies of cytokine$^+$ CD8$^+$ T cells expressed as a percentage of live CD45$^+$ T cells. **(B)** Frequencies of cytokine$^+$ CD4$^+$ T cells expressed as a percentage of total CD45$^+$ T cells. **(C)** Representative flow cytometry dot plots showing IFNγ$^+$ and TNFα$^+$ CD8$^+$ T-cell responses across vaccination groups. Data points on figures represent individual mice; bars show the median, with error bars indicating the 95% CI. Statistical analysis was performed using the Kruskal–Wallis test with Dunn's multiple comparisons (*p < 0.05, **p < 0.01). Colours denote experimental groups: MVA (light grey), Ad (dark grey), MVA/MVA (light blue), Ad/Ad (lavender blue), Ad/MVA (light green), and MVA/Ad (dark green).

Effector-memory CD8$^+$ T-cell responses were most pronounced following adenovirus-containing vaccination regimens, particularly prime–boost strategies. Ad/MVA (median 0.22% IFNγ$^+$TNFα$^+$ CD8$^+$ T cells, IQR: 0.04–0.30), MVA/Ad (median 0.17%, IQR: 0.16–0.21), and Ad/Ad (median 0.16%, IQR: 0.13–0.20), were all significantly greater than GFP controls ($p<0.05$), whereas MVA/MVA was not. No significant differences were observed between heterologous and homologous Ad-based regimens.

Naïve-like (CD44$^-$CD62L$^+$) CD8$^+$ T-cell IFNγ$^+$TNFα$^+$ responses were minimal overall but followed a consistent pattern across vaccination regimens. The highest frequencies were observed following

Ad/MVA vaccination, followed by Ad/Ad and MVA/Ad regimens, while adenoviral prime alone induced similarly low-level responses comparable to those seen with homologous or heterologous regimens. All adenovirus-containing vaccination strategies elicited significantly higher naïve-like $IFN\gamma^{+}TNF\alpha^{+}$ $CD8^{+}$ T-cell frequencies than negative control groups ($p < 0.05$), although responses within this compartment remained substantially lower than those observed in effector and effector-memory populations.

Collectively, these data demonstrate that inclusion of an adenoviral vector is sufficient to drive robust effector and effector-memory $CD8^{+}$ T-cell differentiation, with heterologous Ad-based prime–boost regimens enhancing the magnitude of polyfunctional $IFN\gamma^{+}TNF\alpha^{+}$ responses.

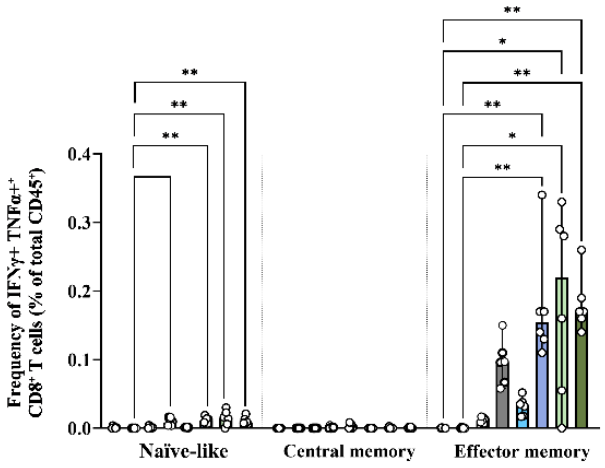


Figure 5.12. Flow cytometric analysis of polyfunctional $CD8^{+}$ and $CD4^{+}$ T-cell cytokine responses and memory phenotypes.

Splenocytes were stimulated overnight with a MERS-CoV spike immunodominant epitope, followed by intracellular cytokine staining to quantify IFNγ- and TNFα-producing T cells. Memory $CD8^{+}$ T-cell subsets were defined based on surface marker expression, with naïve-like cells identified as $CD44^{-}CD62L^{+}$, central memory cells as $CD44^{+}CD62L^{+}$, and effector-memory cells as $CD44^{+}CD62L^{-}CD127^{+}$. Data points represent individual mice; bars indicate the median, with error bars showing the 95% confidence interval. Statistical analysis was performed using the Kruskal–Wallis test with Dunn's multiple-comparisons correction (*$p < 0.05$, **$p < 0.01$). Colours denote experimental groups: MVA (light grey), Ad (dark grey), MVA/MVA (light blue), Ad/Ad (lavender blue), Ad/MVA (light green), and MVA/Ad (dark green).

5.2.4 Determinants of Immune Response

5.2.4.1 High-dose MVA/MVA enhances humoral and cellular immunity compared to low-dose MVA/MVA

Previous studies have indicated that MVA dose can influence vaccine immunogenicity [294, 398]. To assess this, an additional high-dose MVAH/MVAH group (n = 6) was included alongside the standard dose regimen (n = 6), as summarised in Table 5-10. High-dose MVA/MVA vaccination induced significantly higher total MERS-S IgG titres than low-dose MVA/MVA (Figure 5-13A), with similar but non-significant trends for S1- and S2-specific IgG (Figure 5-13A). Neutralising antibody activity measured by PNA was also significantly increased in the high-dose group (Figure 5-13C). IgM and IgA responses were similar (Figure 5-13A) and IgG subclass distributions were comparable between groups (Figure 5-13B). By contrast, cellular responses measured by IFN-γ ELISpot were significantly higher in the high-dose MVA/MVA group (Figure 5-13C).

High-dose MVA/MVA induced significantly stronger binding across multiple FcγRs and antigens, including FcγRI (Spike, S2), FcγRIIB (Spike, S1), FcγRIII (Spike, S1, S2), and FcγRIV (Spike, S1, S2) (Figure 5-15D-F). These findings indicate that dose escalation not only increases antibody titres but also enhances Fc-mediated effector potential.

Group		Spike (MFI, median [IQR])		S1 (MFI, median [IQR])		S2 (MFI, median [IQR])	P-value
MVA/MVA	IgG	3793[2173–6872]	0.0025	217 [161-350]	ns	90 [67–181]	ns
MVA/MVA	IgG	8621 [6883-9629]		366 [5-1097]		54 [7-105]	
MVA/MVA	IgA	183 [102–359]	ns				
MVA/MVA	IgA	104 [20-145]					
MVA/MVA	IgM	461 [292–618]	ns				
MVA/MVA	IgM	1170 [829 -2359]					
MVA/MVA	IgG1	0.37 [0.28–0.50]	ns				
MVA/MVA	IgG1	0.39 [0.34-0.65]					
MVA/MVA	IgG2a	0.46 [0.42–0.54]	ns				
MVA/MVA	IgG2a	0.65 [0.49-0.80]					
MVA/MVA	IgG2b	0.29 [0.21–0.47]	ns				
MVA/MVA	IgG2b	0.30 [0.26-0.34]					
MVA/MVA	IgG3	0.51 [0.32–0.73]	ns				
MVA/MVA	IgG3	0.42 [0.31-0.56]					
MVA/MVA	PNA	2358 [1601–3398]	0.0047				
MVA/MVA	PNA	5012 [3297–8668]					

MVA/MVA	IFN-γ ELISpot	642 [507–1055]	0.0097				
MVA/MVA	IFN-γ ELISpot	1512 [1192–1862]					
MVA/MVA	FcγRI	135 [78–225]	0.0005	578 [343–1040]	ns	118 [45–252]	0.0022
MVA/MVA	FcγRI	1520 [1139–2620]		397 [302–528]		799 [634–1243]	
MVA/MVA	FcγRIIB	105 [50–233]	0.0058	425 [268–967]	0.01	108 [58–181]	ns
MVA/MVA	FcγRIIB	320 [246–392]		1540 [1210–2180]		368 [250–514]	
MVA/MVA	FcγRIII	637 [338–1110]	0.02	1361 [784–3468]	0.01	180 [100–526]	0.001
MVA/MVA	FcγRIII	2092 [1210–3584]		1226 [841–2063]		397 [306–481]	
MVA/MVA	FcγRIV	116 [73–198]	0.0022	320 [206–512]	0.0022	100 [77–195]	<0.0001
MVA/MVA	FcγRIV	770 [599–1235]		1075 [688–1995]		1512 [1192–1862]	

Table 5-10. Median FcγRI responses to MERS-CoV spike, S1, and S2 proteins in low and high dose MVA.

Data are presented as median values with IQR. Antibody responses are expressed as mean fluorescence intensity (MFI). Data are from the MERS-IDT001 experiment (n = 6 animals per group), except for Ad (n = 5) due to missing sample. p-values indicate comparisons with the negative control group. Grey boxes indicate assays that were not performed for the corresponding group.

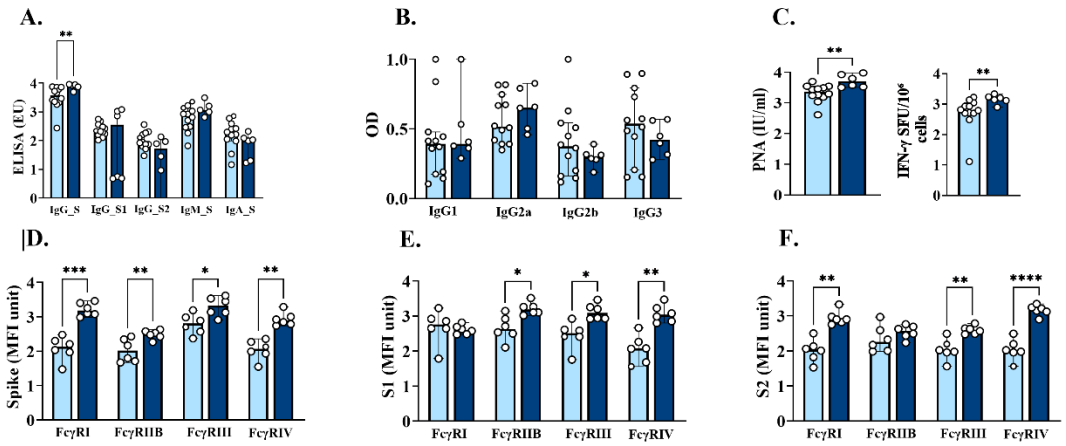


Figure 5-13. Fcγ receptor (FcγR) binding responses following homologous MVA/MVA vaccination at low or high dose.

Individual data points are shown. Colour code: light blue = MVA/MVA (low dose); dark blue = MVA/MVA (high dose). **(A)** IgG, IgM, and IgA binding to full-length spike and its subunits (S1, S2) measured by ELISA. **(B)** IgG subclass distribution (IgG1, IgG2a, IgG2b, IgG3). **(C–E)** Fcγ receptor engagement (FcγRI, FcγRIIB, FcγRIII, FcγRIV) by spike **(C),** S1 **(D),** and S2 **(E).** Data points represent individual animals. Bars show either median values [IQR]. Statistical analysis: Comparisons between two groups were performed using Mann–Whitney U tests. Asterisks (*) denote statistical significance for within-group and between-cohort comparisons, as defined by P-values: * (P<0.05), ** (P<0.01), *** (P<0.001), **** (P<0.0001).

5.2.4.2 Influence of regimen order and dose escalation

To further interpret these findings, an additional comparative analysis was performed to directly compare heterologous and homologous vaccination regimens (Figure 15-17). Since heterologous

schedules (Ad/MVA and MVA/Ad) were evaluated using low-dose MVA, enabling direct comparison with the homologous low-dose MVA/MVA group, the high-dose MVA/MVA arm served as a benchmark to assess whether heterologous vaccination could achieve immune responses comparable to homologous dose escalation.

5.2.4.2.1 Binding and Neutralising antibodies

Serological analysis revealed clear differences between homologous and heterologous regimens (Figure 5-14). Total IgG titres (Figure 5-14A) were significantly higher in the MVA/Ad regimen compared with all other groups. Notably, MVA/Ad induced ~2.6-fold higher IgG than Ad/MVA ($p < 0.0001$). When comparing groups side by side, MVA/Ad responses for S1 were higher than those in low-dose MVA/MVA and Ad/Ad (Figure 5-14B). For S2, MVA/Ad also exceeded responses from homologous MVA at both low and high doses (Figure 5-14C). Interestingly, Ad/MVA responses for S2 appeared higher than those in the high-dose MVA/MVA group, though not when compared with the standard dose MVA/MVA group. This apparent difference may reflect the smaller sample size in the high-dose MVA/MVA arm (n=6) compared with the other groups (n=12), which could contribute to variability (Figure 5-14C). It is possible that higher antigen dosing may induce altered functional responsiveness in a subset of cells, potentially contributing to reduced or heterogeneous responses. Further experimental investigation would be required to directly assess dose-dependent effects on immune responsiveness.

Pseudovirus neutralisation titres (Figure 5-14D) were higher in heterologous regimens compared with homologous vaccination. Notably, high-dose MVA/MVA achieved neutralisation levels comparable to heterologous schedules. Consistent with this, high-dose MVA/MVA also produced IgG2a responses broadly similar to those of heterologous regimens (Figure 5-14H). Class switching to IgM and IgA was particularly evident in the MVA/Ad group, which induced higher IgM than low-dose MVA/MVA and higher IgA than all homologous groups (Figure 5-14E-F). There were no differences between regimens in IgG class switching toward IgG1 and IgG2b, or in antibody avidity (Figure 5-14J,K,L). However, IgG3 levels were higher in Ad/MVA compared with Ad/Ad (Figure 5-14J)

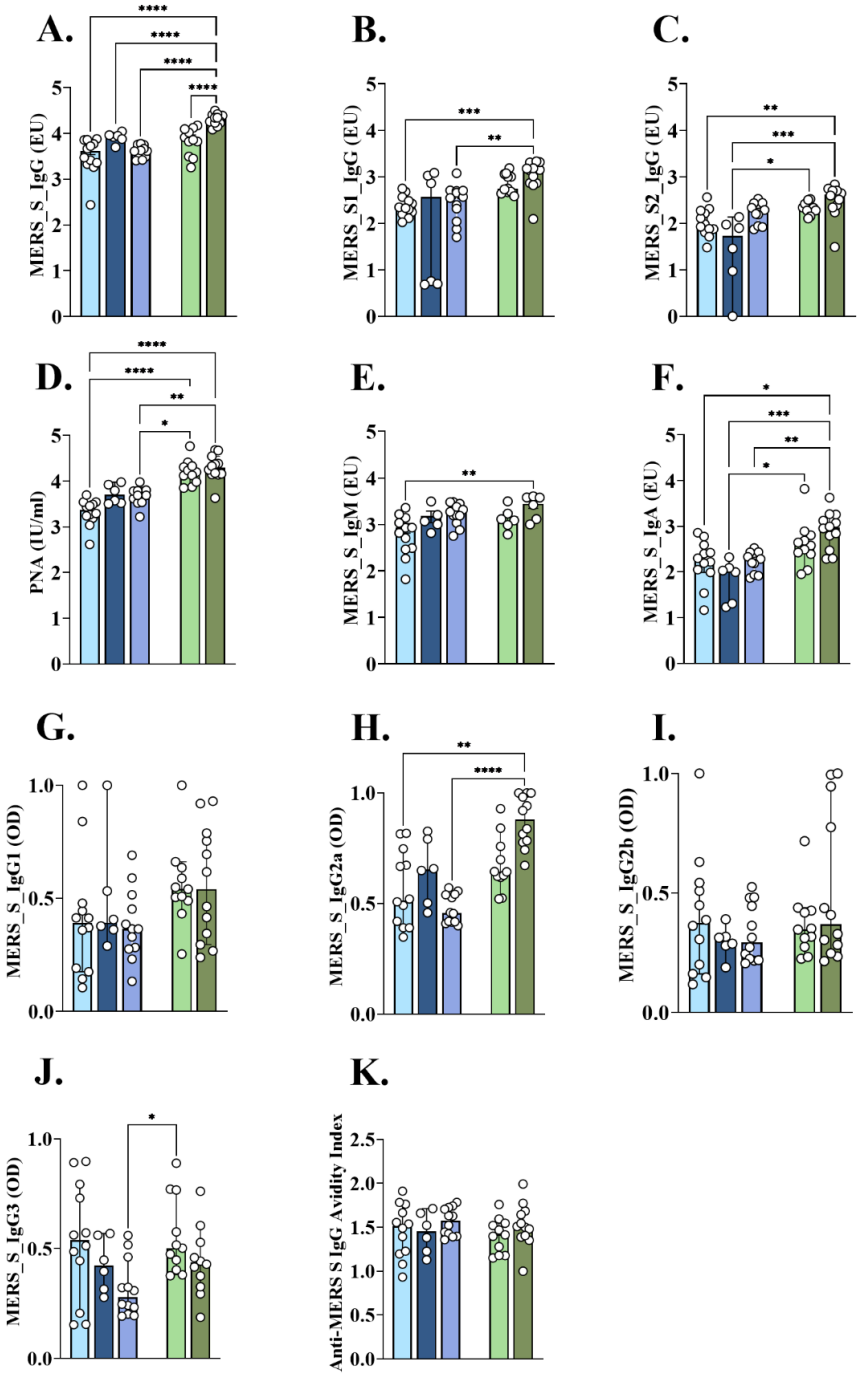


Figure 5-14. Humoral responses following homologous and heterologous prime–boost vaccination.

Humoral immunity was assessed by ELISA and pseudovirus neutralisation. Individual data points represent responses in single mice. Colours denote experimental groups: MVA/MVA low dose (light blue), MVA/MVA high dose (dark blue), Ad/Ad (lavender blue), Ad/MVA (light green), and MVA/Ad (dark green). **(A)** Total MERS-S IgG, **(B)** MERS-S1 IgG, **(C)** MERS-S2 IgG, **(D)** pseudovirus neutralisation assay (PNA), **(E)** MERS-S IgM, **(F)** MERS-S IgA, **(G–J)** IgG subclasses (IgG1, IgG2a, IgG2b, IgG3), and **(K)** IgG avidity index. Data presentation: normally distributed datasets (A, E) are shown as mean ± SEM; all other datasets (B–D, F–K) are shown as median with interquartile range (IQR). Statistical analysis: one-way ANOVA with Tukey's post-hoc test for normally distributed data; Kruskal–Wallis with Dunn's post-test for non-normally distributed data. ns = not significant; *p < 0.05; **p < 0.01; ***p < 0.001; ****p < 0.0001.

5.2.4.2.2 FcγR analysis

FcγR analysis revealed distinct patterns between regimens (Figure 5-15). MVA/Ad consistently produced the highest responses across most readouts, with notable increases against individual subunits. The strongest effect was observed for FcγRIIB binding to S1 (Figure 5-15E), where MVA/Ad was significantly higher than all other groups, including Ad/MVA. Similarly, FcγRIV binding to S2 was higher in MVA/Ad than in homologous regimens (Figure 5-15L).

By contrast, Ad/MVA responses were generally comparable to homologous vaccination, with the exception of FcγRIV binding to S2 (Figure 5-15L) , where Ad/MVA exceeded low-dose MVA/MVA and Ad/Ad. Interestingly, high-dose MVA/MVA was comparable to heterologous regimens across most readouts, with the exception of FcγRIIb binding to S1 (Figure 5-15E), which remained highest in MVA/Ad . Notably, Ad/Ad performed better than heterologous Ad/MVA in inducing FcγRIIB binding (Figure 5-15H).

Collectively, these findings indicate that homologous and heterologous regimens generate distinct FcγR binding signatures, with MVA/Ad standing out as the most potent inducer across multiple receptors and subunits.

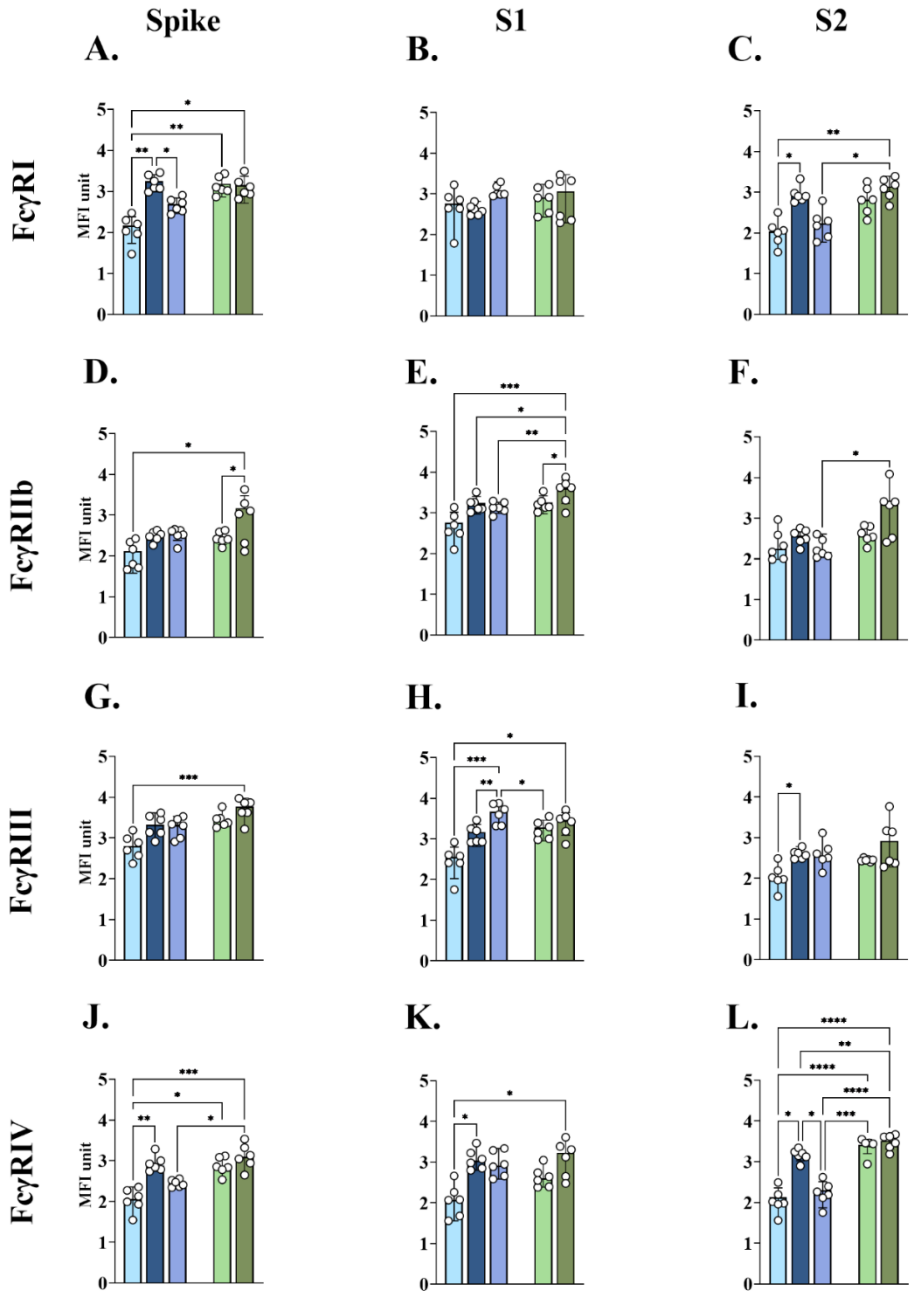


Figure 5-15. Fcγ receptor (FcγR) binding responses following homologous and heterologous prime–boost vaccination.

FcγR binding activity of vaccine-induced antibodies was assessed by Luminex. Individual data points represent responses in single mice. Colours denote experimental groups: MVA/MVA low dose (light blue), MVA/MVA high dose (dark blue), Ad/Ad (lavender blue), Ad/MVA (light green), and MVA/Ad (dark green). **(A–C)** FcγRI binding to spike, S1, and S2; **(D–F)** FcγRIIB binding to spike, S1, and S2; **(G–I)** FcγRIII binding to spike, S1, and S2; **(J–L)** FcγRIV binding to spike, S1, and S2. Heterologous regimens (Ad/MVA and MVA/Ad) induced binding responses comparable to high-dose MVA/MVA but significantly higher than those observed after low-dose MVA/MVA. Data presentation: FcγR binding to spike (FcγRI, FcγRIIB), S1 (FcγRIIB, FcγRIII), and FcγRIV–S2 were normally distributed and are shown as mean ± SEM. All other responses were non-normally distributed and are shown as median with interquartile range (IQR). Statistical analysis: one-way ANOVA with Tukey's post-hoc test for normally distributed data; Kruskal–Wallis with Dunn's multiple comparisons for non-normally distributed data. ns = not significant; *p < 0.05; **p < 0.01; ***p < 0.001; ****p < 0.0001.

5.2.4.2.3 Cellular responses

The high-dose MVA/MVA arm was not included in this analysis, as no spleen or BM samples were available in MERSIDT001. ASC responses in both spleen and BM were higher in the MVA/Ad regimen compared with homologous groups (Figure 5-16A–D). Within the spleen, MVA/Ad also induced more IgG ASC than Ad/MVA (Figure 5-16A).

Cellular responses measured by IFN-γ ELISPOT (Figure 5-16E) were significantly higher in both heterologous regimens compared with homologous vaccination. Flow cytometry further showed that MVA/Ad induced more $CD8^+IFN\text{-}\gamma^+TNF^+$ and $IFN\text{-}\gamma^+$ T cells than homologous MVA/MVA, indicating stronger $CD8^+$ T cell responses in regimens containing Ad vectors (Figure 5-16F-G). In contrast, TNF^+ single-positive cells did not differ between regimens (Figure 5-16H).

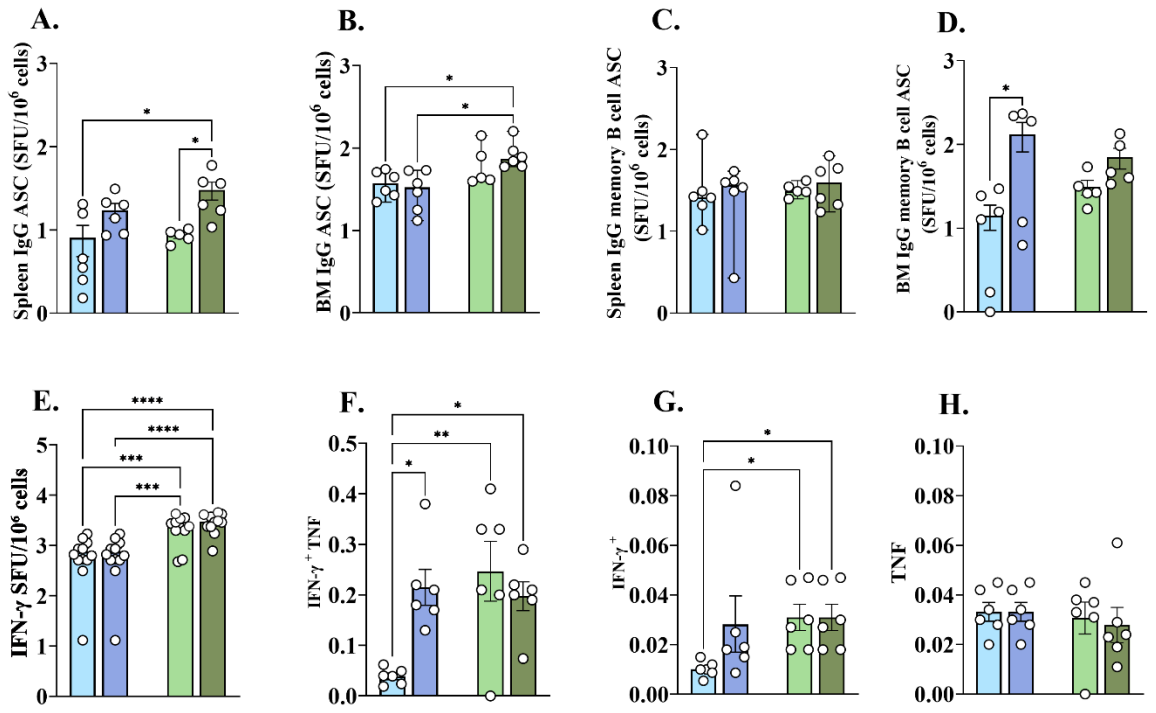


Figure 5-16. Antibody-secreting cell (ASC) and T cell responses following homologous and heterologous prime–boost vaccination.

Individual mouse data are shown. Colours denote experimental groups: MVA/MVA low dose (light blue), MVA/MVA high dose (dark blue), Ad/Ad (lavender blue), Ad/MVA (light green), and MVA/Ad (dark green). **(A)** Frequencies of spike-specific IgG ASCs in spleen. **(B)** Frequencies of IgG ASCs in bone marrow. **(C)** Frequencies of memory IgG B cell ASCs in spleen. **(D)** Frequencies of memory IgG B cell ASCs in bone marrow. **(E)** Splenocyte IFNγ ELISpot responses. **(F–H)** Flow cytometry analysis of $CD8^+$ T cell cytokine responses: $IFN\gamma^+TNF\alpha^+$ double-positive **(F)**, $IFN\gamma^+$ single-positive **(G),** and $TNF\alpha^+$ single-positive **(H).** Data presentation: normally distributed datasets (A, D, E) are shown as mean ± SEM; all other datasets are shown as median with interquartile range (IQR). Statistical analysis: one-way ANOVA with Tukey's post-hoc test for normally distributed data; Kruskal–Wallis with Dunn's post-test for non-normally distributed data. ns = not significant; *p < 0.05; **p < 0.01; ***p < 0.001; ****p < 0.0001.

Collectively, the post hoc analyses show that heterologous regimens enhanced immune responses compared with homologous vaccination, with MVA/Ad consistently inducing the strongest and broadest responses. Notably, heterologous vaccination often achieved responses similar to high-dose MVA/MVA. These findings underscore distinct immune signatures shaped by regimen sequence and dosing, with clear implications for the design of future vaccination strategies.

5.2.4.3 Effect of the heterologous booster dose

Given the higher humoral responses induced by heterologous boosting, we evaluated pre- and post-boost antibody responses following Ad/MVA and MVA/Ad regimens (Figure 5-17). Across both regimens, boosting increased spike-specific antibody responses, with the most pronounced changes observed following MVA/Ad boosting (Figure 5-17A,B). Post-boost responses showed increased IgG reactivity against full-length spike as well as the S1 and S2 subunits compared with pre-boost levels. In contrast, IgM and IgA class switching was limited following MVA boosting but was significantly increased after Ad boosting (Figure 5-17A,B).

Both heterologous regimens induced an increase in IgG2a, consistent with a Th1-skewed humoral response, while other IgG subclasses exhibited limited or variable changes between pre- and post-boost time points (Figure 5-17C,D). Spike-specific Fcγ receptor binding was enhanced following boosting. MVA boosting preferentially increased FcγRIIB and FcγRIII engagement (Figure 5-17E), whereas Ad boosting increased binding across multiple activating Fcγ receptors (Figure 5-17F). Fcγ receptor engagement against S1 and S2 showed differential increases from pre- to post-boost across regimens (Figure 5-17G-J). Notably, heatmap and nightingale plot analyses indicated a preference for S1-directed responses following Ad/MVA boosting, while Ad boosting more effectively enhanced S2-specific antibody responses (Figure 5-18A,B) .

Together, these results demonstrate that heterologous boosting enhances spike-specific humoral immunity, with platform-dependent differences in antibody class switching, IgG subclass distribution, Fcγ receptor engagement, and antigen specificity.

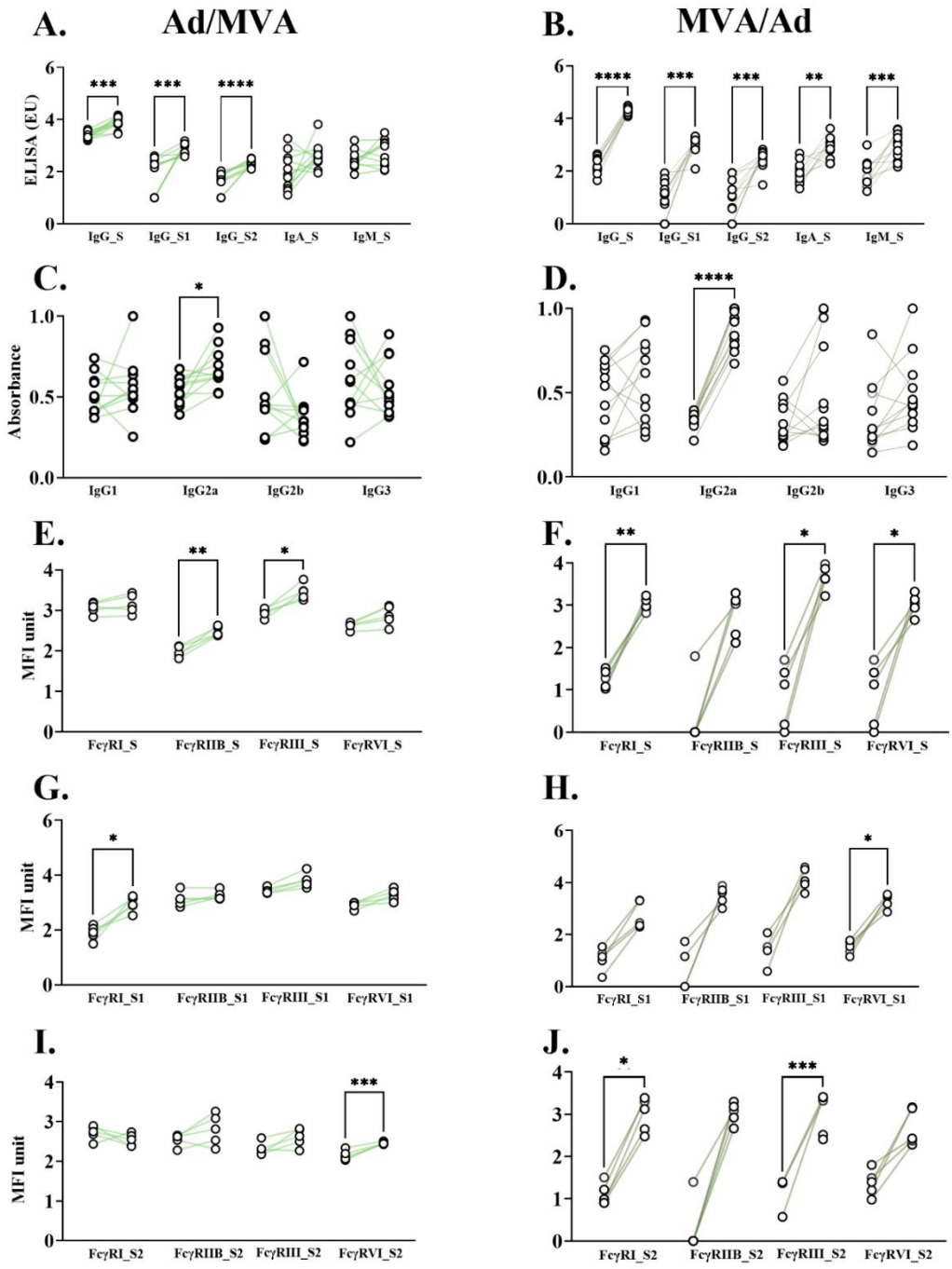


Figure 5-17. Paired analysis of humoral responses following heterologous Ad/MVA and MVA/Ad boosting.

(A–B) Spike-specific antibody isotype responses measured by ELISA before and after boosting with Ad/MVA **(A)** or MVA/Ad **(B).** IgG responses against full-length spike (S), S1, and S2 are shown alongside IgA and IgM responses. **(C–D)** IgG subclass responses following Ad/MVA **(C)** or MVA/Ad **(D)** boosting, shown as absorbance values for IgG1, IgG2a, IgG2b, and IgG3. **(E–F)** Fcγ receptor binding to spike-specific antibodies following Ad/MVA **(E)** or MVA/Ad **(F)** boosting, expressed as mean fluorescence intensity (MFI) units for FcγRI, FcγRIIB, FcγRIII, and FcγRIV. **(G–H)** Fcγ receptor binding to S1-specific antibodies following Ad/MVA **(G)** or MVA/Ad **(H)** boosting. **(I–J)** Fcγ receptor binding to S2-specific antibodies following Ad/MVA **(I)** or MVA/Ad **(J)** boosting. Each point represents an individual mouse, with lines connecting paired pre- and post-boost samples. Statistical significance was determined using a paired Wilcoxon signed-rank test and is indicated as * $p < 0.05$, ** $p < 0.01$, *** $p < 0.001$, **** $p < 0.0001$.

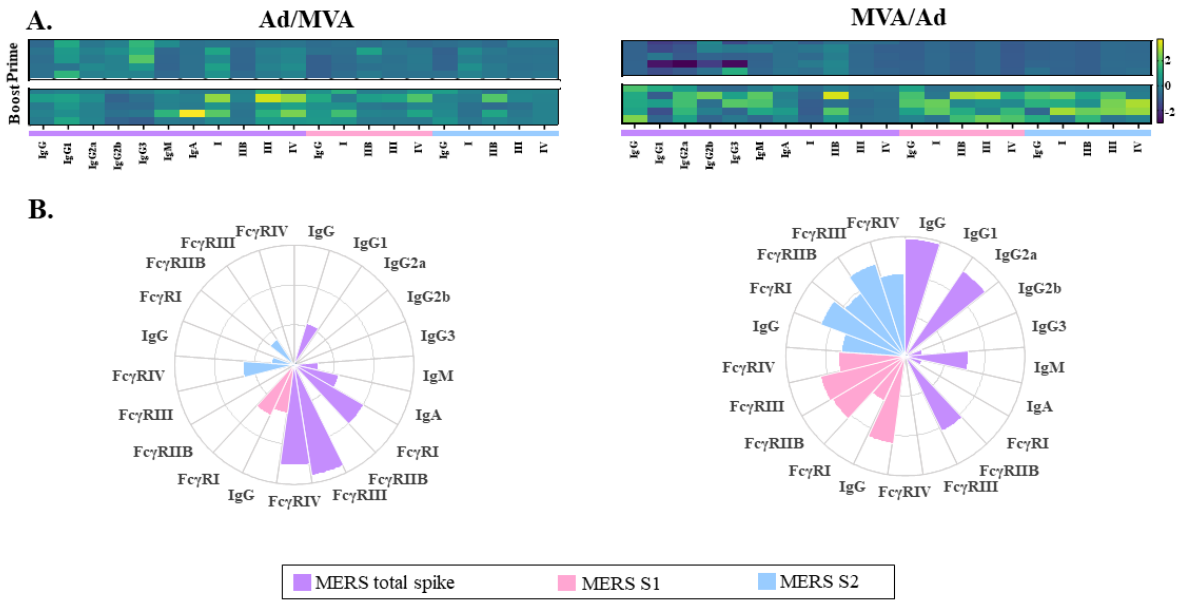


Figure 5-18. Humoral response profiling following heterologous Ad/MVA and MVA/Ad boosting.

(A) Heat maps summarizing pre-boost (Prime) and post-boost (Boost) humoral responses following heterologous Ad/MVA and MVA/Ad regimens. Antibody isotypes, IgG subclasses, and Fcγ receptor–binding profiles against MERS spike antigens are shown, with colour intensity representing normalized response magnitude. **(B)** Nightingale plots depicting fold changes in antibody features following boosting with Ad/MVA (left) or MVA/Ad (right). Responses are shown for total spike, S1, and S2 antigens, including IgG subclasses, IgM, IgA, and Fcγ receptor binding. Radial length represents the relative change in antibody magnitude post-boost compared with pre-boost levels.

5.2.4.4 Antibody pre-boosting modulates post-boost responses.

Because of the marked differences observed between the two heterologous regimens—particularly the stronger induction of IgG against spike and FcγRIIB in the MVA/Ad group—we next examined how pre-boost antibody responses shaped post-boost outcomes (Figure 5-19).

Direct comparison of the two regimens prior to booster administration revealed clear differences in baseline antibody profiles. Ad priming induced significantly higher IgG responses against spike and its subunits, along with elevated IgM (Figure 5-19A). This effect was especially pronounced for IgG2a and IgG3 subclasses (Figure 5-19B), which are associated with strong Fc-mediated effector potential. Consistent with this, Ad priming also drove stronger engagement of all Fcγ receptors compared with MVA priming (Figure 5-19C). Together, these observations suggest that Ad priming establishes a larger and functionally more diverse antibody pool at the time of boosting, which may influence the ability of the subsequent boost to expand or diversify responses.

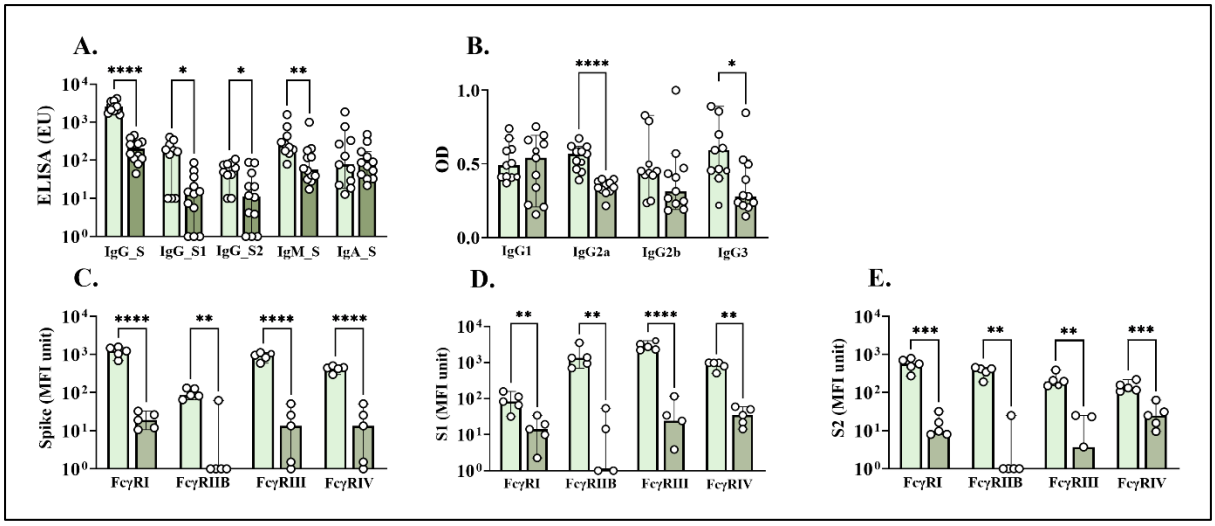


Figure 5-19. Baseline antibody responses prior to heterologous boosting.

Antibody responses were assessed before administration of the booster dose. **(A)** IgG, IgM, and IgA binding to full-length spike and its subunits (S1, S2) measured by ELISA. **(B)** IgG subclass distribution (IgG1, IgG2a, IgG2b, IgG3). **(C–E)** Fcγ receptor engagement (FcγRI, FcγRIIB, FcγRIII, FcγRIV) by spike **(C),** S1 **(D),** and S2 **(E).** Data points represent individual animals. Bars show either median values [IQR]. Statistical analysis: Comparisons between two groups were performed using Mann–Whitney U tests. Asterisks (*) denote statistical significance for within-group and between-cohort comparisons, as defined by P-values: * (P<0.05), ** (P<0.01), *** (P<0.001), **** (P<0.0001). Colours denote groups: Ad prime (light green) and MVA prime (dark grey).

To assess whether baseline serological features influenced boosting, we performed Pearson correlation analyses between pre- and post-boost antibody responses (Figure 5-20). Pre-boost IgG and FcγR-binding responses showed variable associations with post-boost features. While certain pre-boost IgG subclasses, such as IgG1, correlated positively with their post-boost levels, indicating efficient recall, several negative correlations were observed. Notably, higher pre-boost IgG and IgG2a levels were associated with reduced post-boost FcγR capacity and diminished boosting of total IgG responses. In addition, pre-boost IgG and IgG2a negatively correlated with the frequency of ASC in the spleen, suggesting that elevated baseline antibody levels may constrain plasmablast expansion following boosting or that they migrate faster to BM. In contrast, pre-boost IgA and IgG1 levels displayed positive correlations with their respective post-boost values. Collectively, these findings indicate that while baseline serology can promote recall of some features, high pre-existing antibody levels may limit Fc-mediated functions, antibody subclass expansion, and ASC responses.

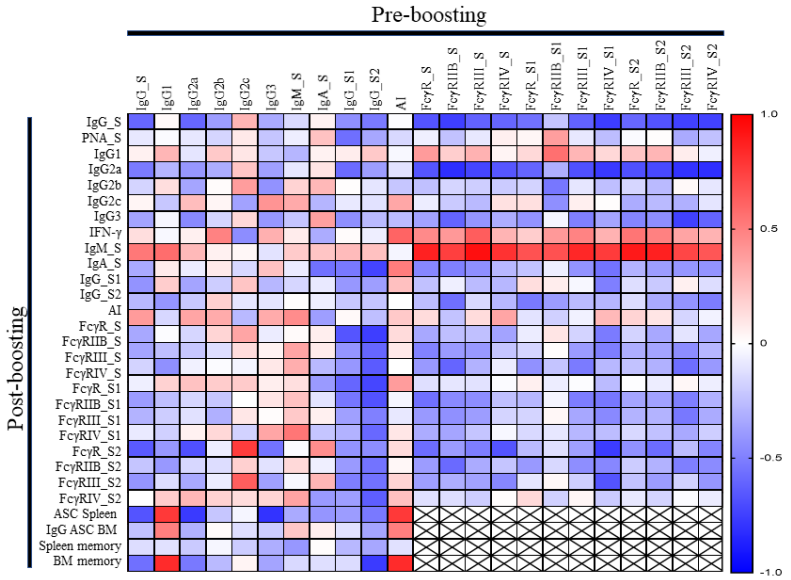


Figure 5-20. Pearson correlation analyses between pre- and post-boost antibody responses.

Heatmap showing Pearson correlation coefficients (R) between antibody features measured pre-boosting (columns) and post-boosting (rows). Blue indicates negative correlations and red indicates positive correlations, with intensity corresponding to the strength of the correlation. Grey boxes indicate features not assessed. Antibody features included binding to spike and subunits (IgG, IgM, IgA, and subclasses), PNA activity, Fcγ receptor engagement (FcγRI, FcγRIIB, FcγRIII, FcγRIV), antibody avidity (AI), and antibody-secreting cell (ASC) responses in spleen and bone marrow.

Principal component analysis (PCA) was performed on all baseline antibody and FcγR binding features in MERS-IDT001 (Figure 5-21) to explore the overall structure and variability of the pre-vaccination humoral landscape. The first two components explained ~64% of the total variance (PC1 = 51.1%, PC2 = 13.2%) (Figure 5-21A). The score plot showed no clear clustering by vaccination regimen, indicating that baseline serology alone did not segregate groups (Figure 5-21B). Projection of the main post-boost outcomes (total IgG, PNA, and IFN-γ ELISpot) as supplementary variables revealed alignment with pre-boost IgG subclass and FcγR features, particularly FcγRIIB_S1 and IgG_S2, which later emerged as key predictors in supervised models (Figure 5-21C).

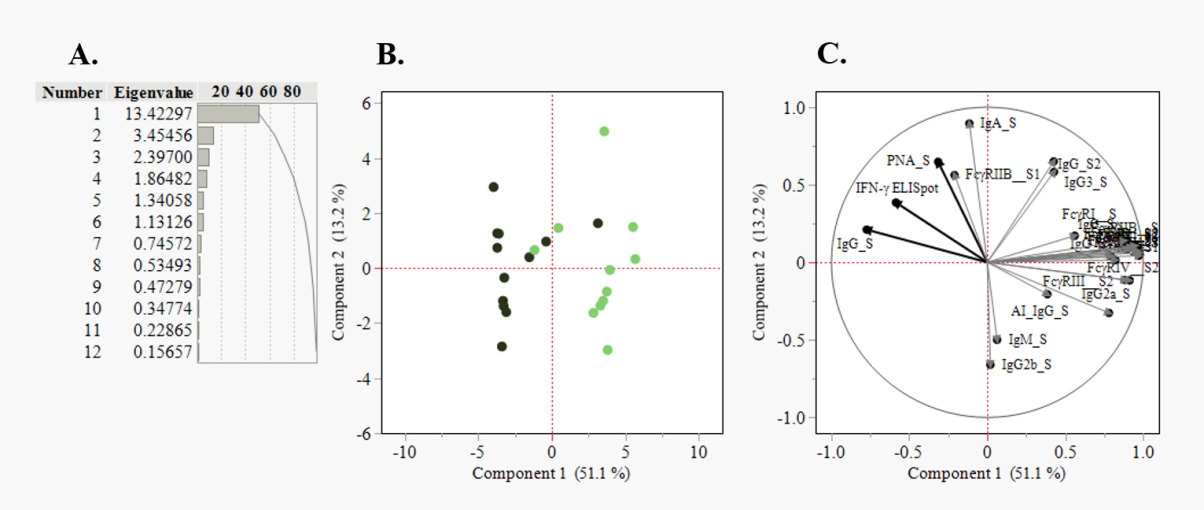


Figure 5-21. Principal component analysis (PCA) of baseline serology with outcomes projected as supplementary variables.

(A) Screen plot showing variance explained by each principal component. **(B)** Score plot of PC1 vs. PC2, which together accounted for 64.2% of the total variance; no strong clustering by vaccination regimen was observed. **(C)** Loading plot showing baseline features (grey vectors) and post-boost outcomes (black vectors). Outcomes (IgG, PNA, IFN-γ ELISPOT) aligned with FcγR binding and IgG subclass features, consistent with supervised models highlighting these predictors as key determinants of boosting.

5.3 Discussion

MERS-CoV remains a global public health threat with the potential to cause outbreaks, underscoring the need for a licensed vaccine to reduce morbidity and mortality. Two leading candidates, ChAdOx1 MERS and MVA-MERS-S, have advanced through phase I clinical evaluation with good safety and immunogenicity profiles [291-295]. While homologous regimens have shown promise, heterologous prime–boost vaccination is a well-established strategy for viral vector vaccines and is expected to enhance immunogenicity against MERS.

Our data demonstrate that heterologous regimens elicited stronger immune responses than homologous schedules across both platforms. Enhanced humoral responses were evident from increased MERS spike-specific IgG or neutralising antibodies, while cellular responses measured by IFN-γ ELISPOT were similarly superior. Importantly, the sequence of administration shaped the outcome: MVA priming followed by ChAdOx1 boosting induced significantly higher IgG titres, splenic IgG ASC responses, and FcγRIIB-binding antibodies compared with the reverse order. These heterologous combinations outperformed homologous vaccination in neutralisation assays and IFN-γ responses. Highlighting that vaccine order is a critical determinant of the quality of the immune response. Notwithstanding the clear effect of vaccine order, the contribution of vaccine dose and prime–boost interval to immune response magnitude cannot be excluded and is examined in the subsequent chapter.

Adenoviruses are potent T-cell inducers and can provide protective efficacy in challenged animal models after single-dose vaccination in several disease models. Repeated vaccination with Adenovirus enhances the transgene humoral responses efficiently but has minimal effects on increasing T cell immunity possibly due to anti-vector immunity.

On the other hand, MVA vaccines are weak priming agents and often require multiple doses to induce immunogenicity. By taking advantage of their ability to boost T cells after Ad priming, consensus has been generally established to boost with MVA after priming with Adenovirus. Few studies have examined them as priming agents alongside adenovirus in a head-to-head comparison of alternative heterologous PB experiments in pre-clinical model before advancing into clinical studies.

The immune profile following heterologous vaccination is shaped by the order of priming and boosting. Several studies have reported that MVA→Ad regimens generate stronger immunogenicity readouts than Ad→MVA, in both humoral [399] and cellular assays in animals [400, 401] as well as in influenza studies in humans [105]. However, in challenge models of malaria and tuberculosis, Ad→MVA often provided superior protection [401, 402]. These contrasting outcomes likely reflect differences in the immune mechanisms engaged by each sequence, which, in these disease models, favoured protective immunity following Ad→MVA. For example, in TB, Ad→MVA induced $CD8^+$ IFN-γ^+ T cells in both spleen and lung, whereas MVA→Ad preferentially expanded $CD4^+$ IFN-γ^+ T cells in the lung but not the spleen [401]. By contrast, in a SARS-CoV-1 model, MVA priming followed by Ad5 boosting induced significantly higher neutralising antibody titers than Ad→MVA in both mice and rabbits, with durable responses persisting for up to four months at levels two- to three-fold greater than other regimens [399]. Nevertheless, protection outcomes across studies are multifactorial and may reflect variation in vaccine dose, prime–boost interval, pathogen, and experimental model, in addition to vaccine sequence.

In the absence of defined correlates of protection for MERS, it remains uncertain which immune profile will best predict protection. Neutralising humoral responses are likely to represent a critical protective mechanism; however, challenge studies using MVA→Ad regimens will ultimately be required to directly assess their protective efficacy against MERS-CoV. Notably, we found that heterologous vaccination, particularly MVA→Ad, enhanced FcγR-binding antibody responses. In closely related SARS-CoV-2 models, antibodies with Fc-mediated effector functions have been identified as key correlates of protection, particularly through FcγRIII engagement [207]. The importance of these mechanisms was further demonstrated in FcγR knockout mice, in which both passive and active immunisation failed to confer protection [207].

Further serological analysis in our experiments identified the pre-boost immune status as an important determinant of booster response. Groups primed with ChAdOx1 had higher levels of circulating

antibodies before the booster given at the 28-day interval, which may have limited the magnitude of the subsequent response. In particular, IgG targeting the conserved S2 subunit appears to play a central role. Elevated S2-specific IgG, including FcγRIV-binding antibodies, can accelerate antigen clearance through Fc-dependent mechanisms and thereby reduce the opportunity for naïve B cell priming. Recent findings from mRNA vaccination similarly demonstrate that pre-existing antibodies constrain boosting by rapidly eliminating antigen [403]. Taken together, these results suggest that both the timing of the booster and the specificity of the pre-boost antibody repertoire—particularly S2-directed IgG—are critical determinants of outcome, with important implications for vaccine design and scheduling.

Our findings also highlight the critical role of dose in shaping MVA-based vaccine immunogenicity. While heterologous regimens are often considered superior because they bypass anti-vector immunity, our data indicate that high-dose homologous administration can elicit immune responses comparable to those induced by heterologous schedules delivered at lower doses. Increasing the vaccine dose may therefore overcome, at least in part, the inhibitory effects of vector-specific immunity that limit homologous boosting. Moreover, extending the prime–boost interval may further enhance immunogenicity, as suggested by recent MVA/MVA clinical studies in which high-dose homologous regimens administered at longer intervals, and complemented by a third booster, produced stronger responses than low-dose homologous regimens given at shorter intervals [295]. Nevertheless, it should be noted that this study was conducted in mice and does not account for pre-existing adenoviral immunity, which may complicate the interpretation and translation of these findings to human populations.

This work has several limitations. First, we did not include challenge experiments, so it remains uncertain whether the immune profiles observed will translate into protection against MERS-CoV. Second, in this animal model, ethical and practical constraints precluded direct assessment of non-antibody effector mechanisms, such as T-cell or NK-cell–mediated responses, which can be evaluated longitudinally in human studies. Future studies should therefore include challenge models for both Ad→MVA and MVA→Ad regimens, as well as passive transfer experiments to test whether booster responses are limited by the level or the quality of priming antibodies. Finally, having explored sequence and interval, the role of dose will also need to be systematically assessed to guide the optimal design of heterologous vaccination strategies.

Together, these findings emphasize the importance of dose, sequence, and interval in shaping vaccine responses, and raise the possibility that careful optimization of these parameters could further improve the efficacy of MERS vaccines.

6 Design of Experiments (DoE) for Optimising MERS-CoV heterologous Prime-Boost Vaccination in Mouse Model

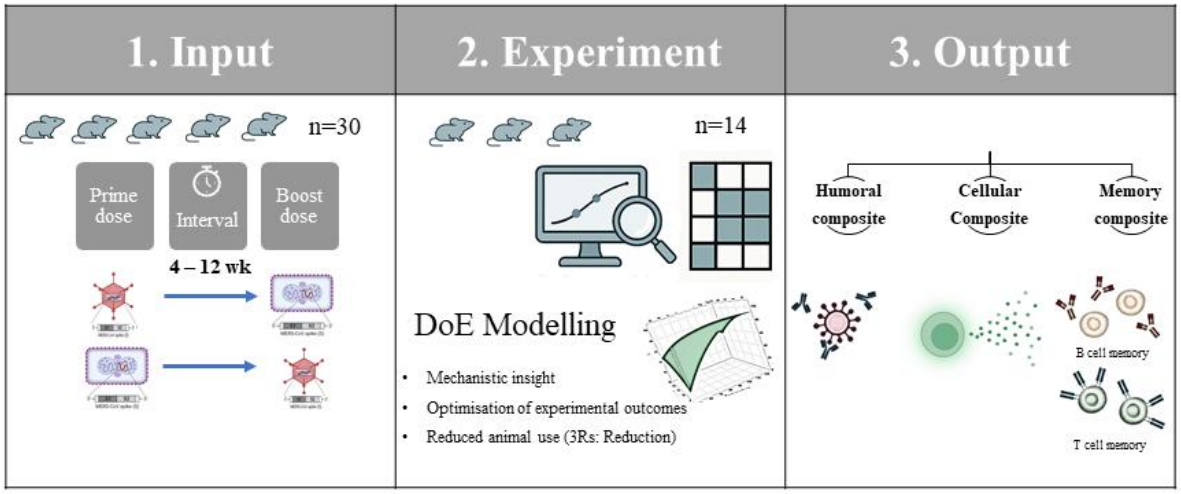


Figure 6-1 Visual abstract of the study methods and results

Highlights

- DoE optimisation identified booster dose as the dominant driver of immunity.
- Ad/MVA elicited robust $CD8^+$ effector T cell responses with strong predictive models, while MVA/Ad promoted stronger humoral responses (IgG, ASC) with higher predictive power.
- Increasing vaccine dose did not consistently enhance immunogenicity or memory.
- T cell hierarchy could be modulated by both interval and dose.
- BM ASC were interval-dependent, underscoring distinct regulation of humoral vs cellular responses

6.1 Introduction

The World Health Organization (WHO) target product profile (TPP) for MERS-CoV vaccines [304] recommends the development of vaccines across three key categories: 1- Dromedary camel vaccine to prevent the transmission of MERS-CoV within camels, and from camels to humans. 2- human vaccine for long-term protection: targeted at high-risk individuals of MERS-CoV, such as healthcare workers (HCW) and those working with potentially infected animals. 3- Human vaccine for reactive use: to provide rapid immunity in outbreak settings.

Heterologous prime-boost is a well-established strategy to enhance immunogenicity. In the previous chapter, we compared MERS-CoV standalone candidates in a homologous and heterologous vaccination regimen using a fixed interval of 28 days in a pre-clinical mouse model. As expected, the heterologous prime-boost regime was more immunogenic than the homologous prime-boost. Interestingly, mice primed with MVA-MERS followed by ChAdOx1 MERS boost elicited higher immunogenicity compared to the reverse order- ChAdOx1 MERS followed by MVA-MERS. At 28 days interval, a significant difference was observed between these two regimens in MERS-spike-specific IgG and spike, S2 subunit measured and IgG2a subclass, indicating a MVA/Ad induced a stronger humoral response with high breadth and a Th1-biased profile. Functional neutralising antibodies to the MERS pseudovirus assay, and IFN-γ ELISPOT responses against the immunodominant domain followed a similar trend, although the difference was not statistically significant.

Further serological analysis suggested an influence of the pre-boost status on the booster response, where the group primed with ChAdOx1 had higher levels of circulating antibodies before the booster was administered at the interval of 28 days set in this experiment, which may interfere with achieving optimal booster response.

These observations raised several important immunological questions. First, does extending the prime–boost (PB) interval enhance immunogenicity in heterologous ChAdOx1-primed, MVA-boosted mice, by allowing antibody levels to wane before boosting? Second, does the superior humoral response observed with the MVA/Ad regimen, compared with Ad/MVA, reflect the lower antigen dose delivered by MVA at priming, or alternatively the higher antigen load provided by the adenovirus boost? Finally, could immunogenicity at shorter intervals be improved by adjusting the dose—either by reducing the priming dose, increasing the booster dose, or combining both strategies?

MERS-CoV vaccines are considered for two main scenarios in humans: for long-term protection in high-risk individuals such as HCW, and abattoir workers, and for reactive use in outbreak situations. In both settings, for ease of distribution and cost effectiveness, a single dose is preferred, and if not possible, short intervals between prime and boost doses in the primary vaccination series is recommended [304].

A single dose of ChAdOx1 MERS has been shown to induce neutralising antibodies (nAbs) and protect against respiratory injury in NHPs; however, a PB regimen was required for protection from viral replication [315]. Similarly, reduction of viral shedding in camels was only achieved after two doses of MVA-MERS [318]. This chapter therefore designed to identify heterologous PB strategy which elicits the most robust immune response.

Determinants of the magnitude of the secondary B cell immune response include: peak primary antibody titres, residual antibodies at time of boost, length of PB interval, and antigen dose at prime and

boost (Figure 6-2) [7]. The way these factors influence the post-boost response is likely to vary with the nature of the immune response to each vaccine platform. Addressing such multifactorial problems is difficult with traditional "one-factor-at-a-time" approaches, which fail to capture interactions between variables and often require large numbers of animals and resources. Therefore, a strategy with a systematic approach to evaluating multiple factors is required.

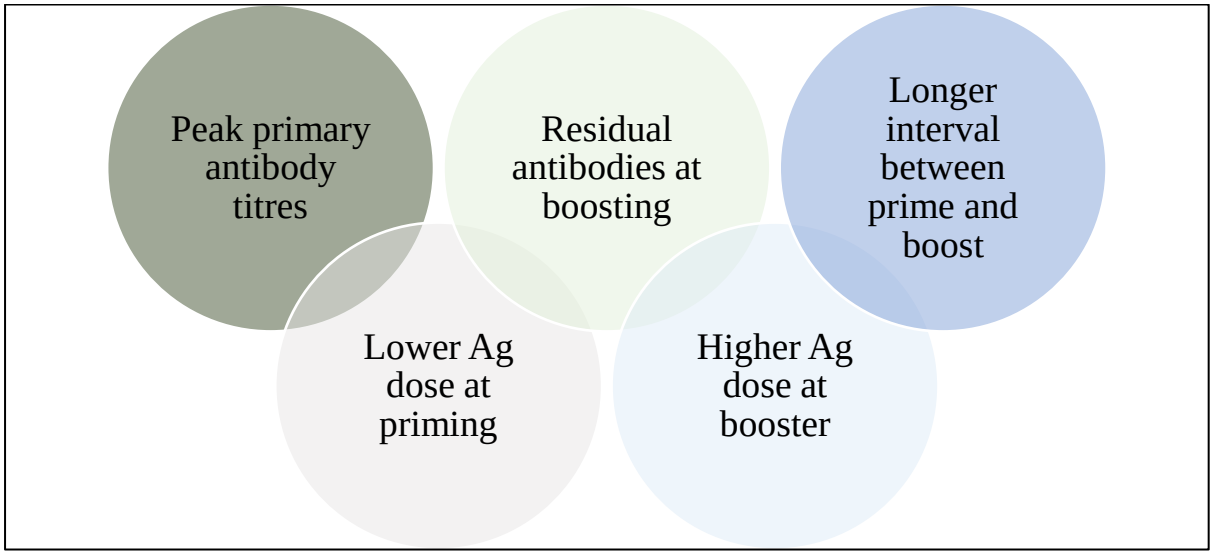


Figure 6-2 Determinants of secondary B cell response

Design of experiments (DoE) is a tool that applies statistical models to explore and understand cause-and-effect relationships between experimental factors and responses. In vaccine development, DoE has been used to optimise the formulation and vaccine composition [404, 405].

Many different experimental designs (numbers of runs, levels of experimental factors, and statistical models applied to the resulting data) have been developed to suit different purposes. A D-optimal design was selected to efficiently evaluate the effects of dose, interval, and vaccination order while minimising animal use and experimental complexity [406].

Dose-escalation studies demonstrated that increasing the dose from 1×10^{6} to 1×10^{7} PFU in mice produced robust immunogenicity, and a 1×10^{9} PFU dose generated strong responses in camels; However, these dose-escalation studies were not directly compared with previously tested regimens, and no impact of pre-existing anti-MVA immunity was detected [398]. In human studies, a reactogenicity threshold emerges at approximately $1.5–2\times10^{8}$ PFU administered intramuscularly [407, 408], beyond which the adverse-event profile shifts noticeably. Participants receiving high doses such as 5×10^{8} PFU experience flu-like symptoms including malaise, nausea or vomiting, and rigors, necessitating modification of the dosing regimen in the study [409]. Consequently, although

immunogenicity increases with dose, a practical upper dosing limit has been reached due to reactogenicity constraints.

Data from the COVID-19 pandemic demonstrated a clear beneficial effect of an extended interval between prime and boost in improving B-cell immunogenicity and protective efficacy [97, 354, 410]. Therefore, healthcare workers seeking long-term protection without the need for repeated vaccinations are likely to benefit from a long PB interval. In contrast, for travellers to endemic areas, a PB interval of more than 12 weeks probably wouldn't be practical; in such cases, a lower priming dose might enhance the post-boost response even after a shorter interval. During outbreak situations, some degree of early protection following the prime would also be advantageous, suggesting that Ad may be preferable to MVA as a priming vaccine. Based on these considerations, we hypothesised that the immunogenicity of heterologous boosting with MVA/Ad—and potentially Ad/MVA—can be further optimised by adjusting the dose of prime and boost, and interval between doses.

In this chapter, we aim to assess the usefulness of a DoE approach for optimising vaccine responses and identifying the key factors influencing heterologous vaccination strategies. We hypothesised that the immune response could be shaped by varying the dose, interval, and order of administration (MVA/Ad versus Ad/MVA). We sought to identify the strategy that elicited the strongest immune response at the shortest feasible interval, in line with the WHO (TPP), which indicated a 4-week interval was preferable. Collectively, these experiments provide proof of concept that immune responses can be adjusted through different vaccination regimens, thereby informing the design of future clinical trials combining ChAdOx1 and MVA candidate vaccines.

6.2 Methods

DoE was applied to systematically explore vaccination parameters and optimise prime–boost strategies. The approach involves five main steps: (i) selecting input parameters and their ranges, (ii) generating treatment combinations that span the design space (including replicates at central points), (iii) performing experimental runs, (iv) analysing the model using ANOVA to assess statistical significance and predictive power, and (v) verifying the model against independent experimental data.

In this study, the key input parameters were the prime dose, booster dose, and interval. Treatment combinations were generated using JMP software. The resulting model was evaluated for fit, robustness, and predictive ability. Steps relevant to this experiment are summarised in Figure 6-3, and each is described in more detail below.

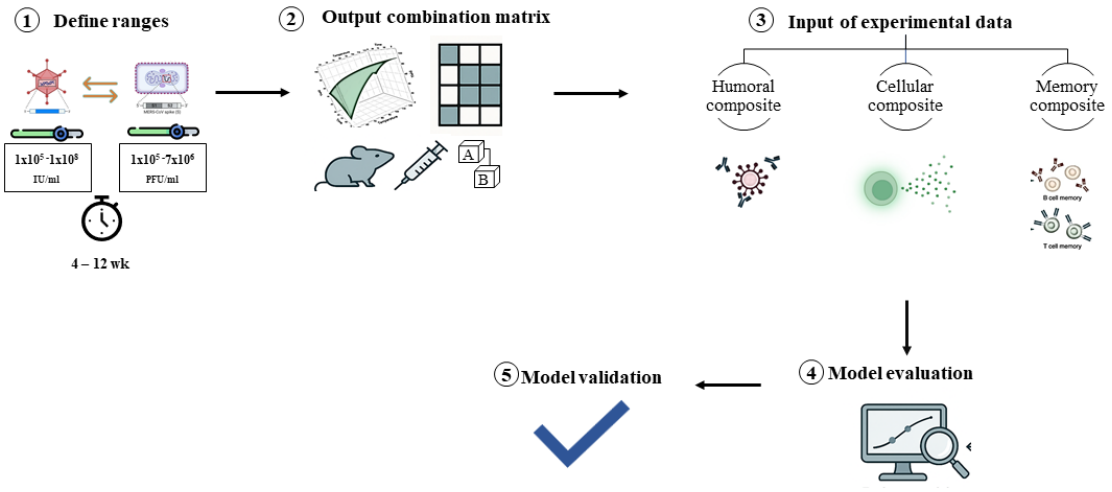


Figure 6-3. DoE workflow applied in this study.

The DoE approach in this study followed five main steps: **(1)** definition of input parameter ranges, including ChAdOx1 and MVA vaccine doses (1×10^5–1×10^8 IU or 1×10^5–1×7^6 PFU respectively) and prime–boost intervals (4–12 weeks); **(2)** generation of treatment combinations using JMP software; **(3)** Incorporation of experimental immunological data into the model, grouped into three composites: humoral (MERS spike–specific IgG, pseudovirus neutralisation, and antibody-secreting cell [ASC] responses in spleen and bone marrow), cellular (IFN-γ ELISPOT and $CD4^+/CD8^+$ T-cell phenotyping), and memory (memory ASC ELISpot in spleen and bone marrow, and T-cell effector memory) **(4)** evaluation of model performance; and **(5)** validation of the predictive model using independent retrospective datasets.

6.2.1 Selection process

To define the vaccination dose of ChAdOx1-MERS and MVA-MERS, the highest vaccination dose of ChAdOx1-MERS and MVA-MERS was defined based on previous performance and batch constraints respectively: $1x10^8$ IU for ChAdOx1-MERS and $7x10^6$ PFU for MVA-MERS. The ChAdOx1-MERS dose was selected based on previous experience within the group using the ChAdOx1 vector in mice, where this moderate-to-high dose produced strong immunogenicity with an acceptable safety profile and without increasing reactogenicity [411-413]. The maximal deliverable dose was constrained by the injection volume (50 µL per leg) permitted under mouse study regulations. In the case of MVA-MERS-S, as discussed in the previous chapter regarding high-dose MVA, a GMP clinical batch with concentration 1×10^8 PFU/mL was employed; consequently maximum dose was restricted to 7×10^6 PFU in 100 µL. The lower end of the dose ranges were defined based on the lowest immunogenic dose previously seen, and midpoint selected to give balanced coverage of the design space

Based on these experimental circumstances, the range was defined as 1×10^5–1×10^8 IU/mL for ChAdOx1 MERS and 1×10^5–7×10^6 PFU for MVA-MERS, ensuring biologically relevant and balanced coverage of design space while retaining the smallest immunogenic dose.

For the prime–boost interval, a lower limit of 4 weeks was chosen to allow sufficient time for antibody responses to develop, while an upper limit of 12 weeks was selected for practicality and feasibility.

After defining these experimental inputs, a D-optimal design was implemented, as it provides an efficient and robust framework for multifactorial study designs.

6.2.2 Treatment generation

The DoE tool generated treatment combinations that spanned the specified parameter ranges. The runs proposed by the DoE tool in JMP are presented in D-optimal design showing treatment combinations of MVA and ChAdOx1 with corresponding doses and vaccination intervals. Model reproducibility was evaluated using central points included in duplicate (n = 4), specifically treatment F (runs 7 and 8) and treatment G (runs 9 and 10). These central point replicates are critical for assessing model adequacy and lack of fit (which ideally should not be statistically significant), estimating experimental error, and confirming that the model provides reliable predictions within the central region of the design space. In addition, treatment C was also included in duplicate (runs 3 and 4).

Treatment number	Treatment reference	MVA dose (PFU/mL)	ChAdOx1 dose (IU/mL)	Interval (weeks)
1	A	1×10^5	1×10^8	12
2	B	1×10^5	1×10^5	12
3	C	3.6×10^6	1×10^5	12
4	C	3.6×10^6	1×10^5	12
5	D	7×10^6	1×10^8	12
6	E	7×10^6	4.3×10^7	12
7	F	3.6×10^6	5×10^7	8
8	F	3.6×10^6	5×10^7	8
9	G	7×10^6	1×10^5	8
10	G	7×10^6	1×10^5	8
11	H	1×10^5	1×10^8	4
12	I	1×10^5	1×10^5	4
13	J	7×10^6	1×10^8	4
14	K	7×10^6	1×10^5	4

Table 6-1. D-optimal design showing treatment combinations of MVA and ChAdOx1 with corresponding doses and vaccination intervals. MVA doses are expressed in plaque-forming units (PFU/mL), ChAdOx1 doses in international units (IU/mL), and intervals in weeks. The table includes 14 treatment regimens, each referencing specific dosing and scheduling conditions. Central points are highlighted in bold.

Treatment levels were generated as continuous output by the DoE design tool. The MVA dose was tested in three levels (1×10^5, 3.6×10^6 and 7×10^6), ChAdOx1 dose in four level (1×10^5, 4.3×10^7, 5×10^7 and 1×10^8). Interval was at three levels (4, 8 and 12 weeks). As the model is designed to assess one sequence at a time, the PB order had to be performed in two separate models with distinct directions: Model 1: MVA prime and Ad boost. Model 2: ChAdOx1 prime and MVA boost.

To enhance the predictive power of the model while minimising animal use and controlling for confounding variables, the study was conducted in two experimental blocks, providing biological

replication at the block level. Blocking ensured that observed effects could be attributed to treatment rather than external factors and substantially reduced unexplained variability, resulting in lower residual variance (a measure of unexplained error in the model). This reduction in variance improved the precision of parameter estimates and strengthened the reliability of model predictions.

Model robustness was further evaluated using standard diagnostic statistics. R^2 was used to quantify the proportion of variability in the response explained by the model, while the adjusted R^2 accounted for model complexity to ensure that improvements in fit were not due to overfitting. RMSE (root mean squared error), reflecting the average magnitude of prediction error, was used to assess how closely the model's predicted values matched the observed data. In addition, the overall model F-test p-value ($p < 0.05$) was examined to confirm that the model provided a statistically significant improvement in predictive ability compared with a null model.

Lack-of-fit assessments were also performed, with non-significant lack-of-fit p-values ($p>0.05$) indicating that the model structure adequately captured the underlying biological relationship and did not show systematic deviations from the observed data. Statistical power was additionally considered to evaluate the model's ability to detect true treatment effects; the reduction in residual error achieved through blocking increased the signal-to-noise ratio, thereby improving power and reducing the likelihood of false negatives. Replicated treatment points within each block (Table 6-1) further enabled reliable estimation of experimental error and provided internal verification that treatment responses were reproducible across blocks. These replications also served as an internal safeguard for assessing assay performance and cell viability throughout the experiment.

Collectively, the reduced residual variance, favourable fit statistics (R^2, adjusted R^2, RMSE), the significant overall model p-value, the non-significant lack-of-fit p-value, and the increased statistical power demonstrate that the blocked design offered the most robust and reliable modelling framework among the alternatives considered.

Importantly, this block design also made the experiment more manageable for the preclinical team, particularly with respect to mouse handling and the logistical challenges of timely tissue processing at termination. Each block (I and II) contained 28 mice (n = 14 per vaccination order: MVA–Ad or Ad–MVA). Negative control mice (n = 2 per block) were included, receiving ChAdOx1-GFP and MVA-GFP (prime–boost at a 4-week interval; one control per vaccination order). The full design table is shown in Table 6-2.

ID	MVA	ChAdOx1	Interval	Gp	Block
1	1×10^5	1×10^8	12	1	I
2	1×10^5	1×10^5	12	1	I
3	3.6×10^6	1×10^5	12	1	I
4	3.6×10^6	1×10^5	12	1	I
5	7×10^6	1×10^8	12	1	I
6	7×10^6	4.3×10^7	12	1	I
13	3.6×10^6	5×10^7	8	3	I
14	3.6×10^6	5×10^7	8	3	I
15	7×10^6	1×10^5	8	3	I
16	7×10^6	1×10^5	8	3	I
21	1×10^5	1×10^8	4	5	I
22	1×10^5	1×10^5	4	5	I
23	7×10^6	1×10^8	4	5	I
24	7×10^6	1×10^5	4	5	I
29	GFP	GFP	4	7	I

ID	ChAdOx1	MVA	Interval	Gp	Block
7	1×10^8	1×10^5	12	2	I
8	1×10^5	1×10^5	12	2	I
9	1×10^5	3.6×10^6	12	2	I
10	1×10^5	3.6×10^6	12	2	I
11	1×10^8	7×10^6	12	2	I
12	4.3×10^7	7×10^6	12	2	I
17	5×10^7	3.6×10^6	8	4	I
18	5×10^7	3.6×10^6	8	4	I
19	1×10^5	7×10^6	8	4	I
20	1×10^5	7×10^6	8	4	I
25	1×10^8	1×10^5	4	6	I
26	1×10^5	1×10^5	4	6	I
27	1×10^8	7×10^6	4	6	I
28	1×10^5	7×10^6	4	6	I
30	GFP	GFP	4	8	I

ID	MVA	ChAdOx1	Interval	Gp	Block
31	1×10^5	1×10^8	12	1	II
32	1×10^5	1×10^5	12	1	II
33	3.6×10^6	1×10^5	12	1	II
34	3.6×10^6	1×10^5	12	1	II
35	7×10^6	1×10^8	12	1	II
36	7×10^6	4.3×10^7	12	1	II
43	3.6×10^6	5×10^7	8	3	II
44	3.6×10^6	5×10^7	8	3	II
45	7×10^6	1×10^5	8	3	II
46	7×10^6	1×10^5	8	3	II
51	1×10^5	1×10^8	4	5	II
52	1×10^5	1×10^5	4	5	II
53	7×10^6	1×10^8	4	5	II
54	7×10^6	1×10^5	4	5	II
59	GFP	GFP	4	7	II

ID	ChAdOx1	MVA	Interval	Gp	Block
37	1×10^8	1×10^5	12	2	II
38	1×10^5	1×10^5	12	2	II
39	1×10^5	3.6×10^6	12	2	II
40	1×10^5	3.6×10^6	12	2	II
41	1×10^8	7×10^6	12	2	II
42	4.3×10^7	7×10^6	12	2	II
47	5×10^7	3.6×10^6	8	4	II
48	5×10^7	3.6×10^6	8	4	II
49	1×10^5	7×10^6	8	4	II
50	1×10^5	7×10^6	8	4	II
55	1×10^8	1×10^5	4	6	II
56	1×10^5	1×10^5	4	6	II
57	1×10^8	7×10^6	4	6	II
58	1×10^5	7×10^6	4	6	II
50	GFP	GFP	4	8	II

Table 6-2. Full experimental design.

This table shows the treatment allocation for each mouse across blocks and models. The treatments are assigned according to the experimental design, which includes the respective prime-boost regimens, doses, and intervals for each block. The treatment allocations are represented for both the MVA and ChAdOx1 vaccines, highlighting the specific model (e.g., prime-boost order) used in each experimental condition.

6.2.3 Experimental data and processing

6.2.3.1 Vaccination protocol

Mice were allocated into six treatment groups according to dosing interval and vaccine combination, with an additional two groups serving as negative controls. The experiment was performed in two blocks under identical conditions, staggered by one month, in order to increase statistical power and minimise confounding effects (Figure 6-4).



			Month 1				Month 2				Month 3				Month 4				Month 5			
			Week				Week				Week				Week				Week			
Block	Group	Interval	1	2	3	4	1	2	3	4	1	2	3	4	1	2	3	4	1	2	3	4
Block I	1-2	12	P												B			Take down				
	3-4	8					P															
	5-8	4									P											
Block II	1-2	12					P												B			Take down
	3-4	8									P											
	5-8	4													P							

Figure 6-4 Experimental design and timeline.

This figure provides a detailed overview of the vaccination group allocation. Mice were grouped based on the intervals between the prime and boost doses, with different doses assigned according to the treatment allocation for each mouse. Treatment groups were replicated in two blocks, which overlapped by one month. Mice within each block were primed at different times but received the booster dose on the same day, and were euthanised 28 days after the boost. The timeline shows vaccination, sample collection, and endpoint procedures: serum collected pre-boost; serum, spleen, and bone marrow collected at takedown.

6.2.3.2 Sample collection

Blood samples were collected a month after the prime dose, two days prior to the booster dose, and at termination one-month post-boost. At the end of the study, mice were euthanised, and BM and spleen were harvested for immunological assays.

6.2.3.3 Immunological assays

Immunogenicity was assessed by serological and cellular assays. Serum samples were tested for total MERS spike-specific IgG and neutralising antibodies; B-cell responses were measured by ELISPOT, and T-cell responses by ELISPOT and flow cytometry (Table 6-3; flow gating strategy in appendix).

Response	Target	Outcome
Humoral	Total MERS spike	Y1: IgG (EU)
		Y2: Pseudovirus neutralisation assay (IU/mL)
		Y:3 Antibody-secreting cells (ASC), spleen (SFU/10^6)
		Y4: Antibody-secreting cells (ASC), bone marrow (SFU/10^6)
		Y5: Memory ASC, spleen (SFU/10^6)

		Y6: Memory ASC, bone marrow (SFU/10^6)
Cellular	Immunodominant epitope of the MERS spike in S1	Y7: IFN-γ ELISPOT (SFU/10^6)
	Immunodominant epitope of the MERS spike in S1	Y8: T-cell phenotyping (frequency, %)
	S1 subunit	Y9: T-cell phenotyping (frequency, %)
	S2 subunit	Y10: T-cell phenotyping (frequency, %)

Table 6-3. Overview of immunological assays performed in this study.
ELISpot assays were used to quantify antibody-secreting cells (ASC) in spleen and bone marrow in response to spike antigen, and to enumerate IFN-γ–producing T cells in spleen following stimulation with spike immunodominant epitope. Flow cytometry was employed to phenotype $CD4^+$ and $CD8^+$ T-cell responses to the S1 and S2 subunits and immunodominant epitope of the MERS-CoV spike protein, and included viability staining for quality control. In addition, effector T-cell phenotyping was carried out using flow cytometry to assess functional subset after *in vitro* stimulation. Memory B-cell assays were performed by in vitro expansion of primary cell cultures to detect spike-specific memory B cells in spleen and bone marrow.

6.2.3.4 Data refinement

6.2.3.4.1 Quality control and sample exclusion

Prior to modelling, datasets were reviewed for quality. Because precision is critical in DoE, a more stringent approach to data exclusion was applied than in our previous analyses. Samples with evidence of poor viability or technical failure were excluded to reduce variability and ensure robust model performance. For ELISPOT assays, spleen samples with <50% viability (as determined by matched flow cytometry with viability staining) were excluded from all downstream analyses, including correlations. In contrast, no independent viability measurements were available for BM preparations, and all samples were therefore included. These factors likely contributed to greater variability in BM assays. Nevertheless, the adoption of stricter QC criteria in this study represents an important methodological improvement, ensuring the robustness and reproducibility of the DoE modelling framework.

To determine which cell counting method (Countess or Casy counter) was most appropriate for downstream ELISPOT analysis, cell counts obtained from each system were compared with independent immunological readouts that reflect the true biological response. For IgG ASC B-cell ELISPOTs in spleen and BM, the corresponding serum IgG titres and pseudovirus neutralisation (PNA) titres were used as reference measures, as increases in antibody-secreting cells should align with higher systemic antibody levels. For IFN-γ ELISPOT assays, total IFN-γ production measured by flow cytometry following stimulation with the immunodominant peptide was used as the reference, as flow cytometry provides a more specific and direct assessment of cytokine-producing T cells. Unlike bulk measurements, flow cytometry quantifies IFN-γ at the single-cell level and allows gating on antigen-specific populations, making it a biologically precise comparator for ELISPOT responses.

Correlation analyses were then performed to determine how well ELISPOT results generated using each cell counting method aligned with these independent immunological outcomes. The cell counting system that demonstrated the strongest and most biologically consistent correlations with its respective reference readouts was selected for all subsequent ELISPOT analysis.

6.1.1.1 Data transformation

ELISPOT and antibody data were log-transformed, while flow cytometry percentages were transformed using an arcsine square-root transformation in Excel to reduce skewness and variance. To enable multivariate modelling and standardised comparisons across assays with different ranges, all values were then normalised by z-score transformation, also performed in Excel. Each outcome was evaluated through model validation, and only validated outcomes were carried forward for composite analyses.

6.1.1.2 Composite definitions

Responses were analysed in three major composites: humoral, cellular, and memory. For flow cytometry, markers were first validated individually, and those passing validation were grouped into composite z-scores representing total, effector, effector memory, and central memory subsets per epitope. Secondary models were also explored, either as individual outcomes or as additional composites, as shown in Table 6-4. The z-score transformation followed established procedures for standardising biological datasets [414], after which composite indices were constructed by summing the corresponding z-scores, consistent with previous applications in biological research [415]. Model evaluation was performed according to widely accepted frameworks for assessing predictive performance and validation in biomedical research [416].

	Layer 1	Layer 2
Humoral outcome	Composite of IgG and PNA	IgG ASC in spleen and BM
Cellular outcome	Composite of ELISPOT, $CD4^+$/$CD8^+$ TNF IFN, effector	Antigenic composite of: immunodominant epitope, S1, S2
Memory outcome	Composite of Memory ASC, TEM	IgG ASC memory in spleen and BM

Table 6-4. Summary of immunological outcomes used in DoE modelling.

Outcomes were grouped into humoral, cellular, and memory compartments, and analysed in two layers. Layer 1 contained primary readouts, combined into composites to represent overall immunogenicity. Layer 2 contained exploratory readouts, analysed individually or in antigen-specific composites to provide additional mechanistic insights. All outcomes were normalised to z-scores, calculated as (value − mean) / standard deviation, and composite scores were generated by summing the corresponding z-scores.

6.2.4 Data analysis and model evaluation

The analysis proceeded in two stages. First, a descriptive analysis of Layer 1 and Layer 2 outcomes was performed to provide an overview of the data and initial group comparisons. Second, predictive modelling was conducted in JMP using least-squares regression based on a D-optimal design. All raw outcome data, including individual animal values and composite readouts (humoral, cellular, and memory), are provided in Appendix Table S and

Table S. Model fitting was performed separately for MVA/Ad and Ad/MVA regimens. Model performance was evaluated using R^2, adjusted R^2, root mean square error (RMSE), ANOVA p-values, and lack-of-fit tests. Correlations between observed and predicted values were examined to assess model robustness. Finally, using the prediction profiler, layer 1 composite outcomes were modelled to identify optimal conditions and to evaluate predicted responses at a 4-week interval. All analysis was performed in JMP Student Edition version 19 (SAS Institute Inc.).

6.2.5 Model validation

Model predictions were validated against retrospective datasets from two independent studies (MERS IDT001 and MERS IDT002) described in chapter 5.

6.3 Results

Female BALB/c mice (n = 60 including GFP control groups), were allocated to vaccination with ChAdOx1 MERS and MVA-MERS S according to the D-optimal design generated by the JMP program (Table 6-1). Three mice from the MVA–Ad regimen and one from the Ad–MVA regimen in Block II were euthanised early after priming for welfare reasons due to spontaneous conditions unrelated to vaccination, which are occasionally observed in inbred BALB/c mice. These animals were excluded from the final analysis. As a result, the final dataset comprised n = 25 mice for MVA/Ad and n = 27 mice for Ad/MVA, from the originally planned 28 per group. All exclusions occurred in the 12-week interval condition and had corresponding replicates in Block I; therefore, their absence did not compromise the D-optimal design. Model fit, reported in the following sections, further confirmed that these exclusions did not adversely affect the analyses. Additional assay-specific exclusions were applied on the basis of low cell viability or technical failure, as detailed in each section. Results are presented below, organised by immunological outcome (Table 6-4).

6.1.2 Descriptive summary

Before subsequent model-based analyses, all treatment conditions were initially considered together within each vaccine order to define overall response patterns. Unless explicitly indicated, all results presented in this section correspond to post-boost responses measured at the final harvest.

6.1.2.1 Humoral responses

6.3.1.1.1 Serum

Both heterologous regimens induced significantly higher IgG and neutralising antibody responses than controls (Figure 6-5A-B); MVA/Ad tended to elicit higher IgG levels, whereas Ad/MVA favoured stronger neutralisation, although differences between the two regimens were not statistically significant. IgG and neutralising antibody titres were strongly correlated (Spearman R = 0.90, p < 0.0001; Figure 6-5C), indicating that higher IgG levels were predictive of stronger neutralising responses.

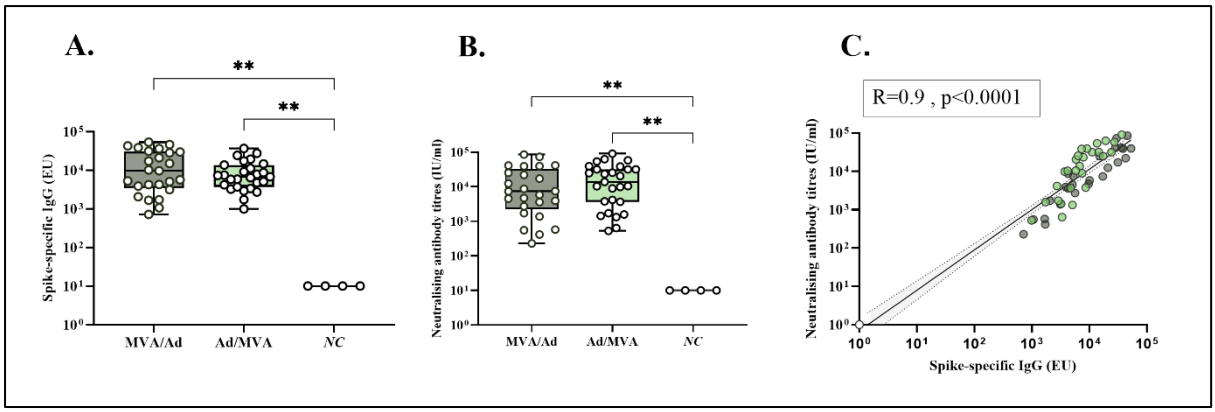


Figure 6-5. Humoral immune responses induced by heterologous vaccination.

(A–B) Spike-specific IgG titres (EU) and neutralising antibody titres (IU/mL) in MVA/Ad, Ad/MVA, and negative control (NC) groups. Box plots show medians with interquartile ranges (IQR); whiskers indicate min–max. Statistical significance was tested by Kruskal–Wallis with Dunn's multiple comparisons (*p < 0.05; **p < 0.01). **(C)** Correlation between IgG and neutralising antibody titres at day 28 post-boost. Linear regression was performed on $\log_{10}$-transformed values, with data displayed on log axes (original units) for consistency with other assays. Regression line (solid) with 95% confidence bands (dashed) is shown. Correlation was significant by Spearman's test (R = 0.9, p < 0.0001). Each point represents one mouse [MVA/Ad, n = 25; Ad/MVA, n = 27; NC, n = 4]. Data are colour-coded: MVA/Ad (dark green), Ad/MVA (light green), NC (white).

6.3.1.2 Cell-based assays

Splenic cell viability was assessed across experimental blocks and regimens. Overall viability differed significantly between groups (p < 0.01, Kruskal–Wallis test), but this variation was driven by block rather than regimen effects. Cells from Block II exhibited higher viability than those from Block I, likely reflecting faster sample processing (Figure 6-6). To ensure data quality, samples with <50% viability (determined by flow cytometry–based viability staining) were excluded from all downstream splenic assays, including both B cell and T cell ELISPOT analyses. This resulted in the removal of 6 MVA/Ad and 8 Ad/MVA samples, leaving 19 mice per regimen for downstream spleen analysis. By contrast, BM viability could not be assessed with a reliable method such as flow cytometry so no data was excluded.

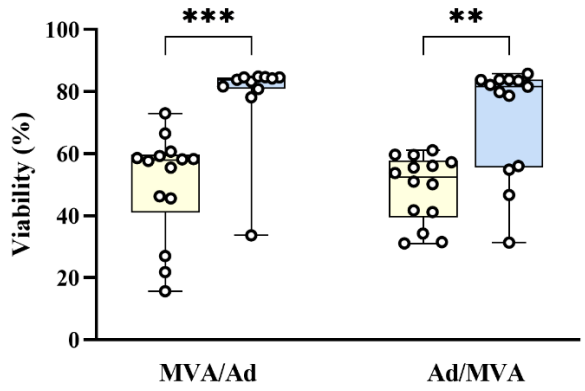


Figure 6-6. Splenic cell viability measured by flow cytometry differed significantly across groups
Box-plots indicate group medians and distributions, with Block I shown in yellow and Block II in blue. Viability was higher in Block II compared with Block I, irrespective of regimen, most likely reflecting faster sample processing. Significance is indicated as follows: *p < 0.05, **p < 0.01, ***p < 0.001, ****p < 0.0001 (Kruskal–Wallis test).

6.1.2.1.1 B cell ELISPOT (ASC)

To identify the most reliable method for quantifying cells in B cell ELISPOT assays, ASC frequencies were calculated using cell counts obtained from either the Casy or Countess counters and correlated with serum anti-spike IgG and PNA titres. Both methods showed significant associations with IgG and PNA responses. For spleen-derived ASC, correlations were comparable between Casy and Countess (IgG: R = 0.89 vs. 0.84; PNA: R = 0.89 vs. 0.81). In contrast, BM ASC frequencies calculated with Casy counts displayed stronger correlations with IgG and PNA than those calculated with Countess counts (IgG R = 0.60 vs. 0.40, and PNA 0.53 vs. 0.45). These findings (Figure 6-7) support the use of Casy-derived counts for subsequent ASC analyses.

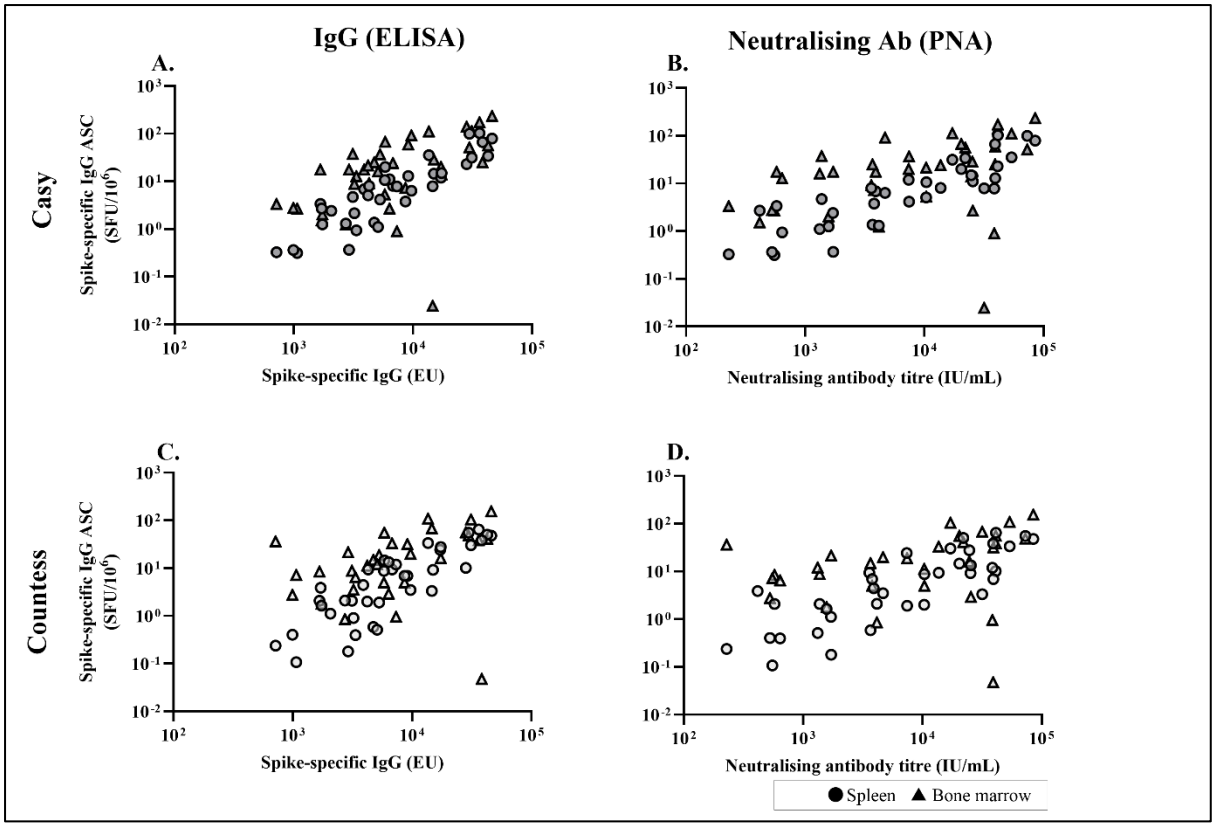


Figure 6-7. Correlations between spike-specific IgG ASC frequencies and serum antibody responses.

(A–B) Correlation of serum spike-specific IgG titres (EU, ELISA) and neutralising antibody titres (IU/mL, PNA) with IgG ASC frequencies in spleen and bone marrow measured using the Casy counter. **(C–D)** The same correlations measured using the Countess counter. Each point shows one mouse; circles = spleen, triangles = bone marrow. Both axes are $\log_{10}$ scaled. Correlations were significant across tissues and methods, with Spearman's R ranging from 0.56–0.70 (all $p < 0.0001$). Group sizes: MVA/Ad (n = 25), Ad/MVA (n = 27), NC (n = 4). Colour code: dark grey = Casy, light grey = Countess.

In the MVA/Ad group, levels of MERS-specific ASC in the spleen and BM were significantly higher than negative controls (spleen: p=0.0045, BM: p=0.002). Conversely, in the Ad/MVA group only ASC in BM were significantly higher compared to the negative control (p=0.02 vs p=0.07 for spleen), as illustrated in Figure 6-8.

The median frequency of ASC in the MVA/Ad group was 8 SFU/10^6 cells [IQR:3-34] in the spleen and 36 [16-102] in the BM. In comparison, the Ad/MVA group exhibited lower median frequencies: 5 [1-11] in the spleen and 18 [5-67] in the BM. These differences were not statistically significant when directly comparing MVA/Ad vs Ad/MVA (spleen: p=0.36; BM=>0.999). These results indicate that the MVA/Ad regimen elicits a more slightly robust induction of MERS-specific ASC in the spleen compared to Ad/MVA.

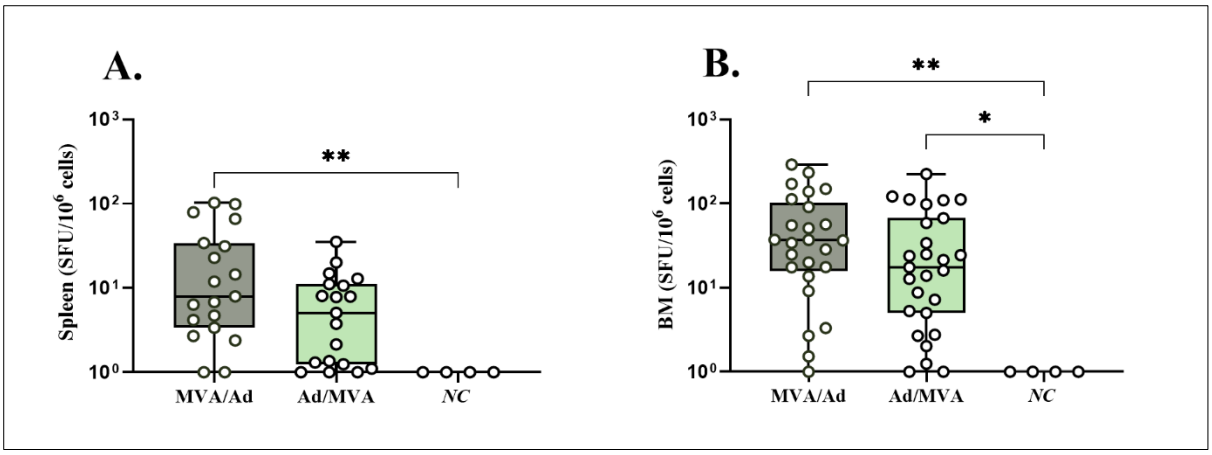


Figure 6-8. Antibody-secreting cell (ASC) responses following heterologous vaccination.
(A) Frequencies of MERS spike–specific IgG ASC in spleen [MVA/Ad, n = 19; Ad/MVA, n = 19; NC, n = 4]. **(B)** Frequencies of MERS spike–specific IgG ASC in bone marrow [MVA/Ad, n = 25; Ad/MVA, n = 27; NC, n = 4]. Box plots show medians with interquartile ranges (IQR); whiskers indicate min–max. Statistical significance was assessed by Kruskal–Wallis test (*p < 0.05). Colours: MVA/Ad (dark green), Ad/MVA (light green), NC (white).

6.1.2.1.2 Correlation between humoral responses

IgG and PNA titres correlated significantly with IgG-ASC frequencies in both spleen and BM (Figure 6-9). Correlations were consistently stronger in the MVA/Ad regimen compared with Ad/MVA. In the spleen, IgG titres correlated strongly with ASC frequencies in both regimens (MVA/Ad: $R = 0.9$, $p < 0.0001$; Ad/MVA: $R = 0.8$, $p < 0.0001$, Figure 6-9A), while neutralising antibody titres correlated equally well (both $R = 0.9$, $p < 0.0001$, Figure 6-9B). In contrast, correlations in the BM were weaker overall, particularly for Ad/MVA (IgG: $R = 0.5$, $p = 0.003$; PNA: $R = 0.5$, $p = 0.0086$) compared with MVA/Ad (IgG: $R = 0.8$, $p < 0.0001$; PNA: $R = 0.7$, $p < 0.0001$) (Figure 6-9C-D). These findings indicate that splenic ASC activity closely mirrors serum antibody titres, whereas BM ASC responses—though still correlated—likely reflect the establishment of long-lived plasma cells. The stronger correlations in MVA/Ad suggest robust coordination of antibody responses at the time of assessment, while the weaker correlations in Ad/MVA may reflect variability in MVA boosting or the delayed kinetics of BM plasma cell establishment, or technical variability related to BM sample viability.

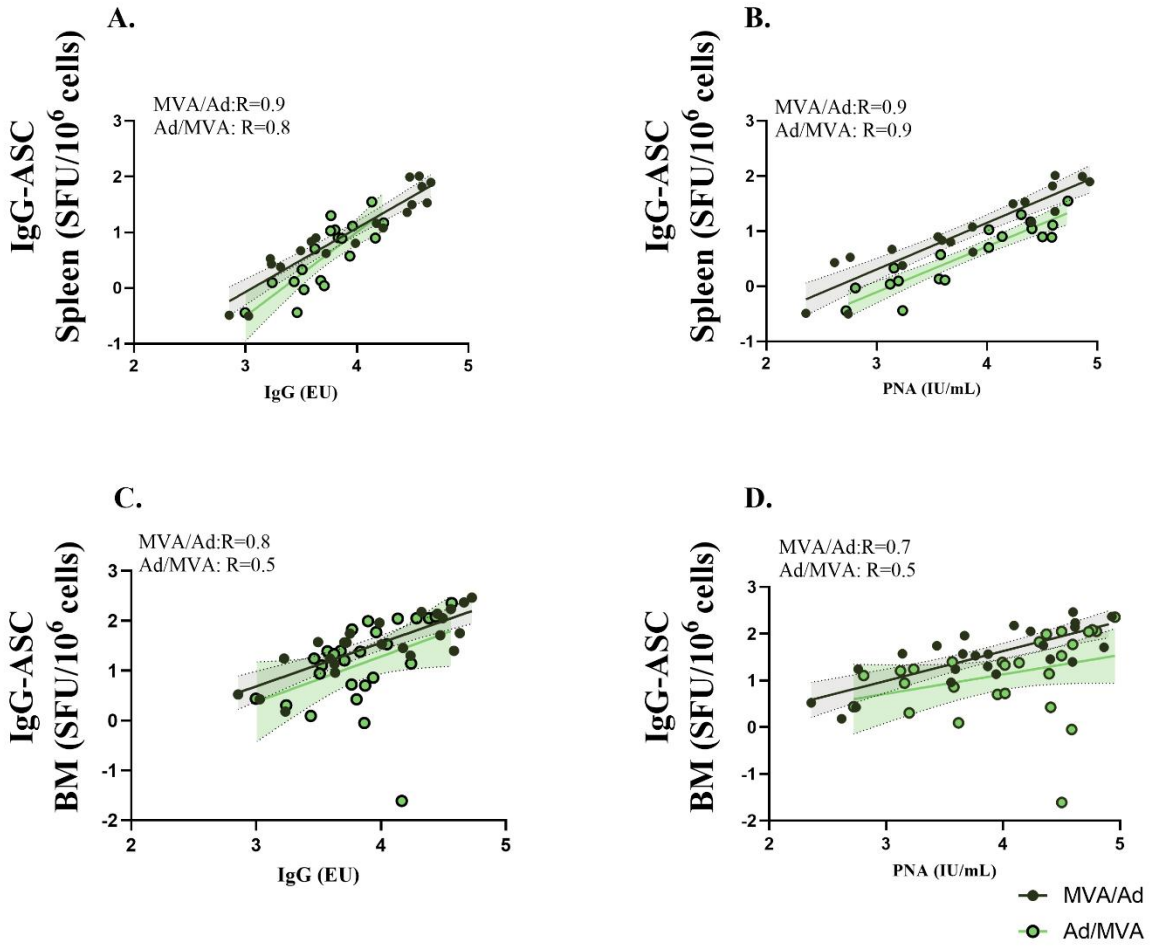


Figure 6-9. Correlation of serum antibody titres with ASC frequencies in spleen and bone marrow.

(A, C) Serum IgG titres (ELISA units) versus IgG-ASC frequencies in spleen **(A)** and bone marrow **(C). (B, D)** PNA titres (IU/mL) versus IgG-ASC frequencies in spleen **(B)** and bone marrow (D). Data are shown for MVA/Ad (grey, filled circles) and Ad/MVA (green, open circles) with linear regression and 95% CI shading. Pearson's Correlation coefficients (R) shown for each group in the panels. P-values were as follows: panel A (spleen IgG-ASC vs IgG), MVA/Ad R = 0.9, $p < 0.0001$ and Ad/MVA R = 0.8, $p < 0.0001$; panel B (spleen IgG-ASC vs neutralising antibody), MVA/Ad R = 0.9, $p < 0.0001$ and Ad/MVA R = 0.9, $p < 0.0001$; panel C (BM IgG-ASC vs IgG), MVA/Ad R = 0.8, $p < 0.0001$ and Ad/MVA R = 0.5, $p = 0.0035$; panel D (BM IgG-ASC vs neutralising antibody), MVA/Ad R = 0.7, $p < 0.0001$ and Ad/MVA R = 0.5, $p = 0.0086$.

6.3.1.2.1 T-cell responses

To identify the most reliable method for quantifying cells in IFN-γ ELISPOT assays, responses calculated using Casy or Countess counts were compared (Figure 6-10). The final analysis included 19 animals per regimen. Both correlated significantly with total IFN-γ levels measured in $CD4^+$ and $CD8^+$ T cells by flow cytometry. Although Casy-derived counts showed a slightly higher correlation ($R = 0.70$, $p < 0.0001$), Countess-derived counts ($R = 0.60$, $p < 0.0001$) provided a better overall model fit in the subsequent DoE analysis. Consequently, Countess counts were used for all subsequent ELISPOT analyses.

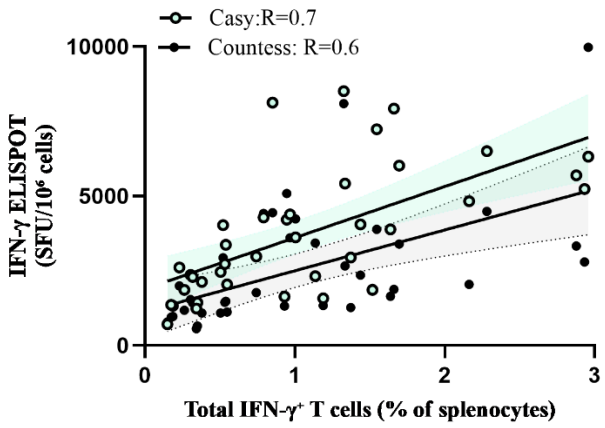


Figure 6-10. Comparison of cell counting methods for T cell ELISPOT.

Correlation between IFN-γ ELISPOT responses (SFU/10^6 cells) and frequencies of IFN-γ^+ $CD4^+$/$CD8^+$ T cells measured by flow cytometry, using counts obtained from either the Casy (open circles) or Countess (filled circles) counters. Both methods showed significant correlations (Spearman), with a stronger association observed for Casy-derived counts ($R = 0.7$, $p < 0.0001$) than for Countess-derived counts ($R = 0.6$, $p < 0.0001$). Data represent n = 19 mice per regimen.

Both regimens induced IFN-γ ELISPOT responses significantly above negative controls (MVA/Ad, $p = 0.029$; Ad/MVA, $p = 0.0008$). Responses were higher in the Ad/MVA group, with a median of 2044 SFU/10^6 [IQR: 1428–4235], compared to 1478 [1087–3333] in the MVA/Ad group. However, the difference between regimens did not reach statistical significance ($p = 0.236$, Kruskal–Wallis test with multiple comparisons;

Figure *6-11*A).

After stimulation of cells with immunodominant, S1, or S2 epitopes, only CD8+ cells showed a significant increase in double-positive IFN-γ^+/TNF-α^+ in MVA/Ad and Ad/MVA vs. negative controls ($p<0.05$;

Figure *6-11*C,E,G); no difference vs. negative controls was seen in $CD4^+$ T cell responses (

Figure *6-11*B,D,F). No significant differences were observed between regimens, although responses tended to be higher in Ad/MVA than MVA/Ad - this trend was most evident for the immunodominant epitope (Ad/MVA: median 0.60 [IQR: 0.26–0.95] vs. MVA/Ad: 0.34 [0.08–0.61],

Figure *6-11*C) and for S1 (Ad/MVA: 0.68 [0.33–1.0] vs. MVA/Ad: 0.53 [0.09–0.88],

Figure *6-11*E), while S2 responses were comparable between regimens (Ad/MVA: 0.22 [0.05–0.40] vs. MVA/Ad: 0.22 [0.039–0.43],

Figure *6-11*G).

ELISPOT responses were modestly higher in MVA/Ad, whereas $CD8^+$ T cell responses by flow cytometry were higher in Ad/MVA. Although not statistically significant, this suggests that some IFN-γ detected in MVA/Ad by ELISPOT—may originate from non-T cell sources such as NK cells.

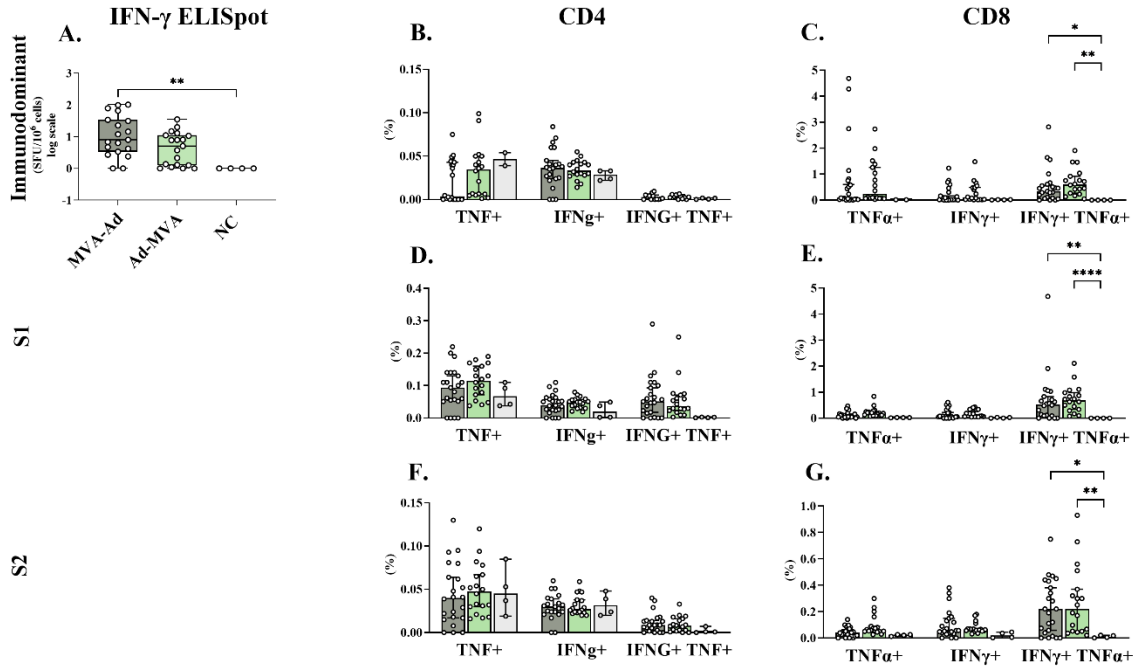


Figure 6-11. IFN-γ responses measured by ELISpot and intracellular cytokine staining.

(A) IFN-γ ELISpot responses against the immunodominant peptide pool in MVA/Ad- and Ad/MVA-immunised mice, with naïve controls (NC) for comparison, shown as box-and-whisker plots. **(B–C)** $CD4^+$ **(B)** and $CD8^+$ **(C)** T-cell cytokine responses to the immunodominant peptide pool, showing proportions of TNF^+, IFN-γ^+, and IFN-γ^+TNF^+ subsets. **(D–E)** $CD4^+$ **(D)** and $CD8^+$ **(E)** T-cell responses to the S1 peptide pool. **(F–G)** $CD4^+$ **(F)** and $CD8^+$ **(G)** T-cell responses to the S2 peptide pool. Panels B–G are shown as bar graphs with medians and 95% confidence intervals. Each symbol represents one mouse: MVA/Ad (n = 19), Ad/MVA (n = 19), naïve controls (NC, n = 4). Colours indicate treatment groups (dark green = MVA/Ad, light green = Ad/MVA, white = NC). Significant differences between regimens are indicated ($p < 0.05$, *$p < 0.01$, **$p < 0.001$, ***$p < 0.0001$; Kruskal–Wallis test with Dunn's post hoc comparison).

6.3.1.2.2 Memory

To assess memory responses following heterologous vaccination, the B-cell compartment was evaluated by measuring the frequencies of spike-specific IgG ASC in spleen and BM after 5 days of in vitro expansion. T-cell memory was assessed in the spleen by quantifying effector and central memory T-cell populations using flow cytometry. Effector memory T cells (TEM) were defined as $CD44^+$ $CD62L^-$, whereas central memory T cells (TCM) were defined as $CD44^+$ $CD62L^+$. Samples with low initial viability were excluded, and three additional samples from the Ad/MVA regimen were removed from B-ELISPOT in the spleen due to a protocol deviation. The final sample sizes were as follows:

spleen IgG ASC memory, MVA/Ad (n = 19) and Ad/MVA (n = 16); BM IgG ASC memory, MVA/Ad (n = 25) and Ad/MVA (n = 27); and T-cell memory in the spleen, n = 19 for both regimens

The MVA/Ad regimen induced significantly higher frequencies of spike-specific IgG ASC after expansion compared with negative controls in both the spleen (p = 0.0019) and BM (p = 0.04). In contrast, the Ad/MVA regimen significantly increased ASC frequencies in the BM (p = 0.0177) but not in the spleen (p = 0.962) (Figure 6-12A,B). The absence of a significant spleen response in Ad/MVA may partly reflect sample exclusions at the 12-week interval (n = 3), a time point expected to yield stronger memory responses, thereby reducing the apparent effect. However, splenic ASC frequencies in Ad/MVA before expansion were similar to those of naïve controls, which also appears to indicate less robust secondary responses from the spleen in this regimen.

Effector-memory T-cell frequencies were low overall. Nevertheless, IFN-γ^+TNF-α^+ double-positive responses were significantly higher than those observed in negative controls (NC). Following S1 peptide stimulation, $CD4^+$ T-cell responses were detected in both vaccination regimens—MVA/Ad: median 0.05 % [IQR: 0.02–0.10] (p=0.002) and Ad/MVA: 0.03 [0.012–0.07] (p=0.003)—compared with NC: 0.0005 [0–0.001]. Induction of $CD8^+$ T-cell responses were more pronounced: after S1 stimulation MVA/Ad yielded 0.36 [0.08–0.64] (p=0.0013) and Ad/MVA 0.49 [0.22–0.69] (p<0.0001) versus NC: 0 [0–0.00097]. Additionally, IFN-γ single-positive $CD8^+$ T cells increased (0.12 [0.043–0.14] vs NC: 0 [0–0.00097]; p=0.009). (Figure 11.C and 11.D). After S2 stimulation, only $CD8^+$ responses remained significantly elevated (MVA/Ad: 0.16 [0.039–0.27], p=0.0007; Ad/MVA: 0.13 [0.042–0.28], p=0.0002) relative to NC: 0.0002 [0–0.001] (

Figure *6-11*C-D) (

Figure *6-11*EF). Central memory T-cell responses were only detected in Block II, likely reflecting higher cell viability; however, frequencies remained low and were undetectable under most conditions.

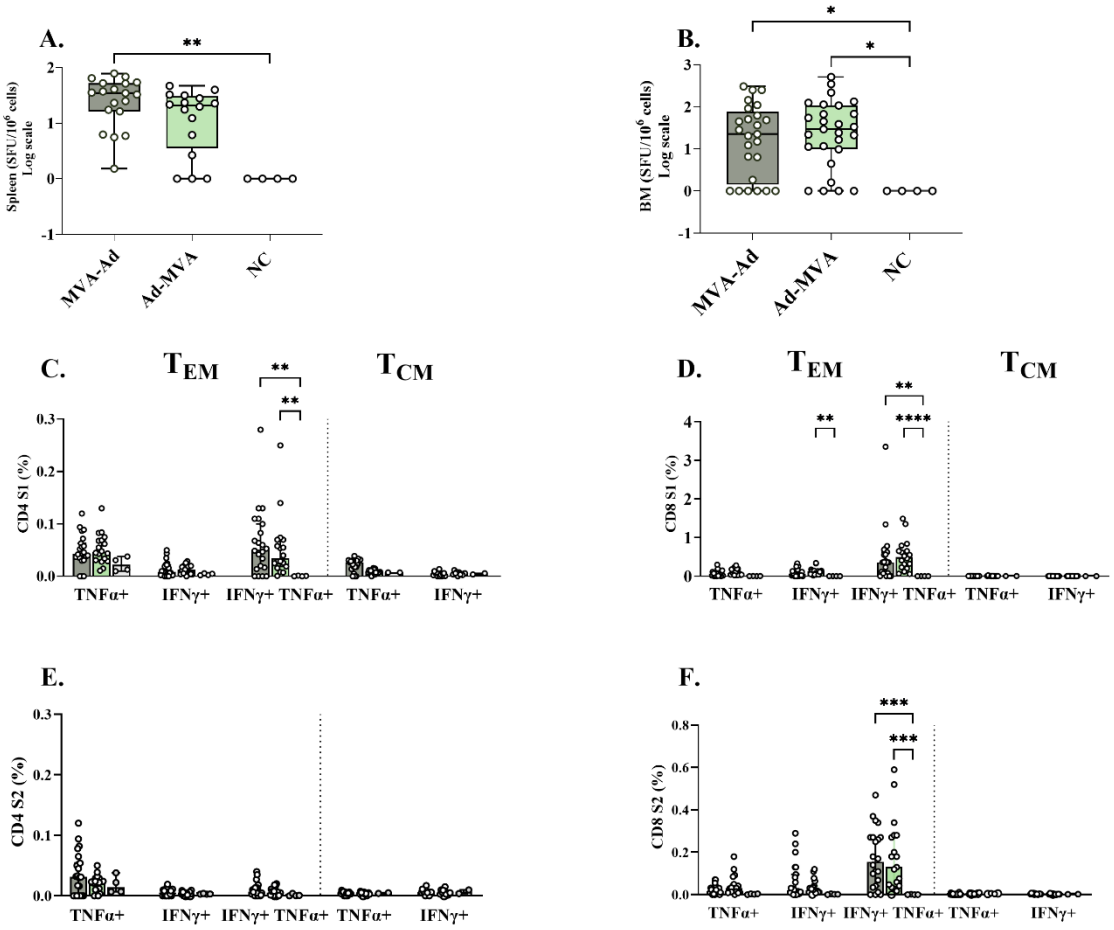


Figure 6-12. Spike-specific humoral and T-cell memory after heterologous vaccination.

(A–B) Frequencies of MERS-CoV spike–specific IgG memory antibody-secreting cells (ASC) in spleen (**A**; MVA/Ad n = 19, Ad/MVA n = 16, NC n = 4) and bone marrow (**B**; MVA/Ad n = 25, Ad/MVA n = 27, NC n = 4) measured by ELISpot. Box plots show medians with interquartile ranges (IQR).**C–F**. Frequencies of cytokine-positive $CD4^+$ **(C, E)** and $CD8^+$ **(D, F)** T cells with effector memory (T_EM) and central memory (T_CM) phenotypes following stimulation with S1 **(C, D)** or S2 **(E, F)** peptide pools. Effector memory T cells (T_EM) were defined as $CD44^+CD62L^-$, and central memory T cells (T_CM) as $CD44^+CD62L^+$. Bars represent group medians with 95% confidence intervals; points represent individual animals. Statistical significance was assessed using the Kruskal–Wallis test ($p < 0.05$). Colours denote experimental groups: black, MVA/Ad; dark green, Ad/MVA; light green, negative controls.

6.3.1.3 Pre-boosting IgG and secondary responses

Based on our previous heterologous prime–boost study, where higher pre-boost IgG titres at a 28-day interval were associated with reduced recall responses, we hypothesised that elevated antibody levels at the time of boosting might limit subsequent immunity by restricting antigen availability and B-cell recruitment. To test this hypothesis in the current DoE design, we analysed whether pre-boost IgG titres

(measured two days prior to boosting) correlated with humoral and cellular responses measured 28 days post-boost.

As expected, pre-boost IgG titres were higher in mice primed with Ad compared to MVA, regardless of interval (Figure 6-13A). When all regimens were pooled, pre-boost titres correlated modestly but significantly with post-boost IgG ($R = 0.3$, $p = 0.02$). Stratification by regimen showed that this effect was driven by Ad-primed animals, where a strong positive correlation was observed ($R = 0.7$, $p = 0.0002$), while no association was detected following MVA priming (Figure 6-13B). These results indicate that higher pre-boost IgG did not suppress boosting but instead reflected priming quality, particularly in Ad-primed groups.

We then asked whether this relationship depended on the prime–boost interval. At the 4-week interval, no correlation was observed (MVA/Ad: $R = –0.2$, $p = 0.7$, $n = 8$; Ad/MVA: $R = 0.6$, $p = 0.2$, $n = 8$, Figure 6-13C). By contrast, at the 12-week interval significant positive correlations were detected in both regimens (MVA/Ad: $R = 0.7$, $p = 0.04$, $n = 9$; Ad/MVA: $R = 0.7$, $p = 0.02$, $n = 11$, Figure 6-13D). Notably, positive correlations emerged only at the longer interval, suggesting that pre-boost IgG titres may act as a marker of effective priming once sufficient germinal centre and memory B-cell maturation has occurred.

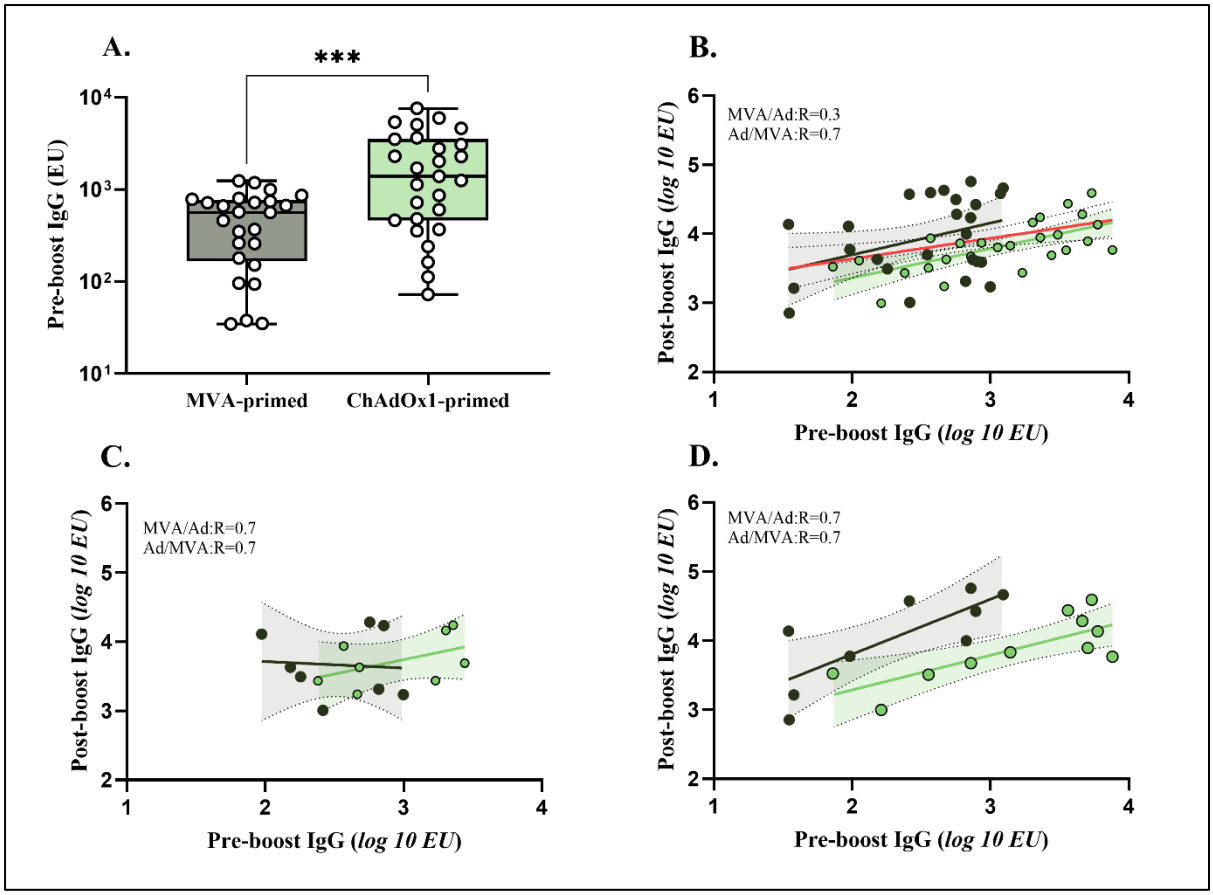


Figure 6-13. Correlation between pre-boosting IgG titres and post-boost IgG responses (Pearson correlation).

(A) Pre-boost anti-spike IgG titres in MVA-primed and ChAdOx1-primed groups (**p < 0.001, Mann–Whitney test). **(B)** Correlation between pre-boost and post-boost IgG titres across all regimens pooled (R = 0.3, p = 0.02, n = 52). Green regression lines show regimen-specific correlations (MVA/Ad: R = 0.3, p = 0.2, n = 25; Ad/MVA: R = 0.7, p = 0.0002, n = 27). The red line indicates the pooled correlation. (C) Short-interval boost (4 weeks; MVA/Ad: R = –0.2, p = 0.7, n = 8; Ad/MVA: R = 0.6, p = 0.2, n = 8). (D) Long-interval boost (12 weeks; MVA/Ad: R = 0.7, p = 0.04, n = 9; Ad/MVA: R = 0.7, p = 0.02, n = 11). Shaded areas represent 95% confidence intervals. Colours: MVA/Ad = light green, Ad/MVA = dark green, pooled = red.

To extend this analysis, we next investigated correlations between pre-boost IgG and a wider range of humoral and cellular outputs (Figure 6-14). Overall, pre-boost IgG correlated modestly but significantly with humoral measures including IgG and ASC in spleen and BM, as well as with IFNγ ELISPOT (R = 0.3–0.4, p < 0.05); the strongest association was seen for PNA (R = 0.6, p<0.05). No consistent correlations were detected in MVA-primed animals, apart from ASC in the spleen (R = 0.5, p = 0.04), again suggesting that these associations were primarily driven by Ad priming.

In Ad-primed groups, pre-boost IgG correlated positively with nearly all humoral readouts, but negatively with the frequencies of $CD8^+$ effector cells specific to the immunodominant and S2 epitopes (R = –0.4, p = 0.03 for both responses). Other effector and memory T-cell responses showed a similar trend but did not reach statistical significance. In contrast, IFNγ ELISPOT responses correlated positively with pre-boost IgG. Taken together, these findings suggest that higher pre-boost titres support

stronger antibody recall, but may at the same time limit expansion of $CD8^+$ effector populations, potentially due to reduced antigen availability. Nevertheless, given the factorial DoE design with multiple doses and intervals, these findings will require confirmation in larger datasets.

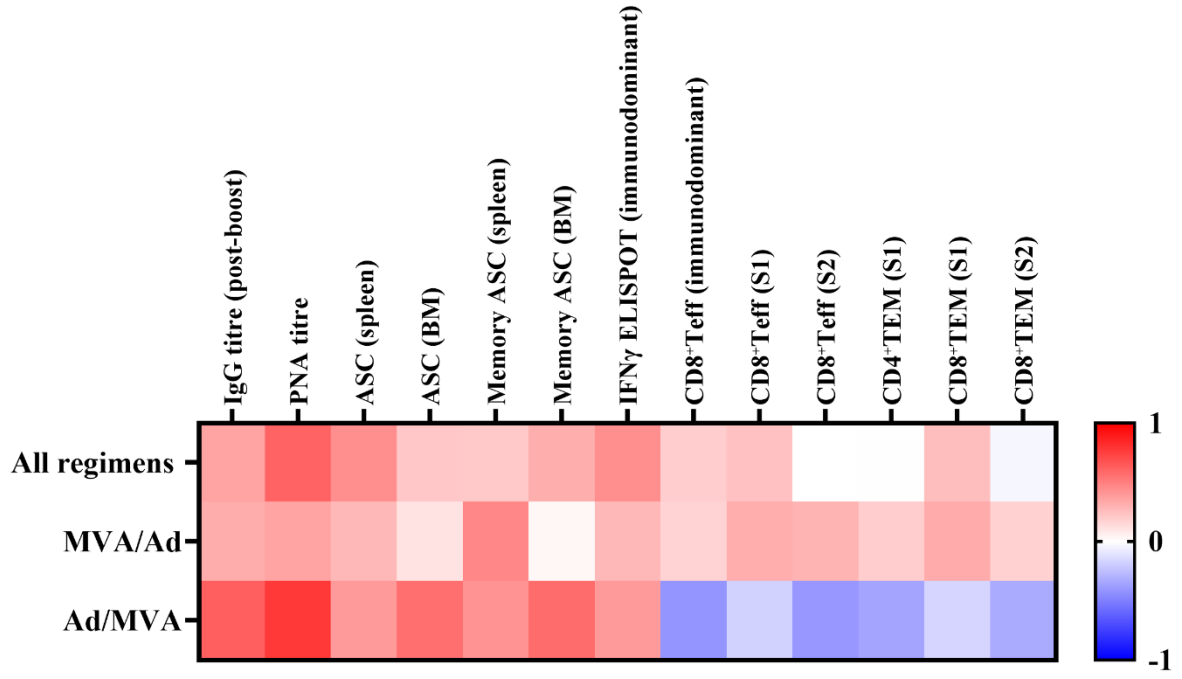


Figure 6-14. Correlation of pre-boost IgG titres with post-boost humoral and cellular immune readouts.

Spearman correlation coefficients (R) are shown for all regimens combined as well as stratified by regimen (MVA/Ad, Ad/MVA). Columns represent humoral readouts (IgG titre, PNA, ASC in spleen, ASC in bone marrow, and memory ASC) and cellular readouts (IFNγ ELISPOT, $CD8^+$ effector [Teff] responses to immunodominant, S1, and S2 epitopes, and $CD4^+$/$CD8^+$ effector memory [TEM] responses). Colour scale indicates correlation strength and direction (blue = negative, red = positive, white = no correlation). Sample sizes: all regimens combined (n = 52), MVA/Ad (n = 25), Ad/MVA (n = 27).

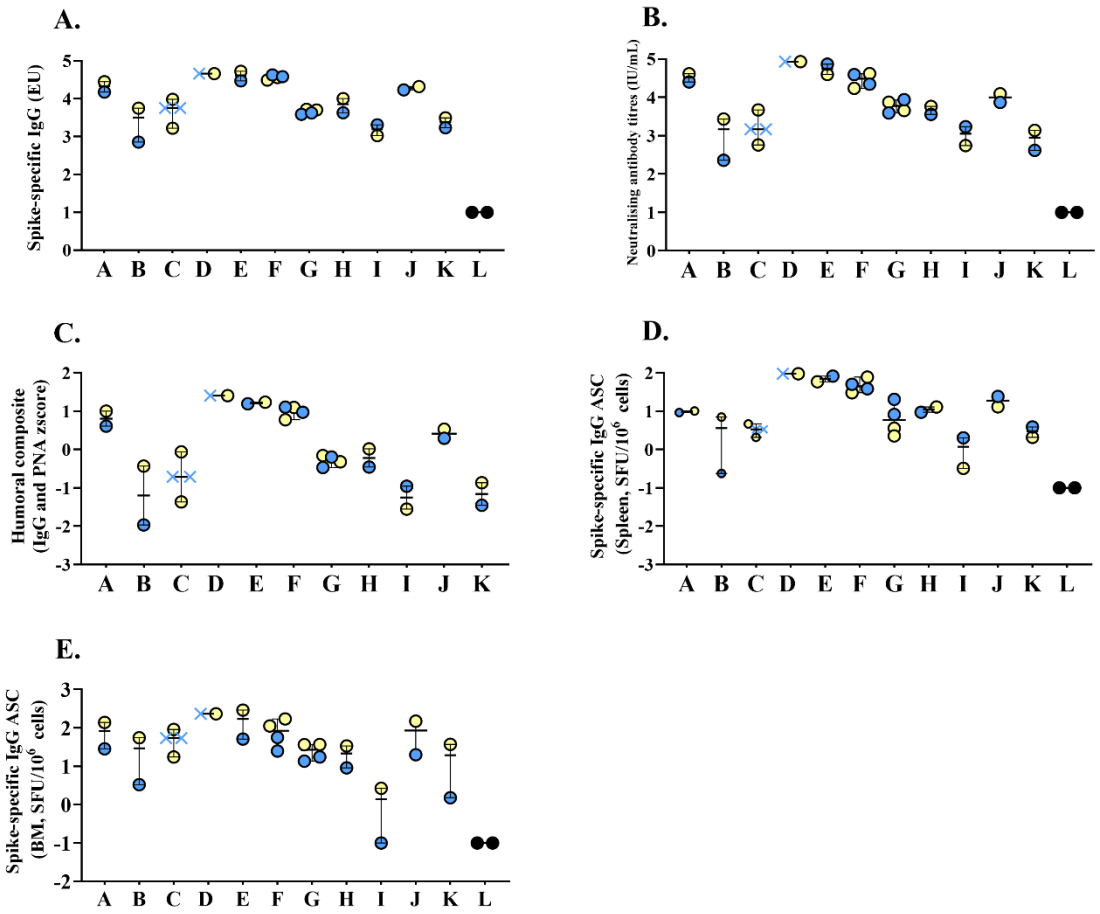
6.3.2 Statistical models

6.3.2.1 Humoral responses

6.3.2.1.1 MVA/Ad

Predictive modelling was performed using data from 11 treatment combinations generated via a D-optimal design. A total of 25 animals were included in the analyses of serum IgG and PNA titres. For ASC responses, spleen models were based on n = 19 mice after exclusion of samples with low viability, while BM ASC analyses included n = 25 mice. Raw data distributions, replicate-level variability, and the distribution of missing samples are shown in

Figure 6-15, with full datasets for individual outcomes and composite readouts summarised in the Supplementary (Table 26).



A	B	C	D	E	F	G	H	I	J	K	L	
1 E5	1 E5	4 E6	7 E6	7 E6	4 E6	7 E6	1 E5	1 E5	7 E6	7 E6	NC	MVA prime
1 E8	1 E5	1 E5	1 E8	4 E7	5 E7	1 E5	1 E8	1 E5	1 E8	1 E5	NC	Ad boost
12	12	12	12	8	8	8	8	4	4	4	4	Interval

Figure 6-15. Primary humoral outcomes for the MVA-prime, ChAdOx1-boost regimen.

(A) Serum anti-spike IgG titres (ELISA units, EU). **(B)** Pseudovirus neutralisation (PNA) IC50 (IU/mL). **(C)** Composite humoral score (IgG + PNA). **(D)** IgG ASC in spleen (SFU/10^6 cells). **(E)** IgG ASC in bone marrow (SFU/10^6 cells). Each symbol represents one mouse: yellow = Block I, blue = Block II, black = negative controls. Horizontal bars show group medians; whiskers (where shown) indicate 95% CIs. Missing observations (n = 3) are marked with "×" and placed at the group median for display only. **(F)** Treatment combinations **A–L**. Cell shading encodes dose/interval intensity (High, Medium, Low; key below). MVA prime doses were 1×10^5, 4×10^6, or 5×10^7 PFU; ChAdOx1 boost doses were 1×10^5, 4.2×10^7, 7×10^7, or 1×10^8 IU. The bottom row indicates the prime–boost interval (weeks). Both y-axes are $\log_{10}$ scaled.

6.4.4.2.1.1.1 Primary humoral readout (IgG and PNA composite)

As shown in

Figure 6-15A-C the highest antibody responses were observed in Treatment D (high prime and booster dose, long interval), with similarly strong responses in most treatments with high-dose ChAdOx1 booster (Treatments A, E, F, and J). These patterns emphasized the dominant role of the booster dose, while substantial within-groups variability (CVs > 50%, up to 109.5%) reflects the inherent biological variability and underscored the need for normalisation. To address this IgG and PNA titres were z-scored and combined into a composite humoral score for modelling, model fit results are shown in Table 6-5. Predictive models for individual composite Anti-MERS IgG ($R^2 = 0.88$) and PNA ($R^2 = 0.85$) were statistically valid, each with non-significant lack-of-fit, indicating good model adequacy. The model for the humoral composite score was similarly robust, with a strong correlation between predicted and observed values ($R^2 = 0.84$, adjusted $R^2 = 0.80$, RMSE = 0.44) and no evidence of lack-of-fit ($p = 0.55$). ANOVA confirmed that the model was highly significant ($p < 0.0001$).

	R2	R2 adjusted	RMSE	Model p-value (ANOVA)	Lack-of-Fit p-value	Significant Effect
IgG	0.88	0.85	0.39	<0.0001	0.76	B, B*B, P
PNA	0.85	0.78	0.46	<0.0001	0.59	B, I
Humoral composite	0.84	0.8	0.44	<0.0001	0.55	B, B*B, P, I

Table 6-5. Model fitting results for primary humoral outcomes in the MVA/Ad regimen.

This table summarizes the R^2, adjusted R^2, RMSE, and model p-values (ANOVA) for the primary humoral readouts: IgG (z-scored EU), PNA (z-scored IC50), and Humoral composite. The lack-of-fit p-values are provided to assess the adequacy of the model. Significant effects are indicated for the main factors and interactions, including B (booster), B*B (booster *booster), P (prime dose), and I (interval).

To further interpret the composite model, effect summary and prediction profiler plots were generated (Figure 6-16A). The most significant contributor was the ChAdOx1 boost dose, with both linear (LogWorth 5.79) and quadratic terms (LogWorth 4) indicating a nonlinear dose-response where increasing the booster dose enhances the response up to a peak, followed by decline in responses as shown in effect summary (Figure 6-16.B). The prediction profiler illustrates the inverted U-shaped relationship (Figure 6-16C).

In addition, the MVA prime dose (LogWorth = 2.1) showed a modest positive effect, while the prime–boost interval (LogWorth = 1.8) also significantly improved the humoral composite response, suggesting that both priming strength and timing contribute meaningfully to immunogenicity. The presence of multiple significant terms, including interactions, supports the conclusion that vaccine regimen parameters interact to shape the humoral response. Finally, desirability optimisation for highest

humoral composite score identified the optimal regimen as one combining a high MVA prime dose and a 12-week interval, with a reduced ChAdOx1 booster dose equal to 6.9×10^7, representing a 30 percent reduction from the original maximum dose and aligning with the plateauing trend observed in the quadratic dose–response curve.

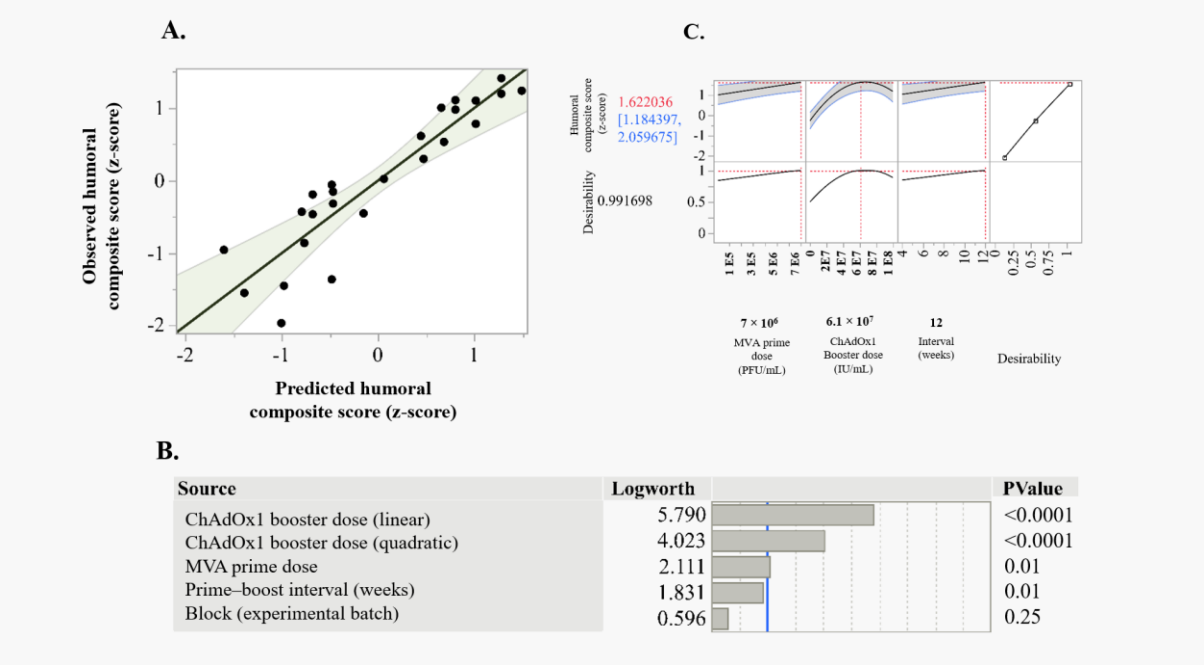


Figure 6-16. Model fitting results for the humoral composite outcome in the MVA/Ad regimen.

(A) Actual versus predicted plot showing z-score–normalized responses for individual mice (n = 25). **(B)** Effect summary ranking factors by their relative contribution to the model. **(C)** Prediction profiler illustrating the influence of each factor, with desirability optimisation identifying the optimal parameter combination.

6.3.2.1.1.1 Secondary humoral readouts (ASC in spleen and BM).

Induction of IgG ASC in the spleen followed a similar trend to serum IgG titres, with Treatment D inducing the highest number of IgG ASC. Samples with low viability (n = 5) generally showed lower responses within replicates, although this was not consistent across all treatments. Variation in ASC responses was considerable, ranging from 32% in the spleen to 75% (with CV up to 135% prior to exclusion), while variation in the BM reached 0–142%, reflecting the substantial biological variability characteristic of cellular assays. ASC frequencies in the BM were also consistently higher in Block I compared to Block II, underscoring the influence of sample processing on the outcome. Inclusion of the block effect in the analysis was therefore necessary to account for this source of variation.

The predictive models for ASC frequencies in both spleen ($R^2 = 0.91$) and BM ($R^2 = 0.89$) were statistically significant and demonstrated strong fits, with non-significant lack-of-fit tests confirming good model adequacy (Figure 6-17, Table 6-6). In the spleen, removal of low-viability samples further

improved robustness, increasing performance from $R^2 = 0.70$ to 0.91 (adjusted R^2: 0.62 → 0.87; RMSE: 0.62 → 0.38), with no evidence of lack-of-fit (p = 0.83).

	R^2	R^2 adjusted	RMSE	Model p-value (ANOVA)	Lack-of-Fit p-value	Significant effect
ASC spleen	0.91	0.87	0.38	<0.0001	0.829	B*B, B, P
ASC BM	0.89	0.86	0.68	<0.0001	0.68	Block, B, I, P, B*B

Table 6-6. Model fitting results for secondary humoral outcomes in the MVA/Ad regimen.
This table summarizes the R^2, adjusted R^2, RMSE, and model p-values (ANOVA) for the secondary humoral readouts: ASC in spleen (z-scored EU), ASC in BM (z-scored IC50), and. Significant effects are indicated for the main factors and interactions, including B (booster), B*B (booster *booster), P (prime dose), and I (interval).

Model analysis confirmed that induction of MERS-specific ASCs was primarily driven by the ChAdOx1 booster dose. In the spleen, ASC responses were almost exclusively dependent on the booster, reflected by high LogWorth values for both quadratic (4.9) and linear (4.5) terms, with only a modest contribution from the MVA prime dose (2.5) (Figure 6-17.B). In contrast, ASC induction in the BM was regulated by a more multifactorial pattern: the booster dose remained the strongest determinant (LogWorth = 5.3), but additional contributions arose from the prime–boost interval (LogWorth = 3.8), the MVA prime dose (3.5), and the quadratic booster term (2.5) (Figure 6-17.E). This multifactorial regulation is consistent with the BM's role in supporting long lived plasma cell (LLPC) generation.

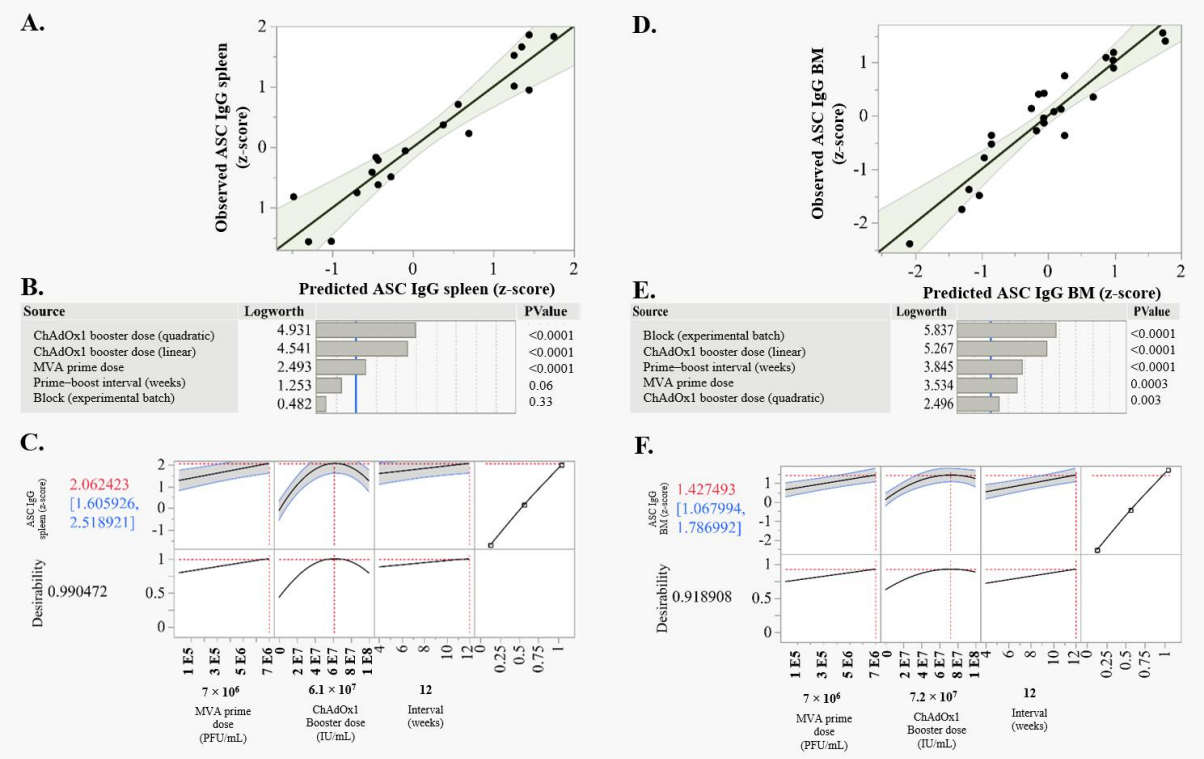


Figure 6-17. Model fitting results for IgG ASC responses in spleen and bone marrow for the MVA/Ad regimen.

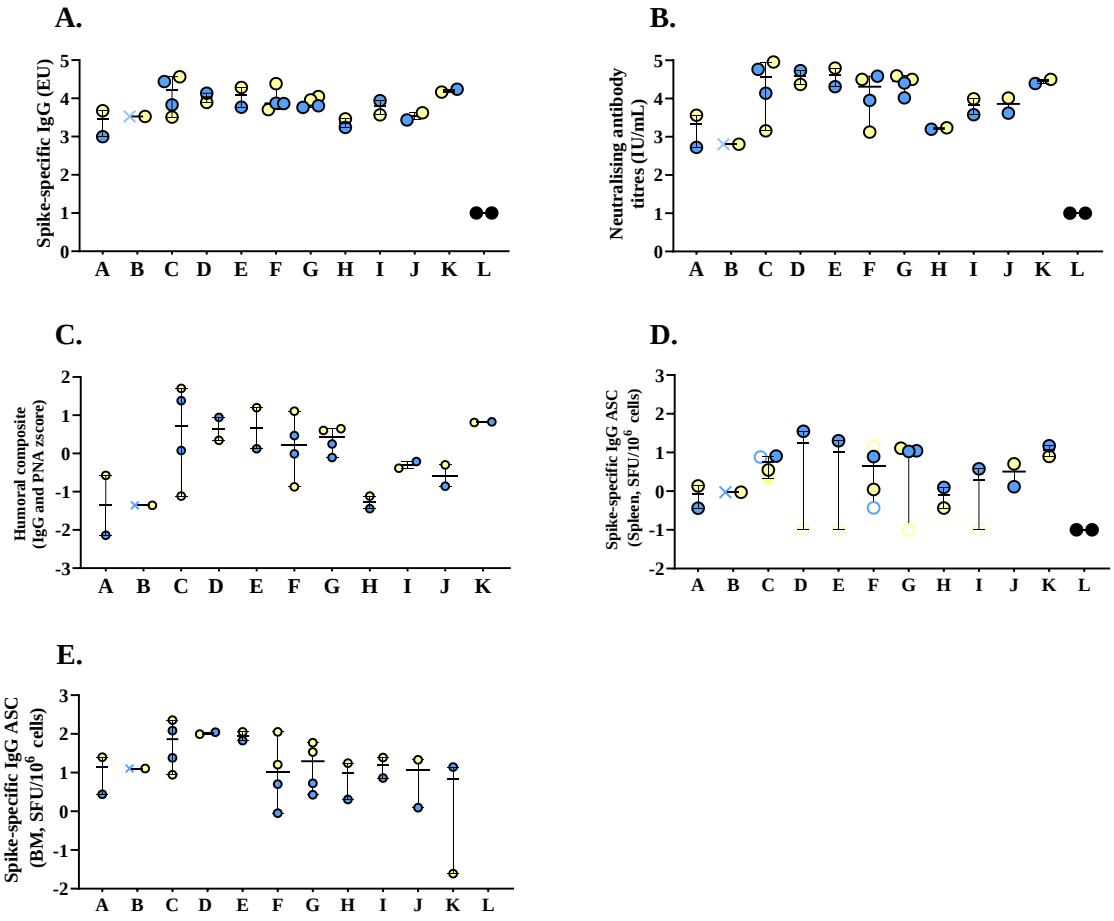
(A–C) Spleen IgG ASC: **(A)** Actual versus predicted plot of z-score–normalized responses (n = 19); **(B)** Effect summary showing ranking of contributing factors; **(C)** Prediction profiler with desirability optimization. **(D–F)** Bone marrow IgG ASC: **(D)** Actual versus predicted plot (n = 25); **(E)** Effect summary of factor contributions; **(F)** Prediction profiler with desirability optimization.

Notably, the effect summary for splenic ASC closely mirrored that of the primary humoral composite in terms of the ranking of contributing factors, whereas the BM ASC effect summary displayed a slightly distinct order. This indicates that serum antibody titres at day 28 post-boost predominantly reflect splenic ASC activity, whereas the establishment of BM ASC is governed by distinct mechanisms, likely requiring additional time and regulation, and is therefore less directly aligned with circulating antibody titres at this early timepoint. This interpretation is consistent with the positive correlations between ASC frequencies and serum IgG titres reported earlier (Figure 8), which were slightly stronger for splenic than BM ASC. Altogether, these results highlight the dominant role of the ChAdOx1 booster in shaping humoral responses, particularly in driving ASC expansion, while also emphasizing the modulatory influence of prime dose and interval in coordinating IgG, PNA, and ASC responses across tissues.

6.3.2.1.2 Ad/MVA model

Female BALB/c mice (n = 27) were analysed for the humoral immune composite, with one mouse excluded from the dataset. Predictive modelling was based on 11 treatment combinations (raw data in Figure 6-18; variability in Table 9). For ASC models, spleen analyses included n = 19 mice after removal of low-viability samples, while BM analyses included all n = 27. Missing spleen samples are

shown in Figure 6-18D, with full raw data and exclusion details are summarised in the Supplementary (Table 27).



A	B	C	D	E	F	G	H	I	J	K	L	
1 E8	1 E5	1 E5	1 E8	4 E7	5 E7	1 E5	1 E8	1 E5	1 E8	1 E5	NC	Ad prime
1 E5	1 E5	4 E6	7 E6	7 E6	4 E6	7 E6	1 E5	1 E5	7 E6	7 E6	NC	MVA boost
12	12	12	12	8	8	8	8	4	4	4	4	Interval

Figure 6-18. Primary humoral outcomes for the Ad-prime, MVA-boost regimen.

(A) Serum anti-spike IgG titres (ELISA units, EU). **(B)** Pseudovirus neutralisation (PNA) IC50 (IU/mL). **(C)** Composite humoral score (IgG + PNA). **(D)** IgG ASC in spleen (SFU/10⁶ cells). **(E)** IgG ASC in bone marrow (SFU/10⁶ cells). Each symbol represents one mouse: yellow = Block I, blue = Block II, black = negative controls. Horizontal bars show group medians; whiskers (where shown) indicate 95% CIs. Missing observations (n = 1) are marked with "×" and placed at the group median for display only. Samples excluded due to <50% viability (n = 6) and excluded IgG ASC values (n = 3) for deviation of protocol are shown as open circles. **(F)** Treatment combinations A–L. Cell shading encodes dose/interval intensity (High, Medium, Low;

key below). MVA prime doses were 1×10^5, 4×10^6, or 5×10^7 PFU; ChAdOx1 boost doses were 1×10^5, 4.2×10^7, 7×10^7, or 1×10^8 IU. The bottom row indicates the prime–boost interval (weeks). Both y-axes are $\log_{10}$ scaled.

6.3.2.1.2.1 Primary humoral readout (IgG and PNA composite)

IgG and PNA showed broadly similar response patterns across treatments, with some differences in magnitude (Figure 6-18A-B). The highest IgG levels were observed in Treatment C and Treatment K, both primed with the lowest ChAdOx dose (1×10^5). Although these groups differed in interval (12 vs 4 weeks), no consistent effect of interval was apparent across the dataset. In contrast, the lowest antibody responses, for both IgG and PNA including composites responses, were found in Treatments A, B, H, and I, all of which received an MVA boost at the lowest dose range. Notably, Treatment D, which received the highest doses for both prime and boost, also ranked among the stronger responders (fifth for IgG and third for PNA). These observations suggest that prime dose and booster dose were more influential than interval in shaping antibody responses.

Modelling of individual humoral outcomes revealed that both anti-MERS IgG and PNA responses were explained by the tested factors, with R^2 values of 0.75 and 0.67, respectively. Neither model showed a significant lack-of-fit, confirming that the underlying structure was appropriate for the data (Table 6-7). The humoral composite model, which integrates both IgG and PNA responses, showed comparable strength ($R^2 = 0.74$, adjusted $R^2 = 0.68$, RMSE = 0.54) as illustrated in Figure 6-19A. Statistical analysis by ANOVA supported the overall model significance ($p < 0.0001$), and lack-of-fit remained non-significant ($p = 0.54$), indicating that the humoral composite model was reliably predicting the responses of antibody-mediated immunity.

	R^2	R^2 adjusted	RMSE	Model p-value (ANOVA)	Lack-of-Fit p-value	Significant effect
IgG	0.75	0.69	0.56	<0.0001	0.62	B, P
PNA	0.67	0.59	0.64	0.0002	0.83	B, P
Humoral composite	0.74	0.68	0.54	<0.0001	0.54	B, P

Table 6-7. Model fitting results for primary humoral outcomes in the Ad/MVA regimen.
This table summarizes the R^2, adjusted R^2, RMSE, and model p-values (ANOVA) for the primary humoral readouts: IgG (z-scored EU), PNA (z-scored IC50), and Humoral composite. The lack-of-fit p-values are provided to assess the adequacy of the model. Significant effects are indicated for the main factors and interactions, including B (booster), B*B (booster *booster), P (prime dose), and I (interval).

The humoral composite model identified the MVA boost dose as the most influential factor (LogWorth = 4.629), followed by the ChAdOx prime dose (2.837). In contrast, the prime–boost interval did not significantly affect responses ($p = 0.218$; Figure 6-19B). Desirability optimisation (Figure 6-19C) predicted that the optimal regimen would include a high ChAdOx1 prime, high MVA boost, and a 12-

week interval. Accordingly, the model suggested that an "all-high" strategy would maximise antibody responses. However, in the experimental DoE, the all-high regimen (Treatment D) ranked only fifth for IgG and third for PNA. The highest observed responses were instead achieved with a low ChAdOx1 prime in combination with a higher boost dose. The overall desirability score of 0.65 (vs. 0.99 for the equivalent for Ad/MVA indicates limitations in the predictive accuracy of this model.

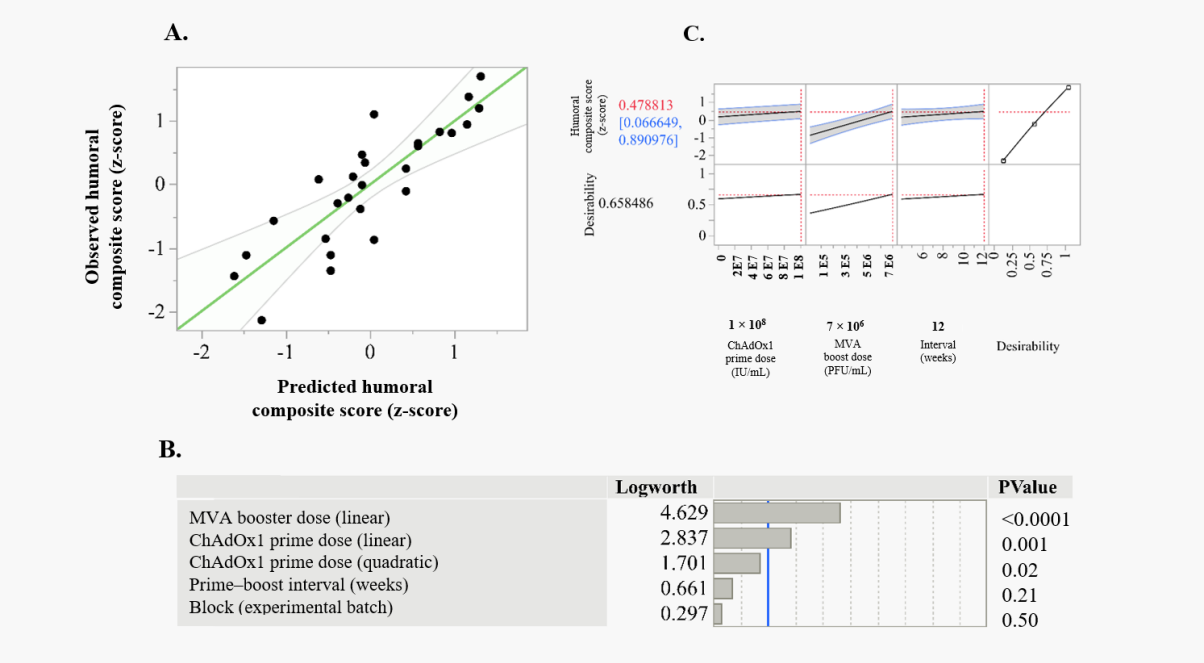


Figure 6-19. Model fitting results for the humoral composite outcome in the Ad/MVA regimen.

(A) Actual versus predicted plot showing z-score–normalized responses for individual mice (n = 27). **(B)** Effect summary ranking factors by their relative contribution to the model. **(C)** Prediction profiler illustrating the influence of each factor, with desirability optimisation identifying the optimal parameter combination.

6.3.2.1.2.2 Secondary humoral readouts (ASC in spleen and BM)

Initial modelling of ASC responses in the spleen showed a relatively poor fit (R^2 = 0.33, p = 0.054). After exclusion of eight low-viability samples identified during quality control, model performance improved substantially (R^2 = 0.77, p = 0.0008), with no evidence of lack of fit after exclusion. This revealed clearer effects of boost dose (LogWorth = 2.7) and prime dose (LogWorth = 2.4), as summarised in Table 6-8 and illustrated in Figure 6-20A-C.

	R^2	R^2 adjusted	RMSE	Model p-value (ANOVA)	Lack-of-Fit p-value	Significant effect
ASC spleen	0.77	0.68	0.5	0.0008	0.80	B, P, P*P

ASC BM	0.68	0.6	0.63	0.0001	0.31	Block, P, P*interval

Table 6-8. Model fitting results for secondary humoral outcomes in the Ad/MVA regimen.
This table summarises the R^2, adjusted R^2, RMSE, and model p-values (ANOVA) for the secondary humoral readouts: ASC in spleen (z-scored EU) and ASC in BM (z-scored IC_{50}). Significant effects are indicated for the main factors and their interactions, including B (booster), B*B (quadratic booster term), P (prime dose), and I (interval).

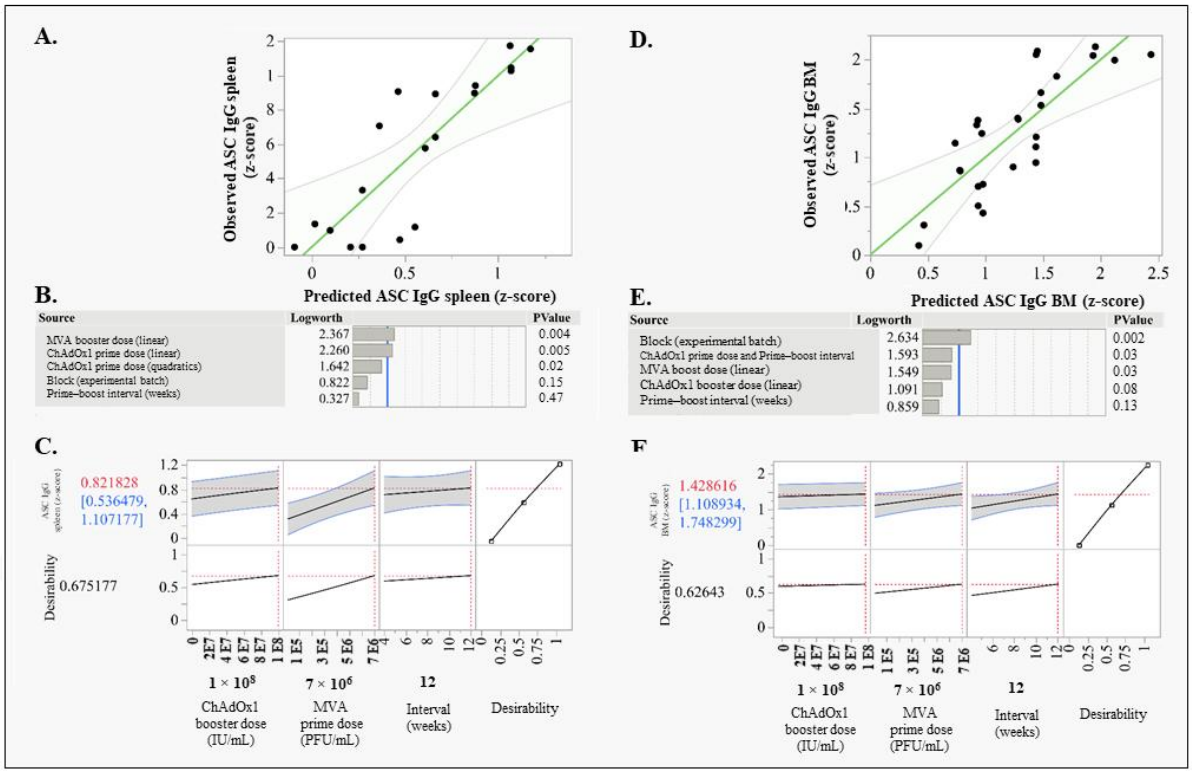


Figure 6-20. Model fitting results for IgG ASC responses in spleen and bone marrow for the Ad/MVA regimen.

(A–C) spleen IgG ASC: **(A)** actual-versus-predicted plot of z-score–normalised responses (n = 19), **(B)** effect summary ranking contributing factors, and **(C)** prediction profiler with desirability optimisation. **(D–F)** bone marrow IgG ASC: **(D)** actual-versus-predicted plot (n = 27), **(E)** effect summary of factor contributions, and **(F)** prediction profiler with desirability optimisation.

In contrast, ASC responses in the BM were significantly influenced by block effects (LogWorth = 2.5), along with contributions from ChAdOx1 prime (LogWorth = 1.7) and the prime × interval interaction (LogWorth = 1.7) Figure 6-20E. The presence of strong block effects in BM ASC was also observed in the MVA/Ad regimen, underscoring that BM readouts are particularly sensitive to technical variability. In the present dataset, ASC counts in block I were on average 2.2-fold higher than in block II, although this difference did not reach statistical significance (p = 0.0784, Mann–Whitney). As no reliable viability measure was available for BM samples, interpretation of these effects is limited. Notably, in

this regimen the desirability scores were 0.90 for spleen and 0.42 for BM, indicating poor predictive performance for the BM model.

Overall, these findings suggest that splenic ASC responses closely mirrored the induction of the primary humoral composite readout, whereas BM ASC responses were more complex, being shaped by both prime vector and interval as well as technical block effects. The involvement of ChAdOx1 prime and interval in BM ASC responses is consistent with the induction of LLPCs, highlighting the BM as a likely contributor to the durability of vaccine-induced antibody responses.

6.3.2.2 Cellular composite

6.3.2.2.1 MVA/Ad model

6.3.2.2.1.1 Primary cellular readout (ELISPOT, $CD4^+/CD8^+$ effector composite)

Predictive models were constructed for IFN-γ ELISPOT and $CD4^+/CD8^+$ effector composite responses (n = 19 mice), based on treatment combination. Results, including the distribution of missing and excluded samples, are shown in Figure 6-21.

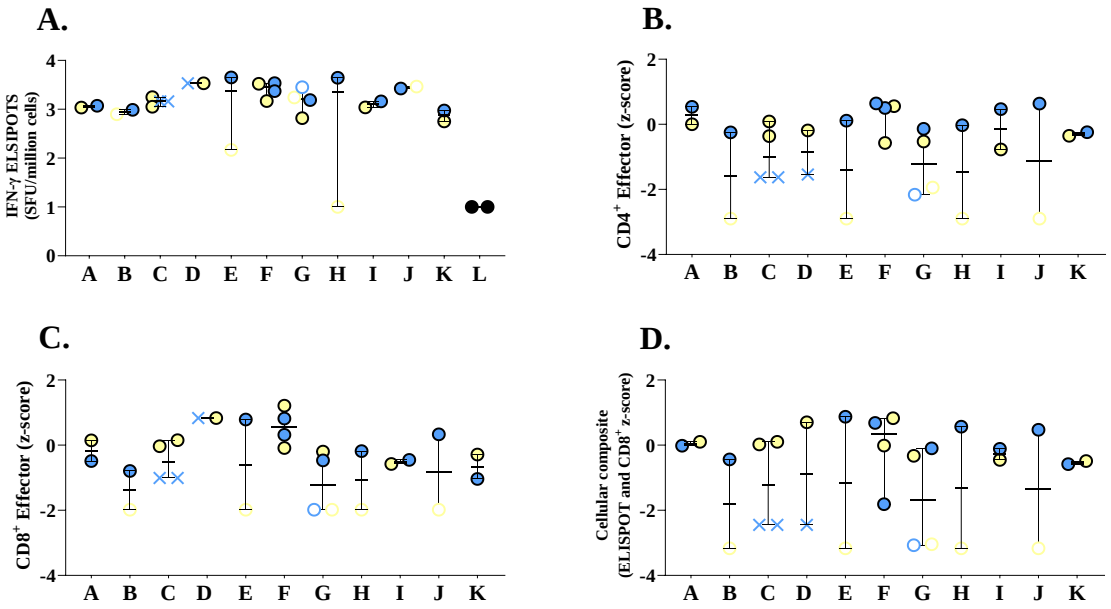


Figure 6-21. Primary cellular outcomes for the MVA-prime, ChAdOx1-boost regimen.

(A) IFN-γ ELISPOT responses (spleen). **(B)** $CD4^+$ effector composite (spleen, z-score). **(C)** $CD8^+$ effector composite (spleen, z-score). **(D)** Cellular composite (spleen; combined ELISpot and $CD8^+$ effector z-scores). Each symbol represents one mouse: yellow = Block I, blue = Block II, black = negative controls. Horizontal bars show group medians; whiskers (where shown) indicate 95% CIs calculated from samples with ≥50% viability. Missing data (n = 3) are marked with "×"; excluded samples with <50% viability (n = 6) are shown as open circles but were not included in summary statistics. (E) Treatment combinations A–L. Cell shading encodes dose/interval intensity (High, Medium, Low; key below). MVA prime doses were 1×10^5, 4×10^6, or

5×10^7 PFU; ChAdOx1 boost doses were 1×10^5, 4.2×10^7, 7×10^7, or 1×10^8 IU. The bottom row indicates the prime–boost interval (weeks).

Modelling of individual cellular outcomes revealed that both IFN-gamma ELISPOT, and $CD8^+$ effector composite responses were explained by the model, with R^2 values of 0.87, 0.58, and 0.69, respectively. However, the $CD4^+$ composite model showed an adjusted R^2 of 0.42, suggesting potential poor model performance. This was expected since $CD4^+$ responses were low and similar to those in the control mice. As a result, $CD4^+$ results were excluded and the cellular composite data were based on $CD8^+$ responses and IFN-gamma ELISPOT (Table 6-9). The initial cellular effector composite model before the removal of low viability spleen samples, which integrated both IFN-gamma and $CD8^+$ responses, was not significant ($R = 0.45$, adjusted $R^2 = 0.26$, RMSE = 1.2, $p = 0.06$). After the removal of low-viability spleen samples (n=6), the model showed improved performance, with robust fit ($R^2 = 0.79$, adjusted $R^2 = 0.68$, RMSE = 0.25). Statistical analysis via ANOVA supported the overall model significance (p 0.0018), and lack-of-fit remained non-significant ($p = 0.95$). These results highlight the importance of cell viability in obtaining accurate and reliable data.

	R^2	R^2 adjusted	RMSE	Model p-value (ANOVA)	Lack-of-Fit p-value	Significant effect
IFN-γ ELISPOT	0.87	0.79	0.16	0.0004	0.92	B, P*I, B*B, B*I
$CD4^+$ effector composite	0.58	0.42	0.336	0.0279	0.94	Block, B
$CD8^+$ effector composite	0.69	0.57	0.39	0.0047	0.92	B*B, B
Cellular composite All	0.64	0.50	0.28	0.013	0.92	B*B, B
Cellular composite (no $CD4^+$)	0.79	0.68	0.25	0.0018	0.95	B. B*B, P*I

Table 6-9. Model fitting results for primary cellular effector outcomes in the MVA/Ad regimen.

This table summarizes the R^2, adjusted R^2, RMSE, and model p-values (ANOVA) for the secondary humoral readouts: IFN-γ ELISPOT (z-scored SFU/million cells), $CD4^+$ (z-scored %), $CD8^+$ (z-scored %), and. Significant effects are indicated for the main factors and interactions, including B (booster), B*B (booster *booster), P (prime dose), and I (interval).

Statistical analysis identified the ChAdOx1 boost dose as the strongest predictor of effector T cell responses ($p = 0.0038$), with an additional interaction between ChAdOx1 prime and boost doses ($p = 0.008$; Figure 6-22B). Both crossed the LogWorth threshold of 2 ($p < 0.01$, blue reference line), indicating strong significance.

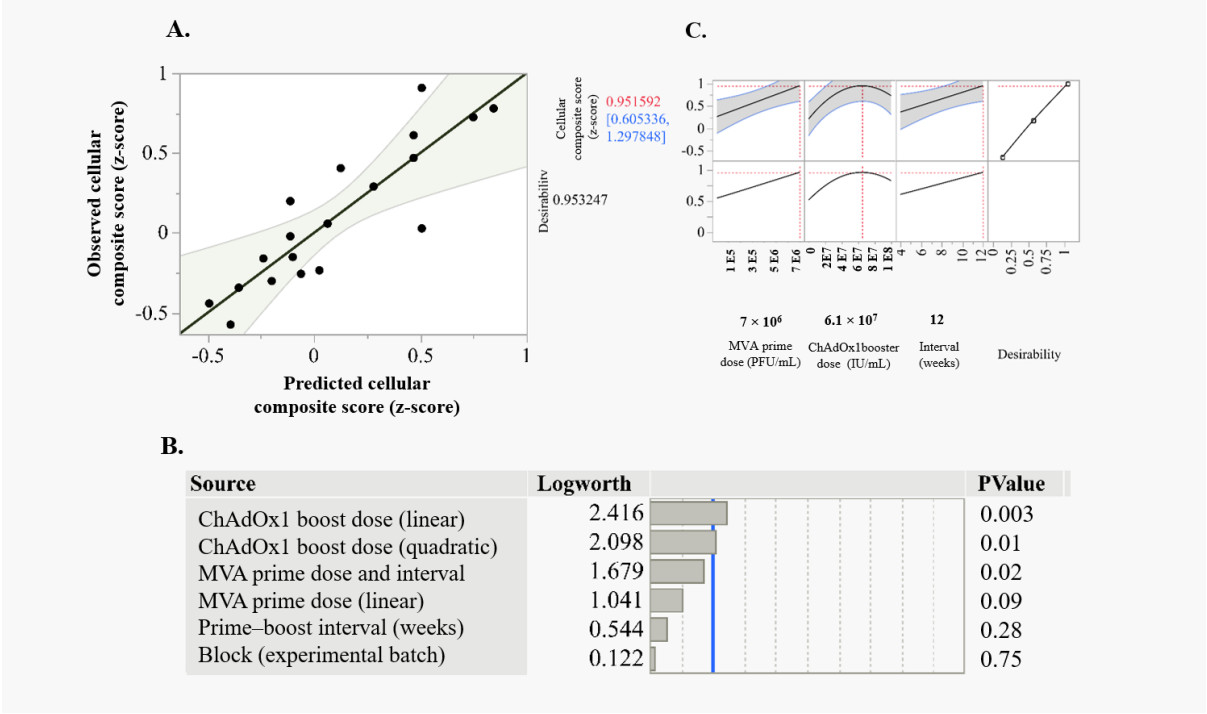


Figure 6-22. Model fitting results for the primary cellular composite outcome in the MVA/Ad regimen.

(A) Actual versus predicted plot showing z-score–normalized responses for individual mice (n = 19). **(B)** Effect summary ranking factors by their relative contribution to the model. **(C)** Prediction profiler illustrating the influence of each factor, with desirability optimisation identifying the optimal parameter combination.

The MVA prime × interval interaction also contributed (p = 0.021), significant at the 0.05 level but below the stricter 0.01 threshold. Interestingly, this interaction indicated that at short intervals (4 weeks), effector T cell responses could be enhanced by decreasing the prime dose, effectively "tricking" the immune system into responding more efficiently (Figure 6-23). Specifically, when boosting with the optimal dose, a low MVA prime (composite z-score 0.52, Figure 6-23A) produced a stronger response than a high MVA prime (0.36, Figure 6-23B). In contrast, at longer intervals, combining a high prime dose with the optimal boost yielded the strongest outcome (0.94, Figure 6-22C), underscoring the critical role of the boost dose in maximising the response. Notably, this enhancement by lowering the prime dose was observed only at short intervals.

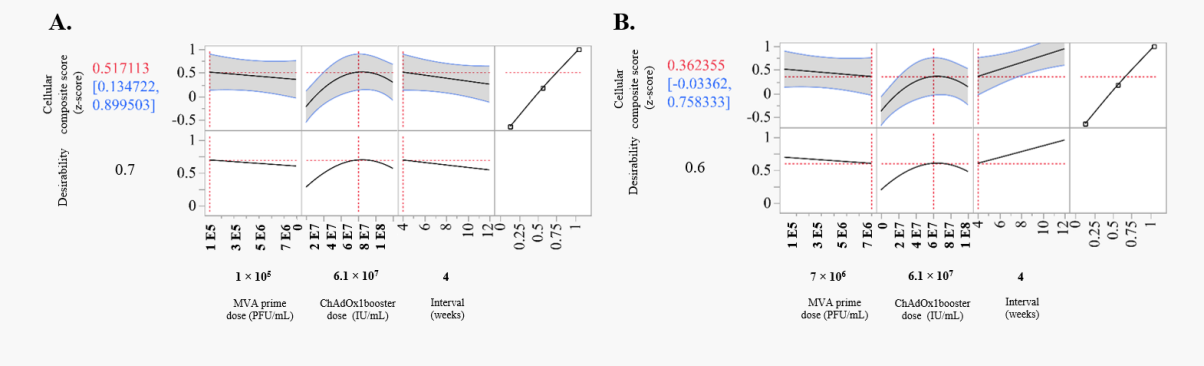


Figure 6-23. Prediction profiler for the primary cellular composite (spleen) in the MVA/ChAd regimen at 4 weeks.

(A) Low MVA prime dose (7×10^6 PFU). **(B)** High MVA prime dose (5×10^7 PFU). The model predicts enhanced responses with the low prime dose compared to the high dose, with composite scores of 0.52 and 0.36, respectively. Shaded areas represent 95% confidence intervals; red dotted lines indicate selected dose/interval settings; desirability scores are shown on the right.

6.3.2.2.1.2 Secondary cellular readout (antigenic determinacy)

Raw data underlying the composite antigenic compartment are shown in Figure 6-24. Modelling of individual linear epitopes showed that composite T cell responses to the immunodominant, S1, and S2 epitopes could be explained by the tested factors, with R^2 values of 0.78, 0.71, and 0.86, respectively. For the immunodominant and S1 epitopes, however, the adjusted R^2 values were low, indicating limited predictive value and possible overfitting despite the apparent fit. In contrast, the S2 model performed better (R^2 = 0.86, adjusted R^2 = 0.78, RMSE = 0.32; Table 6-10). Statistical analysis by ANOVA supported the overall significance of the S2 model (p = 0.0005), and lack-of-fit was non-significant (p = 0.95), suggesting adequate model fit.

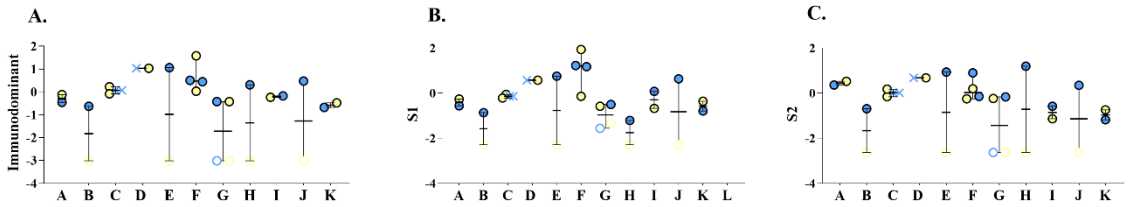


Figure 6-24. Secondary cellular outcomes for the MVA/Ad regimen.

(A) Immunodominant epitope responses (spleen). **(B)** S1 effector composite (spleen, z-score). **(C)** S2 effector composite (spleen, z-score). Each symbol represents one mouse: yellow = Block I, blue = Block II, black = negative controls. Horizontal bars show group medians; whiskers (where shown) indicate 95% CIs calculated from samples with ≥50% viability. Missing data (n = 3) are marked with "×"; excluded samples with <50% viability (n = 6) are shown as open circles but were not included in summary statistics. Treatment combinations (A–L), dose levels, and interval definitions are as described in the previous figure.

	R^2	R^2 adjusted	RMSE	Model p-value (ANOVA)	Lack-of-fit p-value	Significant effect
Immunodominant	0.78	0.59	0.16	0.0065	0.98	B, B*B, P*I
S1	0.71	0.56	0.55	0.0099	0.96	B*B
S2	0.86	0.78	0.32	0.0005	0.95	B, P*I, B*I, I

Table 6-10. Model fitting results for secondary cellular effector outcomes in the MVA/Ad regimen.
This table summarizes the R^2, adjusted R^2, RMSE, and model p-values (ANOVA) for the secondary cellular readouts: Immunodominant (z-scored %), S1 (z-scored %), S2 (z-scored %). Significant effects are indicated for the main factors and interactions, including B (booster), B*B (booster *booster), P (prime dose), and I (interval).

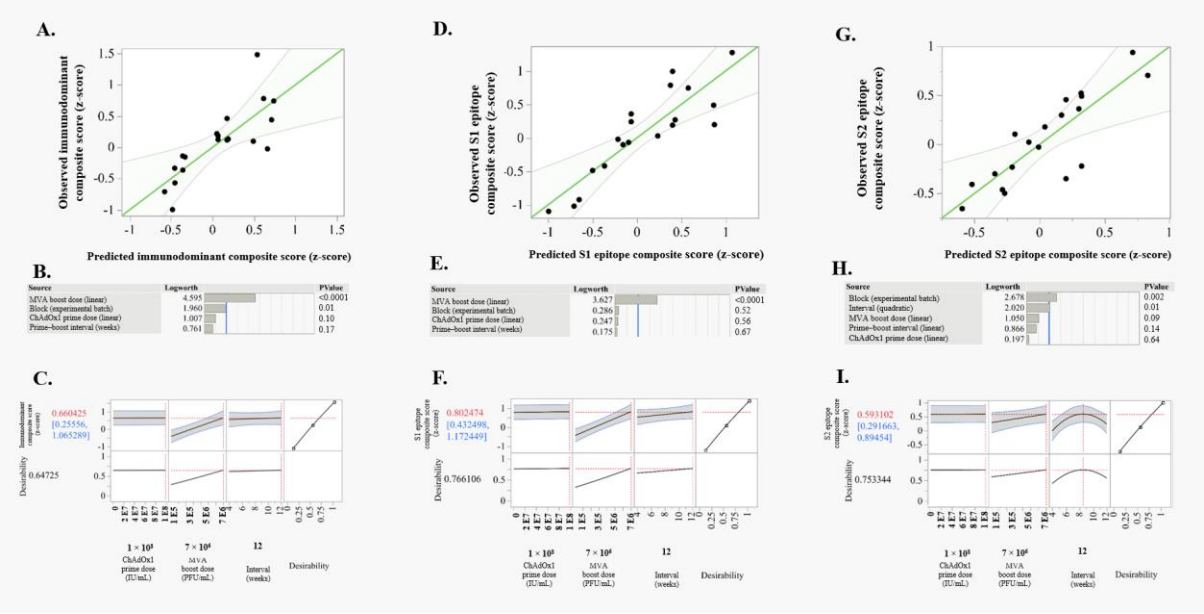


Figure 6-25. Model fitting results for immunodominant, S1, and S2 epitopes in the MVA/Ad regimen.

(A–C) Immunodominant epitope: **(A)** Actual versus predicted plot of z-score–normalized responses (n = 19); **(B)** Effect summary showing ranked factor contributions; **(C)** Prediction profiler with desirability optimization. **(D–F)** S1 epitope: **(D)** Actual versus predicted plot (n = 19); **(E)** Effect summary; **(F)** Prediction profiler. **(G–I)** S2 epitope: **(G)** Actual versus predicted plot (n = 19); **(H)** Effect summary; **(I)** Prediction profiler.

The effect summary for all epitopes in the MVA/Ad regimen is shown in (Figure 6-25B, E, H). Across epitopes, the booster dose was the predominant factor modulating responses. For the immunodominant epitope, effects were broadly similar to those described in (6.3.2.1.2.1), with an additional contribution from the prime dose and interval interaction, although model predictability was limited by a low adjusted R^2. Responses to the S1 epitope were primarily influenced by the quadratic effect of the booster dose, again with low adjusted R^2 suggesting weak predictive value. By contrast, induction of S2

responses was more reliably explained by the tested factors, with significant additional contributions from interval and its interactions with both prime and boost doses (Figure 6-25H).

The prediction profiler indicates that, at short intervals, optimised responses were achieved by lowering the prime dose and maximising the boost dose. Under these conditions, the balance between immunodominant and S2 responses was determined by the boost dose: higher boost doses favoured S2 responses, whereas lower doses favoured S1 (Figure 6-25C,F,I). Together, these findings highlight the importance of dose–interval interactions in shaping T cell responses and demonstrate that modulation of priming and boosting doses can bias epitope selection. Given the stronger predictive performance of the S2 model, the observed prime × interval effect in the composite cellular analysis is most likely driven by changes in S2-specific responses.

6.3.2.2.2 Ad/MVA model

6.3.2.2.2.1 Primary cellular readout (ELISPOT, $CD4^+$/$CD8^+$ effector composite)

Nineteen mice were included in the analysis; the distribution of missing and excluded samples based on predictive model treatment combination is shown in Figure 6-26A-D. Both IFN-γ ELISPOT and $CD8^+$ effector predictive model in Ad/MVA regimen were significant ($p = 0.0008$ and $p = 0.0002$), with explanatory power of $R^2 = 0.72$ and 0.77, respectively (Table 6-11). By contrast, the $CD4^+$ effector model showed poor predictive value ($R^2 = 0.50$, $p = 0.07$) and was excluded from further analyses. Accordingly, the cellular composite was derived from the average of $CD8^+$ effector and IFN-γ ELISPOT responses. This composite model was significant ($R = 0.66$, adjusted $R^2 = 0.56$, $p = 0.0010$) with no evidence of lack-of-fit ($p = 0.38$; Figure 6-27A).

Factor effects showed that responses in Ad/MVA were driven almost exclusively by the MVA booster dose (LogWorth 3.79), with no significant contribution from interval or prime dose. The prediction profiler confirmed the dominant effect of the boost (Figure 6-27B).

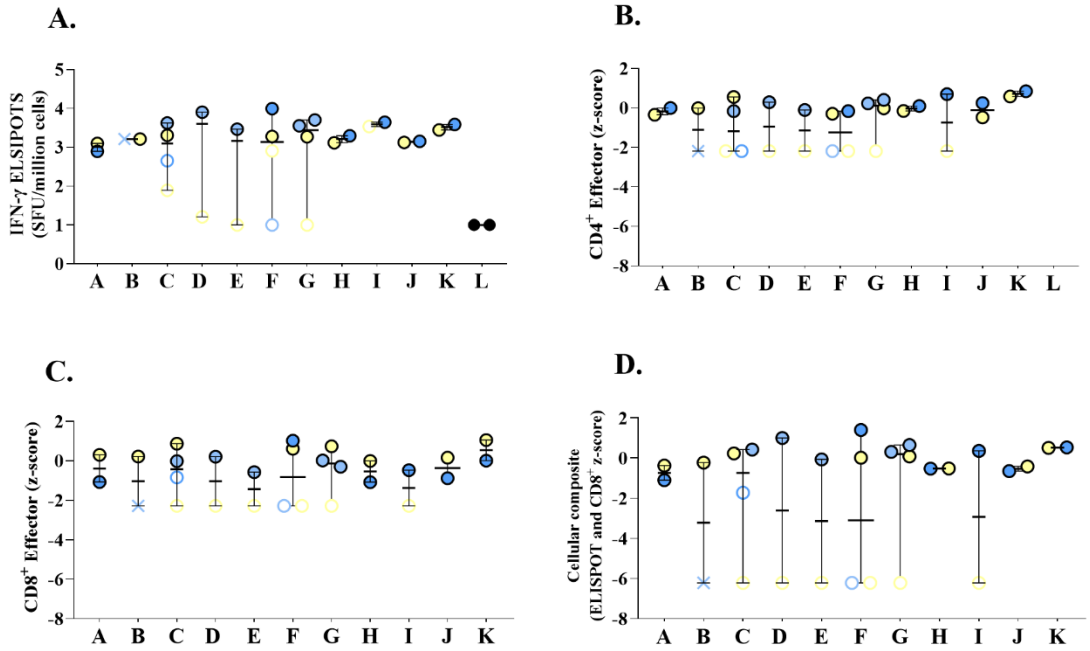


Figure 6-26. Primary cellular outcomes for the Ad/MVA regimen.
(A) IFN-γ ELISPOT responses (spleen), **(B)** CD4⁺ effector composite (z-score), **(C)** CD8⁺ effector composite (z-score), and **(D)** Cellular composite (combined ELISPOT and CD8⁺ effector z-scores). Each point represents one mouse; horizontal lines show medians with 95% confidence intervals. Missing data (n = 3) are indicated by an 'X', and excluded samples due to <50% viability (n = 6) are shown as open circles. Colours indicate experimental blocks (yellow = Block I, blue = Block II). (E) Treatment groups (A–L) are defined by prime and boost doses and intervals, ordered from high to low intensity.

	R^2	R^2 adjusted	RMSE	Model p-value (ANOVA)	Lack-of-Fit p-value	Significant effect
IFN-γ ELISpot	0.72	0.64	0.5288	0.0008	0.2	B, Block
$CD4^+$ effector composite	0.5	0.3	0.309	0.07	0.57	NA
$CD8^+$ effector composite	0.77	0.7	0.3588	0.0002	0.6	Block, B
Cellular composite	0.66	0.56	0.41	0.0010	0.38	Boost

Table 6-11. Model fitting results for primary cellular effector outcomes in the Ad/MVA regimen..
This table summarizes the R^2, adjusted R^2, RMSE, and model p-values (ANOVA) for the secondary humoral readouts: IFN gamma ELISPOT (z-scored SFU/million cells), $CD4^+$ (z-scored %), $CD8^+$ (z-scored %), and cellular composite comprising. Significant effects are indicated for the main factors and interactions, including B (booster), NA.

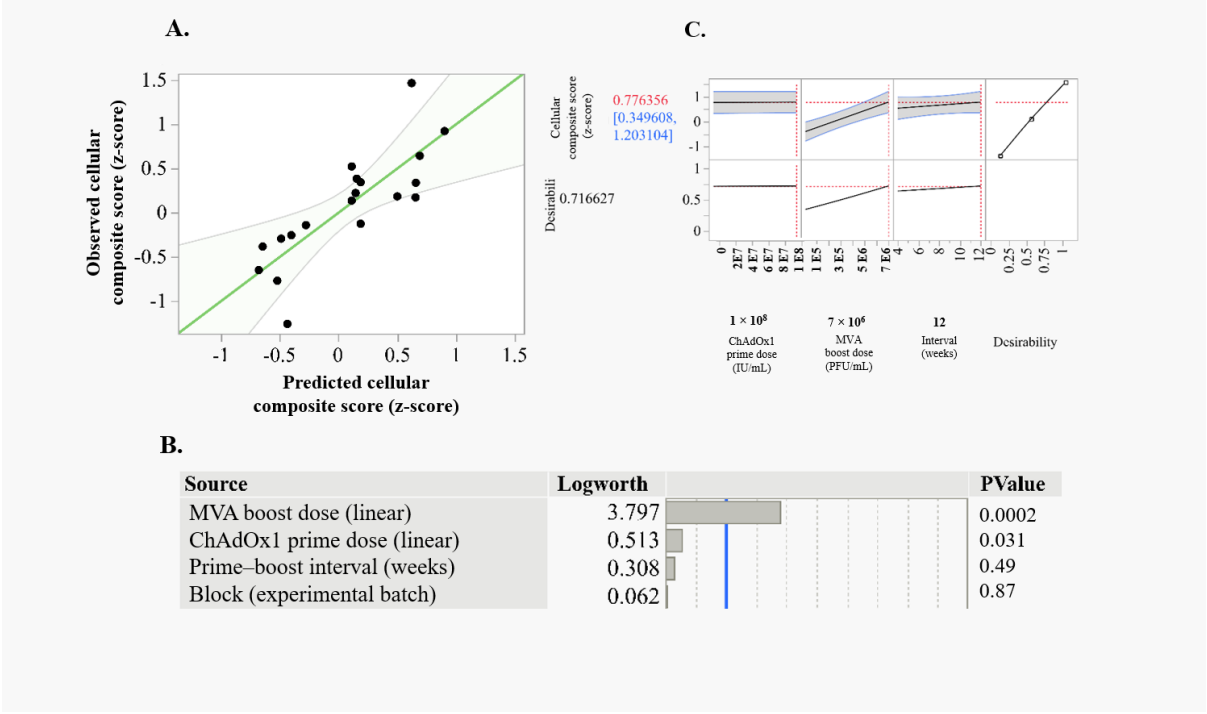


Figure 6-27. Model fitting results for the primary cellular composite outcome in the Ad/MVA regimen. **(A)** Actual versus predicted plot showing z-score–normalized responses for individual mice (n = 19). **(B)** Effect summary ranking factors by their relative contribution to the model. **(C)** Prediction profiler illustrating the influence of each factor, with desirability optimisation identifying the optimal parameter combination.

6.3.2.2.2.2 Secondary cellular readout (antigenic determinacy)

Normalized score composites of each epitope domain is illustrated in Figure 6-28 (A-C). Model fitting results for individual epitopes (Table 6-12) demonstrated relatively strong explanatory power across all three readouts, with R^2 values of 0.64–0.77 and adjusted R^2 values of 0.53–0.70. None of the models showed evidence of lack-of-fit (p = 0.16–0.98), supporting the robustness of the fits. Among the epitopes, S1 gave the strongest explanatory value (R^2 = 0.77, adjusted R^2 = 0.70), followed by S2 (R^2 = 0.72, adjusted R^2 = 0.60), while the immunodominant model was weaker but still significant (R^2 = 0.64, adjusted R^2 = 0.53, p = 0.0046, Figure 6-29 A-C.

Factor contributions differed between epitopes. Immunodominant and S1 responses were predominantly driven by the booster dose, with S1 also influenced by block effects. In contrast, S2 responses were strongly shaped by interval, with a quadratic effect indicating time-dependent modulation of this epitope. The effect summary and prediction profiler for all three epitopes are shown in Figure 27 (B, E, and H).

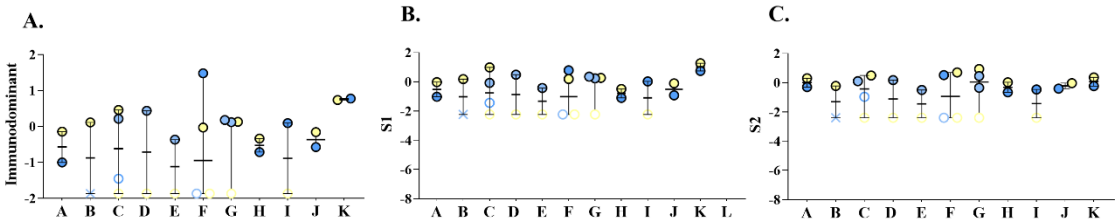


Figure 6-28. Secondary cellular outcomes for the Ad/MVA regimen.

(A) Immunodominant epitope responses (spleen). **(B)** S1 effector composite (spleen, z-score). **(C)** S2 effector composite (spleen, z-score). Each symbol represents one mouse: yellow = Block I, blue = Block II, black = negative controls. Horizontal bars show group medians; whiskers (where shown) indicate 95% CIs calculated from samples with ≥50% viability. Missing data (n = 1) are marked with "×"; excluded samples with <50% viability (n = 8) are shown as open circles but were not included in summary statistics. Treatment combinations (A–L), dose levels, and interval definitions are as described in the previous figure.

	R^2	R^2 adjusted	RMSE	Model p-value (ANOVA)	Lack-of-fit p-value	Significant effect
Immunodominance	0.64	0.53	0.391	0.0046	0.16	B
S1	0.77	0.7	0.357	0.0002	0.7	B, block
S2	0.72	0.6	0.28	0.0029	0.98	Block, I*I

Table 6-12. Model fitting results for secondary cellular effector outcomes in the Ad/MVA regimen.
This table summarizes the R^2, adjusted R^2, RMSE, and model p-values (ANOVA) for the secondary cellular readouts: Immunodominant (z-scored %), S1 (z-scored %), S2 (z-scored %), and. Significant effects are indicated for the main factors and interactions, including B (booster), and I (interval), I*I.

Responses for immunodominant and S1 were influenced by the boost dose. Interestingly, we observe a quadratic effect of interval indicating that T cell responses to S2 linear epitope are time dependent. The prediction profile and effect summary of all three responses are shown in Figure 27 (C, F and I).

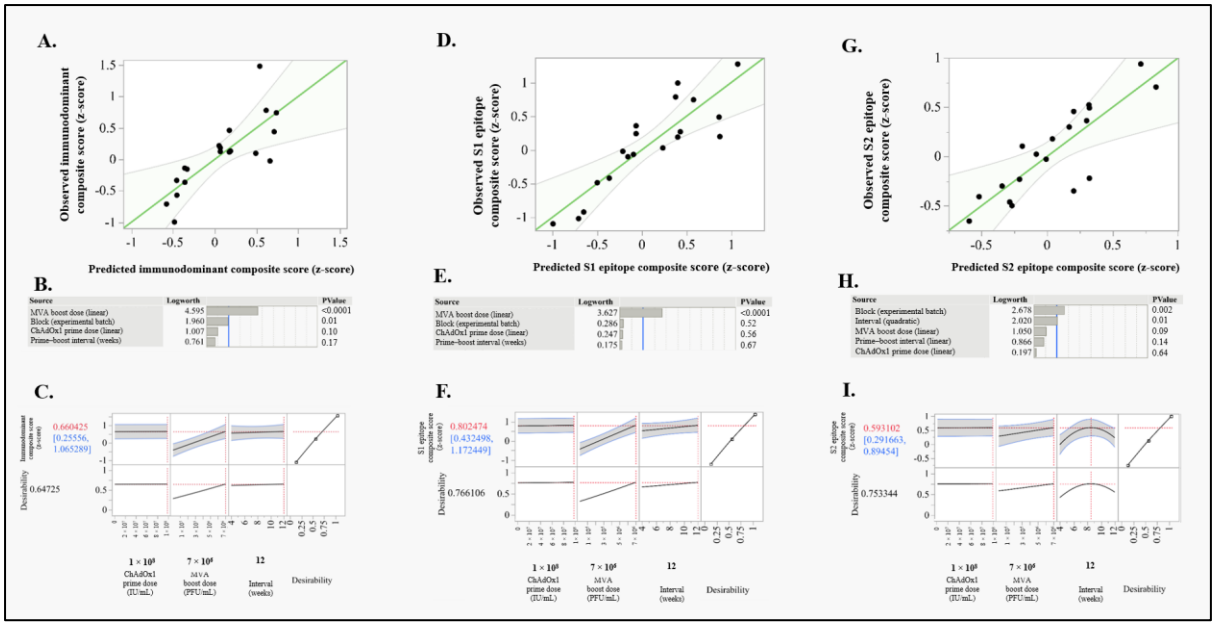


Figure 6-29. Model fitting results for immunodominant, S1, and S2 epitopes in the Ad/MVA regimen.

(A–C) Immunodominant epitope: **(A)** Actual versus predicted plot of z-score–normalized responses (n = 19); **(B)** Effect summary showing ranked factor contributions; **(C)** Prediction profiler with desirability optimization. **(D–F)** S1 epitope: **(D)** Actual versus predicted plot (n = 19); **(E)** Effect summary; **(F)** Prediction profiler. **(G–I)** S2 epitope: **(G)** Actual versus predicted plot (n = 19); **(H)** Effect summary; **(I)** Prediction profiler.

6.3.2.3 Memory responses

6.3.2.3.1 MVA/Ad regimen

6.3.2.3.1.1 Statistical models

Data for humoral and cellular effector memory responses, is shown stratified by treatment group - MVA/Ad in Figure 6-30A-C and Ad/MVA Figure 6-30D-F.

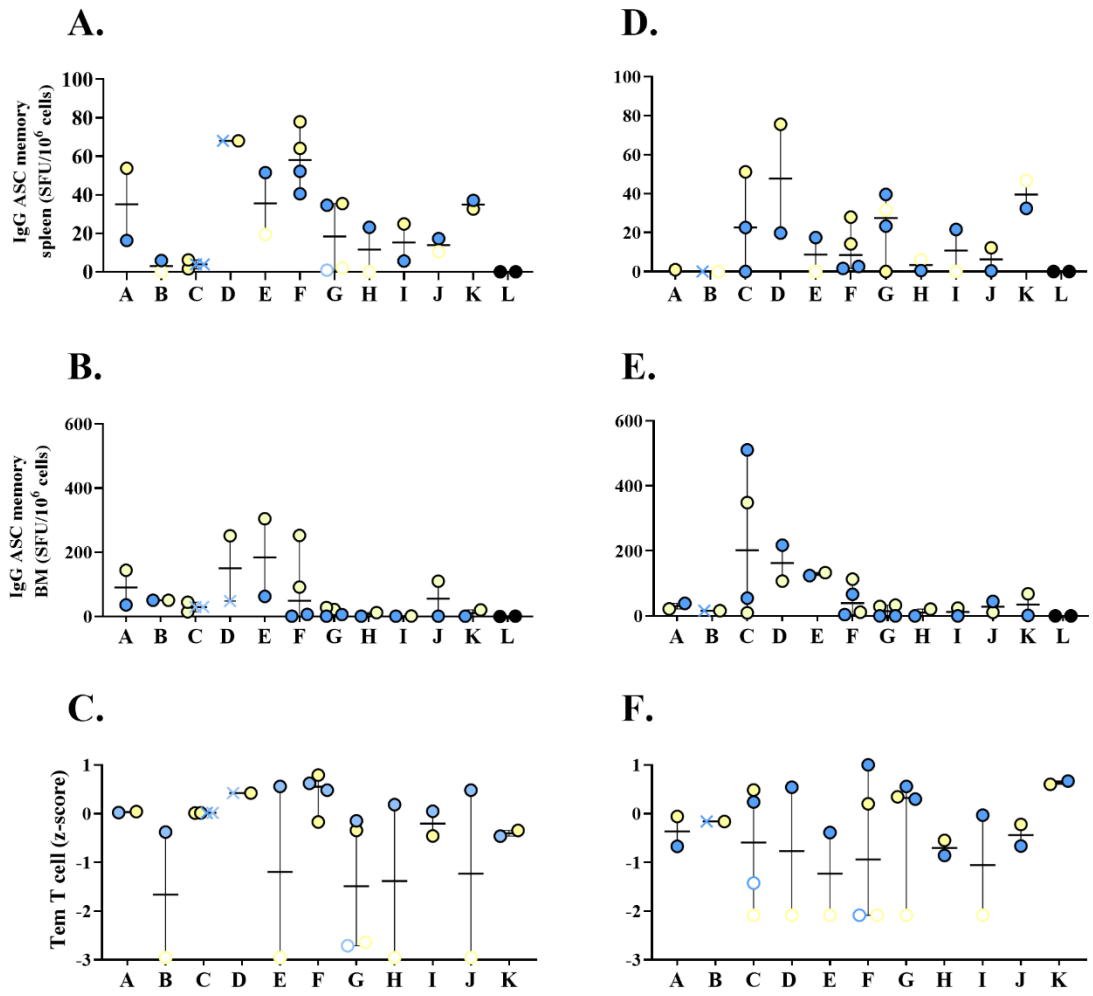


Figure 6-30. Memory outcomes for MVA/Ad and Ad/MVA regimens.
(A–C) show MVA/Ad; **(D–F)**. show Ad/MVA. Individual points represent mice; central bars denote the median, and whiskers indicate 95% confidence intervals (CIs). Antibody-secreting cells (ASC) are shown for spleen **(A, D)** and bone marrow **(BM; B, E);** effector-memory T-cell responses are summarized as z-scores **(C, F).** Missing values are marked with an "X" and, for visualization only, replaced with the group median; specifically, spleen ASC had missing values in MVA/Ad (n=3) and ChAdOx1/MVA (n=1). Excluded spleen ASC observations (n=6) are plotted as empty circles to indicate their position within the distribution but were omitted from summary statistics. Colours denote experimental blocks: yellow, block A; blue, block B; black, negative controls (NC).

Individual and composite predictive models are shown in Table 6-13. These were robust for memory B cells in both spleen (R=0.90) and BM (R=0.89). In contrast, memory T-cell models were weaker: T_EM showed moderate predictability (R=0.63; adjusted R^2=0.49; p=0.01), whereas the T_CM model was not significant (p=0.78), consistent with the very low T_CM frequencies that were comparable to negative controls (NC). To better capture overall memory responses, the composite model by averaging memory

ASC (spleen and BM) and T_EM values demonstrated strong predictive power (R^2=0.94; p<0.0001, Figure 6-31A).

	R^2	R^2 adjusted	RMSE	Model p-value (ANOVA)	Lack-of-fit p-value	Significant effect	N=
Memory ASC spleen	0.9	0.87	0.38	<0.0001	0.75	B*B, B,P	19
Memory ASC BM	0.89	0.86	0.37	<0.0001	0.68	Block, B, I, P, B*B	25
TEM composite	0.63	0.49	0.63	0.0144	0.979	B,B*B	19
TCM composite	0.15	-2.7	0.43	0.78	0.93		10
Memory composite	0.94	0.92	0.22	<0.0001	0.60	B,B*B,P,I,	19

Table 6-13. Model fitting results for memory outcomes in the MVA/Ad regimen.
This table summarizes the R^2, adjusted R^2, RMSE, and model p-values (ANOVA) for the secondary cellular readouts: Immunodominant (z-scored %), S1 (z-scored %), S2 (z-scored %), and. Significant effects are indicated for the main factors and interactions, including B (booster), B*B (booster *booster), P (prime dose), and I (interval).

The induction of memory composite responses was primarily influenced by both the linear and quadratic effects of the ChAdOx1 booster (LogWorth = 6.0 and 5.2, respectively), followed by contributions from the MVA prime (LogWorth = 3.9) and the prime–boost interval (LogWorth = 2.4), as shown in Figure 6-31B. Notably, this trend mirrored the humoral and cellular composites, with the interval also contributing to the modulation of memory outcomes. Importantly, the ChAdOx1 boost emerged as the dominant factor, although higher doses did not always translate into stronger responses.

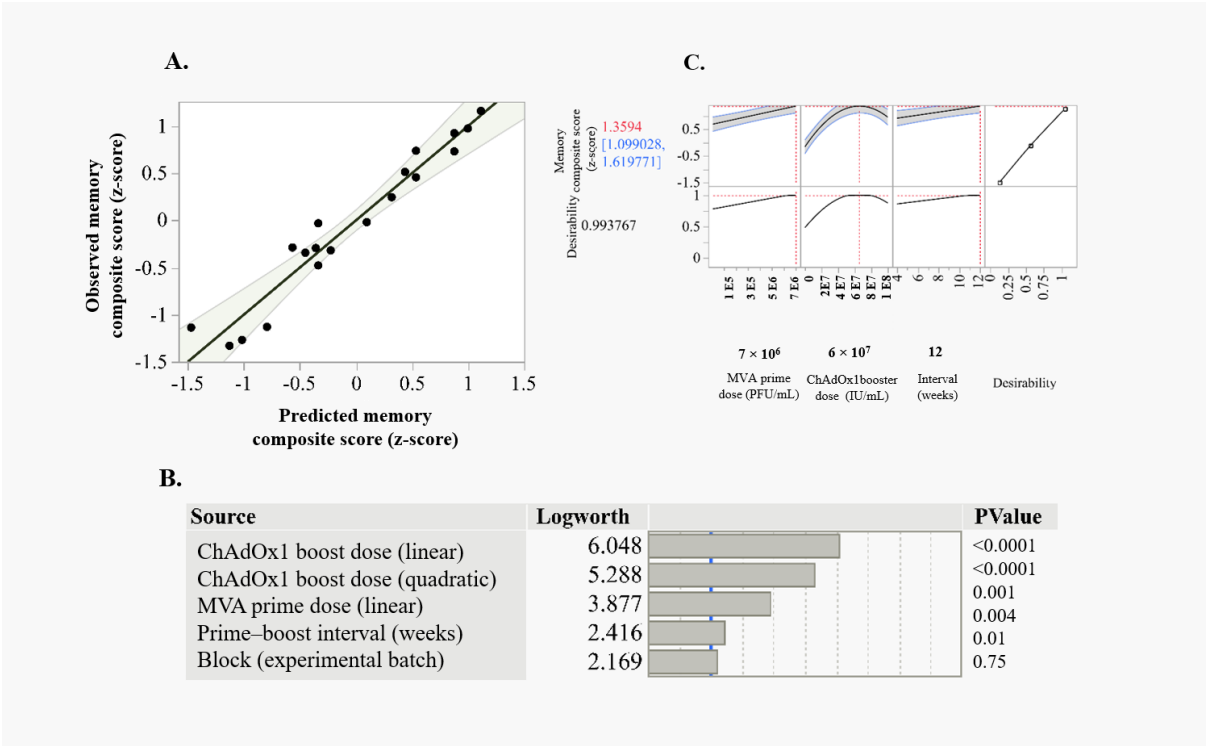


Figure 6-31. Model fitting results for the memory composite outcome in the MVA/Ad regimen.

(A) Actual versus predicted plot showing z-score–normalized responses for individual mice (n = 19). **(B)** Effect summary ranking factors by their relative contribution to the model. **(C)** Prediction profiler illustrating the influence of each factor, with desirability optimisation identifying the optimal parameter combination.

6.3.2.3.2 Ad/MVA regimen

Similar to MVA/Ad, individual models were significant for all memory components except the T central memory (Table 6-14). The booster dose had predominantly influenced the memory formation in both cellular and humoral compartments.

	R^2	R^2 adjusted	RMSE	Model p-value (ANOVA)	Lack-of-fit p-value	Significant effect	N=
Memory ASC spleen	0.8	0.711	0.4175	0.00024	0.3569	B,B*B	16
Memory ASC BM	0.66	0.58	0.6506	0.0002	0.337	I, Block, B*B	27
TEM composite	0.74	0.64	0.3219	0.0017	0.660	B	19
TCM composite	0.35	0.07	0.552	0.3602	0.4277	NA	11
Memory composite	0.73	0.64	0.3044	0.0007	0.0884	B, I, P	19

Table 6-14. Model fitting results for memory outcomes in the Ad/MVA regimen.
This table summarizes the R^2, adjusted R^2, RMSE, and model p-values (ANOVA) for the secondary cellular readouts: Immunodominant (z-scored %), S1 (z-scored %), S2 (z-scored %), and. Significant effects are indicated for the main factors and interactions, including B (booster), B*B (booster *booster), P (prime dose), and I (interval). NA memory composite corresponds to TEM and TCM together.

The memory composite was generated by averaging the z-scores of memory ASC IgG in spleen, ASC memory IgG in BM, and the TEM composite. The predictive performance of this model was significant (R^2 = 0.73, adjusted R^2 = 0.64, p = 0.0007, Figure 6-32A). Induction of the memory composite was primarily influenced by the MVA boost dose (LogWorth = 3.12), followed by the interval (LogWorth = 2.80), ChAdOx1 prime (LogWorth = 1.8), and block (LogWorth = 1.7), as shown in the effect summary. Results are illustrated in Figure 6-32B.

Collectively, in both MVA/Ad and Ad/MVA regimen, the booster and interval emerged as consistent contributors to the memory composite response.

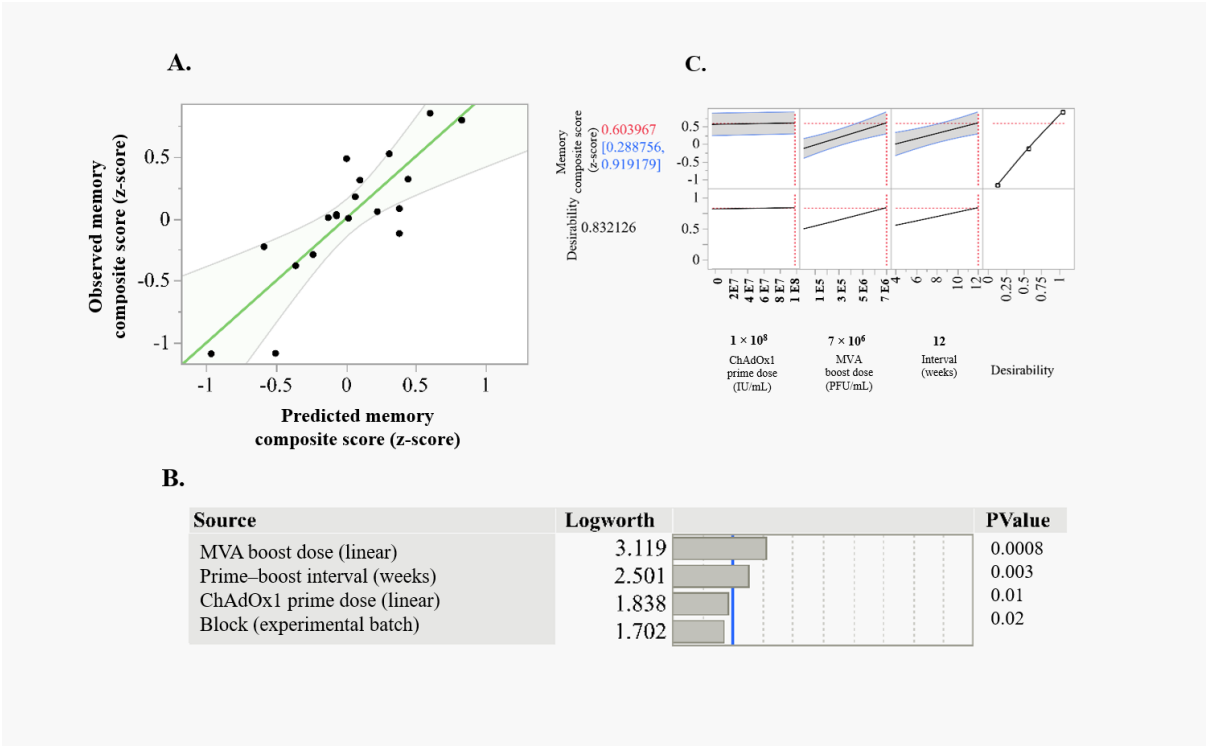


Figure 6-32. Model fitting results for the memory composite outcome in the Ad/MVA regimen.

(A) Actual versus predicted plot showing z-score–normalized responses for individual mice (n = 19). **(B)** Effect summary ranking factors by their relative contribution to the model. **(C)** Prediction profiler illustrating the influence of each factor, with desirability optimisation identifying the optimal parameter combination.

6.3.3 Regimen optimisation

6.3.3.1 Composite immunological outcome integrating humoral, cellular, and memory responses

To define the optimum conditions for each vaccination regimen, the composite outcome of humoral, effector cellular, and memory domains was modelled in a single predictive framework. The predictive power of each component is summarised in Table 6-15 and illustrated in Figure 6-33 and Figure 6-34.

	Regimen Ad/MVA or MVA/Ad	R^2	R^2 adjusted	RMSE	Model p-value (ANOVA)	Lack-of-fit p-value	N=
MVA Ad	Humoral composite	0.87	0.8	0.4871	0.0001	0.69	19
	Effector cellular composite	0.78	0.68	0.25147	0.0018	0.94	19
	Memory composite	0.95	0.92	0.2192	<0.0001	0.6137	19
Ad MVA	Humoral composite	0.67	0.57	0.577	0.0026	0.1142	19
	Effector cellular composite	0.66	0.56	0.4122	0.0030	0.3842	19
	Memory composite	0.73	0.64	0.3044	0.0007	0.0884	19

Table 6-15. Summary of the composite immunological outcome in the combined predictive model

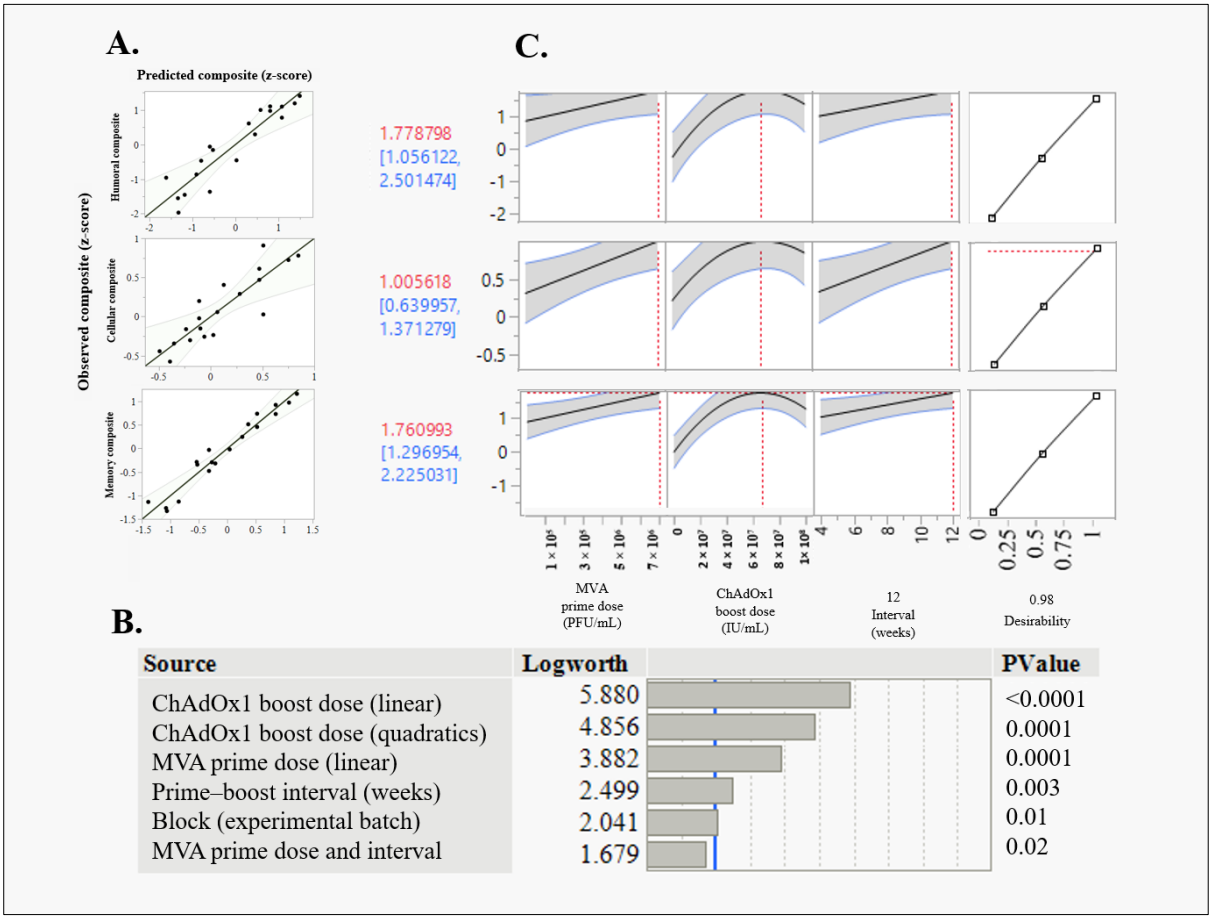


Figure 6-33. Model fitting results for composite immune responses in the MVA/Ad regimen.

(A) Actual versus predicted plots of z-score–normalized composite responses (n = 19), shown separately for humoral, cellular, and memory components. **(B)** Effect summary ranking significant contributing factors (LogWorth and p-values). **(C)** Prediction profiler with desirability optimization across MVA prime dose, ChAdOx1 boost dose, and prime–boost interval.

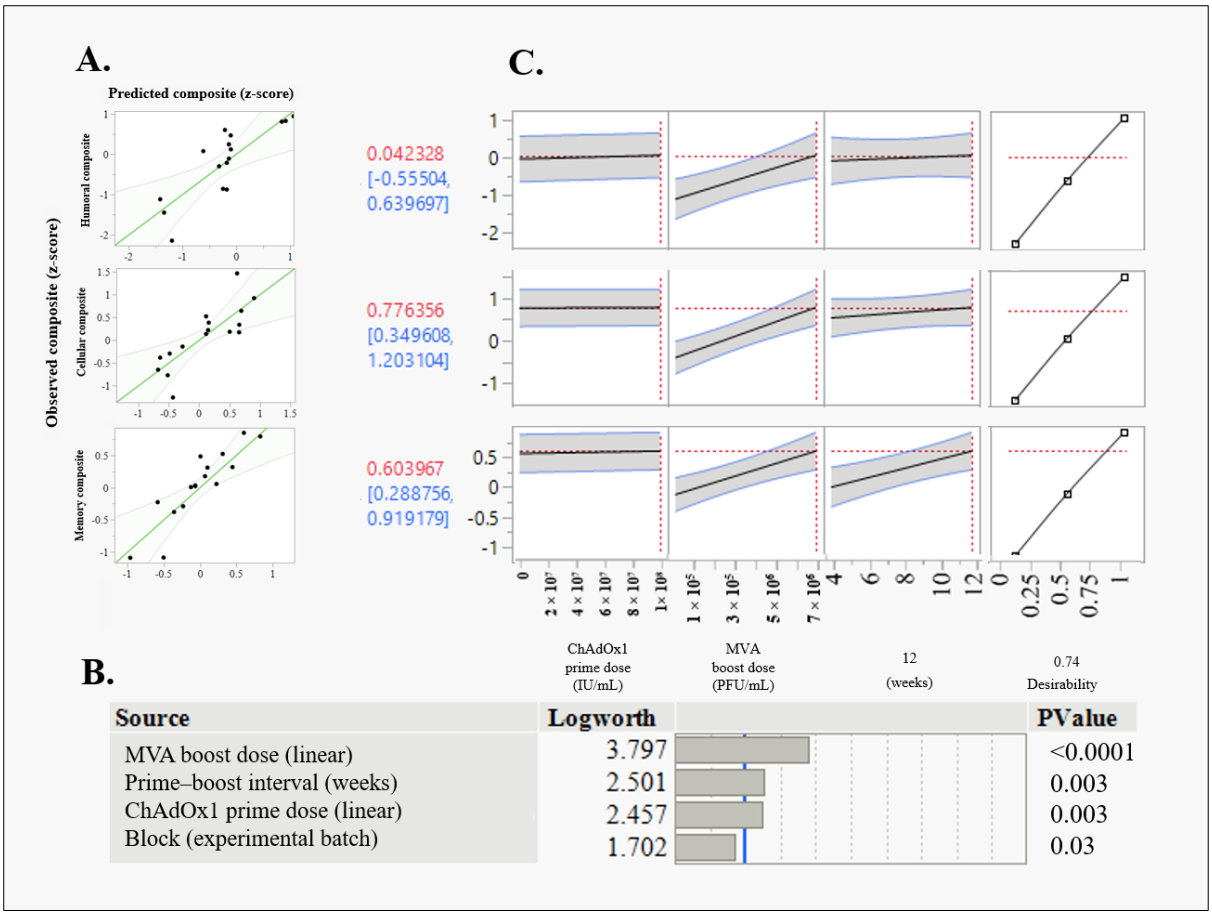


Figure 6-34. Model fitting results for composite immune responses in the Ad/MVA regimen.

(A) Actual versus predicted plots of z-score–normalized composite responses (n = 16), shown separately for humoral, cellular, and memory components. **(B)** Effect summary ranking significant contributing factors (L ogworth and p-values). **(C)** Prediction profiler with desirability optimization across MVA prime dose, ChAdOx1 boost dose, and prime–boost interval.

As expected, the optimal responses were achieved at longer boost intervals in both MVA/Ad and Ad/MVA regimens. The booster dose consistently emerged as the predominant factor influencing immunological outcome. For the Ad/MVA regimen, boosting at the highest tested dose provided a beneficial effect. In contrast, in the MVA/Ad regimen a saturation effect was observed, suggesting that optimisation is required to confirm the threshold dose that maximises responses without exceeding the plateau.

Interestingly, an interaction between the prime dose and interval was identified in the MVA/Ad regimen for the effector T-cell composite. In this case, at a short interval priming with a lower dose appeared to induce higher responses than priming with a higher dose. Although this finding requires confirmation

with additional experiments and larger group sizes, it suggests that dose modulation relative to interval length may be an effective strategy for T-cells. Overall, predictive power was higher for the MVA/Ad than the Ad/MVA regimen, likely reflecting the dominant influence of booster dose and the limited range of MVA doses evaluated at the higher end.

6.3.3.2 Optimised condition at long interval vs short interval

To compare heterologous prime–boost regimens across intervals, optimised doses of MVA/Ad and Ad/MVA were evaluated for humoral, cellular, and memory outcomes. The longest interval, identified as the optimal condition, was compared with a 4-week interval, using prediction intervals to assess differences between regimens (Figure 6-35).

At the long interval, the MVA/Ad regimen induced the strongest overall responses (Figure 6-35), characterised by markedly higher IgG and neutralising antibody (PNA) titres, increased frequencies of BM ASCs, and elevated TE and TEM populations. Cellular responses measured by IFN-γ ELISpot were enhanced in both regimens, although Ad/MVA achieved higher predicted ranges (Figure 6-35C). While ASC induction in the BM was observed for both regimens, Ad/MVA was associated with higher predicted levels of splenic memory ASCs (Figure 6-35F), consistent with stronger stimulation of the peripheral B-cell memory compartment.

At the short interval, MVA/Ad continued to outperform Ad/MVA in humoral outcomes, producing higher IgG titres and neutralising activity (Figure 6-35A,B). In contrast, T-cell responses measured by IFN-γ ELISpot were greater following Ad/MVA (Figure 6-35C), whereas predicted TE frequencies were higher for MVA/Ad (D). Within the memory compartment, MVA/Ad maintained measurable ASC frequencies in both BM and spleen, while Ad/MVA responses were weaker and more variable (Figure 6-35E-F).

Together, these findings indicate that while MVA/Ad at long intervals maximises both antibody and effector T-cell responses, even at short intervals MVA/Ad still provides superior humoral and memory outcomes compared with Ad/MVA. This suggests MVA/Ad as potentially the more effective regimen under both time-constrained and extended boosting schedules. Nevertheless, the induction of B-cell memory by Ad/MVA at long intervals and of T-cell responses measured by ELISpot at short intervals may present advantages in specific contexts. Importantly, in the absence of defined correlates of

protection for MERS-CoV, further studies are needed to determine whether antibody- or T-cell–dominated responses are more advantageous under different immunisation schedules.

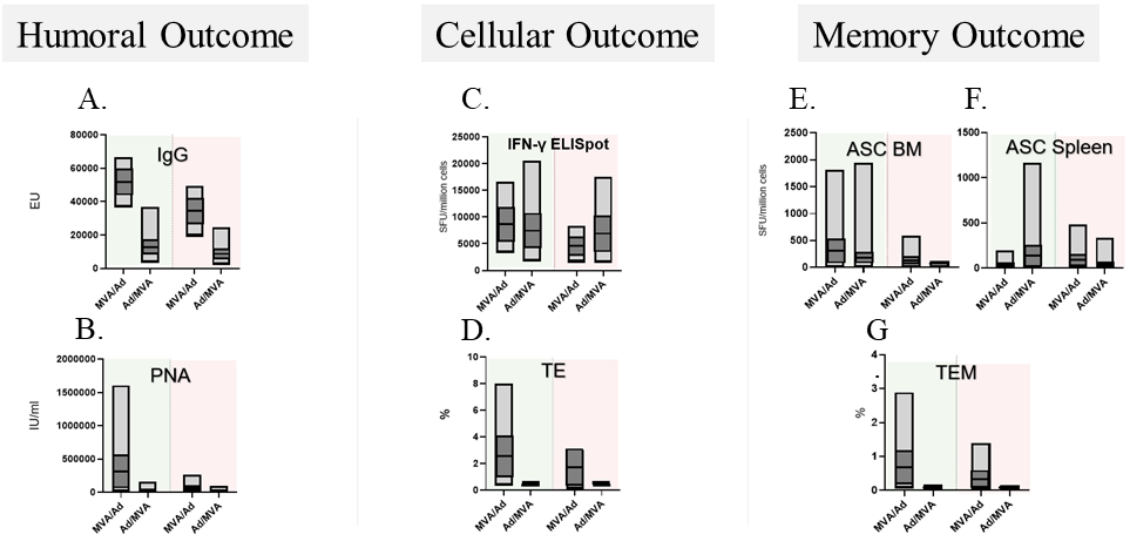


Figure 6-35. Optimized heterologous prime–boost vaccination regimens.

Humoral, cellular, and memory outcomes are shown for MVA/Ad and Ad/MVA regimens with long (green) or short (red) dosing intervals. **(A-B)** Humoral responses included IgG titres and pseudovirus neutralisation assay (PNA). **(C-D)** Cellular immunity was assessed by IFN-γ ELISpot and effector T cell (TE) frequencies. **(E-G)** Memory responses were measured by ASC in bone marrow (BM), ASC in spleen, and effector memory T cells (TEM). Bars represent the median response with 95% CI (dark grey boxes), while shaded areas (light grey box) indicate the model-predicted range of individual responses (95% prediction interval), which is wider than the confidence interval around the median. Overall, MVA/Ad regimens—particularly at the long interval—induced stronger humoral and memory responses, whereas cellular responses were comparable between regimens. For the long interval, doses were Ad 1×10^8/MVA 7×10^5 and MVA 7×10^6/Ad 6.3×10^6; for the short interval, doses were Ad 1×10^8/MVA 7×10^6 and MVA 7×10^6/Ad 1×10^8.

These model outputs indicated that Ad/MVA at high doses might provide effective responses in reactive vaccination scenarios and outbreak settings, with partial protection predicted after a single high-dose Ad prime and further enhancement following a high-dose MVA boost. Longer prime–boost intervals were associated with higher memory B-cell and effector T-cell responses across both regimens. In proactive vaccination of high-risk individuals, where longer intervals might be feasible, both MVA/Ad and Ad/MVA regimens achieved strong predicted responses. Although the higher antibody responses observed with MVA/Ad are notable, the enhanced memory B-cell responses in Ad/MVA may confer greater durability of protection. However, for travellers requiring short-interval protection, MVA/Ad might be predicted to yield higher humoral and memory responses than Ad/MVA. Together, these findings underscore the importance of tailoring heterologous prime–boost regimens to context, balancing the need for rapid onset of protection with the goal of achieving durable immune memory.

6.3.3.3 Validation of data

To retrospectively validate the models, predictions were first generated in the profiler by inputting the experimental dose settings used in MERSIDT001 and MERSIDT002 (MVA, $1x10^6$ PFU; ChAdOx1, $1x10^8$ IU; 4-week PB interval) as described in chapter 5 of this thesis. Z-score outputs were then back-transformed into the original measurement scale using the observed group means and standard deviations for each endpoint. For each readout, both the 95% confidence interval (CI) of the model-predicted mean and the 95% prediction interval (PI) for individual responses were calculated. Independent datasets from MERSIDT001 and MERSIDT002 (n = 12 animals per group) were subsequently compared with these predicted ranges. Validation was performed using prediction profiles derived from individual outcome models as well as z-scores from the composite outcome model.

6.3.3.4 Prediction based on individual model outcomes

When predictions were generated for each immunological readout individually, the models generally aligned well with the independent datasets. For the MVA/Ad regimen, predicted means for IgG, PNA, ASC in spleen, and ASC in BM (both baseline and after expansion) all showed predictive interval ranges, with observed means falling within the corresponding 95% CIs. The exception was IFN-γ ELISpot, where the observed mean lay outside the CI despite positive predicted ranges. Individual-level validation was strong, with 83–100% of animals falling within the 95% PIs (Table 6-16). Prediction model based on is on compsite outcxome is shown in the supplementary (S28).

For the Ad/MVA regimen, predictive performance was weaker. Several readouts, including IFN-γ ELISpot and ASC in BM (baseline and after expansion), had 95% CIs that crossed zero, indicating uncertainty in the model estimates. In addition, ASC spleen after expansion was flagged as not significant due to lack of fit, which was likely driven by missing animals in this dataset as described previously. Nevertheless, individual animal responses still fell within the wide PIs (83–100%), indicating that the model captured inter-animal variability despite reduced precision at the group level.

Overall, these results confirm that the models reproduced the independent datasets at both the group and individual levels, with stronger predictive performance observed for the MVA/Ad regimen compared with Ad/MVA.

	Predicted mean	95% CI (model)	95% PI (model)	Observed mean	Within CI (Y/N	% Animals within PI	
IgG	30919	22348–39491	14863–46975	16721	Y	11/12	92
PNA	15952	1304–30601	-15848–47752	22551	Y	12/12	100
IFN-γ ELISpot	2834	2482–3189	2264–3407	1997	N	10/12	83
ASC spleen	30	13–47	-3–63	26	Y	6/6	100
ASC BM	40	12–68	-26–106	66	Y	5/6	83
ASC memory spleen	38	24–52	11–66	36	Y	6/6	100
ASC memory BM	31	0.7–61	-41–103	59	Y	5/6	83
IgG	5216	621–9811	-5753–16242	9725	Y	11/11	100
PNA	9799	1980–17630	-21895–23100	22435	Y	11/11	100
IFN-γ ELISpot	1005	-285–2297*	-2030–4042	2425	Y	11/11	100
ASC spleen	5	3–8	-0.18–11	5	Y	5/5	100
ASC BM	-0.0	-31–29*	-64–44	39	N	5/5	100
ASC memory spleen	23	13–33	0.2–45	21	Y	5/5	100
ASC memory BM	-57	-135-20*	-235–120	73	N	5/5	100

Table 6-16. Validation of model predictions against independent datasets of individual model.
z-score outputs from the prediction profiler were back-transformed to the original measurement scale using group means and standard deviations for each readout. Data include the model-predicted mean, 95% confidence interval (CI), and 95% prediction interval (PI), alongside observed means from independent experiments (MERSIDT001, MERSIDT002). Validation at the group level was determined by whether the observed mean lay within the model CI (Y/N), while individual-level validation was assessed as the percentage of animals falling within the PI. Readouts with CIs crossing zero (*) indicate uncertainty in prediction. “Model not significant” indicates lack of fit in the profiler. Results for Ad/MVA: light green and MVA/Ad dark green

6.4 Discussion

The selection of vaccine doses and prime–boost intervals is typically informed by established practices described in the literature rather than systematic optimisation. Previous optimisation studies of heterologous viral-vectored vaccines have been limited in scope, focusing mainly on sequence order and interval [400, 401, 417, 418], with antigen dose usually assessed through simple comparisons [419, 420]. Given the immunological complexity of MERS-CoV—where protection involves both antibodies and T cells—there is a clear need for approaches that can assess how dose, interval, and regimen interact to shape multiple arms of the immune response.

In the case of MERS-CoV, optimisation is particularly important because protection is not mediated by a single immune arm. Neutralising antibodies reduce pathology and viral load in animal models after challenge or passive transfer [287, 288]. T-cell studies show that $CD8^+$ cells help control disease but are insufficient for clearance [289], and in human survivors both $CD4^+$ and $CD8^+$ responses are consistently detected, while antibody titres correlate only weakly with viral load during the acute stage [284]. Together, these observations highlight the need for systematic approaches capable of balancing humoral and cellular immunity.

Applying a DoE methodology, we modelled heterologous MVA/Ad and Ad/MVA regimens to evaluate how prime dose, booster dose, and interval interact to shape immune outcomes. Predictive models were statistically valid for humoral, cellular, and memory responses measured 28 days after boosting, and revealed that the booster dose was consistently the dominant factor.

In the MVA/Ad regimen, the Ad booster showed a quadratic effect; the optimal dose for antibody, T-cell, and memory outcomes was slightly below the highest dose tested. A likely explanation is antigen-driven induction of regulatory T cells [421], which suppress germinal centre activity and secondary responses. Lowering the Ad booster dose therefore not only improved immunogenicity but could also enhance safety and tolerability. This dual benefit is particularly relevant for large-scale delivery, as reduced dosing enables fractional dosing approaches to sustain vaccine supply and increase population coverage during outbreaks or supply shortages [422]. At the same time, lower-dose regimens are advantageous in veterinary applications, such as mass vaccination of dromedary camels against MERS-CoV, where minimizing costs and handling demands is critical for practical implementation. These findings require validation in humans and camels, as immune responses and dose–response relationships can differ between species. Importantly, dose reduction may also mitigate the risk of vaccine-induced thrombocytopenia (VITT), although the underlying mechanisms remain unclear as yet [423].

By contrast, in the Ad/MVA regimen higher booster doses were required to achieve optimal outcomes. Others have suggested that higher booster doses may be needed to overcome negative feedback from circulating antibodies induced by the prime, which might otherwise limit B-cell recruitment [421]. This interpretation is supported by Ewer and colleagues [420]. This interpretation aligns with previous reports that higher MVA booster doses enhance neutralising antibody responses following adenoviral priming. However, the maximum MVA dose tested may not have captured the full upper range of the dose–response curve.

In our earlier study, we proposed that high antibody titres at boosting could restrict recall responses through antigen clearance. In contrast, the present factorial analysis showed that pre-boost IgG correlated positively with post-boost responses, particularly following Ad priming and longer intervals, indicating effective priming rather than inhibitory feedback, particularly after Ad priming and when MVA was used as the booster at a 12-week interval. This likely reflects effective maturation of germinal centre and memory B-cell compartments, where higher baseline titres mark successful priming, and therefore have reduced ability to limit recall. Notably, in Ad/MVA regimens pre-boost IgG negatively correlated with $CD8^+$ effector responses, suggesting antibody feedback may still restrict antigen availability for T-cell expansion [403]. Together, these findings refine our initial hypothesis, showing that the impact of pre-boost antibody is highly context-dependent, varying with interval, priming strength, and booster dose.

The interval between prime and boost also proved to be an important determinant of outcome. In the MVA/Ad regimen, longer intervals improved neutralisation and IgG ASC responses in the BM, both before and after expansion. In Ad/MVA, interval effects were less apparent in circulating antibody responses but strongly influenced BM IgG ASC and memory responses. These findings indicate that while interval broadly shapes antibody and ASC responses in MVA/Ad, in Ad/MVA its impact is more compartment-specific. Longer prime–boost intervals have consistently been associated with stronger responses in human studies, including COVID-19 vaccines, where extending the interval increased both IgG and neutralising titres. In our dataset, however, Ad/MVA showed no interval effect on IgG or PNA, likely reflecting the restricted 4–12 week window studied. Transgene-specific antibody responses induced by adenoviral vaccination typically peak around Day 28 and may not have waned sufficiently by the time of boosting, whereas human trials testing broader ranges (28, 56, and 84 days) consistently reported stronger neutralising responses with longer gaps [417, 424]. Despite these differences, in both regimens the interval was consistently associated with stronger IgG ASC responses in BM, which is particularly notable since BM plasma cells are the main source of long-lived, high-avidity IgG. These findings reinforce the importance of interval in shaping durable humoral immunity.

Although memory B cells were not directly measured due to model constraints, BM ASC responses strongly paralleled IgG titres and are likely a reliable proxy for memory potential. BM ASC therefore provide insight into long-term humoral durability [425].

Epitope-specific responses provided further evidence that timing and dose interact to shape immune quality. Interestingly, in MVA/Ad, epitope dominance was flexible at short interval, with lower MVA prime doses shifting responses toward the dominant S1 epitope, while higher Ad booster doses broadened recognition to include the subdominant S2 epitope. In contrast, Ad/MVA responses were more rigid, consistently targeting S and S1, with specificity determined primarily by booster dose and showing little sensitivity to interval. A notable exception was observed at the 8-week interval, where boosting enhanced S2-specific responses. These results are consistent with modelling work by Fernández-Arias et al. [426], which predicted that the interaction of dose and interval depends on the kinetics of T-cell expansion after priming. Experimental studies have shown that the breadth of the T-cell response is transient, typically peaking around week 2 and contracting by week 10, such that the timing of the boost dictates whether subdominant epitopes are expanded or lost. These findings indicate that interval optimisation can reshape epitope breadth and may help overcome immune imprinting.

Interestingly, in the MVA/Ad regimen, lowering the prime dose modulated T cell responses but had little effect on antibody outcomes. This divergence suggests that the two arms of the immune system are regulated differently during priming: cellular responses are more flexible and dynamic, adapting to the strength of the initial stimulus, whereas humoral responses are comparatively insensitive to such adjustments. Nonetheless, both ultimately depended on the booster to achieve the strongest immunity, pointing to a shared mechanism of amplification at the boosting stage. This interpretation is consistent with the DoE models, which consistently ranked the booster dose as the dominant driver of both humoral and cellular outcomes.

When comparing regimens, MVA/Ad generally induced stronger humoral immunity, including greater magnitude and frequency of memory B-cell responses, whereas Ad/MVA elicited robust IFN-γ and TNF-α effector memory T-cell responses in the spleen. Interestingly, prior studies in malaria, tuberculosis, and Ebola models have reported greater protection with Ad/MVA despite lower antibody responses, implicating effector memory T-cell induction as a key protective mechanism [83, 400, 401]. In malaria, protection in the pre-erythrocytic stage was confirmed when splenocytes from Ad/MVA-immunised mice were transferred into naïve recipients. These observations highlight the need for MERS-CoV challenge studies to assess whether the optimised vaccination conditions translate into protective immunity.

Taken together, these results carry direct implications for vaccine deployment. High-dose Ad/MVA at short interval could provide rapid protection in outbreak settings, while extended prime–boost intervals

could enhance memory B-cell and effector T-cell responses, supporting durable immunity. For proactive vaccination of health-care workers and other high-risk groups, longer intervals therefore appear optimal, with Ad/MVA offering a potential advantage in promoting long-term memory. By contrast, for travellers requiring the rapid induction of immunity over a short interval, the MVA/Ad regimen was predicted to elicit stronger humoral and memory responses, although its protective efficacy remains to be confirmed. These findings highlight the trade-off between rapidly induced immunity and long-term durability, illustrating how heterologous prime–boost regimens can be adapted to different epidemiological contexts.

Limitations include dose constraints and the use of inbred mouse models, which may not fully capture human immune diversity. The Ad/MVA regimen was constrained by the maximum MVA dose tested (7×10^6 PFU), which may have underestimated the potential of higher booster doses. The long duration of the study limited the number of dose–interval combinations that could be evaluated, and the models did not explicitly account for pre-boost immune states, which may influence recall responses. Future studies should incorporate higher MVA doses and more diverse experimental models, and extend follow-up to determine whether memory ASC frequencies and flow cytometry measurements obtained one month post-boost correlate with long-term immune durability and, ideally, protection. In addition, approaches such as serum transfer to establish defined baseline immune states could help refine predictive modelling and accelerate translation to clinical settings. Notably, optimal conditions identified for the MVA/Ad models achieved higher desirability scores than those for Ad/MVA, suggesting greater predictive power and indicating that further optimisation of the Ad/MVA regimen remains possible. Despite these limitations, the use of DoE provides a scalable framework that can be applied across diverse vaccine platforms and pathogens.

In conclusion, this work demonstrates the value of a DoE-based modelling approach for vaccine optimisation. By analysing the interactions of dose, interval, and regimen, we identified combinations that enhanced humoral and cellular responses while requiring considerably fewer animals. Our findings show that higher doses do not necessarily yield stronger immunity, and that regimen sequence and timing are critical for balancing rapid onset of protection with durable memory. Ad/MVA was predicted to favour long-term responses, particularly effector T cells in health-care workers and high-risk groups, whereas MVA/Ad offered advantages for travellers requiring short-interval protection. Notably, our results suggest that prime–boost optimisation can reshape the hierarchy of T-cell responses, with the capacity to shift dominance patterns within the response. Ultimately, this study illustrates how systematic modelling can bridge pre-clinical experimentation and translational vaccine design, informing MERS-CoV vaccine development and strengthening preparedness for future emerging pathogens.

7 Discussion

The COVID-19 pandemic has fundamentally reshaped global thinking about how prepared we are for emerging viral threats, particularly regarding the speed at which vaccines must be developed and deployed. CEPI's 100 Days Mission emerged in response to this need. Its goal is to develop and make a safe, effective vaccine available for rollout within 100 days of identifying a new pathogen; this has become a central component of the 2022–2026 CEPI strategy and is now recognised by international bodies such as the G7 and G20 as a key element of future pandemic preparedness [427]. Although COVID-19 vaccines were delivered in record time, modelling suggests that vaccine rollout within the first 100 days could have prevented millions of deaths, particularly in low- and middle-income nations [428]. This understanding reinforces the urgency of accelerating vaccine development not only for novel pathogens but also for known high-threat viruses such as MERS-CoV, which continues to pose a risk of severe outbreaks.

The WHO's target product profiles for MERS-CoV outline three priority areas for vaccine development: reducing transmission through camel vaccination, providing long-term protection for high-risk human populations, and enabling rapid reactive use during outbreaks [304]. These differing priorities highlight the need for flexible vaccine strategies that can support both preparedness and rapid response. Building on this, Saudi Arabia has strengthened its autonomy by expanding diagnostic capacity, enabling local evaluation of ChAdOx1-MERS vaccine candidates, and hosting WHO meetings that enhance cross-sector communication and support One Health implementation for MERS-CoV and other emerging zoonotic coronaviruses [291, 384].

Within this context, and recognising the ongoing need to accelerate vaccine development, our study set out to investigate the humoral immune responses generated by the ChAdOx1-MERS vaccine and to explore strategies that may further optimise its performance. The combination of ChAdOx1 with an MVA boost, or vice versa, together with adjustments to dosing intervals, may help bring these candidates closer to the potential rapid-response and long-term preparedness envisioned by CEPI and the WHO.

The results presented in the previous chapter provide insight into how ChAdOx-based platforms behave under different dosing conditions and how these responses might be predicted, manipulated and enhanced. Importantly, these findings also build on lessons learned from the COVID-19 pandemic, particularly regarding dosing strategies, interval effects, and the value of flexible vaccine platforms. In this chapter, we consider how our results align with or differ from existing literature, what they reveal about the future development of the ChAdOx1 MERS candidate, and how they contribute to the broader goal of strengthening global preparedness for future coronavirus outbreaks.

The ChAdOx1 MERS vaccine candidate has previously been evaluated in dose-escalation trials in both the UK and Saudi Arabia [291, 292]. with the highest humoral and cellular immunogenicity observed in the high-dose group. These findings informed dose selection for ChAdOx1 nCoV-19 during the COVID-19 pandemic [95]. Consistent with earlier observations, our expanded immunoprofiling showed that the high dose elicited responses of greater magnitude, broader Fc-effector activity, and higher seropositivity at both the peak and six-month timepoints. By 12 months binding levels converged, consistent with biphasic waning. The medium-dose group exhibited a slower decline in IgG and a progressive rise in avidity, consistent with prolonged or more selective GC maturation despite lower early titres. In contrast, FcγRIIA-binding activity was more durable in the high-dose group, suggesting that greater antigen availability favours the expansion or maintenance of Fc-competent antibodies.

Overall, these data show that antigen dose differentially shapes both the magnitude and qualitative evolution of the antibody response. These patterns support a model in which intermediate dosing enhances long-term antibody quality through affinity maturation, whereas higher dosing preferentially promotes overall response magnitude and sustained Fc-mediated effector potential. When dose was evaluated alongside dosing interval in post-hoc analyses of the ChAdOx1 nCoV-19 efficacy trials, it became clear that interval length played an important role in shaping protective efficacy [97]. Longer intervals improved durability in our limited sample

Taken together, these data demonstrate a dose-dependent effect from prime (single-dose) vaccination, and highlight the advantage of priming with the highest tolerable dose in outbreak-response settings to achieve rapid early protection. They also support the potential utility of lower doses in wider immunisation strategies where durability and qualitative immune features may be more relevant. The continued increase in avidity observed in the medium-dose group is consistent with ongoing affinity maturation within germinal centres, potentially driven by more effective memory B-cell development. Although memory B-cell populations were not measured in this study, the dose-dependent patterns observed here are consistent with the possibility that lower antigen doses promote improved antibody quality over time. This requires confirmation with direct memory B-cell assays

Recent studies of SARS-CoV-2 have underscored the importance of FcγR engagement, particularly in contributing to enhanced protection against breakthrough infection [339]. As a result, developing assays to measure Fc-mediated correlates of protection is becoming increasingly important for vaccine evaluation. Importantly, the assays used in this study demonstrated good performance, standardisation, and reproducibility, providing reliable readouts to the best of our knowledge. The field of systems serology is rapidly expanding, and our work represents an early step in applying these approaches to MERS vaccine research. A major challenge, however, was the limited ability to perform cellular assays

to directly evaluate Fc-mediated functional activity; therefore, we used FcγR engagement as a surrogate readout. In addition, the absence of glycosylation analysis represents another limitation, particularly given the growing interest in Fc-glycan profiles as determinants of antibody functionality. The importance and predictive value of these assays for assessing protection will likely become clearer as MERS challenge models continue to advance.

Nevertheless, we observed cohort differences: higher, sustained S2-directed FcγRIIA binding in the Saudi cohort, likely linked to greater baseline OC43 reactivity. These results suggest that evaluating vaccines in populations with varying levels of pre-existing coronavirus exposure provides valuable insight into how background immunity shapes post-vaccination responses. This consideration is especially relevant when assessing MERS vaccine responses in the aftermath of widespread SARS-CoV-2 circulation.

In chapter 4, we examined responses to SARS-CoV-2 vaccination in a unique cohort of individuals with a history of MERS infection. Overall, individuals with prior MERS infection exhibited elevated FcγR responses following SARS-CoV-2 vaccination compared with individuals with or without prior SARS-CoV-2 infection. Compared with individuals possessing hybrid SARS-CoV-2 immunity, the MERS-experienced group displayed a distinct FcγR engagement profile against SARS-CoV-2, characterized by enhanced FcγRIIB–S1 activity. In contrast, hybrid SARS-CoV-2 immunity was associated with FcγRIIIA–S2 and FcγRIIIB responses targeting spike. Together, these findings highlight preferential boosting of Fc-mediated responses and suggest that prior coronavirus exposure differentially primes vaccine-induced Fc functionality. However, this comparison is constrained by potential selection bias arising from the use of controls from a separate cohort and differences in sampling schedules. Among MERS003 clinical trial participants, exposure to hybrid immunity from prior SARS-CoV-2 infection appeared to mitigate the effects of age and dosing interval, in contrast to vaccine-induced immunity alone. Taken together, these findings suggest that prior coronavirus exposure may prime the immune system in ways that enhance the functional impact of subsequent vaccination.

Post-pandemic, our results showed that exposure to COVID-19 generated measurable cross-reactive antibody responses to MERS, although these responses remained markedly lower than those induced by a single dose of ChAdOx1-MERS or those observed in pre-pandemic MERS-convalescent individuals. Cross-reactive T-cell responses may also contribute some degree of protection, but their overall impact remains unclear and a detailed assessment was beyond the scope of this thesis.

These immunological observations sit within a broader shift in the post-pandemic epidemiological landscape. Several notable changes have been reported, including fewer documented MERS cases and evidence of reduced disease severity based on contact-tracing data. For example, a recent cluster in April 2025 involved a fatal index case and six secondary infections among healthcare workers, all of

whom experienced only asymptomatic or mild illness [429]. This contrasts sharply with pre-pandemic outbreaks, in which healthcare workers accounted for approximately 26% of cases and had a high fatality rate of 16% [430]. Although these patterns may reflect changes in immunity, they must also be interpreted alongside a substantial reduction in MERS testing, as surveillance efforts have been largely redirected toward SARS-CoV-2, raising the possibility that mild or asymptomatic community infections remain undetected. We did not perform depletion/competition assays, so cross-reactivity conclusions are based on binding data only.

Taken together, these observations raise the possibility that widespread SARS-CoV-2 exposure may modulate disease severity through cross-reactive immunity, even if it does not prevent infection. However, the sporadic re-emergence of MERS — particularly its consistently high mortality among older adults — underscores the continued need for a dedicated MERS-specific vaccine. These considerations highlight the importance of evaluating MERS vaccine immunogenicity in high-risk groups in the post-pandemic period. To explore this further, we next examined vaccine-induced immunogenicity in older individuals post-pandemic.

Immunogenicity data for two homologous doses of ChAdOx1 MERS were derived from the MERS003 clinical trial, which was conducted post-pandemically in healthy older adults, with participant groups defined on the basis of prior ChAdOx1 vector vaccination. Our baseline assessments indicated that IgG and PNA responses to MERS were detectable; however, no correlation was observed with SARS-CoV-2–specific IgG or PNA responses. Unfortunately, due to time limitations within this thesis, we were unable to characterise S1- and S2-specific antibody responses, which may have clarified the basis of this lack of correlation. Nevertheless, the optimised and characterised PNA assay used in this study yielded higher sensitivity for detecting low-level cross-neutralising antibodies at baseline, in contrast to the post-pandemic MVA trial, where no baseline PNA activity was observed (supplementary 8.1.4.1.2). It is possible that this difference reflects variation in assay sensitivity—such as differences in the lower limits of detection or quantification—rather than true biological differences between the study populations. This difference likely reflects both assay performance and variation in pre-existing coronavirus exposure between study populations.

Notably, prior ChAdOx1 exposure had a clear impact on vaccine-induced responses. Compared to ChAdOx1 naïve participants, those with previous exposure showed reduced anti-MERS responses after the first dose and continued to exhibit lower responses after the second dose, consistent with the effects of anti-vector immunity on transgene expression and subsequent immunogenicity. Older adults with no prior ChAdOx1 vaccination mounted antibody responses after the first dose that were comparable to those observed in pre-pandemic prime-vaccination studies in healthy adults aged 18–50 years, indicating that marked immunosenescence was not evident in this cohort. In participants with prior

ChAdOx1 exposure, responses after the first dose were lower than those of the pre-pandemic vaccinees. However, after the booster dose, increased titres in both previously exposed and ChAdOx1-naïve individuals converged, and reached comparable levels to those seen in pre-pandemic MERS-convalescent individuals. This suggests that, despite the presence of anti-vector immunity, robust boosting is still achievable, and no substantial differences in peak antibody responses were observed between these groups following the second dose.

A substantial proportion of the population has now received at least one dose of a ChAdOx1-based vaccine, making strategies to overcome anti-vector immunity increasingly relevant. Chapters 5 and 6 therefore, used pre-clinical models to explore approaches for mitigating anti-vector immunity and enhancing immunogenicity. Heterologous prime–boost strategies offer a practical means of bypassing vector-specific constraints and improving the durability of responses. Although innovations such as hexon modification show promise, they will require considerable time to develop and validate. In the meantime, established platforms with extensive safety data—such as ChAdOx1 and MVA, already progressing through development pipelines—provide the most realistic pathway to achieving the 100 Days Mission proposed by CEPI.

Thus, in Chapter 5, we evaluated the use of heterologous vaccination using Ad/MVA and MVA/Ad regimens. We also compared these responses with the homologous prime–boost (as tested in the clinical trials) and included a group receiving a higher dose of MVA in the homologous MVA/MVA arm. We showed that immunogenicity was strongly influenced by the order of vaccination, with higher responses observed in the MVA/Ad group across most readouts, although only some reached statistical significance. In particular, MVA/Ad induced notably higher levels of IgG and FcγRIIB-binding antibodies to S and S1. These findings are consistent with other studies reporting stronger and more durable humoral responses with this regimen. By using the MVA/Ad approach, it may be theoretically possible to maximise humoral immunogenicity; however, whether such heightened humoral responses translate into meaningful protection—particularly for pathogens in which T-cell immunity is critical—remains uncertain.

Our experiments further demonstrated that increasing the MVA dose in the MVA/MVA regimen produced a significant enhancement in immunogenicity. At the same time, our analysis suggests that pre-boost immune status may have contributed to the variability observed after boosting, consistent with findings from previous studies. These observations prompted key questions regarding how dosing and interval interact to shape pre-boost status and subsequent post-boost vaccine responses. As outlined earlier, post-hoc analyses from other ChAdOx1 platforms have shown that dosing interval is a key determinant of vaccine performance [97]. It also remained unclear whether the higher responses

observed in the MVA/Ad regimen reflected the relatively lower MVA priming dose or the inherently stronger boosting capacity of the adenoviral vector.

Building on this, Chapter 6 sought to determine whether extending the interval or fine-tuning the doses could further enhance immunogenicity. We examined the relationship between these factors in greater depth, and explored how heterologous prime–boost strategies can be tuned to influence response magnitude, durability, and memory induction —areas that remain essential to refine to address MERS-CoV vaccine requirements.

The DoE work presented in this thesis provides a proof of concept for applying this framework to in-vivo studies in mice and to vaccination experiments. Model predictions were largely accurate, particularly for the MVA/Ad regimen in the humoral arm. Importantly, these findings highlight that higher doses do not necessarily translate into superior immunogenicity, especially when adenovirus is used as the booster. In this context, Ad booster doses below an apparent saturation threshold appeared to perform better, offering potential practical advantages such as an improved safety profile, a reduced theoretical risk of VITT, and increased vaccine coverage from reduced dose requirements per individual. One plausible explanation for the diminished performance of high-dose Ad boosters is that excessive antigen delivery may activate regulatory T cells and dampen the secondary response, although this hypothesis requires further confirmation.

Conversely, predictions for the Ad/MVA regimen were less accurate. These limitations may be partly attributable to the use of a relatively low concentration clinical-grade batch, which restricted the feasible dosing range in mice and may have influenced the predictive performance of the model. Interestingly, the predictions also suggested that T-cell hierarchy could be modulated by both dose and interval, consistent with dynamic changes in epitope presentation associated with each vector. Although these findings are intriguing—particularly for applications where directing T-cell responses toward specific epitopes is desired—further confirmation is required.

Using the models, we were able to identify dose and vaccine order conditions that maximised responses at both short (4-week) and longer (12-week) intervals, corresponding to reactive and proactive vaccination scenarios, respectively. These results indicated that, under optimised dose conditions, the MVA/Ad regimen yielded higher IgG and PNA responses than could be achieved with Ad/MVA. In contrast, IFN-γ ELISpot responses in the spleen were maximised by Ad/MVA, as was the induction of memory ASCs at the short interval, whereas the generation of T_{EM} cells was more prominent in the MVA/Ad regimen. At the longer interval, MVA/Ad also appeared to better support the induction of memory responses, including ASC populations in the spleen and BM, as well as T_{EM} cells.

Thus, while MVA/Ad appears promising—particularly for enhancing humoral and memory-associated responses—the utility of this regimen would ultimately need to be evaluated in efficacy studies. Furthermore, the limited predictive performance observed for Ad/MVA should be taken into account when interpreting these findings. Each schedule nevertheless offers distinct immunological advantages that may be suited to different use-case scenarios. Finally, additional T-cell subsets, such as T_{CM} cells, may warrant further investigation given their importance in long-term protection and recall responses. Importantly, these results were generated in inbred mice, and further validation in more diverse models will be essential before extrapolating to human vaccine performance.

In conclusion, the work presented in this thesis supports the continued development of the ChAdOx1 MERS vaccine candidate. It provides important insights into how this platform may be used in settings where pre-existing coronavirus or vector immunity may influence vaccine performance. Overall, the findings demonstrate that ChAdOx1, alone or in combination with MVA, represents a promising approach for future clinical evaluation and contributes meaningfully to the pipeline of MERS vaccine development.

7.1 Future Work

In the absence of ongoing human transmission, licensure of a MERS vaccine will likely rely on bridging studies to define a quantitative immune threshold associated with protection, typically an antibody-based readout because of feasibility and assay practicality. Once such a threshold is derived from animal challenge models, a pivotal clinical immunogenicity trial would be required to show that the vaccine induces this response in humans [431]. Two important considerations should be kept in mind when interpreting and applying these thresholds.

First, NHP models for MERS exhibit well-recognised limitations. MERS-CoV infection in macaques generally results in multifocal, mild-to-moderate interstitial pneumonia, with viral replication largely confined to alveolar pneumocytes. Overall disease severity is substantially reduced compared with humans. This disparity reflects interspecies differences in DPP4 expression and viral tropism, which limit infection in distal lung regions in NHPs. Although other species, such as common marmosets, may develop more severe pathology [432], their small size restricts the depth of immunological and virological sampling that can be performed [308]. Importantly, NHPs often exhibit disproportionately higher antibody concentrations than humans at comparable exposures due to smaller blood volume and species-specific IgG pharmacokinetics, including differences in FcR-mediated recycling.

Second, although FcγR expression and function differ between humans and NHPs, Fc-mediated effector mechanisms can still yield informative immunological signatures. Identifying which FcγR-dependent activities associate with protection in NHPs can guide the selection of functional assays incorporating

human FcγRs, thereby improving translation of qualitative antibody features and enhancing the value of NHP-derived correlates beyond IgG titres alone.

Building on insights from SARS-CoV-2 systems serology, applying similar analytical approaches retrospectively to archived MERS samples collected during the acute stage could help identify immunological signatures associated with survival. A key priority remains the definition of correlates of protection for MERS. Although neutralising antibodies are a central benchmark, accumulating evidence indicates that non-neutralising antibody functions and Fc-mediated effector activity are also likely to contribute to protection, alongside virus-specific T-cell responses. Notably, NHP HIV challenge studies have demonstrated that robust T-cell immunity can lower the antibody threshold required for protection compared with regimens that rely on neutralising antibodies alone [433]. Together, these observations suggest that protective immunity is unlikely to depend on a single immunological parameter; rather, it reflects the coordinated contribution of multiple antibody and cellular pathways. Limited MERS-CoV sequence data from human cases hinders our understanding of viral evolution and adaptation. Future neutralisation studies of post-pandemic MERS trials should consider the potential influence of prior SARS-CoV-2 exposure, as even limited cross-reactive immunity may shape responses to emerging MERS-like viruses. Further work is needed to define the extent and significance of such cross-immunity.

Building on the need to define quantitative correlates of protection, immune thresholds derived from nonhuman primate studies will be evaluated in humans through a planned pivotal clinical immunogenicity trial, the design of which is still being finalized. This randomized, placebo-controlled study will enrol approximately 1,500 participants (9:1 vaccine:placebo), including adults aged 18–64 years and an older adult cohort over 65 years, and will assess the proportion of vaccine recipients achieving neutralising antibody titres at or above the NHP-defined protective threshold, alongside an accelerated (0-1) month vaccination schedule to evaluate rapid protection in outbreak settings. Conducted across regions with historical MERS exposure, including Saudi Arabia, the United Arab Emirates and Jordan, the study will provide key human immunogenicity data to support immunobridging-based licensure strategies in the absence of sustained transmission (planned pivotal trial design; sponsor data on file).

Beyond neutralisation assays directed at MERS antigens, systems-immunology approaches can also be applied to study the ChAdOx1 vector itself to characterise vector-induced humoral and cellular responses. Understanding FcγR-dependent functions, anti-vector antibodies, and vector-driven T-cell activation has broader implications for the use of ChAdOx1 as a vaccine platform, as these features may influence immunogenicity and boosting across different ChAdOx1-based vaccines, including those targeting MERS. Characterising the nature and magnitude of anti-vector immunity may help inform when adjustments to vaccine design or vaccination strategy—such as the use of a different serotype (for

example, ChAdOx2), capsid engineering, mode of delivery [434], altered dosing intervals, or heterologous prime–boost approaches—could be beneficial to optimise immune responses.

An important area that still needs more focused work is understanding how immune responses develop and operate in mucosal tissues. These sites are critical for limiting transmission, yet many aspects of how local immunity is established and maintained remain unclear. Studies in nonhuman primates vaccinated against Simian–Human Immunodeficiency Virus, using HIV Env alone administered subcutaneously or heterologous Ad- and VSV-based vectors delivered intravenously, have reported the presence of CD8+ TRM at mucosal surfaces alongside vaccine-elicited neutralising antibodies [433]. Tissue-resident macrophages and early innate signalling have also been noted in these compartments. Transcriptomic analyses have identified antigen-specific CD4+ T-cell activity and innate pathways at mucosal sites, highlighting the importance of generating T-cell responses directly at the area of infection. Supporting this concept, elevated levels of neutralising antibodies, Fcγ receptor–engaging antibodies, and IgA have been detected in the saliva of individuals following SARS-CoV-2 infection, including those with breakthrough infections [435]. These findings suggest a potential role for infection-induced mucosal antibodies in reducing viral transmission and underscore the need to evaluate HCoV- or SARS-CoV-2–induced mucosal immune responses, as well as their potential contributions to anti-MERS immunity, in parallel with vaccine-elicited responses.

For MERS, developing strong mucosal immunity in humans—and particularly in camels—may be essential for blocking transmission at the primary entry sites. Modelling studies in camels suggest that achieving high vaccination coverage in calves (around 70–90 percent) can lead to a large reduction in incidence in moderate- and high-transmission settings, and may even interrupt transmission in low-transmission areas [214]. Such strategies could substantially reduce viral circulation. In this context, analysis of the respiratory samples collected in the MERS003 study will provide valuable information on the local immune environment and help clarify how mucosal responses develop following vaccination. Together, these observations highlight the need for additional work to define how T cells, innate pathways, and antibody responses interact at mucosal surfaces, and how they can be more effectively engaged in future vaccine strategies.

The DoE analyses presented here provide a quantitative framework for optimising dose and dosing interval, although their translational relevance in humans remains to be formally evaluated. By modelling factor–response interactions, DoE enables the identification of dose–schedule combinations that maximise immunogenicity and supports the rational selection of regimens most likely to achieve predefined antibody thresholds or other putative correlates of protection. Importantly, the principles demonstrated here extend beyond systemic immunity. Applied more broadly, DoE offers a powerful strategy for optimising additional dimensions of vaccine performance—such as mucosal immunity—

by systematically exploring how antigen dose, vector concentration, and delivery route interact within a controlled design space. As such, DoE has wider implications for accelerating vaccine development across platforms and pathogens, providing a structured and efficient approach for guiding evidence-based decisions from preclinical studies through early clinical translation.

Lastly, the continued emergence of MERS-like coronaviruses in bats and the circulation of related merbecoviruses in mammals highlight an ongoing risk of spillover to humans. Conducting MERS-CoV vaccine studies during inter-epidemic periods—and especially in the post–SARS-CoV-2 era—offers a valuable opportunity to generate broadly reactive antibody responses before an outbreak occurs. Importantly, by performing the MERS003 trial at this time and evaluating the ChAdOx1 MERS vaccine candidate, we have established cohorts with prior SARS-CoV-2 exposure and MERS-CoV vaccination that will enable rapid assessment of neutralising capacity against newly emerging MERS-CoV or merbecovirus variants. In our cohort, hybrid MERS/SARS-CoV-2 exposure, or SARS-CoV-2/MERS exposure (MERS003), appears to induce particularly strong neutralising activity. These hybrid immune profiles provide a promising foundation for identifying monoclonal antibodies capable of targeting diverse merbecoviruses and sarbecoviruses. Future work extending these findings may contribute to a preparedness framework that supports rapid and effective responses to the next coronavirus with pandemic potential.

8 Appendix

8.1 Publications and presentations as DPhil student

8.1.1 Publications / Commentaries

- Batawi SA, Alraddadi BM. Revisiting MERS-CoV vaccination in the SARS-CoV-2 era. Lancet Infect Dis. 2025 Feb;25(2):146-148. doi: 10.1016/S1473-3099(24)00453-5. Epub 2024 Oct 7. PMID: 39389072
- Bosaeed M, Balkhy HH, Almaziad S, Aljami HA, Alhatmi H, Alanazi H, Alahmadi M, Jawhary A, Alenazi MW, Almasoud A, Alanazi R, Bittaye M, Aboagye J, Albaalharith N, Batawi S, Folegatti P, Ramos Lopez F, Ewer K, Almoaikel K, Aljeraisy M, Alothman A, Gilbert SC, Khalaf Alharbi N. Safety and immunogenicity of ChAdOx1 MERS vaccine candidate in healthy Middle Eastern adults (MERS002): an open-label, non-randomised, dose-escalation, phase 1b trial. Lancet Microbe. 2022 Jan;3(1):e11-e20. doi: 10.1016/S2666-5247(21)00193-2. Epub 2021 Nov 3. PMID: 34751259; PMCID: PMC8565931.

8.1.2 Oral presentation

- CEPI PADOVAX Scientific Update: Design of Experiments for heterologous vaccination for MERS, Oxford, July 2025.
- Exploring system serology in the context of coronaviruses. Quadripartite Global Technical Meeting on MERS-CoV and Other Emerging Zoonotic Coronaviruses, 27–29 November 2023, Riyadh, Saudi Arabia.

8.1.3 Academic service

- Invited peer reviewer for The Lancet Infectious Diseases (2024) [436]

8.1.4 Supplementary

8.1.4.1 Immunological assay

WHO reference materials previously described in the Comparison of Serologic Assays for Middle East Respiratory Syndrome Coronavirus [322] study, were used as standardized control samples to evaluate the pseudoneutralisation assay (PNA) and Fcγ receptor binding assays. These materials provided well-characterized positive and negative controls and were included to assess assay performance, specificity, and reproducibility.

8.1.4.1.1 WHO reference materials

The WHO reference materials used in this study are summarised in Supplementary Table S1, including sample description and intended use as assay controls.

No.	Name	Description	Expected result
1	Korea 5	Single plasma from laboratory-confirmed MERS patient	Positive
2	Tc Bovine NC	Purified IgG from transchromosomal bovine, negative control	Negative
3	WHO/B	Negative control serum, high titer for other CoV	Negative
4	Tc Bovine SAB 300	Purified IgG from transchromosomal bovine, antigen whole virus	Positive
5	Korea 2	Single plasma from laboratory-confirmed MERS patient	Positive
6	WHO/G	Negative control serum, high titer for other CoV	Negative
7	WHO/A	Negative control serum, high titer for other CoV	Negative
8	WHO/D	Negative control serum, high titer for other CoV	Negative
9	Korea 3	Single plasma from laboratory-confirmed MERS patient	Positive
10	Tc Bovine SAB 301	Purified IgG from transchromosomal bovine, antigen spike protein	Positive
11	Korea 1	Single plasma from laboratory-confirmed MERS patient	Positive
12	Korea 4	Single plasma from laboratory-confirmed MERS patient	Positive
13	WHO/F	Negative control serum, high titer for other CoV	Negative
14	Pool C (low)	Pooled serum samples from laboratory-confirmed MERS patients	Positive
15	WHO/C	Negative control serum, high titer for other CoV	Negative
16	Pool A (high)	Pooled serum samples from laboratory-confirmed MERS patients	Positive
17	WHO/E	Negative control serum, high titer for other CoV	Negative
18	Pool B (medium)	Pooled serum samples from laboratory-confirmed MERS patients	Positive

Table S1. WHO reference materials used in this study.
WHO reference samples were used as standardized positive and negative controls for evaluation of the PNA and Fcγ receptor binding assays.

8.1.4.1.2 Lentivirus-based pseudoneutralisation assay (PNA)

8.1.4.1.2.1 Assay optimisation

Assay optimisation experiments were conducted to determine the optimal cell density, virus input, and assay workflow. Cell seeding densities of 2×10^4 and 4×10^4 cells per well were tested in

combination with virus inputs of 1×10^5 and 2×10^6 RLU per well. Two assay workflows were compared: an in-house PNA protocol established at the University of Oxford (hereafter referred to as the Oxford method), and a protocol developed and used at the NIBSC for MERS-CoV pseudovirus neutralisation assays (hereafter referred to as the NIBSC method). Identical samples were tested on the same day to minimise inter-assay variability. The samples used for assay optimisation are summarised in Table S2.

Briefly, in the Oxford method, all assay steps are performed in a single white 96-well Nunc plate with lid. Following preparation of sample serial dilutions, pseudovirus is added and incubated for one hour, after which Huh-7 cells are added. After 48 hours of incubation, cells are lysed using 30 µL per well, and luciferase activity is measured directly in the same plate. In the NIBSC method, Huh-7 cells are first seeded into a 96-well transparent plate and incubated for two hours. In parallel, sample serial dilutions and pseudovirus are incubated together in a separate plate for one hour before being transferred onto the cells. After 48 hours, cells are lysed using 90 µL per well, and 50 µL of lysate is transferred to a white plate for luminescence measurement. The criteria for selection of optimal assay conditions were based on dynamic range, intra-assay precision, dilutional curve fit, and correlation with total IgG ELISA.

Sample code	Volunteer #	Booster time	Time point
Sample 1	MERS001-044	D182	D0
Sample 2	MERS001-027	-	D28
Sample 3	MERS001-037	-	D28
Sample 4	MERS001-017	-	D28
Sample 5	MERS001-044	D182	D210
Sample 6	MERS001-044	D182	D28
Sample 7	MERS001-032	-	D28
Sample 8	MERS001-052	D28	D0
Sample 9	MERS001-052	D28	D28
Sample 10	MERS001-052	D28	D43

Table S2. Samples used for assay optimisation

Dynamic range was assessed visually by comparing separation of IC50 values across assay conditions, as illustrated in Figure S. Based on these results, a cell density of 4×10^4 cells per well combined with a virus input of 1×10^5 RLU was selected for subsequent experiments due to the improved dynamic range. Assay workflows were compared based on precision, dilutional curve linearity, and correlation with total IgG ELISA, with a summary of quantitative performance metrics shown in Table S . On the basis of these performance metrics, the Oxford method was selected for all subsequent assays.

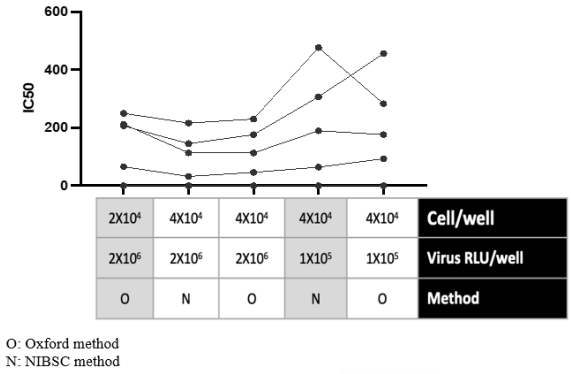


Figure S1. Dynamic range across assay conditions comparing Oxford and NIBSC methods

Representative IC50 values across assay conditions varying by cell density (2×10^4 or 4×10^4 cells per well), virus input (1×10^5 or 2×10^6 RLU per well), and assay workflow. Separation of IC_{50} values across samples was used as a visual assessment of dynamic range. O denotes the Oxford method and N denotes the NIBSC method.

	N	O	n
Intra-assay precision (CV%)	31%	19%	4
Dilutional curve linearity (R^2)	0.86	0.96	10
Correlation with IgG	0.80	0.82	10

Table S3. Summary comparison of Oxford and NIBSC assay workflows.

Correlation p-values were 0.0072 for the NIBSC method and 0.0058 for the Oxford method.

8.1.4.1.2.2 Sample type and handling

Assay performance was evaluated using matched serum and plasma samples collected at day 28 (n = 4). Sample suitability was assessed based on dilutional curve fit and goodness-of-fit values across R curves. Results were significantly different between heat-inactivated serum (HIS) and heat-inactivated plasma (HIP) ($p = 0.02$); with plasma samples demonstrating clearer visual separation of data points and

improved assay discrimination compared with serum Figure S. Therefore, plasma was selected for use in subsequent PNA experiments.

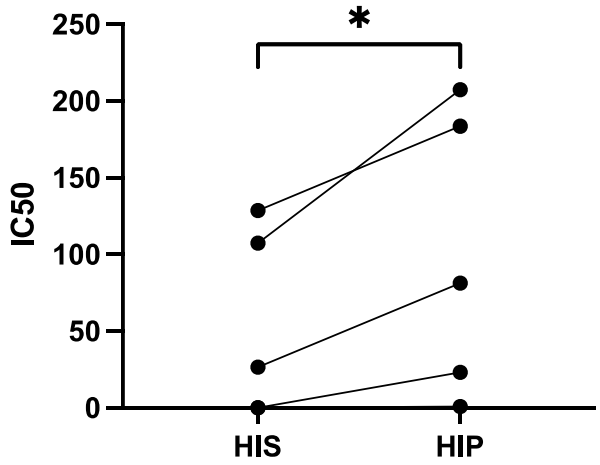


Figure S2. Comparison of heat-inactivated serum (HIS) and heat-inactivated plasma (HIP) performance in the pseudoneutralisation assay .
Lines connect matched samples. Differences were assessed using a Wilcoxon signed-rank test (p = 0.02).

8.1.4.1.2.2.1 Internal control and data normalisation

An internal control (IC) was included on every assay plate to monitor assay performance and enable plate-to-plate normalisation. The internal control consisted of a pooled plasma sample derived from vaccinated individuals with medium to high neutralising antibody titres and was selected based on stability and availability. To minimise variability associated with freeze–thaw cycles, pooled internal control material was aliquoted and stored at −80 ˚C. The internal control was assayed in parallel with test samples using a two-fold serial dilution series starting at 1:50.

Neutralising antibody titres were expressed in international units per millilitre (IU/mL) using calibration to the WHO International Standard for anti-MERS-CoV antibody (NIBSC code 19/178). Due to limited availability of the international standard, it was not included on every assay plate. Instead, the international standard was run alongside the internal control to establish a conversion factor between the two, enabling the internal control to serve as an intermediary for conversion of assay readouts from relative luminescence units to IU/mL. Across 35 assay plates, the internal control demonstrated acceptable consistency (mean CV = 23%), with strong curve-fitting performance (mean $R^2 = 0.98$). The consistency and curve-fitting performance of the internal control dilution series used for normalisation are shown in Figure S. Normalisation of IC50 to IU based on the internal control was applied to all subsequent assay characterisation experiments.

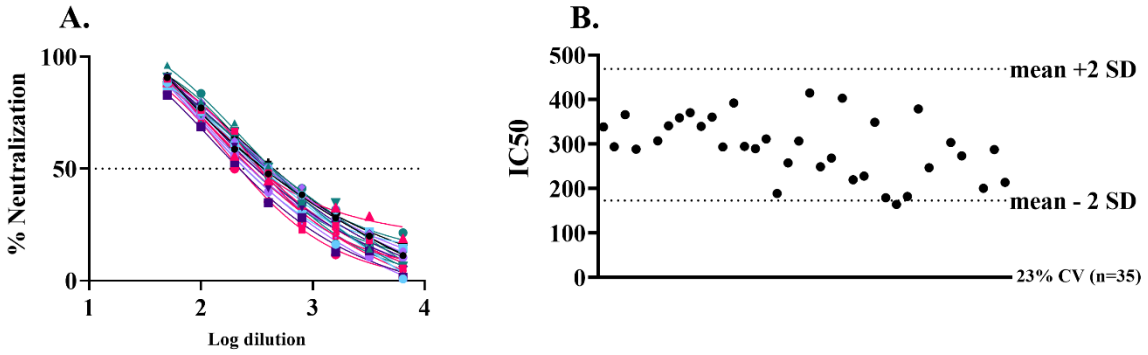


Figure S3. Internal control performance and variability across assay plates.

(A) Internal control dilution curves plotted as percentage neutralisation versus log dilution across multiple assay plates. Curves demonstrate consistent dilutional behaviour with the 50% neutralisation threshold indicated by the dotted line. (B) Distribution of IC50 values for the internal control across 35 assay plates. Dotted lines indicate the mean ± 2 standard deviations. The coefficient of variation across plates was 23%, demonstrating acceptable plate-to-plate consistency for use in assay normalisation.

8.1.4.1.2.3 Assay characterization

Table S summarises the qualification parameters, assessment approaches, acceptance criteria, and outcomes for the pseudovirus neutralisation assay.

Parameter	Assessment approach	Acceptance criteria	Outcome
Specificity	Pre-pandemic negative samples; WHO and NIBSC QC panels; cross-reactivity assessment with non-MERS coronaviruses	No detectable MERS-CoV neutralisation in negative or cross-reactive samples	Criteria met
Sensitivity	Comparison with live virus neutralisation titres; inter-laboratory PV assays; total IgG ELISA; MERS spike monoclonal antibody	Correlation with live virus neutralisation, ELISA, and external assays	Criteria met
Linearity	Evaluation across different starting dilution ranges	Demonstration of acceptable dilutional linearity	Criteria met
Lower limit of quantification	Analysis of pre-pandemic negative samples	Discrimination of positive samples above assay cut-off	Criteria met
Precision	Intra-assay and intermediate precision assessment	CV within acceptable limits for assay use	Criteria met
Accuracy	Recovery experiments using spiked negative samples (25–75%)	Acceptable agreement between expected and observed values	Criteria met

Table S4. Qualification parameters, assessment approach, and acceptance criteria

8.1.4.1.2.3.1 Specificity

Assay specificity was evaluated using pre-pandemic negative samples (n = 29) and quality control panels from the WHO (n = 1) and NIBSC (n = 3). No neutralisation above the assay cut-off was

observed in negative or cross-reactive samples (n = 7), indicating 100% specificity for detection of MERS-CoV neutralising antibodies. Although marginal cross-reactivity was observed in MERS-CoV–specific total IgG measured by the in-house ELISA for a small number of WHO quality control samples containing high titres of NL63 and 229E (WHO A and WHO D), no corresponding neutralising activity was detected in the pseudovirus neutralisation assay. Quantitative specificity results are summarised in Table S.

	Anti-MERS Neutralizing Antibodies	Binding Antibodies				
	IC50 (IU/mL)*	229E**	NL63**	OC43**	HKU-1**	MERS*
WHO A	0.23	160	1280	320	640	222
WHO B	4.22	2560	1280	1280	160	184
WHO C	0.37	160	320	1280	320	75
WHO D	12.05	1280	2560	320	160	215
WHO E	26.86	320	1280	160	160	38
WHO F	0.05	80	320	320	160	126
WHO G	0	320	320	1280	1280	50

Table S5. Binding and neutralising antibodies measurements for cross-reactive seasonal coronavirus.

* Measurements were generated using the Oxford in-house MERS ELISA and MERS pseudoneutralisation assay.
** Binding antibody measurements against HCoVs were provided by the WHO endpoint ELISA.

8.1.4.1.2.3.2 Sensitivity

Assay sensitivity was assessed by comparison with live virus neutralisation titres, external pseudovirus assay data generated in independent laboratories, and total IgG ELISA measurements, with a summary of quantitative sensitivity performance shown in Table S6. Spike-specific neutralisation was further confirmed using a MERS spike-specific monoclonal antibody (Figure S).

Reference method	Strain / isolate	External dataset	Sample source	R	n
Live virus neutralisation	EMC/2012	Lab 1	Convalescents	0.88	8
Live virus neutralisation	EMC/2012	Lab 2	Convalescents	0.88	8
Live virus neutralisation	EMC/2012	Lab 3	Convalescents	0.79	7
Live virus neutralisation	EMC/2012	Lab 4	Vaccinated	1	5
External pseudovirus assay	EMC/2012	Lab 1	Convalescents	0.88	8
External pseudovirus assay	EMC/2012	Lab 2	Convalescents	0.98	9
External pseudovirus assay	EMC/2012	Lab 3	Convalescents	0.9	8
External pseudovirus assay	EMC/2012	Lab 4	Convalescents	0.83	8
External pseudovirus assay	EMC/2012	Lab 5	Convalescents	0.9	8
External pseudovirus assay	EMC/2012	Lab 6	Vaccinated	0.95	5

External pseudovirus assay	England isolate	Lab 1	Vaccinated	0.67 (p=0.26)	5
External pseudovirus assay	Korea isolate	Lab 1	Convalescents	0.88	8
External pseudovirus assay	Korea isolate	Lab 2	Vaccinated	0.95 (p=0.07)	5

Table S6. MERS-CoV isolates used for testing MERS PNA assay sensitivity.

Lab identifiers are strain-specific and do not represent the same laboratory across different isolates.

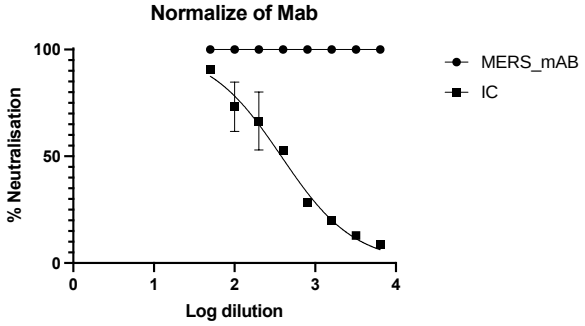


Figure S4. Neutralisation of MERS pseudovirus by a spike-specific monoclonal antibody.

A MERS spike–specific monoclonal antibody was tested in a serial dilution format, demonstrating complete and concentration-dependent neutralisation of pseudovirus infection, confirming assay sensitivity to spike-mediated neutralisation

8.1.4.1.2.3.3 Starting dilution / curve fit

Quality of curve fit for sample diluition series was assessed by comparing different starting dilution points during the optimization phase (n = 5). A fixed starting dilution of 1:50 was selected for subsequent analyses due to a slight improvement in R^2. Supporting data are presented in Table S.

Starting dilution	Mean R^2	SD	n
1:25	0.94	0.02	5
1:50	0.96	0.02	5

Table S7. Curve fit assessment comparing starting dilution points

8.1.4.1.2.3.4 Limit of detection

The lower limit of detection was initially calculated using pre-pandemic negative samples; however, this approach reduced assay specificity. Therefore, the lowest dilution tested 1/50 was selected as the operational assay cut-off.

8.1.4.1.2.3.5 Precision

Precision is defined as the degree of agreement among repeated measurements of the same sample under specified conditions. Precision was evaluated as intra-assay precision (repeatability within the same

plate), inter-plate precision (repeatability between plates on the same day), and intermediate precision (repeatability across assay runs performed on different days), using samples spanning low, medium, high, and very high neutralising antibody levels. Results are summarised in Table S.

Precision level	Sample level	Replicates / runs (n)	Mean IU/mL	SD	CV (%)
Intra-assay	Low	3	81	8	0.3
Intra-assay	Medium	3	188	10	5
Intra-assay	High	3	410	35	9
Intra-assay	Very high	3	709	84	12
Inter-plate	Low	2	88	5	6
Inter-plate	Medium	2	143	3	2
Inter-plate	High	2	349	60	17
Inter-plate	Very high	2	693	41	6
Intermediate	Low	4	82	9	11
Intermediate	Medium	4	144	43	30
Intermediate	High	4	325	60	18
Intermediate	Very high	3	644	61	9

Table S8. Summary of assay precision across different levels.

8.1.4.1.2.3.6 Accuracy

Accuracy is defined as the closeness of agreement between the measured value and the true value. Assay accuracy was assessed using recovery experiments in which negative samples were spiked with defined proportions of positive samples. Results are summarised in Table S.

Concentration Preparation	Observed	Expected	Percent Recovery (R)	Absolute bias (B)	Percent Bias (PB)
25%	181.60	209	87.06	-27.04	-12.94
50%	330.66	418	79.11	-87.34	-20.89
66%	410.68	516	79.59	-105.32	-20.41

Table S9. Accuracy assessment by recovery experiments using spiked samples.

8.1.4.1.2.3.7 Robustness

Assay robustness was evaluated by assessing the effects of virus and sample freeze–thaw cycles. The stability of samples subjected to repeated freeze–thaw cycles following storage at −80 °C was evaluated during the development phase. Samples were allowed to freeze completely and were analysed on consecutive days for four cycles using the same assay protocol, with freshly thawed virus used for each run. A significant reduction in IC50 values was observed between the first cycle and the third and fourth cycles (repeated-measures one-way ANOVA, $p = 0.0099$), with increased variability following repeated freeze–thawing (average CV = 40–51%), as shown in Figure S.

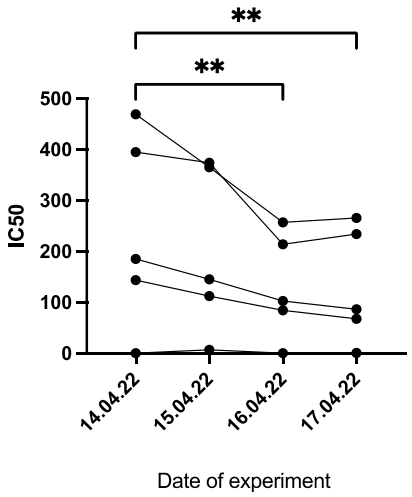


Figure S5. Effect of repeated sample freeze–thaw cycles on assay readouts.
Samples stored at −80 ˚C were subjected to repeated freeze–thaw cycles and analysed on consecutive days using the same assay protocol with freshly thawed pseudovirus. IC50 values decreased with increasing freeze–thaw cycles, with a significant reduction observed at the third and fourth cycles compared with the first cycle (repeated-measures one-way ANOVA, p = 0.0099). Increased variability was observed following repeated freeze–thawing, with average CV values of 40% and 51% between cycle one and cycles three and four, respectively.

8.1.4.1.3 Fcγ receptor binding quantification by Luminex

8.1.4.1.3.1 Assay characterization

8.1.4.1.3.1.1 Limit of quantification

The limits of quantification were determined using standard curves included on each plate. Quantification was based on a pooled sample from MERS001 boosted time-points (n = 4). Antigen targets used for standard curve–based quantification were selected based on assay reproducibility: the full-length spike protein was used for FcγRIIA, FcγRIIIA, and FcγRIIB, while the S1 subunit was used for FcγRIIIB. Limits of quantification were defined using a four-parameter logistic (4PL) nonlinear regression. The lower limit of detection was calculated as the bottom asymptote of the fitted curve plus 3 standard deviations, based on the mean of 7–9 independent experiments. The upper limit was visually determined from curve shape to be 3 log MFI, and was consistent across experiments (Figure S).

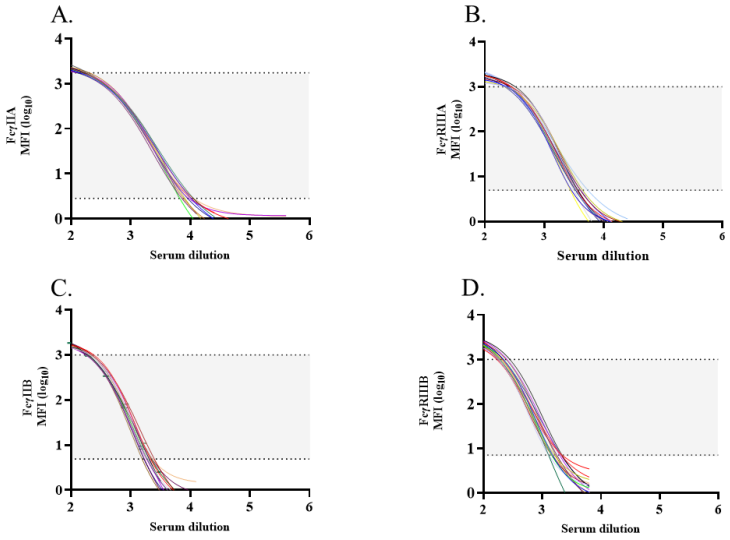


Figure S6. Standard curves and quantification limits for Fcγ receptor assays.

Dashed lines indicate the quantification limits of the standard curves. The lower limit corresponds to the bottom of the 4PL fit plus 3 SD (mean of 7–9 experiments), and the upper limit was visually set at 3 log MFI based on all experiments. All standard curves that passed assay quality control are included in this figure for consistency. Panels: A, FcγRIIA; B, FcγRIIIA; C, FcγRIIB; and D, FcγRIIIB.

8.1.4.1.3.1.2 Specificity and sensitivity

Multiplex assay sensitivity and specificity were evaluated using the WHO reference panel (n = 18; Table S1) and additional SARS-CoV-2 samples (Table S). Full-length MERS spike demonstrated robust and sensitive Fcγ receptor binding across all Fcγ receptors tested, with clear separation from negative controls, whereas S1 and S2 antigens showed detectable and specific binding with reduced signal intensity and dynamic range. Results for MERS antigens are shown in Figure S .

.

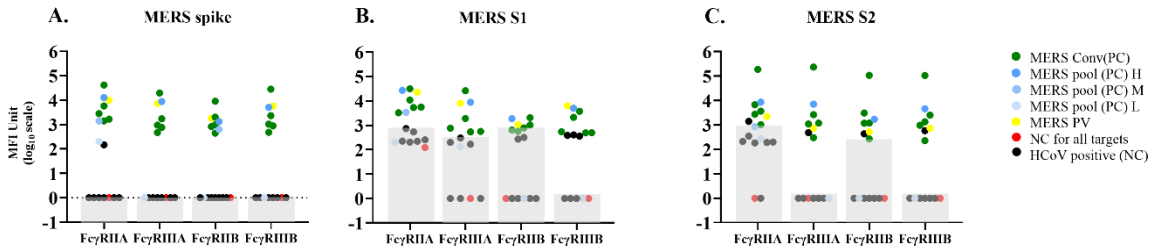


Figure S7. Fcγ receptor binding to MERS-CoV antigens measured by Luminex.
FcγRIIA, FcγRIIIA, FcγRIIB, and FcγRIIIB binding to full-length MERS spike (A), S1 (B), and S2 (C) is shown as MFI on a logarithmic scale. Samples include MERS convalescent plasma, pooled plasma controls (high, medium, and low), MERS positive controls, negative controls for all targets, and HCoV-positive negative controls. Full-length spike demonstrates higher-magnitude Fcγ receptor binding compared to S1 and S2. Colour coding corresponds to sample type as indicated in the figure key. Grey dashed lines indicate the lower limit of quantification.

.

Assay performance for SARS-CoV-2 full-length spike showed reduced specificity, characterized by an increased frequency of false-positive results (Figure S). In contrast, SARS-CoV-2 S1 and S2 antigens demonstrated higher sensitivity and specificity than SARS-CoV-2 spike (Figure SB-C).

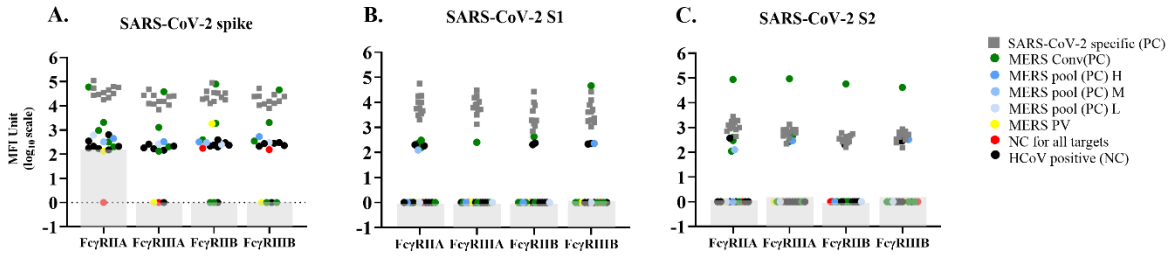


Figure S8. Fcγ receptor binding to SARS-CoV-2 antigens measured by Luminex.

FcγRIIA, FcγRIIIA, FcγRIIB, and FcγRIIIB binding to full-length SARS-CoV-2 spike (A), S1 (B), and S2 (C) is shown as MFI on a logarithmic scale. Samples include SARS-CoV2 convalescent plasma, MERS convalescent plasma, MERS pooled plasma controls (high, medium, and low), MERS positive controls, negative controls for all targets, and HCoV-positive negative controls. Colour coding corresponds to sample type as indicated in the figure key. Grey dashed lines indicate the lower limit of quantification.

Across endemic seasonal coronavirus antigens, Fcγ receptor binding signals showed substantial overlap between samples, with limited dynamic range. In contrast, negative controls were consistently separated at baseline levels (Figure S).

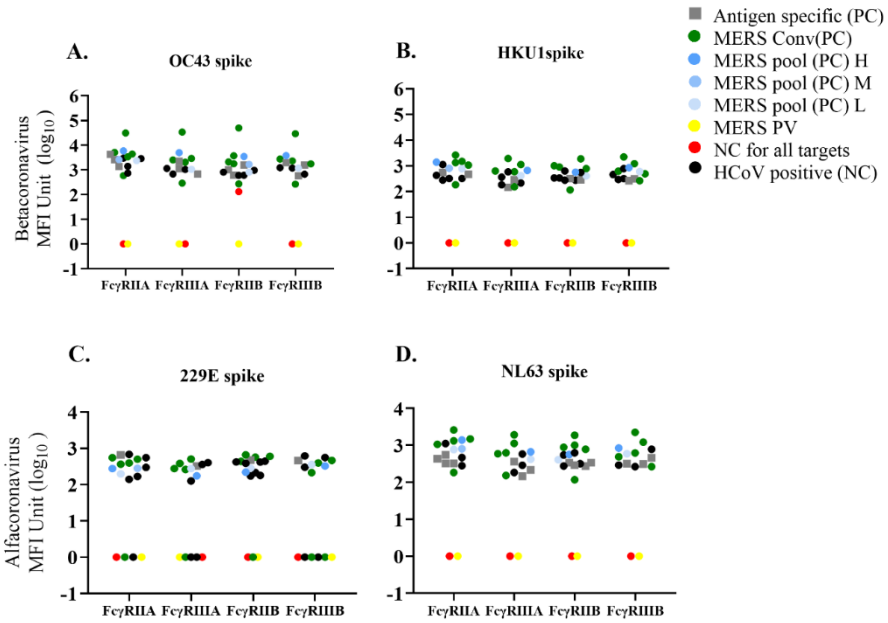


Figure S9. Fcγ receptor binding to endemic human coronavirus spike proteins measured by Luminex.

FcγRIIA, FcγRIIIA, FcγRIIB, and FcγRIIIB binding to OC43 spike (A), HKU1 spike (B), 229E spike (C), and NL63 spike (D) is shown as MFI on a logarithmic scale. Samples include WHO endemic coronavirus–positive control sera, antigen-specific positive controls, negative controls for all targets, and HCoV-positive negative controls (samples positive for other human coronaviruses but negative for the target virus) were included. Antigen-specific positive controls were included to confirm antigen integrity and assay performance. Colour coding corresponds to sample type as indicated in the figure key.

8.1.4.1.3.1.3 Precision

Intra-assay precision was assessed by calculating the coefficient of variation (CV) for each sample across 2–4 technical replicates. CVs were calculated for 13 independent samples per MERS specific antigen–Fcγ receptor pair, and the mean CV across samples is reported Table S3.

Fcγ receptor	Antigen	Mean intra-assay CV (%)	SD
FcγRIIA	MERS_S	16	14
	MERS_S1	16	14
	MERS_S2	18	20
FcγRIIIA	MERS_S	6	8
	MERS_S1	13	17
	MERS_S2	13	19
FcγRIIB	MERS_S	10	9
	MERS_S1	10	12
	MERS_S2	6	7
FcγRIIIB	MERS_S	21	15
	MERS_S1	15	24
	MERS_S2	25	25

Table S3. Intra-assay precision of Fcγ receptor binding assays.
Mean coefficients of variation (CV, %) were calculated for FcγRIIA, FcγRIIIA, FcγRIIB, and FcγRIIIB binding to MERS spike (S), S1, and S2 antigens. For each condition, CVs were calculated per sample across 2–4 technical replicates and averaged across 13 independent samples. The standard deviation (SD) reflects variability in CV values across samples. Inter-assay CV was not tested.

5.1.1.1 Peptide pooling strategy for T-cell assays

8.1.4.1.4 Clinical and mouse peptide pool (MERS001 and MERS003)

		Sequence			Sequence
Pool 1	S	IHARFRRIHSVFLLM	Pool 8		PLGQSLCALPDTPST
		RRIHSVFLLMFLLTP			LCALPDTPSTLTPRS
		VFLLMFLLTPTESYV			DTPSTLTPRSVRSVP
		FLLTPTESYVDVGPD			LTPRSVRSVPGEMRL
		TESYVDVGPDSVKSA			VRSVPGEMRLASIAF
		DVGPDSVKSACIEVD			GEMRLASIAFNHPIQ
		SVKSACIEVDIQQTF			ASIAFNHPIQVDQLN
		CIEVDIQQTFFDKTW			NHPIQVDQLNSSYFK
		IQQTFFDKTWPRPID			VDQLNSSYFKLSIPT
		FDKTWPRPIDVSKAD			SSYFKLSIPTNFSFG
		PRPIDVSKADGIIYP			LSIPTNFSFGVTQEY
		VSKADGIIYPQGRTY			NFSFGVTQEYIQTTI
		GIIYPQGRTYSNITI			VTQEYIQTTIQKVTV
		QGRTYSNITITYQGL			IQTTIQKVTVDCKQY
		SNITITYQGLFPYQG			QKVTVDCKQYVCNGF
		TYQGLFPYQGDHGDM			DCKQYVCNGFQKCEQ
		FPYQGDHGDMYVYSA			VCNGFQKCEQLLREY
		DHGDMYVYSAGHATG			QKCEQLLREYGQFCS
		YVYSAGHATGTTPQK			LLREYGQFCSKINQA
		GHATGTTPQKLFVAN			GQFCSKINQALHGAN
		TTPQKLFVANYSQDV			KINQALHGANLRQDD
Pool 2		LFVANYSQDVKQFAN	Pool 9		LHGANLRQDDSVRNL
		YSQDVKQFANGFVVR			LRQDDSVRNLFASVK
		KQFANGFVVRIGAAA			SVRNLFASVKSSQSS
		GFVVRIGAAANSTGT			FASVKSSQSSPIIPG
		IGAAANSTGTVIISP			SSQSSPIIPGFGGDF
		NSTGTVIISPSTSAT			PIIPGFGGDFNLTLL
		VIISPSTSATIRKIY			FGGDFNLTLLEPVSI
		STSATIRKIYPAFML			NLTLLEPVSISTGSR
		IRKIYPAFMLGSSVG			EPVSISTGSRSARSA
		PAFMLGSSVGNFSDG		S2	STGSRSARSAIEDLL
		GSSVGNFSDGKMGRF			SARSAIEDLLFDKVT
		NFSDGKMGRFFNHTL			IEDLLFDKVTIADPG
		KMGRFFNHTLVLLPD			FDKVTIADPGYMQGY
		FNHTLVLLPDGCGTL			IADPGYMQGYDDCMQ
		VLLPDGCGTLLRAFY			YMQGYDDCMQQGPAS
		GCGTLLRAFYCILEP			DDCMQQGPASARDLI
		LRAFYCILEPRSGNH			QGPASARDLICAQYV
		CILEPRSGNHCPAGN			ARDLICAQYVAGYKV
		RSGNHCPAGNSHTSF			CAQYVAGYKVLPPLM
		CPAGNSHTSFATYHT			AGYKVLPPLMDVNME
		SHTSFATYHTPATDC			LPPLMDVNMEAAYTS
Pool 3		ATYHTPATDCSDGNY	Pool 10		DVNMEAAYTSSLLGS
		PATDCSDGNYNRNAS			AAYTSSLLGSIAGVG
		SDGNYNRNASLNSFK			SLLGSIAGVGWTAGL
		NRNASLNSFKEYFNL			IAGVGWTAGLSSFAA
		LNSFKEYFNLRNCTF			WTAGLSSFAAIPFAQ

		EYFNLRNCTFMYTYN			SSFAAIPFAQSIFYR
		RNCTFMYTYNITEDE			IPFAQSIFYRLNGVG
		MYTYNITEDEILEWF			SIFYRLNGVGITQQV
		ITEDEILEWFGITQT			LNGVGITQQVLSENQ
		ILEWFGITQTAQGVH			ITQQVLSENQKLIAN
		GITQTAQGVHLFSSR			LSENQKLIANKFNQA
		AQGVHLFSSRYVDLY			KLIANKFNQALGAMQ
		LFSSRYVDLYGGNMF			KFNQALGAMQTGFTT
		YVDLYGGNMFQFATL			LGAMQTGFTTTNEAF
		GGNMFQFATLPVYDT			TGFTTTNEAFRKVQD
		QFATLPVYDTIKYYS			TNEAFRKVQDAVNNN
		PVYDTIKYYSIIPHS			RKVQDAVNNNAQALS
		IKYYSIIPHSIRSIQ			AVNNNAQALSKLASE
		IIPHSIRSIQSDRKA			AQALSKLASELSNTF
		IRSIQSDRKAWAAFY			KLASELSNTFGAISA
		SDRKAWAAFYVYKLQ			LSNTFGAISASIGDI
Pool 4		WAAFYVYKLQPLTFL	Pool 11		GAISASIGDIIQRLD
		VYKLQPLTFLLDFSV			SIGDIIQRLDVLEQD
		PLTFLLDFSVDGYIR			IQRLDVLEQDAQIDR
		LDFSVDGYIRRAIDC			VLEQDAQIDRLINGR
		DGYIRRAIDCGFNDL			AQIDRLINGRLTTLN
		RAIDCGFNDLSQLHC			LINGRLTTLNAFVAQ
		GFNDLSQLHCSYESF			LTTLNAFVAQQLVRS
		SQLHCSYESFDVESG			AFVAQQLVRSESAAL
		SYESFDVESGVYSVS			QLVRSESAALSAQLA
		DVESGVYSVSSFEAK			ESAALSAQLAKDKVN
		VYSVSSFEAKPSGSV			SAQLAKDKVNECVKA
		SFEAKPSGSVVEQAE			KDKVNECVKAQSKRS
		PSGSVVEQAEGVECD			ECVKAQSKRSGFCGQ
		VEQAEGVECDFSPLL			QSKRSGFCGQGTHIV
		GVECDFSPLLSGTPP			GFCGQGTHIVSFVVN
		FSPLLSGTPPQVYNF			GTHIVSFVVNAPNGL
		SGTPPQVYNFKRLVF			SFVVNAPNGLYFMHV
		QVYNFKRLVFTNCNY			APNGLYFMHVGYYPS
		KRLVFTNCNYNLTKL			YFMHVGYYPSNHIEV
		TNCNYNLTKLLSLFS			GYYPSNHIEVVSAYG
		NLTKLLSLFSVNDFT			NHIEVVSAYGLCDAA
Pool 5		LSLFSVNDFTCSQIS	Pool 12		VSAYGLCDAANPTNC
		VNDFTCSQISPAAIA			LCDAANPTNCIAPVN
		CSQISPAAIASNCYS			NPTNCIAPVNGYFIK
		PAAIASNCYSSLILD			IAPVNGYFIKTNNTR
		SNCYSSLILDYFSYP			GYFIKTNNTRIVDEW
		SLILDYFSYPLSMKS			TNNTRIVDEWSYTGS
		YFSYPLSMKSDLSVS			IVDEWSYTGSSFYAP
		LSMKSDLSVSSAGPI			SYTGSSFYAPEPITS
		DLSVSSAGPISQFNY			SFYAPEPITSLNTKY
		SAGPISQFNYKQSFS			EPITSLNTKYVAPQV
		SQFNYKQSFSNPTCL			LNTKYVAPQVTYQNI
		KQSFSNPTCLILATV			VAPQVTYQNISTNLP
		NPTCLILATVPHNLT			TYQNISTNLPPPLLG

		ILATVPHNLTTITKP			STNLPPPLLGNSTGI
		PHNLTTITKPLKYSY			PPLLGNSTGIDFQDE
		TITKPLKYSYINKCS			NSTGIDFQDELDEFF
		LKYSYINKCSRLLSD			DFQDELDEFFKNVST
		INKCSRLLSDDRTEV			LDEFFKNVSTSIPNF
		RLLSDDRTEVPQLVN			KNVSTSIPNFGSLTQ
		DRTEVPQLVNANQYS			SIPNFGSLTQINTTL
		PQLVNANQYSPCVSI			GSLTQINTTLLDLTY
Pool 6		ANQYSPCVSIVPSTV	Pool 13		INTTLLDLTYEMLSL
		PCVSIVPSTVWEDGD			LDLTYEMLSLQQVVK
		VPSTVWEDGDYYRKQ			EMLSLQQVVKALNES
		WEDGDYYRKQLSPLE			QQVVKALNESYIDLK
		YYRKQLSPLEGGGWL			ALNESYIDLKELGNY
		LSPLEGGGWLVASGS			YIDLKELGNYTYYNK
		GGGWLVASGSTVAMT			ELGNYTYYNKWPWYI
		VASGSTVAMTEQLQM			TYYNKWPWYIWLGFI
		TVAMTEQLQMGFGIT			WPWYIWLGFIAGLVA
		EQLQMGFGITVQYGT			WLGFIAGLVALALCV
		GFGITVQYGTDTNSV			AGLVALALCVFFILC
		VQYGTDTNSVCPKLE			LALCVFFILCCTGCG
		DTNSVCPKLEFANDT			FFILCCTGCGTNCMG
		CPKLEFANDTKIASQ			CTGCGTNCMGKLKCN
		FANDTKIASQLGNCV			TNCMGKLKCNRCCDR
		KIASQLGNCVEYSLY			KLKCNRCCDRYEEYD
		LGNCVEYSLYGVSGR			RCCDRYEEYDLEPHK
		EYSLYGVSGRGVFQN			YEEYDLEPHKVHVH
		GVSGRGVFQNCTAVG			
		GVFQNCTAVGVRQQR			
		CTAVGVRQQRFVYDA			
Pool 7		VRQQRFVYDAYQNLV			
		FVYDAYQNLVGYYSD			
		YQNLVGYYSDDGNYY			
		GYYSDDGNYYCLRAC			
		DGNYYCLRACVSVPV			
		CLRACVSVPVSVIYD			
		VSVPVSVIYDKETKT			
		SVIYDKETKTHATLF			
		KETKTHATLFGSVAC			
		HATLFGSVACEHISS			
		GSVACEHISSTMSQY			
		EHISSTMSQYSRSTR			
		TMSQYSRSTRSMLKR			
		SRSTRSMLKRRDSTY			
		SMLKRRDSTYGPLQT			
		RDSTYGPLQTPVGCV			
		GPLQTPVGCVLGLVN			
		PVGCVLGLVNSSLFV			
		LGLVNSSLFVEDCKL			
		SSLFVEDCKLPLGQS			
		EDCKLPLGQSLCALP			

8.1.4.1.5 Exploratory peptide pool (MERS001)

Pool	Peptide no	Sequence	Pool	Peptide no	Sequence
Pool A1	tPA1	MDAMKRGLCCVLLLC	Pool A10	MERS140	SRSTRSMLKRRDSTY
	tPA2	RGLCCVLLLCGAVFV		MERS141	SMLKRRDSTYGPLQT
	tPA3	VLLLCGAVFVSASQE		MERS142	RDSTYGPLQTPVGCV
	tPA4	GAVFVSASQEIHARF		MERS143	GPLQTPVGCVLGLVN
	tPA5	SASQEIHARFRRIHS		MERS144	PVGCVLGLVNSSLFV
	MERS1	IHARFRRIHSVFLLM		MERS145	LGLVNSSLFVEDCKL
	MERS2	RRIHSVFLLMFLLTP		MERS146	SSLFVEDCKLPLGQS
	MERS3	VFLLMFLLTPTESYV		MERS147	EDCKLPLGQSLCALP
	MERS4	FLLTPTESYVDVGPD		MERS148	PLGQSLCALPDTPST
	MERS5	TESYVDVGPDSVKSA		MERS149	LCALPDTPSTLTPRS
	MERS6	DVGPDSVKSACIEVD		MERS150	DTPSTLTPRSVRSVP
	MERS7	SVKSACIEVDIQQTF		MERS151	LTPRSVRSVPGEMRL
	MERS8	CIEVDIQQTFFDKTW		MERS152	VRSVPGEMRLASIAF
	MERS9	IQQTFFDKTWPRPID		MERS153	GEMRLASIAFNHPIQ
	MERS10	FDKTWPRPIDVSKAD		MERS154	ASIAFNHPIQVDQLN
	MERS11	PRPIDVSKADGIIYP		MERS155	NHPIQVDQLNSSYFK
Pool A2	MERS12	VSKADGIIYPQGRTY	Pool A11	MERS156	VDQLNSSYFKLSIPT
	MERS13	GIIYPQGRTYSNITI		MERS157	SSYFKLSIPTNFSFG
	MERS14	QGRTYSNITITYQGL		MERS158	LSIPTNFSFGVTQEY
	MERS15	SNITITYQGLFPYQG		MERS159	NFSFGVTQEYIQTTI
	MERS16	TYQGLFPYQGDHGDM		MERS160	VTQEYIQTTIQKVTV
	MERS17	FPYQGDHGDMYVYSA		MERS161	IQTTIQKVTVDCKQY
	MERS18	DHGDMYVYSAGHATG		MERS162	QKVTVDCKQYVCNGF
	MERS19	YVYSAGHATGTTPQK		MERS163	DCKQYVCNGFQKCEQ
	MERS20	GHATGTTPQKLFVAN		MERS164	VCNGFQKCEQLLREY
	MERS21	TTPQKLFVANYSQDV		MERS165	QKCEQLLREYGQFCS
	MERS22	LFVANYSQDVKQFAN		MERS166	LLREYGQFCSKINQA
	MERS23	YSQDVKQFANGFVVR		MERS167	GQFCSKINQALHGAN
	MERS24	KQFANGFVVRIGAAA		MERS168	KINQALHGANLRQDD
	MERS25	GFVVRIGAAANSTGT		MERS169	LHGANLRQDDSVRNL
	MERS26	IGAAANSTGTVIISP		MERS170	LRQDDSVRNLFASVK
	MERS27	NSTGTVIISPSTSAT		MERS171	SVRNLFASVKSSQSS
Pool A3	MERS28	VIISPSTSATIRKIY	Pool A12	MERS172	FASVKSSQSSPIIPG
	MERS29	STSATIRKIYPAFML		MERS173	SSQSSPIIPGFGGDF
	MERS30	IRKIYPAFMLGSSVG		MERS174	PIIPGFGGDFNLTLL
	MERS31	PAFMLGSSVGNFSDG		MERS175	FGGDFNLTLLEPVSI
	MERS32	GSSVGNFSDGKMGRF		MERS176	NLTLLEPVSISTGSR
	MERS33	NFSDGKMGRFFNHTL		MERS177	EPVSISTGSRSARSA
	MERS34	KMGRFFNHTLVLLPD		MERS178	STGSRSARSAIEDLL
	MERS35	FNHTLVLLPDGCGTL		MERS179	SARSAIEDLLFDKVT
	MERS36	VLLPDGCGTLLRAFY		MERS180	IEDLLFDKVTIADPG
	MERS37	GCGTLLRAFYCILEP		MERS181	FDKVTIADPGYMQGY
	MERS38	LRAFYCILEPRSGNH		MERS182	IADPGYMQGYDDCMQ
	MERS39	CILEPRSGNHCPAGN		MERS183	YMQGYDDCMQQGPAS
	MERS40	RSGNHCPAGNSHTSF		MERS184	DDCMQQGPASARDLI
	MERS41	CPAGNSHTSFATYHT		MERS185	QGPASARDLICAQYV
	MERS42	SHTSFATYHTPATDC		MERS186	ARDLICAQYVAGYKV
	MERS43	ATYHTPATDCSDGNY		MERS187	CAQYVAGYKVLPPLM
Pool A4	MERS44	PATDCSDGNYNRNAS	Pool A13	MERS188	AGYKVLPPLMDVNME
	MERS45	SDGNYNRNASLNSFK		MERS189	LPPLMDVNMEAAYTS
	MERS46	NRNASLNSFKEYFNL		MERS190	DVNMEAAYTSSLLGS
	MERS47	LNSFKEYFNLRNCTF		MERS191	AAYTSSLLGSIAGVG
	MERS48	EYFNLRNCTFMYTYN		MERS192	SLLGSIAGVGWTAGL
	MERS49	RNCTFMYTYNITEDE		MERS193	IAGVGWTAGLSSFAA
	MERS50	MYTYNITEDEILEWF		MERS194	WTAGLSSFAAIPFAQ
	MERS51	ITEDEILEWFGITQT		MERS195	SSFAAIPFAQSIFYR
	MERS52	ILEWFGITQTAQGVH		MERS196	IPFAQSIFYRLNGVG
	MERS53	GITQTAQGVHLFSSR		MERS197	SIFYRLNGVGITQQV
	MERS54	AQGVHLFSSRYVDLY		MERS198	LNGVGITQQVLSENQ
	MERS55	LFSSRYVDLYGGNMF		MERS199	ITQQVLSENQKLIAN
	MERS56	YVDLYGGNMFQFATL		MERS200	LSENQKLIANKFNQA
	MERS57	GGNMFQFATLPVYDT		MERS201	KLIANKFNQALGAMQ
	MERS58	QFATLPVYDTIKYYS		MERS202	KFNQALGAMQTGFTT
	MERS59	PVYDTIKYYSIIPHS		MERS203	LGAMQTGFTTTNEAF
Pool A5	MERS60	IKYYSIIPHSIRSIQ	Pool A14	MERS204	TGFTTTNEAFRKVQD
	MERS61	IIPHSIRSIQSDRKA		MERS205	TNEAFRKVQDAVNNN
	MERS62	IRSIQSDRKAWAAFY		MERS206	RKVQDAVNNNAQALS

	MERS63	SDRKAWAAFYVYKLQ		MERS207	AVNNNAQALSKLASE
	MERS64	WAAFYVYKLQPLTFL		MERS208	AQALSKLASELSNTF
	MERS65	VYKLQPLTFLLDFSV		MERS209	KLASELSNTFGAISA
	MERS66	PLTFLLDFSVDGYIR		MERS210	LSNTFGAISASIGDI
	MERS67	LDFSVDGYIRRAIDC		MERS211	GAISASIGDIIQRLD
	MERS68	DGYIRRAIDCGFNDL		MERS212	SIGDIIQRLDVLEQD
	MERS69	RAIDCGFNDLSQLHC		MERS213	IQRLDVLEQDAQIDR
	MERS70	GFNDLSQLHCSYESF		MERS214	VLEQDAQIDRLINGR
	MERS71	SQLHCSYESFDVESG		MERS215	AQIDRLINGRLTTLN
	MERS72	SYESFDVESGVYSVS		MERS216	LINGRLTTLNAFVAQ
	MERS73	DVESGVYSVSSFEAK		MERS217	LTTLNAFVAQQLVRS
	MERS74	VYSVSSFEAKPSGSV		MERS218	AFVAQQLVRSESAAL
	MERS75	SFEAKPSGSVVEQAE		MERS219	QLVRSESAALSAQLA
Pool A6	MERS76	PSGSVVEQAEGVECD	Pool A15	MERS220	ESAALSAQLAKDKVN
	MERS77	VEQAEGVECDFSPLL		MERS221	SAQLAKDKVNECVKA
	MERS78	GVECDFSPLLSGTPP		MERS222	KDKVNECVKAQSKRS
	MERS79	FSPLLSGTPPQVYNF		MERS223	ECVKAQSKRSGFCGQ
	MERS80	SGTPPQVYNFKRLVF		MERS224	QSKRSGFCGQGTHIV
	MERS81	QVYNFKRLVFTNCNY		MERS225	GFCGQGTHIVSFVVN
	MERS82	KRLVFTNCNYNLTKL		MERS226	GTHIVSFVVNAPNGL
	MERS83	TNCNYNLTKLLSLFS		MERS227	SFVVNAPNGLYFMHV
	MERS84	NLTKLLSLFSVNDFT		MERS228	APNGLYFMHVGYYPS
	MERS85	LSLFSVNDFTCSQIS		MERS229	YFMHVGYYPSNHIEV
	MERS86	VNDFTCSQISPAAIA		MERS230	GYYPSNHIEVVSAYG
	MERS87	CSQISPAAIASNCYS		MERS231	NHIEVVSAYGLCDAA
	MERS88	PAAIASNCYSSLILD		MERS232	VSAYGLCDAANPTNC
	MERS89	SNCYSSLILDYFSYP		MERS233	LCDAANPTNCIAPVN
	MERS90	SLILDYFSYPLSMKS		MERS234	NPTNCIAPVNGYFIK
	MERS91	YFSYPLSMKSDLSVS		MERS235	IAPVNGYFIKTNNTR
Pool A7	MERS92	LSMKSDLSVSSAGPI	Pool A16	MERS236	GYFIKTNNTRIVDEW
	MERS93	DLSVSSAGPISQFNY		MERS237	TNNTRIVDEWSYTGS
	MERS94	SAGPISQFNYKQSFS		MERS238	IVDEWSYTGSSFYAP
	MERS95	SQFNYKQSFSNPTCL		MERS239	SYTGSSFYAPEPITS
	MERS96	KQSFSNPTCLILATV		MERS240	SFYAPEPITSLNTKY
	MERS97	NPTCLILATVPHNLT		MERS241	EPITSLNTKYVAPQV
	MERS98	ILATVPHNLTTITKP		MERS242	LNTKYVAPQVTYQNI
	MERS99	PHNLTTITKPLKYSY		MERS243	VAPQVTYQNISTNLP
	MERS100	TITKPLKYSYINKCS		MERS244	TYQNISTNLPPPLLG
	MERS101	LKYSYINKCSRLLSD		MERS245	STNLPPPLLGNSTGI
	MERS102	INKCSRLLSDDRTEV		MERS246	PPLLGNSTGIDFQDE
	MERS103	RLLSDDRTEVPQLVN		MERS247	NSTGIDFQDELDEFF
	MERS104	DRTEVPQLVNANQYS		MERS248	DFQDELDEFFKNVST
	MERS105	PQLVNANQYSPCVSI		MERS249	LDEFFKNVSTSIPNF
	MERS106	ANQYSPCVSIVPSTV		MERS250	KNVSTSIPNFGSLTQ
	MERS107	PCVSIVPSTVWEDGD		MERS251	SIPNFGSLTQINTTL
Pool A8	MERS108	VPSTVWEDGDYYRKQ	Pool A17	MERS252	GSLTQINTTLLDLTY
	MERS109	WEDGDYYRKQLSPLE		MERS253	INTTLLDLTYEMLSL
	MERS110	YYRKQLSPLEGGGWL		MERS254	LDLTYEMLSLQQVVK
	MERS111	LSPLEGGGWLVASGS		MERS255	EMLSLQQVVKALNES
	MERS112	GGGWLVASGSTVAMT		MERS256	QQVVKALNESYIDLK
	MERS113	VASGSTVAMTEQLQM		MERS257	ALNESYIDLKELGNY
	MERS114	TVAMTEQLQMGFGIT		MERS258	YIDLKELGNYTYYNK
	MERS115	EQLQMGFGITVQYGT		MERS259	ELGNYTYYNKWPWYI
	MERS116	GFGITVQYGTDTNSV		MERS260	TYYNKWPWYIWLGFI
	MERS117	VQYGTDTNSVCPKLE		MERS261	WPWYIWLGFIAGLVA
	MERS118	DTNSVCPKLEFANDT		MERS262	WLGFIAGLVALALCV
	MERS119	CPKLEFANDTKIASQ		MERS263	AGLVALALCVFFILC
	MERS120	FANDTKIASQLGNCV		MERS264	LALCVFFILCCTGCG
	MERS121	KIASQLGNCVEYSLY		MERS265	FFILCCTGCGTNCMG
	MERS122	LGNCVEYSLYGVSGR		MERS266	CTGCGTNCMGKLKCN
	MERS123	EYSLYGVSGRGVFQN		MERS267	TNCMGKLKCNRCCDR
Pool A9	MERS124	GVSGRGVFQNCTAVG		MERS268	KLKCNRCCDRYEEYD
	MERS125	GVFQNCTAVGVRQQR		MERS269	RCCDRYEEYDLEPHK
	MERS126	CTAVGVRQQRFVYDA		MERS270	YEEYDLEPHKVHVH
	MERS127	VRQQRFVYDAYQNLV			
	MERS128	FVYDAYQNLVGYYSD			
	MERS129	YQNLVGYYSDDGNYY			
	MERS130	GYYSDDGNYYCLRAC			
	MERS131	DGNYYCLRACVSVPV			
	MERS132	CLRACVSVPVSVIYD			
	MERS133	VSVPVSVIYDKETKT			

	MERS134	SVIYDKETKTHATLF	
	MERS135	KETKTHATLFGSVAC	
	MERS136	HATLFGSVACEHISS	
	MERS137	GSVACEHISSTMSQY	
	MERS138	EHISSTMSQYSRSTR	
	MERS139	TMSQYSRSTRSMLKR	

8.1.4.2 Clinical and vaccination characteristics of study participants with MERS infection, SARS-CoV-2 exposure, and hybrid immunity

Table S11. Clinical and vaccination data of individuals with prior MERS infection and COVID-19 vaccination (hybrid MERS immunity) based on the presence of positive MERS PCR in sputum.

ID	Sex	Age	Years of MERS infection	ICU admission	Sample collection date	Years post-MERS infection	COVID-19 vaccination		
							1st dose	2nd dose	3rd dose
38	M	15	2015	No	Dec 2021	6	BNT162b2	mRNA-1273	
7	M	30	2016	No	Jan 2021	5	Not vaccinated		
40	M	34	2015	No	Dec 2021	6	AZD1222	AZD1222	
51	M	34	2014	Yes	Jan 2022	8	BNT162b2	BNT162b2	
50	F	36	2015	No	Jan 2022	7	BNT162b2	BNT162b2	BNT162b2
45	F	37	2018	Yes	Dec 2021	3	BNT162b2	BNT162b2	
42	M	40	2014	No	Dec 2021	7	AZD1222	BNT162b2	
35	M	44	2016	No	Dec 2021	5	BNT162b2	BNT162b2	
66	F	45	2017	No	Mar 2022	5	BNT162b2	BNT162b2	
56	M	47	2014	No	Feb 2022	8	BNT162b2	BNT162b2	BNT162b2
30	M	57	2014	Yes	Oct 2021	7	BNT162b2	AZD1222	
34	M	64	2018	No	Dec 2021	3	BNT162b2	BNT162b2	
44	M	74	2018	No	Dec 2021	3	BNT162b2	BNT162b2	

Table S12. Clinical and vaccination data of individuals with prior SARS-CoV-2 infection and COVID-19 vaccination (hybrid SARS-CoV2 infection) based on the presence of anti-N antibodies at the time of vaccination.

ID	Sex	Age	History of symptomatic COVID-19 illness	Sample collection date	Days after second dose	COVID-19 vaccination		Days between PB
						1st dose	2nd dose	
Ox-0489	36	M	28/03/2020	07/10/2021	271	17/12/2020	09/01/2021	23
Ox-0117	35	M		28/09/2021	196	12/01/2021	16/03/2021	63
Ox-0013	40	F	11/04/2020	30/09/2021	266	16/12/2020	07/01/2021	22
Ox-0254	38	M		05/10/2021	218	18/01/2021	01/03/2021	42
Ox-0083	47	M	29/03/2020	08/10/2021	183	21/01/2021	08/04/2021	77
Ox-0134	27	M	30/04/2020	05/10/2021	98	22/01/2021	29/06/2021	158
Ox-0035	46	M	10/04/2020	20/07/2021	196	09/12/2020	05/01/2021	27
Ox-0217	30	F		09/11/2021	256	12/12/2020	26/02/2021	76
Ox-0128	49	M		29/10/2021	196	30/01/2021	16/04/2021	76
Ox-0184	43	F	20/03/2020	07/10/2021	276	16/12/2020	04/01/2021	19
Ox-0145	56	M		12/10/2021	176	01/02/2021	19/04/2021	77

Table S13. Clinical and vaccination data of individuals with negative SARS-CoV-2 infection and COVID-19 vaccination (vaccine immunity) based on the absence of anti-N antibodies.

ID	Sex	Age	Sample collection date	Days after second dose	COVID-19 vaccination		Days between PB
					1st dose	2nd dose	
Ox-0246	35	M	08/12/2021	332	11/12/2020	10/01/2021	30
Ox-0529	33	F	25/11/2021	321	15/12/2020	08/01/2021	24
Ox-0511	35	M	30/09/2021	267	11/12/2020	06/01/2021	26
Ox-0531	39	M	30/09/2021	264	23/12/2020	09/01/2021	17
Ox-0491	36	F	28/09/2021	263	11/12/2020	08/01/2021	28
Ox-0507	58	M	28/09/2021	266	11/12/2020	05/01/2021	25
Ox-0516	44	M	23/09/2021	256	22/12/2020	10/01/2021	19
Ox-0146	45	M	23/09/2021	264	11/12/2020	02/01/2021	22
Ox-0286	57	M	23/09/2021	262	14/12/2020	04/01/2021	21
Ox-0588	45	M	08/10/2021	272	19/12/2020	09/01/2021	21
Ox-0143	43	F	12/10/2021	228	28/12/2020	26/02/2021	60
Ox-0596	52	M	02/12/2021	178	25/03/2021	07/06/2021	74
Ox-0591	26	M	17/11/2021	201	12/02/2021	30/04/2021	77

Figure S10. Humoral and cellular immune responses following single-dose MVA-MERS vaccination

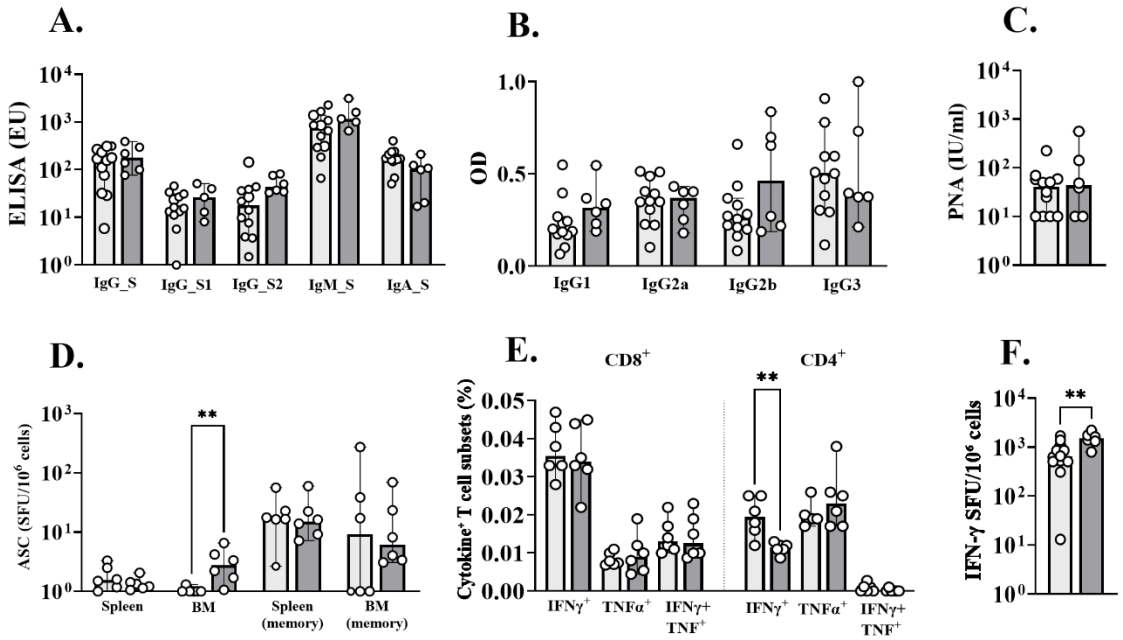
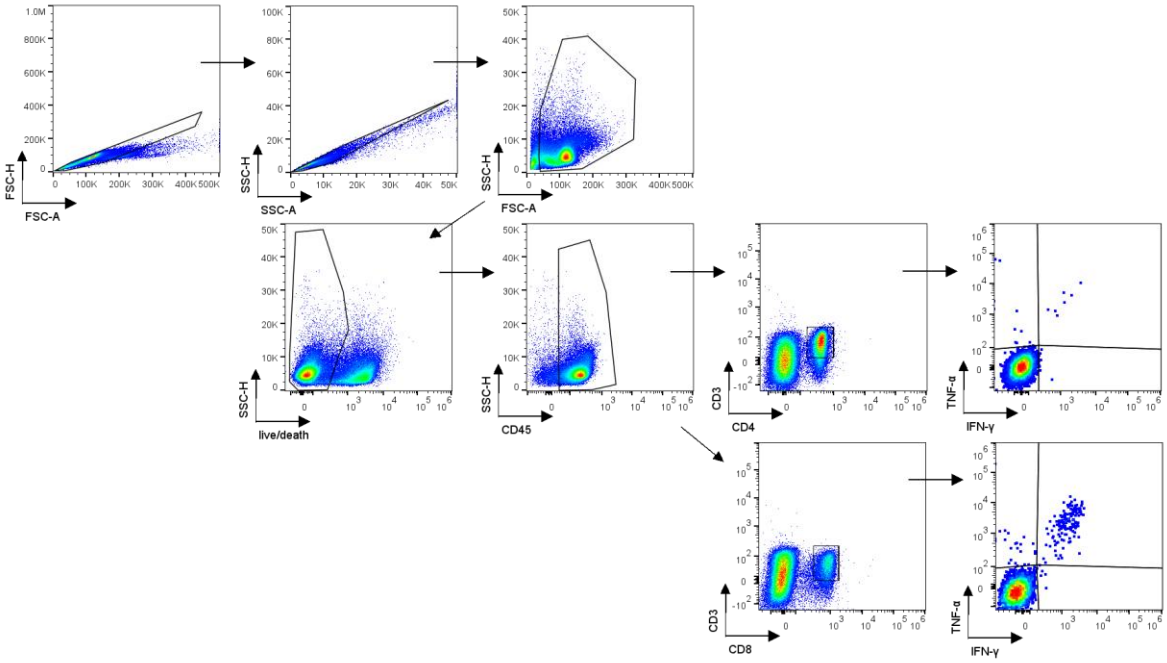


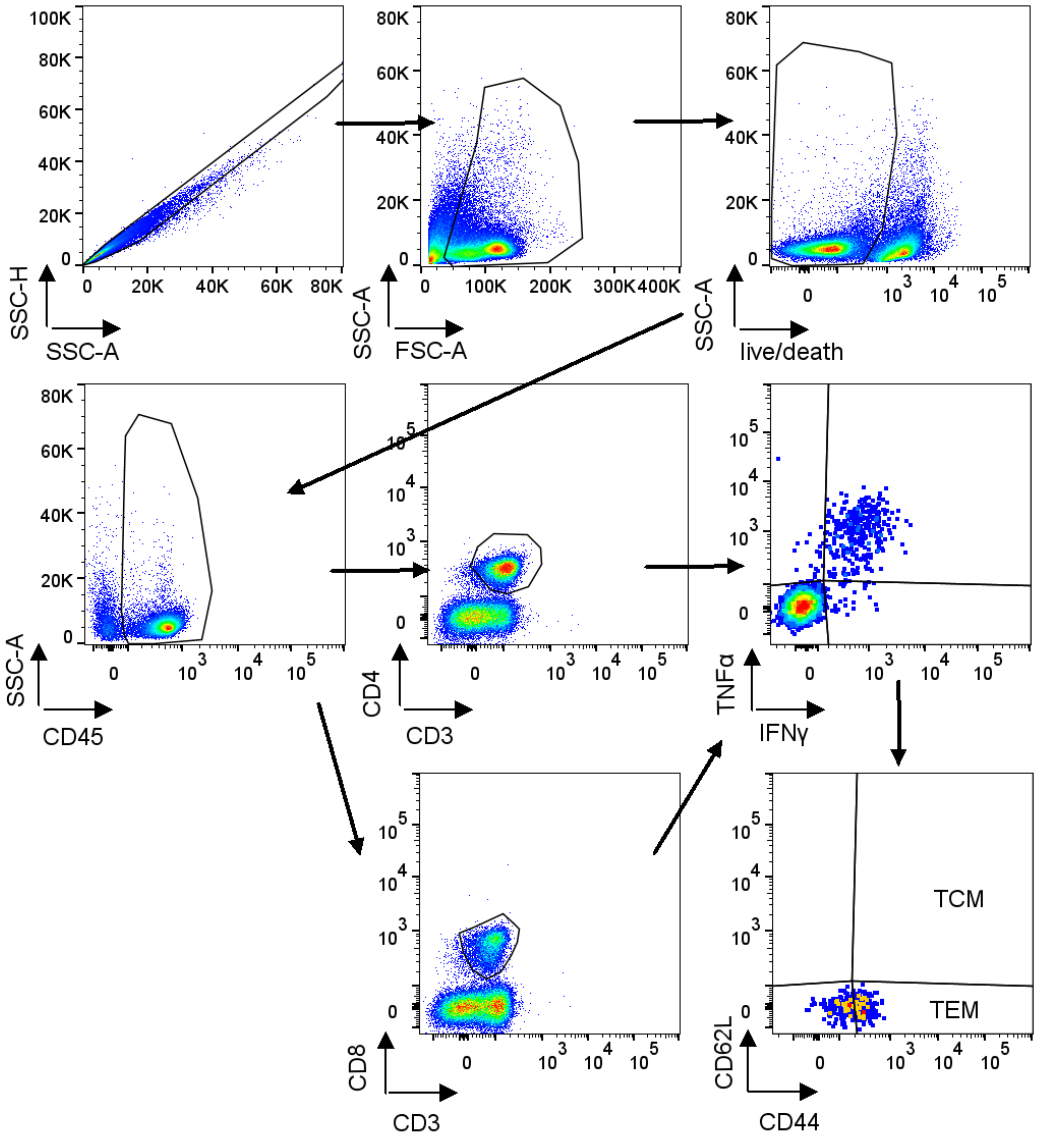
Figure S10. (A) Serum IgG, IgM, and IgA binding antibodies to full Spike, S1, and S2 measured by ELISA. (B) IgG subclass distribution (IgG1, IgG2a, IgG2b, IgG3). (C) Pseudovirus neutralisation assay (PNA) titres. (D) IgG antibody-secreting cells (ASC) and memory IgG ASC in spleen and bone marrow measured by ELISPOT. (E) Frequencies of cytokine$^+$ CD8$^+$ and CD4$^+$ T cells producing IFN-γ and/or TNF-α. (F) IFN-γ ELISPOT responses in splenocytes. Data are shown as [median with 95% CI]] with individual points representing biological replicates (n = 12 for 2-week groups, n = 6 for 4-week groups). Light grey bars = MVA prime-only (2 weeks post-vaccination); dark grey bars = MVA prime-only (4 weeks post-vaccination). Statistical comparisons were performed using two-tailed Mann–Whitney U tests for each readout; *p < 0.05; **p < 0.01; ***p < 0.001; ****p < 0.0001

Figure S11. Gating strategy to identify MERS-specific T cells in mouse splenocytes.



Splenocytes were stimulated for 5 hours with either immunodominant MERS peptide or pooled S1 or S2 peptide libraries, followed by intracellular cytokine staining. Lymphocytes were identified by exclusion of doublets, forward and side scatter properties, and exclusion of dead cells. Live cells were gated on CD45+ leukocytes and CD3+ T cells, and further subdivided into CD4+ and CD8+ populations. Antigen-specific responses were defined by intracellular expression of TNF, IFNγ, or TNF/IFNγ, using the indicated gates. Representative FlowJo dot plots from a single mouse spleen are shown

Figure S12. Gating strategy to identify MERS immunodominant peptide–specific effector and central memory T cells in mouse splenocytes



Following identification of antigen-specific cytokine-producing $CD4^+$ and $CD8^+$ T cells, memory subsets were defined based on CD44 and CD62L expression. Antigen-specific T cells were first gated on IFNγ and/or TNF expression and subsequently analysed for memory phenotype. Central memory T cells (TCM) were defined as CD44^hi^CD62L^$^{+}$^ cells, whereas effector memory T cells (TEM) were defined as CD44^hi^CD62L^–^ cells. Gates were established using unstimulated controls and applied consistently across samples. Representative dot plots illustrate the distribution of TCM and TEM populations within antigen-specific T cells.

Table S14. Summary of primary immunological outcomes for MVA-prime/ChAdOx1-boost regimens.

	MVA prime	ChAd Ox1 boost	Interval	IgG (EU)	PNA (IU/mL)	ASC spleen	ASC BM	IFN-γ ELISPOT	Memory ASC spleen	Memory ASC BM
A	1×10^5	1×10^8	12	21588 [14964–28211] (43%)	33326 [25347–41304] (34%)	9.64 [9.18–10.11] (7%)	84.07 [28.58–139.60] (93%)	1133 [1087–1179] (6%)	35 [16–54] (76%)	90 [36–144] (84%)
B	1×10^5	1×10^8	12	3181 [718–5643] (110%)	1475 [229–2722] (120%)	3.63 [0.24–7.03] (132%)	29.32 [3.32–55.32] (125%)	973 [973–973] (0%)	5.9 [1.5–6.2] (86%)	51 [51–51] (0%)
C	1×10^5	1×10^8	12	5694 [1676–9713] (100%)	2634 [578–4690] (110%)	3.37 [2.07–4.66] (54%)	54.47 [17.52–91.42] (96%)	1449 [1124–1774] (32%)	68 [15–45] (0%)	29 [15–45] (71%)
D	1×10^5	1×10^8	12	46090 [46090–46090] (0%)	85433 [85433–85433] (0%)	94.44 [94.44–94.44] (0%)	234.80 [234.80–234.80] (0%)	3392 [3392–3392] (0%)	51 [51–51] (0%)	48 [48–48] (96%)
E	1×10^5	1×10^8	12	41556 [29808–53304] (40%)	56418 [39805–73032] (42%)	70.53 [58.82–82.24] (24%)	171.80 [51.10–292.60] (99%)	4487 [4487–4487] (0%)	40 [43–58] (27%)	184 [62–305] (93%)
F	1×10^5	1×10^8	8	37161 [32489–41654] (13%)	30694 [18439–40909] (40%)	44.52 [32.31–70.63] (42%)	91.73 [32.89–157.50] (71%)	2842 [1696–3407] (35%)	35 [34–35] (2%)	88 [49–213] (133%)
G	1×10^5	1×10^8	8	4630 [3983–5244] (14%)	5998 [4067–8404] (37%)	5.90 [2.60–17.40] (96%)	26.23 [14.68–36.90] (47%)	1099 [657–1541] (57%)	23 [23–24] (90%)	15 [2.3–27] (89%)
H	1×10^5	1×10^8	4	7211 [4294–10128] (57%)	4702 [3596–5808] (33%)	11.15 [9.40–12.89] (22%)	21.63 [9.14–34.11] (82%)	4421 [4421–4421] (0%)	5.6 [5.6–5.6] (90%)	6.6 [6.6–6.6] (120%)
I	1×10^5	1×10^8	4	1569 [1068–2070] (45%)	1132 [553–1712] (72%)	1.18 [0.32–2.03] (103%)	1.39 [0.10–2.68] (131%)	1269 [1091–1446] (20%)	17 [15–24] (90%)	1.4 [1.0–1.8] (42%)
J	1×10^5	1×10^8	4	19157 [17214–21099] (14%)	9914 [7391–12438] (36%)	18.69 [13.03–24.34] (43%)	85.14 [20.06–150.20] (108%)	2660 [2660–2660] (0%)	17 [17–17] (0%)	56 [56–56] (139%)
K	1×10^5	1×10^8	4	2425 [1718–3132] (41%)	895 [416–1376] (76%)	2.99 [2.08–3.90] (43%)	19.40 [1.52–37.28] (130%)	756 [565–947] (36%)	33 [32–37] (9%)	11 [10–20] (128%)

Data are shown for (Groups A–K). as median [IQR] (CV%). Sample sizes: IgG and PNA (n = 25 per regimen), spleen assays (ASC, IFN-γ ELISPOT, memory ASC; n = 19 per regimen), bone marrow ASC and memory ASC (n = 25 per regimen).

Table S15. Summary of humoral and cellular outcomes for the Ad/MVA regimen.

	MVA prime	ChAdOx 1 boost	Interval	IgG (EU)	PNA (IU/mL)	ASC spleen	ASC BM	IFN-γ ELISPOT	Memory ASC spleen	Memory ASC BM
A	1×10^5	1×10^8	12	2868 [992–4743] (92%)	2106 [529–3684] (106%)	0.86 [0.36–1.36] (82%)	13.9 [2.8–25.1] (113%)	1030 [790–1271] (33%)	-0.37 [-0.67–-0.06] (76%)	30.4 [22–38.8] (39%)
B	1×10^5	1×10^8	12	3361 (NA)	642.9 (NA)	0.94 (NA)	12.8 (NA)	1645 (NA)	-0.16 (NA)	16.5 (NA)
C	1×10^5	1×10^8	12	17112 [3233–36782] (87%)	35951 [4510–82664] (100%)	5.56 [2.49–7.95] (55%)	73.1 [20.1–200] (106%)	4055 [172–8093] (111%)	-0.59 [-1.92–0.42] (63%)	201 [162–470] (104%)
D	1×10^5	1×10^8	12	6804 [3716–13610] (67%)	10987 [2947–25436] (98%)	5 [1–11] (83%)	18 [5–67] (94%)	2044 [1428–4235] (56%)	0.60 [0.26–0.95] (58%)	0.22 [0.05–0.40] (61%)
E	1×10^5	1×10^8	12	5420 [1800–15400] (72%)	8750 [2500–22400] (90%)	4 [2–9] (70%)	22 [6–73] (80%)	1880 [1200–3800] (65%)	0.55 [0.20–0.88] (60%)	0.21 [0.06–0.39] (67%)
F	1×10^5	1×10^8	8	6150 [2000–17400] (68%)	9650 [3000–24800] (84%)	6 [2–12] (75%)	24 [7–81] (85%)	1950 [1350–3900] (60%)	0.58 [0.22–0.91] (59%)	0.23 [0.07–0.41] (64%)
G	1×10^5	1×10^8	8	6480 [2100–18200] (69%)	10200 [3100–25500] (87%)	7 [3–14] (78%)	28 [8–91] (88%)	2000 [1400–4000] (62%)	0.59 [0.23–0.92] (61%)	0.24 [0.08–0.42] (66%)
H	1×10^5	1×10^8	4	7020 [2300–19000] (70%)	11000 [3200–26000] (89%)	8 [3–15] (80%)	30 [9–95] (89%)	2100 [1500–4100] (63%)	0.60 [0.25–0.94] (62%)	0.25 [0.09–0.43] (67%)
I	1×10^5	1×10^8	4	7300 [2400–19500] (71%)	11300 [3300–26500] (90%)	9 [4–16] (81%)	32 [10–98] (90%)	2150 [1550–4200] (64%)	0.61 [0.26–0.95] (63%)	0.26 [0.10–0.44] (68%)
J	1×10^5	1×10^8	4	7600 [2500–20000] (72%)	11500 [3400–27000] (91%)	10 [4–18] (82%)	34 [11–100] (91%)	2200 [1600–4300] (65%)	0.62 [0.27–0.96] (64%)	0.27 [0.11–0.45] (69%)
K	1×10^5	1×10^8	4	7900 [2600–20500] (73%)	11800 [3500–27500] (92%)	11 [5–20] (83%)	36 [12–102] (92%)	2250 [1650–4400] (66%)	0.63 [0.28–0.97] (65%)	0.28 [0.12–0.46] (70%)

Data are shown as median [IQR], with coefficient of variation (CV%) in brackets. Sample sizes: IgG and PNA (n = 27); spleen assays (n = 19); memory ASC in spleen (n = 16); bone marrow ASC and memory ASC (n = 27).

Table S16. Prediction based on composite model outcomes

When the composite model was applied across all readouts, predictive performance was substantially reduced compared with the individual readout models. For most endpoints, the 95% CIs of the model-predicted means crossed zero, reflecting high uncertainty at the group level. This reduction in predictive power likely resulted from the greater variability introduced by combining heterogeneous immunological readouts. Nevertheless, the 95% PIs generally spanned a wide positive range, starting from or near zero, and consistently captured the distribution of independent individual responses. Thus, while the composite model represented inter-animal variability, its precision for estimating group-level means was markedly diminished. These findings suggest that individual readout models provided stronger and more reliable predictions for retrospective validation, whereas the composite model was less informative for distinguishing regimen-specific effects.

	Predicted mean	95% CI (model)	95% PI (model)	Observed mean	Within CI (Y/N	% animals within PI	
IgG	2342	-2381-7131*	-8001-12685	16721	N	1/12	8
PNA	2711	-9906-15505*	-24919-23100	22551	N	9/12	75
IFN-γ ELISpot	2355	1666-3045	858-3852	1997	Y	7/12	58
ASC spleen	1	-2-3*	-5-4	26	N	0/6	0
ASC BM	1	-24-25*	-52-44	66	N	0/6	0
ASC memory spleen	5	0-21	-7-22	36	N	2/6	33
ASC memory BM	-15	-44-14*	-78-49	59	N	3/6	50
IgG	59	-4963-5142*	-11754-11878	9725	N	7/11	63
PNA	-3387	-16802-10192*	-34946-23100	22435	N	9/11	81
IFN-γ ELISpot	1236	230-2241	-1132-3603	2425	N	11/11	100
ASC spleen	-0.59	-3-2*	-7-4	5	N	0/5	0
ASC BM	-11	-37-15*	-72-44	39	N	3/5	60
ASC memory spleen	5	-0.2-21	-7-22*	22	N	0/5	0
ASC memory BM	-2	-38-34*	-86-83	73	Y	5/5	100

Validation of model predictions against independent datasets of composite model.

Z-score outputs from the prediction profiler from composite models were back-transformed to the original measurement scale using group means and standard deviations for each readout. Data include the model-predicted mean, 95% confidence interval (CI), and 95% prediction interval (PI), alongside observed means from independent experiments (MERSIDT001, MERSIDT002). Validation at the group level was determined by

whether the observed mean lay within the model CI (Y/N), while individual-level validation was assessed as the percentage of animals falling within the PI. Readouts with CIs crossing zero (*) indicate uncertainty in prediction. “Model not significant” indicates lack of fit in the profiler. Results for Ad/MVA: light green and MVA/Ad dark green

9 References

1. Ahamed Vp, A., et al., *Jenner's Legacy: How Edward Jenner's Smallpox Vaccine Changed Public Health.* Cureus, 2024. **16**(9): p. e68594.
2. Pollard, A.J. and E.M. Bijker, *A guide to vaccinology: from basic principles to new developments.* Nature Reviews Immunology, 2021. **21**(2): p. 83-100.
3. Nobleprize, *NOBEL PRIZES 2023.* 2023.
4. Watson, O.J., et al., *Global impact of the first year of COVID-19 vaccination: a mathematical modelling study.* The Lancet Infectious Diseases, 2022. **22**(9): p. 1293-1302.
5. Abbas, A.K., A.H. Lichtman, and S. Pillai, *Cellular and Molecular Immunology*. 2021: Elsevier Health Sciences.
6. Pulendran, B. and R. Ahmed, *Immunological mechanisms of vaccination.* Nat Immunol, 2011. **12**(6): p. 509-17.
7. Siegrist, C.-A., *Vaccine Immunology*. 2018. p. 16-34.e7.
8. Randolph, G.J., V. Angeli, and M.A. Swartz, *Dendritic-cell trafficking to lymph nodes through lymphatic vessels.* Nat Rev Immunol, 2005. **5**(8): p. 617-28.
9. Pishesha, N., T.J. Harmand, and H.L. Ploegh, *A guide to antigen processing and presentation.* Nature Reviews Immunology, 2022. **22**(12): p. 751-764.
10. Lieberman, J., *The ABCs of granule-mediated cytotoxicity: new weapons in the arsenal.* Nature Reviews Immunology, 2003. **3**(5): p. 361-370.
11. Wissinger, E. *Cells T CD8+*. Available from: https://www.immunology.org/public-information/bitesized-immunology/cells/cells-t-cd8.
12. Henkart, P.A. and M.V. Sitkovsky, *Cytotoxic Lymphocytes: Two ways to kill target cells.* Current Biology, 1994. **4**(10): p. 923-925.
13. Halle, S., O. Halle, and R. Förster, *Mechanisms and Dynamics of T Cell-Mediated Cytotoxicity In Vivo.* Trends in Immunology, 2017. **38**(6): p. 432-443.
14. Tripathi, S.K. and R. Lahesmaa, *Transcriptional and epigenetic regulation of T-helper lineage specification.* Immunol Rev, 2014. **261**(1): p. 62-83.
15. Geginat, J., et al., *Plasticity of human CD4 T cell subsets.* Front Immunol, 2014. **5**: p. 630.
16. Khader, S.A., S.L. Gaffen, and J.K. Kolls, *Th17 cells at the crossroads of innate and adaptive immunity against infectious diseases at the mucosa.* Mucosal Immunology, 2009. **2**(5): p. 403-411.
17. Fan, X., et al., *Interactions between neutrophils and T-helper 17 cells.* 2023. **Volume 14 - 2023**.
18. Gilliet, M. and R.L. Modlin, *Immunobiology of IL-26.* J Invest Dermatol, 2024. **144**(6): p. 1217-1222.
19. Sakaguchi, S., et al., *FOXP3+ regulatory T cells in the human immune system.* Nat Rev Immunol, 2010. **10**(7): p. 490-500.
20. Mastelic Gavillet, B., et al., *MF59 Mediates Its B Cell Adjuvanticity by Promoting T Follicular Helper Cells and Thus Germinal Center Responses in Adult and Early Life.* J Immunol, 2015. **194**(10): p. 4836-45.
21. Bentebibel, S.E., et al., *Induction of ICOS+CXCR3+CXCR5+ TH cells correlates with antibody responses to influenza vaccination.* Sci Transl Med, 2013. **5**(176): p. 176ra32.
22. Foster, W.S., et al., *Tfh cells and the germinal center are required for memory B cell formation & humoral immunity after ChAdOx1 nCoV-19 vaccination.* Cell Rep Med, 2022. **3**(12): p. 100845.

23. Sallusto, F., et al., *Two subsets of memory T lymphocytes with distinct homing potentials and effector functions.* 1999. **401**(6754): p. 708-712.
24. Sallusto, F., J. Geginat, and A. Lanzavecchia, *Central Memory and Effector Memory T Cell Subsets: Function, Generation, and Maintenance.* 2004. **22**(Volume 22, 2004): p. 745-763.
25. Masopust, D. and A.G. Soerens, *Tissue-Resident T Cells and Other Resident Leukocytes.* Annu Rev Immunol, 2019. **37**: p. 521-546.
26. Xie, D., et al., *Tissue-resident memory T cells in diseases and therapeutic strategies.* MedComm, 2025. **6**(1): p. e70053.
27. MacLennan, I.C., et al., *The changing preference of T and B cells for partners as T-dependent antibody responses develop.* Immunol Rev, 1997. **156**: p. 53-66.
28. Eisenbarth, S.C., et al., *A roadmap for defining “extrafollicular” B cell responses.* Immunity, 2025. **58**(11): p. 2627-2645.
29. Allen, C.D.C., T. Okada, and J.G. Cyster, *Germinal-Center Organization and Cellular Dynamics.* Immunity, 2007. **27**(2): p. 190-202.
30. Ward, J.M., S. Cherian, and M.A. Linden, *19 - Hematopoietic and Lymphoid Tissues*, in *Comparative Anatomy and Histology (Second Edition)*, P.M. Treuting, S.M. Dintzis, and K.S. Montine, Editors. 2018, Academic Press: San Diego. p. 365-401.
31. MacLennan, I.C., et al., *Extrafollicular antibody responses.* 2003. **194**(1): p. 8-18.
32. Liu, Y.J., et al., *Sites of specific B cell activation in primary and secondary responses to T cell-dependent and T cell-independent antigens.* Eur J Immunol, 1991. **21**(12): p. 2951-62.
33. Stavnezer, J., J.E. Guikema, and C.E. Schrader, *Mechanism and regulation of class switch recombination.* Annu Rev Immunol, 2008. **26**: p. 261-92.
34. Victora, G.D. and M.C. Nussenzweig, *Germinal Centers.* Annu Rev Immunol, 2022. **40**: p. 413-442.
35. Li, Z., et al., *The generation of antibody diversity through somatic hypermutation and class switch recombination.* Genes Dev, 2004. **18**(1): p. 1-11.
36. Mesin, L., J. Ersching, and Gabriel D. Victora, *Germinal Center B Cell Dynamics.* Immunity, 2016. **45**(3): p. 471-482.
37. van de Bovenkamp, F.S., et al., *The Emerging Importance of IgG Fab Glycosylation in Immunity.* J Immunol, 2016. **196**(4): p. 1435-41.
38. Nimmerjahn, F. and J.V. Ravetch, *Fcγ receptors as regulators of immune responses.* Nature Reviews Immunology, 2008. **8**(1): p. 34-47.
39. Lu, L.L., et al., *Beyond binding: antibody effector functions in infectious diseases.* Nat Rev Immunol, 2018. **18**(1): p. 46-61.
40. Onoue, K., et al., *Immunoglobulin M antibodies with ten combining sites.* Science, 1968. **162**(3853): p. 574-6.
41. Czajkowsky, D.M. and Z. Shao, *The human IgM pentamer is a mushroom-shaped molecule with a flexural bias.* Proc Natl Acad Sci U S A, 2009. **106**(35): p. 14960-5.
42. Ferrante, A., L.J. Beard, and R.G. Feldman, *IgG subclass distribution of antibodies to bacterial and viral antigens.* Pediatr Infect Dis J, 1990. **9**(8 Suppl): p. S16-24.
43. Bindon, C.I., et al., *Human monoclonal IgG isotypes differ in complement activating function at the level of C4 as well as C1q.* J Exp Med, 1988. **168**(1): p. 127-42.
44. Bruhns, P., et al., *Specificity and affinity of human Fcγ receptors and their polymorphic variants for human IgG subclasses.* Blood, 2009. **113**(16): p. 3716-3725.
45. Corthesy, B., *Multi-Faceted Functions of Secretory IgA at Mucosal Surfaces.* Frontiers in Immunology, 2013. **4**(185).
46. Krugmann, S., et al., *Structural requirements for assembly of dimeric IgA probed by site-directed mutagenesis of J chain and a cysteine residue of the alpha-chain CH2 domain.* J Immunol, 1997. **159**(1): p. 244-9.
47. KERR, M.A., *Function of immunoglobulin A in immunity.* 2000. **47**(6): p. 751-752.
48. Monteiro, R.C. and J.G.J.A.r.o.i. Van De Winkel, *IgA fc receptors.* 2003. **21**(1): p. 177-204.

49. Vidarsson, G., G. Dekkers, and T. Rispens, *IgG subclasses and allotypes: from structure to effector functions.* Front Immunol, 2014. **5**: p. 520.
50. Mevorach, D., *Opsonization of apoptotic cells. Implications for uptake and autoimmunity.* Ann N Y Acad Sci, 2000. **926**: p. 226-35.
51. Dunkelberger, J.R. and W.-C. Song, *Complement and its role in innate and adaptive immune responses.* Cell Research, 2010. **20**(1): p. 34-50.
52. Ricklin, D., et al., *Complement: a key system for immune surveillance and homeostasis.* Nat Immunol, 2010. **11**(9): p. 785-97.
53. Carroll, M.C., *Complement and humoral immunity.* Vaccine, 2008. **26 Suppl 8**(0 8): p. I28-33.
54. Chen, T., et al., *Receptor-Mediated NETosis on Neutrophils.* Front Immunol, 2021. **12**: p. 775267.
55. Monsalve, D.M., et al., *NETosis: A key player in autoimmunity, COVID-19, and long COVID.* Journal of Translational Autoimmunity, 2025. **10**: p. 100280.
56. Thomas, S., et al., *Antibody-Dependent Enhancement (ADE) and the role of complement system in disease pathogenesis.* Molecular Immunology, 2022. **152**: p. 172-182.
57. Zohar, T. and G. Alter, *Dissecting antibody-mediated protection against SARS-CoV-2.* Nature Reviews Immunology, 2020. **20**(7): p. 392-394.
58. Taylor, A., et al., *Fc receptors in antibody-dependent enhancement of viral infections.* Immunol Rev, 2015. **268**(1): p. 340-64.
59. Dejnirattisai, W., et al., *Cross-Reacting Antibodies Enhance Dengue Virus Infection in Humans.* 2010. **328**(5979): p. 745-748.
60. Gartlan, C., et al., *Vaccine-Associated Enhanced Disease and Pathogenic Human Coronaviruses.* Front Immunol, 2022. **13**: p. 882972.
61. Lee, W.S., et al., *Antibody-dependent enhancement and SARS-CoV-2 vaccines and therapies.* Nature Microbiology, 2020. **5**(10): p. 1185-1191.
62. Bournazos, S. and J.V. Ravetch, *Fcγ receptor pathways during active and passive immunization.* Immunol Rev, 2015. **268**(1): p. 88-103.
63. Orange, J.S., *Formation and function of the lytic NK-cell immunological synapse.* Nat Rev Immunol, 2008. **8**(9): p. 713-25.
64. Bruhns, P. and F. Jönsson, *Mouse and human FcR effector functions.* Immunol Rev, 2015. **268**(1): p. 25-51.
65. Zhang, A., et al., *Beyond neutralization: Fc-dependent antibody effector functions in SARS-CoV-2 infection.* Nature Reviews Immunology, 2023. **23**(6): p. 381-396.
66. Doeing, D.C., J.L. Borowicz, and E.T. Crockett, *Gender dimorphism in differential peripheral blood leukocyte counts in mice using cardiac, tail, foot, and saphenous vein puncture methods.* BMC Clin Pathol, 2003. **3**(1): p. 3.
67. Nimmerjahn, F. and J.V. Ravetch, *Fcgamma receptors as regulators of immune responses.* Nat Rev Immunol, 2008. **8**(1): p. 34-47.
68. Smith, P., et al., *Mouse model recapitulating human Fcγ receptor structural and functional diversity.* Proc Natl Acad Sci U S A, 2012. **109**(16): p. 6181-6.
69. Neuberger, M.S. and K. Rajewsky, *Activation of mouse complement by monoclonal mouse antibodies.* Eur J Immunol, 1981. **11**(12): p. 1012-6.
70. Perlmutter, R.M., et al., *Subclass restriction of murine anti-carbohydrate antibodies.* J Immunol, 1978. **121**(2): p. 566-72.
71. Martin, R.M., J.L. Brady, and A.M. Lew, *The need for IgG2c specific antiserum when isotyping antibodies from C57BL/6 and NOD mice.* J Immunol Methods, 1998. **212**(2): p. 187-92.
72. Plotkin, S.A., *Correlates of protection induced by vaccination.* Clin Vaccine Immunol, 2010. **17**(7): p. 1055-65.
73. Taranger, J., et al., *Correlation between pertussis toxin IgG antibodies in postvaccination sera and subsequent protection against pertussis.* J Infect Dis, 2000. **181**(3): p. 1010-3.

74. Jack, A.D., et al., *What level of hepatitis B antibody is protective?* J Infect Dis, 1999. **179**(2): p. 489-92.
75. Edsall, G., *Specific prophylaxis of tetanus.* J Am Med Assoc, 1959. **171**: p. 417-27.
76. Dowdle, W.R., et al., *Inactivated influenza vaccines. 2. Laboratory indices of protection.* Postgrad Med J, 1973. **49**(569): p. 159-63.
77. Lee, L.H., et al., *Correlates of immunity for pneumococcal conjugate vaccines.* Vaccine, 2003. **21**(17-18): p. 2190-6.
78. Roncati, L. and M. Roncati, *Emergency use authorization (EUA), conditional marketing authorization (CMA), and the precautionary principle at the time of COVID-19 pandemic.* J Public Health Policy, 2021. **42**(3): p. 518-521.
79. Cruz, P., et al., *Immunobridging Trials: An Important Tool to Protect Vulnerable and Immunocompromised Patients Against Evolving Pathogens.* Vaccines, 2024. **13**: p. 19.
80. Marinus, R., et al., *Rolling Reviews During COVID-19: The European Union Experience in a Global Context.* Clinical Therapeutics, 2022. **44**(3): p. 352-363.
81. Campbell, J.D., et al., *Immunologic non-inferiority of a newly licensed inactivated trivalent influenza vaccine versus an established vaccine: a randomized study in US adults.* Hum Vaccin, 2011. **7**(1): p. 81-8.
82. Bockstal, V., et al., *Non-human primate to human immunobridging demonstrates a protective effect of Ad26.ZEBOV, MVA-BN-Filo vaccine against Ebola.* npj Vaccines, 2022. **7**(1): p. 156.
83. Roozendaal, R., et al., *Nonhuman primate to human immunobridging to infer the protective effect of an Ebola virus vaccine candidate.* NPJ Vaccines, 2020. **5**(1): p. 112.
84. EMA, *Zabdeno*

ebola vaccine (Ad26.ZEBOV-GP [recombinant]).
85. EMA, *Mvabea.* 2020.
86. Folegatti, P.M., et al., *Comparative assessment of immunogenicity and safety of recombinant influenza vaccine in children, adolescents, and adults: results from a phase 3, immunobridging, open-label, non-randomised study.* The Lancet Infectious Diseases, 2025. **25**(10): p. 1097-1105.
87. Jastorff, A., et al., *Safety and immunogenicity of the Ad26/protein preF RSV vaccine in adults aged 18 to 59 years with and without at-risk comorbidities for severe respiratory syncytial virus disease: A phase 3, randomized, controlled, immunobridging trial.* Vaccine, 2025. **43**: p. 126514.
88. Reiter, L., et al., *Comparable safety and non-inferior immunogenicity of the SARS-CoV-2 mRNA vaccine candidate PTX-COVID19-B and BNT162b2 in a phase 2 randomized, observer-blinded study.* Scientific Reports, 2024. **14**(1): p. 5365.
89. Delaloye, J., et al., *Innate immune sensing of modified vaccinia virus Ankara (MVA) is mediated by TLR2-TLR6, MDA-5 and the NALP3 inflammasome.* PLoS pathogens, 2009. **5**: p. e1000480.
90. Zhu, J., X. Huang, and Y. Yang, *Innate immune response to adenoviral vectors is mediated by both Toll-like receptor-dependent and -independent pathways.* J Virol, 2007. **81**(7): p. 3170-80.
91. Molinier-Frenkel, V., et al., *Adenovirus hexon protein is a potent adjuvant for activation of a cellular immune response.* J Virol, 2002. **76**(1): p. 127-35.
92. Dai, P., et al., *Modified vaccinia virus Ankara triggers type I IFN production in murine conventional dendritic cells via a cGAS/STING-mediated cytosolic DNA-sensing pathway.* PLoS Pathog, 2014. **10**(4): p. e1003989.
93. Graham, F.L. and L. Prevec, *Methods for construction of adenovirus vectors.* Molecular Biotechnology, 1995. **3**(3): p. 207-220.
94. Coughlan, L., *Factors Which Contribute to the Immunogenicity of Non-replicating Adenoviral Vectored Vaccines.* Front Immunol, 2020. **11**: p. 909.

95. Folegatti, P.M., et al., *Safety and immunogenicity of the ChAdOx1 nCoV-19 vaccine against SARS-CoV-2: a preliminary report of a phase 1/2, single-blind, randomised controlled trial.* Lancet, 2020. **396**(10249): p. 467-478.
96. Ramasamy, M.N., et al., *Safety and immunogenicity of ChAdOx1 nCoV-19 vaccine administered in a prime-boost regimen in young and old adults (COV002): a single-blind, randomised, controlled, phase 2/3 trial.* The Lancet, 2020. **396**(10267): p. 1979-1993.
97. Voysey, M., et al., *Safety and efficacy of the ChAdOx1 nCoV-19 vaccine (AZD1222) against SARS-CoV-2: an interim analysis of four randomised controlled trials in Brazil, South Africa, and the UK.* The Lancet, 2021. **397**(10269): p. 99-111.
98. Barouch, D.H., et al., *Durable Humoral and Cellular Immune Responses 8 Months after Ad26.COV2.S Vaccination.* N Engl J Med, 2021. **385**(10): p. 951-953.
99. Sadoff, J., et al., *Safety and Efficacy of Single-Dose Ad26.COV2.S Vaccine against Covid-19.* N Engl J Med, 2021. **384**(23): p. 2187-2201.
100. Logunov, D.Y., et al., *Safety and efficacy of an rAd26 and rAd5 vector-based heterologous prime-boost COVID-19 vaccine: an interim analysis of a randomised controlled phase 3 trial in Russia.* Lancet, 2021. **397**(10275): p. 671-681.
101. Logunov, D.Y., et al., *Safety and immunogenicity of an rAd26 and rAd5 vector-based heterologous prime-boost COVID-19 vaccine in two formulations: two open, non-randomised phase 1/2 studies from Russia.* Lancet, 2020. **396**(10255): p. 887-897.
102. Halperin, S.A., et al., *Final efficacy analysis, interim safety analysis, and immunogenicity of a single dose of recombinant novel coronavirus vaccine (adenovirus type 5 vector) in adults 18 years and older: an international, multicentre, randomised, double-blinded, placebo-controlled phase 3 trial.* Lancet, 2022. **399**(10321): p. 237-248.
103. Zhu, F.C., et al., *Immunogenicity and safety of a recombinant adenovirus type-5-vectored COVID-19 vaccine in healthy adults aged 18 years or older: a randomised, double-blind, placebo-controlled, phase 2 trial.* Lancet, 2020. **396**(10249): p. 479-488.
104. Dicks, M.D.J., et al., *A Novel Chimpanzee Adenovirus Vector with Low Human Seroprevalence: Improved Systems for Vector Derivation and Comparative Immunogenicity.* PLOS ONE, 2012. **7**(7): p. e40385.
105. Coughlan, L., et al., *Heterologous Two-Dose Vaccination with Simian Adenovirus and Poxvirus Vectors Elicits Long-Lasting Cellular Immunity to Influenza Virus A in Healthy Adults.* eBioMedicine, 2018. **29**: p. 146-154.
106. Ewer, K.J., et al., *Protective CD8+ T-cell immunity to human malaria induced by chimpanzee adenovirus-MVA immunisation.* Nat Commun, 2013. **4**: p. 2836.
107. Ewer, K., et al., *A Monovalent Chimpanzee Adenovirus Ebola Vaccine Boosted with MVA.* New England Journal of Medicine, 2015. **374**(17): p. 1635-1646.
108. Ramasamy, M.N., et al., *Safety and immunogenicity of ChAdOx1 nCoV-19 vaccine administered in a prime-boost regimen in young and old adults (COV002): a single-blind, randomised, controlled, phase 2/3 trial.* Lancet, 2021. **396**(10267): p. 1979-1993.
109. Frater, J., et al., *Safety and immunogenicity of the ChAdOx1 nCoV-19 (AZD1222) vaccine against SARS-CoV-2 in HIV infection: a single-arm substudy of a phase 2/3 clinical trial.* Lancet HIV, 2021. **8**(8): p. e474-e485.
110. Airfinity. *AstraZeneca and Pfizer/BioNTech saved over 12 million lives in the first year of vaccination*. 2022; Available from: https://www.airfinity.com/articles/astrazeneca-and-pfizer-biontech-saved-over-12-million-lives-in-the-first.
111. Lopez Bernal, J., et al., *Effectiveness of the Pfizer-BioNTech and Oxford-AstraZeneca vaccines on covid-19 related symptoms, hospital admissions, and mortality in older adults in England: test negative case-control study.* Bmj, 2021. **373**: p. n1088.
112. Greinacher, A., et al., *Thrombotic Thrombocytopenia after ChAdOx1 nCov-19 Vaccination.* N Engl J Med, 2021. **384**(22): p. 2092-2101.

113. Scully, M., et al., *Pathologic Antibodies to Platelet Factor 4 after ChAdOx1 nCoV-19 Vaccination.* N Engl J Med, 2021. **384**(23): p. 2202-2211.
114. Clerici, B., et al., *Thrombosis and Bleeding in Patients with Vaccine-Induced Immune Thrombotic Thrombocytopenia: A Systematic Review of Published Cases.* Thromb Haemost, 2024. **124**(5): p. 423-431.
115. Toh, C.-H., G. Wang, and A.L. Parker, *The aetiopathogenesis of vaccine-induced immune thrombotic thrombocytopenia.* Clinical Medicine, 2022. **22**(2): p. 140-144.
116. Matschke, J., et al., *Fatal Cerebral Venous Sinus Thrombosis and Thrombocytopenia due to Anti-PF4 Disorder Following Adenovirus Infection in a 3-year-old Boy.* Thromb Haemost, 2025. **125**(9): p. 919-922.
117. Uzun, G., et al., *Cerebral venous sinus thrombosis and thrombocytopenia due to heparin-independent anti-PF4 antibodies after adenovirus infection.* Haematologica, 2024. **109**(6): p. 2010-2015.
118. Pavord, S., et al., *Clinical Features of Vaccine-Induced Immune Thrombocytopenia and Thrombosis.* N Engl J Med, 2021. **385**(18): p. 1680-1689.
119. Arman, M. and K. Krauel, *Human platelet IgG Fc receptor FcγRIIA in immunity and thrombosis.* J Thromb Haemost, 2015. **13**(6): p. 893-908.
120. Pombal, R., L. Silva, and D. Ferreira, *Genetic Predisposition to Vaccine-Induced Immune Thrombotic Thrombocytopenia: is there a Family Link?* Eur J Case Rep Intern Med, 2024. **11**(6): p. 004546.
121. Folegatti, P.M., et al., *Vaccines based on the replication-deficient simian adenoviral vector ChAdOx1: Standardized template with key considerations for a risk/benefit assessment.* Vaccine, 2022. **40**(35): p. 5248-5262.
122. Strassburg, M.A., *The global eradication of smallpox.* American Journal of Infection Control, 1982. **10**(2): p. 53-59.
123. Antoine, G., et al., *Corrigendum to "The complete genomic sequence of the modified vaccinia Ankara (MVA) strain: Comparison with other orthopoxviruses" [Virology 244 (1998) 365-396].* Virology, 2006. **350**(2): p. 501-502.
124. Mayr, A., et al., *[The smallpox vaccination strain MVA: marker, genetic structure, experience gained with the parenteral vaccination and behavior in organisms with a debilitated defence mechanism (author's transl)].* Zentralbl Bakteriol B, 1978. **167**(5-6): p. 375-90.
125. Meisinger-Henschel, C., et al., *Genomic sequence of chorioallantois vaccinia virus Ankara, the ancestor of modified vaccinia virus Ankara.* J Gen Virol, 2007. **88**(Pt 12): p. 3249-3259.
126. Meyer, H., G. Sutter, and A. Mayr, *Mapping of deletions in the genome of the highly attenuated vaccinia virus MVA and their influence on virulence.* J Gen Virol, 1991. **72 (Pt 5)**: p. 1031-8.
127. Pischel, L., et al., *Vaccine effectiveness of 3rd generation mpox vaccines against mpox and disease severity: A systematic review and meta-analysis.* Vaccine, 2024. **42**(25): p. 126053.
128. WHO, *MVA-BN (Modified Vaccinia Ankara – Bavarian Nordic) smallpox and mpox vaccine.* 2024.
129. Tscherne, A., et al., *Immunogenicity and efficacy of the COVID-19 candidate vector vaccine MVA-SARS-2-S in preclinical vaccination.* Proc Natl Acad Sci U S A, 2021. **118**(28).
130. Mayer, L., et al., *MVA-based vaccine candidates encoding the native or prefusion-stabilized SARS-CoV-2 spike reveal differential immunogenicity in humans.* npj Vaccines, 2024. **9**(1): p. 20.
131. Masters, P.S., et al., *Genetic and molecular biological analysis of protein-protein interactions in coronavirus assembly.* Adv Exp Med Biol, 2006. **581**: p. 163-73.
132. Bezerra, P.R. and F.C.L. Almeida, *Structural basis for the participation of the SARS-CoV-2 nucleocapsid protein in the template switch mechanism and genomic RNA reorganization.* Journal of Biological Chemistry, 2024. **300**(11): p. 107834.

133. Lai, M.M.C. and D. Cavanagh, *The Molecular Biology of Coronaviruses*, in *Advances in Virus Research*, K. Maramorosch, F.A. Murphy, and A.J. Shatkin, Editors. 1997, Academic Press. p. 1-100.
134. Lang, Y., et al., *Coronavirus hemagglutinin-esterase and spike proteins coevolve for functional balance and optimal virion avidity.* Proceedings of the National Academy of Sciences, 2020. **117**(41): p. 25759-25770.
135. Monto, A.S., et al., *Coronavirus Occurrence and Transmission Over 8 Years in the HIVE Cohort of Households in Michigan.* J Infect Dis, 2020. **222**(1): p. 9-16.
136. Shah, M.M., et al., *Seasonality of Common Human Coronaviruses, United States, 2014-2021(1).* Emerg Infect Dis, 2022. **28**(10): p. 1970-1976.
137. Nickbakhsh, S., et al., *Epidemiology of Seasonal Coronaviruses: Establishing the Context for the Emergence of Coronavirus Disease 2019.* J Infect Dis, 2020. **222**(1): p. 17-25.
138. Reed, S.E., *The behaviour of recent isolates of human respiratory coronavirus in vitro and in volunteers: evidence of heterogeneity among 229E-related strains.* J Med Virol, 1984. **13**(2): p. 179-92.
139. Gagneur, A., et al., *Outbreaks of human coronavirus in a pediatric and neonatal intensive care unit.* Eur J Pediatr, 2008. **167**(12): p. 1427-34.
140. Falsey, A.R., et al., *Long-term care facilities: a cornucopia of viral pathogens.* J Am Geriatr Soc, 2008. **56**(7): p. 1281-5.
141. Monto, A.S., *Medical reviews. Coronaviruses.* Yale J Biol Med, 1974. **47**(4): p. 234-51.
142. Birch, C.J., et al., *Human coronavirus OC43 causes influenza-like illness in residents and staff of aged-care facilities in Melbourne, Australia.* Epidemiol Infect, 2005. **133**(2): p. 273-7.
143. Patrick, D.M., et al., *An Outbreak of Human Coronavirus OC43 Infection and Serological Cross-reactivity with SARS Coronavirus.* Can J Infect Dis Med Microbiol, 2006. **17**(6): p. 330-6.
144. Zaki, A.M., et al., *Isolation of a novel coronavirus from a man with pneumonia in Saudi Arabia.* N Engl J Med, 2012. **367**(19): p. 1814-20.
145. Drosten, C., et al., *Identification of a novel coronavirus in patients with severe acute respiratory syndrome.* N Engl J Med, 2003. **348**(20): p. 1967-76.
146. Cheng, V.C., et al., *Severe acute respiratory syndrome coronavirus as an agent of emerging and reemerging infection.* Clin Microbiol Rev, 2007. **20**(4): p. 660-94.
147. Casassus, B., *MERS: France confirms first cases in 12 years.* 2025. **391**: p. r2577.
148. Alimohamadi, Y., et al., *Case fatality rate of COVID-19: a systematic review and meta-analysis.* J Prev Med Hyg, 2021. **62**(2): p. E311-e320.
149. Zhu, N., et al., *A Novel Coronavirus from Patients with Pneumonia in China, 2019.* N Engl J Med, 2020. **382**(8): p. 727-733.
150. Cucinotta, D. and M. Vanelli, *WHO Declares COVID-19 a Pandemic.* Acta Biomed, 2020. **91**(1): p. 157-160.
151. Markov, P.V., et al., *The evolution of SARS-CoV-2.* Nat Rev Microbiol, 2023. **21**(6): p. 361-379.
152. Wang, L.F. and D.E. Anderson, *Viruses in bats and potential spillover to animals and humans.* Curr Opin Virol, 2019. **34**: p. 79-89.
153. Li, Q., et al., *Early transmission dynamics in Wuhan, China, of novel coronavirus–infected pneumonia.* 2020. **382**(13): p. 1199-1207.
154. Wan, Y., et al., *Receptor recognition by the novel coronavirus from Wuhan: an analysis based on decade-long structural studies of SARS coronavirus.* 2020. **94**(7): p. 10.1128/jvi. 00127-20.
155. Petrosillo, N., et al., *COVID-19, SARS and MERS: are they closely related?* Clinical Microbiology and Infection, 2020. **26**(6): p. 729-734.
156. He, X., et al., *Temporal dynamics in viral shedding and transmissibility of COVID-19.* Nature Medicine, 2020. **26**(5): p. 672-675.
157. Peiris, J.S., et al., *Clinical progression and viral load in a community outbreak of coronavirus-associated SARS pneumonia: a prospective study.* Lancet, 2003. **361**(9371): p. 1767-72.

158. Oh, M.D., et al., *Viral Load Kinetics of MERS Coronavirus Infection.* N Engl J Med, 2016. **375**(13): p. 1303-5.
159. Li, F., *Structure, Function, and Evolution of Coronavirus Spike Proteins.* Annu Rev Virol, 2016. **3**(1): p. 237-261.
160. *Virology: Coronaviruses.* Nature, 1968. **220**(5168): p. 650-650.
161. Focosi, D., et al., *An update on the anti-spike monoclonal antibody pipeline for SARS-CoV-2.* Clinical Microbiology and Infection, 2024. **30**(8): p. 999-1006.
162. Salvatori, G., et al., *SARS-CoV-2 SPIKE PROTEIN: an optimal immunological target for vaccines.* J Transl Med, 2020. **18**(1): p. 222.
163. Premkumar, L., et al., *The receptor-binding domain of the viral spike protein is an immunodominant and highly specific target of antibodies in SARS-CoV-2 patients.* Science Immunology, 2020. **5**(48): p. eabc8413.
164. Silva, R.P., et al., *Identification of a conserved S2 epitope present on spike proteins from all highly pathogenic coronaviruses.* Elife, 2023. **12**.
165. Chau, N., et al., *Investigating spike S2 subunit hairpin proteins of the SARS-CoV-2 virus.* Biophysical Journal, 2024. **123**(3): p. 480a.
166. Corman Victor, M., et al., *Evidence for an Ancestral Association of Human Coronavirus 229E with Bats.* Journal of Virology, 2015. **89**(23): p. 11858-11870.
167. Milewska, A., et al., *Human coronavirus NL63 utilizes heparan sulfate proteoglycans for attachment to target cells.* J Virol, 2014. **88**(22): p. 13221-30.
168. Yeager, C.L., et al., *Human aminopeptidase N is a receptor for human coronavirus 229E.* Nature, 1992. **357**(6377): p. 420-2.
169. Ansil, B.R., et al., *229E- and NL63-like coronaviruses in phyllostomid bats, Belize.* One Health, 2025. **21**: p. 101147.
170. Castillo, G., et al., *Molecular mechanisms of human coronavirus NL63 infection and replication.* Virus Research, 2023. **327**: p. 199078.
171. Stout, A.E., et al., *Furin cleavage sites in the spike proteins of bat and rodent coronaviruses: Implications for virus evolution and zoonotic transfer from rodent species.* One Health, 2021. **13**: p. 100282.
172. Kin, N., et al., *Comparative molecular epidemiology of two closely related coronaviruses, bovine coronavirus (BCoV) and human coronavirus OC43 (HCoV-OC43), reveals a different evolutionary pattern.* Infect Genet Evol, 2016. **40**: p. 186-191.
173. Vlasak, R., et al., *Human and bovine coronaviruses recognize sialic acid-containing receptors similar to those of influenza C viruses.* Proc Natl Acad Sci U S A, 1988. **85**(12): p. 4526-9.
174. Huang, X., et al., *Human Coronavirus HKU1 Spike Protein Uses O-Acetylated Sialic Acid as an Attachment Receptor Determinant and Employs Hemagglutinin-Esterase Protein as a Receptor-Destroying Enzyme.* J Virol, 2015. **89**(14): p. 7202-13.
175. Wang, L.F. and B.T. Eaton, *Bats, civets and the emergence of SARS.* Curr Top Microbiol Immunol, 2007. **315**: p. 325-44.
176. Hoffmann, M., et al., *SARS-CoV-2 Cell Entry Depends on ACE2 and TMPRSS2 and Is Blocked by a Clinically Proven Protease Inhibitor.* Cell, 2020. **181**(2): p. 271-280.e8.
177. Letko, M., A. Marzi, and V. Munster, *Functional assessment of cell entry and receptor usage for SARS-CoV-2 and other lineage B betacoronaviruses.* Nat Microbiol, 2020. **5**(4): p. 562-569.
178. Mathewson, A.C., et al., *Interaction of severe acute respiratory syndrome-coronavirus and NL63 coronavirus spike proteins with angiotensin converting enzyme-2.* J Gen Virol, 2008. **89**(Pt 11): p. 2741-2745.
179. Raj, V.S., et al., *Dipeptidyl peptidase 4 is a functional receptor for the emerging human coronavirus-EMC.* Nature, 2013. **495**(7440): p. 251-254.
180. Yang, D., *Application of Nanotechnology in the COVID-19 Pandemic.* International Journal of Nanomedicine, 2021. **Volume 16**: p. 623-649.

181. Francis, T., *On the Doctrine of Original Antigenic Sin.* Proceedings of the American Philosophical Society, 1960. **104**(6): p. 572-578.
182. Henry, C., et al., *From Original Antigenic Sin to the Universal Influenza Virus Vaccine.* Trends Immunol, 2018. **39**(1): p. 70-79.
183. Lessler, J., et al., *Evidence for Antigenic Seniority in Influenza A (H3N2) Antibody Responses in Southern China.* PLOS Pathogens, 2012. **8**(7): p. e1002802.
184. Fonville, J.M., et al., *Antibody landscapes after influenza virus infection or vaccination.* Science, 2014. **346**(6212): p. 996-1000.
185. Kohler, H., *Novel vaccine concept based on back-boost effect in viral infection.* Vaccine, 2015. **33**(29): p. 3274-5.
186. Murray, S.M., et al., *The impact of pre-existing cross-reactive immunity on SARS-CoV-2 infection and vaccine responses.* Nature Reviews Immunology, 2023. **23**(5): p. 304-316.
187. Ng, K.W., et al., *Preexisting and de novo humoral immunity to SARS-CoV-2 in humans.* Science, 2020. **370**(6522): p. 1339-1343.
188. Wang, C., et al., *A conserved immunogenic and vulnerable site on the coronavirus spike protein delineated by cross-reactive monoclonal antibodies.* Nature Communications, 2021. **12**(1): p. 1715.
189. Aguilar-Bretones, M., et al., *Seasonal coronavirus–specific B cells with limited SARS-CoV-2 cross-reactivity dominate the IgG response in severe COVID-19.* The Journal of Clinical Investigation, 2021. **131**(21).
190. Lin, C.-Y., et al., *Pre-existing humoral immunity to human common cold coronaviruses negatively impacts the protective SARS-CoV-2 antibody response.* Cell Host & Microbe, 2022. **30**(1): p. 83-96.e4.
191. Hu, C., et al., *Pre-existing anti-HCoV-OC43 immunity influences the durability and cross-reactivity of humoral response to SARS-CoV-2 vaccination.* 2022. **Volume 12 - 2022**.
192. Asamoah-Boaheng, M., et al., *Are higher antibody levels against seasonal human coronaviruses associated with a more robust humoral immune response after SARS-CoV-2 vaccination?* Front Immunol, 2022. **13**: p. 954093.
193. Loyal, L., et al., *Cross-reactive CD4(+) T cells enhance SARS-CoV-2 immune responses upon infection and vaccination.* Science, 2021. **374**(6564): p. eabh1823.
194. Mateus, J., et al., *Low-dose mRNA-1273 COVID-19 vaccine generates durable memory enhanced by cross-reactive T cells.* Science, 2021. **374**(6566): p. eabj9853.
195. Ogbe, A., et al., *Durability of ChAdOx1 nCoV-19 vaccination in people living with HIV.* JCI Insight, 2022. **7**(7).
196. Ozono, S., et al., *SARS-CoV-2 D614G spike mutation increases entry efficiency with enhanced ACE2-binding affinity.* Nat Commun, 2021. **12**(1): p. 848.
197. Liu, Y., et al., *The N501Y spike substitution enhances SARS-CoV-2 infection and transmission.* Nature, 2022. **602**(7896): p. 294-299.
198. Xie, X., et al., *Neutralization of SARS-CoV-2 spike 69/70 deletion, E484K and N501Y variants by BNT162b2 vaccine-elicited sera.* Nat Med, 2021. **27**(4): p. 620-621.
199. Faria, N.R., et al., *Genomics and epidemiology of the P.1 SARS-CoV-2 lineage in Manaus, Brazil.* Science, 2021. **372**(6544): p. 815-821.
200. Dougherty, K., et al., *SARS-CoV-2 B.1.617.2 (Delta) Variant COVID-19 Outbreak Associated with a Gymnastics Facility - Oklahoma, April-May 2021.* MMWR Morb Mortal Wkly Rep, 2021. **70**(28): p. 1004-1007.
201. Barut, G.T., et al., *The spike gene is a major determinant for the SARS-CoV-2 Omicron-BA.1 phenotype.* Nat Commun, 2022. **13**(1): p. 5929.
202. Reuschl, A.K., et al., *Evolution of enhanced innate immune suppression by SARS-CoV-2 Omicron subvariants.* Nat Microbiol, 2024. **9**(2): p. 451-463.
203. Willett, B.J., et al., *SARS-CoV-2 Omicron is an immune escape variant with an altered cell entry pathway.* Nature Microbiology, 2022. **7**(8): p. 1161-1179.

204. Viana, R., et al., *Rapid epidemic expansion of the SARS-CoV-2 Omicron variant in southern Africa.* Nature, 2022. **603**(7902): p. 679-686.
205. Cao, Y., et al., *Imprinted SARS-CoV-2 humoral immunity induces convergent Omicron RBD evolution.* Nature, 2023. **614**(7948): p. 521-529.
206. Tegally, H., et al., *Emergence of SARS-CoV-2 Omicron lineages BA.4 and BA.5 in South Africa.* Nat Med, 2022. **28**(9): p. 1785-1790.
207. Mackin, S.R., et al., *Fc-γR-dependent antibody effector functions are required for vaccine-mediated protection against antigen-shifted variants of SARS-CoV-2.* Nat Microbiol, 2023. **8**(4): p. 569-580.
208. Zaki, A.M., et al., *Isolation of a novel coronavirus from a man with pneumonia in Saudi Arabia.* New England Journal of Medicine, 2012. **367**(19): p. 1814-1820.
209. Memish, Z.A., et al., *Middle East respiratory syndrome coronavirus in bats, Saudi Arabia.* Emerg Infect Dis, 2013. **19**(11): p. 1819-23.
210. Müller, M.A., et al., *MERS coronavirus neutralizing antibodies in camels, Eastern Africa, 1983-1997.* Emerg Infect Dis, 2014. **20**(12): p. 2093-5.
211. Park, J.-E., et al., *MERS transmission and risk factors: a systematic review.* BMC Public Health, 2018. **18**(1): p. 574.
212. Control, E.C.f.D.P.a., *Distribution of confirmed cases of MERS by place of infection and month of onset, April 2012 to October 2025.* 2025.
213. Mohd, H.A., J.A. Al-Tawfiq, and Z.A. Memish, *Middle East Respiratory Syndrome Coronavirus (MERS-CoV) origin and animal reservoir.* Virology Journal, 2016. **13**(1): p. 87.
214. Dighe, A., T. Jombart, and N. Ferguson, *Modelling transmission of Middle East respiratory syndrome coronavirus in camel populations and the potential impact of animal vaccination.* Nature Communications, 2025. **16**(1): p. 7679.
215. Conzade, R., et al., *Reported Direct and Indirect Contact with Dromedary Camels among Laboratory-Confirmed MERS-CoV Cases.* Viruses, 2018. **10**(8).
216. Alraddadi, B.M., et al., *Risk Factors for Primary Middle East Respiratory Syndrome Coronavirus Illness in Humans, Saudi Arabia, 2014.* Emerg Infect Dis, 2016. **22**(1): p. 49-55.
217. Azhar, E.I., et al., *Evidence for Camel-to-Human Transmission of MERS Coronavirus.* 2014. **370**(26): p. 2499-2505.
218. Mostafa, A., et al., *Middle East Respiratory Syndrome Coronavirus (MERS-CoV): State of the Science.* Microorganisms, 2020. **8**(7).
219. Oboho, I.K., et al., *2014 MERS-CoV Outbreak in Jeddah — A Link to Health Care Facilities.* 2015. **372**(9): p. 846-854.
220. Alraddadi, B.M., et al., *Risk Factors for Middle East Respiratory Syndrome Coronavirus Infection among Healthcare Personnel.* Emerg Infect Dis, 2016. **22**(11): p. 1915-1920.
221. Lee, J.Y., et al., *The clinical and virological features of the first imported case causing MERS-CoV outbreak in South Korea, 2015.* BMC Infectious Diseases, 2017. **17**(1): p. 498.
222. Cho, S.Y., et al., *MERS-CoV outbreak following a single patient exposure in an emergency room in South Korea: an epidemiological outbreak study.* The Lancet, 2016. **388**(10048): p. 994-1001.
223. Kim, S.W., et al., *Risk Factors for Transmission of Middle East Respiratory Syndrome Coronavirus Infection During the 2015 Outbreak in South Korea.* Clinical Infectious Diseases, 2017. **64**(5): p. 551-557.
224. Lee, S.S. and N.S. Wong, *Probable transmission chains of Middle East respiratory syndrome coronavirus and the multiple generations of secondary infection in South Korea.* International Journal of Infectious Diseases, 2015. **38**: p. 65-67.
225. Ko, J.-H., et al., *Host susceptibility to MERS-CoV infection, a retrospective cohort study of the 2015 Korean MERS outbreak.* Journal of Infection and Chemotherapy, 2018. **24**(2): p. 150-152.

226. Hajeer, A.H., et al., *Association of human leukocyte antigen class II alleles with severe Middle East respiratory syndrome-coronavirus infection.* Ann Thorac Med, 2016. **11**(3): p. 211-3.
227. Azhar, E.I., et al., *The Qatar FIFA World Cup 2022 and camel pageant championships increase risk of MERS-CoV transmission and global spread.* The Lancet Global Health, 2023. **11**(2): p. e189-e190.
228. news, A., *Hajj moves on: Pilgrimage shifts to cooler seasons for next 25 years.* 2025.
229. van Doremalen, N., T. Bushmaker, and V.J. Munster, *Stability of Middle East respiratory syndrome coronavirus (MERS-CoV) under different environmental conditions.* Euro Surveill, 2013. **18**(38).
230. Jiang, S. and F. Wu, *Global surveillance and countermeasures for ACE2-using MERS-related coronaviruses with spillover risk.* Cell, 2025. **188**(6): p. 1465-1468.
231. Wang, Q., L. Sun, and S. Jiang, *Potential recombination between SARS-CoV-2 and MERS-CoV: calls for the development of Pan-CoV vaccines.* Signal Transduction and Targeted Therapy, 2023. **8**(1): p. 122.
232. Sabir, J.S., et al., *Co-circulation of three camel coronavirus species and recombination of MERS-CoVs in Saudi Arabia.* Science, 2016. **351**(6268): p. 81-4.
233. Kim, J.I., et al., *The recent ancestry of Middle East respiratory syndrome coronavirus in Korea has been shaped by recombination.* Sci Rep, 2016. **6**: p. 18825.
234. Ng, D.L., et al., *Clinicopathologic, Immunohistochemical, and Ultrastructural Findings of a Fatal Case of Middle East Respiratory Syndrome Coronavirus Infection in the United Arab Emirates, April 2014.* Am J Pathol, 2016. **186**(3): p. 652-8.
235. Alsaad, K.O., et al., *Histopathology of Middle East respiratory syndrome coronovirus (MERS-CoV) infection - clinicopathological and ultrastructural study.* Histopathology, 2018. **72**(3): p. 516-524.
236. Batawi, S., et al., *Quality of life reported by survivors after hospitalization for Middle East respiratory syndrome (MERS).* Health Qual Life Outcomes, 2019. **17**(1): p. 101.
237. Arabi, Y.M., et al., *Interferon Beta-1b and Lopinavir-Ritonavir for Middle East Respiratory Syndrome.* N Engl J Med, 2020. **383**(17): p. 1645-1656.
238. Falzarano, D., et al., *Treatment with interferon-α2b and ribavirin improves outcome in MERS-CoV-infected rhesus macaques.* Nat Med, 2013. **19**(10): p. 1313-7.
239. Omrani, A.S., et al., *Ribavirin and interferon alfa-2a for severe Middle East respiratory syndrome coronavirus infection: a retrospective cohort study.* The Lancet Infectious Diseases, 2014. **14**(11): p. 1090-1095.
240. Arabi, Y.M., et al., *Ribavirin and Interferon Therapy for Critically Ill Patients With Middle East Respiratory Syndrome: A Multicenter Observational Study.* Clin Infect Dis, 2020. **70**(9): p. 1837-1844.
241. Arabi, Y.M., et al., *Corticosteroid Therapy for Critically Ill Patients with Middle East Respiratory Syndrome.* Am J Respir Crit Care Med, 2018. **197**(6): p. 757-767.
242. Sheahan, T.P., et al., *Comparative therapeutic efficacy of remdesivir and combination lopinavir, ritonavir, and interferon beta against MERS-CoV.* Nature Communications, 2020. **11**(1): p. 222.
243. Arabi, Y.M., et al., *Feasibility of Using Convalescent Plasma Immunotherapy for MERS-CoV Infection, Saudi Arabia.* Emerg Infect Dis, 2016. **22**(9): p. 1554-61.
244. Beigel, J.H., et al., *Safety and tolerability of a novel, polyclonal human anti-MERS coronavirus antibody produced from transchromosomic cattle: a phase 1 randomised, double-blind, single-dose-escalation study.* Lancet Infect Dis, 2018. **18**(4): p. 410-418.
245. de Wit, E., et al., *Prophylactic efficacy of a human monoclonal antibody against MERS-CoV in the common marmoset.* Antiviral Research, 2019. **163**: p. 70-74.
246. Ying, T., et al., *Exceptionally Potent Neutralization of Middle East Respiratory Syndrome Coronavirus by Human Monoclonal Antibodies.* Journal of Virology, 2014. **88**(14): p. 7796-7805.

247. Zhang, N., et al., *An overview of Middle East respiratory syndrome coronavirus vaccines in preclinical studies.* Expert Rev Vaccines, 2020. **19**(9): p. 817-829.
248. Du, L., et al., *MERS-CoV spike protein: a key target for antivirals.* Expert Opin Ther Targets, 2017. **21**(2): p. 131-143.
249. Cotten, M., et al., *Transmission and evolution of the Middle East respiratory syndrome coronavirus in Saudi Arabia: a descriptive genomic study.* Lancet, 2013. **382**(9909): p. 1993-2002.
250. Cotten, M., et al., *Spread, circulation, and evolution of the Middle East respiratory syndrome coronavirus.* mBio, 2014. **5**(1).
251. Lau, S.K., et al., *Polyphyletic origin of MERS coronaviruses and isolation of a novel clade A strain from dromedary camels in the United Arab Emirates.* Emerg Microbes Infect, 2016. **5**(12): p. e128.
252. Hassan, A.M., et al., *Ongoing Evolution of Middle East Respiratory Syndrome Coronavirus, Saudi Arabia, 2023-2024.* Emerg Infect Dis, 2025. **31**(1): p. 57-65.
253. Chu, D.K., et al., *MERS coronaviruses in dromedary camels, Egypt.* Emerg Infect Dis, 2014. **20**(6): p. 1049-53.
254. Chu, D.K.W., et al., *MERS coronaviruses from camels in Africa exhibit region-dependent genetic diversity.* Proc Natl Acad Sci U S A, 2018. **115**(12): p. 3144-3149.
255. Zhou, Z., et al., *Phenotypic and genetic characterization of MERS coronaviruses from Africa to understand their zoonotic potential.* Proceedings of the National Academy of Sciences, 2021. **118**(25): p. e2103984118.
256. Mok, C.K.P., et al., *T-cell responses to MERS coronavirus infection in people with occupational exposure to dromedary camels in Nigeria: an observational cohort study.* The Lancet Infectious Diseases, 2021. **21**(3): p. 385-395.
257. WHO, *Risk evaluation of circulating Middle East respiratory syndrome coronavirus (MERS CoV) clades and lineages* 2025.
258. Zhang, Z., L. Shen, and X. Gu, *Evolutionary Dynamics of MERS-CoV: Potential Recombination, Positive Selection and Transmission.* Scientific Reports, 2016. **6**(1): p. 25049.
259. So Ray, T.Y., et al., *Amino acid substitution L232F in non-structural protein 6 identified as a possible human-adaptive mutation in clade B MERS coronaviruses.* Journal of Virology, 2023. **97**(12): p. e01369-23.
260. Drosten, C., et al., *An Observational, Laboratory-Based Study of Outbreaks of Middle East Respiratory Syndrome Coronavirus in Jeddah and Riyadh, Kingdom of Saudi Arabia, 2014.* Clinical Infectious Diseases, 2014. **60**(3): p. 369-377.
261. Kim, Y., et al., *Spread of Mutant Middle East Respiratory Syndrome Coronavirus with Reduced Affinity to Human CD26 during the South Korean Outbreak.* mBio, 2016. **7**(2): p. 10.1128/mbio.00019-16.
262. Kleine-Weber, H., et al., *Mutations in the Spike Protein of Middle East Respiratory Syndrome Coronavirus Transmitted in Korea Increase Resistance to Antibody-Mediated Neutralization.* J Virol, 2019. **93**(2).
263. Schroeder, S., et al., *Functional comparison of MERS-coronavirus lineages reveals increased replicative fitness of the recombinant lineage 5.* Nat Commun, 2021. **12**(1): p. 5324.
264. Meyerholz, D.K., A.M. Lambertz, and P.B. McCray, Jr., *Dipeptidyl Peptidase 4 Distribution in the Human Respiratory Tract: Implications for the Middle East Respiratory Syndrome.* The American Journal of Pathology, 2016. **186**(1): p. 78-86.
265. Chan, J.F., et al., *Differential cell line susceptibility to the emerging novel human betacoronavirus 2c EMC/2012: implications for disease pathogenesis and clinical manifestation.* J Infect Dis, 2013. **207**(11): p. 1743-52.
266. Yang, Y., et al., *The structural and accessory proteins M, ORF 4a, ORF 4b, and ORF 5 of Middle East respiratory syndrome coronavirus (MERS-CoV) are potent interferon antagonists.* Protein Cell, 2013. **4**(12): p. 951-61.

267. Munasinghe, T.S., et al., *MERS-CoV ORF4b employs an unusual binding mechanism to target IMPα and block innate immunity.* Nature Communications, 2022. **13**(1): p. 1604.
268. Wong, L.R., et al., *Middle East Respiratory Syndrome Coronavirus ORF8b Accessory Protein Suppresses Type I IFN Expression by Impeding HSP70-Dependent Activation of IRF3 Kinase IKKε.* J Immunol, 2020. **205**(6): p. 1564-1579.
269. Menachery, V.D., et al., *MERS-CoV Accessory ORFs Play Key Role for Infection and Pathogenesis.* mBio, 2017. **8**(4).
270. Bello-Perez, M., et al., *MERS-CoV ORF4b is a virulence factor involved in the inflammatory pathology induced in the lungs of mice.* PLoS Pathog, 2022. **18**(9): p. e1010834.
271. Guery, B., et al., *Clinical features and viral diagnosis of two cases of infection with Middle East Respiratory Syndrome coronavirus: a report of nosocomial transmission.* Lancet, 2013. **381**(9885): p. 2265-72.
272. Faure, E., et al., *Distinct immune response in two MERS-CoV-infected patients: can we go from bench to bedside?* PLoS One, 2014. **9**(2): p. e88716.
273. Memish, Z.A., et al., *Middle East respiratory syndrome.* Lancet, 2020. **395**(10229): p. 1063-1077.
274. Zhou, J., et al., *Active replication of Middle East respiratory syndrome coronavirus and aberrant induction of inflammatory cytokines and chemokines in human macrophages: implications for pathogenesis.* J Infect Dis, 2014. **209**(9): p. 1331-42.
275. Chu, H., et al., *Productive replication of Middle East respiratory syndrome coronavirus in monocyte-derived dendritic cells modulates innate immune response.* Virology, 2014. **454-455**: p. 197-205.
276. Tynell, J., et al., *Middle East respiratory syndrome coronavirus shows poor replication but significant induction of antiviral responses in human monocyte-derived macrophages and dendritic cells.* J Gen Virol, 2016. **97**(2): p. 344-355.
277. Zielecki, F., et al., *Human cell tropism and innate immune system interactions of human respiratory coronavirus EMC compared to those of severe acute respiratory syndrome coronavirus.* J Virol, 2013. **87**(9): p. 5300-4.
278. Cockrell, A.S., et al., *A mouse model for MERS coronavirus-induced acute respiratory distress syndrome.* Nat Microbiol, 2016. **2**(2): p. 16226.
279. Jiang, Y., et al., *Complement Receptor C5aR1 Inhibition Reduces Pyroptosis in hDPP4-Transgenic Mice Infected with MERS-CoV.* 2019. **11**(1): p. 39.
280. Jiang, Y., et al., *Blockade of the C5a–C5aR axis alleviates lung damage in hDPP4-transgenic mice infected with MERS-CoV.* Emerging Microbes & Infections, 2018. **7**(1): p. 1-12.
281. Hamed, M.E., et al., *Elevated Expression Levels of Lung Complement Anaphylatoxin, Neutrophil Chemoattractant Chemokine IL-8, and RANTES in MERS-CoV-Infected Patients: Predictive Biomarkers for Disease Severity and Mortality.* J Clin Immunol, 2021. **41**(7): p. 1607-1620.
282. Chu, H., et al., *Middle East Respiratory Syndrome Coronavirus Efficiently Infects Human Primary T Lymphocytes and Activates the Extrinsic and Intrinsic Apoptosis Pathways.* J Infect Dis, 2016. **213**(6): p. 904-14.
283. Shin, H.S., et al., *Immune Responses to Middle East Respiratory Syndrome Coronavirus During the Acute and Convalescent Phases of Human Infection.* Clin Infect Dis, 2019. **68**(6): p. 984-992.
284. Corman, V.M., et al., *Viral Shedding and Antibody Response in 37 Patients With Middle East Respiratory Syndrome Coronavirus Infection.* Clin Infect Dis, 2016. **62**(4): p. 477-483.
285. Arabi, Y.M., et al., *Kinetics of antibody response in critically ill patients with Middle East respiratory syndrome and association with mortality and viral clearance.* Sci Rep, 2021. **11**(1): p. 22548.
286. Ko, J.H., et al., *Serologic responses of 42 MERS-coronavirus-infected patients according to the disease severity.* Diagn Microbiol Infect Dis, 2017. **89**(2): p. 106-111.

287. Zhao, J., et al., *Recovery from the Middle East respiratory syndrome is associated with antibody and T-cell responses.* Sci Immunol, 2017. **2**(14).
288. Zhao, J., et al., *Passive immunotherapy with dromedary immune serum in an experimental animal model for Middle East respiratory syndrome coronavirus infection.* J Virol, 2015. **89**(11): p. 6117-20.
289. Coleman, C.M., et al., *CD8+ T Cells and Macrophages Regulate Pathogenesis in a Mouse Model of Middle East Respiratory Syndrome.* J Virol, 2017. **91**(1).
290. Kim, M.H., H.J. Kim, and J. Chang, *Superior immune responses induced by intranasal immunization with recombinant adenovirus-based vaccine expressing full-length Spike protein of Middle East respiratory syndrome coronavirus.* PLoS One, 2019. **14**(7): p. e0220196.
291. Bosaeed, M., et al., *Safety and immunogenicity of ChAdOx1 MERS vaccine candidate in healthy Middle Eastern adults (MERS002): an open-label, non-randomised, dose-escalation, phase 1b trial.* Lancet Microbe, 2022. **3**(1): p. e11-e20.
292. Folegatti, P.M., et al., *Safety and immunogenicity of a candidate Middle East respiratory syndrome coronavirus viral-vectored vaccine: a dose-escalation, open-label, non-randomised, uncontrolled, phase 1 trial.* Lancet Infect Dis, 2020. **20**(7): p. 816-826.
293. Fathi, A., et al., *Increased neutralization and IgG epitope identification after MVA-MERS-S booster vaccination against Middle East respiratory syndrome.* Nature Communications, 2022. **13**(1): p. 4182.
294. Koch, T., et al., *Safety and immunogenicity of a modified vaccinia virus Ankara vector vaccine candidate for Middle East respiratory syndrome: an open-label, phase 1 trial.* The Lancet Infectious Diseases, 2020. **20**(7): p. 827-838.
295. Raadsen, M.P., et al., *Safety, immunogenicity, and optimal dosing of a modified vaccinia Ankara-based vaccine against MERS-CoV in healthy adults: a phase 1b, double-blind, randomised placebo-controlled clinical trial.* The Lancet Infectious Diseases.
296. Liu, R., et al., *A recombinant VSV-vectored MERS-CoV vaccine induces neutralizing antibody and T cell responses in rhesus monkeys after single dose immunization.* Antiviral Res, 2018. **150**: p. 30-38.
297. Modjarrad, K., et al., *Safety and immunogenicity of an anti-Middle East respiratory syndrome coronavirus DNA vaccine: a phase 1, open-label, single-arm, dose-escalation trial.* The Lancet Infectious Diseases, 2019. **19**(9): p. 1013-1022.
298. Tai, W., et al., *MERS-CoV RBD-mRNA vaccine induces potent and broadly neutralizing antibodies with protection against MERS-CoV infection.* Virus Res, 2023. **334**: p. 199156.
299. O'Donnell, J.S., et al., *Characterization and comparison of novel adjuvants for a prefusion clamped MERS vaccine.* 2022. **Volume 13 - 2022**.
300. Chao, C.W., et al., *Protein nanoparticle vaccines induce potent neutralizing antibody responses against MERS-CoV.* Cell Reports, 2024. **43**(12).
301. Pallesen, J., et al., *Immunogenicity and structures of a rationally designed prefusion MERS-CoV spike antigen.* Proc Natl Acad Sci U S A, 2017. **114**(35): p. E7348-e7357.
302. Gutiérrez-Álvarez, J., et al., *Genetically Engineered Live-Attenuated Middle East Respiratory Syndrome Coronavirus Viruses Confer Full Protection against Lethal Infection.* mBio, 2021. **12**(2).
303. Agrawal, A.S., et al., *Immunization with inactivated Middle East Respiratory Syndrome coronavirus vaccine leads to lung immunopathology on challenge with live virus.* Hum Vaccin Immunother, 2016. **12**(9): p. 2351-6.
304. WHO. *WHO Target Product Profiles for MERS-CoV Vaccines*. 2017 [cited 2025; Available from: https://www.who.int/publications/m/item/who-target-product-profiles-for-mers-cov-vaccines.

305. Agnes, J.T., et al., *Safety, tolerability, and immunogenicity of a DNA-based vaccine (INO-4700) against Middle East respiratory syndrome coronavirus: phase 2a study in healthy volunteers.* 2025. **Volume 16 - 2025**.
306. INOVIO, *INOVIO Provides an Update on Lassa Fever and MERS Programs*. 2022.
307. Alharbi, N.K., et al., *ChAdOx1 and MVA based vaccine candidates against MERS-CoV elicit neutralising antibodies and cellular immune responses in mice.* Vaccine, 2017. **35**(30): p. 3780-3788.
308. van Doremalen, N. and V.J. Munster, *Animal models of Middle East respiratory syndrome coronavirus infection.* Antiviral Res, 2015. **122**: p. 28-38.
309. Agrawal, A.S., et al., *Generation of a transgenic mouse model of Middle East respiratory syndrome coronavirus infection and disease.* J Virol, 2015. **89**(7): p. 3659-70.
310. Falzarano, D., et al., *Infection with MERS-CoV causes lethal pneumonia in the common marmoset.* PLoS Pathog, 2014. **10**(8): p. e1004250.
311. Yao, Y., et al., *An animal model of MERS produced by infection of rhesus macaques with MERS coronavirus.* J Infect Dis, 2014. **209**(2): p. 236-42.
312. Munster, V.J., E. de Wit, and H. Feldmann, *Pneumonia from human coronavirus in a macaque model.* N Engl J Med, 2013. **368**(16): p. 1560-2.
313. de Wit, E., et al., *Middle East respiratory syndrome coronavirus (MERS-CoV) causes transient lower respiratory tract infection in rhesus macaques.* Proc Natl Acad Sci U S A, 2013. **110**(41): p. 16598-603.
314. Munster, V.J., et al., *Protective efficacy of a novel simian adenovirus vaccine against lethal MERS-CoV challenge in a transgenic human DPP4 mouse model.* npj Vaccines, 2017. **2**(1): p. 28.
315. van Doremalen, N., et al., *A single dose of ChAdOx1 MERS provides protective immunity in rhesus macaques.* Sci Adv, 2020. **6**(24): p. eaba8399.
316. Song, F., et al., *Middle East Respiratory Syndrome Coronavirus Spike Protein Delivered by Modified Vaccinia Virus Ankara Efficiently Induces Virus-Neutralizing Antibodies.* Journal of Virology, 2013. **87**(21): p. 11950-11954.
317. Volz, A., et al., *Protective Efficacy of Recombinant Modified Vaccinia Virus Ankara Delivering Middle East Respiratory Syndrome Coronavirus Spike Glycoprotein.* J Virol, 2015. **89**(16): p. 8651-6.
318. Haagmans, B.L., et al., *An orthopoxvirus-based vaccine reduces virus excretion after MERS-CoV infection in dromedary camels.* 2016. **351**(6268): p. 77-81.
319. Mayer, L., et al., *Two-year persistence of MERS-CoV-specific antibody and T cell responses after MVA-MERS-S vaccination in healthy adults.* Nature Communications, 2026. **17**(1): p. 480.
320. Oxford, U.o. *Oxford and Liverpool scientists launch new vaccine trial for Middle East Respiratory Syndrome (MERS)*. 2023 July 8, 2024]; Available from: https://www.ox.ac.uk/news/2023-09-18-oxford-and-liverpool-scientists-launch-new-vaccine-trial-middle-east-respiratory.
321. Giada Mattiuzzo, E.B., Sang Hwan Seo, Nam Hyuk Cho, Jae-Ouk Kim, Samuel , et al., *Establishment of 1st WHO International Standard for anti-MERS-CoV antibody* 2020.
322. Harvey, R., et al., *Comparison of Serologic Assays for Middle East Respiratory Syndrome Coronavirus.* Emerg Infect Dis, 2019. **25**(10): p. 1878-1883.
323. Alosaimi, B., et al., *A 10 Year Long-Lived Cellular and Humoral MERS-CoV Immunity Cross-Recognizing the Wild-Type and Variants of SARS-CoV-2: A Potential One-Way MERS-CoV Cross-Protection Toward a Pan-Coronavirus Vaccine.* J Med Virol, 2025. **97**(1): p. e70071.
324. Angyal, A., et al., *T-cell and antibody responses to first BNT162b2 vaccine dose in previously infected and SARS-CoV-2-naive UK health-care workers: a multicentre prospective cohort study.* The Lancet Microbe, 2022. **3**(1): p. e21-e31.

325. Dichtelmüller, H.O., et al., *Robustness of solvent/detergent treatment of plasma derivatives: a data collection from Plasma Protein Therapeutics Association member companies.* Transfusion, 2009. **49**(9): p. 1931-43.
326. Hall, V.J., et al., *SARS-CoV-2 infection rates of antibody-positive compared with antibody-negative health-care workers in England: a large, multicentre, prospective cohort study (SIREN).* The Lancet, 2021. **397**(10283): p. 1459-1469.
327. Young, A., et al., *A platform technology for generating subunit vaccines against diverse viral pathogens.* 2022. **Volume 13 - 2022**.
328. Demaison, C., et al., *High-level transduction and gene expression in hematopoietic repopulating cells using a human immunodeficiency [correction of imunodeficiency] virus type 1-based lentiviral vector containing an internal spleen focus forming virus promoter.* Hum Gene Ther, 2002. **13**(7): p. 803-13.
329. Ferrara, F. and N. Temperton, *Pseudotype Neutralization Assays: From Laboratory Bench to Data Analysis.* Methods Protoc, 2018. **1**(1).
330. Napolitani, G., et al., *Clonal analysis of Salmonella-specific effector T cells reveals serovar-specific and cross-reactive T cell responses.* Nature Immunology, 2018. **19**(7): p. 742-754.
331. Oguti, B., et al., *The half-life of maternal transplacental antibodies against diphtheria, tetanus, and pertussis in infants: an individual participant data meta-analysis.* Vaccine, 2022. **40**(3): p. 450-458.
332. Lee, W.S., et al., *Decay of Fc-dependent antibody functions after mild to moderate COVID-19.* Cell Rep Med, 2021. **2**(6): p. 100296.
333. WHO. *MERS, Cases*. 2025; Available from: https://data.who.int/dashboards/mers/cases.
334. WHO, *R&D Blueprint.*
335. WHO, *Interim recommendations for use of the ChAdOx1-S*

[recombinant] vaccine against COVID-19

(AstraZeneca COVID-19 vaccine AZD1222, SII Covishield,

SK Bioscience). 2021.
336. Lu, L., et al., *A comparison of mortality-related risk factors of COVID-19, SARS, and MERS: A systematic review and meta-analysis.* Journal of Infection, 2020. **81**(4): p. e18-e25.
337. Rezelj, V.V., et al., *Safety and Humoral Immunogenicity of Different Dose Levels of Ad26.COV2.S as a 2-Dose Regimen in COVID-19 Vaccine-Naïve Healthy Adults: A Phase 3 Randomized Clinical Trial.* Vaccines (Basel), 2024. **12**(10).
338. Anderson, E.J., et al., *Safety and Immunogenicity of SARS-CoV-2 mRNA-1273 Vaccine in Older Adults.* N Engl J Med, 2020. **383**(25): p. 2427-2438.
339. Kaplonek, P., et al., *ChAdOx1 nCoV-19 (AZD1222) vaccine-induced Fc receptor binding tracks with differential susceptibility to COVID-19.* Nat Immunol, 2023. **24**(7): p. 1161-1172.
340. Atyeo, C., et al., *Distinct Early Serological Signatures Track with SARS-CoV-2 Survival.* Immunity, 2020. **53**(3): p. 524-532.e4.
341. Choi, J.H., et al., *Characterization of a human monoclonal antibody generated from a B-cell specific for a prefusion-stabilized spike protein of Middle East respiratory syndrome coronavirus.* PLoS One, 2020. **15**(5): p. e0232757.
342. Weskamm, L.M., et al., *Persistence of MERS-CoV-spike-specific B cells and antibodies after late third immunization with the MVA-MERS-S vaccine.* Cell Rep Med, 2022. **3**(7): p. 100685.
343. Houser, K.V., et al., *Enhanced inflammation in New Zealand white rabbits when MERS-CoV reinfection occurs in the absence of neutralizing antibody.* PLoS Pathog, 2017. **13**(8): p. e1006565.
344. Harrer, C.E., et al., *Identification of a Spike-Specific CD8+ T-Cell Epitope Following Vaccination Against the Middle East Respiratory Syndrome Coronavirus in Humans.* J Infect Dis, 2024. **230**(2): p. e327-e332.

345. Ewer, K.J., et al., *T cell and antibody responses induced by a single dose of ChAdOx1 nCoV-19 (AZD1222) vaccine in a phase 1/2 clinical trial.* Nat Med, 2021. **27**(2): p. 270-278.
346. Hodgson, S.H., et al., *Combining viral vectored and protein-in-adjuvant vaccines against the blood-stage malaria antigen AMA1: report on a phase 1a clinical trial.* Mol Ther, 2014. **22**(12): p. 2142-2154.
347. Dionne, K., et al., *Impact of Vaccine-Elicited Anti-Spike IgG4 Antibodies on Fc-Effector Functions Against SARS-CoV-2.* 2025. **17**(5): p. 666.
348. Vidarsson, G., G. Dekkers, and T. Rispens, *IgG Subclasses and Allotypes: From Structure to Effector Functions.* Frontiers in Immunology, 2014. **5**(520).
349. Andersson, B., *Studies on the regulation of avidity at the level of the single antibody-forming cell. The effect of antigen dose and time after immunization.* J Exp Med, 1970. **132**(1): p. 77-88.
350. Garg, A.K., et al., *Increased B Cell Selection Stringency In Germinal Centers Can Explain Improved COVID-19 Vaccine Efficacies With Low Dose Prime or Delayed Boost.* Front Immunol, 2021. **12**: p. 776933.
351. WHO. *AstraZeneca ChAdOx1-S/nCoV-19 [recombinant], COVID-19 vaccine*. 20 Dec 2021]; Available from: https://www.who.int/publications/m/item/chadox1-s-recombinant-covid-19-vaccine.
352. Leong, D.P., et al., *Comparison of three dosing intervals for the primary vaccination of the SARS-CoV-2 mRNA Vaccine (BNT162b2) on magnitude, neutralization capacity and durability of the humoral immune response in health care workers: A prospective cohort study.* PLoS One, 2023. **18**(2): p. e0281673.
353. Shaw, R.H., et al., *Effect of priming interval on reactogenicity, peak immunological response, and waning after homologous and heterologous COVID-19 vaccine schedules: exploratory analyses of Com-COV, a randomised control trial.* The Lancet Respiratory Medicine, 2022. **10**(11): p. 1049-1060.
354. Nicolas, A., et al., *An extended SARS-CoV-2 mRNA vaccine prime-boost interval enhances B cell immunity with limited impact on T cells.* iScience, 2023. **26**(1).
355. Rodrigues, C.M.C. and S.A. Plotkin, *The influence of interval between doses on response to vaccines.* Vaccine, 2021. **39**(49): p. 7123-7127.
356. Voysey, M., et al., *Single-dose administration and the influence of the timing of the booster dose on immunogenicity and efficacy of ChAdOx1 nCoV-19 (AZD1222) vaccine: a pooled analysis of four randomised trials.* The Lancet, 2021. **397**(10277): p. 881-891.
357. Pettini, E., et al., *Short or Long Interval between Priming and Boosting: Does It Impact on the Vaccine Immunogenicity?* Vaccines (Basel), 2021. **9**(3).
358. Ahmed, J.I., et al., *Improved antibody breadth with an extended primary dose interval of COVID-19 vaccine is overcome by boosters.* 2025. **Volume 16 - 2025**.
359. Koutsakos, M. and A.H. Ellebedy, *Immunological imprinting: Understanding COVID-19.* Immunity, 2023. **56**(5): p. 909-913.
360. Simpson, A.P., et al., *FcγRIIB (CD32B) antibodies enhance immune responses through activating FcγRs.* Clin Exp Immunol, 2025. **219**(1).
361. Wilson, R., et al., *Global Epidemiology and Seasonality of Human Seasonal Coronaviruses: A Systematic Review.* Open Forum Infectious Diseases, 2024. **11**(8): p. ofae418.
362. Al-Romaihi, H.E., et al., *Molecular epidemiology of influenza, RSV, and other respiratory infections among children in Qatar: A six years report (2012–2017).* International Journal of Infectious Diseases, 2020. **95**: p. 133-141.
363. Martin, C.A., et al., *Ethnic differences in cellular and humoral immune responses to SARS-CoV-2 vaccination in UK healthcare workers: a cross-sectional analysis.* eClinicalMedicine, 2023. **58**.

364. Miura, K., et al., *Development and characterization of a standardized ELISA including a reference serum on each plate to detect antibodies induced by experimental malaria vaccines.* Vaccine, 2008. **26**(2): p. 193-200.
365. Lambrou, A.S., et al., *Update on the Epidemiology of Middle East Respiratory Syndrome Coronavirus - Worldwide, 2017-2023.* MMWR Morb Mortal Wkly Rep, 2025. **74**(19): p. 313-320.
366. WHO, *Middle East respiratory syndrome: global summary*

and assessment of risk 2022.
367. Sun, S., et al., *Anti-S2 antibodies responsible for the SARS-CoV-2 infection-induced serological cross-reactivity against MERS-CoV and MERS-related coronaviruses.* Front Immunol, 2025. **16**: p. 1541269.
368. Hicks, J., et al., *Serologic Cross-Reactivity of SARS-CoV-2 with Endemic and Seasonal Betacoronaviruses.* J Clin Immunol, 2021. **41**(5): p. 906-913.
369. Wang, Q., et al., *Deep immunological imprinting due to the ancestral spike in the current bivalent COVID-19 vaccine.* Cell Reports Medicine, 2023. **4**(11): p. 101258.
370. Pušnik, J., et al., *Vaccination impairs de novo immune response to omicron breakthrough infection, a precondition for the original antigenic sin.* Nature Communications, 2024. **15**(1): p. 3102.
371. WHO. *Statement-on-the-antigen-composition-of-covid-19-vaccines*. 2023 July 8, 2024]; Available from: https://www.who.int/news/item/18-05-2023-statement-on-the-antigen-composition-of-covid-19-vaccines.
372. Kopsidas, I., et al., *Global Distribution, Dispersal Patterns, and Trend of Several Omicron Subvariants of SARS-CoV-2 across the Globe.* 2022. **7**(11): p. 373.
373. Whitaker, M., et al., *Variant-specific symptoms of COVID-19 in a study of 1,542,510 adults in England.* Nature Communications, 2022. **13**(1): p. 6856.
374. Bouna, A., et al., *Next generation sequencing shows diversity of Omicron sub-lineages of SARS-COV2 circulating in Jeddah, Saudi Arabia.* Journal of King Saud University - Science, 2024. **36**(2): p. 103081.
375. Obeid, D., et al., *SARS-CoV-2 chronological genomic evolution and epidemiology in the Middle East and North Africa (MENA) region as affected by vaccination, conflict and socioeconomical disparities: a population-based cohort study.* BMJ Open, 2022. **12**(9): p. e060775.
376. Noble, C.C.A., et al., *Characterising the SARS-CoV-2 nucleocapsid (N) protein antibody response.* Journal of Infection, 2025. **90**(3): p. 106436.
377. Edridge, A.W.D., et al., *Seasonal coronavirus protective immunity is short-lasting.* Nature Medicine, 2020. **26**(11): p. 1691-1693.
378. Alhabbab, R.Y., et al., *Middle East Respiratory Syndrome Coronavirus Infection Elicits Long-lasting Specific Antibody, T and B Cell Immune Responses in Recovered Individuals.* Clin Infect Dis, 2023. **76**(3): p. e308-e318.
379. Kim, S.H., et al., *Rise in broadly cross-reactive adaptive immunity against human β-coronaviruses in MERS-recovered patients during the COVID-19 pandemic.* Sci Adv, 2024. **10**(9): p. eadk6425.
380. Kim, Y.-S., et al., *Sustained Responses of Neutralizing Antibodies Against Middle East Respiratory Syndrome Coronavirus (MERS-CoV) in Recovered Patients and Their Therapeutic Applicability.* Clinical Infectious Diseases, 2020. **73**(3): p. e550-e558.
381. Moore, S.C., et al., *Evolution of long-term vaccine-induced and hybrid immunity in healthcare workers after different COVID-19 vaccine regimens.* Med, 2023. **4**(3): p. 191-215.e9.
382. He, X., et al., *Heterogeneous hybrid immunity against Omicron variant JN.1 at 11 months following breakthrough infection.* Signal Transduction and Targeted Therapy, 2024. **9**(1): p. 180.

383. Kaplonek, P., et al., *Hybrid immunity expands the functional humoral footprint of both mRNA and vector-based SARS-CoV-2 vaccines.* Cell Rep Med, 2023. **4**(5): p. 101048.
384. WHO, *Disease Outbreak News_Middle East respiratory syndrome coronavirus - Kingdom of Saudi Arabia.* 2025.
385. Singh, G., et al., *The post-COVID-19 population has a high prevalence of cross-reactive antibodies to spikes from all Orthocoronavirinae genera.* mBio, 2023. **15**(1): p. e02250-23.
386. Grobben, M., et al., *Cross-reactive antibodies after SARS-CoV-2 infection and vaccination.* eLife, 2021. **10**: p. e70330.
387. Duan, L.-J., et al., *SARS-CoV-2 vaccine-induced antibody and T cell response in SARS-CoV-1 survivors.* Cell Reports, 2022. **40**(9).
388. Zedan, H.T., et al., *Assessment of Broadly Reactive Responses in Patients With MERS-CoV Infection and SARS-CoV-2 Vaccination.* JAMA Netw Open, 2023. **6**(6): p. e2319222.
389. Pereira Neto, T.A., et al., *Highly conserved Betacoronavirus sequences are broadly recognized by human T cells.* Cell, 2025. **188**(20): p. 5653-5665.e12.
390. Braun, J., et al., *SARS-CoV-2-reactive T cells in healthy donors and patients with COVID-19.* Nature, 2020. **587**(7833): p. 270-274.
391. Chen, L., et al., *Impact of Immunosenescence on Vaccine Immune Responses and Countermeasures.* 2024. **12**(11): p. 1289.
392. Wang, J., et al., *The Impact of Age Difference on the Efficacy and Safety of COVID-19 Vaccines: A Systematic Review and Meta-Analysis.* Front Immunol, 2021. **12**: p. 758294.
393. Bliss, C.M., et al., *Assessment of novel vaccination regimens using viral vectored liver stage malaria vaccines encoding ME-TRAP.* Scientific Reports, 2018. **8**(1): p. 3390.
394. Davis, C., et al., *Effect of Prior ChAdOx1 COVID-19 Immunisation on T-Cell Responses to ChAdOx1-HBV.* Vaccines (Basel), 2024. **12**(6).
395. CEPI. *MERS*. 2024 October 2024]; Available from: https://cepi.net/MERS.
396. Reyes-Sandoval, A., et al., *Mixed Vector Immunization With Recombinant Adenovirus and MVA Can Improve Vaccine Efficacy While Decreasing Antivector Immunity.* Molecular Therapy, 2012. **20**(8): p. 1633-1647.
397. Reyes-Sandoval, A., et al., *Prime-boost immunization with adenoviral and modified vaccinia virus Ankara vectors enhances the durability and polyfunctionality of protective malaria CD8+ T-cell responses.* Infect Immun, 2010. **78**(1): p. 145-53.
398. Alharbi, N.K., et al., *Immunogenicity of High-Dose MVA-Based MERS Vaccine Candidate in Mice and Camels.* Vaccines (Basel), 2022. **10**(8).
399. Ba, L., et al., *Heterologous MVA-S prime Ad5-S boost regimen induces high and persistent levels of neutralizing antibody response against SARS coronavirus.* Appl Microbiol Biotechnol, 2007. **76**(5): p. 1131-6.
400. Reyes-Sandoval, A., et al., *CD8+ T effector memory cells protect against liver-stage malaria.* J Immunol, 2011. **187**(3): p. 1347-57.
401. Stylianou, E., et al., *Improvement of BCG protective efficacy with a novel chimpanzee adenovirus and a modified vaccinia Ankara virus both expressing Ag85A.* Vaccine, 2015. **33**(48): p. 6800-8.
402. Gilbert, S.C., et al., *Enhanced CD8 T cell immunogenicity and protective efficacy in a mouse malaria model using a recombinant adenoviral vaccine in heterologous prime-boost immunisation regimes.* Vaccine, 2002. **20**(7-8): p. 1039-45.
403. Dangi, T., et al., *Pre-existing immunity modulates responses to mRNA boosters.* Cell Rep, 2023. **42**(3): p. 112167.
404. Rodolfo, C., et al., *Design of Experiments to Achieve an Efficient Chitosan-Based DNA Vaccine Delivery System.* 2021. **13**(9): p. 1369.
405. Poncet, D., et al., *Preclinical optimization of an enterotoxigenic Escherichia coli adjuvanted subunit vaccine using response surface design of experiments.* NPJ Vaccines, 2020. **5**: p. 83.

406. Atkinson, A.C., *The Usefulness of Optimum Experimental Designs.* Journal of the Royal Statistical Society: Series B (Methodological), 1996. **58**(1): p. 59-76.
407. Lillie, P.J., et al., *Preliminary assessment of the efficacy of a T-cell-based influenza vaccine, MVA-NP+M1, in humans.* Clin Infect Dis, 2012. **55**(1): p. 19-25.
408. Gilbert, S.C., *Clinical development of Modified Vaccinia virus Ankara vaccines.* Vaccine, 2013. **31**(39): p. 4241-6.
409. Sheehy, S.H., et al., *Phase Ia clinical evaluation of the safety and immunogenicity of the Plasmodium falciparum blood-stage antigen AMA1 in ChAd63 and MVA vaccine vectors.* PLoS One, 2012. **7**(2): p. e31208.
410. Payne, R.P., et al., *Immunogenicity of standard and extended dosing intervals of BNT162b2 mRNA vaccine.* Cell, 2021. **184**(23): p. 5699-5714.e11.
411. Spencer, A.J., et al., *The ChAdOx1 vectored vaccine, AZD2816, induces strong immunogenicity against SARS-CoV-2 beta (B.1.351) and other variants of concern in preclinical studies.* eBioMedicine, 2022. **77**.
412. Silva-Cayetano, A., et al., *A booster dose enhances immunogenicity of the COVID-19 vaccine candidate ChAdOx1 nCoV-19 in aged mice.* Med, 2021. **2**(3): p. 243-262.e8.
413. Graham, S.P., et al., *Evaluation of the immunogenicity of prime-boost vaccination with the replication-deficient viral vectored COVID-19 vaccine candidate ChAdOx1 nCoV-19.* NPJ Vaccines, 2020. **5**(1): p. 69.
414. Andrade, C., *Z Scores, Standard Scores, and Composite Test Scores Explained.* Indian J Psychol Med, 2021. **43**(6): p. 555-557.
415. Vinhaes, C.L., et al., *An Inflammatory Composite Score Predicts Mycobacterial Immune Reconstitution Inflammatory Syndrome in People with Advanced HIV: A Prospective International Cohort Study.* J Infect Dis, 2021. **223**(7): p. 1275-1283.
416. Steyerberg, E.W., et al., *Assessing the performance of prediction models: a framework for traditional and novel measures.* Epidemiology, 2010. **21**(1): p. 128-38.
417. Pollard, A.J., et al., *Safety and immunogenicity of a two-dose heterologous Ad26.ZEBOV and MVA-BN-Filo Ebola vaccine regimen in adults in Europe (EBOVAC2): a randomised, observer-blind, participant-blind, placebo-controlled, phase 2 trial.* The Lancet Infectious Diseases, 2021. **21**(4): p. 493-506.
418. Anywaine, Z., et al., *Safety and Immunogenicity of a 2-Dose Heterologous Vaccination Regimen With Ad26.ZEBOV and MVA-BN-Filo Ebola Vaccines: 12-Month Data From a Phase 1 Randomized Clinical Trial in Uganda and Tanzania.* J Infect Dis, 2019. **220**(1): p. 46-56.
419. Goldstein, N., et al., *Safety and Immunogenicity of Heterologous and Homologous 2-Dose Regimens of Adenovirus Serotype 26- and Modified Vaccinia Ankara-Vectored Ebola Vaccines: A Randomized, Controlled Phase 1 Study.* J Infect Dis, 2022. **226**(4): p. 595-607.
420. Ewer, K., et al., *A Monovalent Chimpanzee Adenovirus Ebola Vaccine Boosted with MVA.* N Engl J Med, 2016. **374**(17): p. 1635-46.
421. Tas, J.M.J., et al., *Antibodies from primary humoral responses modulate the recruitment of naive B cells during secondary responses.* Immunity, 2022. **55**(10): p. 1856-1871.e6.
422. Roukens, A.H.E. and L.G. Visser, *Fractional-dose yellow fever vaccination: an expert review.* J Travel Med, 2019. **26**(6).
423. Kelton, J.G., D.M. Arnold, and I. Nazy, *Lessons from vaccine-induced immune thrombotic thrombocytopenia.* Nature Reviews Immunology, 2021. **21**(12): p. 753-755.
424. Choi, E.M., et al., *Immunogenicity of an Extended Dose Interval for the Ad26.ZEBOV, MVA-BN-Filo Ebola Vaccine Regimen in Adults and Children in the Democratic Republic of the Congo.* Vaccines (Basel), 2024. **12**(8).
425. Radbruch, A., et al., *Competence and competition: the challenge of becoming a long-lived plasma cell.* Nature Reviews Immunology, 2006. **6**(10): p. 741-750.
426. Fernandez-Arias, C., et al., *Modeling the effect of boost timing in murine irradiated sporozoite prime-boost vaccines.* PLoS One, 2018. **13**(1): p. e0190940.

427. CEPI, *2022-2026-Strategy*. 2022.
428. Barnsley, G., et al., *Impact of the 100 days mission for vaccines on COVID-19: a mathematical modelling study.* The Lancet Global Health, 2024. **12**(11): p. e1764-e1774.
429. WHO, *Middle East respiratory syndrome coronavirus - Kingdom of Saudi Arabia.* (May 2025).
430. Al-Tawfiq, J.A. and Z.A. Memish, *Middle East respiratory syndrome coronavirus in the last two years: Health care workers still at risk.* Am J Infect Control, 2019. **47**(10): p. 1167-1170.
431. Organization, W.H., *Research gaps and needs on Middle East respiratory syndrome coronavirus (MERS-CoV) and other emerging zoonotic coronaviruses*. 2025: Geneva, Switzerland.
432. Falzarano, D., et al., *Infection with MERS-CoV Causes Lethal Pneumonia in the Common Marmoset.* PLOS Pathogens, 2014. **10**(8): p. e1004250.
433. Arunachalam, P.S., et al., *T cell-inducing vaccine durably prevents mucosal SHIV infection even with lower neutralizing antibody titers.* Nat Med, 2020. **26**(6): p. 932-940.
434. Sampson, A.T., et al., *Developing the next-generation of adenoviral vector vaccines.* Human Vaccines & Immunotherapeutics, 2025. **21**(1): p. 2514356.
435. Selva, K.J., et al., *Preexisting immunity restricts mucosal antibody recognition of SARS-CoV-2 and Fc profiles during breakthrough infections.* JCI Insight, 2023. **8**(18).
436. The Lancet Infectious Diseases, E., *Thank you to The Lancet Infectious Diseases statistical and peer reviewers in 2024.* The Lancet Infectious Diseases, 2025. **25**(3): p. e114-e121.